

# **Synthesis and Photophysical Aspects of Fluorescent Biomolecular Probes for Serum Albumins Recognition**

**THESIS SUBMITTED FOR THE  
DEGREE OF DOCTOR OF PHILOSOPHY (SCIENCE)**

**OF**

**JADAVPUR UNIVERSITY**

**MARCH, 2023**



*By*

**MIHIR SASMAL**

**DEPARTMENT OF CHEMISTRY**

**JADAVPUR UNIVERSITY**

**JADAVPUR**

**KOLKATA-700032**

**INDIA**

**2023**

---

Prof. Mahammad Ali,  
Professor,  
Department of Chemistry



JADAVPUR UNIVERSITY  
KOLKATA - 7 0 0 0 3 2, I N D I A  
E-mail: m\_ali2062@yahoo.com  
Mobile: +91-9433249716

---

## CERTIFICATE FROM THE SUPERVISOR

This is to certify that the thesis entitled “ **Synthesis and Photophysical Aspects of Fluorescent Biomolecular Probes for Serum Albumins Recognition**” submitted by **Mr. Mihir Sasmal** who got his name registered on **23.06.2017** (**Index No: 50/17/Chem./25**) for the award of **Ph.D. (Science) degree of Jadavpur University**, is absolutely based upon his own work under my direct supervision and that neither this thesis nor any part of it has been submitted for either any degree / diploma or any other academic award anywhere before.

Date: 30/03/2023

*Mahammad Ali*

(Prof. Mahammad Ali)

Signature of the Supervisor & date with seal

Department of Chemistry  
Jadavpur University  
Kolkata 700 032

Dr. Mahammad Ali  
Professor  
Department of Chemistry  
Jadavpur University  
Kolkata-700 032





***DEDICATED TO MY  
BELOVED PARENTS***

*who made all of this possible, with your  
endless loves, supports, and  
prayers.*

# Acknowledgements

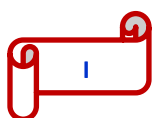
"Analytical Chemistry Building

1<sup>st</sup> floor, Mahammad Ali Research Lab"

The last six years were like a difficult and long test, which directed me to look over my scientific ability. While taking it, I struggled with myself not to give it up several times. This dissertation would not have been possible without the help of so many people in different way throughout my research carrier. Now I want to acknowledge those person who played a role directly or indirectly for the successful completion of my thesis.

First and foremost, I would like to thank my supervisor, Prof. Mahammad Ali, for taking me into his lab and assigning such a challenging project to me. I also like to express my sincere gratitude to him for the continuous support, encourage and to give me confidence for my research and Ph.D. study. I am grateful for the advice and the training that he provides for me to be prepared for anything in my future endeavors and I am greatly proud of being a member of his group. I could not have imagined having a better advisor and mentor for my Ph.D. study.

I would also like to thank the Inorganic Chemistry faculty members at Jadavpur University, specially, present Dean of Science Prof. Subenoy Chakraborty, present Head, Department of Chemistry, Prof. Subratanath Koner, and Prof. Saurabh Das, Sectional in-charge, Inorganic Chemistry for their kind cooperation and encouragement. I am also thankful to Prof. C. R. Sinha, Prof. S. Baitalik, Prof. J. P. Nasakar, Prof. S. Mukhopadhyay, Prof. P. Roy, Prof. T. K. Mandol, and Dr. B. B. Show, Department of Chemistry, Jadavpur University, for providing me their laboratory facilities whenever required. I also sincerely appreciate the constant encouragement of all the faculty members and non-

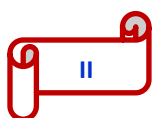


teaching staffs, especially Mr. Baidyanath Paul, Mr. Atikur Rahaman for their helpful attitude. I am also thankful to the authorities of the Jadavpur University for allowing me to use the necessary infrastructure.

I am also grateful to my M. Sc. project guide Prof. Sasankasekhar Mohanta, Department of Chemistry, Inorganic Chemistry Section, Calcutta University for giving me the important knowledge about research which became very helpful in this journey.

This journey would not have been possible without the support of my labmates: Dr. Malay Dolai, Dr. Luna Paul, Dr. Rabiul Alam, Dr. Rahul Bhowmick, Dr. Arindam Giri, Dr. Abu Saleh Musha Islam, Dr. Animesh Mondal, Dr. Ritwik Modak, Dr. Kajari Ghosh, Dr. Dipankar Das, Mr. Habib Ali Molla, Mr. Hasan Mohammad, Mrs. Kaberi Pal, Miss. Debjani Maiti, Miss. Ananya Dutta, Miss Rousunara Khatun, and Miss Dolan Moni. The important discussions with them, dinners, outings to the short trips, general help and friendship were all greatly appreciated. I will never forget the beautiful memories and the difficulty that we shared together.

It is a genuine pleasure to express my appreciation to my close friends for their support and encouragement during the last six years. I am indebted to my friends Prasanta, Dipayan, Subhro, Gurupada, Animesh and Kartic for helping me with data analysis of my research work. Last but not the least, I want to express my heartfelt thanks to some of my very close friends Chayan, Subhajit, Hiranmayee, Mousumi, Sibub, Abani, Avik, Apurba, Saumitra, Basudev, Suman, Santu, and Sandipan for providing me the company and support through every step of this journey. A special thanks are extended to one of my juniors, Rajarshi Panigrahi. They were always beside me during the happy and hard moments to push me and motivate me. Without their support this journey would not be smooth and pleasant.



Finally, No thanks can be enough to acknowledge the people who mean a lot to me, my parents, Ma and Baba, for showing faith in me and giving me liberty to choose what I wanted. I salute you all for the selfless love, care, pain and a lots of sacrifice you did to shape my life. They provide me always both the moral as well as emotional support in my life and prayers on my behalf. I would never be able to pay back the love and affection showered upon by my parents.

Also I want to express a heartfelt gratitude to my brothers, sisters, and sister-in-laws for their selfless love, care, support and valuable prayers which contributed a lot for completion of my thesis.

I would like to thank everybody who was important to the successful insight of the thesis, as well as expressing my apology that I could not mention personally one by one.

I am also thankful to UGC for awarding me JRF and SRF fellowship for the last five years to carry out my research work smoothly. I gratefully acknowledge DST, West Bengal and CSIR, New Delhi for the project funding.

Finally, I would like to thank the almighty for his blessing to journey of completion of my thesis.

Mihir Sasmal; 30/03/23

Department of Chemistry  
Jadavpur University  
Kolkata- 700 032, India.

Mihir Sasmal



## Preface

The work presented in this thesis entitled “**Synthesis and Photophysical Aspects of Fluorescent Biomolecular Probes for Serum Albumins Recognition**” was initiated in January, 2017 and have been carried out in the Department of Chemistry, Jadavpur University.

The thesis consists of six chapters which are summarized below.

**Chapter 1** contains a brief description of serum albumins (HSA/BSA) and describes various popular methods for serum albumin detection and estimation, along with a short review of previously reported HSA/BSA detection probes by fluorometric method. Additionally, a very brief overview of the present work is highlighted.

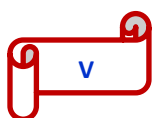
**Chapter 2** describes the synthesis and characterization of a TICT-based small fluorogenic molecular probe HJRA, which can easily *self-assemble* into nonfluorescent nanoaggregates in aqueous solution and undergoes a *disassembly* process towards the monomer formation upon binding with serum albumins (HSA/BSA). The selective trapping of the HJRA monomer in the subdomain IIA of site I in HSA resulted a rapid turn-on red fluorescent response due to suppression of the TICT action by restricting free intramolecular rotation. An analysis of the binding mechanism between HJRA and HSA implies that a combination of various noncovalent interactions encourages the disassembly process. HJRA has a detection limit of 1.13 nM (0.0751 mg/L), which is substantially below the normal HSA concentration in healthy urine signifying the high sensitivity of the probe. The comparable results and quick response toward the quantification of urinary HSA levels by HJRA method with respect to the Bradford method clearly points toward the superiority of this method compared to the existing ones and may lead to biomedical applications for HSA quantification in urine. Additionally, the probe is also least cytotoxic, cell permeable and suitable for imaging of endogenous and exogenous HSA in living cells.

**Chapter 3** deals with the synthesis and characterization of an ICT-based microenvironment sensitive fluorescent probe DCI-MIN, that can selectively interact with HSA in PBS buffer solution and exhibits a ~78-fold enhancement in fluorescence intensity with a significant (~126 nm) Stokes shift. The significant red fluorescence response can be attributed to the suppression of free intramolecular rotation of DCI-MIN probe in the site II hydrophobic

binding cavity of HSA. DCI-MIN displayed high binding affinity to HSA with a  $K_d$  value of  $(0.024 \pm 0.003) \mu\text{M}$ . The probe has a detection limit of 1.01 nM (0.0671 mg/L), which is significantly lower than the normal level of HSA in healthy urine, indicating its high sensitivity. DCI-MIN also shows the ability to perform a variety of useful applications, including the detection and quantification of HSA levels in complex biofluids (human urine and blood samples) as well as the imaging of serum albumin in living cells. As compared to the Bradford assay and the BCG technique, measuring HSA levels in urine and blood samples with DCI-MIN is preferable due to its higher selectivity, faster detection time, and simple operation.

**Chapter 4** describes the interaction of a NBD-embedded olanzapine derivative (OLA-NBD) with HSA protein. A gradual enhancement of the emission intensity of OLA-NBD along with the substantial blue shift of  $\lambda_{\text{em}}^{\text{max}}$  on interaction with HSA vividly indicates the immense modulation of the microenvironment around OLA-NBD within the protein hydrophobic medium compared with the polar aqueous medium. The fluorescence titration of HSA with OLA-NBD resulted in an association constant of  $(9.87 \pm 0.02) \times 10^4 \text{ M}^{-1}$ . The fluorescence quenching study persuaded by OLA-NBD indicates the presence of a static quenching mechanism. The negative value of  $\Delta H^0$  accompanied by a positive value of  $\Delta S^0$  infers the major contribution of electrostatic/ionic interaction for the HSA–OLA-NBD binding process. CD outcome illustrates the alteration of the secondary structure of HSA upon interaction with OLA-NBD. The site-specific binding experiment and molecular docking studies indicate that OLA-NBD binds with HSA in subdomain IIA at the binding site I, that is, close to the Trp 214.

**Chapter 5** deals with a phenanthrene-pyrene-based fluorescent probe (PPI) as a molecular reporter to study the micro heterogeneous environment of BSA protein. The observed blue shift of the emission maximum along with an increment of the fluorescence intensity is due to the movement of PPI from a more polar aqueous environment to a more hydrophobic protein environment. The fluorescence titration of BSA with PPI resulted in a binding constant of  $(1.12 \pm 0.06) \times 10^5 \text{ M}^{-1}$ . The study on fluorescence quenching induced by PPI reveals the occurrence of both static and dynamic quenching mechanisms. The negative  $\Delta H^0$  value accompanied by a negative  $\Delta S^0$  value implies the significant contributions of van der Waals interactions and hydrogen-bonding interactions in stabilizing the BSA-PPI complex. From the FRET study, the average distance between Trp 213 of the BSA donor and the PPI



acceptor is found to be 3.04 nm, and it is close enough for non-radiative energy transfer to occur from BSA to PPI. The CD spectral studies imply the PPI-induced conformational change of the native BSA in terms of decrease of the  $\alpha$ -helix content in BSA. The site-selective binding and molecular docking studies reveal that PPI binds with BSA at site I in subdomain IIA, that is, Trp 213 is near or within the binding site of PPI.

**Chapter 6** represents the highlights of the thesis.

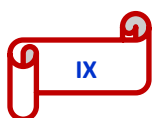
# List of Abbreviations

HSA	Human Serum Albumin
BSA	Bovine Serum Albumin
PDB	Protein Data Bank
ROS	Reactive Oxygen Species
RNS	Reactive Nitrogen Species
NO	Nitric Oxide
FDA	Food and Drug Administration
MO	Methyl Orange
HABA	2-(4'-Hydroxyazobenzene) Benzoic Acid
BCG	Bromocresol Green
BCP	Bromocresol Purple
CMPF	3-carboxy-4-methyl-5-propyl-2-furanpropanoic acid
BPB	Bromophenol Blue
AB	Albumin Blue
SDS	Sodium Dodecyl Sulfate
SPCE	Screen Printed Carbon Electrode
PVA	Polyvinyl Alcohol
RIA	Radioimmunoassay
ELISA	Enzyme-Linked Immunosorbent Assay
LC/MS	Liquid Chromatography/ Mass Spectrometry
ANS	8-Anilino-naphthalene-1-Sulfonic Acid
$\tau$	Fluorescence Lifetime
$\Delta\bar{\nu}$	Stokes Shift
$\Phi$	Quantum Yield
AIE	Aggregation Induced Emission
ACQ	Aggregation Caused Quenching
TICT	Twisted Intramolecular Charge Transfer
MALDI-TOF MS	Matrix Assisted Laser Desorption Ionization-Time of Flight Mass Spectrometry
PET	Photo-Induced Electron Transfer
ICT	Intramolecular Charge Transfer
FRET	Fluorescence Resonance Energy Transfer
ESIPT	Excited-State Intramolecular Proton Transfer
LD	Lipid Droplet
GFP	Green Fluorescent Protein
POC	Point of Care
DLS	Dynamic Light Scattering

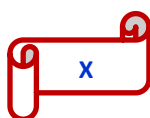


TCSPC	Time Correlated Single Photon Counting
HEPES	4-(2-Hydroxyethyl)piperazine-1-ethanesulfonic acid
TEM	Transmission Electron Microscopy
CD	Circular Dichroism
CT DNA	Calf Thymus Deoxyribonucleic Acid
RNA	Ribonucleic Acid
IgG	Immunoglobulin G
$\beta$ -CD	Beta Cyclodextrin
PNPA	<i>p</i> -Nitrophenyl Acetate
Trp	Tryptophan
Tyr	Tyrosine
Phe	Phenyl Alanine
NBD	4-Chloro-7-nitro-1,2,3-benzoxadiazole
POCl <sub>3</sub>	Phosphorus Oxychloride
MeCN	Acetonitrile
MeOH	Methanol
NaOH	Sodium Hydroxide
NaCl	Sodium Chloride
DCM	Dichloromethane
DMF/dmf	Dimethyl Formamide
H <sub>2</sub> O	Water
DMSO/dmsO	Dimethyl Sulfoxide
mL	Millilitre
$\mu$ M	Micro Molar
$\mu$ L	Micro Litre
nM	Nano Molar
mM	Mili Molar
K <sub>b</sub>	Binding Constant
K <sub>a</sub>	Association Constant
K <sub>d</sub>	Dissociation Constant
K <sub>f</sub>	Formation constant
K <sub>SV</sub>	Stern-Volmer Constant
K <sub>q</sub>	Bimolecular Quenching Rate Constant
$\eta$	Refractive Index
$\Delta H^0$	Standard Enthalpy Change
$\Delta S^0$	Standard Entropy Change
$\Delta G^0$	Standard Gibbs Free Energy Change
ex	Excitation
em	Emission
$\lambda$	Wavelength

HeLa	Human Epithelial Carcinoma Cell
HepG2	Human Hepatocellular Liver Carcinoma Cells
PBS	Phosphate-Buffered Saline
DMEM	Dulbecco's Modified Eagle's Medium
MTT	3-(4,5-di methylthiazol-2-yl)-2,5 diphenyltetrazolium bromide
%T	Percentage of Transmittance
FBS	Fetal Bovine Serum
DAPI	4',6-diamidino-2-phenylindole
LOD	Limit of Detection
MS	Mass Spectroscopy
NMR	Nuclear Magnetic Resonance
FT-IR	Fourier Transform Infrared
Na <sub>2</sub> SO <sub>4</sub>	Sodium Sulfate
TPE	Tetraphenylethylene
LGA	Lamarckian Genetic Algorithm
FI /F.I	Fluorescence Intensity
GSH	Glutathione
Cys	Cysteine
Raw 264.7	Abelson Leukemia Virus Transformed Cell
KB	Human Epithelial Carcinoma Cell
CHO	Chinese Hamster Ovary Cell
NIR	Near-Infrared
MCF7	Acronym of Michigan Cancer Foundation-7 Cell
FE	Fluorescence Enhancement
T	Temperature
s	Second
Tris-HCl	Tris (hydroxymethyl) aminomethane hydrochloride
UV	Ultraviolet
Vis	Visible
h	Hours
RRS	Resonance Rayleigh Scattering
TLC	Thin-Layer Chromatography
HPLC	High-Performance Liquid Chromatography
TMS	Tetramethylsilane
KBr	Potassium Bromide
K <sub>2</sub> CO <sub>3</sub>	Potassium Carbonate
ESI-MS <sup>+</sup>	Electrospray Ionization Mass Spectrometry
HRMS	High-Resolution Mass Spectrometry
CH <sub>2</sub> Cl <sub>2</sub> /DCM	dichloromethane



SOCl <sub>2</sub>	Thionyl Chloride
CDCl <sub>3</sub>	Chloroform-d
DMSO- <i>d</i> <sub>6</sub>	Deuterated Dimethyl sulfoxide
dL	Decilitre
ATP	Adenosine Triphosphate
mg	Milligram
kDa	Kilodalton
CD <sub>3</sub> OD	Methanol- <i>d</i> <sub>4</sub>
Et <sub>3</sub> N	Triethylamine
MHz	Megahertz
<i>f</i>	Oscillator Strength
°	Degree
Å	Angstrom
eV	Electron Volt



# Contents

Acknowledgements	I-III
Preface	IV-VI
List of Abbreviations	VII-X

Chapter 1		Page
<b>Introduction: A Literature Survey</b>		
1.1	Protein: An Overview	2
1.2	Motivation of the Work	3
1.3	Brief Description of Serum Albumins	4
1.3.1	Human Serum Albumin (HSA)	5
1.3.1.1	Structure of HSA	5
1.3.1.2	Synthesis and Metabolic Process of HSA	6
1.3.1.3	Drug Binding Sites of HSA	6
1.3.1.4	Physiological Function of HSA	9
1.3.2	Bovine Serum Albumin (BSA)	10
1.4	Popular Methods for Serum Albumins Detection and Estimation	11
1.4.1	Dye Binding Methods	11
1.4.1.1	Methyl Orange (MO)	12
1.4.1.2	HABA (2-(4'-Hydroxyazobenzene) Benzoic Acid)	13
1.4.1.3	Phenol Red	13
1.4.1.4	8-Anilinoanthralene-1-Sulfonic Acid (ANS)	13
1.4.1.5	Bromocresol Green (BCG)	13
1.4.1.6	Bromocresol Purple (BCP)	14
1.4.1.7	Bromophenol Blue (BPB)	14
1.4.1.8	Albumin Blue (AB) Dyes	15
1.4.1.9	Coomassie Brilliant Blue G-250	15
1.4.2	Electrochemical Methods	15
1.4.3	Immunochemical Methods	16
1.4.3.1	Radial Immunodiffusion	16
1.4.3.2	Radioimmunoassay (RIA)	17
1.4.3.3	Enzyme-Linked Immunosorbent Assay (ELISA)	17
1.4.3.4	Immunoturbidimetry	17
1.4.3.5	Immunonephelometry	18
1.4.4	Chromatography Based Methods	18
1.4.5	Electrophoresis Based Methods	18
1.4.6	Fluorometric Based Methods	19
1.5	Different Strategies for the Detection of Serum Albumins Based on Fluorescent Molecular probes	20
1.5.1	Microenvironment Sensitive Fluorescent Probes	20
1.5.1.1	Dicyanomethylene-4 <i>H</i> -Chromene Based Fluorescent Probes	22
1.5.1.2	Tricyano Dihydrofuran Based Fluorescent Probes	23
1.5.1.3	Dicyanoisophorone Based Fluorescent Probes	24
1.5.1.4	BODIPY Based Fluorescent Probes	26
1.5.1.5	Cyanine Based Fluorescent Probes	28
1.5.1.6	Anthracene Based Fluorescent Probes	31
1.5.1.7	Naphthalene Based Fluorescent Probes	32
1.5.1.8	Carbazole and Coumarin Based Fluorescent Probes	33

1.5.1.9 Pyridinium and Lepidinium Cation Based Fluorescent Probes	34
1.5.1.10 Dimethylaminobenzyl and Rhodanine Based Fluorescent Probes	35
1.5.1.11 Fluorescein Based Fluorescent Probes	38
1.5.1.12 Julolidine and Rosamine Based Fluorescent Probes	39
1.5.1.13 Schiff Base Based Fluorescent Probes	40
1.5.1.14 GFP Based Fluorescent Probes	41
1.5.1.15 Chalcone Based Fluorescent Probes	42
1.5.1.16 Flavonoid Based Fluorescent Probes	43
1.5.1.17 Squaraine Dye Based Fluorescent Probes	45
1.5.2 Aggregation induced emission (AIE) based fluorescent probes	46
1.5.3 Self-assembly/Disassembly Based Fluorescent Probes	52
1.5.4 Enzymatically reactive fluorescent probes	60
1.6 Self-designed Systems Studied in the Thesis	62
1.7 Physical measurements	63
References	65-84

## Chapter 2

Page

### Serum Albumin Inspired Self-Assembly/Disassembly of a Fluorogenic Nanoprobe for Real-Time Monitoring and Quantification of Urinary Albumin with Live Cell Imaging Application

Abstract	86
2.1 Introduction	87
2.2 Experimental Section	89
2.2.1 Materials	89
2.2.2 Instrumentation	90
2.2.3 Synthesis and Characterization of the Compound 1	91
2.2.4 Synthesis and Characterization of the Compound HJRA	93
2.2.5 Experimental Solution	95
2.2.6 UV-Vis and Fluorescence Spectroscopic Studies	95
2.2.7 Steady-State Fluorescence Anisotropy	96
2.2.8 Fluorescence Lifetime Studies	96
2.2.9 Fluorescence Quantum Yield Measurements	97
2.2.10 Detection Limit	97
2.2.11 Determination of Dissociation Constant ( $K_d$ ) for the HSA and HJRA Adduct	98
2.2.12 Dynamic Light Scattering Studies	98
2.2.13 Transmission Electron Microscopy (TEM) Analysis	99
2.2.14 Molecular Docking Study	99
2.2.15 Cell Cytotoxicity Assay	99
2.2.16 Cell Imaging Study	100
2.2.17 Urinary HSA Quantification by Coomassie Brilliant Blue G250	100
2.3 Results and Discussion	101
2.3.1 Rational Design and Synthesis of Probe HJRA	101
2.3.2 Photophysical Properties and Self-Assembly Behavior of HJRA	102
2.3.3 Selectivity Study and Optical Response of HJRA toward HSA/BSA	107
2.3.4 Site-Specific Binding Study and Probable HSA Sensing Mechanism	120
2.3.5 Molecular Docking	123

2.3.6 HSA Quantification in Human Urine Samples	124
2.3.7 Fluorescence Imaging of HSA in Living Cells	126
2.4 Conclusions	129
References	130-139

## Chapter 3

Page

### **A Microenvironment-Sensitive Red Emissive Probe with a Large Stokes Shift for the Specific Recognition and Quantification of Serum Albumin in Complex Biofluids and Live Cells**

Abstract	141
3.1 Introduction	142
3.2 Experimental Section	144
3.2.1 Materials	144
3.2.2 Instrumentation	145
3.2.3 Synthesis and Characterization of the Compound 5-methoxy-1 <i>H</i> -indole-3-carbaldehyde (MIN)	146
3.2.4 Synthesis and Characterization of the Compound DCI-MIN	149
3.2.5 Experimental Solution	151
3.2.6 UV-vis and Fluorescence Spectroscopic Studies	151
3.2.7 Steady-State Fluorescence Anisotropy	152
3.2.8 Fluorescence Lifetime Studies	152
3.2.9 Fluorescence Quantum Yield Measurements	153
3.2.10 Detection Limit	153
3.2.11 Determination of Dissociation Constant ( $K_d$ ) for the Interaction Between HSA and DCI-MIN	154
3.2.12 Molecular Docking Study	154
3.2.13 Cell Cytotoxicity Assay	155
3.2.14 Cell Imaging Study	155
3.2.15 Urinary HSA Quantification by Coomassie Brilliant Blue G250	156
3.2.16 Estimation of HSA in Human Blood Serum	156
3.3 Results and Discussion	157
3.3.1 Photophysical Properties of DCI-MIN	157
3.3.2 Selectivity Analysis and Optical Response of DCI-MIN for HSA/BSA	160
3.3.3 Site-Selective Binding Analysis and Possible HSA sensing Mechanism	170
3.3.4 Molecular Docking	174
3.3.5 HSA Estimation in Human Urine Samples	175
3.3.6 Quantitative Measurement of HSA in Human Serum Samples	176
3.3.7 Fluorescence Imaging of Serum Albumin in Living Cells	178
3.4 Conclusions	179
References	180-188

## Chapter 4

Page

### **Site-Selective Interaction of Human Serum Albumin with 4-Chloro-7-nitro-1,2,3-benzoxadiazole Modified Olanzapine Derivative and Effect of $\beta$ -Cyclodextrin on Binding: In the Light of Spectroscopy and Molecular Docking**

Abstract	190
4.1 Introduction	191
4.2 Experimental Section	192

4.2.1	Materials	192
4.2.2	Instrumentation	193
4.2.3	Synthesis and Characterization of OLA-NBD	193
4.2.4	Experimental Solution	196
4.2.5	UV–Vis and Fluorescence Spectroscopic Studies	196
4.2.6	Steady-State Fluorescence Anisotropy	197
4.2.7	Esterase-Like Activity Study	197
4.2.8	Circular Dichroism (CD) Spectra	198
4.2.9	Detection Limit	198
4.2.10	Fluorescence Lifetime Measurements	198
4.2.11	Molecular Docking Simulation Study	199
4.3	Results and Discussion	199
4.3.1	Effect of OLA-NBD on the Absorption Spectra of HSA	199
4.3.2	Fluorescence Emission Measurement	200
4.3.3	HSA–OLA-NBD Complexation Equilibrium and Stoichiometric Study	203
4.3.4	Intrinsic Fluorescence Quenching of HSA by OLA-NBD	204
4.3.5	Determination of HSA–OLA-NBD Binding Constants and Related Thermodynamic Parameters	207
4.3.6	Steady-State Fluorescence Anisotropy Measurement	208
4.3.7	Fluorescence Lifetime Measurements	210
4.3.8	Hydrophobic Probe ANS Displacement Analysis	212
4.3.9	Site-Specific Binding of OLA-NBD on HSA	213
4.3.10	Resonance Rayleigh Scattering (RRS) Spectral Investigations	215
4.3.11	Conformation Investigations: Circular Dichroism Study	215
4.3.12	OLA-NBD Induced Variation of HSA Functionality: Esterase-Like Activity Assay of HSA	216
4.3.13	Effect of $\beta$ -CD on the Fluorescence Spectra of OLA-NBD	217
4.3.14	Effect of $\beta$ -CD on HSA–OLA-NBD Binding	219
4.3.15	HSA–OLA-NBD Association Kinetics	221
4.3.16	Molecular Docking Results	222
4.4	Conclusions	223
	References	223-231

## Chapter 5

Page

### Domain-Specific Association of a Phenanthrene-Pyrene-Based Synthetic Fluorescent Probe with Bovine Serum Albumin: Spectroscopic and Molecular Docking Analysis

	Abstract	233
5.1	Introduction	234
5.2	Experimental Section	235
5.2.1	Materials	235
5.2.2	Instrumentation	235
5.2.3	Synthesis and Characterization of PPI	236
5.2.4	Experimental Solution	236
5.2.5	UV–Vis and Fluorescence Spectroscopic Studies	239
5.2.6	Steady-State Fluorescence Anisotropy	239

5.2.7 Circular Dichroism (CD) Spectra	239
5.2.8 Detection Limit	240
5.2.9 Fluorescence Lifetime Measurements	240
5.2.10 Molecular Docking Simulation Study	241
5.3 Results and Discussion	241
5.3.1 UV-Visible Absorption Study	241
5.3.2 Fluorescence Emission Study	242
5.3.3 Probe-Protein Binding Study	245
5.3.4 Fluorescence Anisotropy Study	247
5.3.5 ANS Displacement Assay	248
5.3.6 Site-Selective Binding of PPI on BSA	249
5.3.7 Study of Fluorescence Quenching Induced by PPI	250
5.3.8 Analysis of BSA-PPI Binding Equilibria and Determination of Thermodynamic Parameters	253
5.3.9 Fluorescence Lifetime Studies	256
5.3.10 Time-resolved Anisotropy Decay	259
5.3.11 Binding Distance Measurement Using Fluorescence Resonance Energy Transfer (FRET) between PPI and BSA	261
5.3.12 Conformation Investigations: Circular Dichroism (CD) Study	262
5.3.13 Molecular Docking Results	264
5.4 Conclusions	265
References	266-275

## Chapter 6

## Page

Highlights of the Thesis

276-279

## Appendix

## Page

List of Publications

280-281



# Chapter 1

---

## Introduction: A Literature Survey

*"Science is a part of culture. Indeed, it is the only truly global culture because protons and proteins are the same all over the world, and it's the one culture we can all share."*      **Martin Rees**



### 1.1 Protein: An Overview

*“Proteins are the machinery of living tissue that builds the structures and carries out the chemical reactions necessary for life.”* **Michael Behe**

Proteins are the most prevalent biological macromolecules found in cells and essential to all living systems. Their significance emerges from the remarkable variety of functional activities they play inside the living organisms, such as triggering biochemical reactions, DNA replication, delivering materials to the proper locations, keeping the structural integrity of cells and organs, etc.<sup>1-3</sup> The fundamental structural component of a protein is the polypeptide chain, which has a unique protein sequence consisting of twenty frequently occurring amino acid residues connected by peptide bonds.<sup>2</sup> Depending on the physiological state, each of these amino acid residues has a different size, shape and electric charges. The amino acid residues are either hydrophilic or hydrophobic in nature. There are four different types of protein structure (**Figure 1.1**). The arrangement of amino acids in the polypeptide chain constitute the “primary structure” of a protein. Proteins differ from one another based on the particular sequence and composition of amino acid which causes the protein to typically fold into a certain 3D shape and responsible for controlling its function. The term "secondary structure" of a protein refers to the regularly repeating local structures that occur inside a polypeptide backbone arising out of stable hydrogen bonding interactions between  $-C=O$  and  $-NH$  groups of the peptide bonds.

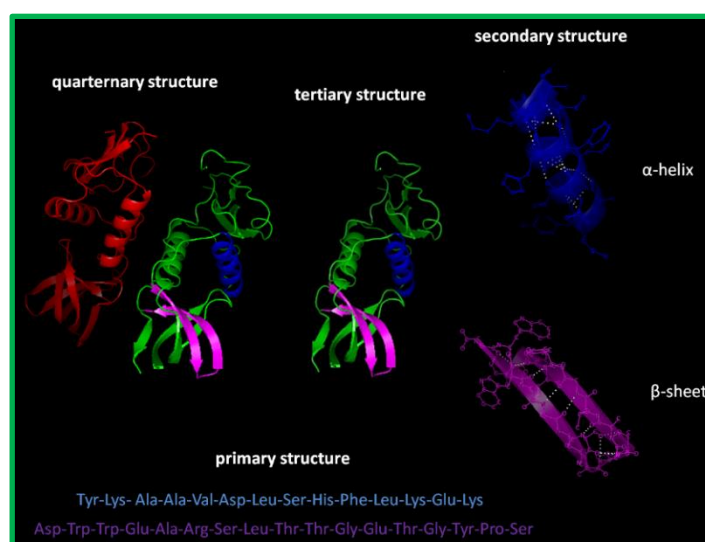


**Figure 1.1** Graphical representation for the primary, secondary, tertiary, and quaternary structures of protein. Source: Wikipedia.

The most prevalent secondary structures are  $\alpha$ -helix,  $\beta$ -sheet, and  $\beta$ -turns. On the other hand, “tertiary structure” of a protein refers to the overall three-dimensional shape of its polypeptide chain in space. It is often stabilized by interactions between the side chains of nonpolar amino acids, externally polar hydrophilic hydrogen and ionic bonds. The two main types of protein tertiary structure are fibrous and globular proteins. Fibrous proteins are often consisting of long and thin strands or sheets and play a structural role. In contrast, globular proteins are generally more compact and spherical or globular form and provide functional role. An organisation of several protein chains or subunits into a compact arrangement is known as a “quaternary structure” of a protein. Hydrogen bonds and van der Waals interactions between nonpolar side chains hold the subunits together.

### 1.2 Motivation of the Work

Recognition of various proteins and their quantitative assessment are very much important for clinical diagnosis and therapeutic monitoring because proteins play a variety of significant roles in the digestive, metabolic, and immunological processes.<sup>4-8</sup> Among the numerous proteins, thiol-containing proteins are abundant in biological systems and perform a variety of key biological roles.<sup>9</sup> Serum albumins (SAs), a family of thiol-containing proteins such as bovine and human serum albumin (BSA and HSA), play a variety of key biological functions, including the removal of free radicals, regulating the pH balance of plasma, fluid transportation, maintenance of the blood osmotic pressure, promoting wound healing, preventing platelet aggregation, inhibiting blood clotting, etc.<sup>10-15</sup> Approximately 55–60% of the total protein in human and bovine blood plasma is mainly composed of serum albumins (SAs),<sup>16,17</sup> and only a small fraction of this protein leaks into the urine through the glomerulus. A healthy adult's blood plasma normally contains 35 to 55 g/L of human serum albumin, which is primarily synthesised in the liver.<sup>18,19</sup> On the other hand, albumin concentrations in urine drop below 30 mg/L, maybe owing to the kidneys ability to prevent the passage of necessary substances like albumin and other proteins into the urine.<sup>20</sup> Nonetheless, a person's health condition is directly related to the content of albumin in urine or blood plasma. Consequently, albumin levels in biofluids (such as blood or urine) are frequently used as an effective biomarker and regularly monitored in medical practice to give the diagnostic information for a wide range of disorders.<sup>19</sup> For instance, an increased plasma albumin concentration ( $> 55$  g/L) can cause hyperalbuminemia, which is associated with

dehydration.<sup>21</sup> However, hypoalbuminemia, a condition caused by a low quantity of albumin (< 35 g/L) in blood plasma, indicates a condition of chronic hepatitis, liver cirrhosis and failure.<sup>22</sup> On the other hand, excess amount of albumin (30–300 mg/L) in the urine can result in microalbuminuria, a condition that has been linked to endothelial dysfunction, diabetes mellitus and hypertension, expressing a primary sign for cardiovascular disease and renal illness (i. e., nephrotic syndrome).<sup>23-25</sup> In addition, a patient is diagnosed with macroalbuminuria if the urine albumin content is greater than 300 mg/L, which denotes an advanced level of renal impairment.<sup>26</sup> Also, a recent research has revealed that albumin detection can assess the health condition of cows, indicating the quality of milk and meat.<sup>27</sup> Therefore, it is crucial to develop an effective fluorescent sensor for selective detection and quantification of albumin content in biofluids which is highly useful for the clinical and biomedical applications.

The protein-ligand interactions are frequently governed by the rearrangement of the protein structure led by the binding of the associated ligand molecules as well as the flexibility of the different protein binding sites.<sup>28</sup> Two important and distinct binding sites, referred to as site I and site II, provide the basis for the specific delivery of ligand molecules by serum albumin.<sup>29,30</sup> Besides, it has also been revealed that compounds with greater serum albumin affinities and preferential site II binding display effective photodynamic therapeutic effects (PDT).<sup>31-33</sup> Therefore, a comprehensive knowledge of interactions between serum albumin and ligands seems to be important for the development of novel drug molecules and biomedicines, as well as for the safe engineering of drug delivery and subsequent control of their therapeutic effectiveness.<sup>34-38</sup>

To this end, the aim of the research work outlined in this thesis is to design and synthesis of fluorescent ligands for the recognition of serum albumins, as well as to estimate the binding affinity and associated thermodynamics of serum albumin-ligand interactions. The underlying mechanism of these interactions was comprehensively explored by utilizing multiple spectroscopic methods and theoretical approaches.

### 1.3 Brief Description of Serum Albumins

The most common blood plasma proteins in a mammal's circulatory system are serum albumins, with an average lifespan of 19 days.<sup>23,39</sup> The most common types of serum albumins utilized in many research disciplines are HSA and BSA.

### 1.3.1 Human Serum Albumin (HSA)

HSA, a single chain globular protein with a molecular weight of ~66.5 kDa, is found most abundantly in the human blood circulation system. There are 585 amino acid residues in HSA.<sup>14</sup>

#### 1.3.1.1 Structure of HSA

First time, the main amino acid sequence of HSA was discovered in 1975.<sup>40</sup> Then the 3D structure of HSA was examined by carter and coworkers in 1989.<sup>41</sup> The crystal structure of HSA reveals that it is a heart-shaped helical protein. The isoelectric point of HSA is around 5, and it has a net charge of  $-15$  at a neutral pH.<sup>13</sup>

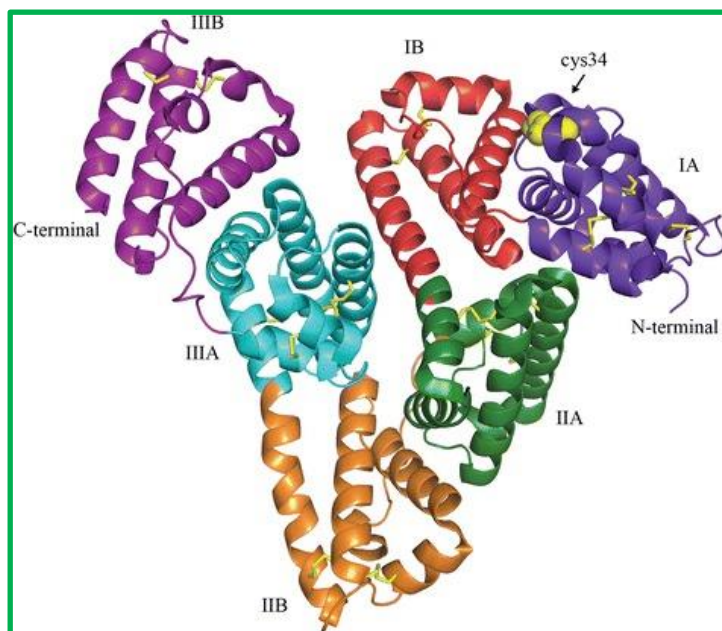


**Figure 1.2** Crystal structure of HSA, displaying domain I, II and III; each domain consists of two subdomains A and B (PDB ID: 1E7E). The disulfide bridges are represented by the yellow sticks, while the free cysteine residue at position 34 (Cys-34) in subdomain IA is represented by the yellow spheres. Adapted with permission from ref. 42. Copyright 2021 American Chemical Society.

As depicted in **Figure 1.2**, HSA has three homologous domains [(I) residues 1–195, (II) residues 196–385, and (III) residues 386–585].<sup>15</sup> Each domain consists of two subdomains (A and B) with 4 and 6  $\alpha$ -helices, respectively.

Its secondary structure is made up of approximately 67%  $\alpha$ -helix and 17 disulfide bridges from 35 cysteine moieties that act as cross-linkers between these three domains.<sup>42</sup> In addition, a single tryptophan (Trp-214) moiety and one free –SH group (Cys-34) are also present in the amino acid sequence, which are located in subdomains IIA and IA, respectively.<sup>14</sup>

### 1.3.1.2 Synthesis and Metabolic Process of HSA

HSA is exclusively produced by polysomes of hepatocytes in the liver at a rate of 10–15 g/day.<sup>43,44</sup> HSA begins to be produced as preproalbumin, which has 24 N-terminal amino acid residues that promote movement into the endoplasmic reticulum.<sup>45,46</sup> Once inside, proalbumin is created by the cleavage of the first 18 amino acids.<sup>46</sup> When the proalbumin reaches the *trans*-Golgi, the remaining 6 N-terminal amino acids are cleaved to create mature albumin.<sup>46</sup> Serum albumin leaks from circulation at a rate of 5% per hour, and returns to it through the lymphatic system at a rate that is comparable to that of the leakage.<sup>43</sup> As a result, though it has a biological half-life of 19 days, it only remains in circulation for 16–18 hours.<sup>42</sup> In instance, the production of HSA is accelerated by insulin, thyroxine, and cortisol as well as circumstances like hypoalbuminemia, but potassium and the prolonged exposure of hepatocytes to high osmotic pressure inhibit its production.<sup>42</sup> In reality, insufficient nutrients adsorption lowers the liver's ability to generate protein. Although albumin can be degraded in any tissue, but it mostly happens in the liver, muscles, and kidneys.<sup>43</sup>

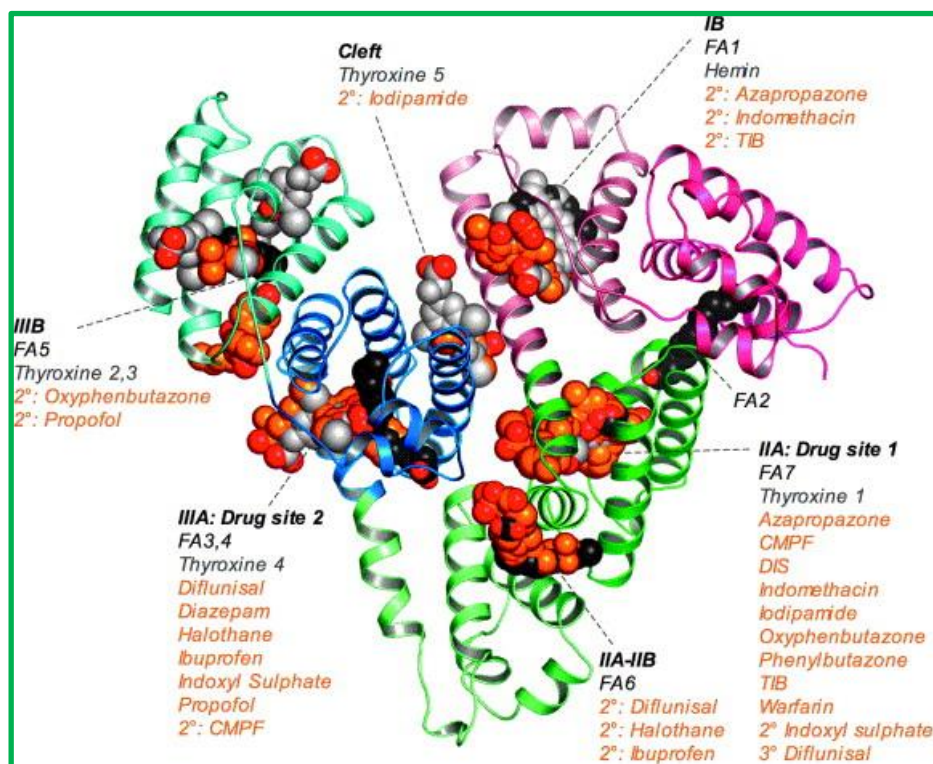
### 1.3.1.3 Drug Binding Sites of HSA

In order to explore the binding sites of HSA, Sudlow *et. al.* initially used drug molecules, and the results showed that most of the drug molecules bind to human serum albumin with high affinity at one or two binding sites, specifically in subdomain IIA at binding site I and subdomain IIIA at binding site II.<sup>29,30</sup> Additionally, studies on drug binding and crystal structure analysis showed that a large number of neutral, bulky, and heterocyclic compounds bind at site I primarily through hydrophobic interactions, while the majority of aromatic carboxylic acid compounds bind at site II through the combination of hydrophobic, van der Waals, ionic, and hydrogen-bonding interactions.<sup>13,14,29,30</sup> The hydrophobic binding zones play an important role in drug deposition and efficacy by enhancing drug solubility in plasma and tailoring drug delivery to *in vivo* and *in vitro* cells.<sup>10</sup>



## Chapter 1: Introduction

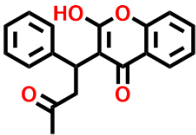
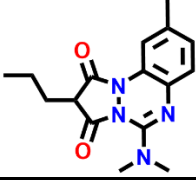
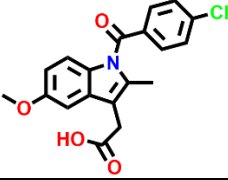
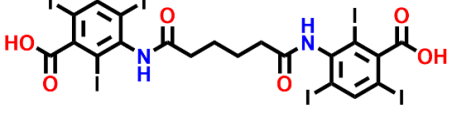
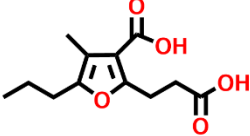
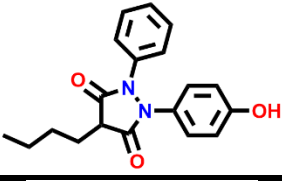
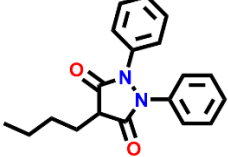
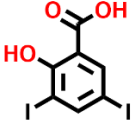
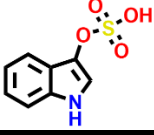
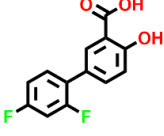
In addition, protein-drug interactions have a substantial impact on the different critical pharmacological characteristics of drugs including absorption, distribution, metabolism, and excretion.<sup>47</sup> Through crystallographic investigation of 17 distinct complexes of HSA with a wide range of drug molecules and small-molecule toxins, Ghuman et al.<sup>48</sup> showed the exact architecture of the two main drug-binding sites on the protein and indicated that amino acid residues are the fundamental determinants of binding selectivity (Figure 1.3). Structural data analysis indicates that the two principal drug binding sites on HSA are highly flexible binding cavities with discrete sub-compartments, some of which can only be accessed through local drug-induced conformational changes and suggest a variety of secondary binding sites dispersed broadly over the protein.<sup>48</sup> Table 1.1 provided a list of the most frequently used small drug molecules and their corresponding human serum albumin binding sites.



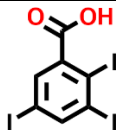
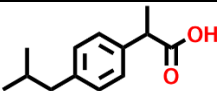
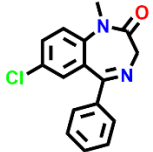
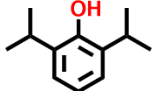
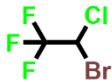
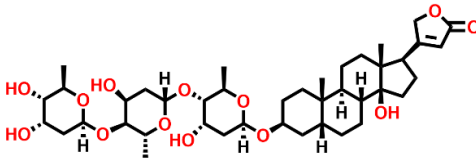
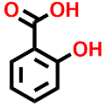
**Figure 1.3** An overview of the ligand binding ability of HSA as determined by crystallographic studies so far. Ligands are shown in space-filling form, and all oxygen atoms are red in colour. All other atoms in endogenous ligands (hemin, thyroxin), fatty acids (myristic acid), and drug molecules are coloured light grey, dark-grey, and orange, respectively. Adapted with permission from ref. 48. Copyright 2005 Elsevier.

## Chapter 1: Introduction

**Table 1.1** Summary of the site-specific binding drugs of human serum albumin.

Site-specific drugs	Structure	Binding site
Warfarin		Subdomain IIA
Azapropazone		Subdomains IIA & IB
Indomethacin		Subdomains IIA & IB
Iodipamide		Subdomain IIA
Carboxy-4-methyl-5-propyl-2-furanpropionic acid (CMPF)		Subdomains IIA & IIIA
Oxyphenbutazone		Subdomains IIA & IIIB
Phenylbutazone		Subdomain IIA
3,5-Diiodosalicylic acid		Subdomain IIA
Indoxyl sulphate		Subdomains IIIA & IIA
Diflunisal		Subdomain IIIA



2,3,5-Triiodobenzoic acid (TIB)		Subdomains IIA & IB
Ibuprofen		Subdomain IIIA
Diazepam		Subdomain IIIA
Propofol		Subdomains IIIA & IIIB
Halothane		Subdomain IIIA
Digitoxin		Subdomain IIIA
Salicylic acid		Subdomains IIA & IB

### 1.3.1.4 Physiological Function of HSA

HSA is the primary regulator of fluid balance across the body's compartments, contributing around 80% of the total plasma osmotic pressure.<sup>17</sup> There are two category of substances that bind to HSA: endogenous and exogenous. The first category consists of all the substances that are already present in the body, including bilirubin, cholesterol, hormones, fatty acids, free radicals, cations, and vitamins.<sup>49,50</sup> The second category of substances comprises the drug molecules that enter into the body from the outside, including hypoglycemic agents, anti-inflammatory drugs, anticoagulants, antibiotics, and pharmaceuticals for the cardiovascular, renal, and central nervous systems.<sup>51</sup> Additionally, HSA is frequently used in clinical practice to treat a variety of illnesses, including haemorrhage, shock, surgical blood loss, burns, trauma, cardiopulmonary bypass, haemodialysis, chronic liver disease, nutrition support, etc.<sup>15</sup> HSA is also the principal source of extracellular reduced -SH groups, which are located at the Cys-34 site and serve as powerful ROS scavengers.<sup>43</sup>

The ability to bind a number of metal ions, including  $\text{Cu}^{2+}$ ,  $\text{Co}^{2+}$ ,  $\text{Ni}^{2+}$ , and  $\text{Zn}^{2+}$  at the N-terminal section of the protein molecule provides another aspect of its antioxidant function. The catalysis of several chemical processes generating free radicals are thus inhibited by these metal ions.<sup>15,52</sup> HSA also helps to maintain normal capillary permeability and stabilize the endothelial layer, likely via lowering oxidative damage and controlling inflammation.<sup>43</sup> Furthermore, HSA has antithrombotic properties that seem to be connected to its ability to bind with nitric oxide (NO) at the Cys-34 site, resulting in the formation of the albumin-NO complex, delaying the quick inactivation of NO and extending its anti-aggregate impact on platelets.<sup>53</sup> In the 1940s, Isidor S. Ravdin, a surgeon, used pure human serum albumin to treat seven patients with severe burns during the Second World War, and all of them recovered successfully.<sup>54</sup> It is important to note that a special attention has been paid to the invention and synthesis of albumin-based nanoparticles for the effective transport of different compounds and biomolecules to the target cells/organs. As a result, Abraxane may be regarded as a representative example of albumin-based nanoparticles authorised by FDA in 2005. Abraxane is primarily used to treat people with metastatic breast cancer.<sup>55</sup> HSA has enzymatic activity, however its turnover is low in comparison to that of other familiar enzymes.<sup>56,57</sup> Hence, it is regarded as a pseudo-esterase. Tyr-411 is considered to be the primary residue involved in the pseudo-esterase activity.<sup>57</sup>

### 1.3.2 Bovine Serum Albumin (BSA)

BSA is a single polypeptide chain with 583 amino acid residues that has a molecular weight of 65000 Da, and is derived from cow serum.<sup>23</sup> When BSA is in water at 25 °C, it has an isoelectric point of 4.7, making it negatively charged at neutral pH levels and positively charged at acidic ones.<sup>58</sup> BSA adsorption on charged surfaces is influenced by the three domains of BSA, each of which has a different surface charge density.<sup>59,60</sup> Both positively and negatively charged molecules may attach to BSA since it contains both positively and negatively charged amino acids. It has been utilised extensively as a carrier for drug delivery since it is readily accessible at cheap cost, easy to filter, and manage. Moreover, the water-soluble BSA protein has a large loading capacity and can bind both hydrophilic and hydrophobic medicines, making it a very flexible carrier. BSA and HSA have a same isoelectric point and shares around 80% sequence homology.

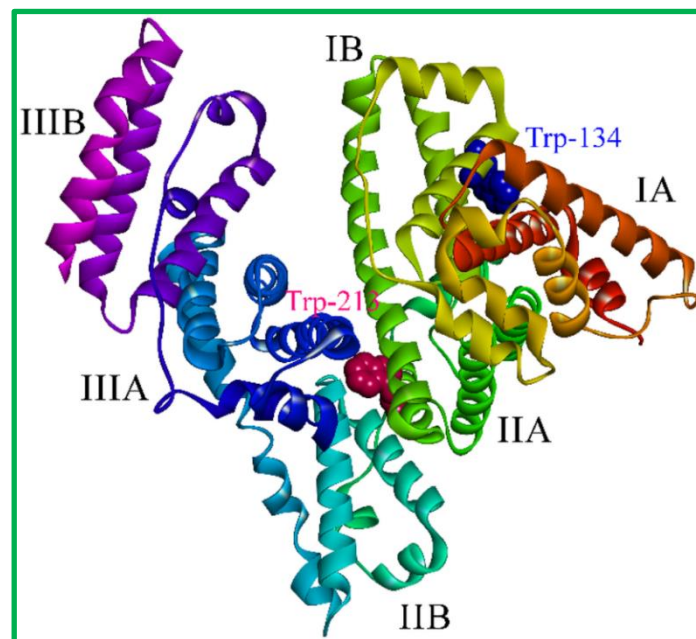


**Figure 1.4** Schematic representation of BSA with two tryptophan amino acid residues (PDB ID: 3V03). Adapted with permission from ref. [61](#). Copyright 2021 Springer Nature.

The primary distinction between the two serum albumins is that, BSA has two tryptophan residues,<sup>[61](#)</sup> Trp-213 in subdomain IIA and Trp-134 in subdomain IB (**Figure 1.4**), while HSA comprises of only one tryptophan residue (Trp-214). Trp-213 is located in a hydrophobic cavity of BSA protein, while Trp-134 is extensively exposed to the hydrophilic zones.<sup>[62,63](#)</sup> The fluorescence property of the protein comes from the presence of tryptophan residue, so HSA and BSA can be discriminated by using spectrofluorimetry. Human exposure to BSA occurs through the ingestion of milk and meat from cows, as well as through immunisations and drugs.<sup>[64](#)</sup>

## 1.4 Popular Methods for Serum Albumins Detection and Estimation

### 1.4.1 Dye Binding Methods

Since the 1950s, dye-binding methods have been widely used to detect and estimate the serum albumin.<sup>[57](#)</sup> In this method, several anionic, cationic, or fluorescence-based dyes are explored for the serum albumin estimation (**Figure 1.5**). Each of these dyes has its advantages and disadvantages.

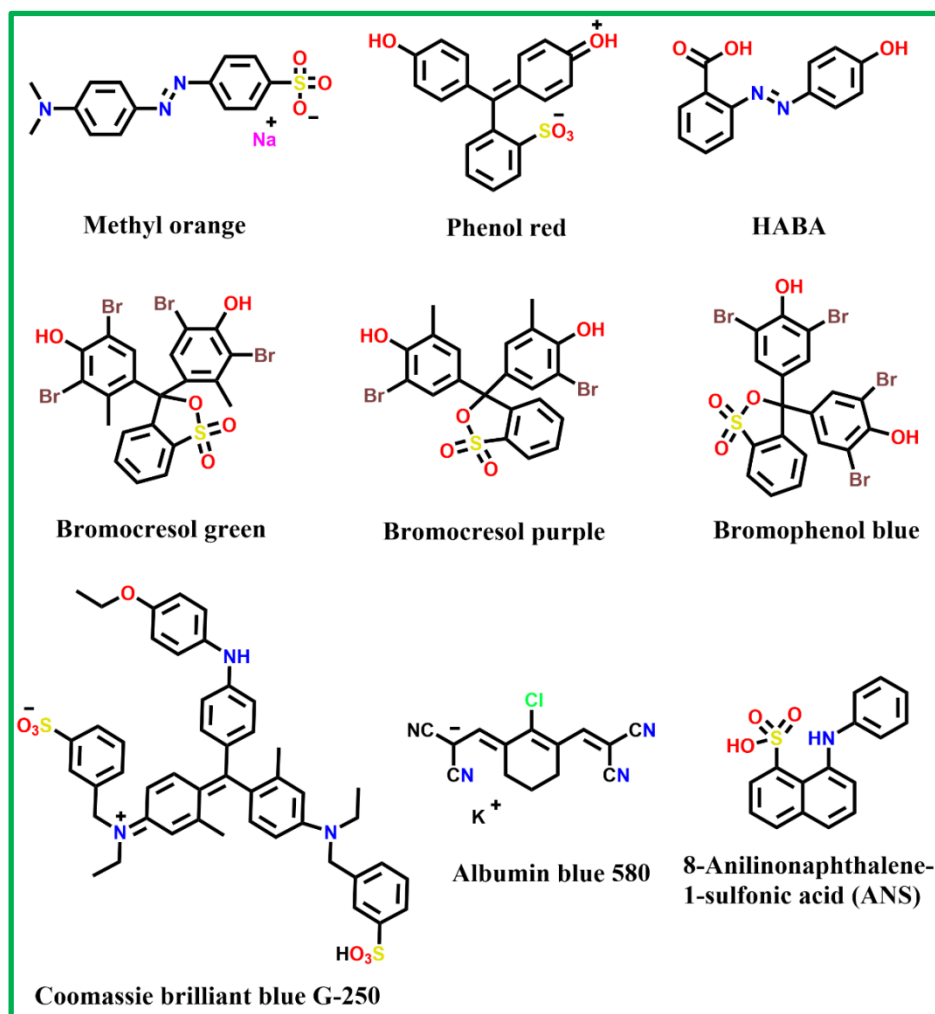


**Figure 1.5** Some commonly used dye molecules for the detection and estimation of serum albumin.

### 1.4.1.1 Methyl Orange (MO)

The first dye used to detect HSA was an anionic dye called methyl orange (MO), which is acidic in nature.<sup>65</sup> The sulfonic group of MO interacts electrostatically with the protonated groups of Lys-444 and Arg-218 to bind with HSA at site I. Here the distinctive colour change is triggered by a proton exchange reaction process between the diazenyl group of MO and the  $\gamma$ -carboxyl group of Glu-292 of HSA.<sup>66</sup> The concentration of serum albumin directly relates to the change in colour intensity. But, in this method, albumin estimation is interfered by the  $\alpha$ - and  $\beta$ -globulins present in the sample. As a result, the dye-globulins binding causes positive errors in the albumin estimation<sup>67</sup> and lowers its specificity.<sup>65</sup>

### 1.4.1.2 HABA (2-(4'-Hydroxyazobenzene) Benzoic Acid)

Similar to methyl orange, HABA (2-(4'-hydroxyazobenzene) benzoic acid) was also the early dye made available to detect HSA in the 1950s.<sup>68</sup> It is an anionic azo dye. Serum albumin detection by HABA dye was originally introduced by Dr. Fred Karush, who employed it to detect BSA. After being motivated by this, David D. Rutstein and his colleagues successfully implemented it to the detection of HSA.<sup>68</sup> However, it is important to note that certain substances, including bilirubin in the plasma, sulphonamides, free fatty acids, and salicylates interfere with HABA for the estimation of HSA.<sup>69</sup>

### 1.4.1.3 Phenol Red

The use of phenol red dye for the measurement of HSA was first introduced by Smith and Smith in 1938.<sup>70</sup> Phenol red binds with HSA at site I. In this method, serum albumin levels are determined by measuring the absorbance of the albumin-dye complex at 560 nm. Fatty acids, bilirubin, and anions such as naphthalene-*p*-sulphonate interfere with the ability of phenol red to assess albumin level.<sup>71-73</sup>

### 1.4.1.4 8-Anilinonaphthalene-1-Sulfonic Acid (ANS)

In aqueous solution, 8-anilinonaphthalene-1-sulfonic acid (ANS) is non-fluorescent, but it emits a distinctive fluorescent signal upon binding with HSA. In this method, the amount of HSA present in the sample is determined by fluorescence intensity. However, its application in clinical chemistry for estimating serum albumin is limited.<sup>70</sup>

### 1.4.1.5 Bromocresol Green (BCG)

The BCG (bromocresol green) dye-binding method was initially introduced by Rodkey in 1965 to detect HSA,<sup>74</sup> but one primary drawback of this approach is that the working dye solution shows a very high absorbance value at pH 7.05. In 1966, the same dye was employed by Bartholomew and Delaney in a direct calorimetric technique to estimate the serum albumin using a pH 3.8 buffer.<sup>75</sup> The main limitation of their approach is that adding a protein solution immediately causes turbidity, making it impossible to obtain reliable data. This dye was also used in 1971 by Doumas et al. to detect serum albumin.<sup>76</sup> In the Doumas method, the introduction of a non-ionic surfactant (Brij-35) decreases the absorbance of the blank, eliminates turbidity, and promotes linearity.

The assay principle is based on the specific binding of the anionic form of BCG dye with serum albumin proteins at an acidic pH of 4.2, which changes the colour from yellow-green to blue-green. Albumin levels in the specimen directly correlate with the intensity of the blue-green colour of albumin-BCG complex, and it is evaluated by measuring the increase in absorbance at 620 nm.<sup>23</sup> Although the approach is reliable in measuring serum albumin, it has some drawbacks, such as a lack of albumin specificity and interactions of BCG dye with  $\alpha$ - &  $\beta$ -globulins and acute-phase proteins that lead to positive errors in the albumin estimation.<sup>65,77</sup> Additionally, Hemoglobin can also interfere with albumin's binding ability with BCG dye.<sup>78</sup> However, in 1976, Gustafsson<sup>79</sup> significantly increased the specificity of the BCG technique by measuring absorbance immediately after combining serum and reagents, inhibiting other proteins from binding.

### 1.4.1.6 Bromocresol Purple (BCP)

Another phthalein dye, bromocresol Purple (BCP), with a similar structure like BCG, was first introduced by Louderback in 1968 to detect HSA.<sup>80,81</sup> Then the method was further improved by P. Carter<sup>82</sup> and Pinnell et al<sup>83</sup>. In contrast to the aforementioned BCG method's lack of specificity, the BCP method is more specific for HSA and is unaffected by precipitation.<sup>83</sup> Hydrophobic interactions enable it to bind with HSA at Site I.<sup>23</sup> In this method, the distinctive colour change is based on a pH-dependent proton transfer reaction between BCP dye and the dissociated carboxyl or protonated amino group of HSA. A spectrophotometric measurement of the HSA-BCP complex's absorbance at 590 nm is used to determine HSA.<sup>84</sup> This method almost completely eliminates salicylate, transferrin, and globulin interference.<sup>80,83</sup> But, in patients receiving hemodialysis and peritoneal dialysis, the BCP method underestimates the HSA level because of the presence of 3-carboxy-4-methyl-5-propyl-2 furanpropanoic acid (CMPF) in plasma and urine.<sup>85-87</sup> Furthermore, research has revealed that heparin can interfere with both the BCG and BCP methods.<sup>88,89</sup>

### 1.4.1.7 Bromophenol Blue (BPB)

In 1978, R. Flores first established the bromophenol blue (BPB) method for the detection of HSA.<sup>90</sup> In the BPB method, HSA is estimated by binding it to BPB at site I<sup>23</sup> in an acidic environment (pH 2.5–3.5) and then determining the absorbance of the blue colour complex at 610 nm.<sup>91</sup>

Globulin interferes with this method, whereas creatinine, bilirubin, and uric acid have very little impact.<sup>92</sup>

### 1.4.1.8 Albumin Blue (AB) Dyes

Albumin blue (AB) dyes are anionic that can selectively target serum albumin by generating a strong fluorescent complex. The derivatives of albumin blue dyes include AB633, AB670, and AB580. Despite being used to detect HSA, AB633 and AB670 have restricted applications due to their lower stability. In contrast, AB580 ( $\lambda_{\text{ex}}$  at 590 nm and  $\lambda_{\text{em}}$  at 616 nm) performs well in terms of stability and HSA detection. The experiment is conducted at pH 7.4, and the fluorescence intensity is immediately recorded once the dye has been added to the sample. According to reports, transferrin, fatty acids, Bence Jones proteins, etc. caused little interference with this procedure, and the interference can also be further minimized by employing excessive dyes.<sup>93</sup> But accurate results also depend on maintaining the temperature at 22 °C and dilution of the sample.<sup>94</sup>

### 1.4.1.9 Coomassie Brilliant Blue G-250

The Coomassie brilliant blue G-250 is a non-azo dye used in the Bradford assay to determine the serum albumin concentration.<sup>95</sup> At an acidic pH, the protonated Coomassie Brilliant Blue G-250 dye exhibits a maximum absorption at 465 nm and is reddish-brown in colour. But, in an acidic environment, the dye binds to albumin predominantly with arginine amino acid residue and to a smaller extent with tryptophan, phenylalanine, histidine, and tyrosine residues, resulting in the formation of a blue colour dye-albumin complex.<sup>96</sup> Due to the dye's stability in its anionic form after binding to albumin, a metachromatic shift from 465 to 595 nm is observed and the increase in absorbance at 595 nm is measured. The dye binding assay is simple, sensitive, rapid and reproducible. Its major drawback is that it fails if the sample contains large amounts of detergents or surfactants (SDS, Triton X-100) or is too basic. Surfactants, in particular, that are frequently employed to solubilize various types of proteins, will affect the test and cause the dye to precipitate out. Another problem with this method is that the Coomassie brilliant blue G-250 dye also stains the walls of working cuvettes.

## 1.4.2 Electrochemical Methods

Electrochemical method is one of the most commonly used detection methods. It measures detectable electrical signals caused by ions or electrons generated when a biorecognizing

element reacts chemically with a target analyte.<sup>97,98</sup> A gold nanoparticle-labeled antibody and a screen-printed carbon electrode (SPCE) surface with polyvinyl alcohol (PVA) modification were used in 2011 by Omidfar et al. to develop an electrochemical immunosensor.<sup>99</sup> It has excellent sensitivity toward HSA with a detection limit of 25 ng/mL. Then, in 2016, Tsai and his colleagues developed an immunosensor based on screen printing that uses a carbon electrode formed by a carbon paste of CaCO<sub>3</sub> and stearic acid.<sup>100</sup> Here, a covalent fixing technique is used to adhere an anti-human albumin antibody to the surface of the screen-printed immunosensor. Then, employing amperometric electrochemical measuring technique, albumin was detected quantitatively. The immunosensor also offers high sensitivity and selectivity for HSA, with a 9.7 mg/mL detection limit. The main disadvantage of this method is that it does not operate in real-time.

### 1.4.3 Immunochemical Methods

Immunochemistry detects albumin by the development of the albumin/anti-albumin antibody complex. HSA concentrations can be measured quantitatively in biological samples (serum, urine) with excellent specificity because of easy access to monoclonal anti-HSA antibodies. However, immunochemical approaches are rarely employed in regular analysis due to their time-consuming procedure, costly equipment, and lack of precision. But, with recent advances in equipment and technology, its application in regular analysis has become simple and precise.<sup>101</sup> This method became widespread in diagnostic laboratories due to automation in the immunochemical detection of HSA in biofluids.

#### 1.4.3.1 Radial Immunodiffusion

In this procedure, anti-HSA antibody is mixed into the agar gel, the newly created agar gel plate is pierced using a gel cutter, and then a sample to be examined is added to the well. Subsequently, the sample disperses into the agar and develops a precipitation complex where interactions between albumin and antibodies take place. Then the diameter of the precipitated protein ring is measured after Coomassie blue staining, and it is correlated with the albumin content in the sample.<sup>102</sup> Although this technology is affordable and efficient, its use in clinical analysis is limited due to a lack of automation and a laborious process.<sup>103</sup>



### 1.4.3.2 Radioimmunoassay (RIA)

In a liquid phase, radioimmunoassay employs a double-antibody approach in which a known quantity of radiolabelled albumin ( $^{125}\text{I}$ -albumin) and albumin from the test sample are in competition for antibody-binding sites. Following free albumin separation, the sample's albumin concentration was calculated by comparing it to a calibration curve.<sup>102</sup> The short shelf life of the radionuclides and radiation-induced problems make the use of the RIA assay difficult, even though it delivers excellent accuracy. Because of this, RIA is not often used in diagnostic laboratories to estimate albumin.<sup>102,103</sup>

### 1.4.3.3 Enzyme-Linked Immunosorbent Assay (ELISA)

Engrall and Perlmann<sup>104</sup> first introduced this ELISA technique in 1971. Both competitive and sandwich ELISA are frequently used to measure the albumin levels in samples.<sup>103</sup> Anti-albumin antibodies are used in sandwich ELISA approach to coat the reaction vessel or plate. After a suitable dilution, the test sample is introduced to the antibody-coated well and washed three times. As the antibodies trap albumin, they are not eliminated during the washing step. After that, a secondary antibody that has been enzyme-labeled is applied, and the labeled antibody binds to the fixed antigen (albumin). The complex is then formed by adding the appropriate enzyme substrate. Following the addition of suitable colouring reagents, this complex produces colour, and the intensity of the colour is proportional to the albumin content in the testing sample.<sup>102</sup> The competitive ELISA method involves putting a diluted test sample with a specific amount of enzyme-labeled antigen on a plate that has been coated with an anti-protein antibody. When a certain substrate and a colouring agent are combined, a colour is produced that is inversely related to the amount of albumin present in the test sample.<sup>102</sup>

### 1.4.3.4 Immunoturbidimetry

The immunoturbidimetric method includes forming an insoluble albumin/anti-albumin complex by interacting an anti-albumin antibody with a test sample containing albumin. A turbidity is produced in the reaction mixture as a result of this interaction. By measuring the absorbance at 340 nm, the turbidity may then be quantitatively examined to determine the albumin level in the test sample.<sup>102,105</sup>

### 1.4.3.5 Immunonephelometry

The concept behind the Immunonephelometry method is the light scattering ability of the albumin-antibody complex. When a particular wavelength of light is emitted from a light source along a horizontal axis, it interacts with the albumin-antibody complex in the solution and scatters in various directions. A photodetector measures the intensity of the scattering light, which is directly proportional to the amount of albumin present in the test sample.<sup>106</sup> The effect of pH and urea is eliminated by diluting the sample in the buffer.

### 1.4.4 Chromatography Based Methods

Chromatography is a popular method for separation and analysis, and in 1977, it was applied to purify HSA.<sup>107</sup> Various researches indicated that this strategy is superior and more accurate than immunochemical techniques.<sup>108,109</sup> Liquid chromatography combined with tandem mass spectrometry (LC/MS) has recently been recognized as promising for identifying trace amounts of albumin in human urine.<sup>110</sup> In comparison to other techniques, chromatography-based approaches are more precise and reliable. However, the need for expensive and sophisticated equipment restricts their application in normal clinical estimation.<sup>107,110</sup>

### 1.4.5 Electrophoresis Based Methods

Electrophoresis is a method for separating charged particle components in a sample based on their mobility caused by charge differences. Albumin is distinguished from other biomolecules using this property, and then its estimation is performed. Tiselius developed electrophoresis equipment in 1935 and was the first to isolate HSA using its electrophoretic mobility.<sup>111</sup> The components are divided into narrow bands as a result of the electric field's action, which causes each component to move at its individual speed in the direction of its matching electrode. Then, using an appropriate detection technique, the electrophoretic band spectrum is recorded. But this approach was too difficult and time-consuming for regular clinical chemistry analysis. In 1950, Tiselius and three other groups of researchers improved this method by using paper as a support matrix for electrophoretic separation, making it more affordable, quick, and reliable.<sup>112</sup> To improve electrophoretic separation, several support matrixes including agarose gel, polyacrylamide gel, starch gel, and cellulose acetate gel are utilized.<sup>113</sup> In 1966, an electrophoresis method using anti-albumin antibodies was developed to effectively measure the quantity of albumin in agarose gel.<sup>114</sup>

This approach is based on the concept that the electrophoretic mobility of the antigen–anti-albumin antibody complex differs from that of unbound albumin. This technique measures albumin quickly and uses a lesser amount of anti-albumin antibodies. In 2003, Duly *et. al.* introduced a capillary zone electrophoresis approach to measure serum albumin, and this approach gives more precise results compared to the BCG method.<sup>115</sup>

### 1.4.6 Fluorometric Based Methods

So far, various analytical techniques, including colorimetric (i. e., dye binding), radiolabeling, immunoassays, electrophoresis, fluorometry, electrochemical, and LC–MS proteomics-based methods have been developed effectively for the detection and quantification of serum albumin in biological fluids (blood, urine, and cell extracts).<sup>95,99-101,115-118</sup> However, among the different techniques, fluorometry is regarded as the most widely used technique owing to its easy operation, non-destructive nature, good selectivity, high sensitivity, quick response, and noninvasive benefits along with high resolution real-time imaging *in vitro* and/or *in vivo*.<sup>19,27,119,120</sup> The term "fluorescent probes" refers to a class of fluorescent chemical compounds with characteristic fluorescence in the visible and near infrared regions, whose fluorescent properties can be sensitively altered in response to the environment through changes in polarity, refractive index, viscosity, and other factors. An ideal fluorescent probe for detecting serum albumins should have the following characteristics:

- (i) highly selective and sensitive towards serum albumins without interference from other bioanalytes (various proteins, enzymes, amino acids, cations, anions, some urine interferents, etc.);
- (ii) real-time detection capability;
- (iii) low cost and easy synthesis;
- (iv) excitation wavelength ( $\lambda_{ex}$ ) of the probe should exceed 340 nm to counter UV-induced cell damage, and emission wavelength should be  $\lambda_{em} \geq 500$  nm to minimize background auto-fluorescence by biomolecules in the living systems;
- (v) higher solubility in relevant buffers, cell culture media or body fluids;
- (vi) good photostability and biocompatibility under relevant conditions;

- (vii) should have functional groups for site-specific binding;
- (viii) good reproducibility ; and
- (ix) finally, it should have potential application in the clinical field and high-resolution cell imaging *in vivo* and/or *in vitro*.

So far, several effective fluorescent sensors that detect serum albumins have been published with their different positive and negative traits. This chapter highlights recent advances in the use of fluorescent molecular probes (by our and other research groups) for the detection of serum albumins with different possible reaction mechanisms.

### 1.5 Different Strategies for the Detection of Serum Albumins Based on Fluorescent Molecular probes

Fluorescent molecular probes include three basic components: a recognition group, a fluorescent group, and a connecting arm.<sup>121</sup> The fluorescent group converts the recognition signal into an optical signal, whereas the recognition group is responsible for determining the selectivity and specificity of the probe molecule. The connecting arm primarily joins the fluorescence group and recognition group. Some common fluorophore moieties are polycyclic aromatic hydrocarbons (naphthalene, anthracene, phenanthrene, pyrene, perylene), coumarin, fluorescein, rhodamine, anthocyanin derivatives, BODIPY, naphthalimide, dansyl, cyanine, carbazole, squaraine etc. In recent years, the organic fluorescent molecular probe-based method has become the most popular and frequently used approach for serum albumin detection and bioimaging application in live cells. The design strategy for the development of organic fluorescent molecular probes is mostly based on the following four aspects:

- (1) Microenvironment sensitive fluorescent probes;
- (2) Aggregation induced emission (AIE) based fluorescent probes;
- (3) Self-assembly/disassembly based fluorescent probes; and
- (4) Enzymatically reactive fluorescent probes.

#### 1.5.1 Microenvironment Sensitive Fluorescent Probes

One of the most widely used designs for developing microenvironment sensitive fluorescent molecular probes is based on the integration of push-pull effects, in which electron-donating

(D) and electron-accepting (A) segments are connected by  $\pi$ -conjugated spacers.<sup>122</sup> This type of probe exhibits variations in fluorescence intensity or emission wavelengths in response to changes in their immediate surroundings (such as polarity, viscosity, etc.).<sup>123-126</sup> The emission of these fluorescent probes is influenced by a mechanism known as intramolecular charge transfer (ICT). After being activated by light, these probes undergo a rapid electron transfer from the donor (D) part to the acceptor (A) part of the molecule. In D-A fluorophores, this effect can develop when the locally excited (LE) state is attained (**Figure 1.6**).

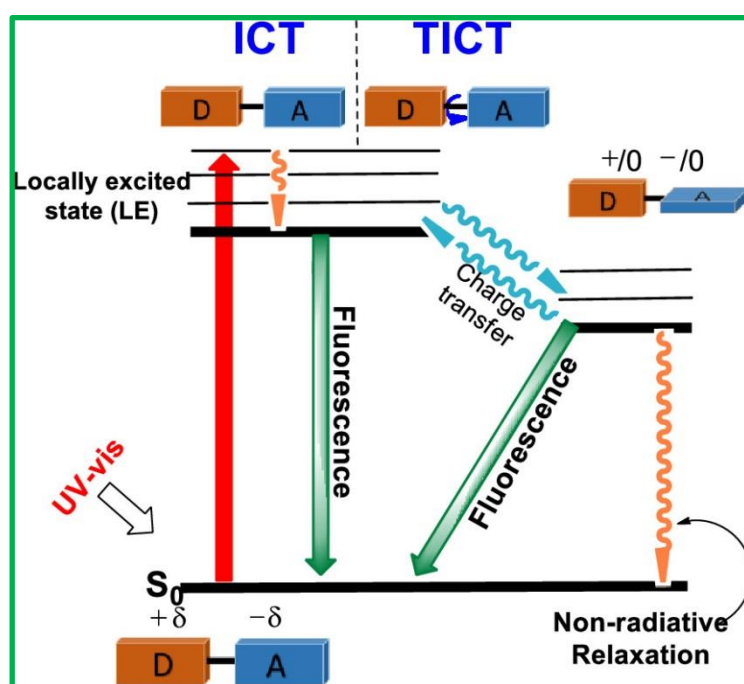


**Figure 1.6** Schematic representation of the TICT state formation from the LE state. Adapted with permission from ref. [122](#). Copyright 2021 American Chemical Society.

Additionally, in polar solvents, such fluorophores also experience intramolecular D-A twisting around a single bond that connects the D and A parts of the molecule (**Figure 1.6**). This twisting process includes a decoupling of the donor and acceptor groups and develops a highly polar, charge-separated, and relaxed perpendicular state with reduced energy, which is defined as the “twisted intramolecular charge transfer” (TICT) state.<sup>126-128</sup> D-A fluorophores showed dual fluorescence in two different energy bands due to relaxation of the locally excited (LE) state and emission from the TICT state. Particularly in the TICT state, molecules in polar media show nonfluorescent or low-fluorescent phenomena. As a result, in case of

nonfluorescent TICT molecules, effective lighting up of the invisible TICT state can be used to design novel fluorescent molecular probes.

In polar aqueous solution, this kind of fluorescent probe is non-fluorescent or exhibits extremely weak fluorescence, but the addition of serum albumins (HSA/BSA) results in a remarkable enhancement in the probe's fluorescence emission intensity. In this case, a variety of non-covalent interactions (such as H-bond, hydrophobic,  $\pi$ - $\pi$ , and so on) between the probe and the inner cavity of serum albumins allow the probe molecules to enter the low-polarity hydrophobic cavity of serum albumins, which restricts the intramolecular rotation of the probe molecules and resulting in an increase in fluorescence intensity. Based on environmental sensitivity, there are various reports on HSA/BSA fluorescent probes.

### 1.5.1.1 Dicyanomethylene-4*H*-Chromene Based Fluorescent Probes

Dicyanomethylene-4*H*-chromene is an important chromophore with excellent photostability. An increasing number of researchers are using it frequently to develop fluorescent probes because of its great optical characteristics.<sup>129</sup> In 2014, Fan *et. al.*<sup>19</sup> developed a fluorescent turn-on HSA probe **1** (Figure 1.7), in which a dicyanomethenyl-4*H*-chromene group is double-bonded to an aromatic amine moiety to form an effective electron push pull system. The aqueous solution of **1** shows a very little fluorescence upon excitation at 520 nm, but when HSA is added, the fluorescence intensity dramatically increases at 620 nm. With a detection limit of 22.0  $\mu\text{g/L}$ , this probe displays a 70-fold increase in fluorescence intensity toward HSA without interference from other biological analytes. The results of the molecular docking study indicate that the probe specifically binds to site I of HSA. Additionally, it also has the ability to measure a trace amount of HSA in healthy human urine.

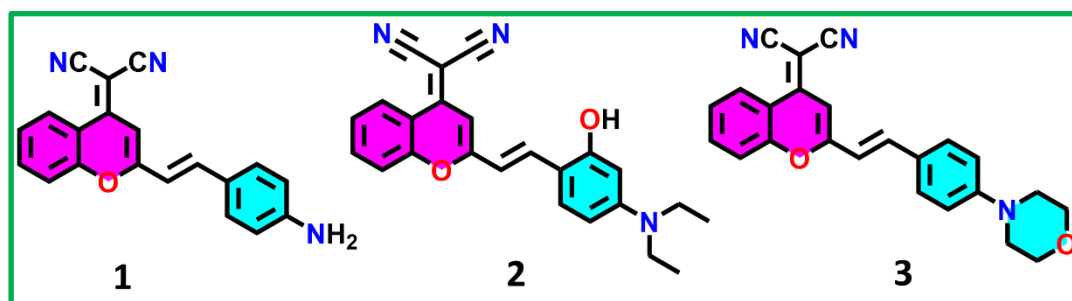


**Figure 1.7** Chemical structure of the probes **1-3** based on dicyanomethylene-4*H*-chromene moiety for HSA detection.

Then, in 2017, Govindaraju *et. al.*<sup>130</sup> also synthesized a red-NIR fluorescent probe **2** (Figure 1.7), based on this dicyanomethylene-4*H*-chromene chromophore for the specific detection of HSA. In an aqueous PBS buffer medium, upon excitation at 530 nm, this probe displays a very weak fluorescence spectra with a  $\lambda_{\text{max}}$  at 733 nm. With the addition of HSA (100 mg/L), the fluorescence spectra of this probe revealed a 100-fold increase in emission intensity, along with a blue shift of emission maxima from 733 nm to 655 nm. It has a detection limit of 1.26 mg/L for HSA. This probe primarily binds with HSA at subdomain IIA of site I, which explains the observed selective increment of the emission intensity. It may be used successfully to stain HSA in gel electrophoresis, quantify and validate HSA in human urine samples, and track serum albumin in living cells.

Similarly, in 2021, another electron push-pull mechanism-based HSA-specific turn-on fluorescent probe **3** (Figure 1.7) was also developed by the Chao group.<sup>131</sup> This probe exhibits excellent photo-stability and showed a 60-fold increase in fluorescence intensity toward HSA at 630 nm with a LOD value of 0.25 mg/mL, upon excitation at 480 nm. Both the drug displacement studies and molecular docking simulations established that this probe binds to HSA at fatty acid site 1 (FA1) rather than the two most often reported binding sites (Sudlow I and II).

### 1.5.1.2 Tricyano Dihydrofuran Based Fluorescent Probes

Tricyano dihydrofuran (TCF) and its derivatives have gained popularity in recent years as red chromophores for the molecular identification and bioimaging of specific targets in complex biological systems, owing to their many inherent benefits, such as their long emission wavelengths (> 600 nm), high water solubility, and capability to suppress the background autofluorescence.<sup>132,133</sup> TCF and its derivatives exhibit exceptional optical properties due to their significant electron-withdrawing capabilities induced by the conjugated structure and presence of three cyano groups.<sup>134</sup> In 2016, Guangbo and colleagues<sup>135</sup> designed and developed a rapid response, turn-on fluorescent probe **4** (Figure 1.8) based on this TCF motif for the selective and sensitive detection of HSA. When this probe is excited at 560 nm in PBS medium, its fluorescence intensity is very low. But, in contrast, binding of probe **4** to HSA results in a 75-fold increase in fluorescence intensity at 612 nm, with no interference from other proteins.

This dramatic fluorescence change can be attributed to the binding of hydrophobic probe **4** within the low-polar hydrophobic cavity of HSA, which inhibits the rotation of probe molecules. It has a detection limit of 2.5 mg/L for HSA, and the response time is around 3 s. Furthermore, the results from the molecular docking study indicate that the probe is located in the subdomain IB of HSA, where the  $\pi$ - $\pi$  interaction and hydrophobicity play an important role in the binding stability. Using this probe, it is also possible to identify trace amounts of HSA in a variety of biological materials, such as diluted plasma and cell culture supernatants.

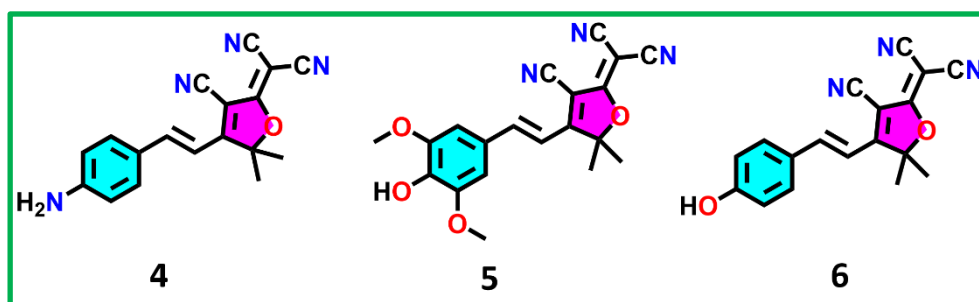


**Figure 1.8** Chemical structure of the probes **4-6** based on TCF moiety for the serum albumins detection.

In 2019, Choudhury *et. al.*<sup>136</sup> also developed two fluorescent probes **5** and **6** based on an electron push pull mechanism by coupling this electron acceptor TCF moiety with an ionizable phenol derivative through a double bond (**Figure 1.8**). These two probes are non-emissive in polar aqueous buffer solution (pH 7.4) because of the energy loss through non-radiative decays. But both the probes show a considerable increase in fluorescence intensity when bound to HSA at site I, resulting in excellent LOD values of 1.0 mg/L and 3.0 mg/L for **5** and **6**, respectively, in HSA-spiked urine samples. Probe **5** responded preferentially to HSA over BSA and other proteins, while probe **6** cannot distinguish between HSA and BSA. The better selectivity of probe **5** for HSA is owing to the constrained movements in the site I binding pocket caused by increased hydrophobic and van der Waals interactions, which inhibit energy loss via radiationless decay routes. Furthermore, the binding of probe **5** with HSA is saturated in less than a minute, whereas probe **6** takes 5 min to attain saturation.

### 1.5.1.3 Dicyanoisophorone Based Fluorescent Probes

In recent years, dicyanoisophorone (DCO) based D- $\pi$ -A type fluorophores have gained popularity due to their simple synthesis, high fluorescence brightness, and outstanding



## Chapter 1: Introduction

chemical and thermal durability.<sup>137</sup> DCO-based fluorescent probes have been widely employed for both fluorescence imaging and the identification of biological species due to their good optical characteristics.<sup>138,139</sup> Importantly, red emission (>600 nm) and a significant Stokes shift (>100 nm) are the two important properties that make DCO fluorophores an appropriate probe skeleton for HSA detection. In 2022, Xu and co-workers<sup>140,141</sup> developed two fluorescent probes **7** and **8** (Figure 1.9) based on a TICT mechanism by coupling this electron acceptor DCO moiety with dimethylamino and julolidine moiety as an electron-donating group via a double bond (Figure 1.9).

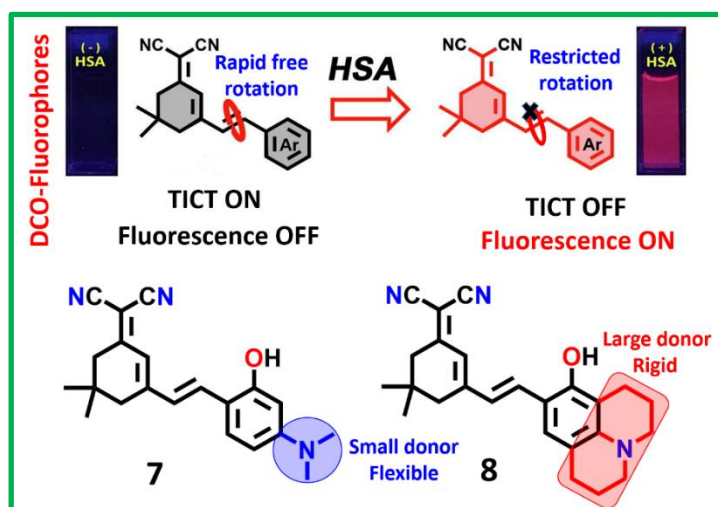


**Figure 1.9** Chemical structure of the TICT based DCO-fluorophores **7** and **8** for the serum albumins detection.

The donor group of both probes freely rotates around the carbon-carbon double bond in pure aqueous solution, generating a TICT state that turns the fluorescence "off". Once the probe attaches within the hydrophobic cavity of HSA or BSA, TICT activity is suppressed by constraining free intramolecular rotation due to the substantial steric hindrance and low-polarity environment inside HSA or BSA, resulting in fluorescence "on" (Figure 1.9). Upon addition of HSA, probes **7** and **8** exhibit 149- and 254-fold fluorescence enhancement, respectively, at 672 and 685 nm, with a LOD value of 11 and 4.64 nM, respectively. Probe **8** binds specifically with HSA over BSA and other proteins, while probe **7** cannot distinguish between HSA and BSA. The selective response toward HSA can be attributed to the rigid donor structure and steric hindrance of probe **8**. The drug displacement studies and molecular docking results indicate that both these probes bind with HSA at site I (subdomain IIA),

where the formation of the H-bond between the hydroxyl group and amino acid residues of HSA is a crucial factor for inhibiting the molecular rotation of probe molecules.

### 1.5.1.4 BODIPY Based Fluorescent Probes

BODIPY (4,4-difluoro-4-bora-3a,4a-diaza-s-indacene) dyes are popular fluorophores because of their exceptional photophysical characteristics, including good photostability, high quantum yields, and molar absorption coefficients.<sup>142</sup> In 2013, the Chang's group<sup>143</sup> synthesized a BODIPY-based HSA turn-on fluorescent probe **9** (Figure 1.10) that specifically binds with HSA at drug site II. Upon excitation at 520 nm, this probe exhibits a 41-fold increment in the emission intensity at 585 nm. More importantly, they observed that the emission of this probe does not overlap with that of dansyl fluorophores. As a result, they combined probe **9** with dansylamide (DNSA), a fluorescent probe that is specific to site I, to develop a straightforward, high-throughput method for the analysis of large collections of therapeutic drugs at HSA binding sites. This multiplex analysis may quickly reveal the HSA binding sites of novel molecular entities that provide a basic understanding of their pharmacodynamic profile and also give crucial information on drug interactions that clinicians may not have been aware of.

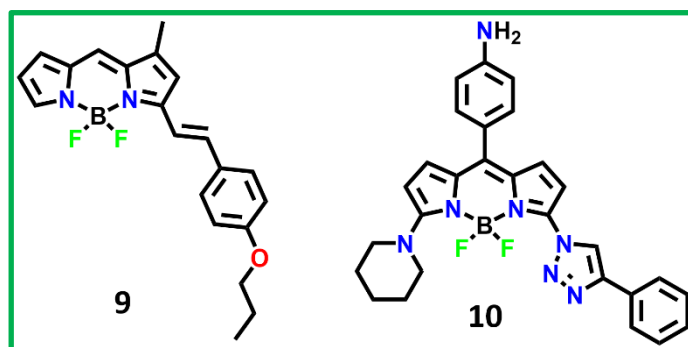


**Figure 1.10** Chemical structure of the probes **9** and **10** based on BODIPY scaffold for HSA detection.

However, one significant disadvantage of BODIPY dyes is their small Stokes shifts, which may restrict their experimental applications. So, in the same year, Chang's group<sup>144</sup> developed 40 BODIPY-triazoles with significant Stokes shifts (between 74 and 160 nm) by incorporating various triazole moieties linked with a piperidinyl substituent at positions 3 and 5 of the BODIPY scaffold.

## Chapter 1: Introduction

Then, after searching through composite libraries, they find a fluorescent probe **10** (Figure 1.10) that is selective for HSA and binds to the FA1 region of the protein with high specificity. Upon excitation at 460 nm, this probe displays a 220 times fluorescence enhancement at 575 nm toward HSA, with a detection limit of 0.3  $\mu\text{g/mL}$ . Additionally, probe **10** can be applied in clinical applications to measure HSA in urine samples that are within the range of microalbuminuria.

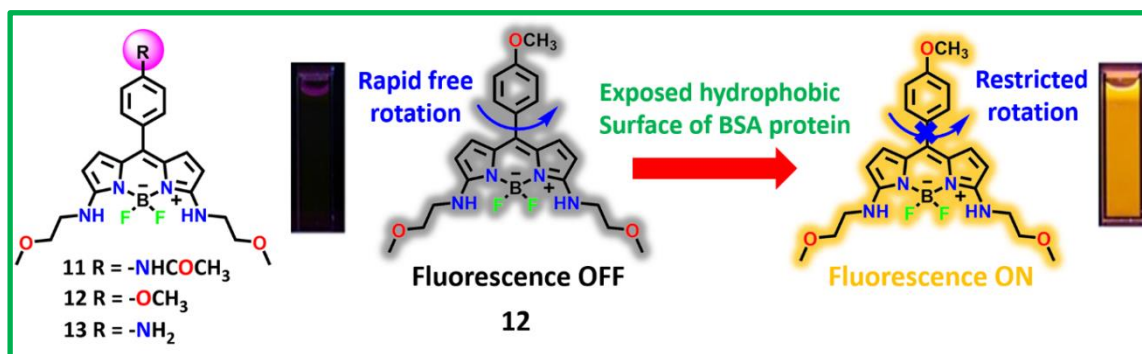


**Figure 1.11** Chemical structure of the probes **11-13** based on BODIPY scaffold and also a schematic representation of probe **12** for BSA detection.

Then, in the year 2015, for the purpose of hydrophobic sensing of proteins, Tiwari and coworkers<sup>145</sup> designed and synthesized three novel BODIPY-based hydrophobic sensors (HPsensors) **11**, **12** and **13** by substituting aryl groups with R = -NH<sub>2</sub>, -NHCOCH<sub>3</sub>, or -OCH<sub>3</sub> at the 8-position (meso) on the BODIPY scaffold (Figure 1.11). They used 2-methoxyethylamine substituent at the 3,5-positions on the BODIPY scaffold to make the dye more stable and soluble in polar environments, by improving the hydrogen bonding ability. These HPsensors exhibit weak fluorescence in aqueous solutions due to the rapid free rotation of the aryl substituents at the 8-position, which results in energy loss via non-radiative decays. In comparison to 8-anilino-1-naphthalenesulfonic acid (ANS), a widely used hydrophobic probe, these three HPsensors provide a substantially greater signal when measuring the surface hydrophobic properties of proteins (BSA, apomyoglobin, and myoglobin). However, HPsensors reveal a 10 to 60 fold enhancement in fluorescence intensity for the BSA protein, and this can be attributed to the restriction of free rotation of the aryl substituents due to their hydrophobic interaction with protein. More interestingly, HPsensor **12** exhibits a 60-fold improvement in fluorescence signal intensity for BSA when compared to ANS.

### 1.5.1.5 Cyanine Based Fluorescent Probes

Quinoline Blue, a compound with "a magnificent blue color," was developed in 1856 by C. H. G. Williams and it is the first cyanine dye.<sup>146</sup> Following that, cyanine dyes with various structural variations were developed further, which are increasingly used in the field of life sciences due to their exceptional photophysical characteristics and the quick advancement of fluorescent labelling technology. This type of dye structure can be easily controlled and modified. Its spectrum range encompasses the full visible light region, as well as the NIR region, providing a strong basis for its diverse uses.<sup>147</sup>

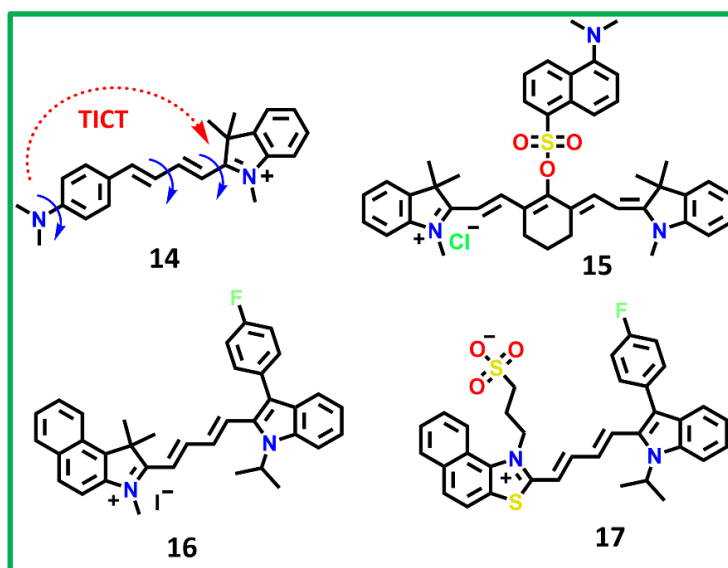


**Figure 1.12** Chemical structure of the probes **14-17** based on cyanine moiety for the serum albumins detection.

In 2015, Kumar's group<sup>148</sup> designed and synthesized a NIR fluorescent probe **14** based on the TICT phenomenon that responds to HSA with a high degree of specificity (**Figure 1.12**). Due to the TICT effect, this probe exhibits very little fluorescence in pure aqueous media. However, when it binds to HSA at subdomain IIA of site I, the hydrophobic protein environment inhibits the TICT effect, causing the probe to stabilize by taking on a planar shape and become highly fluorescent. Upon excitation at 550 nm, the emission intensity of probe **14** is increased by 12 times at 680 nm toward HSA with a LOD value of 11 nM. Then, in 2017, another highly light stable and nontoxic NIR fluorescent probe **15** (**Figure 1.12**) based on the cyanine moiety was also developed by Ghosh *et. al.*<sup>149</sup> for the accurate detection of albumin in various biofluids (blood serum and urine) and the imaging of liver targeting *in*

*vivo* albumin. The NIR excitation and emission ( $\lambda_{\text{ex}} = 740 \text{ nm}$ ,  $\lambda_{\text{em}} = 804 \text{ nm}$ ) of this probe enable improved depth tissue penetration and minimize autofluorescence from other biomolecules present in urine samples, allowing for more accurate serum albumin quantification. This probe exhibits a fluorescent silent emission band at 804 nm in an aqueous media, which is attributed to the development of aggregates. But, upon addition of BSA and HSA, probe **15** showed a 57- and 52-fold increase in fluorescence intensity, owing to the strong binding of the probe in the hydrophobic cavity of serum albumin. This probe has LOD values of 20 nM and 50 nM for BSA and HSA, respectively.

In 2018, Yang's group<sup>150</sup> reported two TICT based red-NIR fluorescent probes **16** and **17** (Figure 1.12) for the differential identification of HSA and BSA. With a detection limit of 0.66 mg/L for HSA, probe **16** exhibits a considerable enhancement of emission intensity toward HSA (100-fold at 676 nm) compared to BSA (33-fold at 664 nm). On the contrary, probe **17** shows the opposite selectivity toward BSA (50-fold at 648 nm), with a detection limit of 2.04 mg/L. The results of site marker displacement experiments and molecular docking indicate that probe **16** binds with HSA at subdomain IIA of site I, which is primarily dependent on the hydrophobic and  $\pi$ - $\pi$  interactions. While probe **17** binds with BSA at the interface between subdomains IIA and IIIA, which is primarily driven by strong H-bond interaction.

In 2020, Yang *et. al.*<sup>151</sup> effectively designed and synthesized a versatile TICT-based NIR fluorescent probe **18** (Figure 1.13) for the selective recognition of albumin proteins (HSA/BSA) in the NIR/far-red region. In an aqueous PBS buffer medium, this probe exhibits a weak broad emission band at 790 nm after being excited at 490 nm, which can be attributed to the participation of the TICT process. However, when probe **18** interacts with either HSA or BSA, its emission intensity is dramatically increased (536-fold for HSA at 668 nm and >500-fold for BSA at 673 nm), and this is due to the probe's strong binding to the hydrophobic pocket of HSA/BSA, where the TICT process is inhibited by the restriction in intramolecular rotation. The LOD value of this probe toward BSA is 23.7 nM. The probe is useful to track precisely the position of sentinel lymph node(s) in the mouse model by fluorescence imaging (NIR/red channel) technique.

In addition, the probe can respond to low polarity conditions and showed a preference for detecting cancer cells over healthy cells, as observed by the unique bioimaging investigations of the lipid droplets in the green emission channel (**Figure 1.13**).

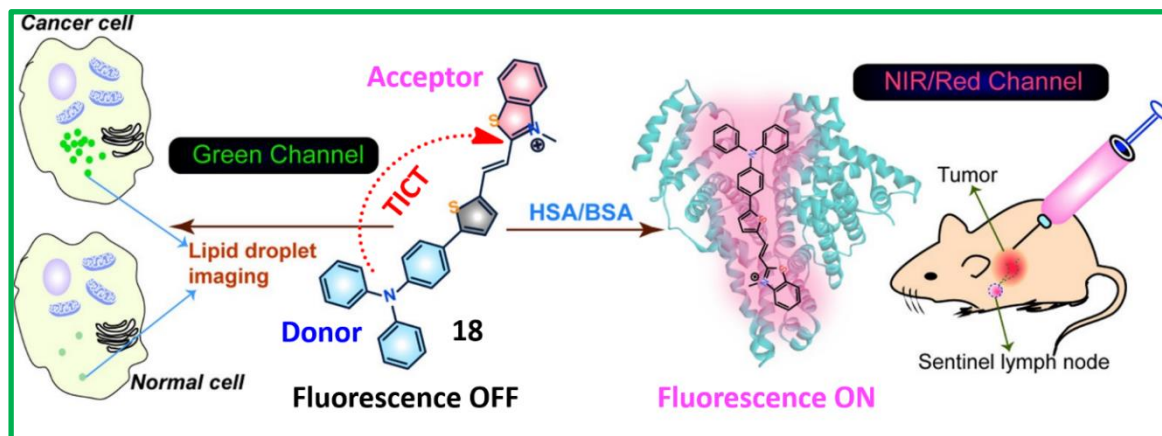


**Figure 1.13** Schematic representation of HSA/BSA recognition by fluorescent turn-on response of a cyanine-based probe **18** along with sentinel lymph node identification and potential cancer diagnosis using different emission channels. Adapted and modified with permission from ref. **151**. Copyright 2019 American Chemical Society.

Then Huang's group<sup>152</sup> also reported two NIR-fluorescent probes **19** and **20** (**Figure 1.14**) with a cyanine framework for the specific recognition of serum albumins. According to the site marker displacement study, MALDI-TOF spectra, and molecular docking theoretical results, **20** has a strong binding affinity ( $K_a = 1.1 \times 10^6 \text{ M}^{-1}$ ) and fluorescence "off-on" property for HSA at site I via hydrophobic, cation- $\pi$  and H-bond interactions, which enabled the quantitative measurement of HSA with a LOD value of  $9.96 \times 10^{-4} \text{ mg/mL}$ . Contrarily, the rigidity of the large 4-(tert-butyl) phenol group in control probe **19** prevented it from entering the hydrophobic pocket of site I in HSA (**Figure 1.14**), leading to the slightly enhanced fluorescence of probe **19** in presence of HSA. As HSA causes probe **20** to emit at 710 nm, it is possible to avoid the autofluorescence of biomolecules and accurately measure the amount of HSA present in real urine and serum samples, which also made it easier to do live cell imaging. Additionally, probe **20** may also be effectively used to track wound healing in live zebrafish.



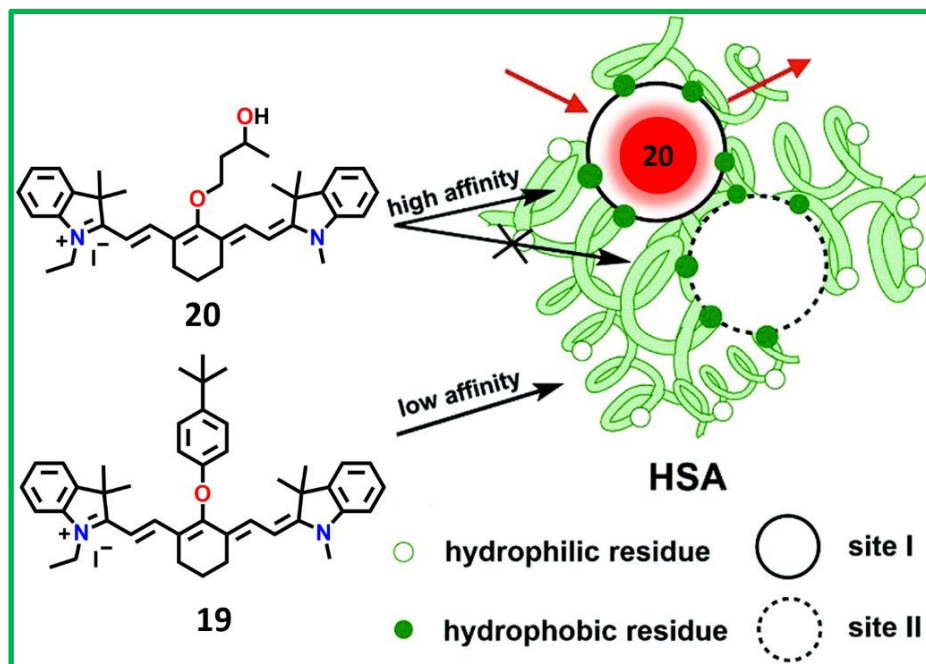


**Figure 1.14** Schematic representation of “turn-on” fluorescence response of cyanine based probes **19** and **20** for HSA. Adapted and modified with permission from ref. **152**. Copyright 2019 Royal Society of Chemistry.

### 1.5.1.6 Anthracene Based Fluorescent Probes

In 2017, Matczyszyn *et. al.*<sup>153</sup> synthesized an anthracene-based water soluble polycationic fluorescent probe **21** (Figure 1.15) and thoroughly investigated its binding interaction with HSA. The addition of increasing concentration of probe **21** resulted in a steady quenching of HSA fluorescence intensity along with a red shift of emission maxima from 346 to 350 nm. The analysis of fluorescence data from temperature dependent quenching experiments using the Stern-Volmer equation indicates that a static quenching process, i.e., the ground state complexation between probe **21** and HSA. When excited at 516 nm, this probe emits a bright fluorescence at 570 nm. The emission intensity of this probe rises with the progressive addition of HSA, accompanied by a 14 nm blue shift of the emission maxima, which is owing to the decrease in radiationless decay caused by the rotational inhibition imposed on the probe molecules. FRET and site-marker displacement studies reveal that binding of probe **21** occurs primarily at subdomain IIA of Site I in HSA.

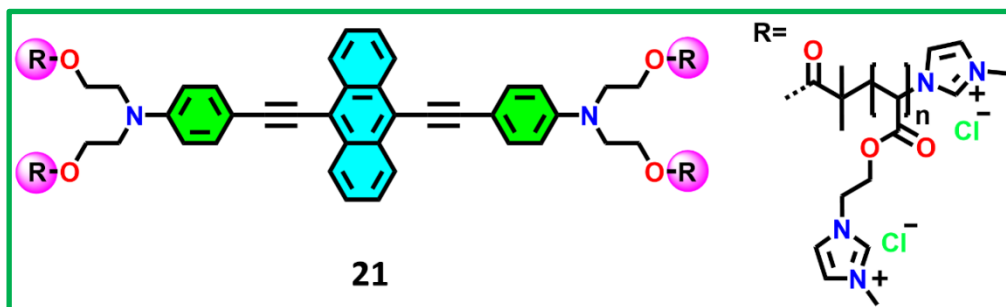


**Figure 1.15** Chemical structure of the probe **21** based on anthracene moiety for the serum albumins detection.

### 1.5.1.7 Naphthalene Based Fluorescent Probes

In 2017, Wang *et. al.*<sup>154</sup> developed a naphthalene moiety based fluorescent probe **22** (**Figure 1.16A**), which is highly selective and sensitive toward HSA over BSA and other biomolecules. When the probe is excited at 482 nm, it exhibits a substantial emission intensity enhancement toward HSA (360-fold at 562 nm) with a detection limit of 50 ng/mL. In addition, the binding of probe **22** to HSA is completed within seconds, and after that fluorescence intensity remains constant. Both site marker displacement assays and molecular docking simulations indicate simultaneous binding of **22** at subdomain IIA of site I and subdomain IIIA of site II of HSA. Moreover, with this probe, it is possible to find HSA concentration in dilute samples of human plasma and urine.

Then, a naphthalene-based amphiphilic fluorescent probe **23** (**Figure 1.16B**) has also been designed and synthesized by Das and colleagues<sup>155</sup> for specific binding and recognition of HSA. Upon excitation at 356 nm, probe shows a weak fluorescence at 500 nm in an aqueous medium. But, when HSA is added, a 14-fold enhancement in emission intensity was noted at 442 nm along with a 58 nm blue shift of emission maxima. The LOD value of this probe for HSA is 80 ng/mL. Probe **23** predominantly binds with HSA at site I mainly through hydrophobic interaction but it also exhibits a weak interaction at site II via both hydrophobic and H-bonding interactions.

In 2022, Xu *et. al.*<sup>156</sup> developed a TICT mechanism-based naphthalene fluorescent probe **24** (**Figure 1.16B**), which can specifically detect HSA/BSA without interference from other biomolecules. When the excitation wavelength is made at 510 nm, it shows a 212-fold enhancement in emission intensity for HSA at 630 nm, with a LOD value of 0.16  $\mu$ M.



The site marker studies reveal that probe **24** binds with both the drug binding sites of HSA i. e., site I and site II. Additionally, this probe may be used to image serum albumin in living cells.

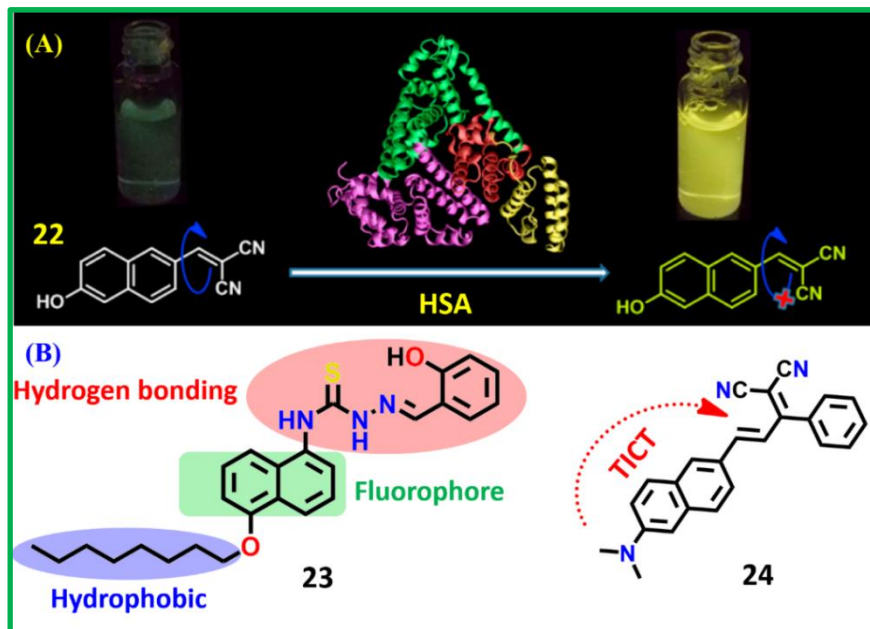


**Figure 1.16** (A) Schematic representation of a naphthalene-based probe **22** for HSA detection. (B) Chemical structure of naphthalene based fluorescent probes **23** and **24**. (A) is adapted and modified with permission from ref. **154**. Copyright 2017 Elsevier.

### 1.5.1.8 Carbazole and Coumarin Based Fluorescent Probes

Carbazole derivatives are a family of highly promising organic optoelectronic functional materials, and researchers are increasingly interested in using them to create organic photoluminescent, electroluminescent, and nonlinear optical materials.<sup>157</sup> In 2016, Ghosh et al.<sup>158</sup> developed a small chemical library of fluorescent molecular probes with various structural designs containing a common carbazole motif. They then screened a carbazole motif-based probe **25** (**Figure 1.17**) with exceptional performance using the structure-optical signaling relationship investigations. This probe not only detects serum albumins in biological fluids (serum and urine samples) with high sensitivity and accuracy, it also does not induce protein denaturation. With the addition of 5  $\mu\text{M}$  of HSA/BSA, probe **25** displays a 42- and 40-fold enhancement in emission intensity for HSA and BSA, respectively. The detection limits of this probe for HSA and BSA are 5 nM and 4 nM, respectively.

The molecular docking analysis reveals that probe **25** binds with HSA mainly at site I through hydrophobic interaction,  $\pi$ - $\pi$  interaction with the Trp unit, and the H-bonding interaction between the -OH group of probe **25** and the -COOH group of glutamine amino acid residue.

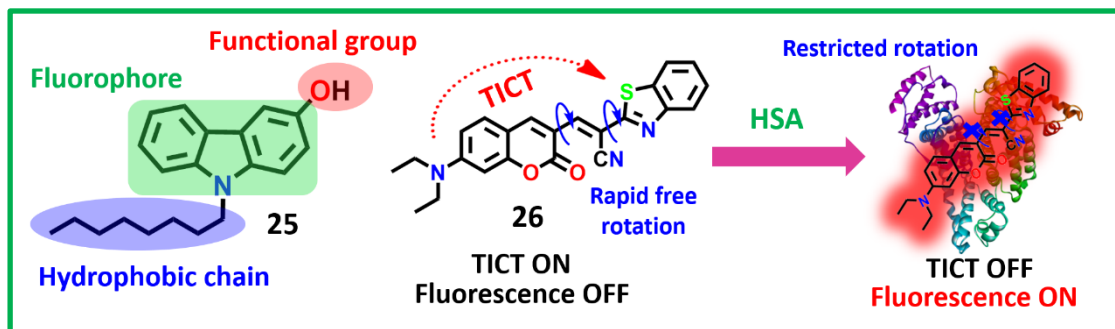


**Figure 1.17** Chemical structure of a carbazole-based probe **25** and a schematic diagram for the coumarin-based probe **26** toward HSA detection.

In 2020, Qu *et. al.*<sup>159</sup> synthesized a coumarin-based fluorescent probe **26** (Figure 1.17), that can selectively detect HSA without any biological interferences. Due to the existence of the TICT effect, this probe displays weak fluorescence at 583 nm in an aqueous buffer solution. But when HSA is added, the emission intensity at 583 nm increases noticeably and reaches equilibrium within 3 min. The estimated LOD value of this probe for HSA is 0.288 nM. Due to the incorporation of probe **26** into a hydrophobic binding cavity of HSA, nonradiative energy loss routes are blocked, and fluorescence is subsequently increased. According to drug displacement studies, probe **26** binds with HSA at both sites, but mostly at site II. Probe **26** can be used to image cells that have exogenously added HSA or that are undergoing endoplasmic reticulum-based HSA synthesis.

### 1.5.1.9 Pyridinium and Lepidinium Cation Based Fluorescent Probes

Pyridinium and lepidinium cations are frequently employed in the structural design of D- $\pi$ -A based TICT molecules because they are electron deficient groups having excellent biocompatibility and cell membrane permeability. In 2019, Ding *et. al.*<sup>160</sup> reported a TICT based fluorescent turn-on HSA/BSA probe **27** (Figure 1.18), in which a modified N, N-dimethylamino group is double-bonded to a pyridinium cation moiety to form an effective D- $\pi$ -A system.

Because of the TICT process, the probe has almost negligible fluorescence in aqueous medium. But, when it enters into the hydrophobic binding site I of HSA, the TICT process is restricted, leading to a strong fluorescence enhancement at 580 nm with a LOD value of 4.8 nM. For this probe, HSA detection process is quite fast and the spectral response remains steady for another 30 min. In 2021, Wang *et. al.*<sup>161</sup> developed another pyridinium cation based TICT probe **28** (Figure 1.18) that can selectively identify HSA over BSA and other biological interferences. Probe **28** displays a weak emission peak at 548 nm after being excited at 368 nm, but when it is trapped in hydrophobic subdomain IB cavity of HSA, the TICT process is suppressed, resulting in a 34-fold enhancement of the fluorescence signal at 540 nm. It has a detection limit of 0.06  $\mu$ M for HSA.

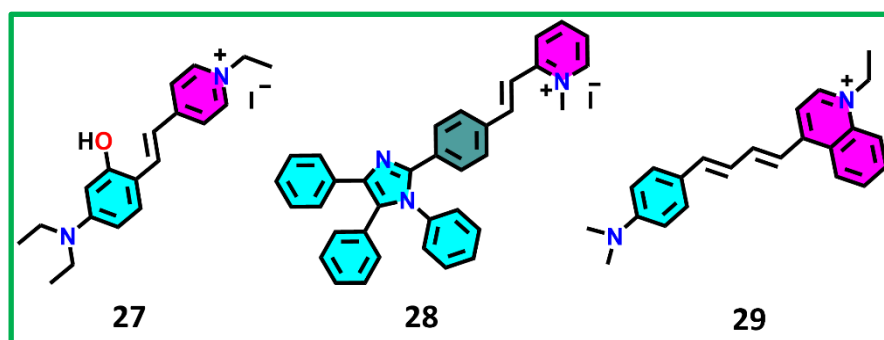


**Figure 1.18** Chemical structure of pyridinium and lepidinium cation based probes **27-29** for the serum albumins detection.

In 2018, Pal *et. al.*<sup>162</sup> synthesized a lepidinium cation based NIR fluorescent probe **29** (Figure 1.18) for the selective and sensitive detection of BSA. In an aqueous PBS buffer solution, probe **29** has an absorption band at 500 nm and it exhibits a very weak fluorescence at 763 nm owing to the TICT effect. But, when BSA is introduced into the medium, it binds with BSA at site I, resulting in a 40 nm red shift of the absorption maxima and a 75 nm blue shift of the emission maxima, along with a dramatic enhancement (500-fold) in fluorescence intensity. The detection limit of this probe is 48 nM for BSA. Moreover, probe **29** can be effectively employed for the quantitative measurement of albumin protein in serum samples.

### 1.5.1.10 Dimethylaminobenzyl and Rhodanine Based Fluorescent Probes

In 2015, Peng's group<sup>163</sup> developed four TICT based fluorescent probes **30-33** (Figure 1.19) on the D- $\pi$ -A framework for the detection of HSA in aqueous solution and solid state.

## Chapter 1: Introduction

Due to the TICT process, all the four probes exhibit extremely weak fluorescence in aqueous media at 541, 647, 620, and 770 nm, respectively. However, their fluorescence emission intensities are increased when they are incorporated into the hydrophobic binding cavity of HSA due to inhibition of the TICT process, along with blue shifts of emission maxima to 535, 590, 585, and 685 nm, respectively. Among them, probe **33** shows a remarkable fluorescence enhancement (428-fold) with a LOD value of 76.3 ng/L. The findings of drug displacement experiments indicate that binding to site I specifically causes the turn-on response of probe **30**, whereas binding to both sites I and II leads to the fluorescence increment of probe **33**. In addition, probe **33** can be used to measure albumin levels in human urine samples for the evaluation and diagnosis of renal function. More importantly, fluorescence imaging in living cells can be done by using **30-33**/HSA complexes.

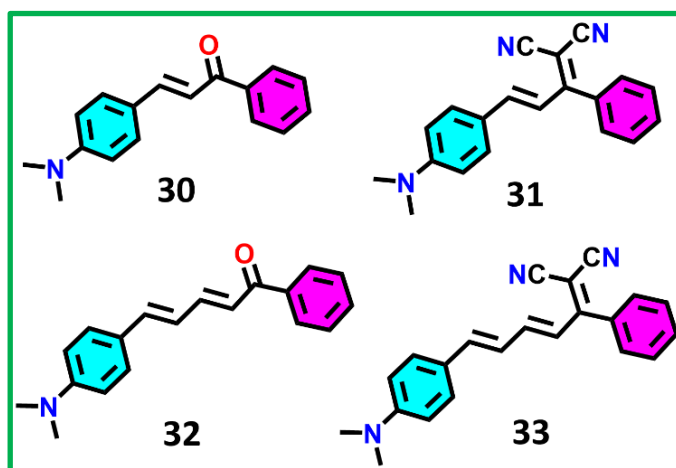


**Figure 1.19** Chemical structure of dimethylaminobenzyl-based probes **30-33** for the serum albumins detection.

The five-membered rhodanine moiety and its derivatives, having extensive pharmacological action, are significant in biomedical and pharmaceutical researches. Several rhodanine compounds are now undergoing clinical trials and show antibacterial, antiviral, and anticancer properties.<sup>164,165</sup> Additionally, due to its excellent electron acceptor properties, the rhodanine moiety is widely used in the structural design of D- $\pi$ -A based TICT probes. Du *et al.*<sup>166</sup> first synthesized a rhodanine moiety-based fluorescent probe **34** (Figure 1.20A) that emits a yellow light when it recognizes HSA with high selectivity and sensitivity.

It has a weak fluorescence at 574 nm due to the existence of the TICT mechanism, but in the presence of HSA the TICT process is inhibited resulting a remarkably fluorescence enhancement (100-fold), with a LOD value of 0.13 mg/L. Its HSA response time is within 10 s. In contrast to the two well-known drug binding sites, probe **34** is located at the FA1 region in HSA. In 2018, Zhu *et al.*<sup>167</sup> developed another rhodanine based TICT probe **35** (**Figure 1.20A**), which is highly selective for HSA detection. It outperforms the earlier probe in terms of excellent selectivity for HSA over BSA, sensitivity (LOD 5 nM, >700-fold increase in fluorescence intensity), and stability of fluorescence signal (over 24 h). However, the probe **35** has certain limitations, including a relatively sluggish HSA reaction time (1 hour) and the fact that it binds with HSA at more than one binding site (i. e., sites I and II). The same year, their research team reported one more TICT probe **36** (**Figure 1.20A**), based on the rhodanine moiety, which is also specific for HSA over BSA.<sup>168</sup> One main difference is that they used a quinoline ring in place of the benzene ring and with this modification, the HSA response time is significantly reduced to 5 s only. Both the probes **34** and **36** can be used for the quantitative measurement of trace HSA in human urine samples.

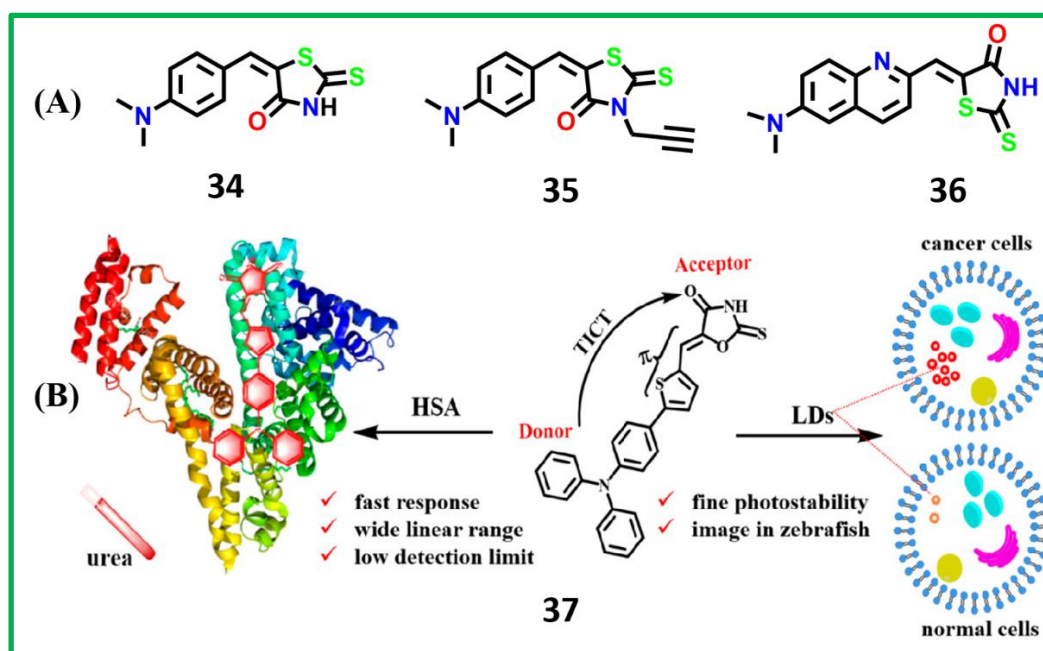


**Figure 1.20** (A) Chemical structure of rhodanine-based fluorescent probes **34-36**. (B) Schematic representation of a rhodanine-based probe **37** for HSA detection. Adapted with permission from ref. **169**. Copyright 2021 American Chemical Society.

Then, in 2022, Dong's group<sup>169</sup> designed and synthesized a TICT probe **37** (Figure 1.20B) based on a rhodanine moiety that has great sensitivity to microenvironment (polarity and viscosity), which can be used to detect HSA in real urine samples along with lipid droplets (LDs) imaging in zebrafish with turn-on red emission. It can specifically detect HSA with moderate response time (10 min), excellent sensitivity (LOD 0.34  $\mu\text{g/mL}$ , ~60-fold emission intensity enhancement at 610 nm), and wide linear detection range (0.00–0.30 mg/mL). Probe **37** enters into the hydrophobic IB domain of HSA, which suppresses the TICT action by restricting the intramolecular rotation, resulting in the bright red fluorescence. Additionally, using microenvironment-guided specific lipid droplet cell imaging, this probe has great capacity to distinguish between cancer and non-cancer cells.

### 1.5.1.11 Fluorescein Based Fluorescent Probes

Fluorescein is a well-known fluorophore moiety that is employed in the structural design of a wide range of fluorescent molecular probes. The two benzene rings are held together through an oxygen bridge bond, giving the molecule a rigid coplanar structure that allows it to produce intense fluorescence when exposed to excitation light. Many researchers have modified its structure to enhance its efficacy in applications. In 2014, Koide *et. al.*<sup>170</sup> successfully synthesized a fluorescein-based fluorescent probe **38** (Figure 1.21) and provide a new method for the measurement of HSA in human serum samples. Upon addition of HSA to a pale yellow-green solution of probe **38**, the solution turns red under natural sunlight, along with red shifts of the absorption maxima from 501 to 514 nm and the emission maxima from 522 to 534 nm, respectively. According to these spectroscopic investigations, the dehydration of probe **38** and/or stability of the tritylic cation species may be the cause of alterations of the absorption and emission spectra upon HSA binding (Figure 1.21). Compared to the BCG approach, this new technique is >30 times more sensitive and superior.

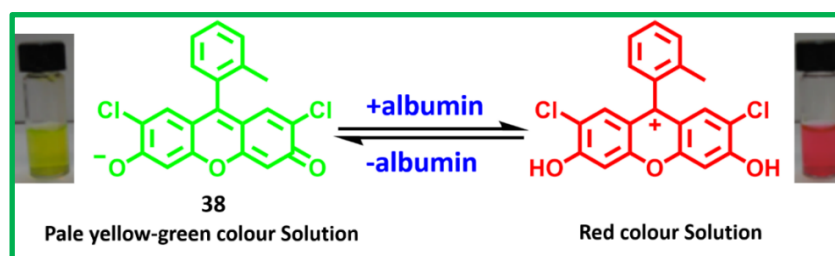


**Figure 1.21** Schematic representation of a fluorescein-based probes **38** for the serum albumins detection.



### 1.5.1.12 Julolidine and Rosamine Based Fluorescent Probes

The julolidine moiety is an excellent fluorophore, and julolidine-containing fluorescent probes often have strong water solubility. In 2014, Tang and colleagues<sup>171</sup> developed a molecular rotor design-based fluorescent probe **39** (Figure 1.22) by coupling the julolidine group with methyl cyanoacetate for urinary albumin detection. In an aqueous PBS buffer medium, it shows very little fluorescence ( $\Phi = 0.0022$ ) as a result of the completely unrestricted torsional rotation. However, when HSA is added, the probe enters the hydrophobic cavity of subdomain IIA, which inhibits the torsional rotation, leading to a significant increase in fluorescence intensity (400-fold). In fact, when HSA is added to the non-emissive solution of probe **39**, it produces a strong blue fluorescence, along with blue shifts of the absorption maxima from 464 to 456 nm and the emission maxima from 500 to 490 nm, respectively. The LOD value of this probe is 6 nM toward the HSA detection. The probe can be used to measure the urinary albumin level effectively.

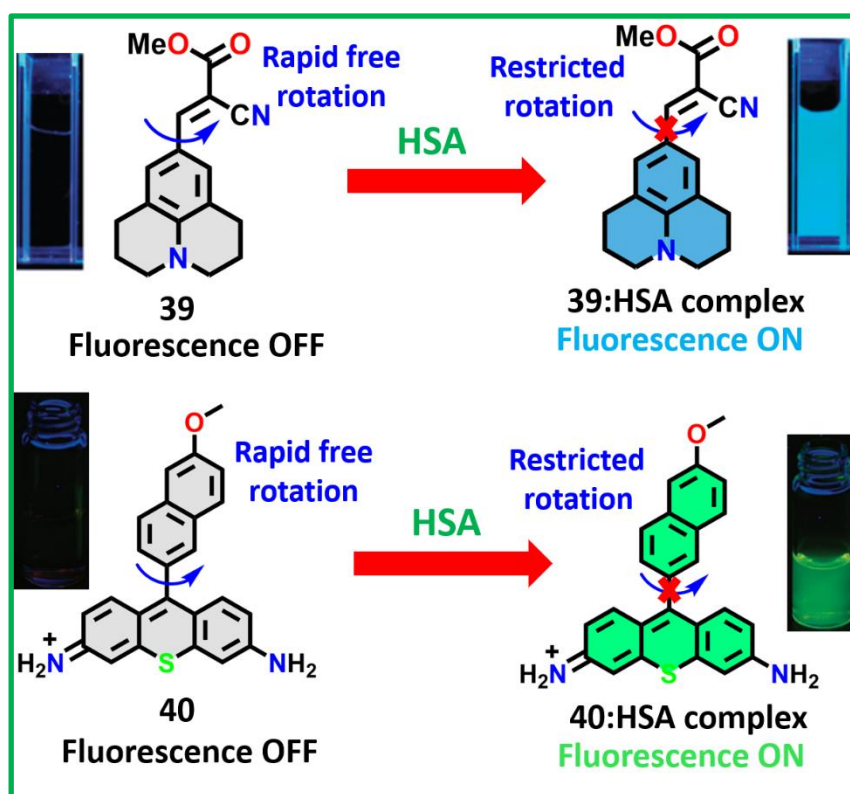


**Figure 1.22** Schematic representation of a Julolidine-based probe **39** and a rosamine-based probe **40** for the recognition of HSA.

Rosamine molecules, unlike rhodamine, lack a carboxyl group in position 2, making it impossible to form an inner five-membered ring structure.<sup>172</sup> Rosamine molecules exhibit excellent photostability, and they are pH insensitive. Nevertheless, the spectroscopic properties of rosamine dyes are comparable to those of rhodamine dye, with a maximum absorption and fluorescence emission (520-600 nm) that are closer to the red region. The use of rosamine moiety in the construction of fluorescent probes has received a lot of attention. In 2008, Chang *et al.*<sup>173</sup> reported a rosamine-based potential HSA sensor **40** (Figure 1.22). In PBS buffer media, it exhibits negligible fluorescence ( $\Phi = 0.019$ ) at 544 nm, but when it is combined with HSA, its emission intensity increases ( $\Phi = 0.20$ ) by nearly 36 times at 554 nm, with a corresponding 10 nm red shift of the emission maxima. It binds to HSA both at site I and Site II.

### 1.5.1.13 Schiff Base Based Fluorescent Probes

In 2017, Yang *et al.*<sup>174</sup> coupled the triphenylamine and benzo-15-crown-5 moieties to develop the Schiff base based fluorescent probe **41** (Figure 1.23), which can detect HSA through the TICT mechanism. It has almost negligible fluorescence in aqueous PBS buffer solution. Following the addition of HSA, the triphenylamine and crown ester groups of the probe **41** bind with HSA at sites I and II, respectively. As a consequence, the TICT process is suppressed and the fluorescence intensity is increased (32-fold). The probe has LOD values of 1.7 nM and 29.5 nM for HSA in PBS solution and a urine sample, respectively.

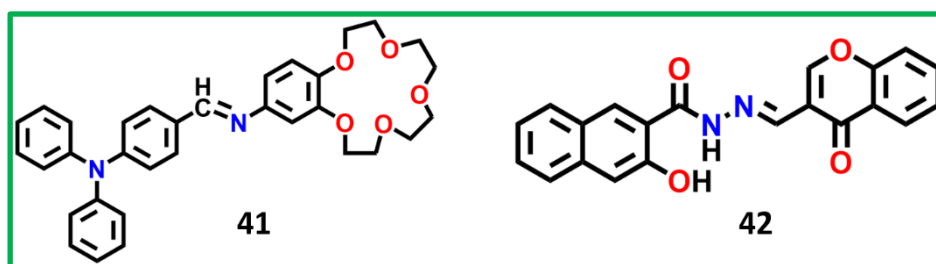


**Figure 1.23** Chemical structure of schiff-base based probes **41** and **42** for the serum albumins detection.

In 2021, Xu *et al.*<sup>175</sup> developed another Schiff base based fluorescent probe **42** (Figure 1.23), which can differentially detect HSA and BSA. When excited at 370 nm, it emits a very faint fluorescent signal ( $\Phi = 0.001$ ) at 424 nm. Upon addition of HSA and BSA, its emission intensity is 141-fold enhanced at 527 nm for HSA and 104-fold enhanced at 492 nm for BSA,



respectively. According to  $3\sigma/\text{slope}$  method, the LOD values of probe **42** for HSA and BSA are 10.62 nM and 16.03 nM, respectively. Site marker studies and molecular docking analysis indicate that probe binds with HSA at site I hydrophobic cavity and with BSA at non-drug binding site. This probe is non-toxic in nature and it can be effectively used for cell imaging of HSA in cancer cells, which differ greatly from normal cells and promotes implementation in medical diagnosis.

### 1.5.1.14 GFP Based Fluorescent Probes

GFP (Green Fluorescent Protein) has been constructed as a fluorescent label to be utilised as a fluorescent sensor for a number of targets, such as pH values, metal ions, and tiny biomolecules. The GFP chromophore was successfully used by the Xiao group in the design of HSA sensors. In 2016, they designed and synthesized an effective HSA sensor **43** (Figure 1.24) based on this GFP chromophoric moiety.<sup>176</sup> Without interference from other biomolecules, it binds with HSA at subdomain IIA of site I via the FRET process with excellent selectivity and sensitivity. When excited at 425 nm, Probe **43** is non-fluorescent, but the addition of HSA (530  $\mu\text{g}/\text{mL}$ ) causes its fluorescence intensity to be 43 times greater at 584 nm with a LOD value of 198.6 ng/L.

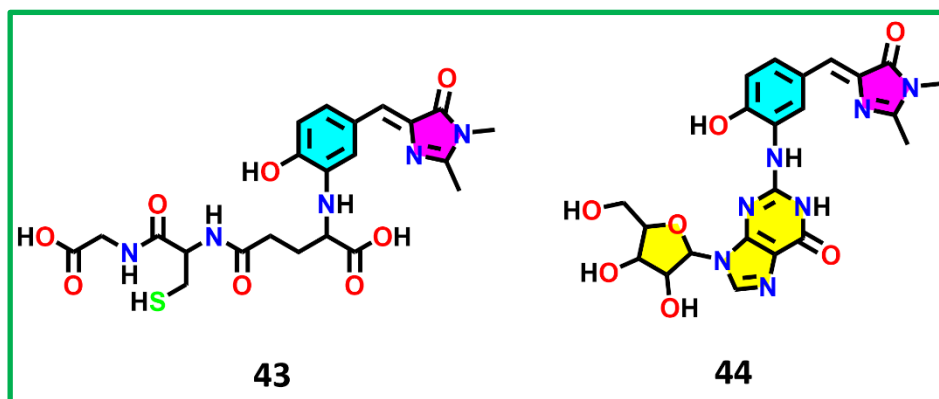


**Figure 1.24** Chemical structure of GFP-based probes **43** and **44** for the HSA detection.

The following year, they improved the original probe by incorporating guanine riboside into the GFP chromophore and created an efficient HSA sensor **44** (Figure 1.24) with a response time of less than 1 min.<sup>177</sup> Due to the bond twisting in the excited state, it is also fluorescent silent, when it is excited at 425 nm. However, the presence of HSA increases the emission intensity by 27 times at 585 nm, with a LOD value of 15.09 ng/mL.

The drug inhibitor investigations show that probe **44** binds with HSA at the site I hydrophobic cavity, which causes the flexibility of the probe to become rigid and leads to an increase in the fluorescence signal.

### 1.5.1.15 Chalcone Based Fluorescent Probes

In 2018, Wang *et. al.*<sup>178</sup> developed a TICT-based environment sensitive fluorescent probe **45** (Figure 1.25) using the chalcone moiety for the specific detection of HSA, with a response time of seconds. Its fluorescence emission intensity dramatically increases at 535 nm with the addition of 1 equivalent of HSA by the inhibition of the TICT mechanism inside the hydrophobic cavity at site I, and the LOD value is 0.57 mg/L. Additionally, the investigation also demonstrated that the probe **45** can effectively measure the HSA levels in blood samples from both healthy individuals and patients with hypoalbuminemia. In the same year, Cui his colleagues<sup>179</sup> also synthesized a TICT-based fluorescent probe **46** (Figure 1.25), which exhibits weak fluorescence in an aqueous PBS buffer solution upon excitation at 436 nm. However, it exhibits exceptional selectivity for HSA among other proteins, with a significant fluorescence increment (160-fold) at 524 nm and provides a broader linear range of HSA (0 to 100 mg/L) with LOD = 1.9 mg/L, determined by  $3\sigma/\text{slope}$  method. Drug inhibition assay and molecular docking analysis reveal that probe **45** binds with HSA at both hydrophobic subdomains IIA and IB.

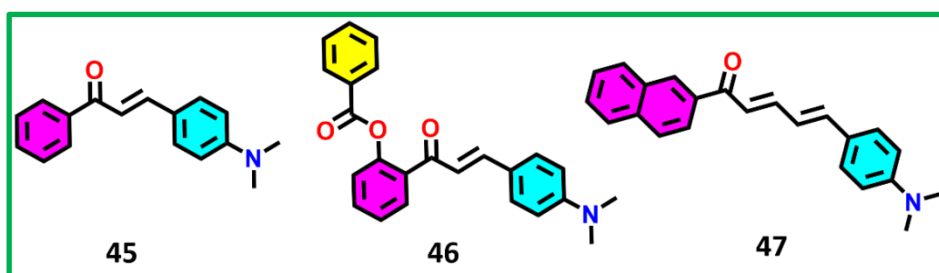


**Figure 1.25** Chemical structure of chalcone-based probes **45-47** for the serum albumins detection.

Then, in 2022, Peng *et. al.*<sup>180</sup> successfully synthesized a highly conjugated novel red-emissive fluorescent probe **47** (Figure 1.25) based on the TICT mechanism for urinary albumin detection. The fluorescence emission intensity of this probe is significantly increased at 610 nm in an aqueous PBS buffer medium upon incremental addition of serum albumin, with response time within 3 min.

The probe has LOD values of 23 nM and 61 nM for HSA in PBS solution and a urine sample, respectively. Additionally, using a straightforward home-made test equipment (POC based), this probe may be used to assess directly both A2-level and A3-level albuminuria in actual urine samples. Probe **47** binds with HSA at both hydrophobic sites I and II.

### 1.5.1.16 Flavonoid Based Fluorescent Probes

Flavonoids are commonly regarded as effective anticancer agents in a variety of natural products. However, recent research has demonstrated that the specific interaction of the chromone ring of flavonoids with the inner hydrophobic cavity of serum albumin may contribute to the increased binding of flavonoids to serum albumin.<sup>181,182</sup> In 2015, Pang *et al.*<sup>183</sup> designed and synthesized a set of fluorescent probes **48a-48f** (Figure 1.26) based on flavone moiety for the recognition of albumin in real blood samples and polyacrylamide gels. Here, the addition of BSA (1.0 mg/mL) increases the fluorescence intensity of probes **48a-48f** by 38, 740, 170, 1100, 7, and 29 times, respectively with corresponding detection limits toward BSA are 2.6, 0.14, 0.59, 0.09, 14, and 3.4  $\mu\text{g/mL}$ . A greater fluorescence response of the probes **48b-48d** suggest that the alkyl group present at the 6-position of flavone moiety may be responsible for the significantly enhanced interactions between flavone and water or protein. The experimental outcomes show that the probe **48d** has better serum albumin sensitivity and selectivity with the capacity to measure the albumin content in samples of monkey serum and may be used effectively for protein staining in polyacrylamide gels.

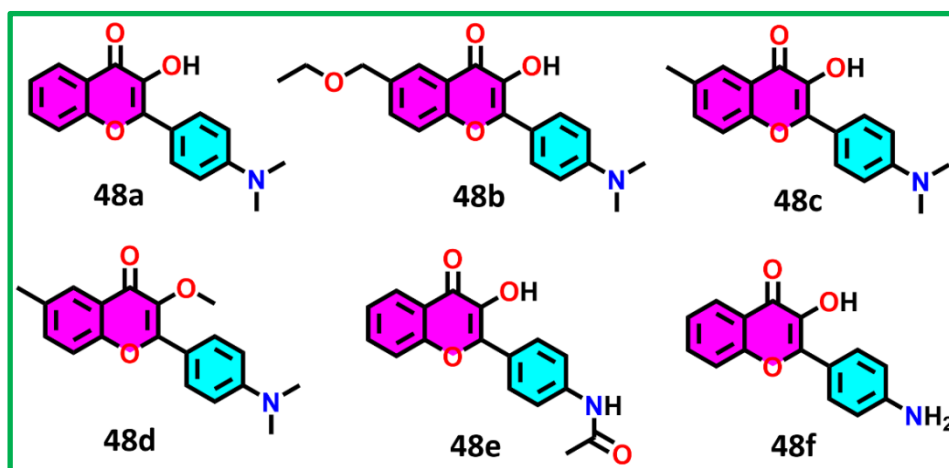
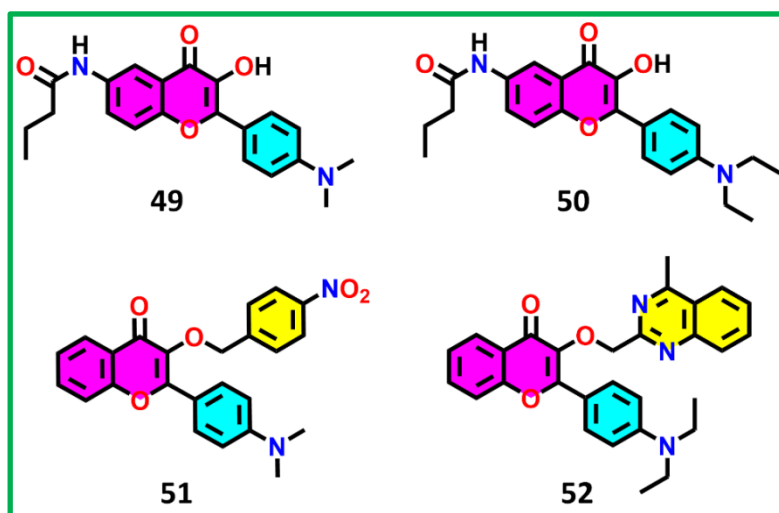


Figure 1.26 Chemical structure of flavonoid-based probes **48a-48f** for the BSA detection.

## Chapter 1: Introduction

In 2016, Liu and colleagues<sup>184</sup> modified the chromone scaffold of flavonoids with an amide group and enhanced the H-bond donors ability to improve the specific binding of the flavonoid derivatives with serum albumin. Keeping this view in mind, they synthesized two D- $\pi$ -A based fluorescent probes **49** and **50** (Figure 1.27) for the selective recognition of HSA. Upon addition of 1 equivalent of HSA, **49** and **50** exhibit significant fluorescence enhancements of 320-fold at 508 nm and 75-fold at 517 nm, respectively. According to the  $3\sigma$ /slope method, the estimated LOD values are 94 nM and 380 nM for **49** and **50**, respectively. Among them, probe **49** shows higher selectivity and sensitivity toward HSA, without interference from other biomolecules. In the comparison test between **49** and BCG methods for the colorimetric assessment of HSA, the relative apparent concentration of HSA measured by the **49** method is generally stable, whereas the apparent concentration of HSA using the BCG method steadily increases for 10 min.



**Figure 1.27** Chemical structure of flavonoid-based probes **49-52** for the HSA detection.

In 2019, Liu *et al.*<sup>185</sup> also developed a flavonoid-based fluorescent probe **51** (Figure 1.27) by integrating a nitrobenzene quencher into a previously described polarity-sensitive fluorescent probe **48a**, enabling the reliable estimation of HSA in a real blood sample without the interference from blood lipids. It exhibits better selectivity for HSA among other proteins, with a substantial fluorescence intensity enhancement (>60-fold) at 490 nm and provide a wide linear range of HSA concentration from 0 to 10  $\mu$ M. Its response time for HSA is very rapid (<10 s). This probe has a low LOD value of 32 nM for HSA. Site marker investigations

and the docking analysis indicate that probe **51** predominantly binds with HSA in the hydrophobic cavity at site I.

In 2022, Yuan group and colleagues<sup>186</sup> proposed an innovative strategy based on TICT and ESIPT mechanisms for the development of another fluorescent probe **52** (Figure 1.27), which can selectively detect HSA over BSA and other biomolecules. Upon excitation at 405 nm, the addition of HSA to the solution of this probe increases the emission intensity by 1042 times ( $\Phi = 0.45$ ) at 463 nm with a strong blue fluorescence, but only by 1.8 times when BSA is added. Here, it should be mentioned that the fluorescence response time of probe **52** for HSA is within 3 minutes, and its emission intensity displays excellent linearity in the region of 0 to 0.25  $\mu\text{M}$  HSA. The estimated binding constant ( $K_b$ ) between probe **52** and HSA is  $7.71 \times 10^5 \text{ M}^{-1}$ , indicating a strong binding affinity for HSA. According to  $3\sigma/\text{slope}$  method, the LOD value of this probe toward HSA is 4.14 nM. This probe primarily binds with HSA at subdomain IB. Additionally, probe **52** provides faster and more accurate microalbumin detection in human urine samples than the commercial BCG approach.

### 1.5.1.17 Squaraine Dye Based Fluorescent Probes

A typical squaraine dye structure consists of two electron donating (D) groups and an electron accepting (A) four-membered quaternary acid ring core, resulting in a strong intramolecular D–A–D electronic structure. In 2010, Ramaiah *et. al.*<sup>187</sup> synthesized three squaraine dyes **53-55** (Figure 1.28), which can effectively interact with HSA/BSA and show site selectivity, involving combine effects of hydrophobic, H-bonding, and electrostatic interactions. These dyes absorb strongly between 580 and 620 nm. Unfortunately, they are unable to discriminate between HSA and BSA. The addition of HSA enhances the fluorescence intensity of all these three dyes, with bathochromic shifts in emission maxima from 600 to 623 nm, 625 to 640 nm, and 634 to 646 nm, respectively, for the dyes **53**, **54**, and **55**. The binding constants between these dyes with HSA/BSA have been calculated and are found to be  $1.4 \times 10^6$ ,  $4.9 \times 10^6$  and  $4.1 \times 10^5 \text{ M}^{-1}$ , respectively, for the dyes **53**, **54**, and **55** with BSA, whereas HSA shows relatively higher binding constants of  $1.4 \times 10^6$ ,  $6.0 \times 10^6$  and  $9.9 \times 10^5 \text{ M}^{-1}$ . The site marker analysis indicates that halogenated dyes **54** and **55** bind predominantly at site II of HSA/BSA than at site I due to steric restrictions, while dye **53** binds at both sites I and II.

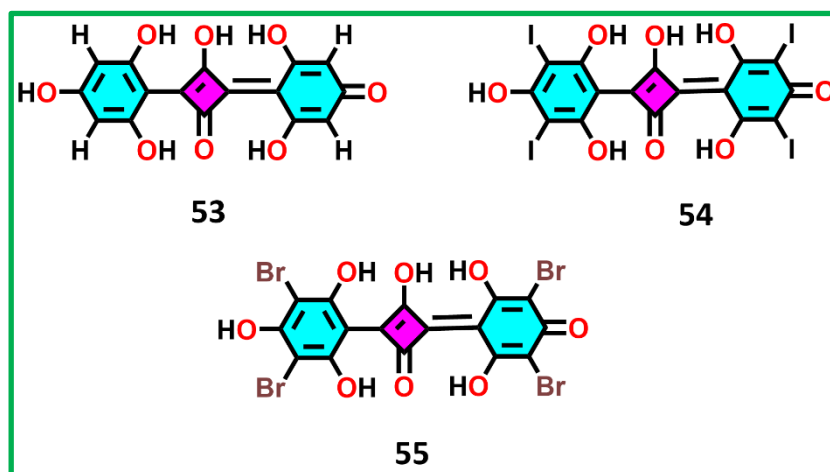


**Figure 1.28** Chemical structure of squaraine dye-based probes **53-55** for the serum albumins detection.

### 1.5.2 Aggregation induced emission (AIE) based fluorescent probes

The second design strategy for the development of serum albumin sensors is based on the aggregation-induced emission (AIE) properties of fluorophores. The AIE phenomenon was first reported in 2001 by Tang and colleagues.<sup>188</sup> Since then, several AIE-active compounds have been employed effectively as fluorescent sensors for metal ions, pH, temperature, and various bioanalytes.

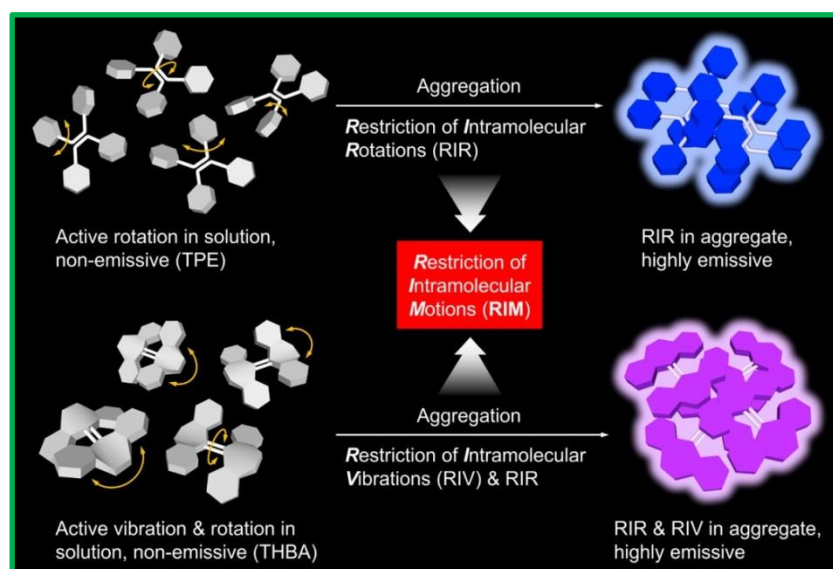


**Figure 1.29** Schematic representation depicting the mechanisms of the AIE phenomenon. Adapted with permission from ref. **189**. Copyright 2018 American Chemical Society.

In summary, AIE fluorophores are a type of substances that are slightly emissive or completely non-emissive in dilute aqueous solutions (i.e., discrete molecular state) but produces extremely bright fluorescence in aggregated and solid forms. Generally, it is believed that the restriction of intramolecular rotations (e.g., propeller-like tetraphenylethene, TPE moiety) and restriction of intramolecular vibrations (e.g., shell-like THBA moiety) are the main mechanisms used to explain the AIE phenomena (**Figure 1.29**).<sup>189</sup>

In 2010, Tang *et. al.*<sup>190</sup> developed a water-soluble AIE fluorescent probe **56** (**Figure 1.30A**) based on tetraphenylethylene (TPE) moiety for the selective recognition and quantification of HSA. In PBS buffer, this probe is weakly luminescent at 390 nm, but after the addition of 10  $\mu\text{M}$  HSA its fluorescence intensity is significantly enhanced ( $\sim 300$ -fold at 475 nm) with a low LOD value of 1 nM. This AIE probe has a wide linear operating range of HSA concentration from 0 to 100 nM. According to computational studies, charge neutralization, H-bonding, and hydrophobic interactions help this probe to bind with HSA at the hydrophobic cleft between subdomains IIA and IIIA, making it strongly emissive due to the restriction of intramolecular rotations of the probe in the entrapped state. Additionally, this probe may be used to identify urinary albumin as well as a quick and sensitive protein staining dye for the detection of HSA in gel electrophoresis analysis.

In 2013, Wenjing *et. al.*<sup>191</sup> used the anthracene moiety to synthesize another water-soluble AIE-based BSA sensor **57** (**Figure 1.30A**). The probe has weak fluorescence in PBS buffer, but upon addition of BSA (70  $\mu\text{g}/\text{mL}$ ), its fluorescence intensity is increased at 525 nm by 600 times with a linear correlation of HSA concentration from 0 to 60  $\mu\text{g}/\text{mL}$ . According to the further experimental outcomes, it is evident that the interaction between this probe and BSA is mostly hydrophobic in nature. In the same year, Tong and colleagues<sup>192</sup> also designed and synthesized a Schiff-base based AIE fluorescent probe **58** (**Figure 1.30B**), which can give a ratiometric response to BSA/HSA via hydrophobic interactions. It is observed that this probe experienced deprotonation in PBS buffer (pH 7.4) and produced blue fluorescence at 436 nm. When BSA/HSA is added to this probe's solution, the emission intensity drops at 436 nm and increases at 518 nm, resulting in a visible change in the fluorescence colour from blue to green. The emission intensity ratios,  $I_{518}/I_{436}$  are linearly correlated with the added concentrations of BSA (0-900  $\mu\text{g}/\text{mL}$ ), and HSA (100-700  $\mu\text{g}/\text{mL}$ ). The LOD values for BSA and HSA are 16.12  $\mu\text{g}/\text{mL}$  and 10.5  $\mu\text{g}/\text{mL}$ , respectively.



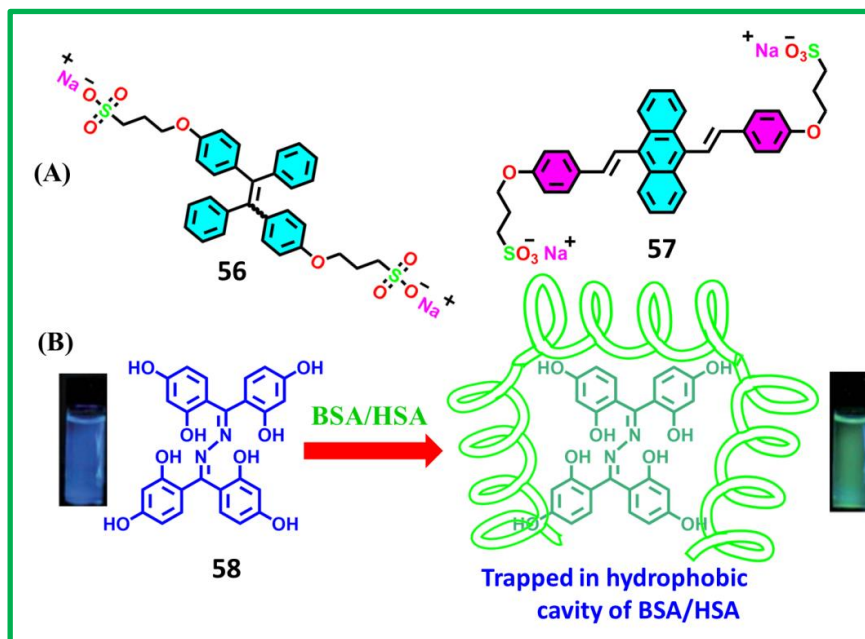


**Figure 1.30** (A) Chemical structure of AIE fluorescent probes **56** and **57** based on TPE and anthracene moiety, respectively. (B) Schematic representation of a Schiff-base based AIE fluorophore **58** toward BSA/HSA detection.

In 2015, Dong's group<sup>193</sup> designed and developed an AIE active fluorescent probe **59** (**Figure 1.31**), which can quantitatively detect HSA/BSA in blood serum. Upon photoexcitation at 310 nm, this probe produces a weak fluorescence at 443 nm in PBS buffer. However, upon addition of BSA (150  $\mu\text{g/mL}$ ), its fluorescence intensity is increased at 443 nm by 9 times with a linear correlation of BSA concentration from 2.18 to 70  $\mu\text{g/mL}$ . Similarly, the emission intensity is also linearly correlated with the concentration of added HSA from 1.68 to 100  $\mu\text{g/mL}$ . For BSA and HSA, the LOD values are as low as 2.18  $\mu\text{g/mL}$  and 1.68  $\mu\text{g/mL}$ , respectively. Additionally, this probe has a rapid response time ( $< 6$  s) towards BSA. According to an unfolding process triggered by guanidine hydrochloride, selective hydrophobic and H-bonding interactions between this probe and HSA/BSA are the primary cause of the fluorescence light up in the binding state. The quantitative measurement of BSA in fatal bovine serum is successfully accomplished with this probe.

Then, in 2017, Hu *et al.*<sup>194</sup> synthesized an AIE active amphiphilic fluorescent probe **60** (**Figure 1.31**) for the selective detection of HSA. This probe has a rotatable N-N single bond joining two fluorophore moieties together.



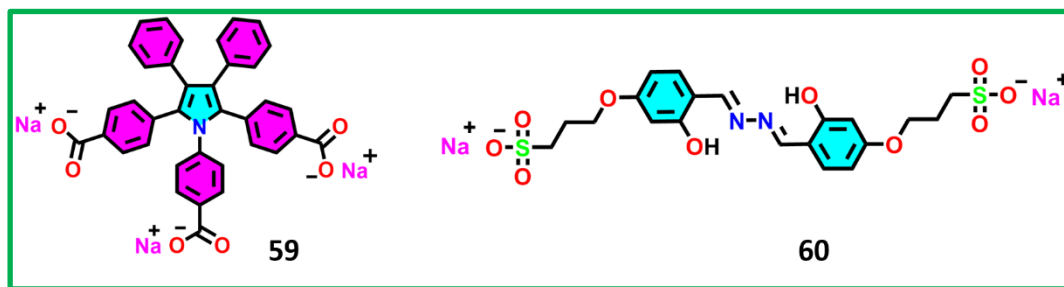


**Figure 1.31** Chemical structure of AIE fluorophores **59** and **60** for the HSA/BSA detection.

Upon excitation at 355 nm, this probe exhibits a weak fluorescence at 517 nm owing to the flexible rotation around the N-N single bond. Whereas, addition of 1000 µg/mL HSA causes a substantial increase in fluorescence intensity (50-fold) at 508 nm, which is ascribed to the inhibition of intramolecular rotation around the N-N bond inside the hydrophobic binding cavity of HSA through the hydrophobic and H-bonding interactions. In addition, its fluorescence intensity is linearly correlated with the added concentration of HSA from 0 to 100 µg/mL and it has a low LOD value of 6.11 µg/mL for HSA. Molecular docking study reveals that probe **60** binds at the long and narrow cavity in the core of HSA rather than drug sites I and II.

In 2018, Bhattacharya *et al.*<sup>195</sup> synthesized an amphiphilic fluorescent probe **61** (**Figure 1.32A**) with a carbazole moiety that can produce thermoreversible, pH-sensitive nanoaggregates in water at pH 6.0. Though this probe displays monomeric emission at 400 nm due to the existence of uniformly distributed building components, the addition of HSA quickly alters the fluorescence colour from blue to cyan by generating a new emission band at 454 nm. A concentration-dependent fluorescence study using HSA shows that at low HSA concentrations (0-25 mg/L), quenching of fluorescence arises at 400 nm, but at high HSA concentrations (30-80 mg/L), fluorescence amplification occurs at 454 nm. The estimated LOD value for HSA is 0.27 mg/L. Mechanistic studies show that the probe binds non-specifically to the negatively charged surfaces of HSA via electrostatic interactions, producing a "turn-off" response at 400 nm, whereas enclosing the probe molecule in the hydrophobic binding cavity of subdomain IIA induces a "turn-on" response at 454 nm (MICE effect). Additionally, this probe is capable of accurately measuring the amount of HSA present in a variety of biofluids, such as saliva, blood plasma, and healthy urine.

## Chapter 1: Introduction

In 2021, Hong and coworkers<sup>196</sup> developed an AIE fluorescent probe **62** (Figure 1.32B) based on D- $\pi$ -A mechanism, which can selectively and sensitively detect HSA over BSA and other biomolecules.

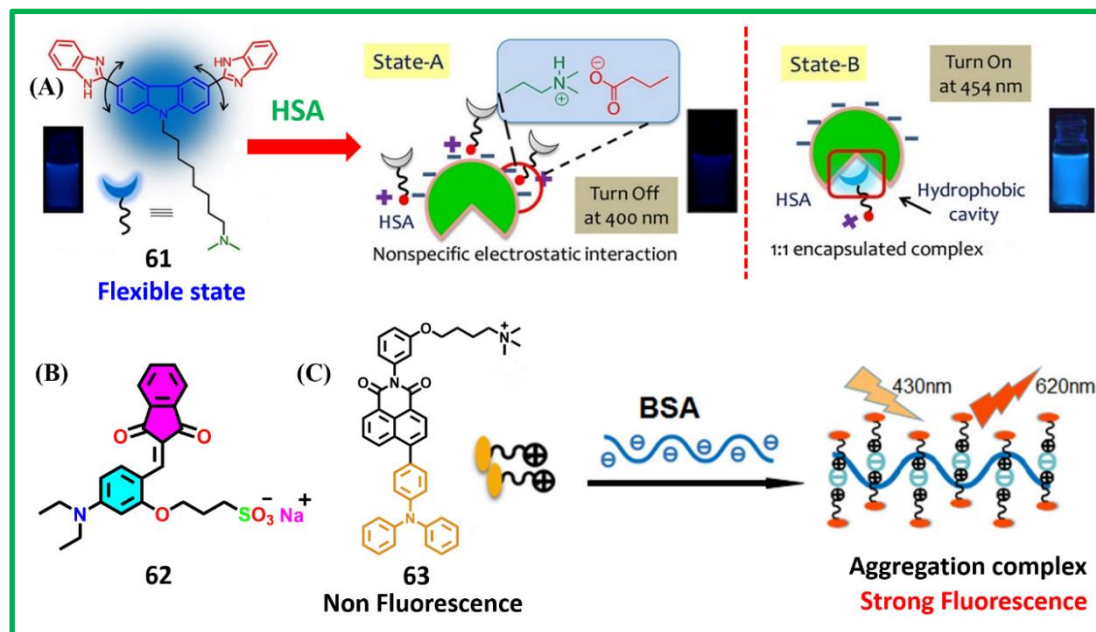


**Figure 1.32** (A) Pictorial representation of a carbazole-based AIE fluorescent probe **61** towards HSA detection. (B) Chemical structure of a AIE fluorophores **62**. (C) An illustration of an AIE fluorophore **63** based on naphthalimide for BSA detection. (A) and (C) are adapted and modified with permission from ref. **195** and **197**. Copyright 2018 Wiley-VCH, 2021 Elsevier, respectively.

This probe has weak fluorescence because the sulphonate functional group helps it to dissolve in water. However, upon addition of HSA (1000 mg/mL), its fluorescence intensity is increased at 550 nm by 450 times, and this can be attributed to the movement of probe molecules from the polar aqueous microenvironment to the low polar hydrophobic cavity inside HSA. It has a detection limit for HSA of 3.74 nM and a linear correlation of HSA concentrations ranging from 0 to 1000 mg/mL. The probe **62** reacts to HSA quickly, and its fluorescence intensity is stable for 60 min. In addition, this probe can accurately measure the HSA concentration in healthy human urine samples.

In the same year, Cao *et. al.*<sup>197</sup> also designed and synthesized a water-soluble NIR fluorescent probe **63** (Figure 1.32C) based on the AIE phenomena for the sensitive “turn-on”

fluorescence response toward BSA. The free probe has almost no fluorescence in aqueous medium, but after addition of 2  $\mu\text{M}$  BSA, its fluorescence intensity is raised by 6-fold at 620 nm, and its fluorescence colour changes noticeably from colourless to orange-red. This increase in emission intensity is caused by the formation of a nano-aggregated state through the electrostatic and hydrophobic interactions between the negatively charged BSA and the positively charged ammonium group of the probe. The calculated LOD value for BSA is 0.027  $\mu\text{M}$ . According to DLS analysis, the average diameter of the probe/BSA complex is bigger (600 nm) than that of the free probe and BSA, which establishes that the presence of BSA causes the probe molecule to aggregate into nanoparticles.

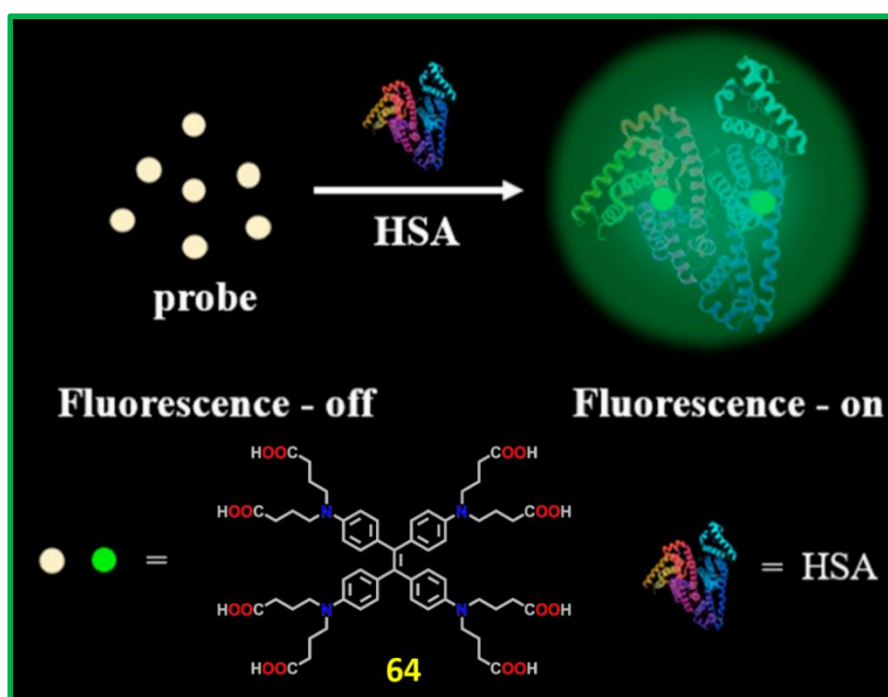


**Figure 1.33** Schematic representation of a TPE-based AIE fluorophore **64** for HSA detection. Adapted with permission from ref. **198**. Copyright 2022 American Chemical Society.

In 2022, Wu *et. al.*<sup>198</sup> successfully developed a tetraphenylethylene (TPE) moiety based AIE fluorescent probe **64** (Figure 1.33), which has the longest negatively charged branch (the terminal  $-\text{COOH}$  group) and the lowest background fluorescence. When HSA is added, the fluorescence intensity rises by 136 times, and it is thought that  $\text{COOH}$ -terminals play essential roles in the particular identification of HSA, presumably via positively charged amino acid residues situated at the mouth of the Site II hydrophobic pocket.

According to the Job's plot, the molar ratio of this probe to HSA is 2:1. The drug displacement studies indicate that probe **64** binds with HSA at both sites i.e., site I and site II. In conclusion, both the polarity shift and rotational limitation of the TPE ring inside the hydrophobic cavity of HSA act synergistically to provide the sensing mechanism that allows this probe to recognize HSA. At a 5  $\mu\text{M}$  probe concentration, it has a low LOD value of 56 nM for HSA.

### 1.5.3 Self-assembly/Disassembly Based Fluorescent Probes

Molecular self-assembly is a process by which individual organic molecules spontaneously associate themselves into well-ordered structures (e.g., nanofibers, nanotubes, and nanoparticles), and it is aided by various non-covalent interactions including hydrophobic, H-bond,  $\pi$ - $\pi$ , Van der Waals, and electrostatic interactions.<sup>199</sup> In recent times, self-assembled molecular probes are emerging as an effective material for protein sensing research with a significant advantage over their individual molecular forms.<sup>200,201</sup>

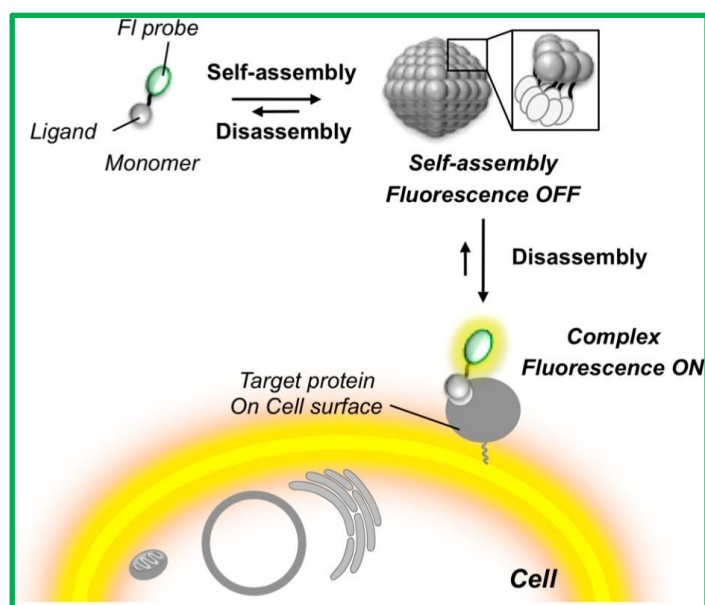


**Figure 1.34** Pictorial representation of a self-assembled turn-on fluorescent probe for cell surface protein recognition. Adapted with permission from ref. **202**. Copyright 2012 American Chemical Society.

Additionally, a wide range of flexibility in chemical design and fine-tuning of the optical characteristic is provided by molecular self-assembled nanoaggregates with remarkable photostability and biocompatibility.

For example, the aggregation caused quenching (ACQ) effect causes a self-assembled probe to exhibit little to no fluorescence, but when the probe reacts to the specific target analytes (e.g., protein) by undergoing disassembly, it emits intense fluorescence (**Figure 1.34**).<sup>199,202</sup> Therefore, the transition from self-assembly to disassembly usually results in the recovery or augmentation of fluorescence signals, and thus opening up a new route for the development of "turn-on" HSA/BSA fluorescent probes. Upon addition of HSA/BSA, the self-assembled fluorescent probes are disassembled owing to the secondary bond interaction inside the hydrophobic pocket of HSA/BSA, resulting in the re-opening of original fluorescence and subsequently enables the quantitative measurement of HSA/BSA in biofluids (human urine and blood serum samples).

Squaraine dyes are fluorescence silent in aqueous solution because they frequently form nanoaggregates as a result of their poor water solubility. Using this property, in 2014, Ajayaghosh *et. al.*<sup>203</sup> first successfully developed a squaraine moiety-based self-assembled fluorescent probe **65** (**Figure 1.35A**) for the selective detection of HSA/BSA in the blood serum through the recognition-induced disassembly approach without interference from other thiol-containing compounds and proteins. In aqueous solution, this probe ( $\lambda_{\text{abs}} = 670 \text{ nm}$ ,  $\lambda_{\text{em}} = 700 \text{ nm}$ ) self-assembles into nonfluorescent spherical nanoaggregates with an average diameter of 200 nm. When BSA is added to this probe in PBS buffer, the absorption band at 670 nm is decreased with the appearance of a new absorption band at 380 nm. However, upon excitation at 380 nm, the addition of BSA/HSA increases the fluorescence intensity at 480 nm with the emergence of green color fluorescence. The estimated LOD value for BSA and HSA is 3 nM. Here, the addition of BSA/HSA causes these spherical nanoaggregates to disassemble into monomers with an average diameter of 10 nm, which makes it easier to encapsulate the monomeric probe in the hydrophobic binding cavity of the protein. This process triggers the selective interaction of this probe with the free Cys-34 residue of the protein, resulting in the breakdown of probe's conjugation to develop a new chromophore *in situ* that emits a bright green fluorescence.

However, the aforementioned self-assembled nanoaggregate probe has not yet been employed for *in vivo* cell imaging. Therefore, in 2016, Xu and colleagues<sup>204</sup> improved the above work by combining a pyrene moiety with a squaraine fluorophore to create a fluorescent probe **66** (**Figure 1.35A**), which can effectively self-assemble into

nanoaggregates in aqueous medium via multiple noncovalent interactions (such as  $\pi$ - $\pi$ , C-H $\cdots\pi$  and hydrophobic interactions) and specifically detect HSA/BSA in blood serum over other biological interferences. This probe has the capacity to enter into cells and can be successfully employed for fluorescence imaging in living cells. The probe has two absorption peaks at 610 and 668 nm that correspond to the aggregate and monomeric forms of the probe molecules, respectively. The absorbance at 610 nm gradually decreases with the addition of HSA, whereas the absorbance at 668 nm gradually increases. When the excitation is made at 600 nm, this probe is fluorescence silent due to the ACQ effect. But, with the addition of 16  $\mu\text{M}$  HSA, fluorescence intensity is greatly enhanced (38-fold) at 674 nm, with a broad linear operating range of HSA concentration from 0 to 16  $\mu\text{M}$ . The estimated HSA detection limit is 140 nM. Here, the addition of BSA/HSA leads these nanoaggregates (average diameter of 145 nm) to disintegrate into monomers with an average diameter of 6 nm, making it easier to enclose the monomeric probe in the hydrophobic binding cavity (site II) of the protein.

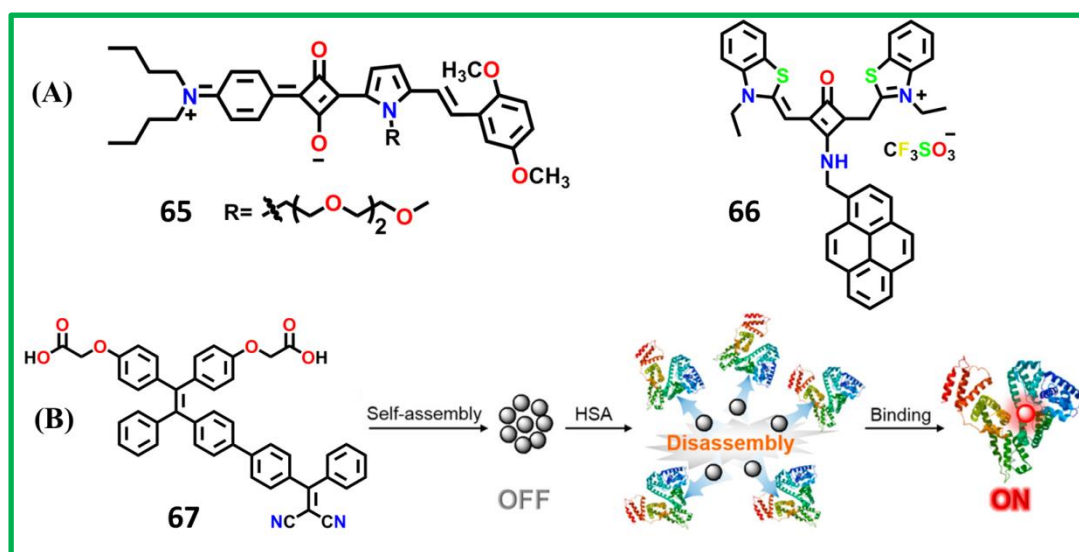


**Figure 1.35** (A) Chemical structure of self-assembled fluorescent probes **65** and **66** based on squaraine moiety. (B) Schematic representation of a TPE-based self-assembled fluorophore **67** toward HSA detection. (B) is adapted and modified with permission from ref. **205**. Copyright 2016 American Chemical Society.

Then, in 2016, Zhao's group<sup>205</sup> designed and synthesized a water soluble self-assembled fluorescent probe **67** (Figure 1.35B) using tetraphenylethylene (TPE) moiety for the selective and sensitive detection of HSA.



In a PBS buffer, this probe self-assembles into nanoaggregates with an average diameter of 34 nm and it is nonemissive owing to the presence of TICT effect and loose molecular packing. However, when HSA is added, the nanoaggregates breakdown into monomers of average diameter 6 nm within 5 min, and the released monomers are trapped inside the site I hydrophobic binding cavity of HSA, resulting in a red emission at 610 nm caused by restriction of the probe's intramolecular rotation. This self-assembled probe provides a wide linear operating range of HSA concentration from 10 to 2000 nM with a LOD value of 2.7 nM. The mechanism analysis reveals that a combination of several noncovalent interactions (H-bond,  $\pi$ - $\pi$  stacking, and cation- $\pi$ ) are responsible for the disassembly and trapping of monomers inside HSA.

In 2017, Cheng *et. al.*<sup>206</sup> developed an amphiphilic self-assembled fluorescent probe **68** (Figure 1.36), which has a modified imidazole core as the fluorophore moiety, an alkyl chain as the hydrophobic component, and a pyridinium cation moiety as the hydrophilic group. This probe can self-assemble into nanoparticles with an average diameter of 180 nm in PBS buffer and it has a quick response time (15 s) towards HSA. This nanoprobe is fluorescence silent upon excitation at 380 nm, but when HSA is added, it exhibits a strong fluorescent enhancement at 480 nm with a LOD value of 0.14  $\mu$ M. This nanoprobe also has an excellent linear operating range of HSA concentration from 0 to 15  $\mu$ M. According to the analysis of operating mechanism, several noncovalent interactions (electrostatic, H-bond,  $\pi$ - $\pi$ , and cation- $\pi$ ) help to disassemble the nanoprobe and trapping the released monomer inside the Site I hydrophobic binding cavity of HSA. The probe's intramolecular rotation is then inhibited in the hydrophobic cavity, resulting in an enhancement of fluorescence intensity. More significantly, this nanoprobe may be used to detect and measure HSA in real human serum samples.

In the year 2018, Kumar *et. al.*<sup>207</sup> synthesized a self-assembled fluorescent probe **69** (Figure 1.36) based on perylene diimide moiety, which can specifically detect HSA/BSA over other proteins. In a HEPES buffer media, this probe self-assembles into nanoaggregates, with an absorbance maximum at 500 nm and exhibits weak fluorescence peak at 577 nm. The progressive addition of HSA/BSA from 1 nM to 50 nM into the aqueous solution of this probe resulted in a reduction of fluorescence intensity at 577 nm.

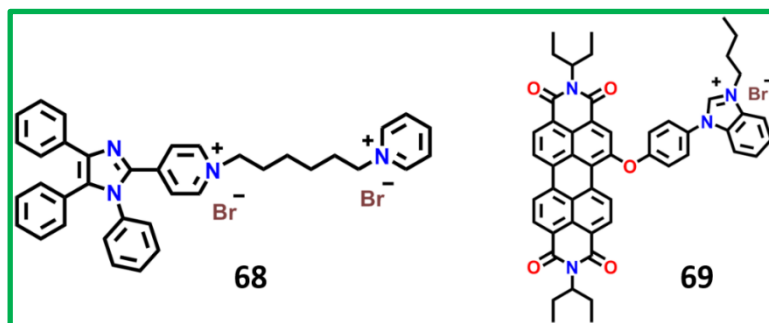


**Figure 1.36** Chemical structure of self-assembled fluorescent probes **68** and **69** for HSA detection.

But, when the added concentration of HSA/BSA increases further, a new blue-shifted emission band begins to develop at 540 nm. It has a low LOD value of 0.301 nM for HSA/BSA at 577 nm. Upon addition of BSA, the average diameter of the nanoaggregates decreases from 100-250 nm to 10 nm, which is attributed to microencapsulation-driven disintegration of the nanoaggregates, resulting in the fluorescent “turn-on” response. According to the site-marker investigations, the probe predominantly binds at the site I hydrophobic pocket of HSA/BSA proteins. Additionally, this probe may be utilized to monitor and image serum albumin proteins.

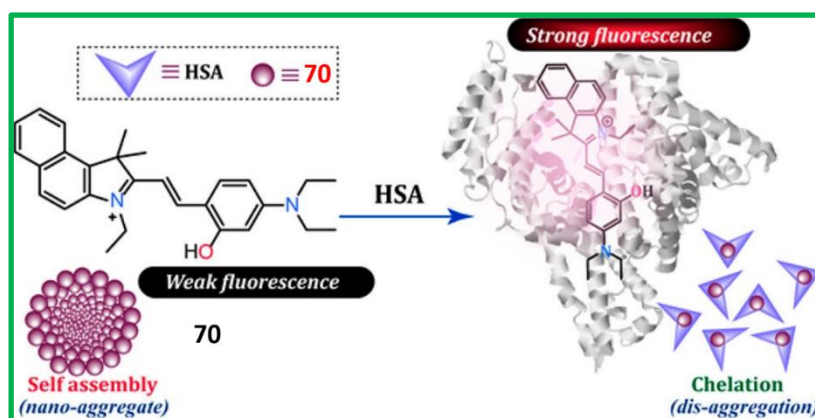


**Figure 1.37** Pictorial representation of a cyanine moiety-based self-assembled fluorescent probe **70** for HSA detection. Adapted with permission from ref. **208**. Copyright 2018 American Chemical Society.

In this year, a simple TICT-based fluorescent probe **70** (**Figure 1.37**), has also been developed by Das *et. al.*,<sup>208</sup> which can self-assemble into nanoaggregates with an average diameter of 200 nm in an aqueous buffer media. The probe exhibits a selective and rapid



fluorescence turn-on response (within seconds) toward HSA/BSA over other biological interferences. When this probe interacts with HSA in a PBS buffer medium, its absorbance maxima is red-shifted from 567 to 575 nm. Because of the existence of the TICT process, it exhibits a very faint emission band at 585 nm when the excitation wavelength is made at 540 nm. However, upon addition of HSA, its fluorescence intensity is increased at 596 nm by 30 times with a detection limit of 6.5 nM. TEM investigations show that the addition of HSA reduces the average diameter of nanoaggregates from 200 nm to <50 nm, which is ascribed to the chelation-induced disassembly of the nanoaggregates, resulting in the fluorescent "turn-on" response. According to site-marker displacement studies and molecular docking simulation, this probe binds with HSA at a position other than the common drug binding sites (i.e., sites I and II). Furthermore, this probe can precisely measure the amount of HSA in body fluids and an artificial urine sample.

Then, in the same year, Xu and colleagues<sup>209</sup> also developed a self-assembled fluorescent probe **71** (Figure 1.38) by coupling two squaraine moieties together via a disulfide connection, which can selectively and sensitively detect BSA in both aqueous media and living cells. This probe can self-assemble to form "compact" nanoaggregates that provide extremely low background fluorescence owing to the combination of ACQ and homoFRET effects. However, upon addition of BSA, its fluorescence intensity is 25-fold increased at 678 nm with a linear correlation of BSA concentration from 0 to 1.2 g/L. According to  $3\sigma/\text{slope}$  method, the LOD value of this probe is 0.53 nM. The selective fluorescent response of this nanoaggregate to BSA results from a two-step disintegration via cascade interactions that include first quick (30 s) noncovalent binding with the hydrophobic cavity of BSA and second slow covalent binding with the Cys-34 amino acid residue in BSA.

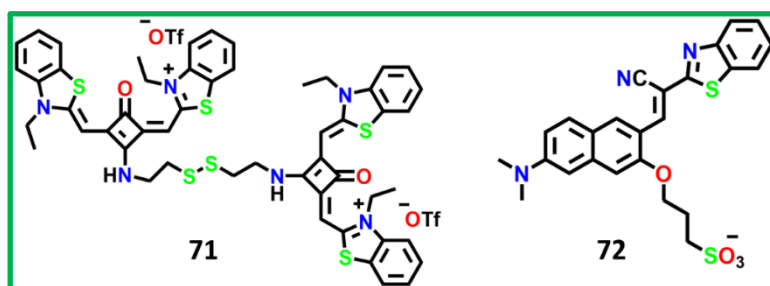


**Figure 1.38** Chemical structure of self-assembled fluorescent probes **71** and **72** based on squaraine and naphthalene moiety, respectively, for the serum albumins recognition.

## Chapter 1: Introduction

In 2019, Kim *et. al.*<sup>210</sup> synthesized a naphthalene moiety based fluorescent probe **72** (Figure 1.38) which allows a quick ( $\leq 2$  s) fluorimetric measurement of HSA in aqueous medium, urine and blood serum. It shows a very weak fluorescent signal ( $\Phi = 0.01$ ) at 708 nm after being excited at 450 nm because of the formation of colloidal nanoaggregates with an average diameter of  $(1050 \pm 100)$  nm. However, upon addition of HSA (133 mg/L) the nanoaggregates disintegrate into monomers with an average diameter  $(15 \pm 10)$  nm, and the released monomers are trapped inside the hydrophobic binding pocket of HSA, resulting in the dramatic fluorescence enhancement (1000-fold) along with a blue-shift of emission maxima from 708 to 592 nm. Moreover, the emission intensity enhances linearly at 592 nm with HSA concentrations between 0 and 333 mg/L, and the probe has a LOD value of 0.30 mg/L.

Then, Xie's group<sup>211</sup> developed a coumarin moiety-based self-assembled fluorescent probe **73** (Figure 1.39) in the year 2020 for the specific detection of HSA and its applications in the monitoring of renal illness. In aqueous medium, this probe can easily self-assemble into nanoaggregates with an average diameter of 258 nm owing to the hydrophobic interaction between organic molecules.

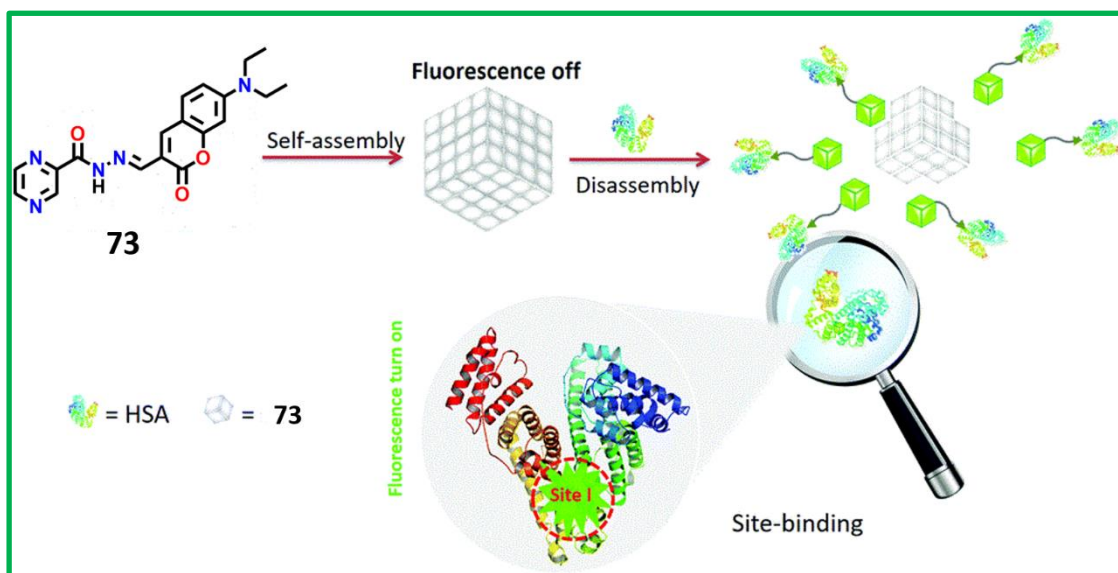


**Figure 1.39** Schematic description of a Schiff-based self-assembled fluorophore **73** for HSA detection. Adapted and modified with permission from ref. **211**. Copyright 2020 Royal Society of Chemistry.

## Chapter 1: Introduction

The probe is fluorescence silent in PBS buffer media ( $\Phi = 0.004$ ) when the excitation wavelength is made at 450 nm due to the ACQ effect, but it displays a considerable fluorescence augmentation ( $\Phi = 0.034$ ) at 513 nm with the addition of HSA through the recognition-induced disassembly mechanism. Here, adding 1 equivalent of HSA results in a shift in the average diameter of the nanoaggregates from 258 nm to 157 nm, suggesting the disassembly of the nanoaggregates and allowing probe molecules to be encapsulated in the hydrophobic pockets (site I) of HSA. The fluorescent response of this probe to HSA occurs within 30 s. According to the  $3\sigma/\text{slope}$  method, the calculated LOD values in PBS media and urine samples are 8.97 nM and 8.42 nM, respectively. Additionally, the fluorescence imaging of HSA in MCF-7 cells suggests that this probe can be employed to monitor the amount of HSA *in vivo*.

Then, in 2021, Mula *et. al.*<sup>212</sup> reported a NIR-emitting BODIPY-based self-assembled fluorescent probe **74** (Figure 1.40), in which the inclusion of hydrophilic glucose moieties to the hydrophobic BODIPY scaffold results in the development of the probe's amphiphilic nature. The PBS buffer solution of this probe is fluorescence silent upon excitation at 620 nm, but when BSA (405  $\mu\text{M}$ ) is added, the solution turns red fluorescent and exhibits a 150-fold enhancement in emission intensity at 665 nm with a detection limit of 157.7 nM. Such a large modification of the fluorescence intensity clearly indicates the disassembly of the nanoaggregates to form the **74**–BSA complex. The molecular docking analysis indicates that this probe binds with BSA at the site I hydrophobic binding pocket. Additionally, this probe may be used to measure serum albumin in clinical samples.

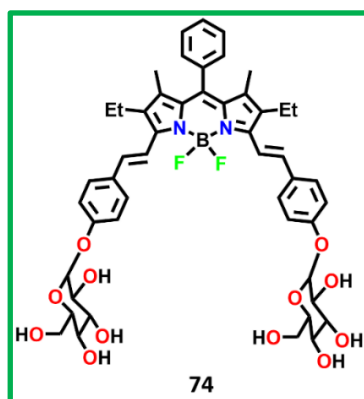


**Figure 1.40** Chemical structure of a BODIPY-based self-assembled fluorescent probe **74** for BSA recognition.

### 1.5.4 Enzymatically reactive fluorescent probes

HSA/BSA functions as an enzyme and exhibits pseudo esterase activity. When combined with HSA/BSA, the substrate goes through a hydrolysis reaction in which the ester group splits to generate an acyl group and a hydroxyl group. This acyl end binds with the amino acid residues of HSA/BSA (i.e., Lys, Tyr), while the hydroxyl end transforms into a free fluorescent molecule. Therefore, some fluorescent molecular probes has been successfully developed for the detection of serum albumins through enzymatic reactions.

In 2013, Kim *et. al.*<sup>213</sup> developed a fluorescent probe **75a** (Figure 1.41) for the detection of HSA based on its pseudo-esterase activity. In this probe, the fluorescent reporter is a dansyl group, while the fluorescent quencher is 4-nitrophenylcarbamate. The reactive acyl part of the probe is hydrolyzed by HSA, which can also break the carbamate bond to liberate CO<sub>2</sub> and 4-nitroaniline, resulting in the formation of a temporary, unstable intermediate quinone methide. Following that, a covalent link is established between this quinone methide moiety and a nucleophile close to the active region of the enzyme, leading to the development of a probe-protein complex **75b**. The fluorescence intensity of the probe **75a** is completely quenched by 4-nitrophenylcarbamate moiety in HEPES buffer media, but upon addition of 10 μM HSA, fluorescent intensity is significantly increased (35-fold) at 477 nm due to the formation of complex **75b**. By using size-exclusion/gel-filtration column chromatography technique, **75b** is effectively purified. Additionally, this probe is capable of identifying HSA in samples of human tissue contaminated with blood.

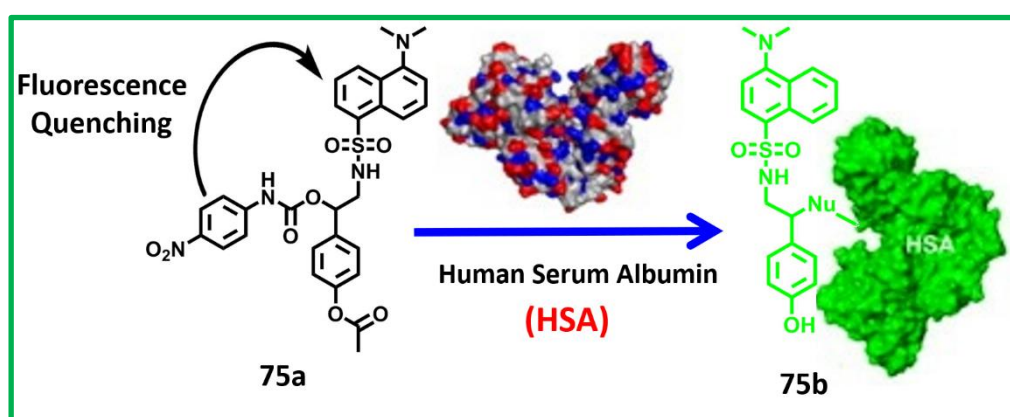


**Figure 1.41** Mechanism underlying the binding of fluorescent probe **75a** to HSA. Adapted and modified with permission from ref. **213**. Copyright 2013 Elsevier.

## Chapter 1: Introduction

In 2017, Qian's group<sup>214</sup> synthesized an enzymatic reaction-based fluorescent probe **76a** (Figure 1.42) by coupling of a coumarin fluorophore moiety with a dioxaborine core for the specific and sensitive detection of HSA/BSA over other biological interferences. The probe itself absorbs at 515 nm, but when HSA is introduced (1.0 mg/mL), the absorption maxima at 515 nm gradually disappears with the emergence of a new absorption maxima at 475 nm. Upon excitation at 495 nm, this probe is non-fluorescent in PBS buffer medium, but with the introduction of HSA, a broad emission band at 585 nm and a shoulder at 540 nm appeared within 1 min. Then after 15 min of incubation with HSA, its fluorescent intensity is 1000-fold enhanced at 540 nm with a LOD value of 0.21  $\mu\text{g/mL}$ . Actually, HSA hydrolyzes the dioxaborine group into  $\beta$ -diketonate compound **76b** with a shorter conjugation structure, which is attributed to the fluorescence amplification accompanied by blue shifts of absorption and emission maxima of about 40 nm and 45 nm, respectively. The molecular docking analysis reveals that both **76a** and **76b** bind with HSA at the site I hydrophobic cavity, where two H-bonds with Arg-257 and hydrophobic interactions are important for the stabilization of the protein-probe interaction. Additionally, the bioimaging findings indicate that probe **76a** may be useful in cancer detection.

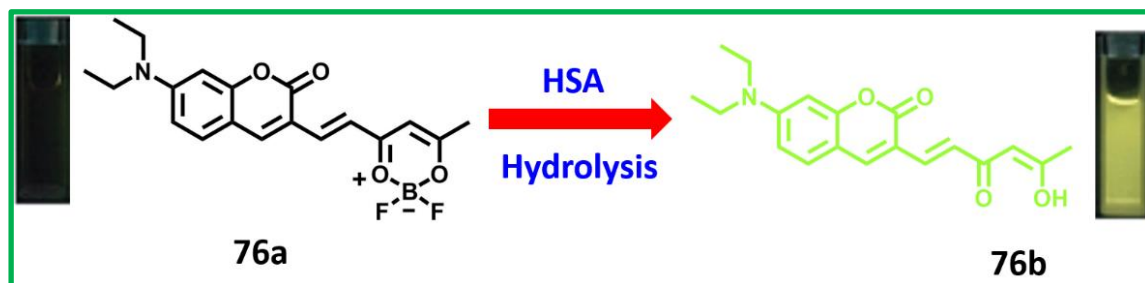


**Figure 1.42** Schematic representation of a coumarin-based fluorescent probe **76a** for HSA recognition through enzymatic reaction.

In the same year, Guo *et. al.*<sup>215</sup> also developed an enzymatic reaction based NIR fluorescent probe **77a** (Figure 1.43), which can specifically detect HSA in human serum and hepatocyte cell culture supernatants. The probe has an absorption band at 430 nm, but when HSA is added, the absorption maxima at 430 nm gradually decreases with the development of a new absorption maxima at 646 nm. This probe exhibits weak fluorescence in PBS buffer medium when the excitation wavelength is set at 600 nm, but with the addition of HSA, its emission intensity is greatly enhanced at 662 nm with a wide linear operating range of HSA

concentration from 0 to 200 mg/L. According to  $3\sigma$ /slope method, it has a low LOD value of 6.51 mg/L. In this case, HSA triggers the cleavage of ester bond of probe **77a**, releasing a hydrolyzed product **77b**, which is attributed to the fluorescence augmentation. In addition, this probe has the ability to pass across the cell membranes, making it useful for bioimaging of endocytosis serum albumin in living renal cells. Furthermore, this probe has also been effectively utilised to monitor serum albumin uptake and degradation in *ex vivo* mouse models.

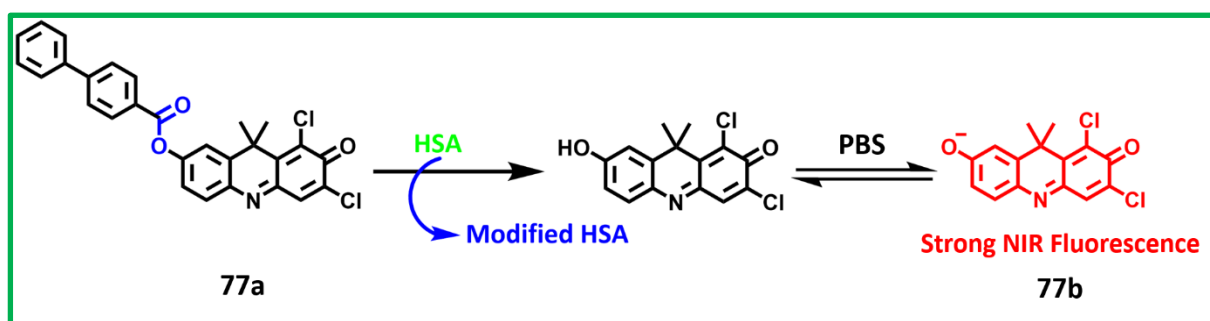


**Figure 1.43** Recognition mechanism of a NIR fluorescent probe **77a** for HSA recognition through enzymatic reaction.

### 1.6 Self-designed Systems Studied in the Thesis

In this thesis, we have developed some simple fluorescent molecular probes (**Figure 1.44**), which can selectively and sensitively detect HSA/BSA over other biological interferences in purely aqueous medium. The selective recognition of HSA/BSA has been studied by using fluorescence and absorbance change on binding with varying concentrations of HSA/BSA to determine the binding constant by using a suitable computer-fit program. Important parameters like quantum yield ( $\Phi$ ) and limit of detection are also determined, which generally dictate the suitability of the probe to be used in biological systems. The underlying mechanism of protein-probe interactions has been comprehensively explored by utilizing multiple spectroscopic methods and molecular docking analysis. We have also monitored the time-based change in fluorescence intensity using fluorometric technique. Additionally, accurate measurement of serum albumin in body fluids (human blood serum and urine samples) has been accomplished, which has great importance in clinical diagnosis.

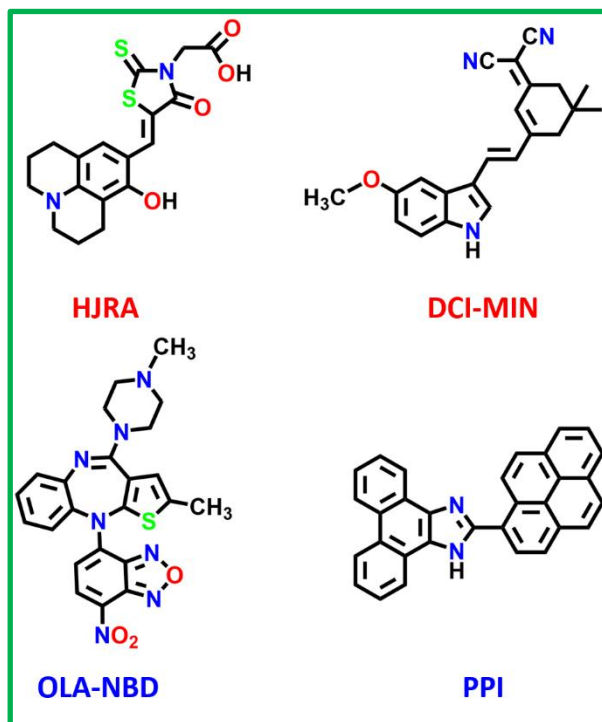


**Figure 1.44** Chemical structure of the self-designed fluorescent molecular probes for HSA/BSA recognition.

### 1.7 Physical Measurements

- (i) **FT-IR spectra:** Infrared spectra ( $400\text{--}4000\text{ cm}^{-1}$ ) were recorded in solid state on a Perkin-Elmer RX I FT-IR spectrophotometer.
- (ii)  **$^1\text{H}$  NMR spectra:**  $^1\text{H}$ -NMR spectra were recorded in DMSO- $d_6$ ,  $\text{CDCl}_3$ ,  $\text{CH}_3\text{OD}$ ,  $\text{CD}_3\text{CN}$  on a Bruker 300/400/600 MHz NMR spectrometer using tetramethylsilane ( $\delta = 0$ ) as an internal standard.
- (iii) **UV-vis spectra:** The UV-Vis absorbance spectral studies were carried out on an Agilent diode-array Spectrophotometer (Agilent 8453) using a 1 cm path length quartz cuvette in the wavelength range of 190-900 nm.
- (iv) **Mass spectra:** The ESI- $\text{MS}^+$  ( $m/z$ ) spectra of the probes were recorded on a HRMS spectrophotometer (model: QTOF Micro YA263).
- (v) **Fluorescence spectra:** Steady-state fluorescence measurements were performed with a PTI QM-40 spectrofluorometer by using a fluorescence free quartz cuvette of 1 cm path length.
- (vi) **Lifetimes measurements:** Fluorescence lifetimes were determined from time-resolved intensity decay by the method of time correlated single photon counting



(TCSPC) measurements using a picosecond diode laser (IBH Nanoled-07) in an IBH fluorocube apparatus. The fluorescence decay data were collected on a Hamamatsu MCP photomultiplier (R3809) and examined by the IBH DAS6 software.

- (vii) **Dynamic light scattering studies:** The dynamic light scattering (DLS) measurements were carried out at 25 °C on a Malvern Zetasizer Nano ZS instrument.
- (viii) **Transmission electron microscopy (TEM) analysis:** TEM characterization were carried out on a FEI Tecnai G2 F20 microscope TEM instrument by drop casting of the sample separately on carbon-coated copper grids (400 meshes) and drying them in a vacuum.
- (ix) **Molecular docking study:** The molecular docking study between proteins (HSA and BSA) and probes were performed using docking program AutoDock (version 4.2). The X-ray crystal structure of HSA/BSA was taken from RCSB Protein Data Bank. To draw the chemical structure of different probes, Chem3D Ultra 12.0 was used and further modification was carried out by using Gaussian 09W and AutoDock 4.2 programs. The Lamarckian genetic algorithm (LGA) was used to accomplish docking calculations and the grid maps for energy were calculated by AutoGrid. The best optimized docked model with lowest binding energy was considered for further study of docking simulations and the output was best viewed by using Discovery Studio and PyMOL software.
- (x) **Circular dichroism (CD) studies:** CD spectral studies were recorded on a PC-driven JASCO J815 (Japan) spectropolarimeter.
- (xi) **Cell imaging:** Cell imaging studies have been performed under fluorescence microscope. Bright field and fluorescence images of the CHO and KB cells were taken using a fluorescence microscope (Olympus, model IX-81) with an objective lens of 40x, 20x magnification.
- (xii) **pH study:** The pH of the solutions was recorded using a Systronics digital pH meter (Model 335, India) with the pH range 2–12. The pH meter was calibrated using standard buffer solutions (Acros Organics) of pH 4.0, 7.0 and 10.0.

### References

- 1) Nelson, D. L.; Cox, M. M. *Lehninger Principles of Biochemistry*, 5th ed.; W. H. Freeman & Company: New York, 2008.
- 2) Berg, J. M.; Tymoczko, J. L.; Stryer, L. *Biochemistry*, 5th ed.; W. H. Freeman & Company: New York, 2002.
- 3) Eftink, M.; Pedigo, S. In *Encyclopedia of Physical Science and Technology*, 3rd ed.; Meyers, R. A., Ed.; Academic Press: New York, 2003; pp 179–190.
- 4) Mizukami, S.; Hori, Y.; Kikuchi, K. Small-molecule-based protein-labeling technology in live cell studies: probe-design concepts and applications. *Acc. Chem. Res.* **2014**, *47*, 247–256.
- 5) Kobayashi, H.; Ogawa, M.; Alford, R.; Choyke, P. L.; Urano, Y. New strategies for fluorescent probe design in medical diagnostic imaging. *Chem. Rev.* **2010**, *110*, 2620–2640.
- 6) Whitcombe, M. J.; Chianella, I.; Larcombe, L.; Piletsky, S. A.; Noble, J.; Porter, R.; Horgan, A. The rational development of molecularly imprinted polymer-based sensors for protein detection. *Chem. Soc. Rev.* **2011**, *40*, 1547–1571.
- 7) Chan, J.; Dodani, S. C.; Chang, C. J. Reaction-based Small-molecule Fluorescent Probes for Chemoselective Bioimaging. *Nat. Chem.* **2012**, *4*, 973–984.
- 8) Vendrell, M.; Zhai, D.; Er, J. C.; Chang, Y. T. Combinatorial Strategies in Fluorescent Probe Development. *Chem. Rev.* **2012**, *112*, 4391–4420.
- 9) Ying, J.; Clavreul, N.; Sethuraman, M.; Adachi, T.; Cohen, R. A. Thiol Oxidation in Signaling and Response to Stress: Detection and Quantification of Physiological and Pathophysiological Thiol Modifications. *Free Radical Biol. Med.* **2007**, *43*, 1099–1108.
- 10) Olson, R. E.; Christ, D. D. Chapter 33. Plasma Protein Binding of Drugs. *Annu. Rep. Med. Chem.* **1996**, *31*, 327–336.
- 11) Nicholson, J. P.; Wolmarans, M. R.; Park, G. R. The role of albumin in critical illness. *Br. J. Anaesth.* **2000**, *85*, 599–610.

- 12) Wen, J.; Geng, Z.; Yin, Y.; Wang, Z. A versatile water soluble fluorescent probe for ratiometric sensing of  $\text{Hg}^{2+}$  and bovine serum albumin. *Dalton Trans.* **2011**, *40*, 9737–9745.
- 13) Peters, T., Jr. Serum Albumin. *Adv. Protein Chem.* **1985**, *37*, 161–245.
- 14) He, X. M.; Carter, D. C. Atomic structure and chemistry of human serum albumin. *Nature* **1992**, *358*, 209–215.
- 15) Fanali, G.; di Masi, A.; Trezza, V.; Marino, M.; Fasano, M.; Ascenzi, P. Human serum albumin: from bench to bedside. *Mol. Aspects Med.* **2012**, *33*, 209–290.
- 16) Sethi, P. K.; White, C. A.; Cummings, B. S.; Hines, R. N.; Muralidhara, S.; Bruckner, J. V. Ontogeny of plasma proteins, albumin and binding of diazepam, cyclosporine, and deltamethrin. *Pediatr. Res.* **2016**, *79*, 409–415.
- 17) Ding, F.; Liu, W.; Zhang, L.; Yin, B.; Sun, Y. J. Sulfometuron-methyl binding to human serum albumin: Evidence that sulfometuron-methyl binds at the Sudlow's site I. *J. Mol. Struct.* **2010**, *968*, 59–66.
- 18) Belinskaia, D. A.; Voronina, P. A.; Batalova, A. A.; Goncharov, N. V. Serum Albumin. *Encyclopedia* **2021**, *1*, 65–75.
- 19) Fan, J.; Sun, W.; Wang, Z.; Peng, X.; Li, Y.; Cao, J. A fluorescent probe for site I binding and sensitive discrimination of HSA from BSA. *Chem. Commun.* **2014**, *50*, 9573–9576.
- 20) Alino, V. J.; Yang, K. L. Using liquid crystals as a readout system in urinary albumin assays. *Analyst* **2011**, *136*, 3307–3313.
- 21) Rani, S.; Gupta, S.; Luxami, V.; Paul, K. A novel target and biomarker benzothiazolyl–naphthalimide probes for precise and selective detection of serum albumin and anticancer activity. *New J. Chem.* **2022**, *46*, 12082–12092.
- 22) Murch, S. H.; Winyard, P. J. D.; Koletzko, S.; Wehner, B.; Cheema, H. A.; Risdon, R. A.; Phillips, A. D.; Meadows, N.; Klein, N. J.; Walker-Smith, J. A. Congenital enterocyte heparan sulphate deficiency with massive albumin loss, secretory diarrhoea, and malnutrition. *Lancet* **1996**, *347*, 1299–1301.
- 23) Peters, T., Jr. *All About Albumins: Biochemistry, Genetics and Medical Applications*; Academic Press: San Diego, CA, 1996; pp 76–132.

- 24) Hoogenberg, K.; Sluiter, W. J.; Dullaart, R. P. Effect of growth hormone and insulin-like growth factor I on urinary albumin excretion: studies in acromegaly and growth hormone deficiency. *Eur. J. Endocrinol.* **1993**, *129*, 151–157.
- 25) de Zeeuw, D.; Parving, H. H.; Henning, R. Microalbuminuria as an early marker for cardiovascular disease. *J. Am. Soc. Nephrol.* **2006**, *17*, 2100–2105.
- 26) Amin, R.; Widmer, B.; Prevost, A. T.; Schwarze, P.; Cooper, J.; Edge, J.; Marcovecchio, L.; Neil, A.; Dalton, R. N.; Dunger, D. B. Risk of microalbuminuria and progression to macroalbuminuria in a cohort with childhood onset type 1 diabetes: prospective observational study. *BMJ.* **2008**, *336*, 697–701.
- 27) Jahanban-Esfahlan, A.; Ostadrahimi, A.; Jahanban-Esfahlan, R.; Roufegarinejad, L.; Tabibiazar, M.; Amarowicz, R. Recent developments in the detection of bovine serum albumin. *Int. J. Biol. Macromol.* **2019**, *138*, 602–617.
- 28) Gao, M.; Skolnick, J. A Comprehensive Survey of Small Molecule Binding Pockets in Proteins. *PLoS Comput. Biol.* **2013**, *9*, e1003302.
- 29) Sudlow, G.; Birkett, D. J.; Wade, D. N. The Characterization of Two Specific Drug Binding Sites on Human Serum Albumin. *Mol. Pharmacol.* **1975**, *11*, 824–832.
- 30) Sudlow, G.; Birkett, D. J.; Wade, D. N. Further Characterization of Specific Drug Binding Sites on Human Serum Albumin. *Mol. Pharmacol.* **1976**, *12*, 1052–1061.
- 31) Szacilowski, K.; Macyk, W.; Drzewiecka-Matuszek, A.; Brindell, M.; Stochel, G. Bioinorganic Photochemistry: Frontiers and Mechanisms. *Chem. Rev.* **2005**, *105*, 2647–2694.
- 32) Pandey, R. K.; Constantine, S.; Tsuchida, T.; Zheng, G.; Medforth, C. J.; Aoudia, M.; Kozyrev, A. N.; Rodgers, M. A. J.; Kato, H.; Smith, K. M.; Dougherty, T. J. Synthesis, photophysical properties, in vivo photosensitizing efficacy, and human serum albumin binding properties of some novel bacteriochlorins. *J. Med. Chem.* **1997**, *40*, 2770–2779.
- 33) Bonnett, R. *Chemical Aspects of Photodynamic Therapy*; Gordon and Breach Science Publishers: The Netherlands, 2000.
- 34) Royer, C. A. Probing Protein Folding and Conformational Transitions with Fluorescence. *Chem. Rev.* **2006**, *106*, 1769–1784.

- 35) Cohen, B. E.; McAnaney, T. B.; Park, E. S.; Jan, Y. N.; Boxer, S. G.; Jan, L. Y. Probing Protein Electrostatics with a Synthetic Fluorescent Amino Acid. *Science* **2002**, *296*, 1700–1703.
- 36) Abou-Zied, O. K.; Al-Shihi, O. I. K. Characterization of Subdomain IIA Binding Site of Human Serum Albumin in its Native, Unfolded, and Refolded States Using Small Molecular Probes. *J. Am. Chem. Soc.* **2008**, *130*, 10793–10801.
- 37) Er, J. C.; Vendrell, M.; Tang, M. K.; Zhai, D.; Chang, Y.-T. Fluorescent Dye Cocktail for Multiplex Drug-Site Mapping on Human Serum Albumin. *ACS Comb. Sci.* **2013**, *15*, 452–457.
- 38) Lazaro, E.; Lowe, P. J.; Briand, X.; Faller, B. New approach to measure protein binding based on a parallel artificial membrane assay and human serum albumin. *J. Med. Chem.* **2008**, *51*, 2009–2017.
- 39) Carter, D. C.; Ho, J. X. Structure of Serum Albumin. *Adv. Protein Chem.* **1994**, *45*, 153–203.
- 40) Meloun, B.; Moravek, L.; Kotska, V. Complete Amino-Acid Sequence of Human-Serum Albumin. *FEBS Lett.* **1975**, *58*, 134–137.
- 41) Carter, D. C.; He, X. M.; Munson, S. H.; Twings, P. D.; Gernert, K. M.; Broom, M. B.; Miller, T. Y. Three-dimensional structure of human serum albumin. *Science* **1989**, *244*, 1195–1198.
- 42) Spada, A.; Emami, J.; Tuszyński, J. A.; Lavasanifar, A. The uniqueness of albumin as a carrier in nanodrug delivery. *Mol. Pharmaceutics* **2021**, *18*, 1862–1894.
- 43) Caraceni, P.; Tufoni, M.; Bonavita, M. E. Clinical use of albumin. *Blood Transfus.* **2013**, *11*, s18–s25.
- 44) Belinskaia, D. A.; Voronina, P. A.; Batalova, A. A.; Goncharov, N. V. Serum Albumin. *Encyclopedia* **2021**, *1*, 65–75.
- 45) Sabbioni, G.; Turesky, R. J. Biomonitoring Human Albumin Adducts: The Past, the Present, and the Future. *Chem. Res. Toxicol.* **2017**, *30*, 332–366.
- 46) Brennan, S. O.; Carrell, R. W. A circulating variant of human proalbumin. *Nature* **1978**, *274*, 908–909.
- 47) Kandagal, P. B.; Shaikh, S. M. T.; Manjunatha, D. H.; Seetharamappa, J.; Nagaralli, B. S. Spectroscopic studies on the binding of bioactive phenothiazine compounds to human serum albumin. *J. Photochem. Photobiol., A* **2007**, *189*, 121–127.

- 48) Ghuman, J.; Zunszain, P. A.; Petitpas, I.; Bhattacharya, A. A.; Otagiri, M.; Curry, S. Structural Basis of the Drug-Binding Specificity of Human Serum Albumin. *J. Mol. Biol.* **2005**, *353*, 38–52.
- 49) Fasano, M.; Curry, S.; Terreno, E.; Galliano, M.; Fanali, G.; Narciso, P.; Notari, S.; Ascenzi, P. The extraordinary ligand binding properties of human serum albumin. *IUBMB Life* **2005**, *57*, 787–769.
- 50) Curry, S.; Mandelkow, H.; Brick, P.; Franks, N. Crystal structure of human serum albumin complexed with fatty acid reveals an asymmetric distribution of binding sites. *Nat. Struct. Biol.* **1998**, *5*, 827–835.
- 51) Arroyo, V.; García-Martinez, R.; Salvatella, X. Human serum albumin, systemic inflammation, and cirrhosis. *J. Hepatol.* **2014**, *61*, 396–407.
- 52) Sadler, P. J., Tucker, A., and Viles, J. H. Involvement of a lysine residue in the N-terminal Ni<sup>2+</sup> and Cu<sup>2+</sup> binding site of serum albumins. Comparison with Co<sup>2+</sup>, Cd<sup>2+</sup> and Al<sup>3+</sup>. *Eur. J. Biochem.* **1994**, *220*, 193–200.
- 53) Kim, S. B.; Chi, H. S.; Park, J. S.; Hong, C. D.; Yang, W. S. Effect of increasing serum albumin on plasma D-dimer, von Willebrand factor, and platelet aggregation in CAPD patients. *Am. J. Kidney Dis.* **1999**, *33*, 312–317.
- 54) Lee, P.; Wu, X. Review: Modifications of Human Serum Albumin and Their Binding Effect. *Curr. Pharm. Des.* **2015**, *21*, 1862–1865.
- 55) Jahanban-Esfahlan, A.; Dastmalchi, S.; Davaran, S. A simple improved desolvation method for the rapid preparation of albumin nanoparticles. *Int. J. Biol. Macromol.* **2016**, *91*, 703–709.
- 56) Ranjbar, S.; Shokoohinia, Y.; Ghobadi, S.; Bijari, N.; Gholamzadeh, S.; Moradi, N.; Ashrafi-Kooshk, M. R.; Aghaei, A.; Khodarahmi, R. Studies of the interaction between isoimperatorin and human serum albumin by multispectroscopic method: identification of possible binding site of the compound using esterase activity of the protein. *Sci. World J.* **2013**, *2013*, 1–13.
- 57) Kumar, D.; Banerjee, D. Methods of albumin estimation in clinical biochemistry: Past, present, and future. *Clin. Chim. Acta* **2017**, *469*, 150–160.
- 58) Kopac, T.; Bozgeyik, K.; Yener, J. Effect of pH and temperature on the adsorption of bovine serum albumin onto titanium dioxide. *Colloids Surf., A* **2008**, *322*, 19–28.

- 59) McClellan, S. J.; Franses, E. I. Effect of concentration and denaturation on adsorption and surface tension of bovine serum albumin. *Colloids Surf., B* **2003**, *28*, 63–75.
- 60) Majorek, K. A.; Porebski, P. J.; Dayal, A.; Zimmerman, M. D.; Jablonska, K.; Stewart, A. J.; Chruszcz, M.; Minor, W. Structural and Immunologic Characterization of Bovine, Horse, and Rabbit Serum Albumins. *Mol. Immunol.* **2012**, *52*, 174–182.
- 61) Wang, X.; Zhang, G.; Yu, D.; Wang, N.; Guan, Q. The interaction of folate-modified Bletilla striata polysaccharide-based micelle with bovine serum albumin. *Glycoconj. J.* **2021**, *38*, 585–597.
- 62) Jana, S.; Dalapati, S.; Ghosh, S.; Guchhait, N. Binding interaction between plasma protein bovine serum albumin and flexible charge transfer fluorophore: A spectroscopic study in combination with molecular docking and molecular dynamics simulation. *J. Photochem. Photobiol., A* **2012**, *231*, 19–27.
- 63) Sahoo, B. K.; Ghosh, K. S.; Dasgupta, S. Investigating the Binding of Curcumin Derivatives to Bovine Serum Albumin. *Biophys. Chem.* **2008**, *132*, 81–88.
- 64) Mogues, T.; Li, J.; Coburn, J.; et al. IgG antibodies against bovine serum albumin in humans—their prevalence and response to exposure to bovine serum albumin. *J. Immunol. Methods* **2005**, *300*, 1–11.
- 65) Doumas, B. T.; Peters, T., Jr. Origins of Dye-Binding Methods for Measuring Serum Albumin. *Clin. Chem.* **2009**, *55*, 583–584.
- 66) Ito, S.; Yamamoto, D. Structure of the Methyl Orange-Binding Site on Human Serum Albumin and Its Color-Change Mechanism. *Biomed. Res.* **2015**, *36*, 247–252.
- 67) Crowley, L. V. Evaluation of Serum Protein Fraction Using Methyl Orange Method for Determination of Albumin. *Clin. Chem.* **1964**, *10*, 1131–1136.
- 68) Rutstein, D. D.; Ingenito, E. F.; Reynolds, W. E. The Determination of Albumin in Human Blood Plasma and serum; A Method Based on the Interaction of Albumin with an Anionic Dye-2(4'-hydroxybenzeneazo) Benzoic Acid. *J. Clin. Invest.* **1954**, *33*, 211–221.
- 69) Aryan, D. A.; Ritz, A. Measurement of Serum Albumin by HABA-Dye Technique—a Study of Effect of Free and Conjugated Bilirubin, of Bile Acids and of Certain Drugs. *Clin. Chim. Acta* **1969**, *26*, 505–516.



- 70) Rees, V. H.; Fildes, J. E.; Laurence, D. J. R. The Dye-Binding Capacity of Human Plasma Determined Fluorimetrically and Its Relation to the Determination of Plasma Albumin. *J. Clin. Pathol.* **1954**, *7*, 336–340.
- 71) Kragh-Hansen, U. Effects of Aliphatic Fatty-Acids on the Binding of Phenol red to Human-Serum Albumin. *Biochem. J.* **1981**, *195*, 603–613.
- 72) Sengupta, A.; Hage, D. S. Characterization of minor site probes for human serum albumin by high-performance affinity chromatography. *Anal. Chem.* **1999**, *71*, 3821–3827.
- 73) Rodkey, F. L. Binding of Phenol Red by Human Serum Albumin. *Arch. Biochem. Biophys.* **1961**, *94*, 526–531.
- 74) Rodkey, F. L. Direct Spectrophotometric Determination of Albumin in Human Serum. *Clin. Chem.* **1965**, *11*, 478–487.
- 75) Bartholomew, R. J.; Delaney, A. M. Sulphonphthaleins as specific reagents for albumin: determination of albumin in serum. *Proc. Aust. Assoc. Clin. Biochem.* **1966**, *1*, 214–218.
- 76) Doumas, B. T.; Watson, W. A.; Biggs, H. G. Albumin Standards and Measurement of Serum Albumin with Bromocresol Green. *Clin. Chim. Acta.* **1971**, *31*, 87–96.
- 77) Doumas, B. T.; Peters, T. Jr. Serum and urine albumin: a progress report on their measurement and clinical significance. *Clin. Chim. Acta* **1997**, *258*, 3–20.
- 78) Javed, M. U. H.; Waqar, S. N. An enzymatic method for the detection of human serum albumin. *Exp. Mol. Med.* **2001**, *33*, 103–105.
- 79) Gustafsson, J. E. C. Improved Specificity of Serum-Albumin Determination and Estimation of Acute Phase Reactants by Use of Bromocresol Green Reaction. *Clin. Chem.* **1976**, *22*, 616–622.
- 80) Hill, P. G. The Measurement of Albumin in Serum and Plasma. *Ann. Clin. Biochem.* **1985**, *22*, 565–578.
- 81) Louderback, A. A new dye binding technic using bromocresol purple for determination of albumin in serum. *Clin. Chem.* **1968**, *14*, 793–794.
- 82) Carter, P. Ultramicroestimation of Human Serum Albumin- Binding of Cationic Dye 5,5'-Dibromo-o-Cresolsulfonphthalein. *Microchem. J.* **1970**, *15*, 531–539.
- 83) Pinnell, A. E.; Northam, B. E. New Automated Dye-Binding Method for Serum-Albumin Determination with Bromocresol Purple. *Clin. Chem.* **1978**, *24*, 80–86.

- 84) Ito, S.; Yamamoto, D. Mechanism for the Color Change in Bromocresol Purple Bound to Human Serum Albumin. *Clin. Chim. Acta* **2010**, *411*, 294–295.
- 85) Brackeen, G. L.; Dover, J. S.; Long, C. L. Serum Albumin. Differences in Assay Specificity. *Nutr. Clin. Pract.* **1989**, *4*, 203–205.
- 86) Coley-Grant, D.; Herbert, M.; Cornes, M. P.; Barlow, I. M.; Ford, C.; Gama, R. The Impact of Change in Albumin Assay on Reference Intervals, Prevalence of 'Hypoalbuminaemia' and Albumin Prescriptions. *Ann. Clin. Biochem.* **2016**, *53*, 112–116.
- 87) Kamphuis, S.; Salden, H. J. M.; Zuijderhoudt, F. M. J. Albumin Analysis in Plasma: Comparison between Bromocresol Green, Bromocresol Purple and Immunoassay in Adult (Non) Hemodialysis Patients. *Ned. Tijdschr. voor Klin. Chemie.* **2001**, *26*, 9–12.
- 88) Bonvicini, P.; Ceriotti, G.; Plebani, M.; Volpe, G. Heparin Interferes with Albumin Determination by Dye-Binding Methods. *Clin. Chem.* **1979**, *25*, 1459–1460.
- 89) Perry, B. W.; Doumas, B. T. Effect of Heparin on Albumin Determination by Use of Bromocresol Green and Bromocresol Purple. *Clin. Chem.* **1979**, *25*, 1520–1522.
- 90) Flores, R. A rapid and reproducible assay for quantitative estimation of proteins using bromophenol blue. *Anal. Biochem.* **1978**, *88*, 605–611.
- 91) Pugia, M. J.; Lott, J. A.; Profitt, J. A.; Cast, T. K. High-Sensitivity Dye Binding Assay for Albumin in Urine. *J. Clin. Lab. Anal.* **1999**, *13*, 180–187.
- 92) Schosinsky, K. H.; Vargas, M.; Luz Esquivel, A.; Chavarria, M. A. Simple Spectrophotometric Determination of Urinary Albumin by Dye-Binding with Use of Bromphenol Blue. *Clin. Chem.* **1987**, *33*, 223–226.
- 93) Kessler, M. A.; Meinitzer, A.; Wolfbeis, O. S. Albumin Blue 580 Fluorescence Assay for Albumin. *Anal. Biochem.* **1997**, *248*, 180–182.
- 94) Kessler, M. A.; Meinitzer, A.; Petek, W.; Wolfbeis, O. S. Microalbuminuria and Borderline-Increase Albumin Excretion Determined with a Centrifugal Analyzer and the Albumin Blue 580 Fluorescence Assay. *Clin. Chem.* **1997**, *43*, 996–1002.
- 95) Bradford, M. M. A rapid and sensitive method for the quantitation of microgram quantities of protein utilizing the principle of protein-dye binding. *Anal. Biochem.* **1976**, *72*, 248–254.

- 96) de Moreno, M. R.; Smith, J. F.; Smith, R. V. Mechanism studies of coomassie blue and silver staining of proteins. *J. Pharm. Sci.* **1986**, *75*, 907–911.
- 97) Bhardwaj, J.; Devarakonda, S.; Kumar, S.; Jang, J. Development of a Paper-Based Electrochemical Immunosensor Using an Antibody-Single Walled Carbon Nanotubes Bio-Conjugate Modified Electrode for Label-Free Detection of Foodborne Pathogens. *Sens. Actuators B: Chem.* **2017**, *253*, 115–123.
- 98) Santharaman, P.; Das, M.; Singh, S. K.; Sethy, N. K.; Bhargava, K.; Claussen, J. C.; Karunakaran, C. Label-Free Electrochemical Immunosensor for the Rapid and Sensitive Detection of the Oxidative Stress Marker Superoxide Dismutase 1 at the Point-of-Care. *Sens. Actuators B: Chem.* **2016**, *236*, 546–553.
- 99) Omidfar, K.; Dehdast, A.; Zarei, H.; Sourkoghi, B. K.; Larijani, B. Development of Urinary Albumin Immunosensor Based on Colloidal AuNP and PVA. *Biosens. Bioelectron.* **2011**, *26*, 4177–4183.
- 100) Tsai, J. Z.; Chen, C. J.; Settu, K.; Lin, Y. F.; Chen, C. L.; Liu, J. T. Screen-Printed Carbon Electrode-Based Electrochemical Immunosensor for Rapid Detection of Microalbuminuria. *Biosens. Bioelectron.* **2016**, *77*, 1175–1182.
- 101) Spencer, K.; Price, C. P. Kinetic immunoturbidimetry: the estimation of albumin. *Clin Chim Acta* **1979**, *95*, 263–276.
- 102) Watts, G. F.; Bennett, J. E.; Rowe, D. J.; Morris, R. W.; Gatling, W.; Shaw, K. M. Polak, A. Assessment of immunochemical methods for determining low concentrations of albumin in urine. *Clin. Chem.* **1986**, *32*, 1544–1548.
- 103) Ide, L. E. Y.; Akani, N. A. Microalbuminuria: It's Significance, risk factors and methods of detection. *Nig. Health J.* **2011**, *11*, 1–7.
- 104) Engvall, E.; Perlmann, P. Enzyme-linked immunosorbent assay (ELISA) quantitative assay of immunoglobulin G. *Immunochemistry*, **1971**, *8*, 871–874.
- 105) Larijani, B.; Javadi, A.; Shafae, A.; Mahmoudi, M.; Hemati, P. Screening for microalbuminuria in the early detection of diabetic nephropathy: a cheap and simple method. *Acta med. Iran.* **2002**, *40*, 65–68.
- 106) Killingsworth, L. M.; Savory, J. Nephelometric Methods for the Determination of Urinary Albumin, Transferrin and Alpha-2 Macroglobulin. *Ann. Clin. Lab. Sci.* **1974**, *4*, 46–52.

- 107) Curling, J. M.; Berglöf, J.; Lindquist, L. O.; Eriksson, S. Chromatographic Procedure for Purification of Human-Plasma Albumin. *Vox Sang.* **1977**, *33*, 97–107.
- 108) Redon, J. Measurement of microalbuminuria—what the nephrologist should know. *Nephrol. Dial. Transplant.* **2006**, *21*, 573–576.
- 109) Brinkman, J. W.; Bakker, S. J. L.; Gansevoort, R. T.; Hillege, H. L.; Kema, I. P.; Gans, R. O. B.; De Jong, P. E.; De Zeeuw, D. Which method for quantifying urinary albumin excretion gives what outcome? A comparison of immunonephelometry with HPLC *Kidney Int.* **2004**, *66*, S69–S75.
- 110) Ketha, H.; Singh, R. J. Quantitation of Albumin in Urine by Liquid Chromatography Tandem Mass Spectrometry. In *Methods in Molecular Biology*; Springer: Clifton, NJ, 2016; Vol. *1378*, pp 31–36.
- 111) Luetscher, J. A. Electrophoretic Analysis of Plasma and Urinary Proteins. *J. Clin. Invest.* **1940**, *19*, 313–320.
- 112) Martin, N. H.; Franglen, G. T. The Use and Limitations of Filter-Paper Electrophoresis. *J. Clin. Pathol.* **1954**, *7*, 87–105.
- 113) Keyser, J. W.; Watkins, G. L. Estimation of Serum-Proteins by Electrophoresis on Cellulose-Acetate. *Clin. Chem.* **1972**, *18*, 1541–1542.
- 114) Laurell, C. B. Quantitative Estimation of Proteins by Electrophoresis in Agarose Gel Containing Antibodies. *Anal. Biochem.* **1966**, *15*, 45–52.
- 115) Duly, E. B.; Grimason, S.; Grimason, P.; Barnes, G.; Trinick, T. R. Measurement of serum albumin by capillary zone electrophoresis, bromocresol green, bromocresol purple, and immunoassay methods. *J. Clin. Pathol.* **2003**, *56*, 780–781.
- 116) Seegmiller, J. C.; Sviridov, D.; Larson, T. S.; Borland, T. M.; Hortin, G. L.; Lieske, J. C. Comparison of urinary albumin quantification by immunoturbidimetry, competitive immunoassay, and protein-cleavage liquid chromatography-tandem mass spectrometry. *Clin. Chem.* **2009**, *55*, 1991–1994.
- 117) Seegmiller, J. C.; Barnidge, D. R.; Burns, B. E.; Larson, T. S.; Lieske, J. C.; Kumar, R. Quantification of urinary albumin by using protein cleavage and LC-MS/MS. *Clin. Chem.* **2009**, *55*, 1100–1107.
- 118) Lowry, O. H.; Rosebrough, N. J.; Farr, A. L.; Randall, R. J. Protein Measurement with Folin Phenol Reagent. *J. Biol. Chem.* **1951**, *193*, 265–275.

- 119) He, X. P.; Zang, Y.; James, T. D.; Li, J.; Chen, G. R. Probing Disease-related Proteins with Fluorogenic Composite Materials. *Chem. Soc. Rev.* **2015**, *44*, 4239–4248.
- 120) Jin, Q.; Feng, L.; Wang, D. D.; Dai, Z. R.; Wang, P.; Zou, L. W.; Liu, Z. H.; Wang, J. Y.; Yu, Y.; Ge, G. B.; Cui, J. N.; Yang, L. A two photon ratiometric fluorescent probe for imaging carboxylesterase 2 in living cells and tissues. *ACS Appl. Mater. Interfaces* **2015**, *7*, 28474–28481.
- 121) Czarnik, A. W. Chemical Communication in Water Using Fluorescent Chemosensors. *Acc. Chem. Res.* **1994**, *27*, 302–308.
- 122) Belmonte-Vázquez, J. L.; Amador-Sánchez, Y. A.; Rodríguez-Cortés, L. A.; Rodríguez-Molina, B. Dual-state emission (DSE) in organic fluorophores: design and applications. *Chem. Mater.* **2021**, *33*, 7160–7184.
- 123) Klymchenko, A. S. Solvatochromic and fluorogenic dyes as environment-sensitive probes: design and biological applications. *Acc. Chem. Res.* **2017**, *50*, 366–375.
- 124) Chen, C.; Fang, C. Devising Efficient Red-Shifting Strategies for Bioimaging: A Generalizable Donor-Acceptor Fluorophore Prototype. *Chem. Asian J.* **2020**, *15*, 1514–1523.
- 125) Haidekker, M. A.; Theodorakis, E. A. Molecular rotors—fluorescent biosensors for viscosity and flow. *Org. Biomol. Chem.* **2007**, *5*, 1669–1678.
- 126) Sasaki, S.; Drummen, G. P.; Konishi, G. I. Recent advances in twisted intramolecular charge transfer (TICT) fluorescence and related phenomena in materials chemistry. *J. Mater. Chem. C* **2016**, *4*, 2731–2743.
- 127) Grabowski, Z. R.; Rotkiewicz, K.; Rettig, W. Structural Changes Accompanying Intramolecular Electron Transfer: Focus on Twisted Intramolecular Charge-Transfer States and Structures. *Chem. Rev.* **2003**, *103*, 3899–4032.
- 128) Rettig, W. Photoinduced Charge Separation Via Twisted Intramolecular Charge Transfer States. *Top. Curr. Chem.* **1994**, *169*, 253–299.
- 129) Chen, S.; Zhang, M.; Zhu, C.; Lu, H.; Zhao, M.; Tian, X.; Zhang, Q.; De Souza, S. C.; Rong, F.; Zhou, H.; et al. Rational Design of Two-Photon Absorbing Dicyanomethylene-4H-Chromene Derivatives and Their Application in Bioimaging. *Dyes Pigm.* **2018**, *148*, 429–436.

- 130) Rajasekhar, K.; Achar, C. J.; Govindaraju, T. A red-NIR Emissive Probe for the Selective Detection of Albumin in Urine Samples and Live Cells. *Org. Biomol. Chem.* **2017**, *15*, 1584–1588.
- 131) Chao, X.; Yao, D.; Qi, Y.; Yuan, C.; Huang, D. A fluorescent sensor recognized by the FA1 site for highly sensitive detection of HSA. *Anal. Chim. Acta* **2021**, *1188*, 339201.
- 132) Wu, M. Y.; Li, K.; Li, C. Y.; Hou, J. T.; Yu, X. Q. A water-soluble near-infrared probe for colorimetric and ratiometric sensing of SO<sub>2</sub> derivatives in living cells. *Chem. Commun.* **2014**, *50*, 183–185.
- 133) Yuan, L.; Lin, W.; Zheng, K.; He, L.; Huang, W. Far-red to near infrared analyte-responsive fluorescent probes based on organic fluorophore platforms for fluorescence imaging. *Chem. Soc. Rev.* **2013**, *42*, 622–661.
- 134) Peng, P.; Strohecker, D.; Liao, Y. Negative photochromism of a TCF chromophore. *Chem. Commun.* **2011**, *47*, 8575–8577.
- 135) Wang, Y. R.; Feng, L.; Xu, L.; Li, Y.; Wang, D. D.; Hou, J.; Zhou, K.; Jin, Q.; Ge, G. B.; Cui, J. N.; Yang, L. A rapid-response fluorescent probe for the sensitive and selective detection of human albumin in plasma and cell culture supernatants. *Chem. Commun.* **2016**, *52*, 6064–6067.
- 136) Choudhury, R.; Patel, S. R.; Ghosh, A. Selective Detection of Human Serum Albumin by near Infrared Emissive Fluorophores: Insights into Structure-Property Relationship. *J. Photochem. Photobiol. A: Chem.* **2019**, *376*, 100–107.
- 137) Zhang, X.; Chen, Y. Synthesis and fluorescence of dicyanoisophorone derivatives. *Dyes Pigm.* **2013**, *99*, 531–536.
- 138) Zhang, Y.; Ma, Y.; Wang, Z.; Zhang, X.; Chen, X.; Hou, S.; Wang, H. A novel colorimetric and far-red emission ratiometric fluorescent probe for the highly selective and ultrafast detection of hypochlorite in water and its application in bioimaging. *Analyst* **2020**, *145*, 939–945.
- 139) Shu, W.; Zang, S.; Wang, C.; Gao, M.; Jing, J.; Zhang, X. An endoplasmic reticulum-targeted ratiometric fluorescent probe for the sensing of hydrogen sulfide in living cells and zebrafish. *Anal. Chem.* **2020**, *92*, 9982–9988.
- 140) Liu, B.; Zhao, X.; Zhou, M.; Song, C.; Zeng, C.; Qin, T.; Zhang, M.; Xu, Z. Modulating donor of dicyanoisophorone-based fluorophores to detect human serum

- albumin with NIR fluorescence. *Spectrochim. Acta A: Mol. Biomol. Spectrosc.* **2022**, *268*, 120666.
- 141) Liu, B.; Zeng, C.; Zheng, D.; Zhao, X.; Song, C.; Qin, T.; Xu, Z. A near-infrared dicyanoisophorone-based fluorescent probe for discriminating HSA from BSA. *Spectrochim. Acta A: Mol. Biomol. Spectrosc.* **2022**, *274*, 121081.
- 142) Shu, T.; Yang, Z.; Cen, Z.; Deng, X.; Deng, Y.; Dong, C.; Yu, Y. A Novel Ratiometric Fluorescent Probe Based on a BODIPY Derivative for Cu<sup>2+</sup> Detection in Aqueous Solution. *Anal. Methods* **2018**, *10*, 5755–5762.
- 143) Er, J. C.; Vendrell, M.; Tang, M. K.; Zhai, D.; Chang, Y. T. Fluorescent Dye Cocktail for Multiplex Drug-Site Mapping on Human Serum Albumin. *ACS Comb Sci.* **2013**, *15*, 452–457.
- 144) Er, J. C.; Tang, M. K.; Chia, C. G.; Liew, H.; Vendrell, M.; Chang, Y. T. MegaStokes BODIPY-Triazoles as Environmentally Sensitive Turn-on Fluorescent Dyes. *Chem. Sci.* **2013**, *4*, 2168–2176.
- 145) Dorh, N.; Zhu, S.; Dhungana, K. B.; Pati, R.; Luo, F. T.; Liu, H.; Tiwari, A. BODIPY-based fluorescent probes for sensing protein surface-hydrophobicity. *Sci. rep.* **2015**, *5*, 1–10.
- 146) Ilina, K.; Henary, M. Cyanine dyes containing quinoline moieties: history, synthesis, optical properties, and applications. *Chem. Eur. J.* **2021**, *27*, 4230–4248.
- 147) Xu, Z.; Huang, X.; Zhang, M.-X.; Chen, W.; Liu, S. H.; Tan, Y.; Yin, J. Tissue Imaging of Glutathione-Specific Naphthalimide-Cyanine Dye with Two-Photon and near Infrared Manners. *Anal. Chem.* **2019**, *91*, 11343–11348.
- 148) Reja, S. I.; Khan, I. A.; Bhalla, V.; Kumar, M. A TICT Based NIR-Fluorescent Probe for Human Serum Albumin: A Preclinical Diagnosis in Blood Serum. *Chem. Commun.* **2016**, *52*, 1182–1185.
- 149) Dey, G.; Singh, V.; Dewangan, J.; Daniel, P. V.; Kamthan, M.; Ghosh, D.; Mondal, P.; Ghosh, S. Renal clearable new NIR probe: precise quantification of albumin in biofluids and fatty liver disease state identification through tissue specific high contrast imaging in vivo. *Anal. chem.* **2017**, *89*, 10343–10352.
- 150) Liu, C.; Yang, W.; Gao, Q.; Du, J.; Luo, H.; Liu, Y.; Yang, C. Differential Recognition and Quantification of HSA and BSA Based on Two red-NIR Fluorescent Probes. *J. Lumin.* **2018**, *197*, 193–199.



- 151) Samanta, S.; Huang, M.; Lin, F.; Das, P.; Chen, B.; Yan, W.; Chen, J. J.; Ji, K.; Liu, L.; Qu, J.; Yang, Z. Solo smart fluorogenic probe for potential cancer diagnosis and tracking in vivo tumorous lymphatic systems via distinct emission signals. *Anal. Chem.* **2019**, *92*, 1541–1548.
- 152) Zhao, R.; Jia, T.; Shi, H.; Huang, C. A versatile probe for serum albumin and its application for monitoring wounds in live zebrafish. *J. Mater. Chem. B* **2019**, *7*, 2782–2789.
- 153) Deiana, M.; Mettra, B.; Mazur, L. M.; Andraud, C.; Samoc, M.; Monnereau, C.; Matczyszyn, K. Two-photon macromolecular probe based on a Quadrupolar Anthracenyl scaffold for sensitive recognition of serum proteins under simulated physiological conditions. *ACS omega* **2017**, *2*, 5715–5725.
- 154) Wang, Y. R.; Feng, L.; Xu, L.; Hou, J.; Jin, Q.; Zhou, N.; Lin, Y.; Cui, J. N.; Ge, G. B. An Ultrasensitive and Conformation Sensitive Fluorescent Probe for Sensing Human Albumin in Complex Biological Samples. *Sens. Actuators B Chem.* **2017**, *245*, 923–931.
- 155) Kar, C.; Ojha, B.; Das, G. A novel amphiphilic thiosemicarbazone derivative for binding and selective sensing of human serum albumin. *Luminescence* **2013**, *28*, 339–344.
- 156) Wang, Q.; Fan, J.; Zhou, Y.; Xu, S. Development of a human serum albumin structure-based fluorescent probe for bioimaging in living cells. *Spectrochim. Acta A: Mol. Biomol. Spectrosc.* **2022**, *269*, 120769.
- 157) Li, W.; Hu, Y. H.; Song, Y. Y.; Gu, Y. Y.; Yang, W. E. New Carbazole Fluorescent Sensor for Ultrasensitive and Ratiometric Sensing of SO<sub>2</sub> Derivatives and Hydrazine. *J. Photochem. Photobiol. A: Chem.* **2020**, *389*, 112269.
- 158) Dey, G.; Gaur, P.; Giri, R.; Ghosh, S. Optical Signaling in Biofluids: A Nondenaturing Photostable Molecular Probe for Serum Albumins. *Chem. Commun.* **2016**, *52*, 1887–1890.
- 159) Liang, Z.; Sun, Y.; Zeng, H.; Sun, K.; Yang, R.; Li, Z.; Zhang, K.; Chen, X.; Qu, L. Simultaneous detection of human serum albumin and sulfur dioxide in living cells based on a catalyzed michael addition reaction. *Anal. Chem.* **2020**, *92*, 16130–16137.
- 160) Zhang, P.; Guo, X.; Xiao, Y.; Zhang, Q.; Ding, C. Twisted Intramolecular Charge Transfer (TICT) Based Fluorescent Probe for Lighting up Serum Albumin with High

- Sensitivity in Physiological Conditions. *Spectrochim. Acta A: Mol. Biomol. Spectrosc.* **2019**, *223*, 117318.
- 161) Luo, Y.; Yu, Q. Q.; Gao, J. J.; Lang, X. X.; Li, H. Y.; Yu, X. F.; Qi, X. Y.; Wang, M. Q. Design, synthesis and mechanistic studies of a TICT based fluorogenic probe for lighting up protein HSA. *Bioorg. Med. Chem. Lett.* **2021**, *53*, 128438.
- 162) Chakraborty, G.; Ray, A. K.; Singh, P. K.; Pal, H. A highly fluorescent turn-on probe in the near-infrared region for albumin quantification in serum matrix. *Chem. Commun.* **2018**, *54*, 8383–8386.
- 163) Zhu, T.; Du, J.; Cao, W.; Fan, J.; Peng, X. Microenvironment-Sensitive Fluorescent Dyes for Recognition of Serum Albumin in Urine and Imaging in Living Cells. *Ind. Eng. Chem. Res.* **2016**, *55*, 527–533.
- 164) Akhavan, M.; Foroughifar, N.; Pashar, H.; Bekhradnia, A. Green Synthesis, Biological Activity Evaluation, and Molecular Docking Studies of Aryl Alkylidene 2, 4-Thiazolidinedione and Rhodanine Derivatives as Antimicrobial Agents. *Comb. Chem. High Throughput Screen.* **2019**, *22*, 716–72.
- 165) Wu, Y.; Ding, X.; Xu, S.; Yang, Y.; Zhang, X.; Wang, C.; Lei, H.; Zhao, Y. Design and Synthesis of Biaryloxazolidinone Derivatives Containing a Rhodanine or Thiohydantoin Moiety as Novel Antibacterial Agents against Gram-Positive Bacteria. *Bioorg. Med. Chem. Lett.* **2019**, *29*, 496–502.
- 166) Du, J.; Zhu, T.; Gu, Q.; Cao, W.; Fan, J.; Peng, X. Fabrication of Artificial Fluorescent Protein Probe for HSA Recognition and Relay Sensing Ag<sup>+</sup> by Functional Microenvironment-Sensitive Fluorescent Dye. *Sens. Actuators B: Chem.* **2018**, *263*, 661–667.
- 167) Xu, Y. J.; Su, M. M.; Li, H. L.; Liu, Q. X.; Xu, C.; Yang, Y. S.; Zhu, H. L. A Fluorescent Sensor for Discrimination of HSA from BSA through Selectivity Evolution. *Anal. Chim. Acta* **2018**, *1043*, 123–131.
- 168) Zheng, D. J.; Xu, J.; Su, M. M.; Sun, Z. G.; Jiao, Q. C.; Yang, Y. S.; Zhu, H. L. A Small, Steady, Rapid and Selective TICT Based Fluorescent HSA Sensor for Pre-Clinical Diagnosis. *Sens. Actuators B: Chem.* **2018**, *271*, 82–89.
- 169) Pei, S.; Li, J.; Zhang, C.; Zhang, G.; Zhou, Y.; Fan, L.; Wang, W.; Shuang, S.; Dong, C. TICT-Based Microenvironment-Sensitive Probe with Turn-on Red Emission for

- Human Serum Albumin Detection and for Targeting Lipid Droplet Imaging. *ACS Biomater. Sci. Eng.* **2021**, *8*, 253–260.
- 170) Smith, S. E.; Williams, J. M.; Ando, S.; Koide, K. Time-Insensitive Fluorescent Sensor for Human Serum Albumin and Its Unusual Red Shift. *Anal. Chem.* **2014**, *86*, 2332–2336.
- 171) Wu, Y. Y.; Yu, W. T.; Hou, T. C.; Liu, T. K.; Huang, C. L.; Chen, I. C.; Tan, K. T. A Selective and Sensitive Fluorescent Albumin Probe for the Determination of Urinary Albumin. *Chem. Commun.* **2014**, *50*, 11507–11510.
- 172) Yang, L.; Niu, J. Y.; Sun, R.; Xu, Y. J.; Ge, J. F. Rosamine with Pyronine-Pyridinium Skeleton: unique Mitochondrial Targetable Structure for Fluorescent Probes. *Analyst* **2018**, *143*, 1813–1819.
- 173) Ahn, Y. H.; Lee, J. S.; Chang, Y. T. Selective Human Serum Albumin Sensor from the Screening of a Fluorescent Rosamine Library. *J. Comb. Chem.* **2008**, *10*, 376–380.
- 174) Shen, P.; Hua, J.; Jin, H.; Du, J.; Liu, C.; Yang, W.; Gao, Q.; Luo, H.; Liu, Y.; Yang, C.; Recognition and Quantification of HSA: A Fluorescence Probe across  $\alpha$ -Helices of Site I and Site II. *Sens. Actuators B: Chem.* **2017**, *247*, 587–594.
- 175) Yan, X. J.; Li, Z.; Liu, H. B.; Wang, Z. G.; Fan, J.; Xie, C. Z.; Li, Q. Z.; Xu, J. Y. A chromone hydrazide Schiff base fluorescence probe with high selectivity and sensitivity for the detection and discrimination of human serum albumin (HSA) and bovine serum albumin (BSA). *J. Photochem. Photobiol. A: Chem.* **2022**, *422*, 113576.
- 176) Liao, C.; Li, F.; Huang, S.; Zheng, B.; Du, J.; Xiao, D. A Specific and Biocompatible Fluorescent Sensor Based on the Hybrid of GFP Chromophore and Peptide for HSA Detection. *Biosens. Bioelectron.* **2016**, *86*, 489–495.
- 177) Huang, S.; Li, F.; Liao, C.; Zheng, B.; Du, J.; Xiao, D. A Selective and Sensitive Fluorescent Probe for the Determination of HSA and Trypsin. *Talanta* **2017**, *170*, 562–568.
- 178) Luo, Z.; Liu, B.; Zhu, K.; Huang, Y.; Pan, C.; Wang, B.; Wang, L. An environment-sensitive fluorescent probe for quantification of human serum albumin: Design, sensing mechanism, and its application in clinical diagnosis of hypoalbuminemia. *Dyes Pigm.* **2018**, *152*, 60–66.

- 179) Li, P.; Wang, Y.; Zhang, S.; Xu, L.; Wang, G.; Cui, J. An ultrasensitive rapid-response fluorescent probe for highly selective detection of HSA. *Tetrahedron Lett.* **2018**, *59*, 1390–1393.
- 180) Zhao, X.; Zheng, W.; Qin, T.; Du, X.; Lei, Y.; Lv, T.; Zhou, M.; Xu, Z.; Wang, L.; Liu, B.; Peng, X. An anti-interference fluorescent probe for point-of-care diagnosis of albuminuria. *Sens. Actuators B: Chem* **2022**, *351*, 130980.
- 181) Nijveldt, R. J.; van Nood, E.; van Hoorn, D. E.; Boelens, P. G.; van Norren, K.; van Leeuwen, P. A. Flavonoids: A Review of Probable Mechanisms of Action and Potential Applications. *Am. J. Clin. Nutr.* **2001**, *74*, 418–425.
- 182) Sytnik, A.; Litvinyuk, I. Energy Transfer to a Proton-Transfer Fluorescence Probe: Tryptophan to a Flavonol in Human Serum Albumin. *Proc. Natl. Acad. Sci. USA.* **1996**, *93*, 12959–12963.
- 183) Liu, B.; Pang, Y.; Bouhenni, R.; Duah, E.; Paruchuri, S.; McDonald, L. A step toward simplified detection of serum albumin on SDS-PAGE using an environment-sensitive flavone sensor. *Chem. Commun.* **2015**, *51*, 11060-11063.
- 184) Liu, B.; Bi, X.; McDonald, L.; Pang, Y.; Liu, D.; Pan, C.; Wang, L. Solvatochromic Fluorescent Probes for Recognition of Human Serum Albumin in Aqueous Solution: Insights into Structure-Property Relationship. *Sens. Actuators B: Chem.* **2016**, *236*, 668–674.
- 185) Zhu, K.; Lv, T.; Qin, T.; Huang, Y.; Wang, L.; Liu, B. A flavonoid-based fluorescent probe enables the accurate quantification of human serum albumin by minimizing the interference from blood lipids. *Chem. Commun.* **2019**, *55*, 13983–13986.
- 186) Su, L.; Yang, F.; Li, W.; Li, H.; Wang, C.; Wang, Q.; Yuan, L. Engineering a selective fluorescent sensor with a high signal-to-background ratio for microalbumin detection and imaging. *Mater. Chem. Front.* **2022**, *6*, 3084–3093.
- 187) Jisha, V. S.; Arun, K. T.; Hariharan, M.; Ramaiah, D. Site-Selective Interactions: Squaraine Dye-Serum Albumin Complexes with Enhanced Fluorescence and Triplet Yields. *J. Phys. Chem. B.* **2010**, *114*, 5912–5919.
- 188) Luo, J.; Xie, Z.; Lam, J. W.; Cheng, L.; Chen, H.; Qiu, C.; Kwok, H. S.; Zhan, X.; Liu, Y.; Zhu, D.; Tang, B. Z. Aggregation-induced emission of 1-methyl-1, 2, 3, 4, 5-pentaphenylsilole. *Chem. commun.* **2001**, *18*, 1740–1741.

- 189) Zhu, C.; Kwok, R. T.; Lam, J. W.; Tang, B. Z. Aggregation-induced emission: a trailblazing journey to the field of biomedicine. *ACS Appl. Bio Mater.* **2018**, *1*, 1768–1786.
- 190) Hong, Y.; Feng, C.; Yu, Y.; Liu, J.; Lam, J. W. Y.; Luo, K. Q.; Tang, B. Z. Quantitation, Visualization, and Monitoring of Conformational Transitions of Human Serum Albumin by a Tetraphenylethene Derivative with Aggregation-Induced Emission Characteristics. *Anal. Chem.* **2010**, *82*, 7035–7043.
- 191) Wang, Z.; Ma, K.; Xu, B.; Li, X.; Tian, W. A highly sensitive “turn-on” fluorescent probe for bovine serum albumin protein detection and quantification based on AIE-active distyrylanthracene derivative. *Sci. China Chem.* **2013**, *56*, 1234–1238.
- 192) Peng, L.; Wei, R.; Li, K.; Zhou, Z.; Song, P.; Tong, A. A ratiometric fluorescent probe for hydrophobic proteins in aqueous solution based on aggregation-induced emission. *Analyst* **2013**, *138*, 2068–2072.
- 193) Li, W.; Chen, D.; Wang, H.; Luo, S.; Dong, L.; Zhang, Y.; Shi, J.; Tong, B.; Dong, Y. Quantitation of albumin in serum using “turn-on” fluorescent probe with aggregation-enhanced emission characteristics. *ACS Appl. Mater. Interfaces* **2015**, *7*, 26094–26100.
- 194) Li, J.; Wu, J.; Cui, F.; Zhao, X.; Li, Y.; Lin, Y.; Li, Y.; Hu, J.; Ju, Y. A dual functional fluorescent sensor for human serum albumin and chitosan. *Sens. Actuators B: Chem.* **2017**, *243*, 831–837.
- 195) Dey, N.; Maji, B.; Bhattacharya, S. Motion-Induced Changes in Emission as an Effective Strategy for the Ratiometric Probing of Human Serum Albumin and Trypsin in Biological Fluids. *Chem. Asian J.* **2018**, *13*, 664–671.
- 196) Hu, Q.; Yao, B.; Owyong, T. C.; Prashanth, S.; Wang, C.; Zhang, X.; Wong, W. W. H.; Tang, Y.; Hong, Y. Detection of Urinary Albumin Using a “Turn-on” Fluorescent Probe with Aggregation-Induced Emission Characteristics. *Chem. Asian J.* **2021**, *16*, 1245–1252.
- 197) Zheng, J.; Cao, J.; Tu, Y.; Huang, C.; Liu, M.; Zhang, M. Water-soluble naphthalimide derivatives probe with near-infrared fluorescence “turn-on” characteristics for the detection of bovine serum albumin. *J. Mol. Struct.* **2022**, *1250*, 131868.

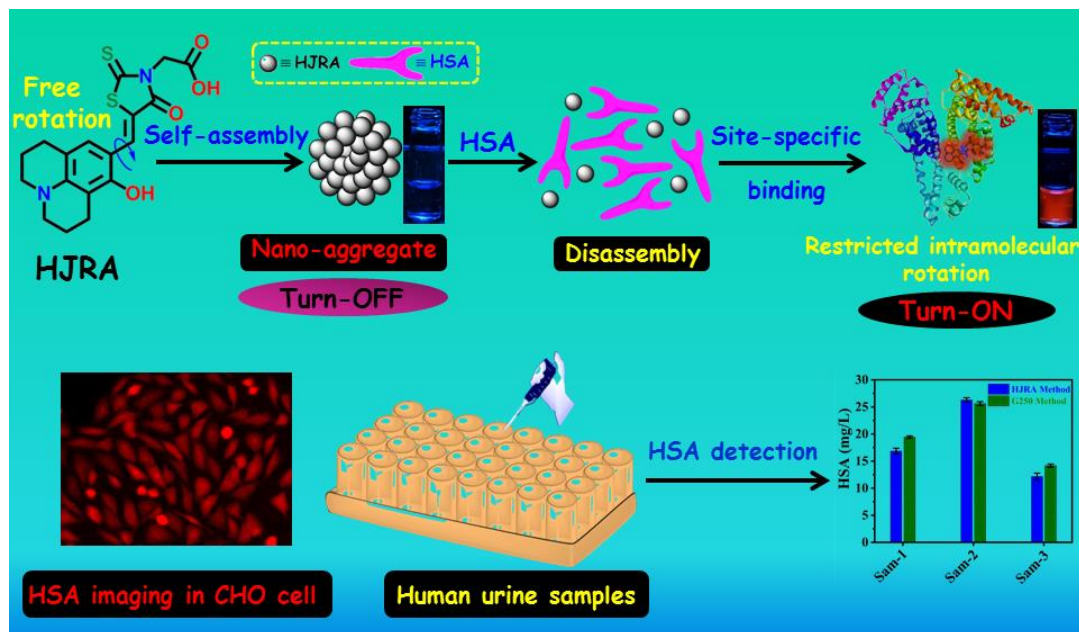
- 198) Zang, S.; Wu, S.; Xiao, L.; Deng, X.; Zhao, Y. Hyperbranched Tetraphenylethylene Derivatives with Low Non-specific Aggregation-Induced Emission for Fluorescence Recognition of Proteins with Hydrophobic Pockets. *Anal. Chem.* **2022**, *94*, 8365–8372.
- 199) Ren, C.; Zhang, J.; Chen, M.; Yang, Z. Self-assembling small molecules for the detection of important analytes. *Chem. Soc. Rev.* **2014**, *43*, 7257–7266.
- 200) Molla, M. R.; Prasad, P.; Thayumanavan, S. Protein-induced supramolecular disassembly of amphiphilic polypeptide nanoassemblies. *J. Am. Chem. Soc.* **2015**, *137*, 7286–7289.
- 201) Wang, H.; Zhuang, J.; Raghupathi, K. R.; Thayumanavan, S. A supramolecular dissociation strategy for protein sensing. *Chem. Commun.* **2015**, *51*, 17265–17268.
- 202) Mizusawa, K.; Takaoka, Y.; Hamachi, I. Specific cell surface protein imaging by extended self-assembling fluorescent turn-on nanoprobe. *J. Am. Chem. Soc.* **2012**, *134*, 13386–13395.
- 203) Anees, P.; Sreejith, S.; Ajayaghosh, A. Self-assembled near-infrared dye nanoparticles as a selective protein sensor by activation of a dormant fluorophore. *J. Am. Chem. Soc.* **2014**, *136*, 13233–13239.
- 204) Fan, X.; He, Q.; Sun, S.; Li, H.; Pei, Y.; Xu, Y. Nanoparticles self-assembled from multiple interactions: a novel near-infrared fluorescent sensor for the detection of serum albumin in human sera and turn-on live-cell imaging. *Chem. Commun.* **2016**, *52*, 1178–1181.
- 205) Yu, Y.; Huang, Y.; Hu, F.; Jin, Y.; Zhang, G.; Zhang, D.; Zhao, R. Self-assembled nanostructures based on activatable red fluorescent dye for site-specific protein probing and conformational transition detection. *Anal. Chem.* **2016**, *88*, 6374–6381.
- 206) Gao, T.; Yang, S.; Cao, X.; Dong, J.; Zhao, N.; Ge, P.; Zeng, W.; Cheng, Z. Smart self-assembled organic nanoprobe for protein-specific detection: design, synthesis, application, and mechanism studies. *Anal. Chem.* **2017**, *89*, 10085–10093.
- 207) Singh, P.; Mittal, L. S.; Kaur, S.; Kaur, S.; Bhargava, G.; Kumar, S. Self-assembled small molecule based fluorescent detection of serum albumin proteins: Clinical detection and cell imaging. *Sens. Actuators B: Chem.* **2018**, *255*, 478–489.

- 208) Samanta, S.; Halder, S.; Das, G. Twisted-intramolecular-charge-transfer-based turn-on fluorogenic nanoprobe for real-time detection of serum albumin in physiological conditions. *Anal. chem.* **2018**, *90*, 7561–7568.
- 209) Zheng, Z.; Li, H.; Sun, S.; Xu, Y. Media dependent switching of selectivity and continuous near infrared turn-on fluorescence response through cascade interactions from noncovalent to covalent binding for detection of serum albumin in living cells. *ACS Appl. Mater. Interfaces* **2018**, *10*, 44336–44343.
- 210) Park, J.; Kim, Y. Colloidal fluorophore aggregates for the selective detection of albumins in solution and on electrophoresis gels. *ChemBioChem* **2019**, *20*, 350–354.
- 211) Wang, Z. G.; Yan, X. J.; Liu, H. B.; Zhang, D. L.; Liu, W.; Xie, C. Z.; Li, Q. Z.; Xu, J. Y. A novel hydrazone Schiff base self-assembled nanoprobe for selective detection of human serum albumin and its applications in renal disease surveillance. *J. Mater. Chem. B* **2020**, *8*, 8346–8355.
- 212) Shivran, N.; Koli, M.; Chakraborty, G.; Srivastava, A. P.; Chattopadhyay, S.; Mula, S. A BODIPY-O-glycoside based near-infrared fluorescent sensor for serum albumin. *Org. Biomol. Chem.* **2021**, *19*, 7920–7929.
- 213) Kim, S. J.; Rhee, H. W.; Park, H. J.; Kim, H. Y.; Kim, H. S.; Hong, J. I. Fluorescent Probes Designed for Detecting Human Serum Albumin on the Basis of Its Pseudo-Esterase Activity. *Bioorg. Med. Chem. Lett.* **2013**, *23*, 2093–2097.
- 214) Sun, Q.; Wang, W.; Chen, Z.; Yao, Y.; Zhang, W.; Duan, L.; Qian, J. A fluorescence turn-on probe for human (bovine) serum albumin based on the hydrolysis of a dioxaborine group promoted by proteins. *Chem. Commun.* **2017**, *53*, 6432–6435.
- 215) Jin, Q.; Feng, L.; Zhang, S. J.; Wang, D. D.; Wang, F. J.; Zhang, Y.; Cui, J. N.; Guo, W. Z.; Ge, G. B.; Yang, L. Real-time tracking the synthesis and degradation of albumin in complex biological systems with a near-infrared fluorescent probe. *Anal. chem.* **2017**, *89*, 9884–9891.



## Chapter 2

Serum Albumin Inspired Self-Assembly/Disassembly of a Fluorogenic Nanoprobe for Real-Time Monitoring and Quantification of Urinary Albumin with Live Cell Imaging Application



### Abstract:

Abnormal levels (high/low) of urinary human serum albumin (HSA) are associated with a number of diseases and thus act as an essential biomarker for quick therapeutic monitoring and biomedical diagnosis, entailing the urgent development of an effective chemosensor to quantify the albumin levels. Herein, we have rationally designed and developed a small fluorogenic molecular probe, (Z)-2-(5-((8-hydroxy-2,3,6,7-tetrahydro-1H,5H-pyrido[3,2,1-ij]quinolin-9-yl)methylene)-4-oxo-2-thioxothiazolidin-3-yl)acetic acid (HJRA) with a twisted intramolecular charge transfer (TICT) property, which can easily self-assemble into nonfluorescent nanoaggregates in aqueous solution. However, HJRA nanoaggregates can selectively bind with serum albumin proteins (HSA/BSA) in ~100% PBS medium thereby facilitating the disassembly of nanoaggregates into monomers, exhibiting a clear turn-on red fluorescent response toward HSA and BSA. Analysis of the specific binding mechanism between HJRA and HSA using a site-selective fluorescence displacement assay and molecular docking simulations indicates that a variety of noncovalent interactions are responsible for the disassembly of nanoaggregates with the concomitant trapping of the HJRA monomer at site I in HSA yielding a substantial red emission caused by the inhibition of intramolecular rotation of HJRA probe inside the hydrophobic cavity of HSA. The limit of detection (LOD) determined by the  $3\sigma/\text{slope}$  method was found to be 1.13 nM, which is substantially below the normal HSA concentration in healthy urine signifying the very high sensitivity of the probe toward HSA. The comparable results and quick response toward quantification of HSA in urine by HJRA with respect to the Bradford method clearly point toward the superiority of this method compared to the existing ones and may lead to biomedical applications for HSA quantification in urine. It may also find potential application in live-cell imaging of HSA.

### 2.1 Introduction

Protein detection and quantification are very much crucial in fundamental research, biomedical diagnosis and therapeutic monitoring.<sup>1,2</sup> Human serum albumin (HSA), a most abundant thiol-containing protein, present in very high concentration in blood serum, serves a number of key biological functions including blood osmotic pressure regulation, plasma pH buffering, and fluid transportation in the body and also possesses some antioxidant properties.<sup>3,4</sup> HSA, by virtue of its exceptional ligand-binding ability, functions as a transporter for a wide range of endogenous and exogenous substances, and hence has a significant influence on therapeutic efficacy, cell metabolism, and disease detection.<sup>5-7</sup>

HSA is synthesized exclusively in the liver, primarily in the polysomes of hepatocytes maintaining a normal level of 35 to 55 g/L in blood plasma in a healthy adult.<sup>8,9</sup> Contrarily, albumin levels in urine fall below 30 mg/L, probably due to the kidneys preventing essential materials like albumin and other proteins from entering the urine.<sup>10</sup> Nevertheless, an aberrant concentration of albumin in the blood plasma and urine has a direct impact on an individual's health. Hence, albumin levels in body fluids (blood/urine) are commonly employed as health indicators.<sup>9</sup> For example, an HSA deficit in the blood plasma, a case of hypoalbuminemia, may cause chronic hepatitis, kidney disease, liver cirrhosis and failure.<sup>11</sup> Conversely, excess albumin (30–300 mg/L) in urine can cause microalbuminuria, which has been identified in diabetes mellitus and hypertension, manifesting an early sign of cardiovascular and renal disease.<sup>12-14</sup> Moreover, a patient with an urinary albumin concentration >300 mg/L is diagnosed with macroalbuminuria, indicating a stage where renal damage has progressed to an advanced stage.<sup>15</sup>

Thus, in the last few decades bioanalytical chemists have paid attention to developing an effective chemosensor for the accurate detection of albumin protein in biological fluids, particularly in urine samples. So far, several analytical approaches like colorimetric (Lowry, Bradford etc.), radiolabeling, immunoassays, electrophoresis, fluorometry and LC–MS proteomics-based methods have been established effectively for serum albumin detection in body fluids.<sup>16-19</sup> Traditionally, ELISA technique is used for the measuring of HSA concentration in body fluid like blood, urine etc.<sup>20</sup> But, its accurate point-of-care testing is limited by the involvement of multistep and time-consuming preparations. However, fluorometry is considered as the most popularly used technique for the accurate quantification

of proteins owing to its high selectivity, sensitivity, technical simplicity, rapid responsivity and noninvasive benefits along with high-resolution real-time imaging in living cells.<sup>21-25</sup>

In the past few years, fluorophores with typical aggregation-induced emission (AIE) activity have garnered the attention of chemists and biologists to explore the possibility of their biomedical applications.<sup>26-28</sup> As a consequence, a number of AIEgen-based fluorescent molecular probes have been developed for the detection of HSA and BSA.<sup>29-33</sup> Recently, self-assembled molecular probes have been emerging with unique superiority to their individual molecular form as a potent material for protein sensing analysis.<sup>34-36</sup> Molecular self-assembled nanoaggregates with exceptional photostability and biocompatibility offer a wide range of flexibility in chemical design and fine-tuning of optical properties. For instance, a self-assembled probe exhibits no or very little fluorescence due to the aggregation caused quenching (ACQ) effect, but when the probe responds to the target analytes by undergoing disassembly, it will emit strong fluorescence.<sup>37</sup> Besides, there are also few reports where some near-infrared (NIR) dyes bind with HSA to generate HSA-dye nanocomposites for applications in bioimaging, tumor therapeutic diagnosis and potential drug delivery.<sup>38</sup> However, Thayumanavan and colleagues have successfully employed the *polymer-nanoparticle-disassembly* strategy as a unique technique for the detection of both protein and enzyme.<sup>39-41</sup> On the contrary, only a few examples exist where this disassembly technique was utilized successfully for *small-molecule derived self-assembled nanoaggregated* probes for the HSA and BSA detection.<sup>42-49</sup>

Despite the difficult task in comprehending HSA's complex multidomain structure and remarkable ligand binding ability,<sup>3,50</sup> targetable nanoaggregates with activatable signals based on molecular *self-assembly* may also be useful for exploring noncovalent site-selective interactions. Very recently a number of fluorescent molecular probes for HSA detection<sup>9,20,51-61</sup> have been published; however, they are incapable of self-assembling into nanoaggregates and have a number of drawbacks, including low sensitivity and selectivity issues, delayed reaction time, poor biocompatibility, etc. Furthermore, several bioprobes have been found to be ineffective and have limited uses in advanced biomedical research because most of them struggle to measure nanomolar level of HSA present in complex biological fluids owing to their high detection limits, large background signal and excitation/emission occurring at comparatively shorter wavelengths.

Therefore, in this article, we rationally designed and developed a TICT-based small organic molecular probe HJRA that can easily self-assemble into nonfluorescent nanoaggregates in aqueous solution. However, HJRA nanoaggregates can selectively bind with serum albumins (HSA/BSA), which facilitates the disassembly of nanoaggregates into monomers, exhibiting a noticeable turn-on red fluorescent response toward HSA and BSA in biological environments. Some particular advantages of the probe may be include (i) the coupling of disassembly induced emission enhancement with the site-specific recognition mechanism favors the enhancement of the sensitivity and selectivity of the probe; (ii) a very fast (~15 s) fluorescence response time of HJRA toward HSA; (iii) very low LOD value (1.13 nM), substantially below the normal level of HSA in healthy urine, signifying the high sensitivity of the probe toward HSA; (iv) most strikingly, the outstanding HSA detection capabilities of HJRA in urine, allowing us develop a rapid and effective way to monitor the health status of people; and (v) finally, the probe may also find potential applications for live-cell imaging of HSA. Here, in addition to the detailed morphological characterization, HSA site marker displacement studies, molecular docking, steady-state fluorescence, and lifetime spectroscopic studies were also conducted to understand the underlying sensing mechanism.

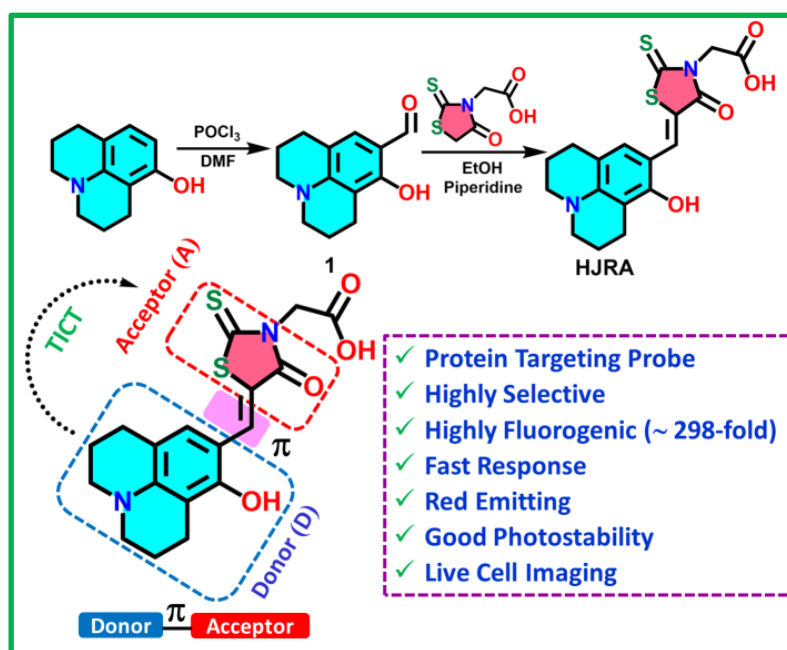
## 2.2 Experimental Section

### 2.2.1 Materials

8-Hydroxyjulolidine, rhodanine-3-acetic acid, Coomassie Brilliant Blue G-250, ibuprofen, warfarin and glycerol were purchased from Sigma-Aldrich and used as received. All the proteins and enzymes (HSA, BSA,  $\beta$ -lactoglobulin, lysozyme, CT-DNA, hemoglobin, cytochrome C, proteinase K, collagen, pepsin and trypsin) as well as other biomolecules like glutathione (GSH), creatinine, uric acid, glucose, urea and all amino acids were also obtained from Sigma Aldrich. The sodium salts of various anions ( $F^-$ ,  $Cl^-$ ,  $Br^-$ ,  $I^-$ ,  $PO_4^{3-}$ ,  $BrO_3^-$ ,  $ClO_4^-$ ,  $N_3^-$ ,  $NO_2^-$ ,  $NO_3^-$ ,  $SCN^-$ ,  $CH_3COO^-$ ,  $H_2PO_4^-$ ,  $S_2O_3^{2-}$ ,  $SH^-$ ,  $HSO_4^-$ ) and perchlorate salts of different cations ( $Na^+$ ,  $K^+$ ,  $Ca^{2+}$ ,  $Mg^{2+}$ ,  $NH_4^+$ ,  $Mn^{2+}$ ,  $Co^{2+}$ ,  $Ni^{2+}$ ,  $Cu^{2+}$ ,  $Al^{3+}$ ,  $Hg^{2+}$ ,  $Fe^{2+}$ ,  $Zn^{2+}$ ,  $Fe^{3+}$ ) were procured either from Sigma-Aldrich or from other commercial suppliers. Reagent grade (Merck, India) solvents were used for the synthetic purposes and dried prior to use according to the standard procedures. For the spectroscopic studies deionized water from Milli-Q source and HPLC-grade solvents were used.

### 2.2.2 Instrumentation

The  $^1\text{H}$  NMR and  $^{13}\text{C}$  NMR spectra were recorded on a Bruker 400 MHz spectrophotometer using tetramethylsilane as an internal standard in  $\text{DMSO-}d_6$ . The following abbreviations were used to explain multiplicities: s = singlet, d = doublet, t = triplet, q = quartet, m = multiplet, br = broad. Coupling constants,  $J$  were reported in Hertz unit (Hz). The  $\text{ESI-MS}^+$  ( $m/z$ ) spectra of the probe was recorded on a HRMS spectrophotometer (model: QTOF Micro YA263). The Fourier transform infrared spectra ( $4000\text{--}400\text{ cm}^{-1}$ ) of the probe was recorded on a Perkin-Elmer RX I FT-IR spectrophotometer with a solid KBr disc. The UV-Vis absorbance spectral studies were carried out on an Agilent diode-array Spectrophotometer (Agilent 8453) using a 1 cm path length quartz cuvette in the wavelength range of 190-900 nm. Steady-state fluorescence spectroscopic measurements were performed on a PTI spectrofluorimeter (Model QM-40) by using a fluorescence free quartz cuvette of 1 cm path length. The excitation and emission slit widths were fixed at 3 nm. Fluorescence lifetimes were determined from time-resolved intensity decay by the method of time correlated single photon counting (TCSPC) measurements using a picosecond diode laser (IBH Nanoled-07) in an IBH fluorocube apparatus. The fluorescence decay data were collected on a Hamamatsu MCP photomultiplier (R3809) and examined by the IBH DAS6 software.



Scheme 2.1 Rational Design and Synthesis of HJRA.

### 2.2.3 Synthesis and Characterization of the Compound 1

In the first step (Scheme 2.1), compound **1** was synthesized according to the method described in literature.<sup>62</sup> A solution of 8-Hydroxyjulolidine (1.892 g, 10 mmol) in 2 mL of freshly distilled DMF was added dropwise to a cold solution of POCl<sub>3</sub> (10.5 mmol, 1.609 g, 0.978 mL) in 4 mL of DMF and stirred for 30 min at room temperature. After this, the solution was heated at 100 °C under N<sub>2</sub> atmosphere for an additional 30 min. Then the solution was cooled to room temperature and 15 mL of water was added with constant stirring and a light green solid formed slowly. The precipitate was filtered, washed with water, and dried in a vacuum desiccator. The solid was dissolved in benzene/5% ethyl acetate and filtered through silica gel bed. The filtrate was collected and solvent was evaporated by a rotary, leaving yellowish oil which was solidified on standing. Compound **1** was obtained as a yellow solid (79% yield) after recrystallization of the crude residue in hexane. <sup>1</sup>H NMR (400 MHz, DMSO-*d*<sub>6</sub>):  $\delta$  in ppm = 11.84 (s, 1H), 9.35 (s, 1H), 6.96 (s, 1H), 3.28–3.24 (m, 4H), 2.60 (t, *J* = 6.4 Hz, 2H), 2.53 (t, *J* = 6.4 Hz, 2H), 1.86–1.78 (m, 4H) (Figure 2.1). <sup>13</sup>C NMR (101 MHz, DMSO-*d*<sub>6</sub>):  $\delta$  in ppm = 192.1, 158.9, 149.7, 131.4, 113.9, 110.5, 104.7, 50.0, 49.6, 27.0, 21.5, 20.4, 19.7 (Figure 2.2). HRMS (ESI) *m/z*: calcd for [M + H<sup>+</sup>], 218.1181; found, 218.1179 (Figure 2.3).

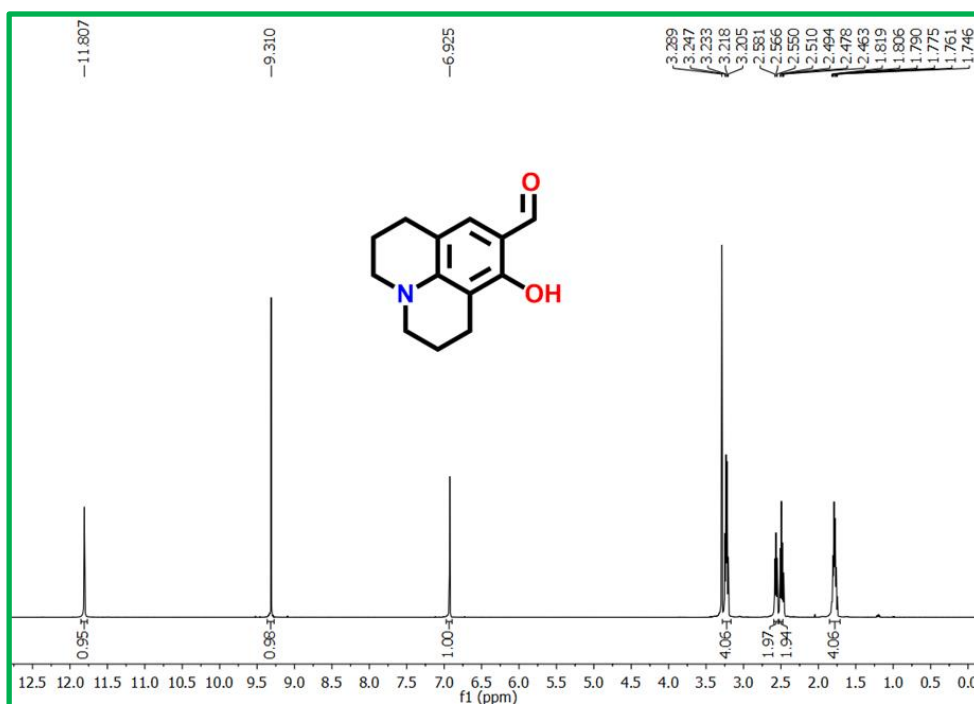


Figure 2.1 <sup>1</sup>H-NMR spectrum of compound **1** in DMSO-*d*<sub>6</sub>.



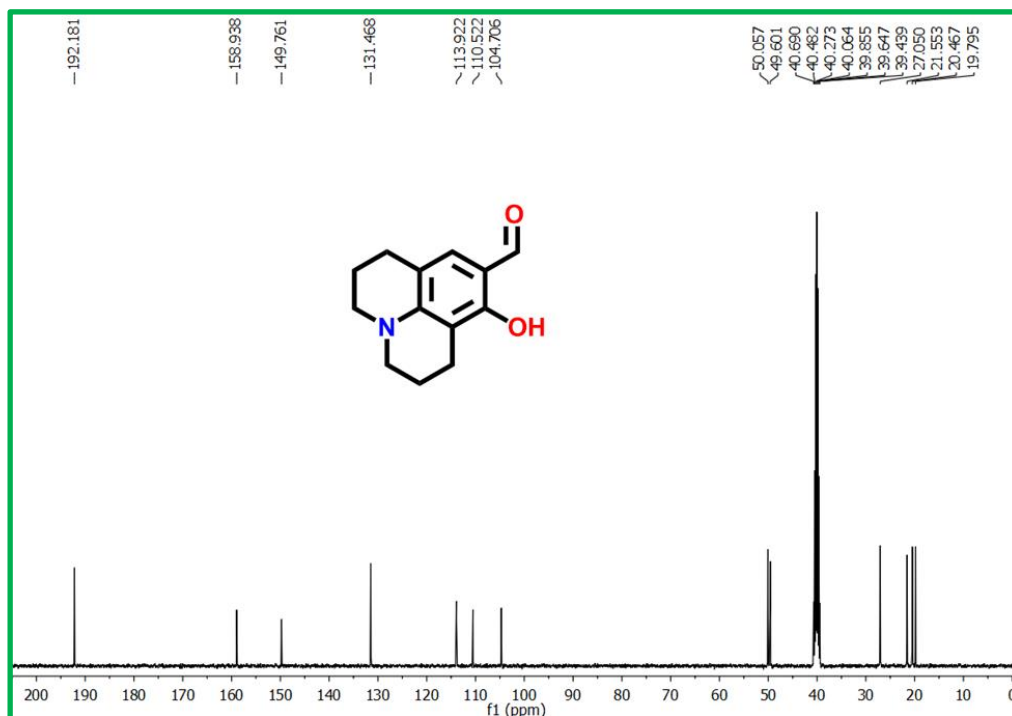


Figure 2.2  $^{13}\text{C}$ -NMR spectrum of compound **1** in  $\text{DMSO-}d_6$ .

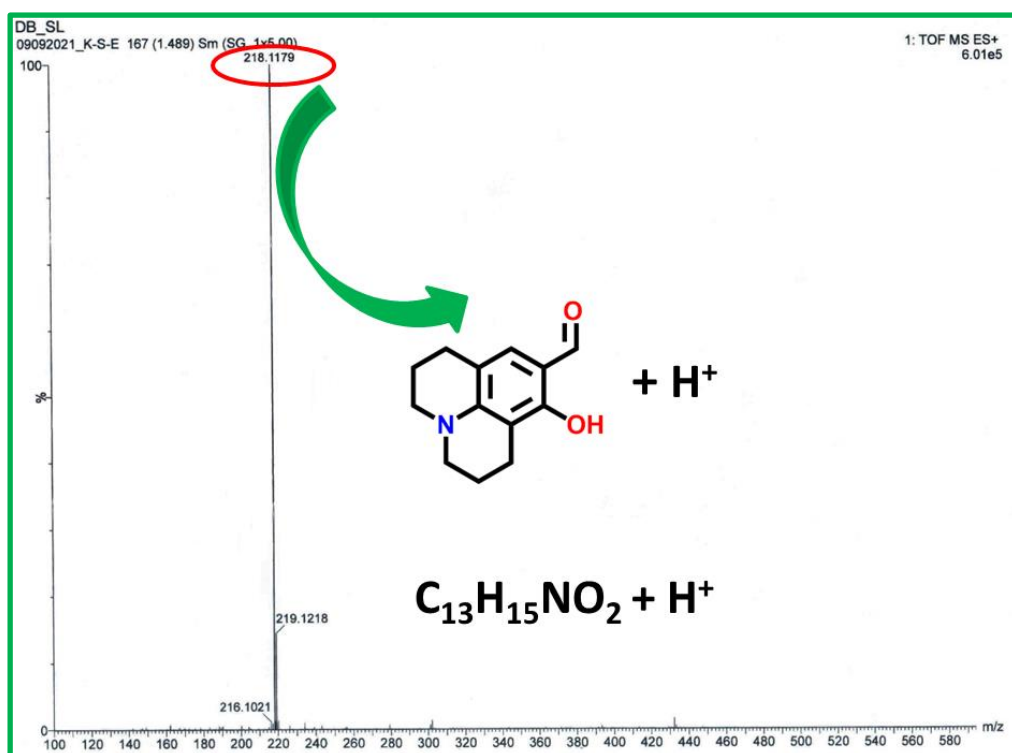
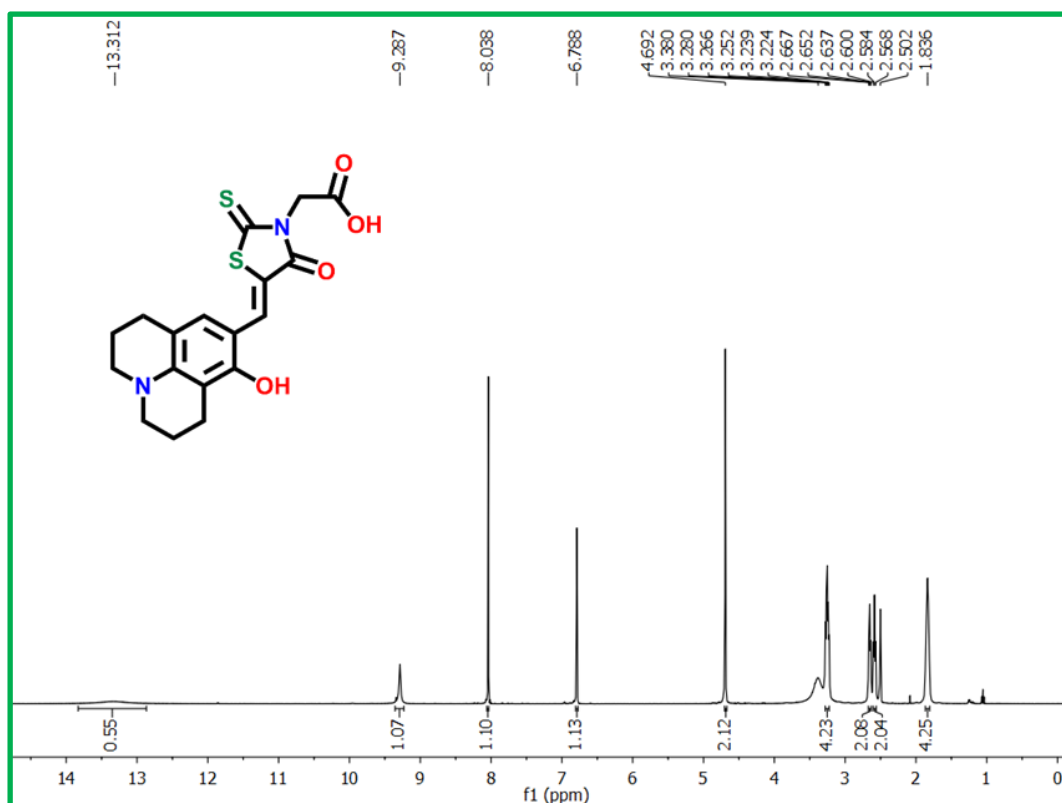


Figure 2.3 Mass spectrum of compound **1** in  $\text{MeOH}$ .

### 2.2.4 Synthesis and Characterization of the Compound HJRA

In the next step, for the synthesis of HJRA, compound **1** (0.217 g, 1 mmol) and rhodanine-3-acetic acid (0.191 g, 1 mmol) were dissolved in 10 mL of dry ethanol and a catalytic amount of piperidine was added. Then the reaction mixture was refluxed for 8 h with constant stirring. The residue was then filtered, washed thoroughly with ethanol and dried in vacuum desiccator overnight to get a solid crude product. The product was then purified by using column chromatography to afford a purple color solid (71% yield) (**Scheme 2.1**).  $^1\text{H}$  NMR (400 MHz,  $\text{DMSO-}d_6$ ):  $\delta$  in ppm = 13.312 (s, 1H), 9.287 (s, 1H), 8.038 (s, 1H), 6.788 (s, 1H), 4.692 (s, 2H), 3.280–3.224 (m, 4H), 2.652 (t,  $J = 6.1$  Hz, 2H), 2.584 (t,  $J = 6.3$  Hz, 2H), 1.836 (s, 4H) (**Figure 2.4**).  $^{13}\text{C}$  NMR (101 MHz,  $\text{DMSO-}d_6$ ):  $\delta$  in ppm = 192.37, 167.73, 166.50, 155.15, 147.74, 131.54, 127.45, 115.32, 109.37, 107.03, 49.65, 48.88, 44.90, 26.92, 21.18, 21.06, 20.28 (**Figure 2.5**). HRMS (ESI)  $m/z$ : calcd for  $[\text{M} + \text{H}^+]$ , 391.0786; found, 391.0788 (**Figure 2.6**). IR Spectrum:  $\tilde{\nu}$  in  $\text{cm}^{-1}$  = 3330, 2823, 1718, 1660, 1170 (**Figure 2.7**).



**Figure 2.4**  $^1\text{H}$ -NMR spectrum of probe HJRA in  $\text{DMSO-}d_6$ .

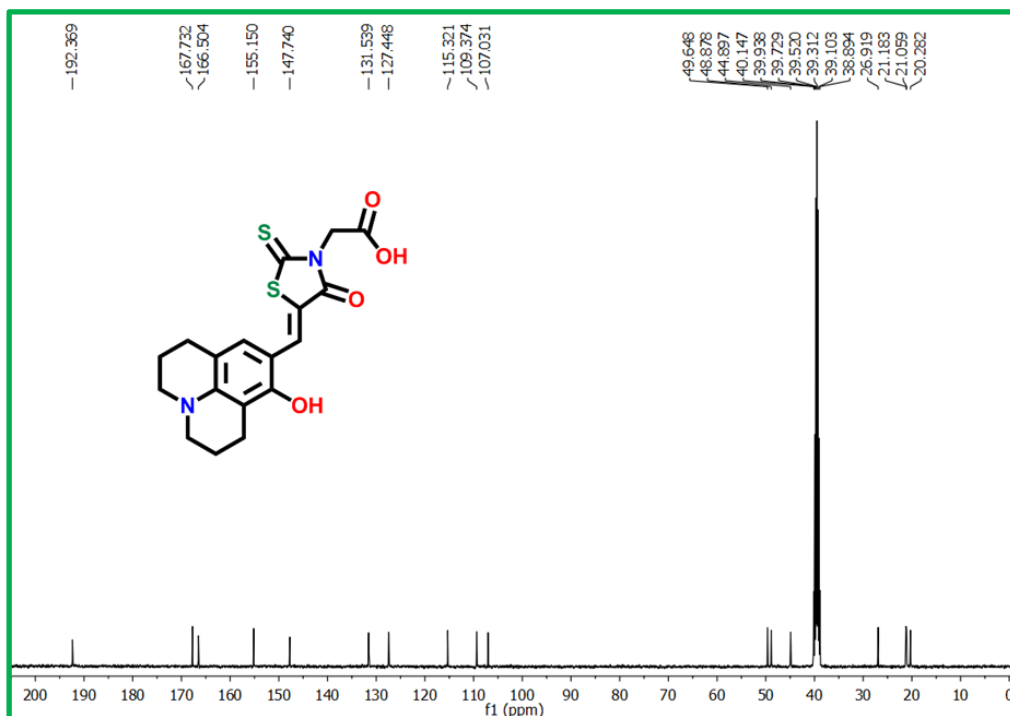


Figure 2.5 <sup>13</sup>C-NMR spectrum of probe HJRA in DMSO-*d*<sub>6</sub>.

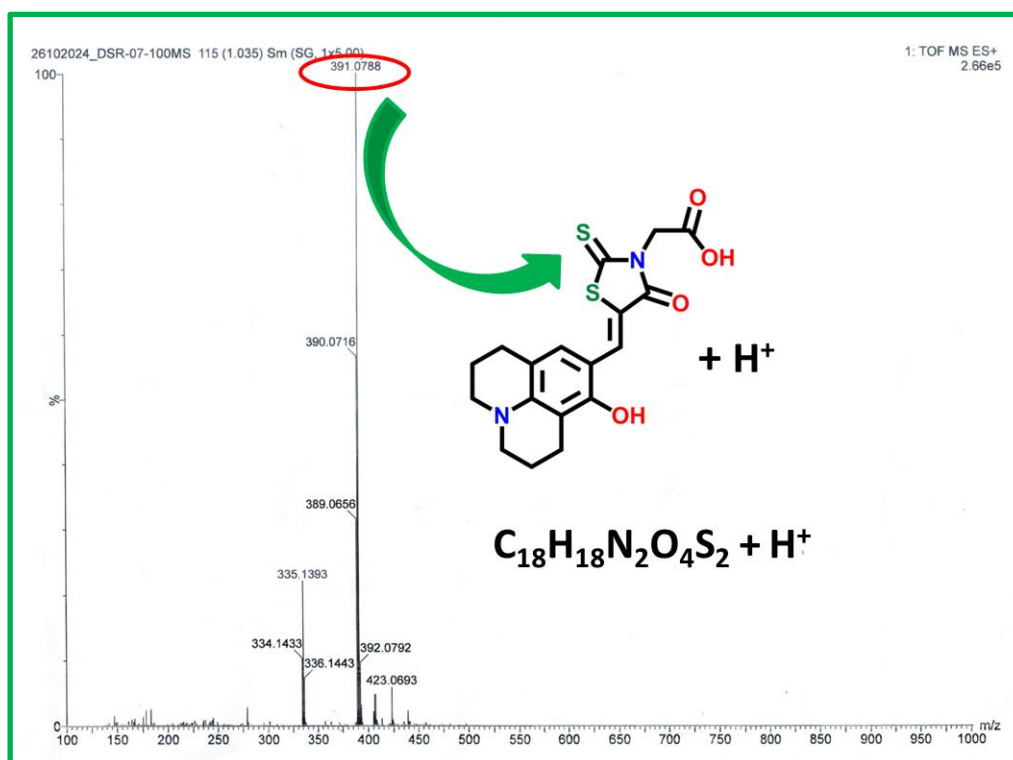


Figure 2.6 Mass spectrum of probe HJRA in MeOH.

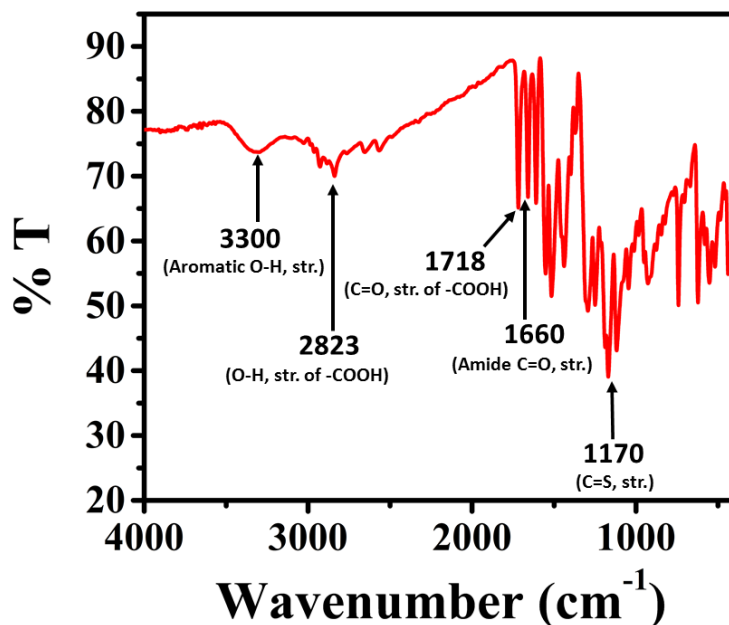


Figure 2.7 IR spectrum of probe HJRA.

### 2.2.5 Experimental Solution

A 500 mL 10 mM phosphate-buffered saline (PBS) solution of pH 7.4 was prepared in deionized Milli pore water and used in all studies. Stock solutions of BSA and HSA (20 mg/mL) were prepared in deionized water. The stock solutions of other proteins, enzymes and biomolecules were prepared as required, and the exact concentrations of the protein stock solutions were evaluated spectrophotometrically by considering the absorbance and molar extinction coefficient values at particular wavelengths as relevant. Stock solutions of different cations (5 mM for each) and anions (5 mM for each) were prepared by dissolving the required amount of inorganic salts in deionized water. A 10 mL stock solution of HJRA (1 mM) was prepared in spectroscopic grade DMSO and stored in a refrigerator before use.

### 2.2.6 UV-Vis and Fluorescence Spectroscopic Studies

Stock solution of HJRA ( $1 \times 10^{-3}$  M) in DMSO was diluted to 2  $\mu$ M for various spectroscopic studies by placing only 4  $\mu$ L of the stock solution of HJRA into PBS solution (pH 7.4) to a final volume of 2 mL. In the fluorescence selectivity experiment, the test samples were prepared by adding the appropriate amounts of the stock solutions of the respective proteins, enzymes, metal ions, anions and other analytes into 2 mL of probe HJRA solution (2  $\mu$ M). For the fluorescence-titration experiments, another set of HSA standard solution ( $1 \times 10^{-4}$  M) was prepared by diluting the earlier prepared 20 mg/mL stock solution in PBS medium. Then

a Quartz cuvette was filled with 2 mL of HJRA solution (2  $\mu\text{M}$ ) for the fluorescence-titration experiment, to which the newly prepared stock solution of HSA ( $1 \times 10^{-4}$  M) was gradually added using a micropipette as required. For the fluorescence experiments, excitation wavelength was set at 539 nm and emission was recorded from 550 to 750 nm. For the UV-Vis studies the probe concentration was also fixed at 2  $\mu\text{M}$  and the spectra were collected with proper background correction. For the competitive fluorescence binding experiments, stock solutions of warfarin and ibuprofen (1 mM for each) were prepared in deionized water and DMSO, respectively. In a typical assay, HSA solution was premixed with HJRA at a molar ratio 1:4. Then, this mixed solution was further spiked with different amounts of warfarin or ibuprofen and the resultant ternary mixtures were subjected for the fluorescence measurement. All the spectral data were recorded within 1 min after the addition of the analytes, except in the kinetic studies.

### 2.2.7 Steady-State Fluorescence Anisotropy

Fluorescence anisotropy ( $r$ ) measurements were carried out by considering the following equation described by Larsson *et al.*<sup>63</sup>

$$r = \frac{I_{VV} - GI_{VH}}{I_{VV} + 2GI_{VH}} \quad (1)$$

Where, the polarizer positions were set at ( $0^\circ, 0^\circ$ ), ( $0^\circ, 90^\circ$ ), ( $90^\circ, 0^\circ$ ), and ( $90^\circ, 90^\circ$ ) to get  $I_{VV}$ ,  $I_{VH}$ ,  $I_{HV}$ ,  $I_{HH}$  for excitation and emission signals respectively.  $G$  factor is defined as

$$G = \frac{I_{HV}}{I_{HH}} \quad (2)$$

Where,  $I_{HV}$  and  $I_{HH}$  are respectively the vertical and horizontal component of emission polarizer, keeping the excitation polarizer horizontal.  $G$  depends on slit widths and monochromator wavelength. The excitation and emission wavelengths were fixed at 539 and 582 nm respectively.

### 2.2.8 Fluorescence Lifetime Studies

The TCSPC measurements were carried out in 10 mM PBS buffer solution of pH 7.4 for the fluorescence decay of HJRA in the absence and in the presence of increasing concentration of HSA at 25  $^\circ\text{C}$ . During the TCSPC measurements the photoexcitation was fixed at 532 nm. The fluorescence decay curves were fitted to a triple-exponential function:<sup>64</sup>

$$I(t) = A + B_1 \cdot e^{(-t/\tau_1)} + B_2 \cdot e^{(-t/\tau_2)} + B_3 \cdot e^{(-t/\tau_3)} \quad (3)$$

Where,  $B_i$  represents the  $i$ th pre-exponential factor and  $\tau_i$  denotes the decay time of component  $i$  (here  $i = 1, 2, 3$ ). The average lifetimes ( $\tau_{avg}$ ) for the fluorescence decay profiles were calculated by using the following equation:

$$\tau_{avg} = \sum_{i=1}^3 \alpha_i \cdot \tau_i \quad (4)$$

Where,  $\alpha_i$  is the relative ratio factor and it is calculated by

$$\alpha_i = B_i / \left( \sum_{i=1}^3 B_i \right) \quad (5)$$

### 2.2.9 Fluorescence Quantum Yield Measurements

Fluorescence quantum yield were calculated by adopting the reported strategy<sup>65</sup> where relative measurement was carried out using Rhodamine 6G as reference ( $\Phi_s = 0.94$  in ethanol) and by considering the following equation:

$$\Phi_u = \frac{A_s F_u \eta_u^2}{A_u F_s \eta_s^2} \times \Phi_s \quad (6)$$

Where, " $\Phi$ " is the quantum yield; "A" is the optical density; "F" is the measured integrated emission intensity; and " $\eta$ " is the refractive index of the medium. The subscript "u" refers to the unknown sample, and subscript "s" refers to the standard reference with a known quantum yield.

### 2.2.10 Detection Limit

The detection limit was calculated on the basis of the fluorescence titration with HSA. The fluorescence emission spectrum of HJRA was measured 10 times to calculate the standard deviation of blank measurement. Then, the fluorescence emission at 582 nm was plotted as a function of the concentration of HSA from the corresponding titration experiment to evaluate the slope. The detection limit was then calculated using the following equation:<sup>58</sup>

$$\text{Detection limit} = 3\sigma/k \quad (7)$$

Where " $\sigma$ " is the standard deviation of blank measurement, and "k" is the slope between the fluorescence emission intensity versus [HSA].

### 2.2.11 Determination of Dissociation Constant ( $K_d$ ) for the HSA and HJRA Adduct

The evaluation of  $K_d$  value in this study was performed by following the previously published method<sup>66,67</sup> with some modification to fulfil our specific purpose. In principle, the dissociation constant  $K_d$  is calculated as follows:



$$K_d = \frac{([HSA]_T - [HSA : HJRA])([HJRA]_T - [HSA : HJRA])}{[HSA : HJRA]} \quad (9)$$

Where,  $[HSA]_T$  and  $[HJRA]_T$  are the total concentrations of HSA and HJRA, respectively.  $[HSA : HJRA]$  represents the concentration of HSA–HJRA complex.  $[HSA : HJRA]$  is given by

$$[HSA : HJRA] = \frac{1}{2} [( [HJRA]_T + [HSA]_T + K_d ) \pm \sqrt{([HJRA]_T + [HSA]_T + K_d)^2 - (4[HJRA]_T[HSA]_T)}] \quad (10)$$

To obtain  $K_d$  by fluorescence assay, we simply converted the calculation parameter into fluorescence intensity and solution concentration as follows:

$$\frac{I - I_0}{I_\infty - I_0} = \frac{1}{2[HJRA]_T} [( [HJRA]_T + [HSA]_T + K_d ) - \sqrt{([HJRA]_T + [HSA]_T + K_d)^2 - (4[HJRA]_T[HSA]_T)}] \quad (11)$$

Where,  $I_0$  and  $I$  denote the fluorescence intensities of HJRA in initial state and at different concentration of HSA, respectively.  $I_\infty$  is the saturated fluorescence intensity with HSA. Then experimental data are best fitted with the eq 11 and the dissociation constant ( $K_d$ ) value was obtained.

### 2.2.12 Dynamic Light Scattering Studies

The particle sizes of HJRA and the aggregates of HJRA with 1 equiv. of HSA were measured by dynamic light scattering (DLS) measurements at 25 °C on a Malvern Zetasizer Nano ZS instrument. At first, DLS measurement was performed with 2 μM HJRA in PBS buffer solution (pH 7.4). Then, to determine the change in particle size of HJRA upon interaction with HSA, a DLS study was also performed with of 2 μM HJRA in the presence of 1 equiv. HSA in PBS buffer solution (pH 7.4).



### 2.2.13 Transmission Electron Microscopy (TEM) Analysis

The morphology of HJRA (2  $\mu$ M) and the aggregates of HJRA (2  $\mu$ M) with 1 equiv. HSA in PBS buffer solution (pH 7.4) were characterized in a FEI Tecnai G2 F20 microscope TEM instrument by drop casting of the sample separately on carbon-coated copper grids (400 meshes) and drying them in a vacuum.

### 2.2.14 Molecular Docking Study

To know the probable binding sites within HSA and the mode of binding of HJRA with HSA, molecular docking study was performed using docking program AutoDock (version 4.2). The X-ray crystal structure of HSA was taken from RCSB Protein Data Bank having PDB ID: 1AO6. To draw the structure of HJRA, Chem3D Ultra 12.0 was used and further modification was carried out by using Gaussian 09W and AutoDock 4.2 programs. Gasteiger charges and polar hydrogen atoms were added to the protein and probe. Grid box with dimensions of 110 Å  $\times$  110 Å  $\times$  110 Å and 0.403 Å grid spacing were specified to enclose the protein using AutoGrid program. The default values shown by the AutoDock program were used for other sets of parameters. The Lamarckian genetic algorithm (LGA) was used to accomplish docking calculations and the grid maps for energy were calculated by AutoGrid.<sup>68,69</sup> The best optimized docked model with lowest binding energy was considered for further study of docking simulations and the output was best viewed by using Discovery Studio.

### 2.2.15 Cell Cytotoxicity Assay

The cell cytotoxicity study of HJRA was performed by MTT assay. At first, CHO cells were cultured in 24-well plates in Dulbecco's modified Eagle's (DMEM) medium (supplemented with 10% FBS and 1% penicillin–streptomycin) at 37 °C and under 5% CO<sub>2</sub>. After overnight growth, cells were incubated with different doses of HJRA for 24 h. Next, cells were washed with PBS buffer (pH 7.4), and then 500  $\mu$ L of DMEM media was added to each well. Then, 50  $\mu$ L of an aqueous solution of MTT (5 mg/mL) was added to each well and incubated for 4 h. The produced purple formazan was dissolved in a DMF–water (1:1) solution mixture of sodium dodecyl sulfate, and the absorbance of the solution was measured at 570 nm in a microplate reader. The relative cell viability was measured by assuming 100% cell viability for cells without any HJRA.

### 2.2.16 Cell Imaging Study

CHO cells were cultured in 24-well plate in DMEM (with 10% fetal bovine serum and 1% penicillin-streptomycin) at 37 °C and 5% CO<sub>2</sub> atmosphere. After overnight growth, for live cell imaging of endogenous HSA, CHO cells were incubated with 2 μM HJRA for 30 min and DAPI dye for 10 min (for nucleus staining) in serum free DMEM media. The cells were washed with PBS buffer (pH 7.4) for three times to remove the residual molecules. Then fresh DMEM media was added to the washed cells and imaged under fluorescence microscope (Olympus, model IX-81) upon excitation at 352 nm and 540 nm for imaging of DAPI and HJRA, respectively. For the warfarin inhibition study, CHO cells (pretreated with 30 μM warfarin for 15 min) were treated with HJRA (2 μM) for 30 min and then with DAPI for another 10 min. Next the cells were washed and imaged under microscope.

For live cell imaging of HSA exogenously, CHO cells were incubated with HSA (20 μM) in serum free DMEM media for 24 h. Then, cells were washed with PBS buffer (pH 7.4) for three times. Subsequently, cells were treated with 2 μM HJRA for 30 min and DAPI dye for 10 min (for nucleus staining) in serum free DMEM media. Next, the cells were washed with PBS buffer (pH 7.4) to remove unbound molecules and imaged under microscope upon excitation at 352 nm and 540 nm for imaging of DAPI and HJRA, respectively. For the drug inhibition study, CHO cells (incubated with 20 μM HSA for 24 h) pretreated with 30 μM of warfarin and ibuprofen separately for 15 min, then with HJRA (2 μM) for another 30 min and then further loaded with DAPI for 10 min. Next the cells were washed and imaged under microscope.

### 2.2.17 Urinary HSA Quantification by Coomassie Brilliant Blue G250

#### (A) Reagent Preparation:

(1) **Coomassie Brilliant Blue G250 Solution.** 100 mg of Coomassie Brilliant Blue G250 was dissolved in 50 mL of 95% ethanol. To this solution 100 mL of 85% (W/V) phosphoric acid was added. Finally, the resulting solution was diluted to 1000 mL with deionized water.

(2) **0.9% NaCl.** 900 mg NaCl was dissolved in 100 mL deionized water.

(3) **HSA Standard Solution.** A 100 mL of 0.05 mg/mL HSA standard solution was prepared by diluting the previously prepared 20 mg/mL HSA stock solution with deionized water.

**(B) Preparation of Standard Curve:**

For the generation of Standard curve, 11 test tubes were taken and the reagents were added according to the following table:

**Preparation of standard samples**

Sample	1	2	3	4	5	6	7	8	9	10	11
HSA standard solution (mL)	0	0.1	0.2	0.3	0.4	0.5	0.6	0.7	0.8	0.9	1.0
0.9% NaCl (mL)	1.0	0.9	0.8	0.7	0.6	0.5	0.4	0.3	0.2	0.1	0
Coomassie Brilliant Blue G250 (mL)	4.0	4.0	4.0	4.0	4.0	4.0	4.0	4.0	4.0	4.0	4.0
HSA concentration (mg/L)	0	1.0	2.0	3.0	4.0	5.0	6.0	7.0	8.0	9.0	10.0

Draw a standard addition curve with Absorbance at 595 nm versus HSA content (mg/L).

**(C) Endogenous HSA Determination in Urine:**

1 mL urine sample was taken in a fresh test tube. Then 4 mL Coomassie Brilliant Blue G250 reagent was added to react for 5 minutes. Finally, the absorbance at 595 nm was measured to determine the amount of HSA. The final data obtained by Coomassie Brilliant Blue G250 method is measured value × 5.

**2.3 Results and Discussion**

**2.3.1 Rational Design and Synthesis of Probe HJRA**

In this article, our main intention was to synthesize a suitably designed novel fluorescent molecular probe that might potentially bind to albumin protein in a site-specific manner. Keeping this in mind, we have developed a TICT mechanism-based molecular probe, HJRA, by incorporating a ‘donor- $\pi$ -acceptor’ system with julolidine as the electron donor and rhodanine as the electron acceptor moieties (Scheme 2.1). Here, the selection of modified julolidine fluorophore is based on its outstanding quantum yield<sup>20</sup> and emission wavelength that is nearly as feasible as the Red/NIR region, which in turn is necessary for achieving improved tissue depth penetration and less autofluorescence. The intension to incorporate hydroxyl group was two fold: (i) to boost the electron-donating ability of the overall moiety as a secondary donor and (ii) to facilitate the formation of stable hydrogen bonds with the amino acid residues of serum albumin protein, which in turn prevents the free molecular rotation of

the probe within the protein binding pocket. Moreover, the presence of the hydroxyl group on HJRA may also enhance the aqueous solubility of the probe. A neutral rhodanine moiety was selected for avoiding nonspecific electrostatic interactions and the carboxylic acid functionality makes additional conjugation to a specific protein much easier. Some similar frameworks to the structure of the rhodanine benzylidene conjugates have also been previously reported as protein or RNA aptamer fluorogens, which encourage us to select this probe for our present investigation.<sup>70,71</sup> To achieve our goal, the probe HJRA was synthesized by a simple condensation reaction between compound **1** and rhodanine-3-acetic acid in ethanol (Scheme 2.1) and well characterized by <sup>1</sup>H NMR (Figure 2.4), <sup>13</sup>C NMR (Figure 2.5), HRMS (Figure 2.6) and IR (Figure 2.7) spectroscopies.

### 2.3.2 Photophysical Properties and Self-Assembly Behavior of HJRA

Small organic molecules may undergo self-assembly via noncovalent interactions leading to the formation of nanoaggregates, which can greatly alter their optical (absorbance and fluorescence) characteristics.<sup>49</sup> Therefore, to establish the formation of nanoaggregates, we examined the optical properties of HJRA in DMSO/PBS binary mixtures, where a solution of HJRA (2 μM) in pure DMSO exhibited an intrinsic absorption maximum at 521 nm and a strong emission peak at 585 nm.

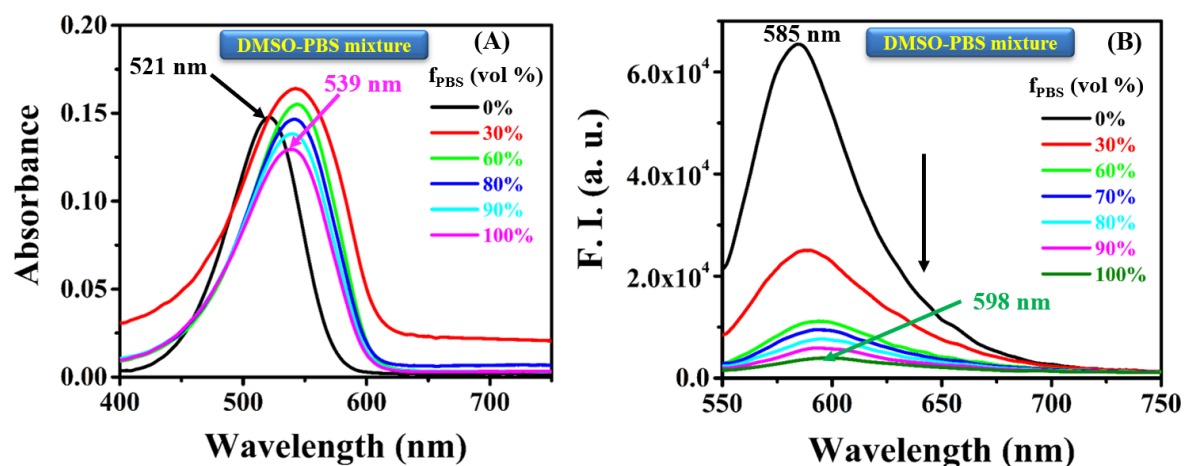


**Figure 2.8** (A) UV-vis absorption spectra of HJRA (2 μM) in DMSO/PBS buffer mixtures with different PBS fractions ( $f_{\text{PBS}}$ ). (B) Fluorescence emission spectra of HJRA (2 μM) in DMSO/PBS buffer mixtures with different PBS fractions ( $f_{\text{PBS}}$ ).  $\lambda_{\text{ex}} = 539$  nm.

With the progressive switch of solvent composition from pure DMSO to PBS buffer (pH 7.4), the absorption maximum of HJRA gets shifted from 521 to 539 nm (Figure 2.8A) and a significant diminishing of emission intensity along with a red shift of emission maxima from 585 nm to 598 nm (Figure 2.8B) was observed. All the aforementioned changes in spectral behavior clearly indicate the aggregation of HJRA in aqueous PBS buffer medium, mainly due to the hydrophobic interactions among the HJRA molecules.<sup>48</sup> The nanoaggregate formation was further ascertained by dynamic light scattering (DLS) experiments on a 2  $\mu$ M HJRA in PBS buffer that displayed the formation of nanoparticles with a 105 nm average diameter (Figure 2.9A). Moreover, TEM investigation (Figure 2.9B) vividly established the development of spherical HJRA nanoaggregates with an average diameter of  $\sim$ 97 nm (Figure 2.9C).

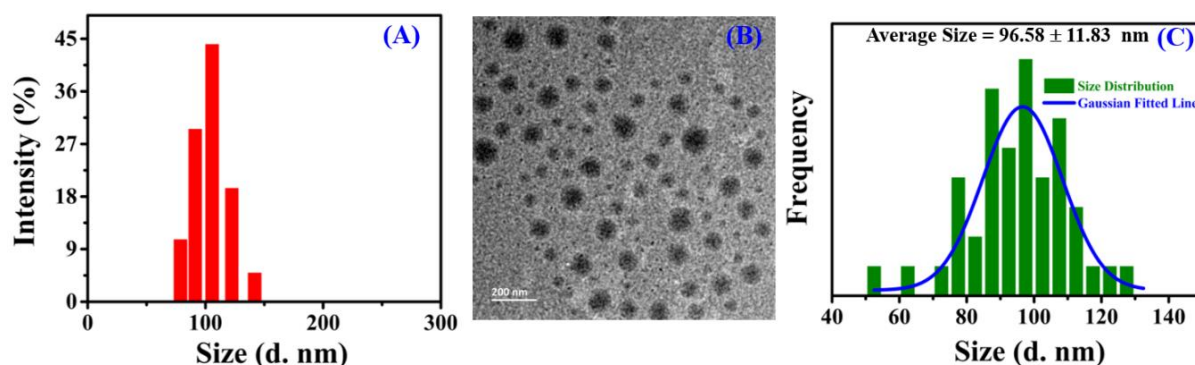


**Figure 2.9** (A, B) DLS and TEM images of the nanoaggregates of 2  $\mu$ M HJRA. (C) Particle size distribution plot of HJRA (2  $\mu$ M) nanoaggregates from the TEM image characterization. Scale bar: 200 nm.

The probe HJRA (2  $\mu$ M) displays fluorescent-silent emission band at 598 nm (Figure 2.10) in  $\sim$  100% PBS buffer (pH 7.4, containing 0.2% DMSO) upon excitation at 539 nm. The nonemissive status may be due to the formation of loosely packed nanoaggregates resulting aggregation caused quenching (ACQ) effect<sup>46-48</sup> and the presence of twisted intramolecular charge transfer process. Therefore, to establish this, change in photophysical (UV-vis absorption and fluorescence) behavior of probe was explored. Thus, HJRA (2  $\mu$ M) was added to various organic solvents with different polarity and changes in the absorbance and fluorescence behavior were monitored. As the solvent polarity increases, it was found that the probe showed red shifts of absorption and emission maxima from 495 and 548 nm to 521 and 585 nm, in 1,4-dioxane and DMSO, respectively (Figure 2.11).

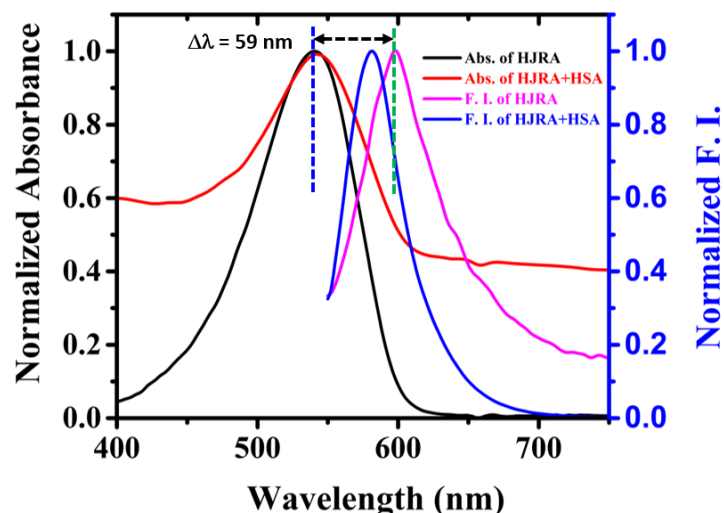


**Figure 2.10** Normalized absorbance and fluorescence spectra of HJRA (2  $\mu\text{M}$ ) in the absence or presence of HSA (19.6  $\mu\text{M}$ ) in  $\sim$ 100% PBS buffer solution of pH 7.4.

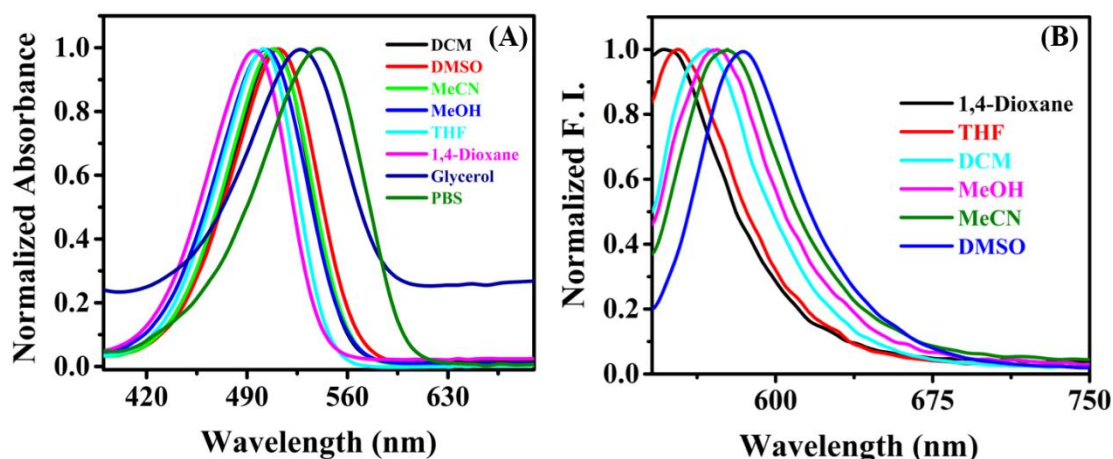


**Figure 2.11** (A) Normalized absorption spectra of HJRA (2  $\mu\text{M}$ ) in different solvents. (B) Normalized fluorescent spectra of HJRA (2  $\mu\text{M}$ ) in different solvents.

Additionally, we have examined the effect of solvent polarity on the fluorescence intensity of HJRA in mixed solvent media of different polarity using PBS/1,4-dioxane and PBS/ethanol in variable compositions. It is expected that the addition of low polarity solvents (1,4-dioxane or ethanol) may disintegrate HJRA nanoaggregates. Indeed, the emission peak of HJRA was blue shifted with the concomitant enhancement in fluorescence intensity when the volume fraction of 1,4-dioxane and ethanol in the binary combination (PBS/1,4-dioxane and PBS/ethanol) were increased (**Figure 2.12**), suggesting the disintegration of HJRA nanoaggregates in low polarity medium.



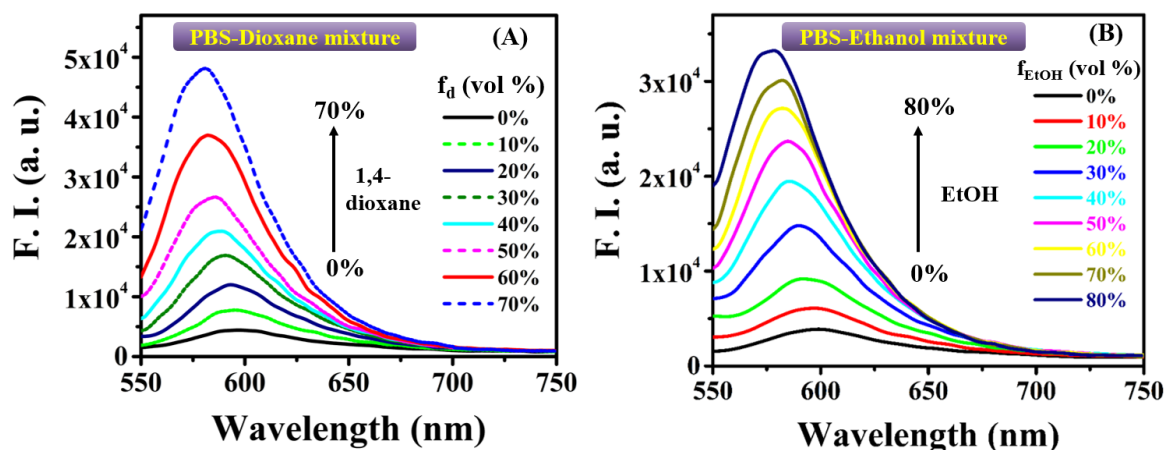


**Figure 2.12** (A) Fluorescence emission spectra of HJRA (2  $\mu\text{M}$ ) in PBS/1,4-dioxane mixtures with different dioxane fractions ( $f_d$ ). (B) Fluorescence emission spectra of HJRA (2  $\mu\text{M}$ ) in PBS/ethanol mixtures with different ethanol fractions ( $f_{\text{EtOH}}$ ).  $\lambda_{\text{ex}} = 539 \text{ nm}$ .

To further corroborate the occurrence of TICT mechanism, we recorded the fluorescence spectra of HJRA (2  $\mu\text{M}$ ) in mixed solvent media of variable compositions using PBS/glycerol, ethanol/glycerol and ethylene glycol/glycerol having different viscosity.

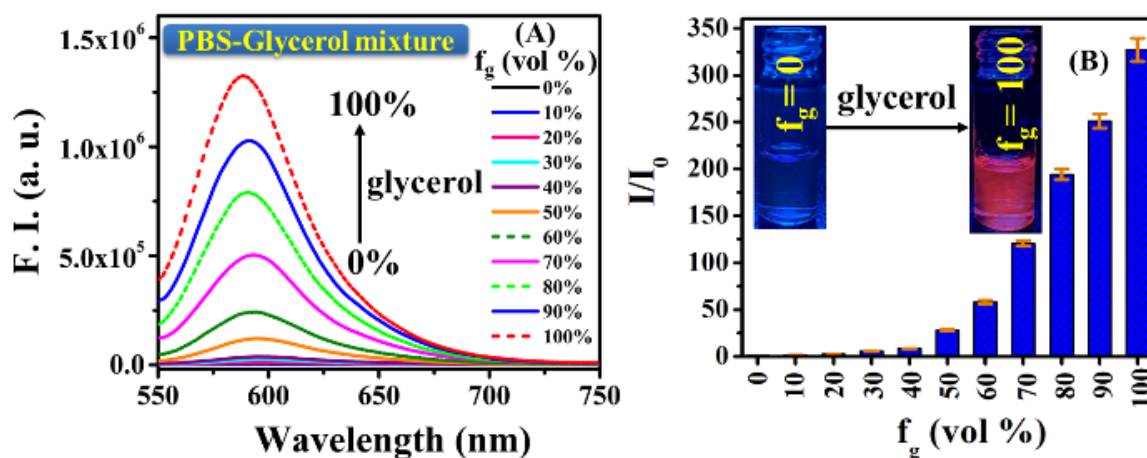


**Figure 2.13** (A and B) Fluorescence spectra and corresponding variations in  $I/I_0$  (at 590 nm) of HJRA (2  $\mu\text{M}$ ) in PBS buffer with different fractions of glycerol (v/v, from 0 to 100%). Inset of (B) Fluorescent photoimages of HJRA with two different  $f_g$  values.  $\lambda_{\text{ex}} = 539 \text{ nm}$ . Error bars: standard deviation ( $n = 3$ ).

As shown in **Figure 2.13A**, the emission intensity of HJRA was increased consistently with the increase in glycerol fraction in PBS/glycerol binary mixture indicating the regular



increment in viscosity of the medium. Actually, an ~314-fold increase in emission intensity of HJRA was observed at 590 nm upon increment of the glycerol proportion from 0% to 100% (Figure 2.13B).

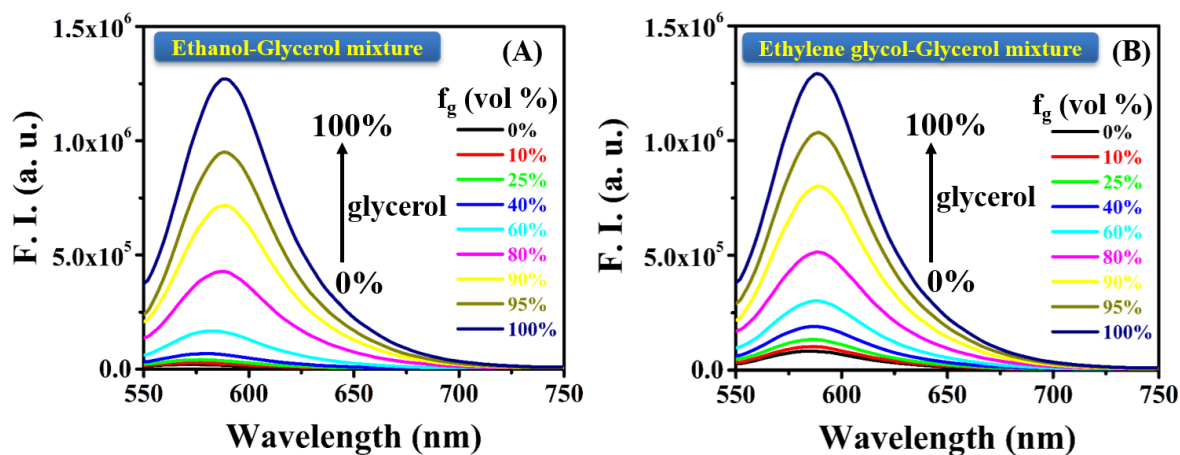
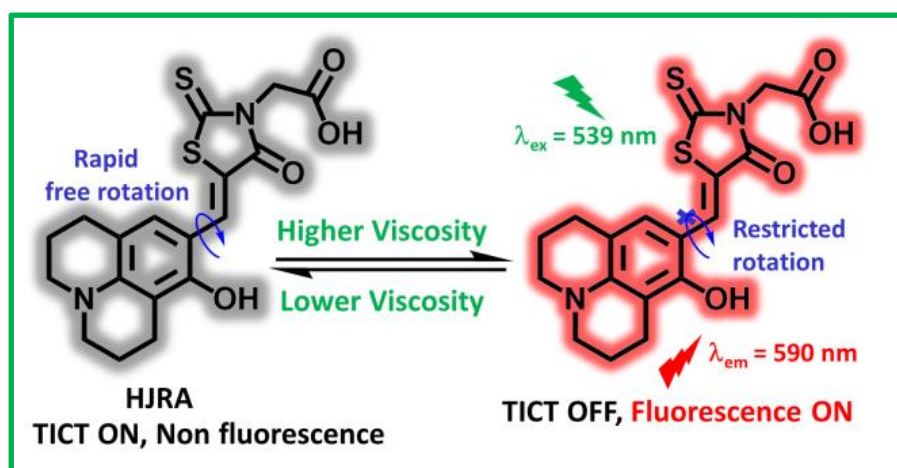


**Figure 2.14** (A) Fluorescence emission spectra of HJRA (2  $\mu$ M) in ethanol/glycerol mixtures with different glycerol fractions ( $f_g$ ). (B) Fluorescence emission spectra of HJRA (2  $\mu$ M) in ethylene glycol/glycerol mixtures with different glycerol fractions ( $f_g$ ).  $\lambda_{ex} = 539$  nm.

Similar changes in fluorescence were also observed upon increasing the glycerol volume fraction in ethanol/glycerol and ethylene glycol/glycerol mixtures (Figure 2.14). As a consequence, these viscosity-dependent fluorescence modifications evidently demonstrate the



**Scheme 2.2** Response mechanism of HJRA towards viscosity.

restriction imposed on the free intramolecular rotation of HJRA probe by the increase in viscosity, which in turn enhances the fluorescence intensity of HJRA by blocking the

nonradiative decay pathways (Scheme 2.2). Here, it was also worth mentioning that irradiation of the HJRA solution ( $2 \mu\text{M}$ ) with a 539 nm light at a power source of 75 W for a period of 30 min did not result in any noticeable changes in the fluorogenic behavior of HJRA (Figure 2.15). This emphasizes the good photostability of HJRA in its operating environment, which is necessary for a biosensor to work effectively.

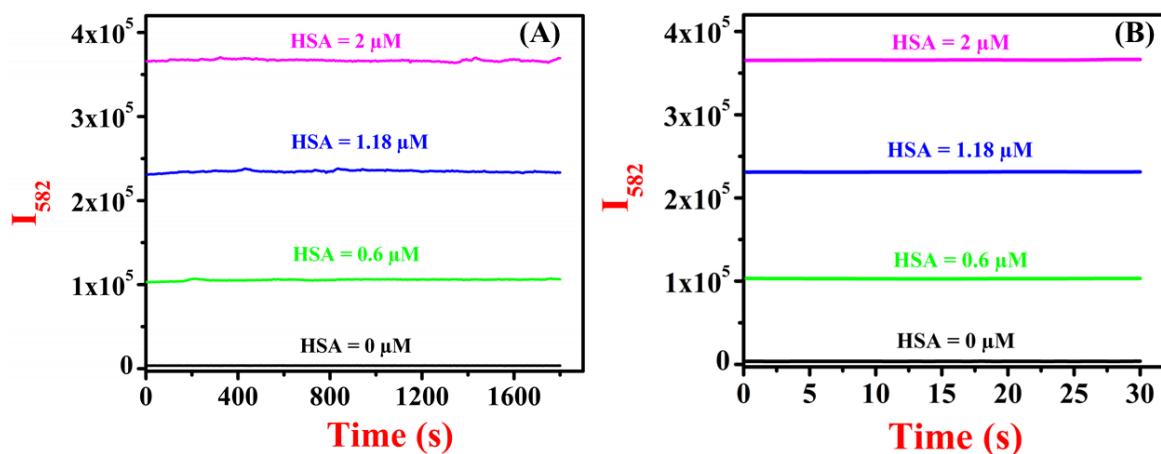


**Figure 2.15** (A, B) Time dependent fluorescent intensity changes at 582 nm of HJRA ( $2 \mu\text{M}$ ) in the presence of 0  $\mu\text{M}$ , 0.6  $\mu\text{M}$ , 1.18  $\mu\text{M}$ , 2.0  $\mu\text{M}$  of HSA in  $\sim 100\%$  PBS buffer of pH 7.4,  $\lambda_{\text{ex}} = 539 \text{ nm}$ .

### 2.3.3 Selectivity Study and Optical Response of HJRA toward HSA/BSA

To explore the selectivity of HJRA, at first, we systematically recorded absorption and fluorescence responses of HJRA ( $2 \mu\text{M}$ ) in  $\sim 100\%$  PBS buffer (pH 7.4) by the addition of excess amount (10 equiv) of different proteins and enzymes, including  $\beta$ -lactoglobulin, lysozyme, CT-DNA, hemoglobin, cytochrome C, proteinase K, collagen, pepsin, trypsin, HSA and BSA. In PBS buffer medium, HJRA ( $2 \mu\text{M}$ ) displays an absorbance maximum at 539 nm (Figure 2.10). Here, it was found that upon addition of excess HSA/BSA proteins (10 equiv.) to a solution of HJRA, induced certain variations in the absorbance behavior of HJRA. Besides this, no such change in the absorption band of HJRA was noticed in the presence of other proteins, enzymes and bioanalytes tested (Figure 2.16A). There is a gradual increase in absorbance at 542 nm was observed upon gradual addition of HSA to a solution of HJRA (Figure 2.16B). Here, it was also worth noting that only HSA and BSA were capable of

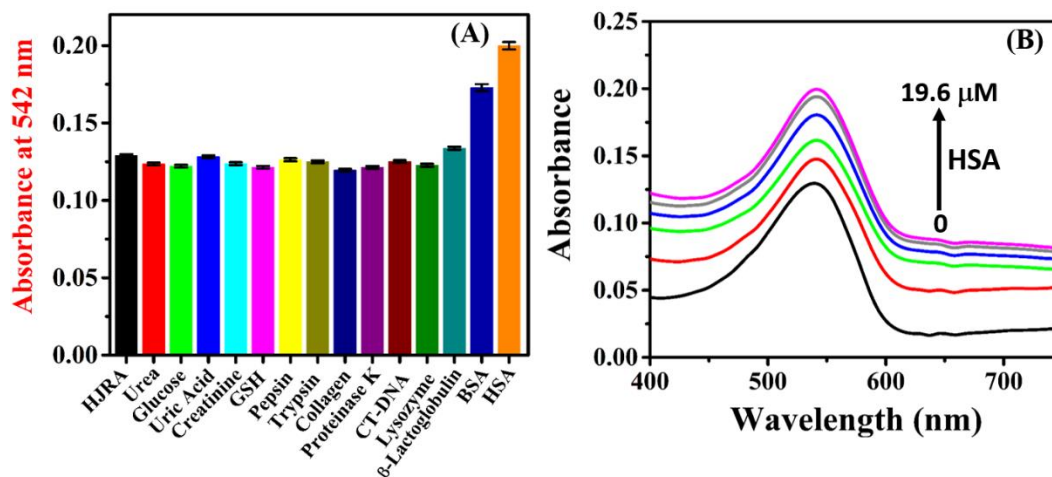


**Figure 2.16** (A) Absorption responses of HJRA (2 μM) at 542 nm in ~100% PBS buffer (pH = 7.4) by the addition of excess amount (10 equiv) of different proteins, enzymes and bioanalytes. Error bars: standard deviation (n = 3). (B) UV-vis absorption spectra of HJRA (2 μM) in ~100% PBS buffer of pH 7.4 with the gradual addition HSA.

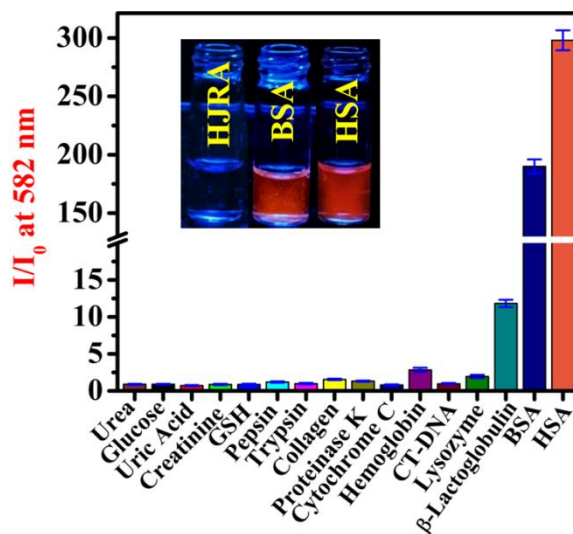


**Figure 2.17** Variations in emission intensity ( $I/I_0$ ) of HJRA (2 μM) at 582 nm in ~100% PBS buffer (pH = 7.4) by the addition of excess amount (10 equiv.) of different proteins, enzymes and urine interferences. Inset: visual fluorescence changes of HJRA upon addition of HSA and BSA under 356 nm UV light.  $\lambda_{ex}$  = 539 nm. Error bars: standard deviation (n = 3).

providing a substantial turn-on fluorescent response at 582 nm among the different proteins and enzymes tested (Figure 2.17). As the HJRA probe has the potential to be used in urine analysis, we further investigated the impact of other key organic components present in human urine, such as GSH, glucose, urea, uric acid and creatinine (each at 10 equiv.) on the

selective detection of HSA and BSA by HJRA. According to the investigational findings presented in **Figure 2.17**, it can be concluded that the fluorescence emission of HJRA is negligibly changed by these urine interferents under identical experimental environments.

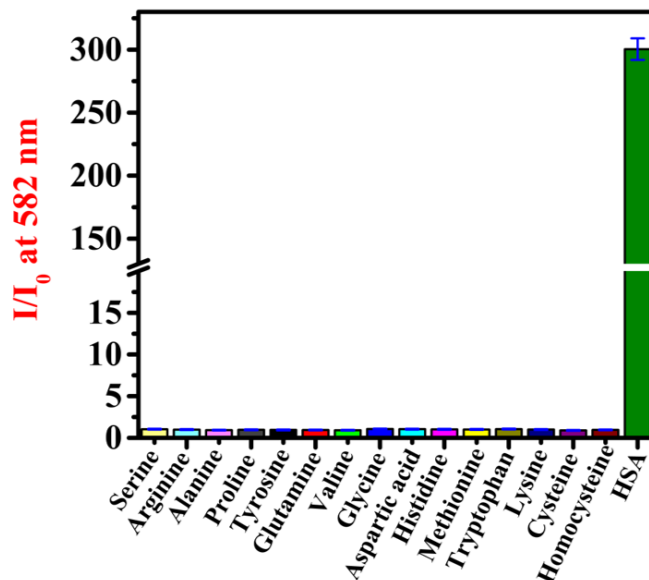


**Figure 2.18** Fluorescence responses of HJRA (2 μM) toward HSA (10 equiv.) and various amino acids (10 equiv.) at 582 nm in ~100% PBS buffer of pH 7.4,  $\lambda_{ex} = 539$  nm. Error bars: standard deviation (n = 3).

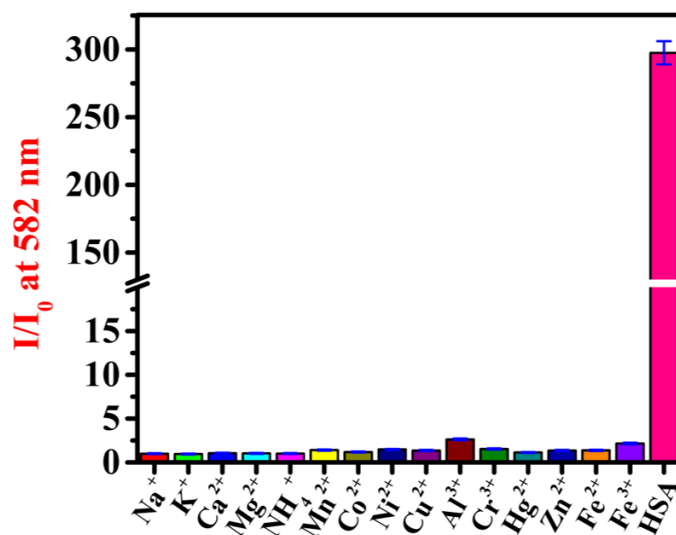


**Figure 2.19** Fluorescence responses of HJRA (2 μM) toward HSA (10 equiv.) and various cations (15 equiv.) at 582 nm in ~100% PBS buffer of pH 7.4,  $\lambda_{ex} = 539$  nm. Error bars: standard deviation (n = 3).

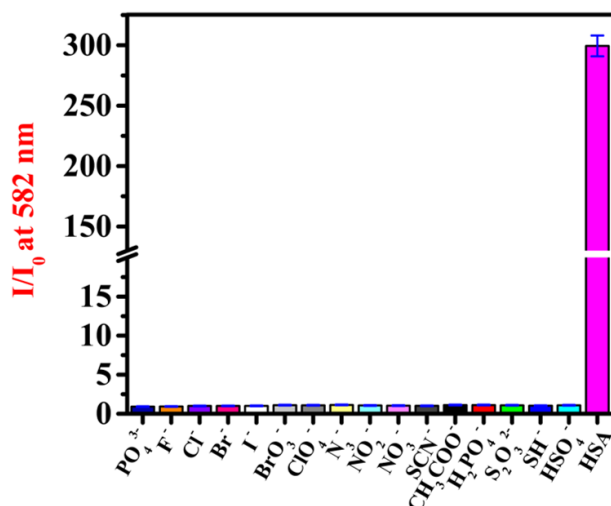


**Figure 2.20** Fluorescence responses of HJRA (2 μM) toward HSA (10 equiv.) and various anions (15 equiv.) at 582 nm in ~100% PBS buffer of pH 7.4,  $\lambda_{ex}$  = 539 nm. Error bars: standard deviation (n = 3).

Additionally, the selectivity of HJRA (2 μM) toward 10 equiv. of different amino acids, 15 equiv of different cations and 15 equiv. of various anions was also investigated, resulting in negligible influence on the fluorescence behavior of HJRA at 582 nm (Figures 2.18–2.20). This suggests that HJRA can serve as a useful analytical method for independently identifying and detecting HSA/BSA.

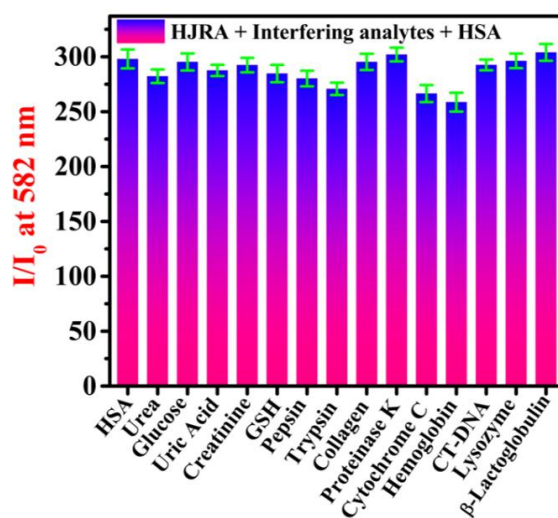


**Figure 2.21** Fluorescence responses of HJRA (2 μM) toward HSA (10 equiv.) in the presence of excess amount (10 equiv.) of different proteins, enzymes and urine interferents at 582 nm in ~100% PBS buffer of pH 7.4,  $\lambda_{ex}$  = 539 nm. Error bars: standard deviation (n = 3).

In this study, the anti-interference capability of HJRA was also investigated by measuring the fluorescence response of HJRA toward HSA in the presence of typical urine interferents as well as other proteins, enzymes, different amino acids, cations and anions. As shown in **Figure 2.21**, and **Figures 2.22–2.24**, when additional interferents were present in the detection system, the fluorescence response of HJRA toward HSA at 582 nm did not alter appreciably in PBS (pH 7.4) buffer medium. Thus, all of them exhibited an interference-free selective fluorescence response of HJRA toward HSA. These findings show that the HJRA probe has exceptional selectivity toward HSA, which can be useful for further cell imaging applications and HSA detection in complicated biological samples.

Interestingly, when the nonemissive HJRA ( $\Phi = 0.0015$ ) interacts with an excess of HSA and BSA in PBS buffer media, it becomes strongly emissive ( $\Phi = 0.4317$  in the presence of HSA) and displays a turn-on red fluorescent response, which in turn allows the scope to identify HSA and BSA with the naked eye under UV light (**Figure 2.17**, inset). In fact, it was noticed that the interaction of HJRA (2  $\mu\text{M}$ ) with HSA and BSA (10 equiv. of each) resulted in  $\sim 298$ -fold and  $\sim 190$ -fold increases in emission intensity at 582 nm, respectively (**Figure 2.17**).

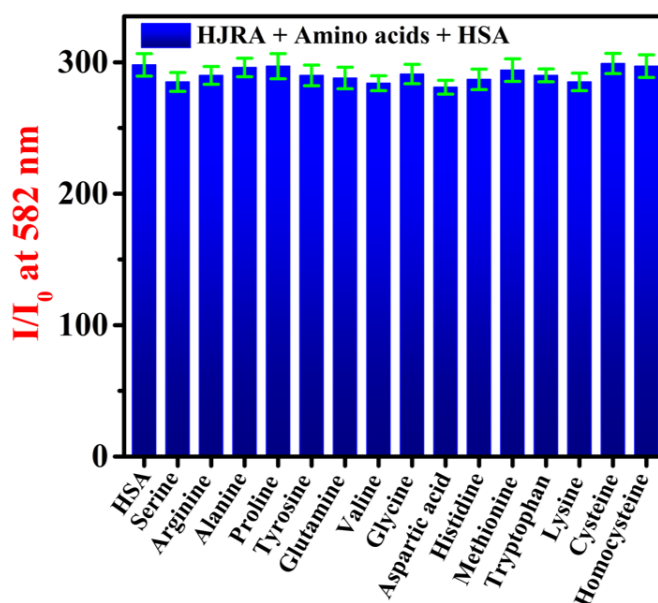


**Figure 2.22** Fluorescence responses of HJRA (2  $\mu\text{M}$ ) toward HSA (10 equiv.) in the presence of various amino acids (10 equiv.) at 582 nm in  $\sim 100\%$  PBS buffer of pH 7.4,  $\lambda_{\text{ex}} = 539$  nm. Error bars: standard deviation ( $n = 3$ ).

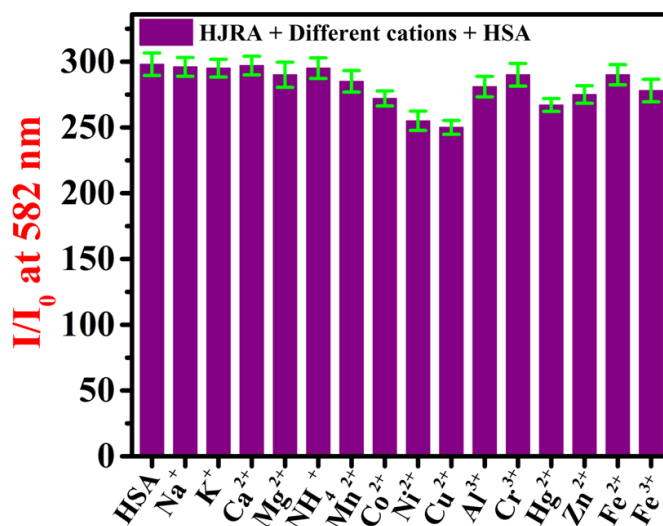


**Figure 2.23** Fluorescence responses of HJRA (2  $\mu$ M) toward HSA (10 equiv.) in the presence of different cations (15 equiv.) at 582 nm in ~100% PBS buffer of pH 7.4,  $\lambda_{ex}$  = 539 nm. Error bars: standard deviation (n = 3).

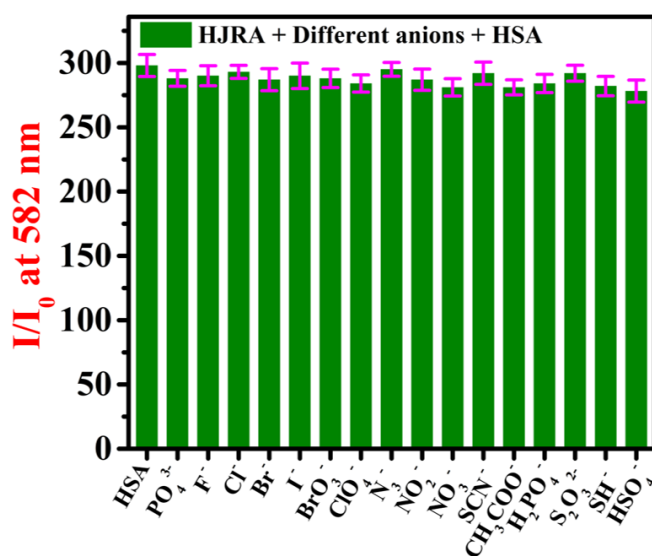
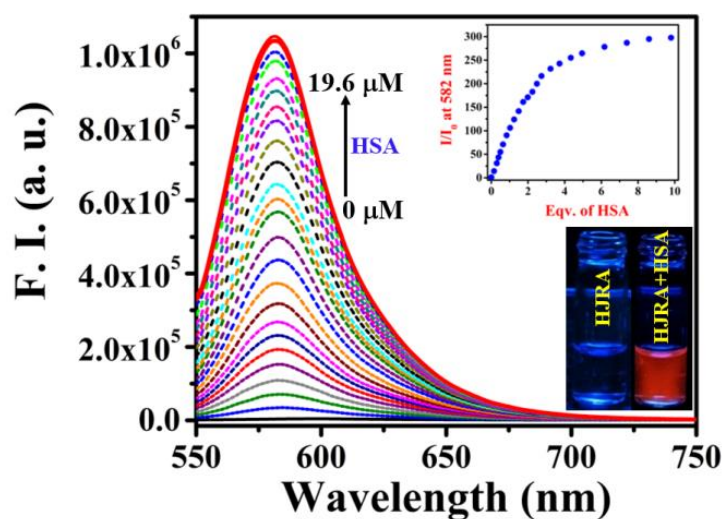


**Figure 2.24** Fluorescence responses of HJRA (2  $\mu$ M) toward HSA (10 equiv.) in the presence of different anions (15 equiv.) at 582 nm in ~100% PBS buffer of pH 7.4,  $\lambda_{ex}$  = 539 nm. Error bars: standard deviation (n = 3).

HSA and BSA have comparable form and functional behaviors, but the difference in microstructure and milieu within their hydrophobic binding zones may affect the extent of interaction of HJRA with proteins and hence the extent of rigidity imposed on the probe. However, in order to comprehend the fluorescent turn-on response of HJRA probe imposed



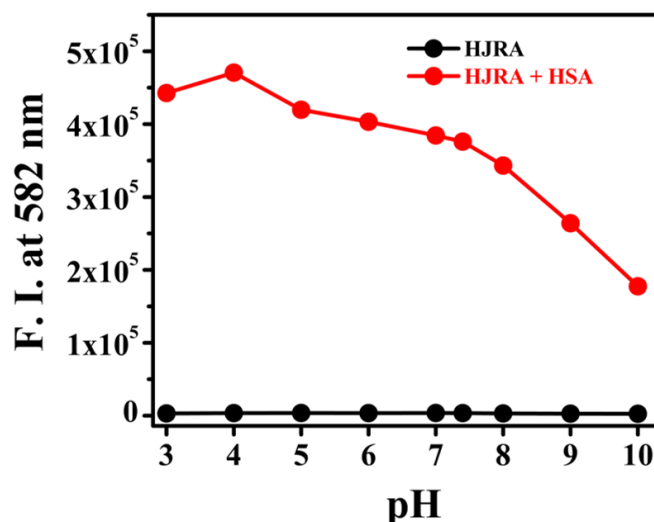
by serum albumin proteins, a quantitative assessment of the interaction between HJRA and HSA is essential. Therefore, a fluorescence titration was carried out keeping [HJRA] = 2  $\mu$ M with the varying HSA concentration between 0 and 19.6  $\mu$ M in PBS buffer at pH 7.4. It was noticed that the emission intensity of HJRA was enhanced significantly ( $\sim$ 298-fold) in a 19.6  $\mu$ M concentration of HSA along with a simultaneous blue shift ( $\sim$ 16 nm) of the emission maxima from 598 to 582 nm upon excitation at 539 nm (Figure 2.25 and Figure 2.10). Here, it is important to note that as all the emission spectra were collected within 1 min of the bioanalytes being added, the fluorescent response of HJRA to HSA appears to be very quick.



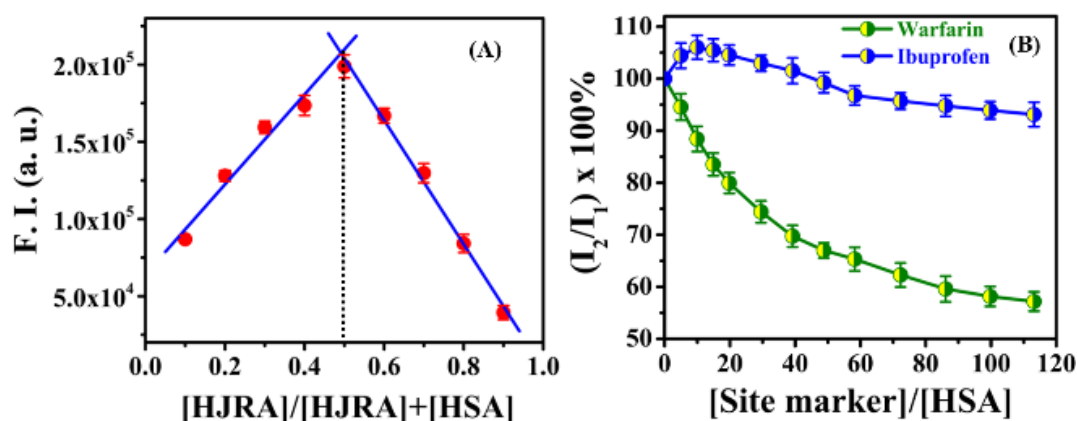
**Figure 2.25** Fluorescence spectral changes of HJRA (2  $\mu$ M) in  $\sim$ 100% PBS buffer (pH = 7.4) upon successive addition of HSA. Insets: plot of emission intensity variations ( $I/I_0$ ) at 582 nm versus equivalent of HSA and visual fluorescence changes of HJRA with the addition of HSA.  $\lambda_{ex}$  = 539 nm.

Hence, the time-dependent fluorescence assay of HJRA was conducted in the absence and presence of different HSA concentration to determine the response time. Figure 2.15 shows that after adding HSA, the emission intensity was increased rapidly and gets saturated within the time of measurement ( $\sim$ 15 s). Therefore, HJRA might be an excellent probe for the real-time measurement of HSA in biological fluids. Here, we also looked at the influence of pH of the medium on HSA sensing by HJRA in the range pH 3 to 10. Without HSA, the emission behavior of the probe (2  $\mu$ M) remained unchanged across the experimental pH range (Figure 2.26), suggesting that HJRA was relatively stable in various microenvironment. On the other hand, upon addition of 1 equiv. of HSA, the emission intensity of HJRA was greatly increased

and remained almost constant in the range pH 5 to 7.4, manifesting that the probe is suitable for the detection of HSA in the physiological pH range. The stoichiometry of the reaction between HSA and HJRA was determined by Job's method which clearly indicates a 1:1 complexation (Figure 2.27A).

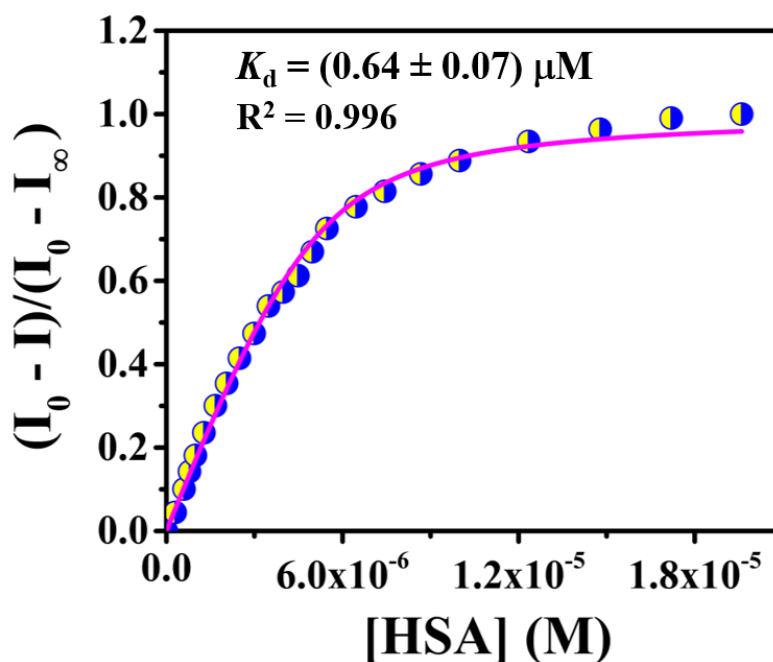


**Figure 2.26** The fluorescence emission intensities of HJRA (2  $\mu$ M) at 582 nm in the absence and presence of HSA (1 equiv.) at different pHs. All the experiments were performed in PBS buffer.  $\lambda_{ex}$  = 539 nm.

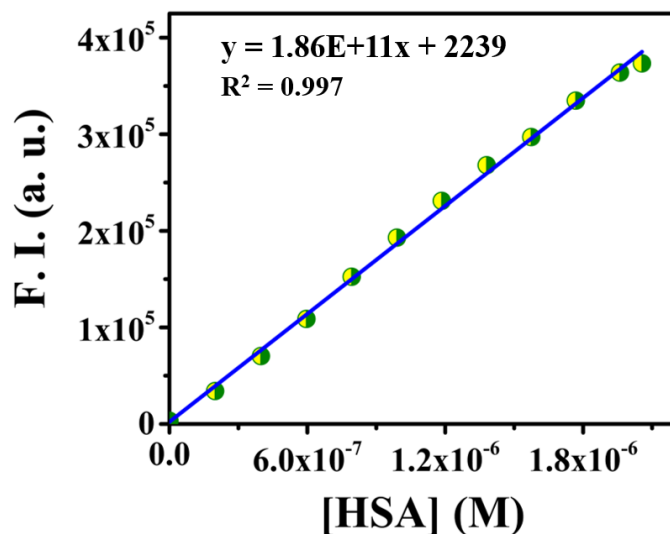


**Figure 2.27** (A) Job's plot analysis of HJRA with HSA in different molar ratios keeping the overall concentration at 2  $\mu$ M. (B) Emission intensity variations of HJRA-HSA composite (HJRA = 2  $\mu$ M, HSA = 0.5  $\mu$ M) in pH 7.4 PBS buffer with the successive addition of warfarin and ibuprofen site markers (0-56.6  $\mu$ M).  $\lambda_{ex}$  = 539 nm and  $\lambda_{em}$  = 582 nm. Error bars: standard deviation (n = 3).

In this study, the fluorescence titration data of HJRA with HSA (*vide supra*) were used to evaluate the dissociation constant ( $K_d$ ) value between the probe and HSA. Following eq 11 when we plot  $(I_0 - I)/(I_0 - I_\infty)$  vs. HSA concentration, a nonlinear curve was obtained (Figure 2.28), which was then solved by using a nonlinear curve fitting approach to give a high binding affinity of HJRA to HSA in terms of the dissociation constant value,  $K_d = (0.64 \pm 0.07) \mu\text{M}$ . Moreover, the emission intensity of HJRA at 582 nm displayed a good linear relationship with the incremental addition of HSA within the concentration range 0–2.05  $\mu\text{M}$  (Figure 2.29). Based on the  $3\sigma/\text{slope}$  method,<sup>58</sup> the limit of detection (LOD) value was estimated to be 1.13 nM (0.0751 mg/L). A quick inspection of the literature revealed that the present LOD is substantially below the normal HSA concentration in healthy urine signifying the high sensitivity of the probe and superior to the recently reported other HSA sensing probes.<sup>32,42-44,48,49,51-56,60,61,72-91</sup> Besides this, a comparison table has been prepared (Table 2.1) to list the advantages of this developed method in terms of sensitivity, selectivity, response time, and binding site as compared to the previously reported HSA/BSA detection strategies.

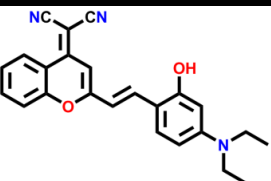
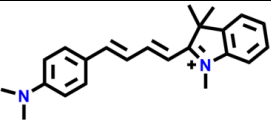
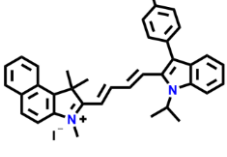


**Figure 2.28** Plot of  $(I_0 - I)/(I_0 - I_\infty)$  vs. HSA concentration for the determination of dissociation constant ( $K_d$ ) between HJRA and HSA. The solid line displays the best fit assuming a 1:1 HJRA:HSA complex using a nonlinear curve-fitting method.

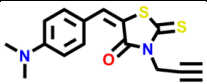
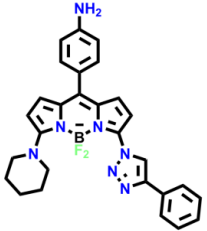
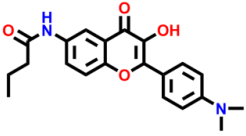
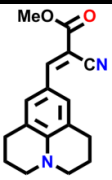
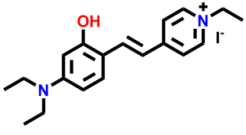
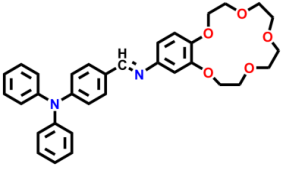
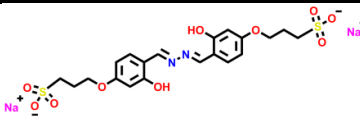
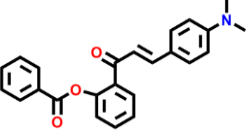
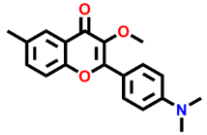


**Figure 2.29** Linear fluorescence response of HJRA (2  $\mu\text{M}$ ) to HSA (0-2.05  $\mu\text{M}$ ) at 582 nm in  $\sim 100\%$  PBS buffer of pH 7.4 for determination of detection limit. LOD value is estimated as 1.13 nM. The LOD value was estimated from 10 times the standard deviation ( $\sigma$ ) of the fluorescence intensity corresponding to the blank sample (HJRA only). Here,  $\sigma$  value is 70.332. From the graph we get slope =  $1.86 \times 10^{11} \text{ M}^{-1}$ .

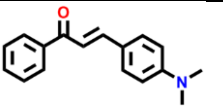
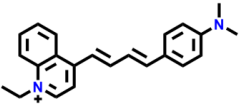
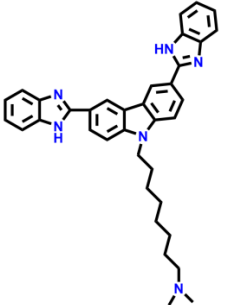
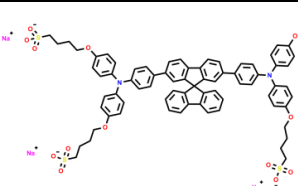
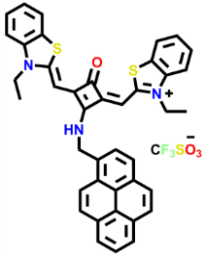
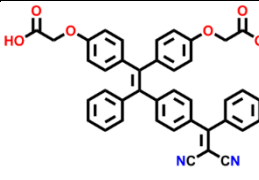
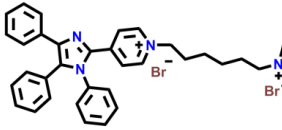
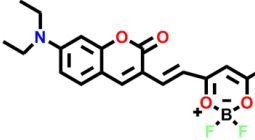
**Table 2.1** Comparison of the fluorescent molecular probes for the detection of serum albumins.

Structure of the probe	$\lambda_{\text{ex}}/\lambda_{\text{em}}$ (nm)	Selectivity	LOD	Response time	Binding site	Ref.
	530/650	HSA	1.26 mg/L	–	Site I	54
	550/680	HSA	11 nM	–	Site I	52
	540/676	HSA	0.66 mg/L	–	Site I	72

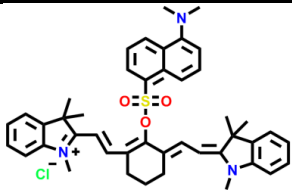
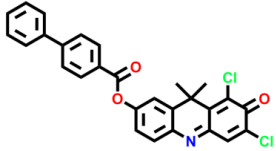
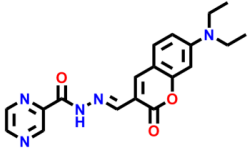
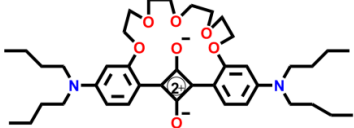
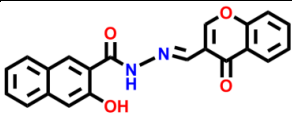
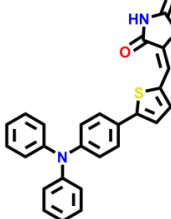
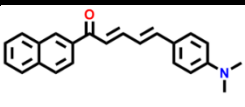
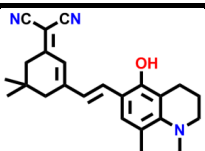
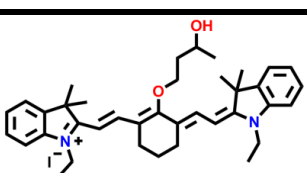
## Chapter 2: Serum Albumin.....Live Cell Imaging Application

	436/508	HSA	5 nM	60 min	More than one site	<b>73</b>
	460/575	HSA	0.30 mg/L	–	Fatty acid site I	<b>74</b>
	400/508	HSA	94 nM	<30 sec	Site I	<b>75</b>
	440/490	HSA	0.40 mg/L	–	Site I	<b>20</b>
	480/580	HSA	4.8 nM	30 sec	Site I	<b>76</b>
	360/500	HSA	1.7 nM	–	Site I & Site II	<b>77</b>
	355/508	HSA	6.11 mg/L	–	–	<b>78</b>
	426/524	HSA	1.91 mg/L	–	Site I	<b>79</b>
	400/480	BSA	0.09 mg/L	–	Hydrophobic site	<b>80</b>

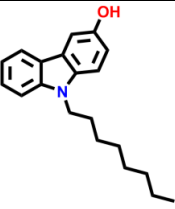
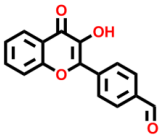
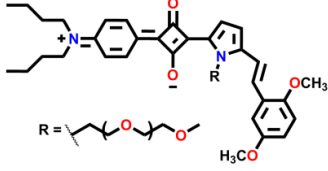
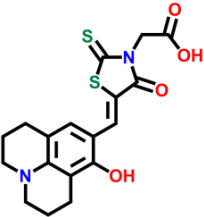
## Chapter 2: Serum Albumin.....Live Cell Imaging Application

	400/535	HSA	0.57 mg/L	<1 min	Site I	<b>81</b>
	525/688	BSA	47.25 nM	–	Site I	<b>82</b>
	350/454	HSA	0.27 mg/L	2 h	Site I	<b>83</b>
	378/461	BSA	7.3 nM	–	Site I & Site II	<b>84</b>
	600/674	HSA	140 nM	–	Site II	<b>42</b>
	405/610	HSA	2.7 nM	<5 min	Site I	<b>47</b>
	380/480	HSA	0.14 μM	~15 sec	Site I	<b>44</b>
	495/540	HSA	0.21 mg/L	<15 min	Site I & Site II	<b>85</b>

## Chapter 2: Serum Albumin.....Live Cell Imaging Application

	740/804	HSA	50 nM	–	Site II	<b>60</b>
	600/662	HSA	6.51 mg/L	–	Reaction site	<b>86</b>
	450/513	HSA	0.59 mg/L	<30 sec	Site I	<b>48</b>
	650/675	HSA	1.03 mg/L	–	Site I & Site II	<b>49</b>
	370/527	HSA	0.93 mg/L	–	Site I	<b>87</b>
	497/610	HSA	0.34 mg/L	~10 min	Subdoma in IB	<b>61</b>
	480/610	HSA	23 nM	~3 min	Site I & Site II	<b>88</b>
	590/685	HSA	4.64 nM	~15 min	Site I	<b>89</b>
	630/710	HSA	0.996 mg/L	<5 min	Site I	<b>90</b>



	295/400	HSA	4 nM	–	Site I	56
	420/507	HSA	20.7 nM	~1 min	Site I & Site II	91
	380/480	BSA	3 nM	~150 sec	Cys34 thiol group	43
	539/582	HSA	1.13 nM (0.0751 mg/L)	~15 sec	Site I	This work

#### 2.3.4 Site-Specific Binding Study and Probable HSA Sensing Mechanism

The 1:1 complexation between HJRA and HSA, as delineated by Job's plot, confirms that HJRA binds with HSA protein primarily at one site only. According to the crystal structure study, HSA is a ~66.5 kDa complex protein with three distinct domains (domains I, II, and III), each of which contains two subdomains (A and B).<sup>4</sup> The major ligand binding sites of HSA are mostly found in hydrophobic regions of subdomain IIA (binding site I) and subdomain IIIA (binding site II).<sup>92,93</sup> Site I interact with compounds primarily through strong hydrophobic interactions, whereas site II employs a mixture of ionic, van der Waals, and hydrogen bonding interactions.<sup>4,92,93</sup> Therefore, the competitive fluorescence displacement assays were conducted to determine the probable binding location of HJRA on HSA employing two famous site-specific drugs (warfarin for site I and ibuprofen for site II). Here, in the displacement experiments the site-specific drugs were incrementally added to a solution of HSA and HJRA in a molar ratio of 1:4 to minimize the nonspecific binding of the

site-specific drugs.<sup>94</sup> The change in emission intensity of this ternary mixture were monitored by using the approach stated by Sudlow *et al.*<sup>93</sup>

$$\frac{I_2}{I_1} \times 100\%$$

Here,  $I_2$  and  $I_1$  are the emission intensities of the HSA–HJRA mixture in the presence and absence of site-specific drugs, respectively. In the presence of 56.6  $\mu\text{M}$  warfarin, the emission intensity of the HSA–HJRA combination was noticeably reduced by about 43%, implying the displacement of HSA bound HJRA by warfarin (Figure 2.27B), whereas, ibuprofen exhibited no significant change in emission intensity. Hence, these experimental findings clearly indicate that HJRA is most probably housed at subdomain IIA of Site I in HSA.

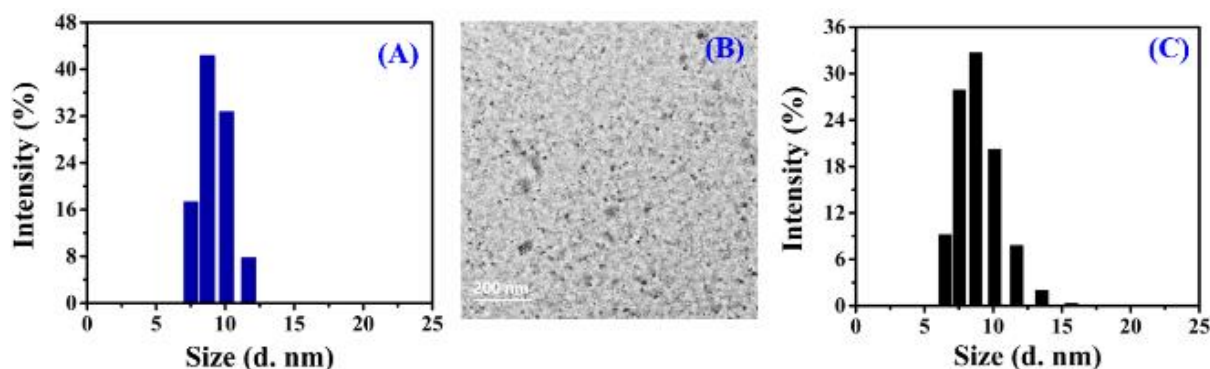


**Figure 2.30** (A, B) DLS and TEM images of the HJRA (2  $\mu\text{M}$ ) after the addition of 1 equiv. of HSA in  $\sim 100\%$  PBS buffer solution (pH 7.4). (C) DLS analysis of only 2  $\mu\text{M}$  HSA. Scale bar: 200 nm.

Then the HSA detection process was explored further to know more about the underlying sensing mechanism. DLS experiment of 2  $\mu\text{M}$  HJRA in  $\sim 100\%$  PBS buffer (pH 7.4) indicated that HJRA can form nanoaggregates with a mean diameter of 105 nm (Figure 2.9A). As the most common cause of AIEgens fluorescence light-up is molecular aggregation, DLS analysis was employed to see if bigger nanoaggregates developed in the presence of HSA protein. Interestingly, after adding of 1 equiv. HSA, the peak at 105 nm related to the HJRA nanoaggregates was vanished with the emergence of a new peak at 9 nm (Figure 2.30A) corresponding to the size of the HSA protein in solution (Figure 2.30C).<sup>38,42</sup> Furthermore,

TEM imaging investigations vividly displayed that after the addition of 1 equiv HSA, nanoaggregates of HJRA with an average diameter of  $\sim 97$  nm (Figure 2.9B, C) converted into considerably smaller particles (Figure 2.30B). These experimental outcomes undoubtedly established the disassembly of the self-assembled nanoaggregates of HJRA upon complexation with HSA. Thus, the fluorescent turn-on response of HJRA to HSA can be attributed to the site-specific binding of HJRA within the hydrophobic cavity of HSA, which in turn suppresses the TICT action by restricting free intramolecular rotation, because of the severe steric hindrance and low-polarity environment inside HSA. Moreover, a steady-state fluorescence anisotropy study was carried out to collect important information about the rigidity of the environment in the immediate proximity of the HJRA probe and it is reflected by the change in anisotropy value.<sup>95,96</sup>

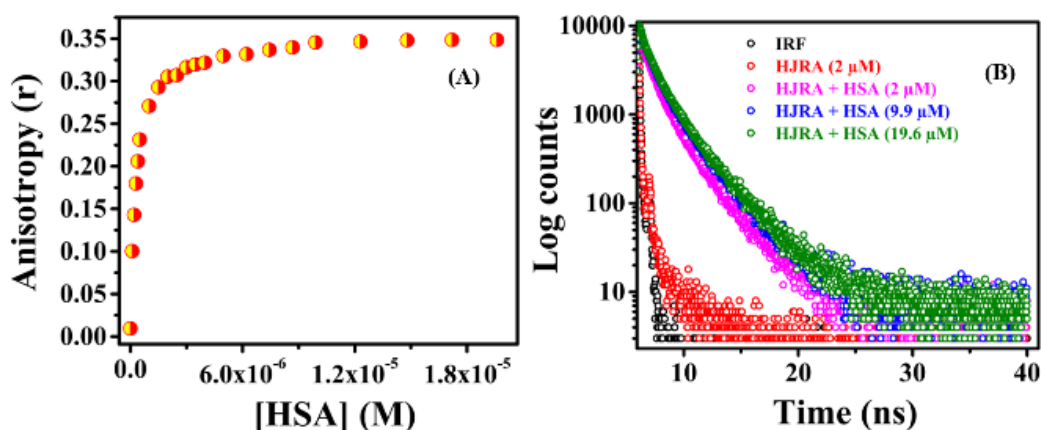


**Figure 2.31** Steady-state anisotropy variation of HJRA ( $2 \mu\text{M}$ ) with the increasing concentration of HSA ( $\lambda_{\text{ex}} = 539$  nm and  $\lambda_{\text{em}} = 582$  nm). (B) Time-resolved fluorescence decay spectra of HJRA ( $2 \mu\text{M}$ ) with the addition of HSA (0-19.6  $\mu\text{M}$ ).

At first, a quick augmentation in the anisotropy value of HJRA ( $2 \mu\text{M}$ ) was noticed from 0.009 to 0.292 upon addition of only  $1.5 \mu\text{M}$  HSA and then the value slowly improved to 0.348 until the addition of  $19.6 \mu\text{M}$  HSA (Figure 2.31A). Hence, the rising value of anisotropy evidently reveals that considerable motional restriction is imposed on HJRA probes within HSA. Additionally, to determine the source of fluorescence amplification we have also performed the fluorescence lifetime analysis of probe HJRA with the addition of HSA (Figure 2.31B). Table 2.2 summarizes the decay related parameters. In  $\sim 100\%$  PBS buffer medium, free HJRA probe displays a triexponential decay with lifetimes of 0.46 ns (34.62%), 0.02 ns (30.96%) and 0.45 ns (34.42%), while after the addition of  $19.6 \mu\text{M}$  of

HSA, probe HJRA exhibits a triexponential decay with lifetimes of 1.21 ns (44.17%), 0.29 ns (10.85%) and 2.97 ns (44.98%). The longer lifetime value of HJRA-HSA composite implies that binding of HJRA to HSA decreases the molecular rotational flexibility and blocks the TICT process, thereby lowering the energy loss through nonradiative decay routes.

**Table 2.2** Time-resolved fluorescence lifetime decay parameters of HJRA (2  $\mu$ M) with the increasing concentration of HSA in ~100% aqueous PBS buffer (pH 7.4).

[HSA] ( $\mu$ M)	$\tau_1$ (ns)	$\tau_2$ (ns)	$\tau_3$ (ns)	$\alpha_1$	$\alpha_2$	$\alpha_3$	$\tau_{avg}$ (ns)	$\chi^2$
0	0.46	0.02	0.45	0.0483	0.9026	0.0491	0.06	1.091
2	1.11	0.27	2.77	0.3586	0.5378	0.1036	0.83	0.955
9.9	1.16	0.28	2.89	0.4060	0.4310	0.1630	1.06	1.028
19.6	1.21	0.29	2.97	0.4163	0.4128	0.1709	1.13	1.023

### 2.3.5 Molecular Docking

Here, we have conducted the molecular docking simulations to determine the probable binding site of HJRA within HSA and the role of relevant interactions during the complexation process.<sup>50,69</sup> From the ten distinct conformers, the docking conformation with lowest binding energy was selected for further investigations. **Figure 2.32A** shows the molecular docking pose of HJRA with HSA, indicating that subdomain IIA of site I in HSA is the preferred binding site for the HJRA probe, as evidenced by site-specific drug displacement studies. Several hydrophobic amino acid residues, like Trp 214, Ala 291, Leu 198, Leu 219 and Val 343 provided a better stability to the housed HJRA within HSA through hydrophobic and van der Waals interactions (**Figure 2.32B, D**). Some basic and cationic amino acid residues, such as Lys 199, Arg 257, Arg 222 and His 242 are important in forming hydrogen bonds with the oxygen atoms of different functional groups of HJRA (**Figure 2.32C, D**). Furthermore, Lys 195 engages with the aromatic skeleton of HJRA probe through cation- $\pi$  interaction. The indole ring of Trp 214 residue was projected into the binding domain to form a  $\pi$ - $\pi$  bond with HJRA. As shown in **Figure 2.32D**, a  $\pi$ -sulfur interaction also occurs between the Tyr 150 residue and the exocyclic sulfur atom of the HJRA probe. Based on the docking experiment, the binding energy for the interaction of HJRA with HSA is  $-6.36$

kcal/mol, suggesting that the interaction process is energetically favorable. The probable HSA sensing mechanism is portrayed in **Figure 2.32E**. Primarily, these hydrophobic, electrostatic and cation- $\pi$  interactions are responsible for the disassembly of the HJRA nanoaggregates which, in turn, facilitated the release and movement of HJRA monomer inside the HSA's hydrophobic cavity. Consequently, various noncovalent bonds that were developed in Site I are responsible for restricting the free rotation of the HJRA probe, making it highly emissive inside the protein domain.

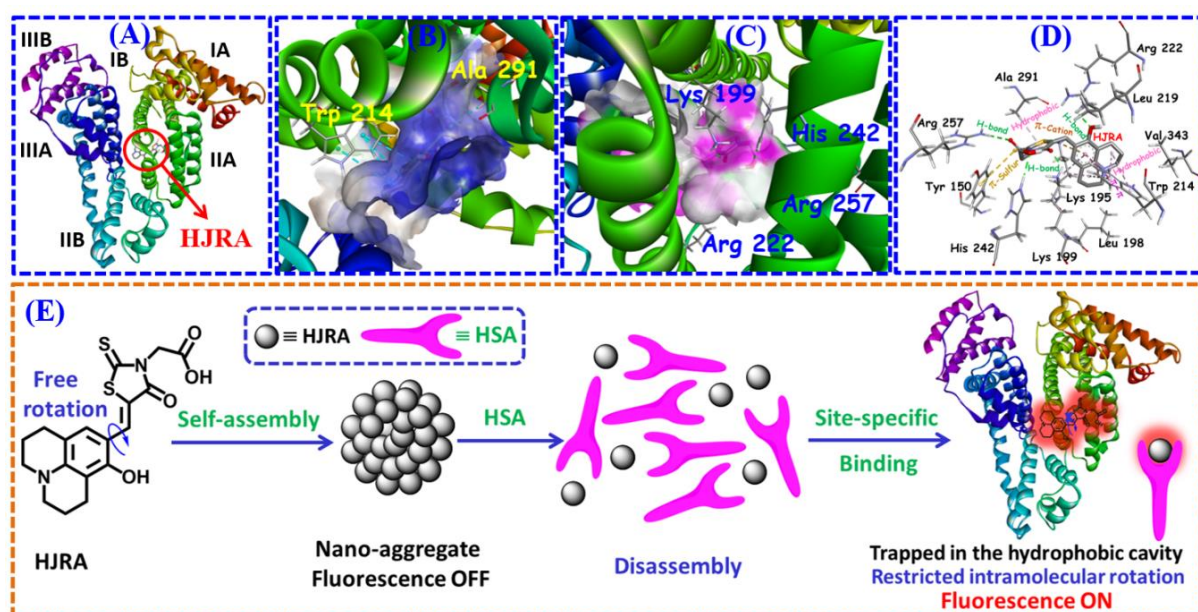


**Figure 2.32** (A) Molecular docking posture of HJRA with HSA protein (PDB ID: 1AO6) shown by red circle. (B, C) Magnified view of hydrophobic and hydrogen bonding interactions, respectively, made by HJRA in site I of HSA. (D) Neighboring amino acid residues and responsible forces directly interact for the accommodation of HJRA in site I of HSA. Hydrophobic and  $\pi$ - $\pi$  interactions are displayed as dotted purple lines; H-bonds,  $\pi$ -cation and  $\pi$ -sulfur bonds are indicated as dotted green, orange and dark orange lines, respectively. (E) Schematic representation of the HSA mediated disassembly of HJRA nanoaggregates and fluorescence turn-on process.

### 2.3.6 HSA Quantification in Human Urine Samples

The quantitative detection of urinary albumin levels has immense clinical importance, although it is often complicated by the presence of other biological interferences and strong auto fluorescence of urine. However, we believe that the probe HJRA may be utilized for



selective identification and quantification of the albumin level in urine samples due to its ability of HSA detection over a range of pH 5 to 7.4 (Figure 2.26) through strong turn-on fluorescence response. Therefore, to establish the practical applicability of the probe HJRA, we collected three urine samples from three healthy male volunteers with no past medical history and diluted ten times by ~100% PBS buffer (pH 7.4) to assess the endogenous HSA concentration in urine samples using standard addition curve technique. Dilution of urine samples was used to reduce the pH effect and urine background fluorescence.

In our experiment, when HSA (0-20.13  $\mu\text{M}$ ) was added to a urine-PBS system containing 2  $\mu\text{M}$  HJRA, the fluorescence intensity increased with the increasing concentration of HSA and reached saturation at 20.13  $\mu\text{M}$  (Figure 2.33A). Furthermore, in the concentration range of 0–2.05  $\mu\text{M}$ , the fluorescence intensity increased linearly with HSA (Figure 2.33B) and the detection limit was 1.72 nM (0.1143 mg/L) by the  $3\sigma/\text{slope}$  method. From the linear relationship of HJRA emission intensity at 582 nm with the increasing HSA concentration, the urinary HSA levels of the three male volunteers were estimated to be 16.84 mg/L, 26.28 mg/L and 12.76 mg/L, respectively.

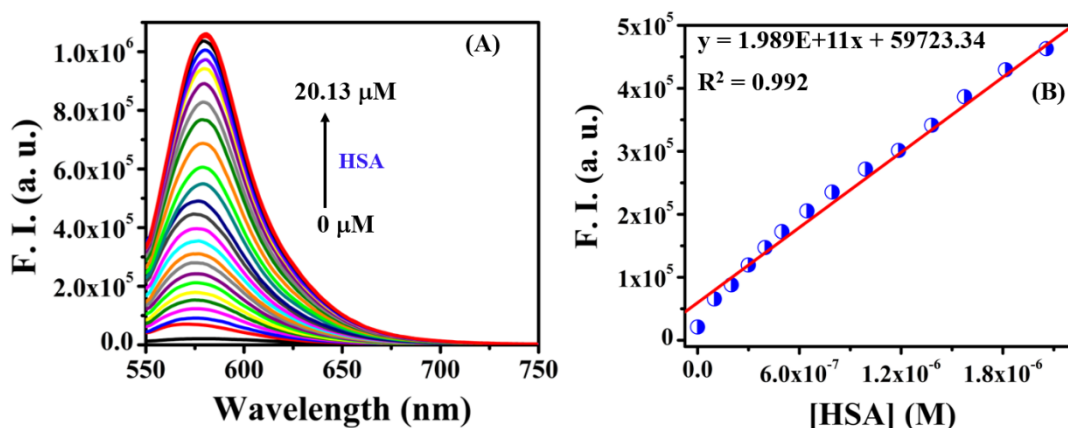


**Figure 2.33** (A) Fluorescence emission spectra of HJRA (2  $\mu\text{M}$ ) with the addition of HSA (0–20.13  $\mu\text{M}$ ) in treated urine sample. (B) Linear fluorescence response of HJRA (2  $\mu\text{M}$ ) to HSA (0-2.05  $\mu\text{M}$ ) at 582 nm for determination of detection limit.  $\lambda_{\text{ex}} = 539 \text{ nm}$ . From the graph we get slope =  $1.989 \times 10^{11} \text{ M}^{-1}$ .

For the validation of HSA levels determined by HJRA (fluorescence technique), urine samples were also examined using the Coomassie Brilliant Blue G250 technique.<sup>97</sup> Due to the limited sensitivity of Coomassie Brilliant Blue G250 (an albumin binding dye), undiluted

urine samples were used in this technique. Based on the standard addition curve of absorbance at 595 nm versus HSA content (mg/L) (Figure 2.34A), the urinary HSA levels were evaluated to be 19.43 mg/L, 25.61 mg/L and 14.05 mg/L, respectively. Remarkably, the urinary HSA levels estimated by the HJRA (Fluorescence) approach were shown to be in good accordance with the G250 method (Figure 2.34B). Hence, HJRA is an excellent red fluorescent probe for the accurate monitoring and quantifying the endogenous HSA in urine samples.

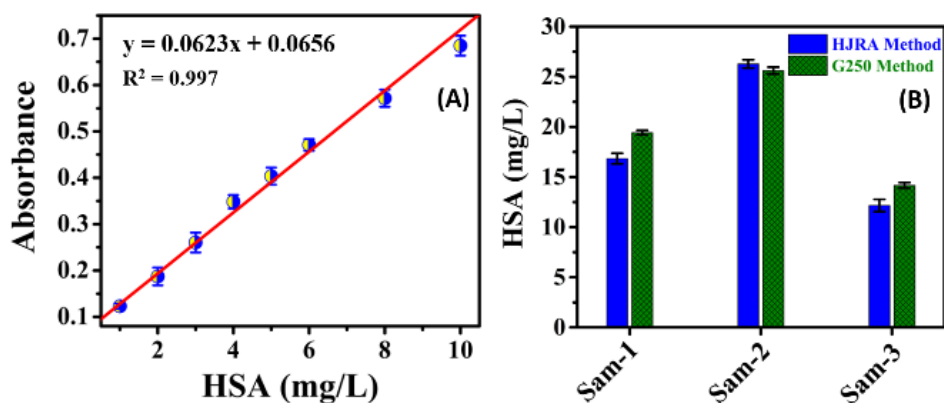


**Figure 2.34** (A) Standard addition curve of absorbance versus HSA content (mg/L) by the Coomassie Brilliant Blue G250 method.  $\lambda_{\text{abs}} = 595$  nm. (B) Endogenous HSA quantification in human urine samples by a spectrofluorometric technique using HJRA in comparison with the G250 method. Error bars: standard deviation (n = 3).

### 2.3.7 Fluorescence Imaging of HSA in Living Cells

Prior to the intracellular fluorescence imaging studies, a well-known MTT based assay was performed in the CHO cell line to examine the cytotoxicity of the probe HJRA.

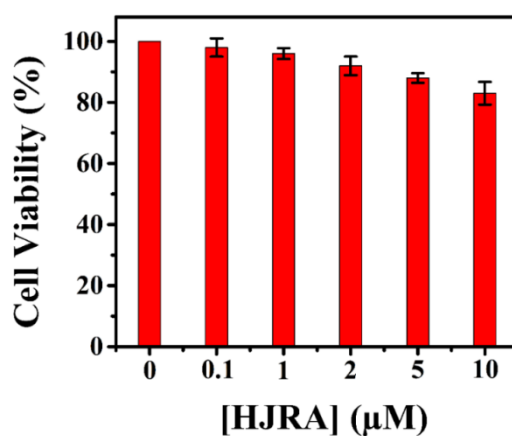


**Figure 2.35** Cell viabilities of CHO cells treated with different concentrations of HJRA.



As shown in **Figure 2.35**, after 24 h of incubation with 10  $\mu\text{M}$  of HJRA, the viability of CHO cells was remained over 82%, suggesting that the probe HJRA has very low cytotoxicity and might be useful in biological applications. Then the cell imaging of endogenous HSA in CHO cells was performed using HJRA. Upon incubation of CHO cells with HJRA (2  $\mu\text{M}$ ) for 30 min a weak red fluorescence was observed (**Figure 2.36B2**).

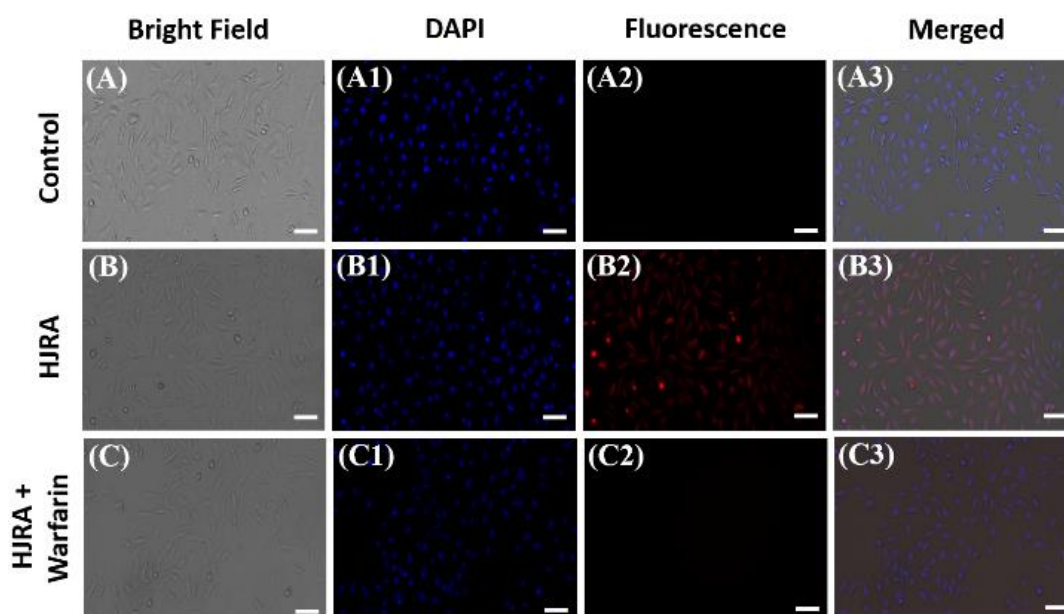


**Figure 2.36** Confocal fluorescence imaging of endogenous HSA in living CHO cells. (A-A3) CHO cells as control. (B-B3) CHO cells treated with HJRA (2  $\mu\text{M}$ ) for 30 min and then with DAPI for another 10 min. (C-C3) CHO cells (pretreated with 30  $\mu\text{M}$  warfarin for 15 min) treated with HJRA (2  $\mu\text{M}$ ) for 30 min and then with DAPI for another 10 min.  $\lambda_{\text{ex}}$  for DAPI and HJRA are 352 and 540 nm, respectively. Scale bar = 50  $\mu\text{m}$ .

Interestingly, the intracellular fluorescence intensity was dramatically reduced in CHO cells when warfarin (30  $\mu\text{M}$ ) was initially incubated for 15 min, followed by incubation with HJRA (2  $\mu\text{M}$ ) for an additional 30 min (**Figure 2.36C2**). These findings demonstrated that HJRA has good permeability to the cell membrane, enabling cells to interact with endogenous HSA. However, the fluorescence intensity was significantly enhanced when CHO cells were initially treated with 20  $\mu\text{M}$  HSA for 24 h, followed by further 30 min incubation with 2  $\mu\text{M}$  HJRA (**Figure 2.37A2**). In a control study, the intracellular fluorescence intensity was obviously decreased when the CHO cells (incubated with 20  $\mu\text{M}$  HSA for 24 h) were loaded with warfarin (30  $\mu\text{M}$ ) for inhibition (**Figure 2.37B2**).

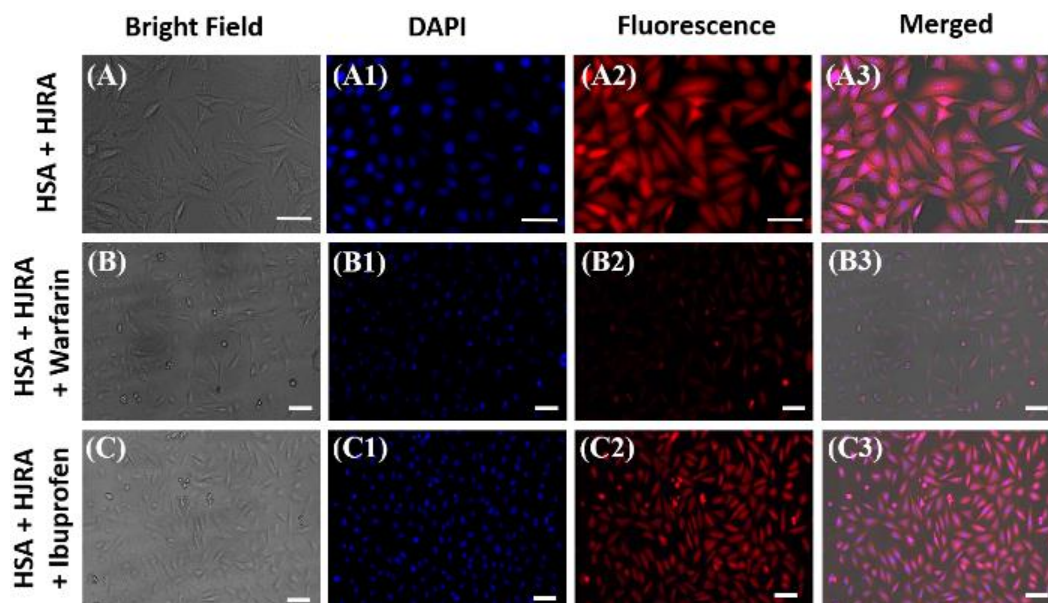


**Figure 2.37** Confocal fluorescence imaging of exogenous HSA in living CHO cells. (A-A3) CHO cells (incubated with 20  $\mu$ M HSA for 24 h) loaded with HJRA (2  $\mu$ M) for 30 min and then with DAPI for another 10 min. (B-B3) CHO cells (incubated with 20  $\mu$ M HSA for 24 h) pretreated with warfarin (30  $\mu$ M) for 15 min, then with HJRA (2  $\mu$ M) for another 30 min and then further loaded with DAPI for 10 min. (C-C3) CHO cells (incubated with 20  $\mu$ M HSA for 24 h) pretreated with ibuprofen (30  $\mu$ M) for 15 min, then with HJRA (2  $\mu$ M) for another 30 min and then further loaded with DAPI for 10 min.  $\lambda_{ex}$  for DAPI and HJRA are 352 and 540 nm, respectively. Scale bar = 50  $\mu$ m.

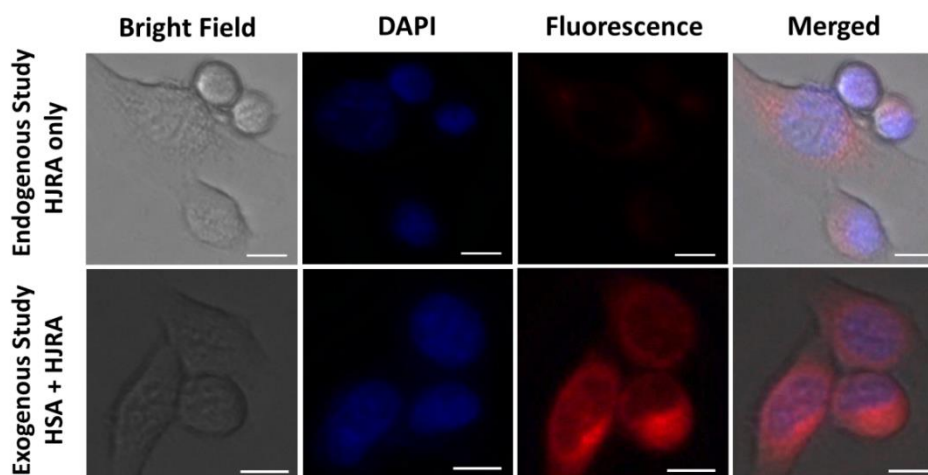


**Figure 2.38** Magnified fluorescence microscopic imaging of endogenous and exogenous HSA in living CHO cells using HJRA (2  $\mu$ M).  $\lambda_{ex}$  = 540 nm, Scale bar = 10  $\mu$ m.

In contrast, HSA treated CHO cells loaded with 30  $\mu\text{M}$  ibuprofen followed by incubation with 2  $\mu\text{M}$  HJRA for an additional 30 min, showed no change in intracellular fluorescence intensity (**Figure 2.37C2**), supporting the spectrum analysis shown in **Figure 2.27B**. Costaining with DAPI, a nucleus-targeting dye, followed by microscopic image analysis indicates that HJRA probes are mostly localized in the cytoplasm of CHO cells. (**Figure 2.38**). These outcomes showed the capability of HJRA to image exogenous HSA in living cells.

### 2.4 Conclusions

In this article, a TICT-based small fluorogenic molecular probe HJRA has been rationally designed and synthesized, which can easily *self-assemble* into nonfluorescent nanoaggregates in aqueous PBS buffer at pH 7.4. The HJRA nanoaggregates can selectively bind with serum albumin proteins (HSA/BSA) in physiological conditions which facilitates the *disassembly* process toward monomer formation. The selective trapping of the HJRA monomer in the subdomain IIA of site I in HSA resulted a rapid turn-on red fluorescent response due to suppression of the TICT action by restricting free intramolecular rotation. A similar turn-on response was also noticed in the case of BSA. The limit of detection (LOD) value was estimated to be 1.13 nM (0.0751 mg/L), which is substantially below the normal HSA concentration in healthy urine signifying the high sensitivity of the probe and superior to the recently reported other HSA sensing probes. The underlying HSA sensing mechanism has been well supported by molecular docking, competitive fluorescent displacement assay, and DLS and TEM studies. Analysis of the binding mechanism between HJRA and HSA implies that a combination of various noncovalent bonds including hydrophobic interactions, hydrogen bonds, and  $\pi$ - $\pi$  and cation- $\pi$  interactions are the fundamental forces for encouraging the disassembly process and trapping of the HJRA probe at the site I in HSA. The cell viability experiment reveals the low cytotoxicity of the HJRA probe. The practical applications of the probe were demonstrated by analyzing the healthy urine samples collected from three adults with no previous medical history. The comparable results and quick response toward quantification of HSA in urine by HJRA with respect to the Bradford method clearly points toward the superiority of this method compared to the existing ones and may lead to biomedical applications for HSA quantification in urine. Additionally, the probe may be used to image endogenous and exogenous HSA in living cells. Therefore, one

can safely conclude that the HJRA probe can serve as an effective biomarker for the quick biomedical diagnosis of HSA-associated diseases. In conclusion, self-assembly/disassembly strategy opens up a new potential platform for the specific and sensitive detection of various target analytes.

### References

- (1) Mizukami, S.; Hori, Y.; Kikuchi, K. Small-molecule-based protein-labeling technology in live cell studies: probe-design concepts and applications. *Acc. Chem. Res.* **2014**, *47*, 247–256.
- (2) Kobayashi, H.; Ogawa, M.; Alford, R.; Choyke, P. L.; Urano, Y. New strategies for fluorescent probe design in medical diagnostic imaging. *Chem. Rev.* **2010**, *110*, 2620–2640.
- (3) Fanali, G.; di Masi, A.; Trezza, V.; Marino, M.; Fasano, M.; Ascenzi, P. Human serum albumin: from bench to bedside. *Mol. Aspects Med.* **2012**, *33*, 209–290.
- (4) He, X. M.; Carter, D. C. Atomic structure and chemistry of human serum albumin. *Nature* **1992**, *358*, 209–215.
- (5) Fasano, M.; Curry, S.; Terreno, E.; Galliano, M.; Fanali, G.; Narciso, P.; Notari, S.; Ascenzi, P. The extraordinary ligand binding properties of human serum albumin. *IUBMB Life* **2005**, *57*, 787–769.
- (6) Curry, S.; Mandelkow, H.; Brick, P.; Franks, N. Crystal structure of human serum albumin complexed with fatty acid reveals an asymmetric distribution of binding sites. *Nat. Struct. Biol.* **1998**, *5*, 827–835.
- (7) Ha, C. E.; Bhagavan, N. V. Novel insights into the pleiotropic effects of human serum albumin in health and disease. *Biochim. Biophys. Acta* **2013**, *1830*, 5486–5493.
- (8) Belinskaia, D. A.; Voronina, P. A.; Batalova, A. A.; Goncharov, N. V. Serum Albumin. *Encyclopedia* **2021**, *1*, 65–75.
- (9) Fan, J.; Sun, W.; Wang, Z.; Peng, X.; Li, Y.; Cao, J. A fluorescent probe for site I binding and sensitive discrimination of HSA from BSA. *Chem. Commun.* **2014**, *50*, 9573–9576.
- (10) Alino, V. J.; Yang, K. L. Using liquid crystals as a readout system in urinary albumin assays. *Analyst* **2011**, *136*, 3307–3313.

- (11) Murch, S. H.; Winyard, P. J. D.; Koletzko, S.; Wehner, B.; Cheema, H. A.; Risdon, R. A.; Phillips, A. D.; Meadows, N.; Klein, N. J.; Walker-Smith, J. A. Congenital enterocyte heparan sulphate deficiency with massive albumin loss, secretory diarrhoea, and malnutrition. *Lancet* **1996**, *347*, 1299–1301.
- (12) Peters, T. All About Albumin: Biochemistry, Genetics and Medical Application; Academic Press: San Diego, CA, 1996; pp 234–240.
- (13) Hoogenberg, K.; Sluiter, W. J.; Dullaart, R. P. Effect of growth hormone and insulin-like growth factor I on urinary albumin excretion: studies in acromegaly and growth hormone deficiency. *Eur. J. Endocrinol.* **1993**, *129*, 151–157.
- (14) de Zeeuw, D.; Parving, H. H.; Henning, R. Microalbuminuria as an early marker for cardiovascular disease. *J. Am. Soc. Nephrol.* **2006**, *17*, 2100–2105.
- (15) Amin, R.; Widmer, B.; Prevost, A. T.; Schwarze, P.; Cooper, J.; Edge, J.; Marcovecchio, L.; Neil, A.; Dunger, D. B. Risk of microalbuminuria and progression to macroalbuminuria in a cohort with childhood onset type 1 diabetes: prospective observational study. *BMJ.* **2008**, *336*, 697–701.
- (16) Seegmiller, J. C.; Sviridov, D.; Larson, T. S.; Borland, T. M.; Hortin, G. L.; Lieske, J. C. Comparison of urinary albumin quantification by immunoturbidimetry, competitive immunoassay, and protein-cleavage liquid chromatography–tandem mass spectrometry. *Clin. Chem.* **2009**, *55*, 1991–1994.
- (17) Seegmiller, J. C.; Barnidge, D. R.; Burns, B. E.; Larson, T. S.; Lieske, J. C.; Kumar, R. Quantification of urinary albumin by using protein cleavage and LC-MS/MS. *Clin. Chem.* **2009**, *55*, 1100–1107.
- (18) Lowry, O. H.; Rosebrough, N. J.; Farr, A. L.; Randall, R. J. Protein Measurement with Folin Phenol Reagent. *J. Biol. Chem.* **1951**, *193*, 265–275.
- (19) Bradford, M. M. A rapid and sensitive method for the quantitation of microgram quantities of protein utilizing the principle of protein-dye binding. *Anal. Biochem.* **1976**, *72*, 248–254.
- (20) Wu, Y. Y.; Yu, W. T.; Hou, T. C.; Liu, T. K.; Huang, C. L.; Chen, I. C.; Tan, K. T. A selective and sensitive fluorescent albumin probe for the determination of urinary albumin. *Chem. Commun.* **2014**, *50*, 11507–11510.



- (21) Kubota, R.; Hamachi, I. Protein Recognition Using Synthetic Small-molecular Binders toward Optical Protein Sensing in vitro and in Live Cells. *Chem. Soc. Rev.* **2015**, *44*, 4454–4471.
- (22) He, X. P.; Zang, Y.; James, T. D.; Li, J.; Chen, G. R. Probing Disease-related Proteins with Fluorogenic Composite Materials. *Chem. Soc. Rev.* **2015**, *44*, 4239–4248.
- (23) Thurley, S.; Roglin, L.; Seitz, O. Hairpin peptide beacon: Dual-labeled PNA-peptide-hybrids for protein detection. *J. Am. Chem. Soc.* **2007**, *129*, 12693–12695.
- (24) Wang, B.; Yu, C. Fluorescence turn-on detection of a protein through the reduced aggregation of a perylene probe. *Angew. Chem., Int. Ed.* **2010**, *49*, 1485–1488.
- (25) Jin, Q.; Feng, L.; Wang, D. D.; Dai, Z. R.; Wang, P.; Zou, L. W.; Liu, Z. H.; Wang, J. Y.; Yu, Y.; Ge, G. B.; Cui, J. N.; Yang, L. A two-photon ratiometric fluorescent probe for imaging carboxylesterase 2 in living cells and tissues. *ACS Appl. Mater. Interfaces* **2015**, *7*, 28474–28481.
- (26) Hu, F.; Huang, Y.; Zhang, G.; Zhao, R.; Yang, H.; Zhang, D. Targeted bioimaging and photodynamic therapy of cancer cells with an activatable red fluorescent bioprobe. *Anal. Chem.* **2014**, *86*, 7987–7995.
- (27) Mei, J.; Leung, N. L. C.; Kwok, R. T. K.; Lam, J. W. Y.; Tang, B. Z. Aggregation-induced emission: together we shine, united we soar!. *Chem. Rev.* **2015**, *115*, 11718–11940.
- (28) Ding, D.; Li, K.; Liu, B.; Tang, B. Z. Bioprobes Based on AIE Fluorogens. *Acc. Chem. Res.* **2013**, *46*, 2441–2453.
- (29) Yuan, C. X.; Tao, X. T.; Wang, L.; Yang, J. X.; Jiang, M. H. Fluorescent turn-on detection and assay of protein based on lambda ( $\Lambda$ )-shaped pyridinium salts with aggregation-induced emission characteristics. *J. Phys. Chem. C* **2009**, *113*, 6809–6814.
- (30) Li, W., Chen, D., Wang, H., Luo, S., Dong, L., Zhang, Y., Shi, J.; Tong, B.; Dong, Y. Quantitation of albumin in serum using “turn-on” fluorescent probe with aggregation-enhanced emission characteristics. *ACS Appl. Mater. Interfaces* **2015**, *7*, 26094–26100.
- (31) Hong, Y. N.; Feng, C.; Yu, Y.; Liu, J. Z.; Lam, J. W. Y.; Luo, K. Q.; Tang, B. Z. Quantitation, visualization, and monitoring of conformational transitions of human serum albumin by a tetraphenylethene derivative with aggregation-induced emission characteristics. *Anal. Chem.* **2010**, *82*, 7035–7043.

- (32) Hu, Q.; Yao, B.; Owyong, T. C.; Prashanth, S.; Wang, C.; Zhang, X.; Wong, W. W. H.; Tang, Y.; Hong, Y. Detection of Urinary Albumin Using a “Turn-on” Fluorescent Probe with Aggregation-Induced Emission Characteristics. *Chem. - Asian J.* **2021**, *16*, 1245–1252.
- (33) Yu, Y.; Gong, Q. T.; Lu, W. F.; Liu, Y. H.; Yang, Z. J.; Wang, N.; Yu, X. Q. Aggregation-Induced Emission Probes for Specific Turn-on Quantification of Bovine Serum Albumin. *ACS Appl. Bio Mater.* **2020**, *3*, 5193– 5201.
- (34) Molla, M. R.; Prasad, P.; Thayumanavan, S. Protein-induced supramolecular disassembly of amphiphilic polypeptide nanoassemblies. *J. Am. Chem. Soc.* **2015**, *137*, 7286–7289.
- (35) Azagarsamy, M. A.; Yesilyurt, V.; Thayumanavan, S. Disassembly of dendritic micellar containers due to protein binding. *J. Am. Chem. Soc.* **2010**, *132*, 4550–4551.
- (36) Wang, H.; Zhuang, J.; Raghupathi, K. R.; Thayumanavan, S. A supramolecular dissociation strategy for protein sensing. *Chem. Commun.* **2015**, *51*, 17265–17268.
- (37) Ren, C.; Zhang, J.; Chen, M.; Yang, Z. Self-assembling small molecules for the detection of important analytes. *Chem. Soc. Rev.* **2014**, *43*, 7257–7266.
- (38) Chen, Q.; Liu, X.; Zeng, J.; Cheng, Z.; Liu, Z. Albumin-NIR dye self-assembled nanoparticles for photoacoustic pH imaging and pH-responsive photothermal therapy effective for large tumors. *Biomaterials* **2016**, *98*, 23–30.
- (39) Azagarsamy, M. A.; Sokkalingam, P.; Thayumanavan, S. Enzyme-triggered disassembly of dendrimer-based amphiphilic nanocontainers. *J. Am. Chem. Soc.* **2009**, *131*, 14184–14185.
- (40) Guo, J.; Zhuang, J.; Wang, F.; Raghupathi, K. R.; Thayumanavan, S. Protein AND enzyme gated supramolecular disassembly. *J. Am. Chem. Soc.* **2014**, *136*, 2220–2223.
- (41) Amado Torres, D.; Garzoni, M.; Subrahmanyam, A. V.; Pavan, G. M.; Thayumanavan, S. Protein-Triggered Supramolecular Disassembly: Insights Based on Variations in Ligand Location in Amphiphilic Dendrons. *J. Am. Chem. Soc.* **2014**, *136*, 5385–5399.
- (42) Fan, X.; He, Q.; Sun, S.; Li, H.; Pei, Y.; Xu, Y. Nanoparticles Self-assembled from Multiple Interactions: a Novel Near-infrared Fluorescent Sensor for the Detection of Serum Albumin in Human Sera and Turn-on Live-cell Imaging. *Chem. Commun.* **2016**, *52*, 1178–1181.



- (43) Anees, P.; Sreejith, S.; Ajayaghosh, A. Self-assembled near-infrared dye nanoparticles as a selective protein sensor by activation of a dormant fluorophore. *J. Am. Chem. Soc.* **2014**, *136*, 13233–13239.
- (44) Gao, T.; Yang, S.; Cao, X.; Dong, J.; Zhao, N.; Ge, P.; Zeng, W.; Cheng, Z. Smart self-assembled organic nanoprobe for protein-specific detection: design, synthesis, application, and mechanism studies. *Anal. Chem.* **2017**, *89*, 10085–10093.
- (45) Samanta, S.; Halder, S.; Das, G. Twisted-intramolecular-charge-transfer-based turn-on fluorogenic nanoprobe for real-time detection of serum albumin in physiological conditions. *Anal. Chem.* **2018**, *90*, 7561–7568.
- (46) Zheng, Z.; Li, H.; Sun, S.; Xu, Y. Media Dependent Switching of Selectivity and Continuous near Infrared Turn-on Fluorescence Response through Cascade Interactions from Noncovalent to Covalent Binding for Detection of Serum Albumin in Living Cells. *ACS Appl. Mater. Interfaces* **2018**, *10*, 44336–44343.
- (47) Yu, Y.; Huang, Y.; Hu, F.; Jin, Y.; Zhang, G.; Zhang, D.; Zhao, R. Self-assembled nanostructures based on activatable red fluorescent dye for site-specific protein probing and conformational transition detection. *Anal. Chem.* **2016**, *88*, 6374–6381.
- (48) Wang, Z. G.; Yan, X. J.; Liu, H. B.; Zhang, D. L.; Liu, W.; Xie, C. Z.; Li, Q. Z.; Xu, J. Y. A novel hydrazide Schiff base self-assembled nanoprobe for selective detection of human serum albumin and its applications in renal disease surveillance. *J. Mater. Chem. B* **2020**, *8*, 8346–8355.
- (49) Guo, Y.; Chen, Y.; Zhu, X.; Pan, Z.; Zhang, X.; Wang, J.; Fu, N. Self-assembled nanosensor based on squaraine dye for specific recognition and detection of human serum albumin. *Sens. Actuators B: Chem.* **2018**, *255*, 977–985.
- (50) Sasmal, M.; Islam, A. S. M.; Bhowmick, R.; Maiti, D.; Dutta, A.; Ali, M. Site-selective interaction of human serum albumin with 4-chloro-7-nitro-1, 2, 3-benzoxadiazole modified olanzapine derivative and effect of  $\beta$ -cyclodextrin on binding: In the light of spectroscopy and molecular docking. *ACS Appl. Bio Mater.* **2019**, *2*, 3551–3561.
- (51) Wang, Y. R.; Feng, L.; Xu, L.; Li, Y.; Wang, D. D.; Hou, J.; Zhou, K.; Jin, Q.; Ge, G. B.; Cui, J. N.; Yang, L. A rapid-response fluorescent probe for the sensitive and selective

- detection of human albumin in plasma and cell culture supernatants. *Chem. Commun.* **2016**, 52, 6064–6067.
- (52) Reja, S. I.; Khan, I. A.; Bhalla, V.; Kumar, M. A TICT based NIR-fluorescent probe for human serum albumin: a pre-clinical diagnosis in blood serum. *Chem. Commun.* **2016**, 52, 1182–1185.
- (53) Wang, Y. R.; Feng, L.; Xu, L.; Hou, J.; Jin, Q.; Zhou, N.; Lin, Y.; Cui, J. N.; Ge, G. B. An ultrasensitive and conformation sensitive fluorescent probe for sensing human albumin in complex biological samples. *Sens. Actuators B: Chem.* **2017**, 245, 923–931.
- (54) Rajasekhar, K.; Achar, C. J.; Govindaraju, T. A red-NIR emissive probe for the selective detection of albumin in urine samples and live cells. *Org. Biomol. Chem.* **2017**, 15, 1584–1588.
- (55) Zhu, K., Lv, T., Qin, T., Huang, Y., Wang, L., Liu, B. A flavonoid-based fluorescent probe enables the accurate quantification of human serum albumin by minimizing the interference from blood lipids. *Chem. Commun.* **2019**, 55, 13983–13986.
- (56) Dey, G.; Gaur, P.; Giri, R.; Ghosh, S. Optical signaling in biofluids: a nondenaturing photostable molecular probe for serum albumins. *Chem. Commun.* **2016**, 52, 1887–1890.
- (57) Smith, S. E.; Williams, J. M.; Ando, S.; Koide, K. Time-insensitive fluorescent sensor for human serum albumin and its unusual red shift. *Anal. Chem.* **2014**, 86, 2332–2336.
- (58) Zhu, T.; Du, J.; Cao, W.; Fan, J.; Peng, X. Microenvironment-sensitive fluorescent dyes for recognition of serum albumin in urine and imaging in living cells. *Ind. Eng. Chem. Res.* **2016**, 55, 527–533.
- (59) Green, A. M.; Abelt, C. J. Dual-Sensor Fluorescent Probes of Surfactant-Induced Unfolding of Human Serum Albumin. *J. Phys. Chem. B* **2015**, 119, 3912–3919.
- (60) Dey, G.; Singh, V.; Dewangan, J.; Daniel, P. V.; Kamthan, M.; Ghosh, D.; Mondal, P.; Ghosh, S. Renal clearable new NIR probe: precise quantification of albumin in biofluids and fatty liver disease state identification through tissue specific high contrast imaging in vivo. *Anal. Chem.* **2017**, 89, 10343–10352.
- (61) Pei, S.; Li, J.; Zhang, C.; Zhang, G.; Zhou, Y.; Fan, L.; Wang, W.; Shuang, S.; Dong, C. TICT-Based Microenvironment-Sensitive Probe with Turn-on Red Emission for Human

- Serum Albumin Detection and for Targeting Lipid Droplet Imaging. *ACS Biomater. Sci. Eng.* **2022**, *8*, 253–260.
- (62) Van Gompel, J.; Schuster, G. B. Chemiluminescence of organic peroxides: Intramolecular electron-exchange luminescence from a secondary perester. *J. Org. Chem.* **1987**, *52*, 1465–1468.
- (63) Larsson, A.; Carlsson, C.; Jonsson, M.; Albinsson, B. Characterization of the Binding of the Fluorescent Dyes YO and YOYO to DNA by Polarized Light Spectroscopy. *J. Am. Chem. Soc.* **1994**, *116*, 8459–8465.
- (64) Tang, L.; Ji, R.; Li, X.; Teng, K. S.; Lau, S. P. Energy-level structure of nitrogen-doped graphene quantum dots. *J. Mater. Chem. C* **2013**, *1*, 4908–4915.
- (65) Brouwer, A. M. Standards for photoluminescence quantum yield measurements in solution (IUPAC Technical Report). *Pure Appl. Chem.* **2011**, *83*, 2213–2228.
- (66) Babendure, J. R.; Adams, S. R.; Tsien, R. Y. Aptamers switch on fluorescence of triphenylmethane dyes. *J. Am. Chem. Soc.* **2003**, *125*, 14716–14717.
- (67) Li, Q.; Min, J.; Ahn, Y. H.; Namm, J.; Kim, E. M.; Lui, R.; Kim, H. Y.; Ji, Y.; Wu, H.; Winsniewski, T.; Chang, Y. T. Styryl-Based Compounds as Potential in vivo Imaging Agents for  $\beta$ -Amyloid Plaques. *ChemBioChem* **2007**, *8*, 1679–1687.
- (68) Morris, G. M.; Goodsell, D. S.; Huey, R.; Olson, A. J. Distributed Automated Docking of Flexible Ligands to Proteins: Parallel Applications of AutoDock 2.4. *J. Comput.-Aided Mol. Des.* **1996**, *10*, 293–304.
- (69) Morris, G. M.; Goodsell, D. S.; Halliday, R. S.; Huey, R.; Hart, W. E.; Belew, R. K.; Olson, A. J. Automated Docking Using a Lamarckian Genetic Algorithm and Empirical Binding Free Energy Function. *J. Comput. Chem.* **1998**, *19*, 1639–1662.
- (70) Pellerano, M.; Naud-Martin, D.; Peyressatre, M.; Prével, C.; Teulade-Fichou, M. P.; Morris, M.; Mahuteau-Betzer, F. TP-2Rho Is a Sensitive Solvatochromic Red-Shifted Probe for Monitoring the Interactions between CDK4 and Cyclin D. *ChemBioChem* **2016**, *17*, 737–744.
- (71) You, M.; Jaffrey, S. R. Structure and mechanism of RNA mimics of green fluorescent protein. *Annu. Rev. Biophys.* **2015**, *44*, 187–206.

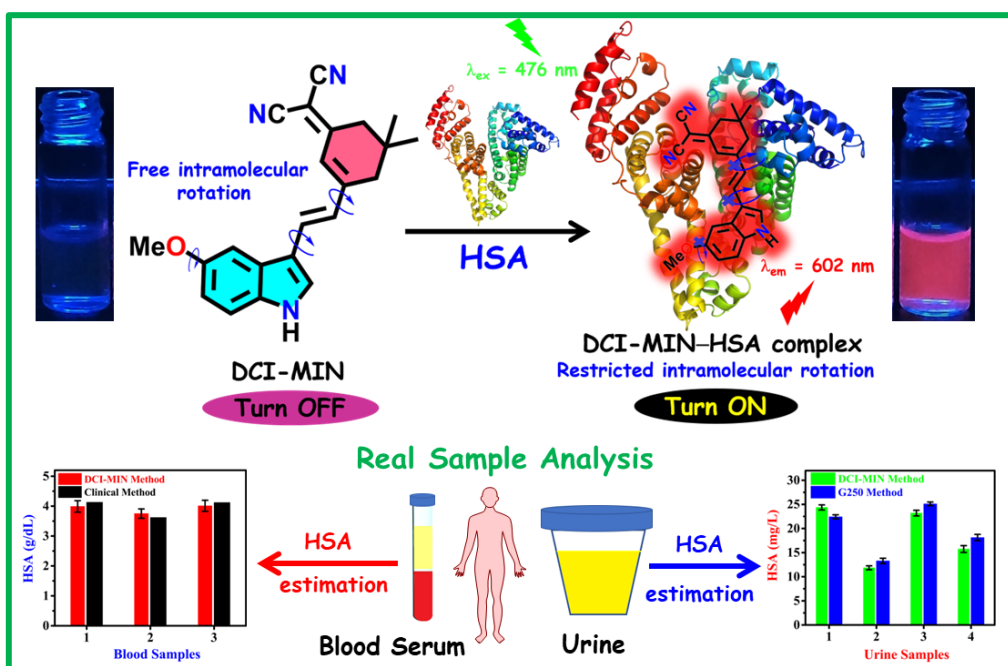
- (72)Liu, C.; Yang, W.; Gao, Q.; Du, J.; Luo, H.; Liu, Y.; Yang, C. Differential recognition and quantification of HSA and BSA based on two red-NIR fluorescent probes. *J. Lumin.* **2018**, *197*, 193–199.
- (73)Xu, Y. J.; Su, M. M.; Li, H. L.; Liu, Q. X.; Xu, C.; Yang, Y. S.; Zhu, H. L. A fluorescent sensor for discrimination of HSA from BSA through selectivity evolution. *Anal. Chim. Acta* **2018**, *1043*, 123–131.
- (74)Er, J. C.; Tang, M. K.; Chia, C. G.; Liew, H.; Vendrell, M.; Chang, Y. T. MegaStokes BODIPY-triazoles as environmentally sensitive turn-on fluorescent dyes. *Chem. Sci.* **2013**, *4*, 2168–2176.
- (75)Liu, B.; Bi, X.; McDonald, L.; Pang, Y.; Liu, D.; Pan, C.; Wang, L. Solvatochromic fluorescent probes for recognition of human serum albumin in aqueous solution: insights into structure-property relationship. *Sens. Actuators B: Chem.* **2016**, *236*, 668–674.
- (76)Zhang, P.; Guo, X.; Xiao, Y.; Zhang, Q.; Ding, C. Twisted intramolecular charge transfer (TICT) based fluorescent probe for lighting up serum albumin with high sensitivity in physiological conditions. *Spectrochim. Acta A: Mol. Biomol. Spectrosc.* **2019**, *223*, 117318.
- (77)Shen, P.; Hua, J.; Jin, H.; Du, J.; Liu, C.; Yang, W.; Gao, Q.; Luo, H.; Liu, Y.; Yang, C. Recognition and quantification of HSA: A fluorescence probe across  $\alpha$ -helices of site I and site II. *Sens. Actuators B: Chem.* **2017**, *247*, 587–594.
- (78)Li, J.; Wu, J.; Cui, F.; Zhao, X.; Li, Y.; Lin, Y.; Li, Y.; Hu, J.; Ju, Y. A dual functional fluorescent sensor for human serum albumin and chitosan. *Sens. Actuators B: Chem.* **2017**, *243*, 831–837.
- (79)Li, P.; Wang, Y.; Zhang, S.; Xu, L.; Wang, G.; Cui, J. An ultrasensitive rapid-response fluorescent probe for highly selective detection of HSA. *Tetrahedron Lett.* **2018**, *59*, 1390–1393.
- (80)Liu, B.; Pang, Y.; Bouhenni, R.; Duah, E.; Paruchuri, S.; McDonald, L. A step toward simplified detection of serum albumin on SDS-PAGE using an environment-sensitive flavone sensor. *Chem. Commun.* **2015**, *51*, 11060–11063.
- (81)Luo, Z.; Liu, B.; Zhu, K.; Huang, Y.; Pan, C.; Wang, B.; Wang, L. An environment-sensitive fluorescent probe for quantification of human serum albumin: Design, sensing

- mechanism, and its application in clinical diagnosis of hypoalbuminemia. *Dyes Pigm.* **2018**, *152*, 60–66.
- (82) Chakraborty, G.; Ray, A. K.; Singh, P. K.; Pal, H. A highly fluorescent turn-on probe in the near-infrared region for albumin quantification in serum matrix. *Chem. Commun.* **2018**, *54*, 8383–8386.
- (83) Dey, N.; Maji, B.; Bhattacharya, S. Motion Induced Change in Emission as an Effective Strategy for Ratiometric Probing of Human Serum Albumin and Trypsin in Biological Fluids. *Chem. Asian J.* **2018**, *13*, 664–671.
- (84) Schlüter, F.; Riehemann, K.; Kehr, N. S.; Quici, S.; Daniliuc, C. G.; Rizzo, F. A highly fluorescent water soluble spirobifluorene dye with a large Stokes shift: synthesis, characterization and bio-applications. *Chem. Commun.* **2018**, *54*, 642–645.
- (85) Sun, Q.; Wang, W.; Chen, Z.; Yao, Y.; Zhang, W.; Duan, L.; Qian, J. A fluorescence turn-on probe for human (bovine) serum albumin based on the hydrolysis of a dioxaborine group promoted by proteins. *Chem. Commun.* **2017**, *53*, 6432–6435.
- (86) Jin, Q.; Feng, L.; Zhang, S. J.; Wang, D. D.; Wang, F. J.; Zhang, Y.; Cui, J. N.; Guo, W. Z.; Ge, G. B.; Yang, L. Real-time tracking the synthesis and degradation of albumin in complex biological systems with a near-infrared fluorescent probe. *Anal. Chem.* **2017**, *89*, 9884–9891.
- (87) Yan, X. J.; Li, Z.; Liu, H. B.; Wang, Z. G.; Fan, J.; Xie, C. Z.; Li, Q. J.; Xu, J. Y. A chromone hydrazide Schiff base fluorescence probe with high selectivity and sensitivity for the detection and discrimination of human serum albumin (HSA) and bovine serum albumin (BSA). *J. Photochem. Photobiol. A: Chem.* **2022**, *422*, 113576.
- (88) Zhao, X.; Zheng, W.; Qin, T.; Du, X.; Lei, Y.; Lv, T.; Zhou, M.; Xu, Z.; Wang, L.; Liu, B.; Peng, X. An anti-interference fluorescent probe for point-of-care diagnosis of albuminuria. *Sens. Actuators B: Chem.* **2022**, *351*, 130980.
- (89) Liu, B.; Zeng, C.; Zheng, D.; Zhao, X.; Song, C.; Qin, T.; Xu, Z. A near-infrared dicyanoisophorone-based fluorescent probe for discriminating HSA from BSA. *Spectrochim. Acta A: Mol. Biomol. Spectrosc.* **2022**, *274*, 121081.

- (90) Zhao, R.; Jia, T.; Shi, H.; Huang, C. A versatile probe for serum albumin and its application for monitoring wounds in live zebrafish. *J. Mater. Chem. B*. **2019**, *7*, 2782–2789.
- (91) Liu, B.; Lv, T.; Zhao, X.; Zhou, M.; Song, C.; Zeng, C.; Quin, T.; Xu, Z. Fluorescence discrimination of HSA from BSA: A close look at the albumin-induced restricted intramolecular rotation of flavonoid probe. *Spectrochim. Acta A Mol. Biomol. Spectrosc.* **2022**, *264*, 120306.
- (92) Sudlow, G.; Birkett, D. J.; Wade, D. N. The Characterization of Two Specific Drug Binding Sites on Human Serum Albumin. *Mol. Pharmacol.* **1975**, *11*, 824–832.
- (93) Sudlow, G.; Birkett, D. J.; Wade, D. N. Further Characterization of Specific Drug Binding Sites on Human Serum Albumin. *Mol. Pharmacol.* **1976**, *12*, 1052–1061.
- (94) Ibrahim, N.; Ibrahim, H.; Kim, S.; Nallet, J. P.; Nepveu, F. Interactions between Antimalarial Indolone-*N*-oxide Derivatives and Human Serum Albumin. *Biomacromolecules* **2010**, *11*, 3341–3351.
- (95) Lakowicz, J. R. Fluorescence Anisotropy. In *Principles of Fluorescence Spectroscopy*, 3rd ed.; Springer: New York, **2006**; pp 353–381.
- (96) Sasmal, M.; Bhowmick, R.; Islam, A. S. M.; Bhuiya, S.; Das, S.; Ali, M. Domain-Specific Association of a Phenanthrene–Pyrene-Based Synthetic Fluorescent Probe with Bovine Serum Albumin: Spectroscopic and Molecular Docking Analysis. *ACS Omega* **2018**, *3*, 6293–6304.
- (97) Sedmak, J. J.; Grossberg, S. E. A rapid, sensitive, and versatile assay for protein using Coomassie brilliant blue G250. *Anal. Biochem.* **1977**, *79*, 544–552.

## Chapter 3

A Microenvironment-Sensitive Red Emissive Probe with a Large Stokes Shift for the Specific Recognition and Quantification of Serum Albumin in Complex Biofluids and Live Cells





### Abstract:

Human serum albumin (HSA) is regarded as a useful biomarker for rapid medical diagnosis of various disorders. Hence, it is crucial to identify and monitor the HSA level in complex biofluids (urine and blood samples) using a simple approach. Herein, we have designed and synthesized an intramolecular charge transfer (ICT) based environment-sensitive fluorescent molecular probe, (E)-2-(3-(2-(5-methoxy-1H-indol-3-yl)vinyl)-5,5-dimethylcyclohex-2-en-1-ylidene)malononitrile (DCI-MIN), that can selectively interact with HSA in PBS buffer solution and exhibits a ~78-fold enhancement in fluorescence intensity with a significant (~126 nm) Stokes shift, which is important to avoid interference from the excitation light. The significant red fluorescence response can be attributed to the suppression of free intramolecular rotation of DCI-MIN probe in the site II hydrophobic binding cavity of HSA, which was corroborated by fluorescence displacement assays and molecular docking analysis. According to the  $3\sigma$ /slope method, the detection limit was found to be 1.01 nM (0.0671 mg/L) in aqueous solution, which is significantly lower than the normal level of HSA in healthy urine, indicating its high sensitivity. DCI-MIN has the ability to perform a variety of useful applications, including the detection and quantification of HSA concentration levels in complex biofluids (human urine and blood samples) as well as the imaging of serum albumin in living cells. In comparison to the Bradford assay and the BCG technique, measuring HSA levels in urine and blood samples with DCI-MIN is preferable due to its higher selectivity, faster detection time, and simple operation.

### 3.1 Introduction

Serum albumins (SAs), a family of thiol-containing proteins such as bovine and human serum albumins (BSA and HSA), play key roles in various biological functions, including the removal of free radicals, regulating the pH balance of plasma, fluid transportation, maintenance of the blood osmotic pressure, promoting wound healing, preventing platelet aggregation, etc.<sup>1-6</sup> Approximately 55–60% of the total protein in human and bovine blood plasma is mainly composed of serum albumins (SAs),<sup>7,8</sup> and only a small fraction of this protein leaks into the urine through the glomerulus. Though HSA includes 35 cysteine residues, only one of them, Cys-34, is in free thiol form and can potentially interact with reactive oxygen/nitrogen species.<sup>9</sup> Hence, HSA serves as the most significant antioxidant in the blood, and it possesses a variety of biological properties, including anti-inflammatory and anticoagulant actions.<sup>10</sup>

HSA is exclusively produced by polysomes of hepatocytes in the liver at a rate of 10–15 g/day<sup>9,11</sup> and secreted into the blood circulation in its unmodified form.<sup>12</sup> Though it has a biological half-life of 19 days, it only remains in blood circulation for 16–18 hours.<sup>13</sup> In the kidney, glomerulus filters the circulating HSA, and subsequently reabsorbs it along the proximal tubules by endocytosis,<sup>14</sup> maintaining a normal level of HSA between 35 and 55 g/L in the blood plasma of a healthy adult.<sup>15</sup> On the other hand, albumin concentrations in urine drops below 30 mg/L, maybe owing to the kidneys ability to prevent the passage of necessary substances like albumin and other proteins into the urine.<sup>16</sup> Nonetheless, a person's health is directly correlated with an abnormal albumin content in urine or blood plasma. Consequently, albumin levels in biofluids (such as blood or urine) are frequently used as an effective health marker and regularly monitored in medical practice to give the diagnostic information for a wide range of disorders.<sup>15</sup> For instance, an increased plasma albumin concentration (> 55 g/L) can cause hyperalbuminemia, which is associated with dehydration.<sup>17</sup> However, hypoalbuminemia, a condition caused by a low quantity of albumin (< 35 g/L) in blood plasma, is an indication of chronic hepatitis, liver cirrhosis, heart failure, atrial fibrillation, and stroke.<sup>18,19</sup> On the other hand, excessive amount of albumin (30–300 mg/L) in the urine can result in microalbuminuria, a condition that has been linked to endothelial dysfunction, post-streptococcal glomerulonephritis, diabetes mellitus and hypertension expressing a primary sign for cardiovascular disease and renal illness (i.e.,

nephrotic syndrome).<sup>20-22</sup> In addition, a patient is diagnosed with macroalbuminuria if the urine albumin content is greater than 300 mg/L, which denotes an advanced level of renal impairment.<sup>23</sup>

Therefore, it is crucial to develop an effective chemosensor to accurately detect and quantify the serum albumin level in biofluids (blood or urine samples), which has enormous clinical importance and biomedical research applications. So far, three different approaches have been successfully employed for the detection and measurement of HSA in biofluids: (i) optical (fluorometry and colorimetric) methods; (ii) antibody-based immunoassays; and (iii) LC-MS proteomics-based techniques.<sup>24-28</sup> Among these approaches, the colorimetric one is the most affordable, least laborious, and most user-friendly method, requiring the minimum steps in sample preparation. The colorimetric dyes like bromocresol green (BCG)<sup>29</sup> and bromocresol purple (BCP)<sup>30</sup> have been utilized frequently in diagnostic laboratories to measure the serum albumin level in blood plasma, but they are not effective to quantify the trace urine albumin concentration due to their limited sensitivity and specificity.<sup>31</sup> Moreover, LC-MS proteomics-based techniques provide poor limit of detection (LOD) values, which are higher than the typical albumin levels in urine.<sup>32</sup> Therefore, traditional immunochemical techniques (such as, Enzyme-Linked Immunosorbent Assay, etc.) are the only ones that can be used to quantitatively measure the HSA levels in urine samples. But these methods are rarely employed in regular analysis due to the time-consuming procedure, multistep operation, and the high prices of antibodies.<sup>33,34</sup> On the contrary, fluorometry is regarded as the most widely used method for the real-time measurement of proteins because of its easy operation, non-destructive nature, excellent selectivity, high sensitivity, quick response time, and noninvasive advantages, as well as high resolution imaging *in vitro* and/or *in vivo*.<sup>35-39</sup> Until now, several fluorescent molecular probes have been reported for HSA detection.<sup>15, 40-63</sup> In this regard, fluorescent probes with great sensitivity to the polarity and viscosity of the medium are highly attractive and provide a crucial selection criterion for the detection of serum albumins. Nevertheless, they have some disadvantages, such as low sensitivity, less specificity, slow response time, poor biocompatibility, etc. Additionally, it has been found that a number of fluorescent probes are ineffective in real practical applications because the majority of them suffer to detect trace amount of HSA in complex biofluids due to their poor LOD values (> 30 mg/L), significant background signals, and comparatively shorter emission wavelengths (< 600 nm). Hence, it is extremely desirable to develop fluorescent probes with

Red/NIR emission ( $> 600$  nm), which in turn is also necessary to achieve improved tissue penetration depth and lower autofluorescence.

In recent years, fluorescent molecular probes based on the dicyanoisophorone (DCI) moiety have gained popularity owing to their easy synthesis, high fluorescence brightness, relatively longer emission wavelengths ( $>600$  nm), large Stokes shifts ( $\geq 100$  nm), excellent photostability, and the capability of avoiding background autofluorescence.<sup>64,65</sup> Moreover, DCI-based fluorescent probes have been widely employed for both fluorescence imaging and the identification of biological species due to their good optical characteristics.<sup>66-69</sup> The remarkable optical characteristics of DCI and its fluorescent probes can be ascribed to the strong electron-accepting properties triggered by the presence of conjugated structure and two cyano groups. Keeping these in mind, in this context, we rationally designed and developed an intramolecular charge transfer (ICT)-based environment-sensitive fluorescent turn-on HSA probe, DCI-MIN, that involves coupling of a methoxy substituted indole moiety as the electron donor with the electron acceptor dicyanoisophorone moiety via a double bond to form of an effective ‘*donor- $\pi$ -acceptor*’ system. Some specific advantages of the probe may be listed as follows: (i) it exhibits a selective turn-on red fluorescent response toward HSA in complex samples containing other biological interferents, and predominantly binds to the site II hydrophobic region of HSA; (ii) a large Stokes shift ( $\sim 126$  nm) in the fluorescent turn-on response of the probe towards HSA provides an added advantage, assuring the minimum interference from the excitation light; (iii) a very low detection limit (1.01 nM; 0.0671 mg/L), significantly lower than the normal concentration of HSA in healthy urine, indicates its high sensitivity; and (iv) most impressively, its excellent HSA detection abilities in both urine and blood serum samples provides a quick and efficient method for tracking health status. Here, steady-state fluorescence studies, site marker displacement assays, molecular docking simulations, and lifetime analysis were performed to comprehend the underlying sensing process.

## 3.2 Experimental Section

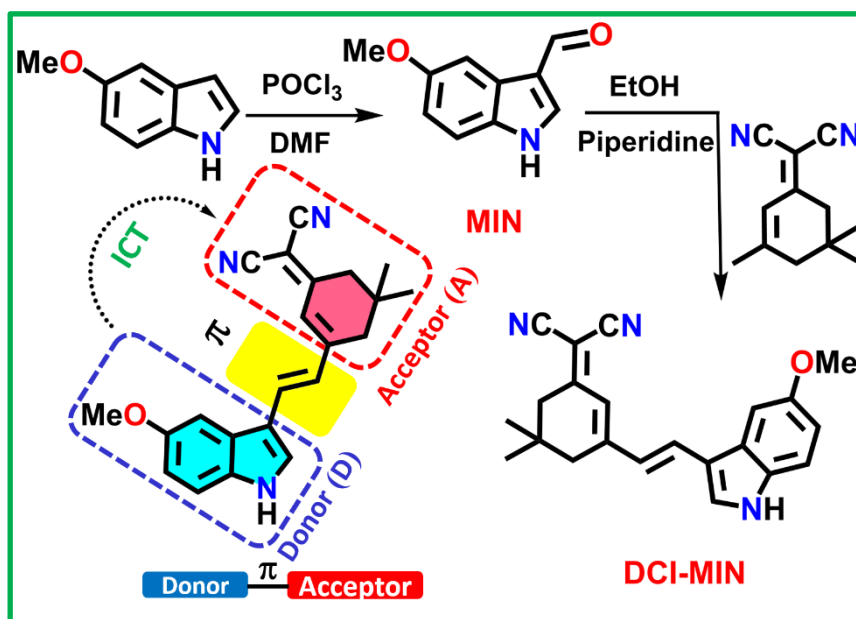
### 3.2.1 Materials

5-Methoxy-1*H*-indole, 2-(3,5,5-trimethylcyclohex-2-en-1-ylidene)malononitrile, Coomassie Brilliant Blue G-250, diflunisal, warfarin and glycerol were procured from Sigma-Aldrich and used as received.

All the proteins and enzymes (lysozyme, proteinase K, HSA, BSA,  $\beta$ -lactoglobulin, pepsin, CT-DNA, peroxidase, hemoglobin, cytochrome C, collagen, cholesterol, transferrin, human IgG, and trypsin) along with other bioanalytes like urea, uric acid, glucose, creatinine, glutathione (GSH), and all amino acids were also purchased from Sigma Aldrich. The sodium salts of different anions ( $\text{SH}^-$ ,  $\text{HSO}_4^-$ ,  $\text{CH}_3\text{COO}^-$ ,  $\text{H}_2\text{PO}_4^-$ ,  $\text{F}^-$ ,  $\text{Cl}^-$ ,  $\text{Br}^-$ ,  $\text{I}^-$ ,  $\text{BrO}_3^-$ ,  $\text{NO}_2^-$ ,  $\text{NO}_3^-$ ,  $\text{SCN}^-$ ,  $\text{ClO}_4^-$ ,  $\text{N}_3^-$ ,  $\text{PO}_4^{3-}$ , and  $\text{S}_2\text{O}_3^{2-}$ ) and perchlorate salts of various cations ( $\text{Mg}^{2+}$ ,  $\text{NH}_4^+$ ,  $\text{Ca}^{2+}$ ,  $\text{Na}^+$ ,  $\text{K}^+$ ,  $\text{Al}^{3+}$ ,  $\text{Hg}^{2+}$ ,  $\text{Mn}^{2+}$ ,  $\text{Co}^{2+}$ ,  $\text{Ni}^{2+}$ ,  $\text{Cu}^{2+}$ ,  $\text{Fe}^{2+}$ ,  $\text{Fe}^{3+}$ , and  $\text{Zn}^{2+}$ ) were obtained either from Sigma-Aldrich or from other commercial vendors. For the synthesis purposes, reagent grade solvents (Merck, India) were dried before use in accordance with the standard methods. The HPLC-grade solvents and Millipore water were employed for the spectroscopic experiments.

### 3.2.2 Instrumentation

The  $^1\text{H}$  NMR and  $^{13}\text{C}$  NMR spectra were recorded on a Bruker 300 and 400 MHz spectrophotometer using tetramethylsilane as an internal standard in  $\text{DMSO}-d_6$ . The following abbreviations were used to explain multiplicities: s = singlet, d = doublet, t = triplet, q = quartet, m = multiplet, br = broad. Coupling constants,  $J$  were reported in Hertz unit (Hz). The ESI-MS<sup>+</sup> (m/z) spectra of the probe were recorded on a HRMS spectrophotometer (model: QTOF Micro YA263). The Fourier transform infrared spectrum ( $4000\text{--}400\text{ cm}^{-1}$ ) of the probe was recorded on a Perkin-Elmer RX I FT-IR spectrophotometer with a solid KBr disc. The UV-Vis absorbance spectral studies were carried out on an Agilent diode-array Spectrophotometer (Agilent 8453) using a 1 cm path length quartz cuvette in the wavelength range of 190-900 nm. Steady-state fluorescence spectroscopic measurements were performed on a PTI spectrofluorimeter (Model QM-40) by using a fluorescence free quartz cuvette of 1 cm path length. The excitation and emission slit widths were fixed at 3 nm. Fluorescence lifetimes were determined from time-resolved intensity decay by the method of time correlated single photon counting (TCSPC) measurements using a picosecond diode laser (IBH Nanoled-07) in an IBH fluorocube apparatus. The fluorescence decay data were collected on a Hamamatsu MCP photomultiplier (R3809) and examined by the IBH DAS6 software.



**Scheme 3.1** Rational Design and Synthesis of DCI-MIN.

### 3.2.3 Synthesis and Characterization of the Compound 5-methoxy-1*H*-indole-3-carbaldehyde (MIN)

In the first step, a homogeneous mixture of 5-methoxy-1*H*-indole (5.15 g, 35.0 mmol) in 40 mL DMF was slowly added to an ice-cold solution of POCl<sub>3</sub> (20 mL) in DMF (40 mL) under vigorous stirring. The overall composition at 0° C was allowed to react for 2 h where the progress of the reaction was monitored by thin-layer chromatography (TLC) for a specified time interval. After the complete conversion of starting material, the reaction mixture was poured into 300 mL ice water and mixed thoroughly using a glass-rod. The pH of the solution was maintained at ~9.0 through the addition of required quantities of NaOH pellets. Subsequently, the reaction mixture was filtered and washed with ethyl acetate. Then the filtrate was extracted with ethyl acetate and the organic layer was dried over Na<sub>2</sub>SO<sub>4</sub>. Finally, the solvent was concentrated and dried under vacuum to get a solid crude product of 5-methoxy-1*H*-indole-3-carbaldehyde (MIN). The product was then purified by using column chromatography to afford a yellow solid (~82% yield) (**Scheme 3.1**). <sup>1</sup>H NMR (300 MHz, DMSO-*d*<sub>6</sub>): δ in ppm = 12.035 (s, 1H), 9.906 (s, 1H), 8.217 (s, 1H), 7.601 (d, *J* = 2.4 Hz, 1H), 7.415 (d, *J* = 8.8 Hz, 1H), 6.892 (dd, *J* = 8.8, 2.5 Hz, 1H), 3.793 (s, 3H) (**Figure 3.1**). <sup>13</sup>C NMR (75 MHz, DMSO-*d*<sub>6</sub>): δ in ppm = 185.28, 156.09, 138.87, 132.26, 125.35, 118.50, 113.75, 113.64, 102.94, 55.72 (**Figure 3.2**).

HRMS (ESI)  $m/z$ : calcd for  $[M + H]^+$ , 176.0712; found, 176.0716 (Figure 3.3). IR Spectrum:  $\tilde{\nu}$  in  $\text{cm}^{-1}$  = 3127, 3042, 2890, 2720, 1614 (Figure 3.4).

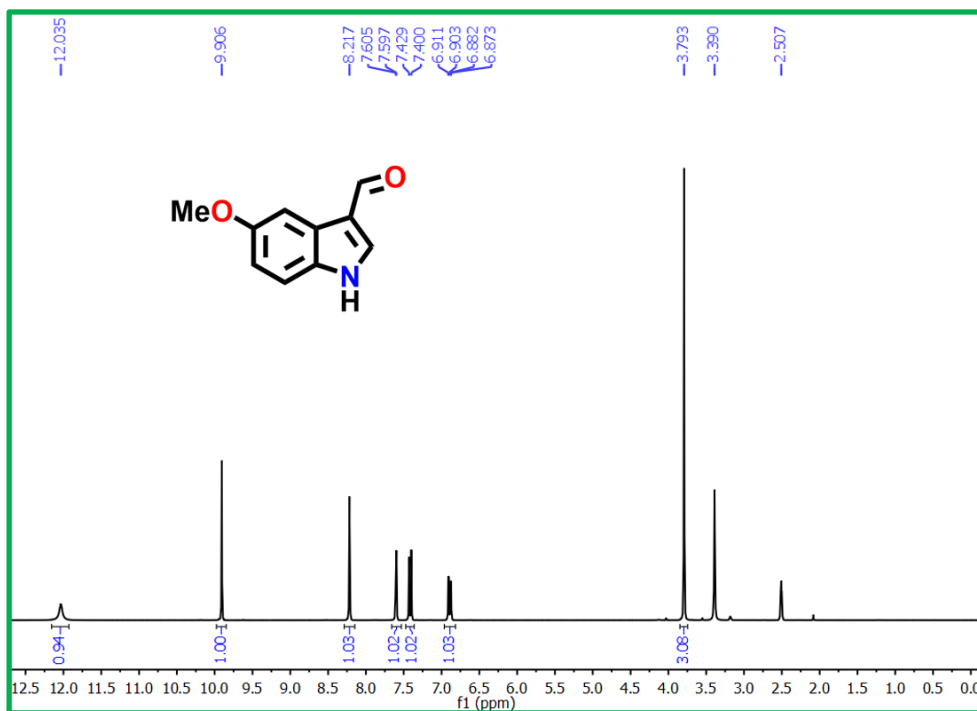


Figure 3.1  $^1\text{H}$ -NMR spectrum of compound MIN in  $\text{DMSO-}d_6$ .

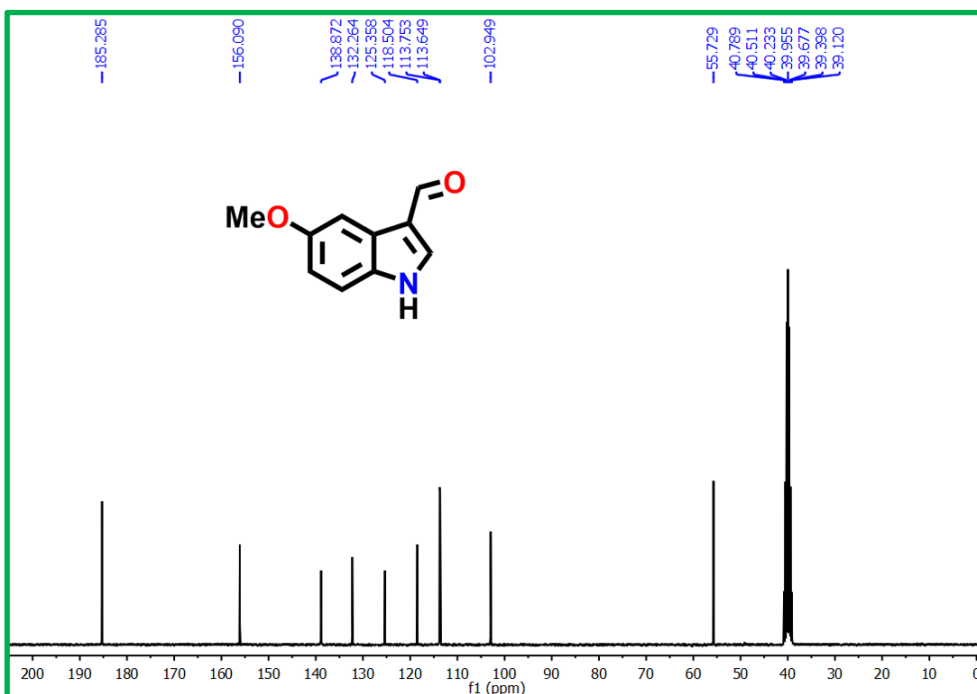


Figure 3.2  $^{13}\text{C}$ -NMR spectrum of compound MIN in  $\text{DMSO-}d_6$ .



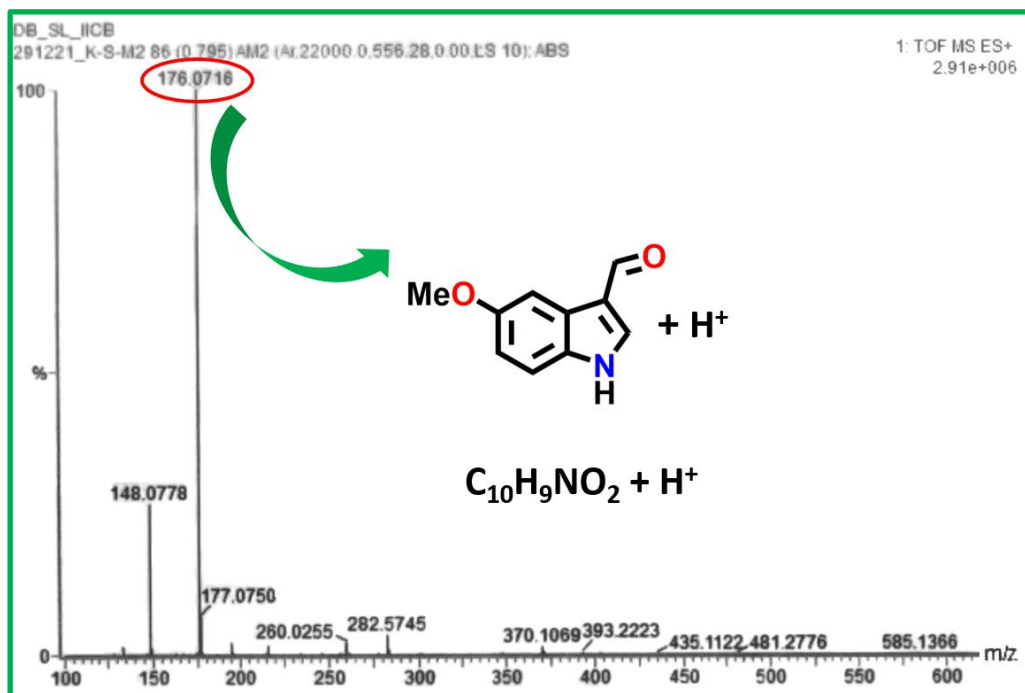


Figure 3.3 Mass spectrum of compound MIN in MeOH.

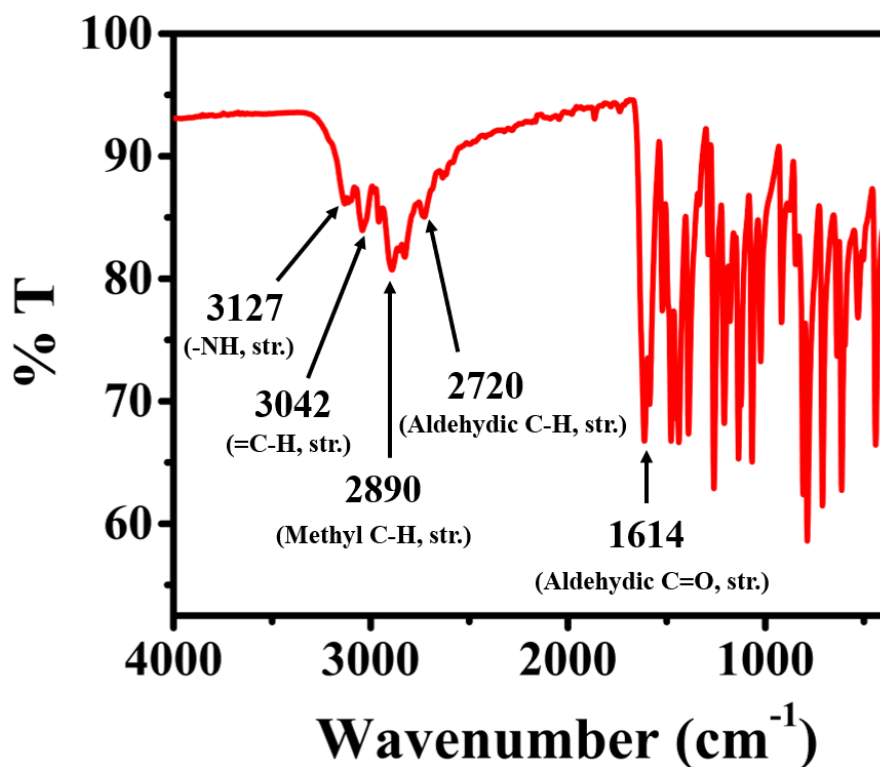
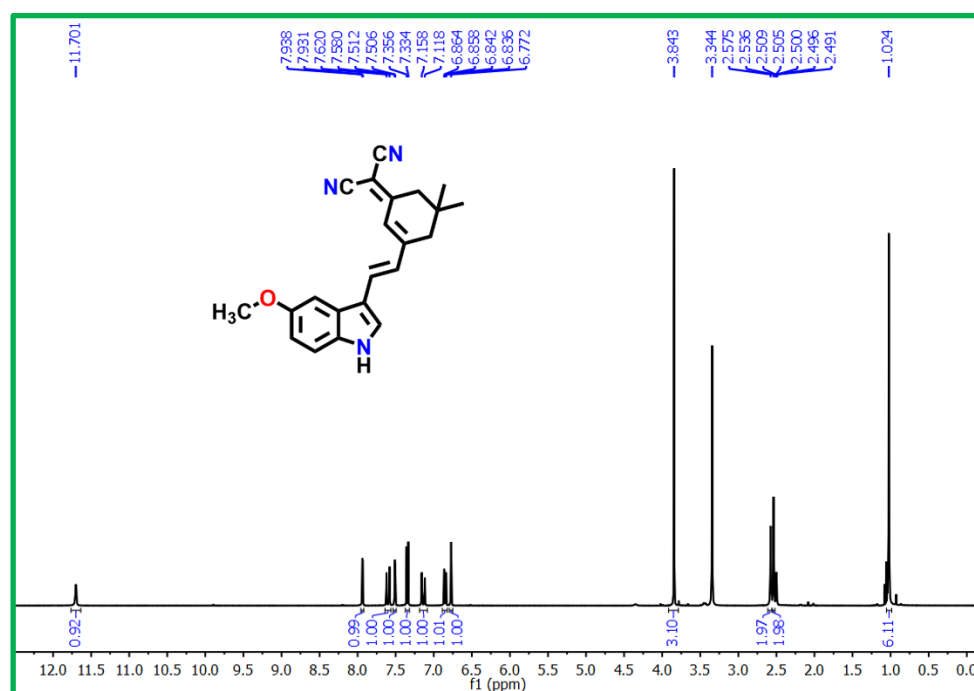


Figure 3.4 IR spectrum of compound MIN.

### 3.2.4 Synthesis and Characterization of the Compound DCI-MIN

In the next step, for the synthesis of DCI-MIN, compound MIN (0.35 g, 2 mmol) and 2-(3,5,5-trimethylcyclohex-2-en-1-ylidene)malononitrile (0.372 g, 2 mmol) were dissolved in 12 mL of dry ethanol in a 250 mL round bottom flask. The solution was then refluxed for 12 h in the presence of catalytic amount of piperidine under an inert atmosphere. The progress of the condensation reaction was monitored by thin-layer chromatography (TLC). After completion of the reaction, solvent was removed under vacuum. Then the obtained residues were purified by silica gel column chromatography using PE/DCM (10/1, V/V) solvent system to afford a reddish brown color solid of DCI-MIN (~76% yield) (**Scheme 3.1**).  $^1\text{H}$  NMR (400 MHz,  $\text{DMSO-}d_6$ ):  $\delta$  in ppm = 11.701 (s, 1H), 7.935 (d,  $J = 2.9$  Hz, 1H), 7.600 (d,  $J = 16.0$  Hz, 1H), 7.509 (d,  $J = 2.4$  Hz, 1H), 7.345 (d,  $J = 8.8$  Hz, 1H), 7.138 (d,  $J = 16.0$  Hz, 1H), 6.850 (dd,  $J = 8.8, 2.4$  Hz, 1H), 6.772 (s, 1H), 3.843 (s, 3H), 2.575 (s, 2H), 2.536 (s, 2H), 1.024 (s, 6H) (**Figure 3.5**).  $^{13}\text{C}$  NMR (101 MHz,  $\text{DMSO-}d_6$ ):  $\delta$  in ppm = 169.80, 158.31, 154.83, 133.59, 132.19, 130.76, 125.94, 123.38, 119.05, 114.78, 114.14, 113.95, 112.93, 112.12, 102.63, 71.73, 55.68, 42.34, 38.08, 31.60, 27.49 (**Figure 3.6**). HRMS (ESI)  $m/z$ : calcd for  $[\text{M} + \text{H}^+]$ , 344.1763; found, 344.1750 (**Figure 3.7**). IR Spectrum:  $\tilde{\nu}$  in  $\text{cm}^{-1} = 3277, 2959, 2220$  (**Figure 3.8**).



**Figure 3.5**  $^1\text{H}$ -NMR spectrum of probe DCI-MIN in  $\text{DMSO-}d_6$ .

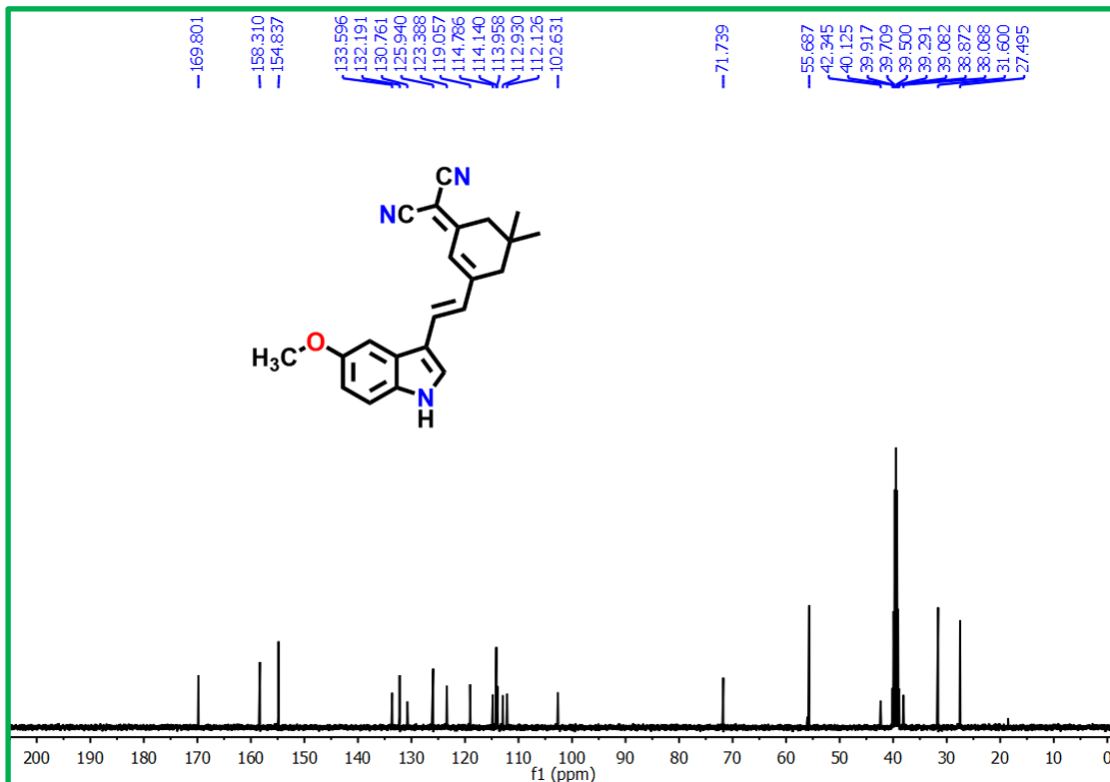


Figure 3.6 <sup>13</sup>C-NMR spectrum of probe DCI-MIN in DMSO-*d*<sub>6</sub>.

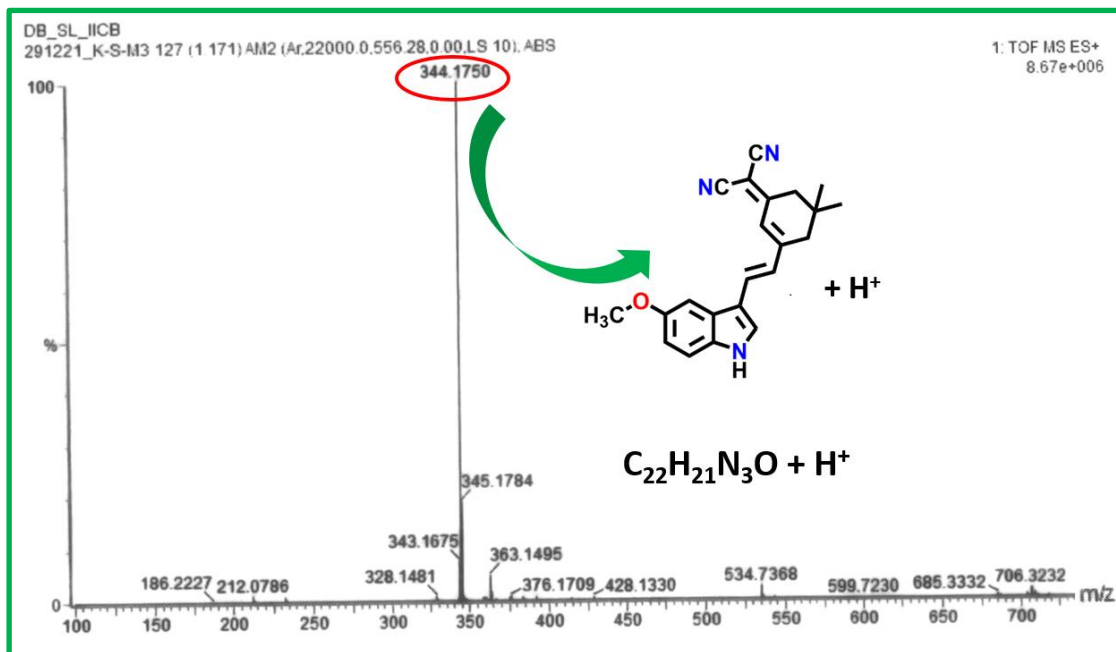


Figure 3.7 Mass spectrum of probe DCI-MIN in MeOH.

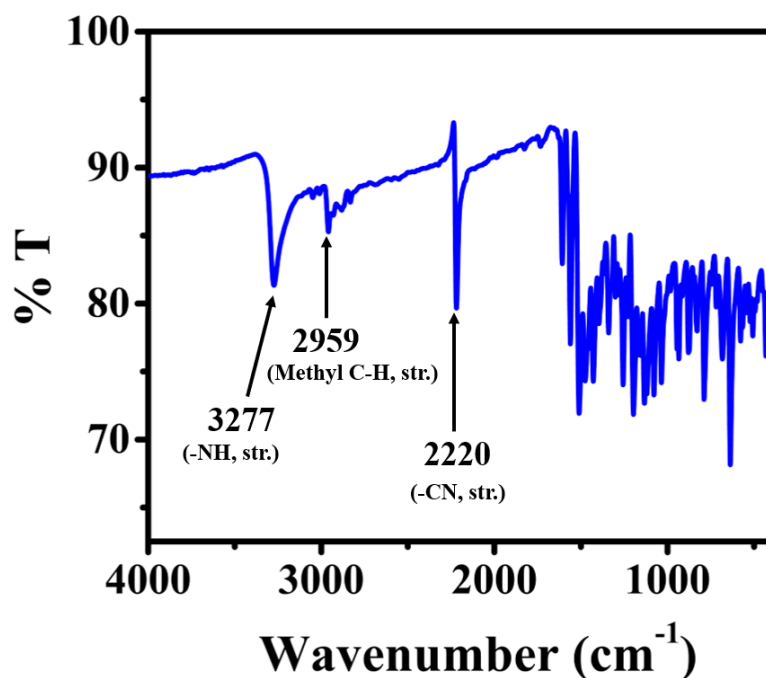


Figure 3.8 IR spectrum of probe DCI-MIN.

### 3.2.5 Experimental Solution

A 250 mL PBS solution (10 mM, pH 7.4) was prepared in Millipore water and used for all experiments. The stock solutions of HSA and BSA (25 mg/mL) were prepared in PBS solution. The stock solutions of other required proteins, enzymes and various bioanalytes were prepared in PBS solution, and concentrations of the protein solutions were determined by using the absorbance and molar extinction coefficient values at specific wavelengths as appropriate. The required amount of various inorganic salts were dissolved in Millipore water to prepare the stock solutions (10 mM) of cations and anions. A 10 mL stock solution of DCI-MIN ( $1 \times 10^{-3}$  M) was prepared in absolute dimethyl sulfoxide (DMSO) solvent and kept in a refrigerator before use.

### 3.2.6 UV-vis and Fluorescence Spectroscopic Studies

Stock solution of DCI-MIN ( $1 \times 10^{-3}$  M) in DMSO was diluted to 2  $\mu$ M for various spectroscopic studies by placing only 4  $\mu$ L of the stock solution of DCI-MIN into PBS solution (pH 7.4) to a final volume of 2 mL. In the fluorescence selectivity experiment, the test samples were prepared by adding the appropriate amounts of the stock solutions of the respective proteins, enzymes, cations, anions and other bioanalytes into 2 mL of probe DCI-MIN solution (2  $\mu$ M). For the fluorescence-titration experiments, another set of HSA

standard solution ( $1 \times 10^{-4}$  M) was prepared by diluting the earlier prepared 25 mg/mL stock solution in PBS medium. Then a Quartz cuvette was filled with 2 mL of DCI-MIN solution (2  $\mu$ M) for the fluorescence-titration experiment, to which the newly prepared stock solution of HSA ( $1 \times 10^{-4}$  M) was gradually added using a micropipette as required. For the fluorescence experiments, excitation wavelength was set at 476 nm and emission was recorded from 490 to 780 nm. For the UV-vis studies the probe concentration was also fixed at 2  $\mu$ M and the spectra were collected with proper background correction. For the competitive fluorescence binding experiments, stock solutions of warfarin and diflunisal (1 mM for each) were prepared in deionized water and DMSO, respectively. In a typical assay, HSA solution was premixed with DCI-MIN at a molar ratio 1:4. Then, this mixed solution was further spiked with different amounts of warfarin or diflunisal and the resultant ternary mixtures were subjected for the fluorescence measurement. All the spectral data were recorded within 1 min after the addition of the analytes, except in the kinetic studies.

### 3.2.7 Steady-State Fluorescence Anisotropy

Fluorescence anisotropy ( $r$ ) measurements were carried out by considering the following equation described by Larsson *et al.*<sup>70</sup>

$$r = \frac{I_{VV} - GI_{VH}}{I_{VV} + 2GI_{VH}} \quad (1)$$

Where, the polarizer positions were set at  $(0^\circ, 0^\circ)$ ,  $(0^\circ, 90^\circ)$ ,  $(90^\circ, 0^\circ)$ , and  $(90^\circ, 90^\circ)$  to get  $I_{VV}$ ,  $I_{VH}$ ,  $I_{HV}$ ,  $I_{HH}$  for excitation and emission signals respectively.  $G$  factor is defined as

$$G = \frac{I_{HV}}{I_{HH}} \quad (2)$$

Where,  $I_{HV}$  and  $I_{HH}$  are respectively the vertical and horizontal component of emission polarizer, keeping the excitation polarizer horizontal.  $G$  depends on slit widths and monochromator wavelength. The excitation and emission wavelengths were fixed at 476 and 602 nm respectively.

### 3.2.8 Fluorescence Lifetime Studies

The TCSPC measurements were carried out in 10 mM PBS buffer solution of pH 7.4 for the fluorescence decay of DCI-MIN in the absence and presence of increasing concentration of HSA at 25 °C. Besides this lifetime decay of DCI-MIN was also performed with the addition

of different glycerol fraction ranging from 0% to 100%. During the TCSPC measurements the photoexcitation was fixed at 480 nm. The fluorescence decay curves were fitted to a biexponential function:

$$I(t) = A + \alpha_1 \cdot e^{(-t/\tau_1)} + \alpha_2 \cdot e^{(-t/\tau_2)} \quad (3)$$

Where,  $\alpha_i$  represents the  $i$ th pre-exponential factor and  $\tau_i$  denotes the decay time of component  $i$  (here  $i = 1, 2$ ). The average lifetimes ( $\tau_{avg}$ ) for the fluorescence decay profiles were calculated by using the following equation:<sup>71</sup>

$$\tau_{avg} = \sum_{i=1}^2 \alpha_i \cdot \tau_i / \alpha_i \quad (4)$$

### 3.2.9 Fluorescence Quantum Yield Measurements

Fluorescence quantum yield were calculated by adopting the reported strategy<sup>72</sup> where relative measurement was carried out using Rhodamine 6G as reference ( $\Phi_s = 0.94$  in ethanol) and by considering the following equation:

$$\Phi_u = \frac{A_s F_u \eta_u^2}{A_u F_s \eta_s^2} \times \Phi_s \quad (5)$$

Where, " $\Phi$ " is the quantum yield; " $A$ " is the optical density; " $F$ " is the measured integrated emission intensity; and " $\eta$ " is the refractive index. The subscript " $u$ " refers to the unknown sample, and subscript " $s$ " refers to the standard reference with a known quantum yield.

### 3.2.10 Detection Limit

The detection limit was calculated on the basis of the fluorescence titration with HSA. The fluorescence emission spectrum of DCI-MIN was measured 10 times to calculate the standard deviation of blank measurement. Then, the fluorescence emission at 602 nm was plotted as a function of the concentration of HSA from the corresponding titration experiment to evaluate the slope. The detection limit was then calculated using the following equation:<sup>73</sup>

$$\text{Detection limit} = 3\sigma/k \quad (6)$$

Where " $\sigma$ " is the standard deviation of blank measurement, and " $k$ " is the slope between the fluorescence emission intensity versus [HSA].

### 3.2.11 Determination of Dissociation Constant ( $K_d$ ) for the Interaction Between HSA and DCI-MIN

The evaluation of  $K_d$  value in this study was followed by the previously published method<sup>74,75</sup> with slight modification for our specific purpose. In principle, the dissociation constant  $K_d$  is calculated as follows:



$$K_d = \frac{([HSA]_T - [HSA : DCI - MIN])([DCI - MIN]_T - [HSA : DCI - MIN])}{[HSA : DCI - MIN]} \quad (8)$$

Where,  $[HSA]_T$  and  $[DCI - MIN]_T$  are the total concentrations of HSA and DCI-MIN, respectively.  $[HSA : DCI - MIN]$  represents the concentration of HSA-DCI-MIN complex.  $[HSA : DCI - MIN]$  is given by

$$[HSA : DCI - MIN] = \frac{1}{2} [(DCI - MIN)_T + [HSA]_T + K_d] \pm \sqrt{[(DCI - MIN)_T + [HSA]_T + K_d]^2 - (4[DCI - MIN]_T[HSA]_T)} \quad (9)$$

To obtain  $K_d$  by fluorescence assay, we simply converted the calculation parameter into fluorescence intensity and solution concentration as follows:

$$\frac{I - I_0}{I_\infty - I_0} = \frac{1}{2[DCI - MIN]_T} [(DCI - MIN)_T + [HSA]_T + K_d] - \sqrt{[(DCI - MIN)_T + [HSA]_T + K_d]^2 - (4[DCI - MIN]_T[HSA]_T)} \quad (10)$$

Where,  $I_0$  and  $I$  denote the fluorescence intensities of DCI-MIN in initial state and at different concentration of HSA, respectively.  $I_\infty$  is the saturated fluorescence intensity with HSA. Then experimental data are best fitted with the eq 10 and the dissociation constant ( $K_d$ ) value was obtained.

### 3.2.12 Molecular Docking Study

To determine the plausible binding sites within HSA and the mode of binding of DCI-MIN with HSA, molecular docking simulations was carried using docking program AutoDock (version 4.2).



The X-ray crystal structure of HSA was taken from RCSB Protein Data Bank having PDB ID: 2BXE. To draw the structure of DCI-MIN, Chem3D Ultra 19.1 was used and further modification was carried out by using Gaussian 09W and AutoDock 4.2 programs. Gasteiger charges and polar hydrogen atoms were added to the protein and probe. Using the AutoGrid tool, a grid box with dimensions of  $120 \text{ \AA} \times 120 \text{ \AA} \times 120 \text{ \AA}$  and  $0.403 \text{ \AA}$  grid spacing were selected to accommodate the protein. The default values shown by the AutoDock program were used for other sets of parameters. The grid maps for energy were computed using AutoGrid, and docking calculations were carried out using the Lamarckian genetic algorithm (LGA).<sup>76,77</sup> The best optimized docked model with lowest binding energy was chosen for further analysis of docking simulations and the output was best viewed using Discovery Studio.

### 3.2.13 Cell Cytotoxicity Assay

The cell cytotoxicity study of DCI-MIN was performed by MTT assay. At first, CHO and KB cells were cultured in 24-well plates in Dulbecco's modified Eagle's (DMEM) medium (supplemented with 10% FBS and 1% penicillin–streptomycin) at  $37 \text{ }^\circ\text{C}$  and under 5%  $\text{CO}_2$ . After overnight growth, cells were incubated with different doses of DCI-MIN for 24 h. Next, cells were washed with PBS buffer (pH 7.4), and then  $500 \text{ }\mu\text{L}$  of DMEM media was added to each well. Then,  $50 \text{ }\mu\text{L}$  of an aqueous solution of MTT (5 mg/mL) was added to each well and incubated for 4 h. The produced purple formazan was dissolved in a DMF–water (1:1) solution mixture of sodium dodecyl sulfate, and the absorbance of the solution was measured at 570 nm in a microplate reader. The relative cell viability was measured by assuming 100% cell viability for cells without any DCI-MIN.

### 3.2.14 Cell Imaging Study

CHO and KB cells were cultured in 24-well plate in DMEM (with 10% fetal bovine serum and 1% penicillin–streptomycin) at  $37 \text{ }^\circ\text{C}$  and 5%  $\text{CO}_2$  atmosphere. After overnight growth, for live cell imaging, CHO and KB cells were incubated with  $2 \text{ }\mu\text{M}$  DCI-MIN for 30 min and DAPI dye for 10 min (for nucleus staining) in serum free DMEM media. The cells were washed with PBS buffer (pH 7.4) for three times to remove the residual molecules. Then fresh DMEM media was added to the washed cells and imaged under fluorescence microscope (Olympus, model IX-81) upon excitation at 352 nm and 488 nm for imaging of DAPI and DCI-MIN, respectively.

### 3.2.15 Urinary HSA Quantification by Coomassie Brilliant Blue G250

**(A) Reagent preparation:**

(1) **Coomassie Brilliant Blue G250 Solution.** 100 mg of Coomassie Brilliant Blue G250 was dissolved in 50 mL of 95% ethanol. To this solution 100 mL of 85% (W/V) phosphoric acid was added. Finally, the resulting solution was diluted to 1000 mL with deionized water.

(2) **0.9% NaCl.** 900 mg NaCl was dissolved in 100 mL deionized water.

(3) **HSA standard solution.** A 100 mL of 0.05 mg/mL HSA standard solution was prepared by diluting the previously prepared 20 mg/mL HSA stock solution with deionized water.

**(B) Preparation of standard curve:**

For the generation of Standard curve, 11 test tubes were taken and the reagents were added according to the following table:

**Preparation of standard samples**

Sample	1	2	3	4	5	6	7	8	9	10	11
HSA standard solution (mL)	0	0.1	0.2	0.3	0.4	0.5	0.6	0.7	0.8	0.9	1.0
0.9% NaCl (mL)	1.0	0.9	0.8	0.7	0.6	0.5	0.4	0.3	0.2	0.1	0
Coomassie Brilliant Blue G250 (mL)	4.0	4.0	4.0	4.0	4.0	4.0	4.0	4.0	4.0	4.0	4.0
HSA concentration (mg/L)	0	1.0	2.0	3.0	4.0	5.0	6.0	7.0	8.0	9.0	10.0

Draw a standard addition curve with Absorbance at 595 nm versus HSA content (mg/L).

**(C) Endogenous HSA determination in urine:**

1 mL urine sample was taken in a fresh test tube. Then 4 mL Coomassie Brilliant Blue G250 reagent was added to react for 5 minutes. Finally, the absorbance at 595 nm was measured to determine the amount of HSA. The final data obtained by Coomassie Brilliant Blue G250 method is measured value  $\times$  5.

### 3.2.16 Estimation of HSA in Human Blood Serum

Blood samples (5 mL each) were collected from healthy donors into a blood collecting tube using a sterilized syringe and needle. Then, the blood samples were centrifuged at 5000 rpm for 10 min to separate the serum from the red blood cells.

Serum on the top portion is then pipetted out into another vial which was used for the analysis. The HSA content in blood serum was estimated with DCI-MIN by using standard addition method. Fluorescence response of DCI-MIN (2  $\mu\text{M}$ ) in diluted plasma sample (1000-fold dilution) upon addition of different concentrations of HSA (0–3.98  $\mu\text{M}$ ). A calibration plot was prepared by measuring the emission maximum at 602 nm ( $I_{602}$ ). The unknown concentration of HSA protein in the blood serum was calculated from the calibration curve by diluting the serum sample appropriately within the linear range.

### 3.3 Results and Discussion

#### 3.3.1 Photophysical Properties of DCI-MIN

DCI-MIN probe belongs to a group of fluorescent dyes known as molecular rotors. This type of molecules exhibit a charge transfer-excited singlet state that can be quickly deactivated by intramolecular rotation around the donor-acceptor bond. The fluorescence of molecular rotors is significantly influenced by the viscosity of the microenvironment and to a lesser extent, the polarity of the solvent. Therefore, first, we have examined the photophysical (UV-vis absorption and fluorescence) properties of DCI-MIN (2  $\mu\text{M}$ ) in  $\sim 100\%$  PBS buffer solution (pH 7.4, 0.2% DMSO). The absorption spectra exhibited a well-defined absorbance maximum at 476 nm (Figure 3.9), which can be attributed to the probe's intramolecular charge transfer transition.

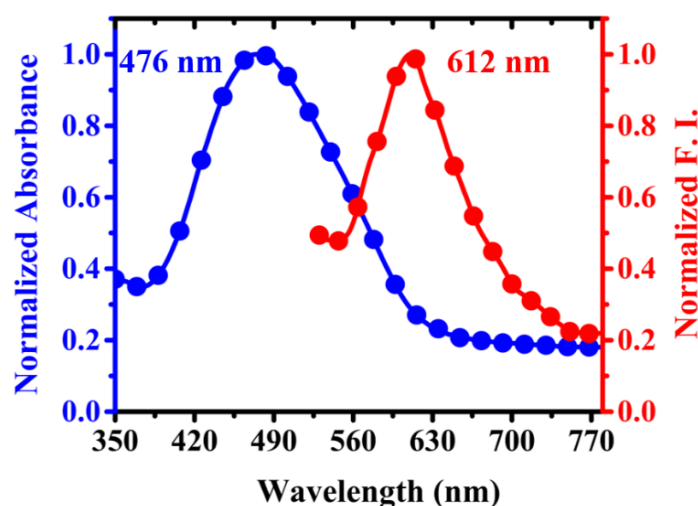


**Figure 3.9** Normalized absorption and fluorescence spectra of DCI-MIN (2  $\mu\text{M}$ ) in  $\sim 100\%$  PBS buffer (pH 7.4).

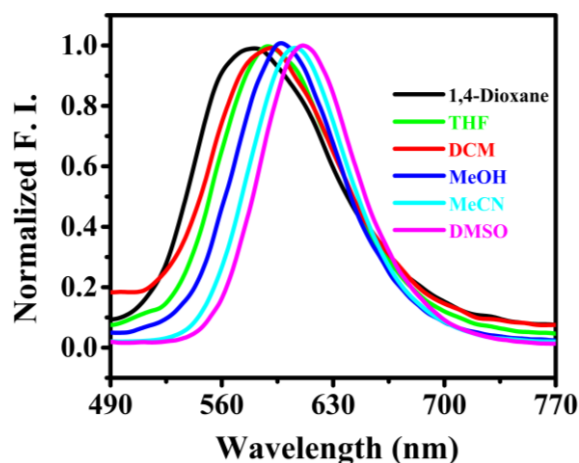


**Figure 3.10** Normalized fluorescence spectra of DCI-MIN ( $2 \mu\text{M}$ ) in different solvents.

Upon excitation at 476 nm, DCI-MIN ( $2 \mu\text{M}$ ) shows a fluorescence-silent emission maxima at 612 nm (**Figure 3.9**) in PBS buffer solution, and this nonemissive nature is due to the completely unrestricted torsional intramolecular rotation of the probe molecules. Following that, DCI-MIN ( $2 \mu\text{M}$ ) was added to several organic solvents of varying polarities, and variations in fluorescence behaviour were recorded. The probe displayed red shifts in emission maxima from 580 to 611 nm when the solvent polarity increased from 1,4-dioxane to DMSO (**Figure 3.10**).

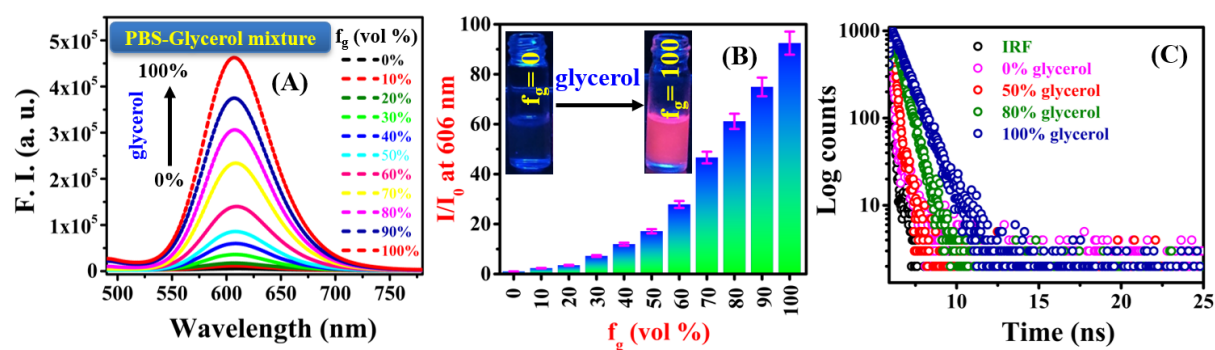


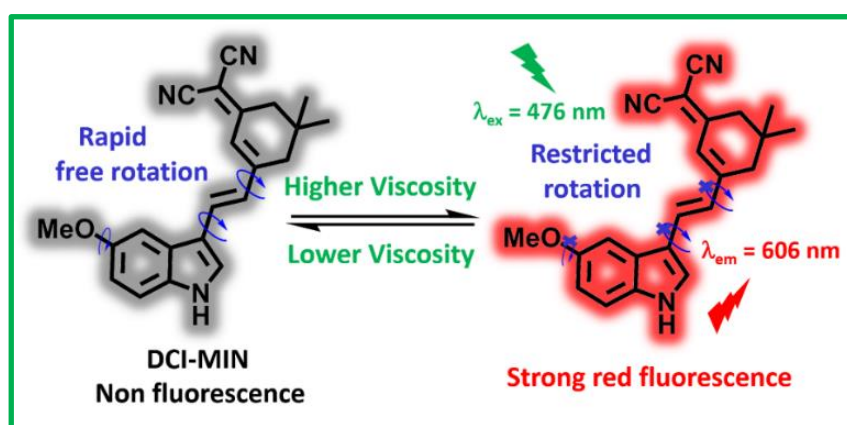
**Figure 3.11** (A and B) Fluorescence spectra and variations in emission intensity ( $I/I_0$ ) at 606 nm of DCI-MIN ( $2 \mu\text{M}$ ) with the increasing in glycerol fractions ranging from 0 to 100%. Inset of B, visual changes in fluorescence of DCI-MIN from 0 to 100% glycerol.  $\lambda_{\text{ex}} = 476$  nm. Error bars: standard deviation ( $n = 3$ ). (C) Lifetime decay of DCI-MIN ( $2 \mu\text{M}$ ) with different fractions of glycerol (0, 50, 80 and 100%).

Here, to corroborate the influence of viscosity on the molecular rotation of the probe molecules, we have measured the emission spectra of DCI-MIN ( $2 \mu\text{M}$ ) in mixed solvent

systems of varying compositions using PBS/glycerol, which have different viscosities. The fluorescence intensity of DCI-MIN was continuously enhanced with the rise in glycerol percentage in the PBS/glycerol binary mixture, implying a regular increase in medium viscosity (Figure 3.11A). In fact, increasing the glycerol fraction from 0% to 100% resulted in a ~92-fold increase fluorescence intensity of DCI-MIN at 606 nm (Figure 3.11B). In addition, we have also conducted the lifetime experiment of the probe DCI-MIN with different glycerol fractions ranging from 0 to 100% (Figure 3.11C). The lifetime decay-associated parameters are compiled in Table 3.1.

**Table 3.1** Time-resolved fluorescence lifetime decay parameters of DCI-MIN (2 μM) with different glycerol fractions ranging from 0 to 100%.

Glycerol, $f_g$ (vol %)	$\tau_1$ (ns)	$\tau_2$ (ns)	$\alpha_1$ (%)	$\alpha_2$ (%)	$\tau_{avg}$ (ns)	$\chi^2$
0	0.034	0.861	93.02	6.98	0.091	1.045
50	0.129	0.191	39.26	60.74	0.166	1.017
80	0.215	0.503	17.06	82.94	0.453	1.029
100	0.521	0.878	11.19	88.81	0.838	0.996



**Scheme 3.2** Response of DCI-MIN towards change in viscosity of the medium.

In ~100% PBS buffer solution, free DCI-MIN probe exhibits a biexponential decay with lifetimes of 0.034 ns (93.02%), and 0.861 ns (6.98%), whereas in 100% glycerol medium, probe DCI-MIN shows a biexponential decay with lifetimes of 0.521 ns (11.19%), and 0.878

ns (88.81%). It is evident from the viscosity-dependent fluorescence changes and the longer lifetime value of DCI-MIN in glycerol medium that the increase in viscosity inhibits the free intramolecular rotation of the probe molecules, which in turn increases the emission intensity of DCI-MIN by obstructing the operation of nonradiative decays (Scheme 3.2). Here, it is also important to note that there was no any appreciable change in the maximum fluorescence intensity of DCI-MIN after 30 min of exposure to a 476 nm light at a power supply of 75 W (Figure 3.12). This shows the excellent photostability of DCI-MIN in its working environment, which is crucial for a biosensor to function properly.

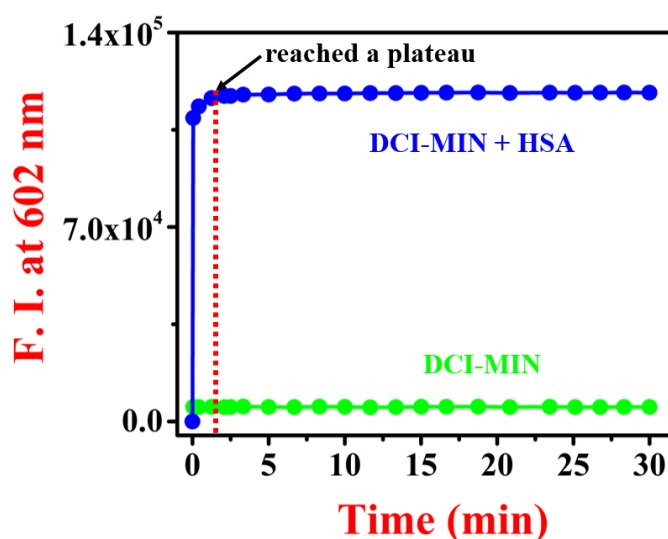
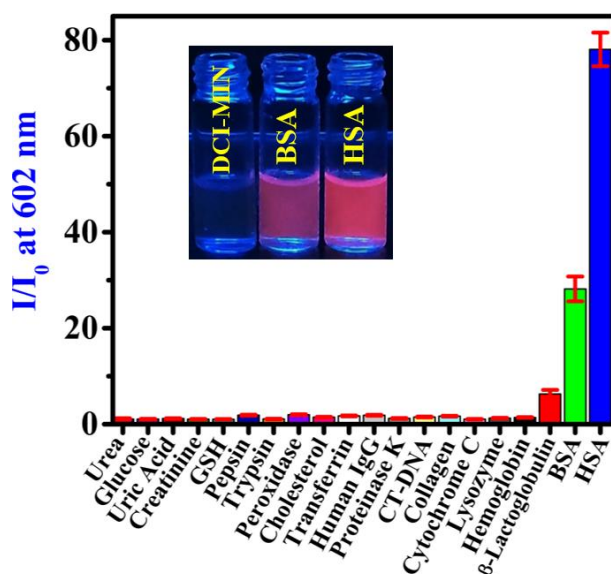


**Figure 3.12** Time dependent fluorescence intensity changes at 602 nm of DCI-MIN (2  $\mu\text{M}$ ) in the presence of 0 and 0.50  $\mu\text{M}$  of HSA in  $\sim 100\%$  PBS buffer of pH 7.4,  $\lambda_{\text{ex}} = 476$  nm.

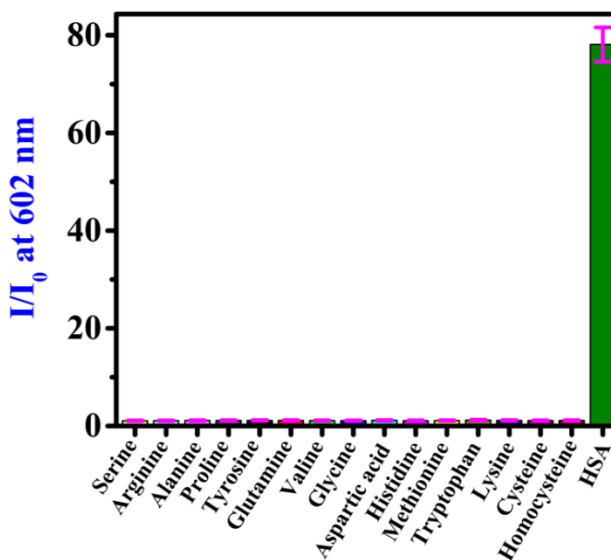
### 3.3.2 Selectivity Analysis and Optical Response of DCI-MIN for HSA/BSA

To investigate the selectivity of DCI-MIN, we initially measured the fluorescence responses of DCI-MIN (2  $\mu\text{M}$ ) in PBS buffer solution by adding excess amounts (20  $\mu\text{M}$ ) of various proteins and enzymes (lysozyme, hemoglobin, cytochrome C,  $\beta$ -lactoglobulin, CT-DNA, proteinase K, peroxidase, collagen, cholesterol, pepsin, human IgG, trypsin, transferrin, BSA, and HSA) as well as in the presence of some common urine components, including urea, uric acid, glucose, GSH, and creatinine (each at 20  $\mu\text{M}$ ). Here, it should be noted that among the several proteins, enzymes, and urine interferences, only HSA and BSA were able to provide a significant turn-on fluorescence response at 602 nm (Figure 3.13), which can be visualized directly with naked eye under UV light (Figure 3.13, inset). Actually, it was observed that the

binding of DCI-MIN (2  $\mu\text{M}$ ) with HSA and BSA (each at 20  $\mu\text{M}$ ) resulted in  $\sim 78$ -fold and  $\sim 28$ -fold enhancement of fluorescence intensity at 602 nm, respectively (Figure 3.13).

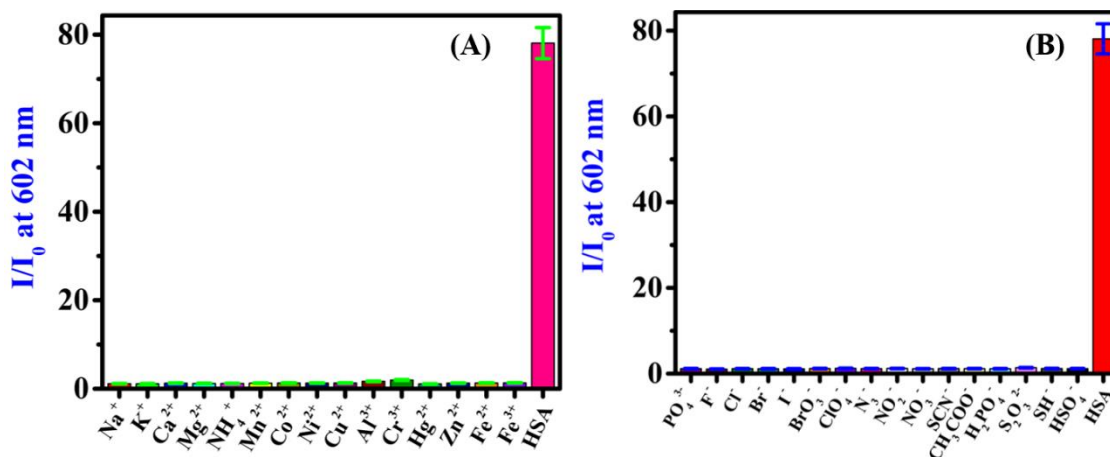


**Figure 3.13** Emission intensity variations ( $I/I_0$ ) of DCI-MIN (2  $\mu\text{M}$ ) at 602 nm in PBS buffer in the presence of excess amount (20  $\mu\text{M}$ ) of various proteins, enzymes and urine interferents. Inset: fluorescence images of DCI-MIN under UV light in the absence and presence of HSA and BSA, respectively.  $\lambda_{\text{ex}} = 476$  nm. Error bars: standard deviation ( $n = 3$ ).



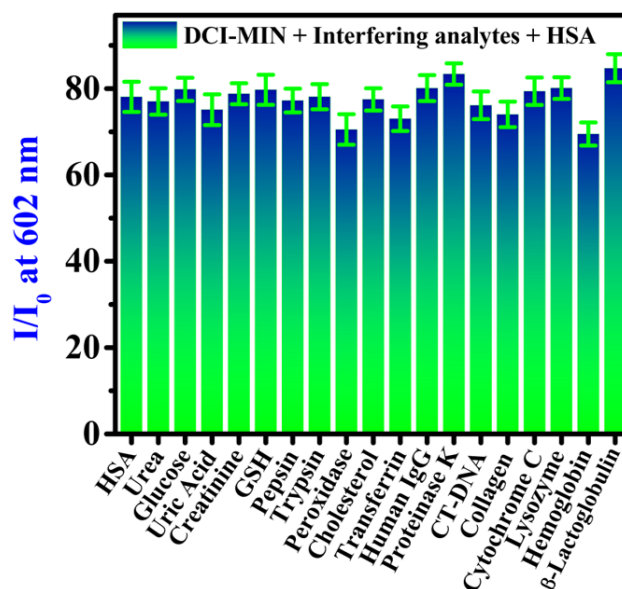
**Figure 3.14** Emission intensity variations ( $I/I_0$ ) of DCI-MIN (2  $\mu\text{M}$ ) for HSA (20  $\mu\text{M}$ ) and various amino acids (each at 20  $\mu\text{M}$ ) at 602 nm in PBS buffer solution of pH 7.4,  $\lambda_{\text{ex}} = 476$  nm. Error bars: standard deviation ( $n = 3$ ).



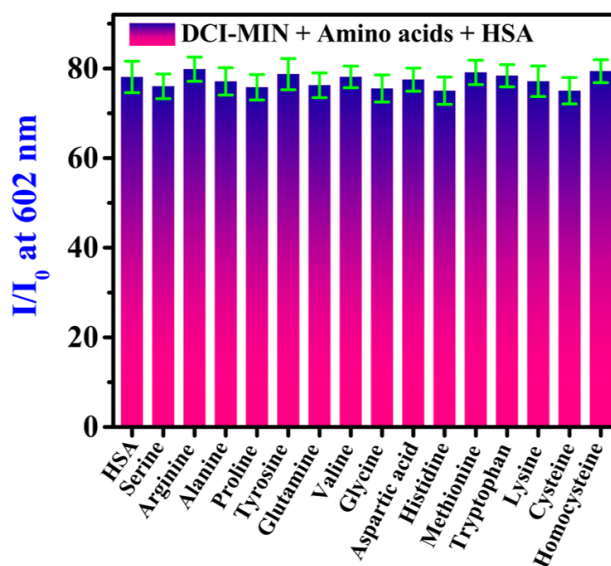


**Figure 3.15** (A and B) Emission intensity variations ( $I/I_0$ ) of DCI-MIN (2  $\mu\text{M}$ ) for HSA (20  $\mu\text{M}$ ) and various cations and anions (each at 30  $\mu\text{M}$ ) at 602 nm in PBS buffer solution of pH 7.4,  $\lambda_{\text{ex}} = 476$  nm. Error bars: standard deviation ( $n = 3$ ).

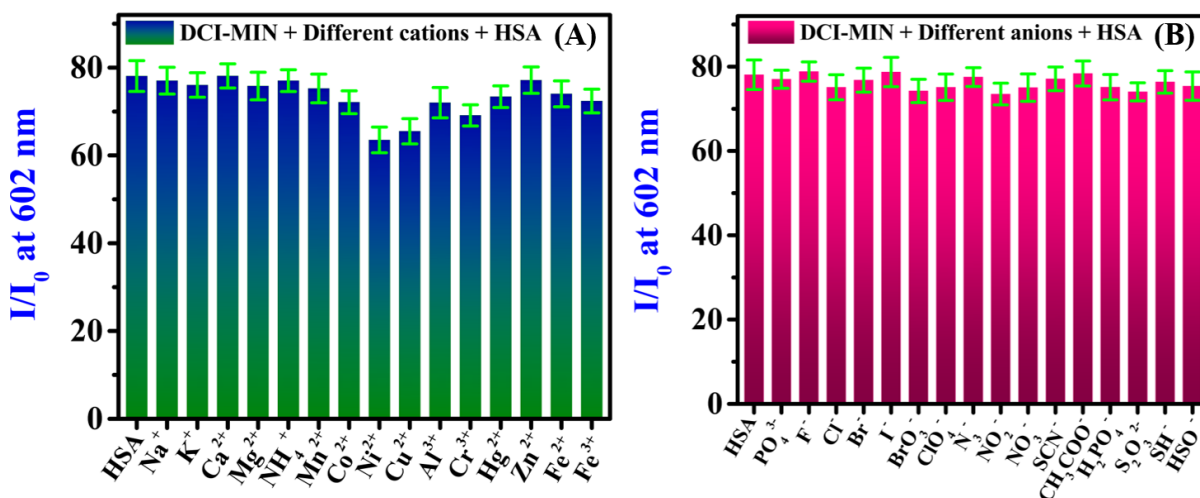
Moreover, the selectivity of DCI-MIN (2  $\mu\text{M}$ ) towards 20  $\mu\text{M}$  of various amino acids, 30  $\mu\text{M}$  of various cations, and 30  $\mu\text{M}$  of various anions was also tested, but they exhibited negligible fluorescence response at 602 nm (**Figures 3.14 and 3.15**). This indicates that DCI-MIN may serve as an effective analytical technique for the recognition and quantification of HSA/BSA.



**Figure 3.16** Emission intensity variations ( $I/I_0$ ) of DCI-MIN (2  $\mu\text{M}$ ) for HSA (20  $\mu\text{M}$ ) with the addition of excess amounts (20  $\mu\text{M}$ ) of various proteins, enzymes and urine interferents at 602 nm in PBS buffer solution,  $\lambda_{\text{ex}} = 476$  nm. Error bars: standard deviation ( $n = 3$ ).



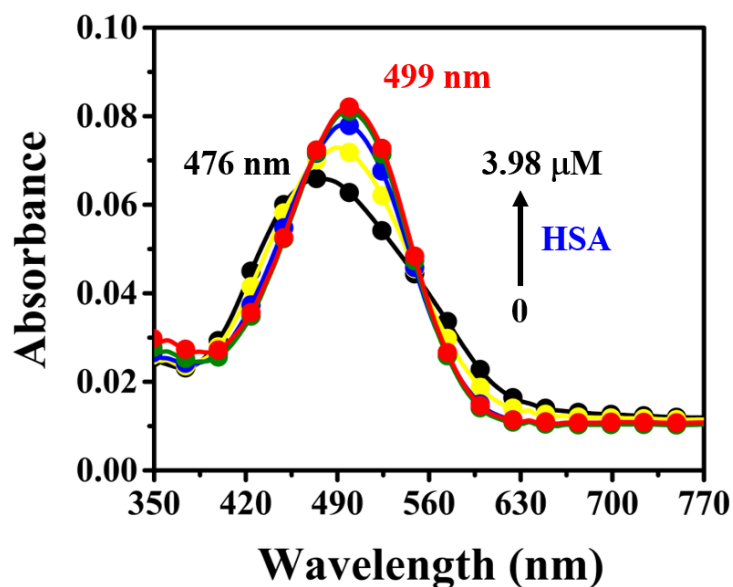
**Figure 3.17** Emission intensity variations ( $I/I_0$ ) of DCI-MIN (2  $\mu$ M) for HSA (20  $\mu$ M) in the presence of various amino acids (20  $\mu$ M) at 602 nm in PBS buffer solution of pH 7.4,  $\lambda_{ex}$  = 476 nm. Error bars: standard deviation (n = 3).



**Figure 3.18** (A and B) Emission intensity variations ( $I/I_0$ ) of DCI-MIN (2  $\mu$ M) for HSA (20  $\mu$ M) in the presence of different cations and anions (each at 30  $\mu$ M) at 602 nm in PBS buffer solution of pH 7.4,  $\lambda_{ex}$  = 476 nm. Error bars: standard deviation (n = 3).

Here, the anti-interference ability of DCI-MIN was further examined by recording its emission intensity for HSA in the presence of common urine interferents along with different other proteins, enzymes, amino acids, cations, and anions. **Figures 3.16-3.18** demonstrating the fact that the emission intensity of DCI-MIN towards HSA in PBS buffer solution at 602

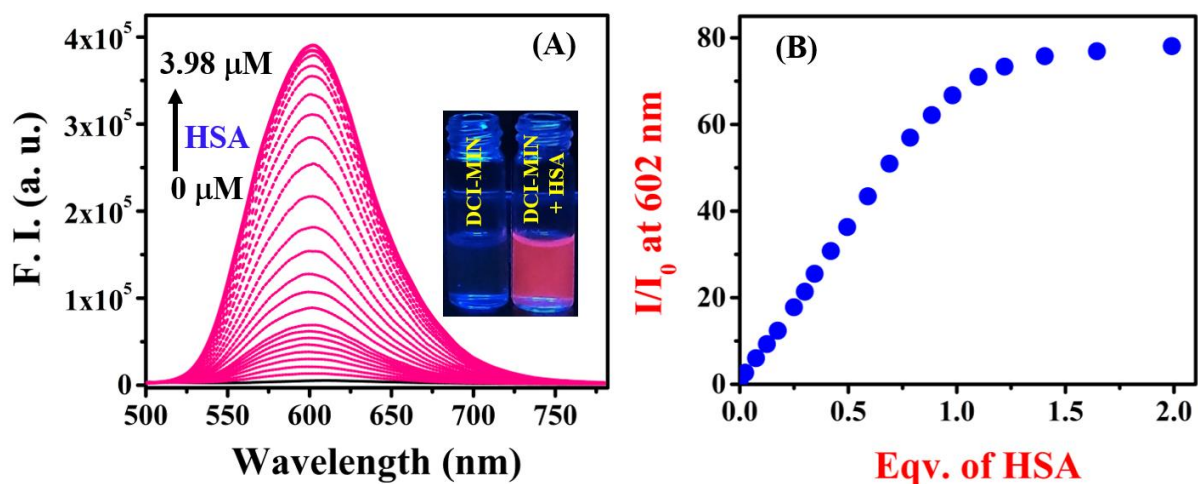
nm did not change significantly when different interfering bioanalytes were introduced in the detection system. Hence, the DCI-MIN probe offers an interference-free selective fluorescence response for HSA, which may be used to detect HSA in the complex biological samples.



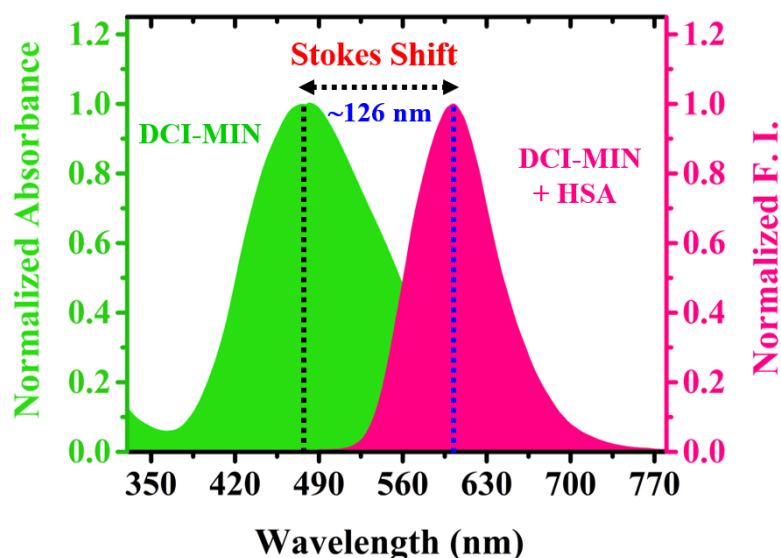
**Figure 3.19** UV-vis absorption spectra of DCI-MIN (2  $\mu\text{M}$ ) in  $\sim 100\%$  PBS buffer of pH 7.4 with the gradual addition HSA ranging from 0 to 3.98  $\mu\text{M}$ .

DCI-MIN (2  $\mu\text{M}$ ) exhibited an absorbance maximum at 476 nm ( $32964 \text{ M}^{-1} \text{ cm}^{-1}$ ) in PBS buffer solution, but when HSA (0-3.98  $\mu\text{M}$ ) was added, its absorbance progressively increased to a new red-shifted absorbance maximum ( $41025 \text{ M}^{-1} \text{ cm}^{-1}$ ) at 499 nm (**Figure 3.19**). On the other hand, upon interaction with HSA in PBS buffer solution, the nonemissive DCI-MIN ( $\Phi = 0.0029$ ) becomes substantially emissive ( $\Phi = 0.2136$ ) and exhibits a red fluorescence response. However, a quantitative analysis of the association between DCI-MIN and HSA is necessary to understand the fluorescence switching behavior of the DCI-MIN probe that is enforced by HSA. Thus, upon excitation at 476 nm, a fluorescence titration was performed at  $[\text{DCI-MIN}] = 2 \mu\text{M}$  in PBS buffer solution with the incremental addition of HSA ranging from 0 to 3.98  $\mu\text{M}$ . It was observed that upon addition of only 2 equiv. HSA (3.98  $\mu\text{M}$ ), the emission intensity of DCI-MIN was greatly increased (about 78-fold) accompanied by a blue shift ( $\sim 10 \text{ nm}$ ) of the emission maximum from 612 to 602 nm (**Figure 3.20A, B**).

Also, it should be noted that there was a difference of  $\sim 126$  nm between the excitation and the emission wavelengths when DCI-MIN interacted with HSA (Figure 3.21). This association of the significant Stokes shift of  $\sim 126$  nm in the fluorescent turn-on response of the probe DCI-MIN towards HSA is beneficial since it assures the minimum interference from the excitation light.

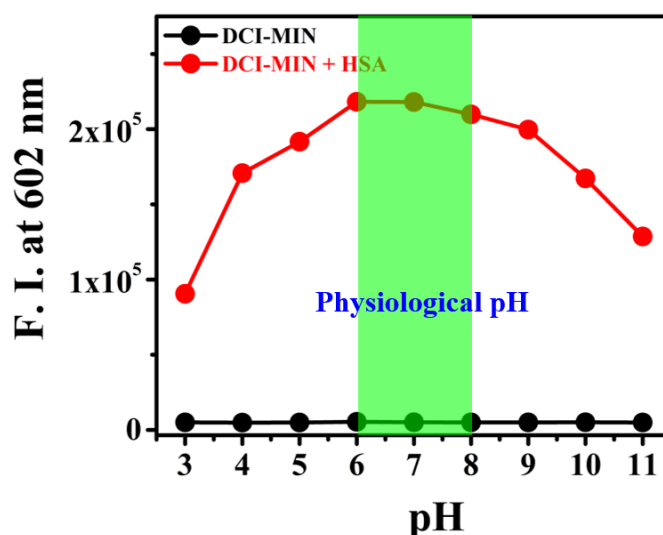


**Figure 3.20** (A) Fluorescence spectra of DCI-MIN ( $2 \mu\text{M}$ ) in PBS buffer solution with the incremental addition of HSA. Inset shows the visual fluorescence changes of DCI-MIN with the addition of HSA. (B) Emission intensity alterations ( $I/I_0$ ) at 602 nm with equivalents of HSA added.  $\lambda_{\text{ex}} = 476$  nm.



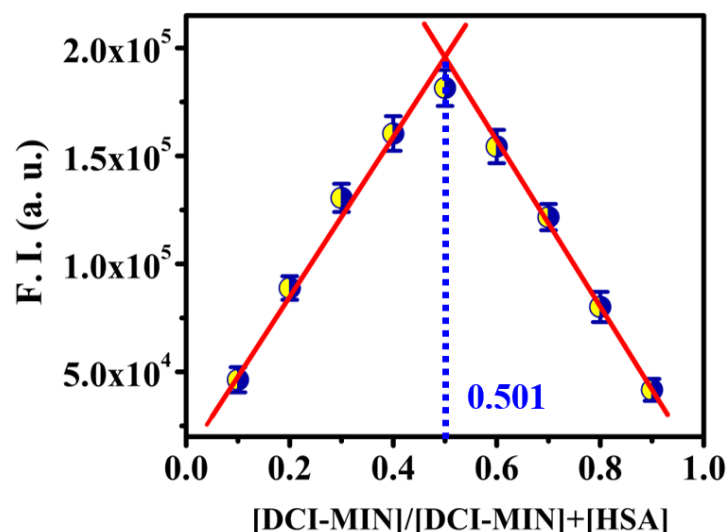
**Figure 3.21** Stokes shift of the probe DCI-MIN ( $2 \mu\text{M}$ ) for HSA sensing.

Here, we also measured the reaction time by performing a time-dependent fluorescence study of the DCI-MIN (2  $\mu\text{M}$ ) in the presence of 0.5  $\mu\text{M}$  HSA. **Figure 3.12** reveals that the emission intensity of DCI-MIN was enhanced quickly after the addition of HSA and reached saturation within  $\sim 1.5$  min. In light of this, DCI-MIN may be a superior probe for the quick detection of HSA in complex biological samples. In this study, we also examined the effect of medium pH ranging from 3 to 11 on HSA sensing by DCI-MIN. In the absence of HSA, the emission intensity of DCI-MIN (2  $\mu\text{M}$ ) remains unaltered throughout the experimental pH range (**Figure 3.22**), indicating that DCI-MIN was reasonably stable in different microenvironments. Nevertheless, when 2  $\mu\text{M}$  HSA was added, the emission intensity of DCI-MIN significantly raised and nearly stayed constant in the pH range of 6 to 8, demonstrating that the probe is appropriate for the measurement of HSA in the physiological pH range.

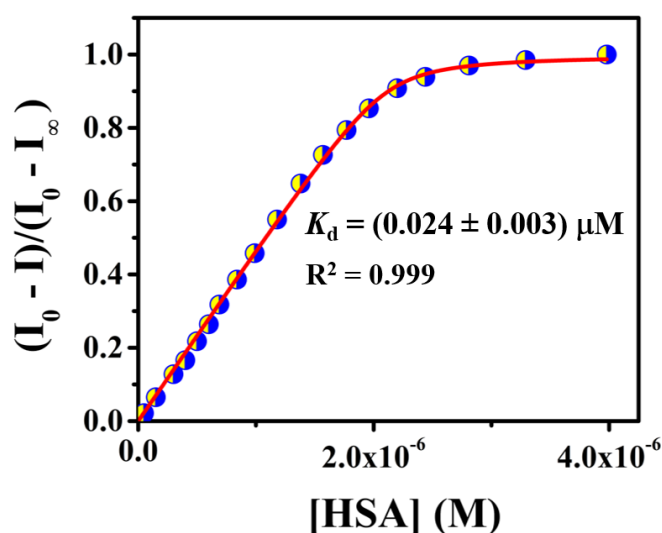


**Figure 3.22** Emission intensities of DCI-MIN (2  $\mu\text{M}$ ) at 602 nm in the absence and presence of HSA (2  $\mu\text{M}$ ) at different pHs. All the experiments were performed in PBS buffer solution.  $\lambda_{\text{ex}} = 476$  nm.

Using Job's plot analysis, the stoichiometry of the association between DCI-MIN and HSA was calculated, and this evidently shows a 1:1 complexation (**Figure 3.23**). Here, the dissociation constant ( $K_d$ ) of the interaction between DCI-MIN and HSA was also determined using the emission titration data of DCI-MIN with HSA (**Figure 3.20**). Using **eq 10**, we obtained a nonlinear curve by plotting  $(I_0 - I)/(I_0 - I_\infty)$  vs. [HSA] (**Figure 3.24**).



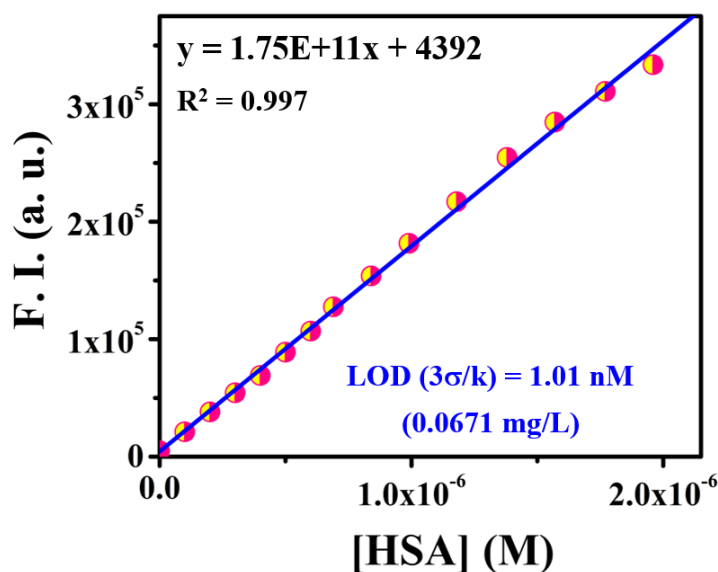
**Figure 3.23** Job's plot experiment of DCI-MIN with HSA in various molar ratios maintaining the overall concentration at 2  $\mu\text{M}$ . Error bars: standard deviation ( $n = 3$ ).



**Figure 3.24** Plot of  $(I_0 - I)/(I_0 - I_\infty)$  vs. HSA concentration for the determination of dissociation constant ( $K_d$ ) between DCI-MIN and HSA. The solid line displays the best fit assuming a 1:1 DCI-MIN:HSA complex using a nonlinear curve-fitting method.

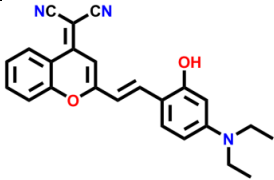
This was subsequently solved by adopting a nonlinear curve-fitting strategy, which yields a  $K_d$  value of  $(0.024 \pm 0.003) \mu\text{M}$ , indicating a strong binding affinity of DCI-MIN to HSA. Moreover, we also observed an excellent linear correlation ( $R^2 = 0.997$ ) between the emission intensity of DCI-MIN at 602 nm and the concentration of HSA ranging from 0 to 1.96  $\mu\text{M}$  (Figure 3.25). According to the  $3\sigma/\text{slope}$  technique,<sup>73</sup> the limit of detection (LOD) value was evaluated to be 1.01 nM (0.0671 mg/L). A quick inspection of the literature reveals that the

current LOD is significantly lower than the typical HSA content in healthy urine, demonstrating the probe's great sensitivity and superiority to other HSA sensing probes that have recently been reported.<sup>40,41,44,45,50,52,55,57,59-62,78</sup> In addition, a comparison table (Table 3.2) has been created to show the benefits of this proposed approach in terms of sensitivity, Stokes shift, reaction time, and binding site in comparison to the earlier reported HSA detection methods.

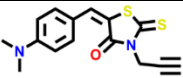
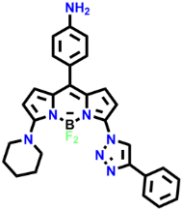
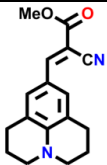
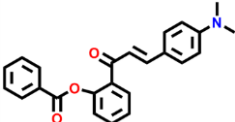
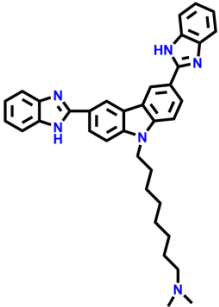
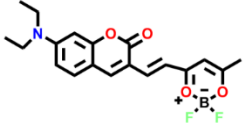
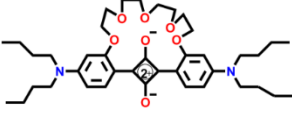
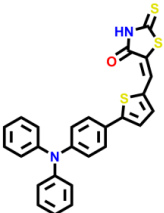


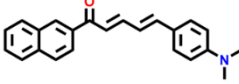
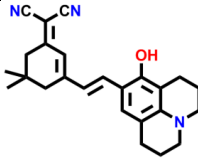
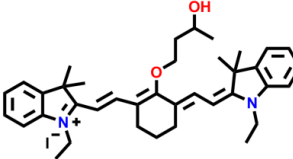
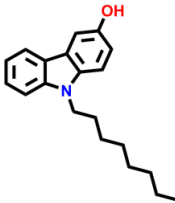
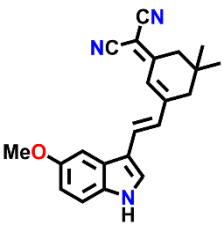
**Figure 3.25** Linear fluorescence response of DCI-MIN (2 μM) to HSA (0-1.96 μM) at 602 nm in ~100% PBS buffer of pH 7.4 for determination of detection limit. LOD value is estimated as 1.01 nM. The LOD value was estimated from 10 times the standard deviation (σ) of the fluorescence intensity corresponding to the blank sample (DCI-MIN only). Here, σ value is 59.172. From the graph we get slope =  $1.75 \times 10^{11} \text{ M}^{-1}$ .

**Table 3.2** Comparison of the fluorescent molecular probes for the detection of human serum albumin.

Structure of the probe	$\lambda_{\text{ex}}/\lambda_{\text{em}}$ (Stokes shift) (nm)	Selectivity	LOD	Response time	Binding site	Ref.
	530/650 (120)	HSA	1.26 mg/L	–	Site I	41



	436/508 (72)	HSA	5 nM	60 min	More than one site	<b>44</b>
	460/575 (115)	HSA	0.30 mg/L	–	Fatty acid site I	<b>45</b>
	440/490 (50)	HSA	0.40 mg/L	–	Site I	<b>40</b>
	426/524 (98)	HSA	1.91 mg/L	–	Site I	<b>50</b>
	350/454 (104)	HSA	0.27 mg/L	2 h	Site I	<b>52</b>
	495/540 (45)	HSA	0.21 mg/L	<15 min	Site I & Site II	<b>55</b>
	650/675 (25)	HSA	1.03 mg/L	–	Site I & Site II	<b>57</b>
	497/610 (113)	HSA	0.34 mg/L	~10 min	Subdomain IB	<b>59</b>

	480/610 (130)	HSA	23 nM	~3 min	Site I & Site II	<b>60</b>
	590/685 (95)	HSA	4.64 nM	~15 min	Site I	<b>61</b>
	630/710 (80)	HSA	0.996 mg/L	<5 min	Site I	<b>78</b>
	295/400 (105)	HSA	4 nM	–	Site I	<b>62</b>
	476/602 (126)	HSA	1.01 nM (0.0671 mg/L)	~1.5 min	Site II	<b>This work</b>

### 3.3.3 Site-Selective Binding Analysis and Possible HSA sensing Mechanism

The crystal structure investigation revealed that HSA is a complex protein of ~66.5 kDa and it has three different domains (domains I, II, and III), each including two subdomains (A and B).<sup>5</sup> The principal ligand binding sites of HSA are mainly located in the hydrophobic zones of subdomain IIA (site I) and subdomain IIIA (site II).<sup>79,80</sup> Site I bind with molecules predominantly via strong hydrophobic interactions, while site II uses a combination of hydrogen bonding, ionic, and van der Waals interactions.<sup>5,78,80</sup> Thus, fluorescence displacement assays were carried out to identify the possible binding position of DCI-MIN on HSA using two well-known site-markers (warfarin for site I and diflunisal for site II).

In the displacement assays the site-markers were gradually added to a solution of HSA and DCI-MIN at a molar ratio of 1:4 to reduce the nonspecific binding of the site-markers.<sup>81</sup> The

emission intensity variations of this ternary mixture were recorded employing the method outlined by Sudlow *et al.*<sup>80</sup>

$$\frac{I_2}{I_1} \times 100\%$$

Where,  $I_2$  and  $I_1$  denote the emission intensities of the HSA–DCI-MIN composite in the presence and absence of site-markers, respectively. Upon addition of 46.03  $\mu\text{M}$  diflunisal, the emission intensity of the HSA–DCI-MIN composite was considerably lowered by  $\sim 76.70\%$ , while warfarin showed only  $\sim 22.73\%$  reduction in emission intensity (Figure 3.26). Hence, the experimental outcomes evidently indicate that DCI-MIN binds to both sites but predominantly to site II.

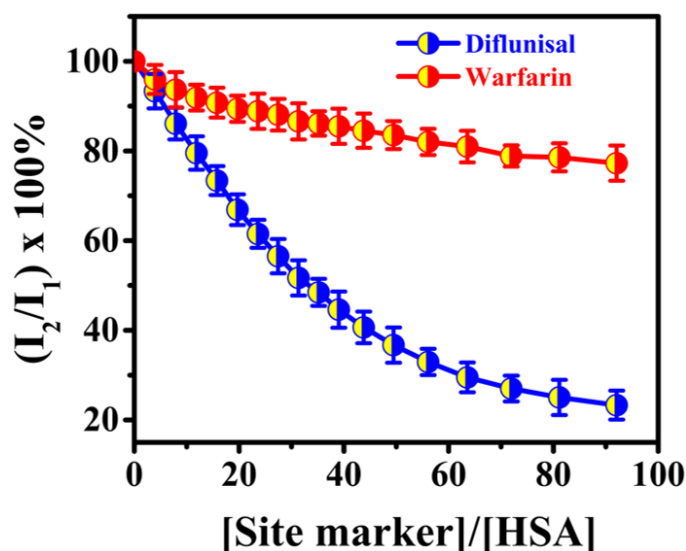


**Figure 3.26** Emission intensity alterations of DCI-MIN–HSA composite ([DCI-MIN] = 2  $\mu\text{M}$ , [HSA] = 0.5  $\mu\text{M}$ ) with the increasing concentration of warfarin and dlflunisal site-markers (0–46.03  $\mu\text{M}$ ).  $\lambda_{\text{ex}}$  = 476 nm and  $\lambda_{\text{em}}$  = 602 nm. Error bars: standard deviation (n = 3).

Since DCI-MIN constructs a strong ‘pull–push’ system, it is very sensitive to variations in the external microenvironment. For DCI-MIN both within and outside the HSA cavities, the microenvironment (polarity, viscosity, steric influence, etc.) varied significantly. The cavity of serum albumins creates a microenvironment with low polarity and severe steric hindrance, in contrast to the PBS buffer, which is a polar solution with low viscosity.

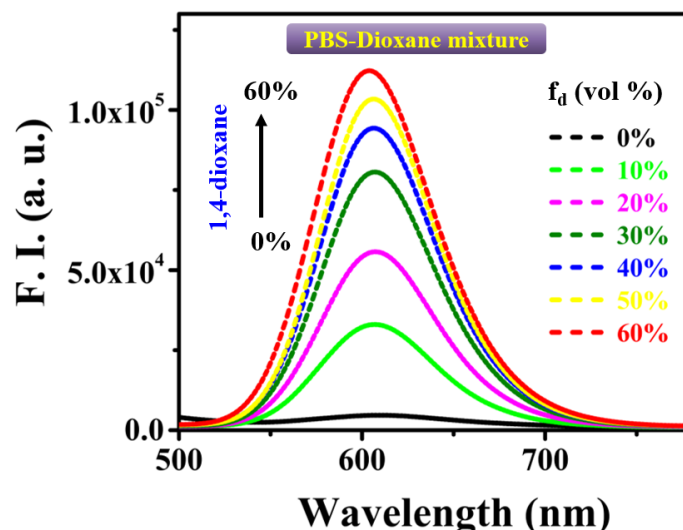
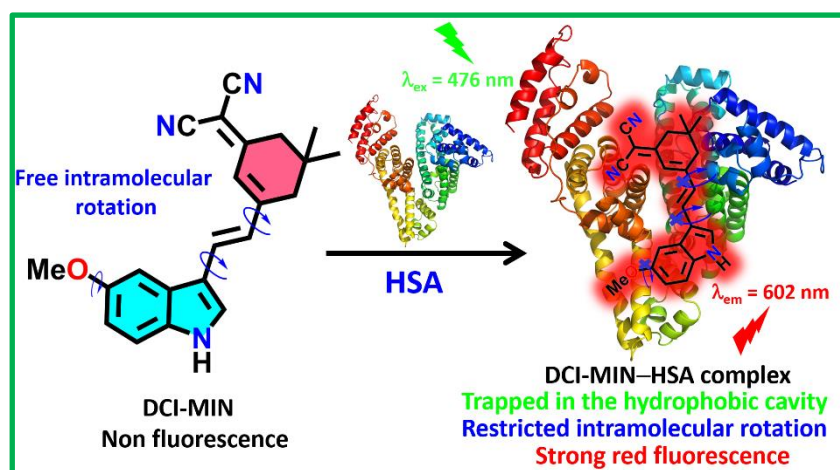


**Figure 3.27** Fluorescence emission spectra of DCI-MIN (2  $\mu\text{M}$ ) in PBS/1,4-dioxane mixtures with different dioxane fractions ( $f_d$ ).  $\lambda_{\text{ex}} = 476 \text{ nm}$ .

According to **Figure 3.27**, DCI-MIN was anticipated to be polarity sensitive in various proportions of 1,4-dioxanes in PBS buffer, and the emission intensity rises as the environment gets more hydrophobic. In addition to this, **Figure 3.11** also shows that DCI-MIN is viscosity sensitive probe. We thus proposed that the incorporation of DCI-MIN into the hydrophobic cavity of HSA prevents the probe molecules from rotating freely due to the severe steric hindrance and low polarity microenvironment present inside HSA, which results in intense red fluorescence (**Scheme 3.3**).



**Scheme 3.3** Schematic representation of the fluorescent probe DCI-MIN for HSA detection

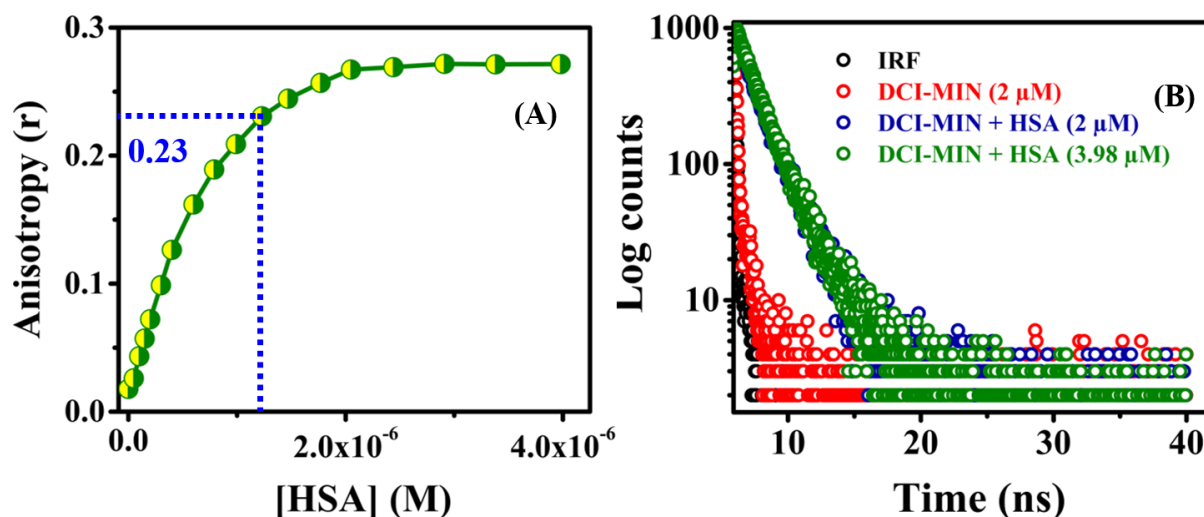


**Figure 3.28** Fluorescence anisotropy alterations of DCI-MIN (2  $\mu\text{M}$ ) with the successive addition of HSA ( $\lambda_{\text{ex}} = 476 \text{ nm}$  and  $\lambda_{\text{em}} = 602 \text{ nm}$ ). (B) Lifetime decay spectra of DCI-MIN (2  $\mu\text{M}$ ) with the incremental addition of HSA (0-3.98  $\mu\text{M}$ ).

Furthermore, a fluorescence anisotropy experiment was conducted to gather crucial information on the rigidity of the microenvironment in close vicinity to the DCI-MIN probe, which is expressed by the variation in anisotropy value.<sup>82,83</sup> The anisotropy value of DCI-MIN (2  $\mu\text{M}$ ) was quickly increased from 0.017 to 0.23 with the addition of just 1.23  $\mu\text{M}$  HSA, and then gradually improved to 0.271 till the addition of 3.98  $\mu\text{M}$  HSA (**Figure 3.28A**). Thus, the increasing anisotropy value clearly demonstrates that significant motional constraint is exerted on DCI-MIN probes within HSA. Here, in order to identify the cause of fluorescence augmentation, we have also conducted a fluorescence lifetime investigation of probe DCI-MIN with the increasing concentration of HSA (**Figure 3.28B**).

**Table 3.3** Lifetime decay parameters of DCI-MIN (2  $\mu\text{M}$ ) with the increasing concentration of HSA in PBS buffer solution.

[HSA] ( $\mu\text{M}$ )	$\tau_1$ (ns)	$\tau_2$ (ns)	$\alpha_1$ (%)	$\alpha_2$ (%)	$\tau_{\text{avg}}$ (ns)	$\chi^2$
0	0.034	0.861	93.02	6.98	0.091	1.045
2	0.592	1.843	27.11	72.89	1.503	1.031
3.98	0.594	1.857	25.15	74.85	1.539	1.023

The lifetime decay-associated parameters are summarized in **Table 3.3**. Free DCI-MIN probe shows a biexponential decay with an average lifetime ( $\tau_{avg}$ ) of 0.091 ns in PBS buffer solution, whereas upon addition of 3.98  $\mu\text{M}$  of HSA, the probe displays a biexponential decay with  $\tau_{avg}$  of 1.539 ns. The higher lifetime of the DCI-MIN–HSA composite suggests that the interaction of DCI-MIN with HSA restricts the intramolecular rotation, which in turn reduces the energy loss via nonradiative decay pathways.

### 3.3.4 Molecular Docking

Here, we have performed the molecular docking study to identify the potential DCI-MIN binding location inside the HSA and the involvement of pertinent interactions during the association process.<sup>77</sup> The lowest-binding energy docked conformer was chosen among the ten unique conformers for additional analysis. **Figure 3.29A** depicts the molecular docking posture of DCI-MIN with HSA, revealing that the primary binding site of DCI-MIN is subdomain IIIA of site II in HSA, as indicated by site-marker displacement assays.

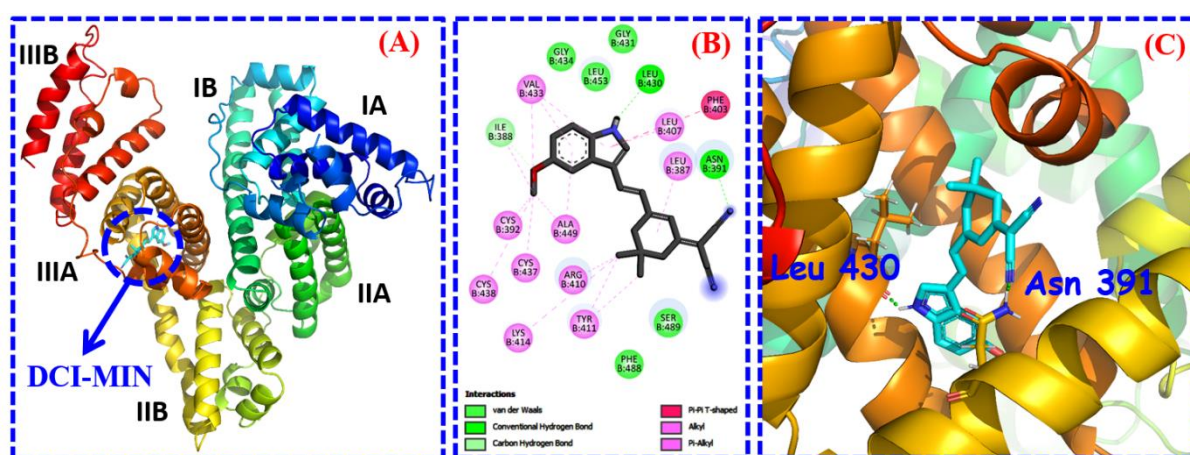


**Figure 3.29** (A) Stereo view of DCI-MIN with HSA (PDB ID: 2BXE) shown by blue circle. (B) Adjacent residues and forces responsible for the accommodation of DCI-MIN at site II of HSA. (C) Enlarged view of hydrogen bonding interactions made by DCI-MIN at site II of HSA.

According to **Figures 3.29B and C**, it was clearly revealed that the indole -NH group of DCI-MIN formed one hydrogen bond with Leu 430 and one cyano group of DCI-MIN made another hydrogen bond with Asn 391, providing better stability to DCI-MIN inside the HSA. A number of hydrophobic amino acid residues, including Gly 434, Gly 431, Leu 453, Leu

430, and Phe 488, also contributed to the stability of the DCI-MIN-HSA complex through van der Waals interactions. (Figure 3.29B). Furthermore, a T-shaped  $\pi$ - $\pi$  bond was formed between DCI-MIN and the Phe 403 amino acid residue. The low binding energy ( $-7.79$  kcal/mol) also suggests the strong interaction of DCI-MIN with HSA.

### 3.3.5 HSA Estimation in Human Urine Samples

The quantitative measurement of urinary HSA concentration has enormous therapeutic significance, while it is frequently hampered by the presence of various biological interferents and significant auto fluorescence of urine samples. However, we believe that the probe DCI-MIN may be employed for the detection and measurement of the urinary HSA levels owing to its selective binding ability with HSA and red emissive response. So, we took four urine samples from four healthy male donors who had no prior medical history, diluted with PBS buffer solution, and used the conventional standard addition curve method to measure the urinary HSA levels.

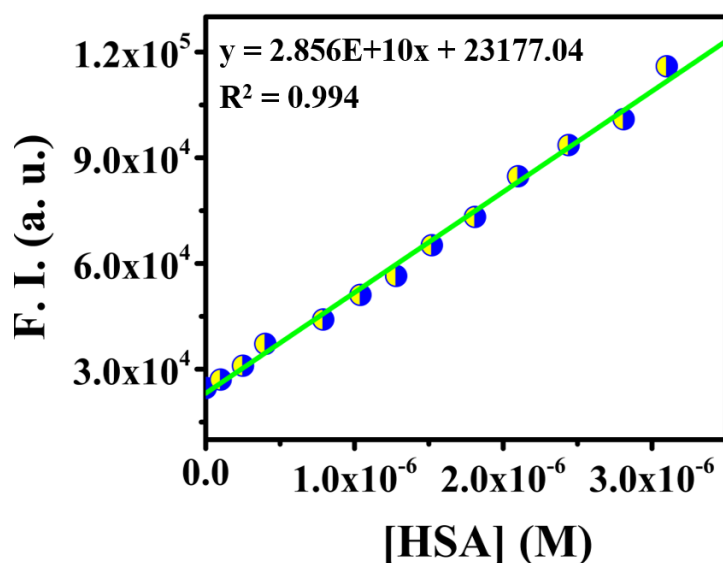


**Figure 3.30** Linear fluorescence response of DCI-MIN (2  $\mu$ M) in a urine-PBS system (1:1, v/v) spiked with different HSA concentrations (0-3.10  $\mu$ M) at 602 nm.  $\lambda_{\text{ex}} = 476$  nm. From the graph we get slope =  $2.856 \times 10^{10} \text{ M}^{-1}$ .

In our study, a urine-PBS system (1:1, v/v) containing 2  $\mu$ M DCI-MIN was spiked with various concentrations of HSA (0-3.10  $\mu$ M), and the fluorescence signals were recorded. Here, we noticed an excellent linear correlation ( $R^2 = 0.994$ ) between the increase in emission intensity of DCI-MIN at 602 nm and the amount of HSA in the urine-PBS system (Figure



3.30). Using the standard addition technique, the urinary HSA levels of the four male donors were evaluated to be 24.37 mg/L, 11.85 mg/L, 23.19 mg/L, and 15.74 mg/L respectively.

The same urine samples were also investigated by the Coomassie Brilliant Blue G250 method<sup>84</sup> to verify the HSA levels measured by the DCI-MIN method. From the standard addition plot of  $A_{595}$  vs. HSA (mg/L) (Figure 3.31A), the urinary HSA levels were estimated to be 22.42 mg/L, 13.29 mg/L, 25.10 mg/L, and 18.13 mg/L, respectively. Interestingly, it was found that the G250 technique exhibited good agreement with the urinary HSA levels determined by the DCI-MIN approach (Figure 3.31B). In light of this, we believe that DCI-MIN can serve as an effective fluorescent probe for the specific detection, monitoring, and quantification of HSA concentration in urine samples.

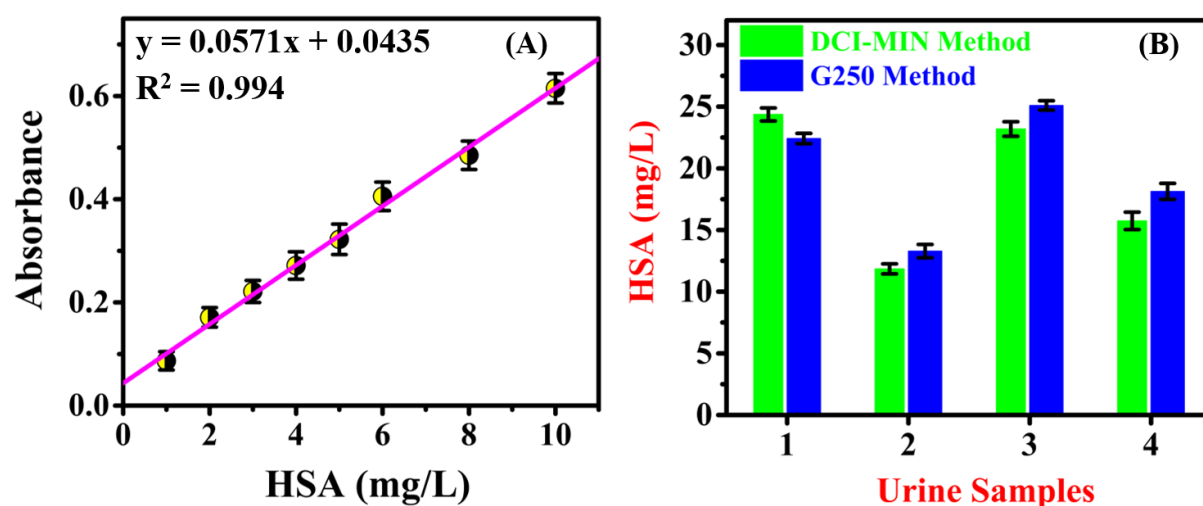


**Figure 3.31** (A) Standard addition plot of absorbance (at 595 nm) versus amount of HSA (mg/L) by the Coomassie Brilliant Blue G250 method. (B) Comparison of the DCI-MIN technique for measuring urinary HSA to the G250 method. Error bars: standard deviation ( $n = 3$ ).

### 3.3.6 Quantitative Measurement of HSA in Human Serum Samples

To further establish the applicability for the real sample, DCI-MIN was utilized to measure the concentrations of HSA in human blood serum samples. Initially, the fluorescence responses of probe DCI-MIN (2  $\mu$ M) in a PBS buffer diluted serum sample spiked with varying amounts of HSA (0-3.98  $\mu$ M) were recorded. With the addition of HSA, the emission intensity of DCI-MIN was significantly enhanced (Figure 3.32A).

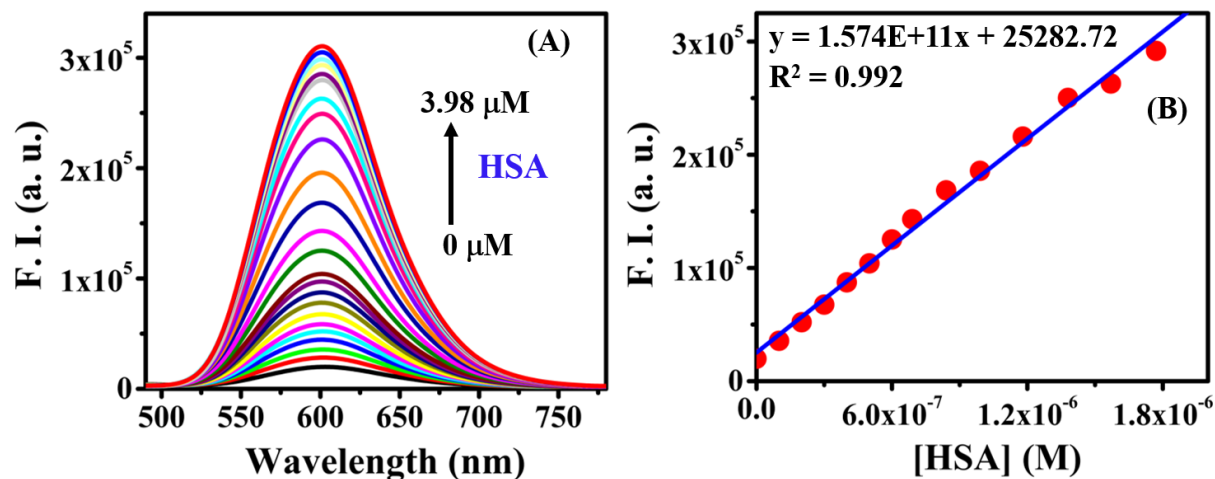


**Figure 3.32** (A) Fluorescence spectra of DCI-MIN (2 μM) with the addition of HSA (0-3.98 μM) in a PBS diluted human blood sample. (B) Linear fluorescence response between emission intensity and different HSA concentrations (0-1.77 μM) at 602 nm  $\lambda_{ex} = 476$  nm. From the graph we get slope =  $1.574 \times 10^{11} M^{-1}$ .

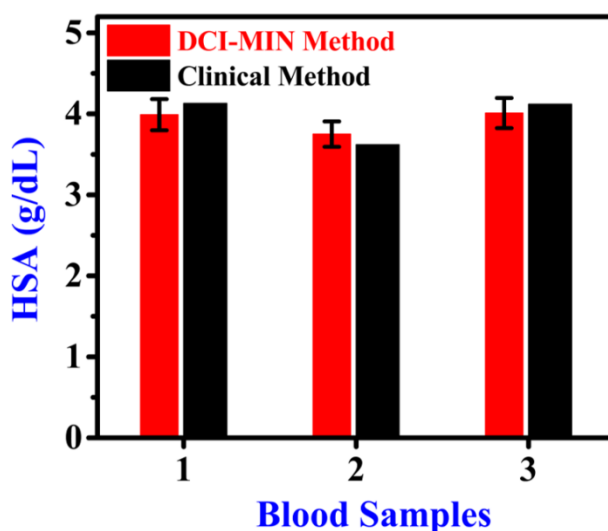


**Figure 3.33** Validation of the HSA estimation data in human blood samples by DCI-MIN method with those obtained independently from a diagnostic laboratory using the conventional clinical method. Error bars: standard deviation (n = 3).

As seen in **Figure 3.32B**, an excellent linear relationship ( $R^2 = 0.992$ ) between the emission intensity at 602 nm and HSA concentrations ranging from 0 to 1.77 μM was observed. After that, we measured the HSA concentrations in three blood samples collected from three healthy donors using DCI-MIN, and the estimated values were 3.99 g/dL, 3.75 g/dL, and 3.62 g/dL, respectively.

The same three blood samples assessed by the conventional clinical method (obtained independently from a diagnostic laboratory) were used as a control. According to [Figure 3.33](#), the HSA levels found in three blood samples were within the reference range of normal human blood, and furthermore, the HSA concentrations evaluated by the DCI-MIN method agreed well with the conventional clinical method.

However, the most common method for measuring the serum albumin is a dye-binding method that makes use of the albumin's capability to produce a stable complex with the BCG dye. The BCG technique may overestimate serum albumin owing to the binding ability of this dye with other proteins like globulin.<sup>85</sup> Furthermore, this technique normally needs a 5-30 min reaction time. Thus, for the recognition of serum albumin, DCI-MIN demonstrated better selectivity and a quicker reaction time than the BCG technique. These results showed that the DCI-MIN probe may be used to detect HSA in human blood samples with good sensitivity and reproducibility.

### 3.3.7 Fluorescence Imaging of Serum Albumin in Living Cells

A well-established MTT-based assay was carried out in the KB and CHO cell lines to determine the cytotoxicity of the probe DCI-MIN before the fluorescence imaging experiments. According to [Figure 3.34](#), the cell viabilities of KB and CHO cells were still over 76% and 72%, respectively, after 24 h of incubation with 10  $\mu\text{M}$  of DCI-MIN, indicating that the probe DCI-MIN has low cytotoxicity and may be suitable in biological applications.

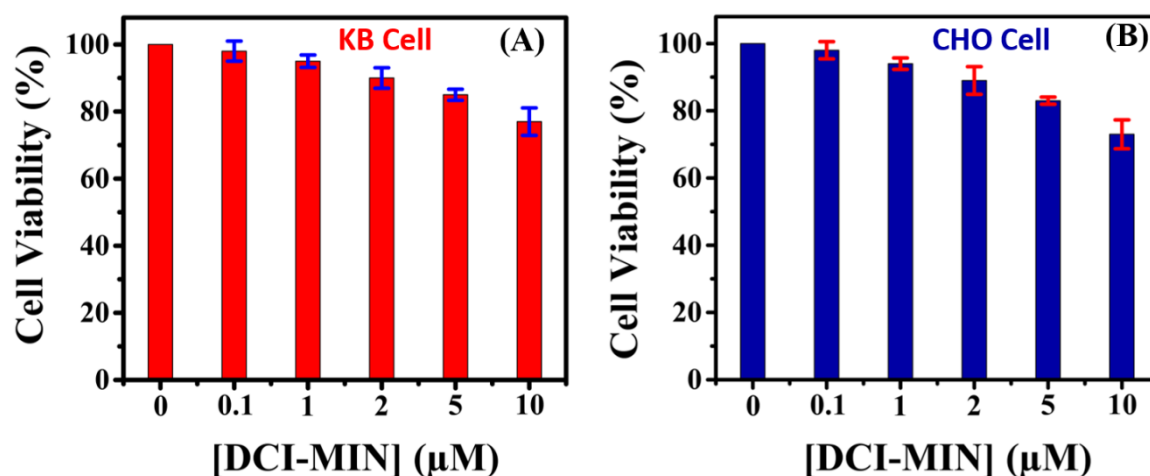


**Figure 3.34** (A and B) Cell viabilities of KB and CHO cells treated with different concentrations of DCI-MIN.

For cell culture investigations, serum albumin is a significant and crucial component of the culture medium. Thus, the intracellular imaging of serum albumin in KB and CHO cells was performed using DCI-MIN. Upon incubation of KB and CHO cells with DCI-MIN (2  $\mu\text{M}$ ) for 30 min a strong red fluorescence was observed (Figure 3.35). DAPI staining and microscopic image analysis showed that DCI-MIN probes are primarily localized in the cytoplasm of both KB and CHO cells.

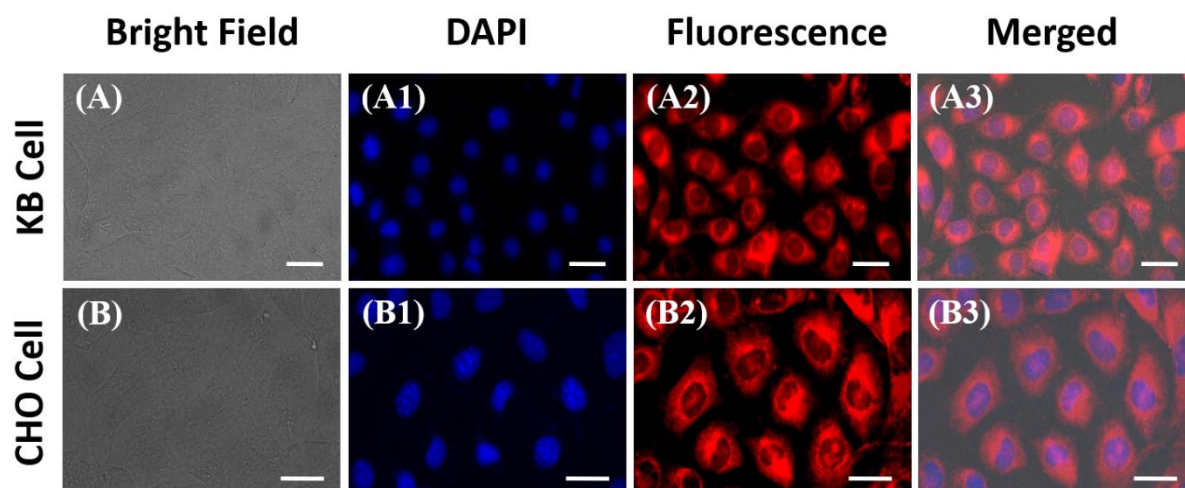


**Figure 3.35** Confocal fluorescence imaging of serum albumin in living KB and CHO cells. (A-A3) KB cells treated with DCI-MIN (2  $\mu\text{M}$ ) for 30 min and then with DAPI for another 10 min. (B-B3) CHO cells treated with DCI-MIN (2  $\mu\text{M}$ ) for 30 min and then with DAPI for another 10 min.  $\lambda_{\text{ex}}$  for DAPI and DCI-MIN are 352 and 488 nm, respectively. Scale bar = 50  $\mu\text{m}$ .

### 3.4 Conclusions

In summary, we have developed an ICT-based environment sensitive fluorescent probe DCI-MIN for the detection and quantification of HSA in complicated biological samples with high selectivity and sensitivity. DCI-MIN has excellent photostability and exhibits a clear HSA induced large enhancement in emission intensity ( $\sim 78$ -fold) without interference from various ions (cations and anions) and other bioanalytes that are often present in the environment or biological systems. The strong red fluorescence response of DCI-MIN in the presence of HSA can be attributed to the incorporation of DCI-MIN into the site II hydrophobic binding cavity of HSA, that restricts the free rotation of DCI-MIN due to the severe steric hindrance as well as the low polarity of the microenvironment. The fluorescence displacement assay

and the molecular docking analysis are in conformity of the above proposition. DCI-MIN displayed high binding affinity to HSA with a  $K_d$  value of  $(0.024 \pm 0.003) \mu\text{M}$ . The probe has a detection limit of 1.01 nM (0.0671 mg/L) in aqueous solution, which is significantly lower than the normal level of HSA in healthy urine, indicating its high sensitivity and superiority to the earlier reported HSA detection probes. Interestingly, a substantial Stokes shift of  $\sim 126$  nm in the fluorescent turn-on response of DCI-MIN towards HSA seems to be highly beneficial, which assures the minimum interference from the excitation light. DCI-MIN has the ability to perform a variety of useful applications, including the detection and quantification of HSA levels in complex biofluids (human urine and blood samples) as well as the imaging of serum albumin in living cells. As compared to the Bradford assay, measuring the urinary HSA level with DCI-MIN is favorable due to its inexpensive cost, rapid detection time and a simple operating technique. Besides this, DCI-MIN demonstrated better selectivity and a faster reaction time than the BCG technique for the recognition and monitoring HSA levels in human blood samples. Therefore, it is reasonable to infer that the DCI-MIN probe can be used as an effective biomarker for the rapid diagnosis of disorders linked with HSA and will draw the attention of researchers in developing other sensors capable of detecting HSA through non-covalent interactions.

### References

- 1) Olson, R. E.; Christ, D. D. Chapter 33. Plasma Protein Binding of Drugs. *Annu. Rep. Med. Chem.* **1996**, *31*, 327–336.
- 2) Nicholson, J. P.; Wolmarans, M. R.; Park, G. R. The role of albumin in critical illness. *Br. J. Anaesth.* **2000**, *85*, 599–610.
- 3) Wen, J.; Geng, Z.; Yin, Y.; Wang, Z. A versatile water soluble fluorescent probe for ratiometric sensing of  $\text{Hg}^{2+}$  and bovine serum albumin. *Dalton Trans.* **2011**, *40*, 9737–9745.
- 4) Peters, T., Jr. Serum Albumin. *Adv. Protein Chem.* **1985**, *37*, 161–245.
- 5) He, X. M.; Carter, D. C. Atomic structure and chemistry of human serum albumin. *Nature* **1992**, *358*, 209–215.
- 6) Fanali, G.; di Masi, A.; Trezza, V.; Marino, M.; Fasano, M.; Ascenzi, P. Human serum albumin: from bench to bedside. *Mol. Aspects Med.* **2012**, *33*, 209–290.

- 7) Sethi, P. K.; White, C. A.; Cummings, B. S.; Hines, R. N.; Muralidhara, S.; Bruckner, J. V. Ontogeny of plasma proteins, albumin and binding of diazepam, cyclosporine, and deltamethrin. *Pediatr. Res.* **2016**, *79*, 409–415.
- 8) Ding, F.; Liu, W.; Zhang, L.; Yin, B.; Sun, Y. J. Sulfometuron-methyl binding to human serum albumin: Evidence that sulfometuron-methyl binds at the Sudlow's site I. *J. Mol. Struct.* **2010**, *968*, 59–66.
- 9) Caraceni, P.; Tufoni, M.; Bonavita, M. E. Clinical use of albumin. *Blood Transfus.* **2013**, *11*, s18–s25.
- 10) Lee, H.; Cha, M. K.; Kim, I. H. Activation of Thiol-Dependent Antioxidant Activity of Human Serum Albumin by Alkaline pH Is Due to the B-like Conformational Change. *Arch. Biochem. Biophys.* **2000**, *380*, 309–318.
- 11) Belinskaia, D. A.; Voronina, P. A.; Batalova, A. A.; Goncharov, N. V. Serum Albumin. *Encyclopedia* **2021**, *1*, 65–75.
- 12) Levitt, D. G.; Levitt, M. D. Human serum albumin homeostasis: a new look at the roles of synthesis, catabolism, renal and gastrointestinal excretion, and the clinical value of serum albumin measurements. *Int. J. Gen. Med.* **2016**, *9*, 229–255.
- 13) Spada, A.; Emami, J.; Tuszyński, J. A.; Lavasanifar, A. The uniqueness of albumin as a carrier in nanodrug delivery. *Mol. Pharmaceutics* **2021**, *18*, 1862–1894.
- 14) Pollock, C. A.; Poronnik, P. Albumin transport and processing by the proximal tubule: physiology and pathophysiology. *Curr. Opin. Nephrol. Hypertens.* **2007**, *16*, 359–364.
- 15) Fan, J.; Sun, W.; Wang, Z.; Peng, X.; Li, Y.; Cao, J. A fluorescent probe for site I binding and sensitive discrimination of HSA from BSA. *Chem. Commun.* **2014**, *50*, 9573–9576.
- 16) Alino, V. J.; Yang, K. L. Using liquid crystals as a readout system in urinary albumin assays. *Analyst* **2011**, *136*, 3307–3313.
- 17) Rani, S.; Gupta, S.; Luxami, V.; Paul, K. A novel target and biomarker benzothiazolyl–naphthalimide probes for precise and selective detection of serum albumin and anticancer activity. *New J. Chem.* **2022**, *46*, 12082–12092.
- 18) Murch, S. H.; Winyard, P. J. D.; Koletzko, S.; Wehner, B.; Cheema, H. A.; Risdon, R. A.; Phillips, A. D.; Meadows, N.; Klein, N. J.; Walker-Smith, J. A. Congenital



- enterocyte heparan sulphate deficiency with massive albumin loss, secretory diarrhoea, and malnutrition. *Lancet* **1996**, *347*, 1299–1301.
- 19) Verhave, J. C.; Hillege, H. L.; Burgerhof, J. G. M.; Gansevoort, R. T.; Zeeuw, D. D.; Jong, P. E. D. The association between atherosclerotic risk factors and renal function in the general population. *Kidney Int.* **2005**, *67*, 1967–1973.
- 20) Peters, T., Jr. *All About Albumins: Biochemistry, Genetics and Medical Applications*; Academic Press: San Diego, CA, 1996; pp 76–132.
- 21) Hoogenberg, K.; Sluiter, W. J.; Dullaart, R. P. Effect of growth hormone and insulin-like growth factor I on urinary albumin excretion: studies in acromegaly and growth hormone deficiency. *Eur. J. Endocrinol.* **1993**, *129*, 151–157.
- 22) de Zeeuw, D.; Parving, H. H.; Henning, R. Microalbuminuria as an early marker for cardiovascular disease. *J. Am. Soc. Nephrol.* **2006**, *17*, 2100–2105.
- 23) Amin, R.; Widmer, B.; Prevost, A. T.; Schwarze, P.; Cooper, J.; Edge, J.; Marcovecchio, L.; Neil, A.; Dalton, R. N.; Dunger, D. B. Risk of microalbuminuria and progression to macroalbuminuria in a cohort with childhood onset type 1 diabetes: prospective observational study. *BMJ.* **2008**, *336*, 697–701.
- 24) Bradford, M. M. A rapid and sensitive method for the quantitation of microgram quantities of protein utilizing the principle of protein-dye binding. *Anal. Biochem.* **1976**, *72*, 248–254.
- 25) Seegmiller, J. C.; Sviridov, D.; Larson, T. S.; Borland, T. M.; Hortin, G. L.; Lieske, J. C. Comparison of urinary albumin quantification by immunoturbidimetry, competitive immunoassay, and protein-cleavage liquid chromatography–tandem mass spectrometry. *Clin. Chem.* **2009**, *55*, 1991–1994.
- 26) Seegmiller, J. C.; Barnidge, D. R.; Burns, B. E.; Larson, T. S.; Lieske, J. C.; Kumar, R. Quantification of urinary albumin by using protein cleavage and LC-MS/MS. *Clin. Chem.* **2009**, *55*, 1100–1107.
- 27) Watts, G. F.; Bennett, J. E.; Rowe, D. J.; Morris, R. W.; Gatling, W.; Shaw, K. M. Polak, A. Assessment of immunochemical methods for determining low concentrations of albumin in urine. *Clin. Chem.* **1986**, *32*, 1544–1548.
- 28) Engvall, E.; Perlmann, P. Enzyme-linked immunosorbent assay (ELISA) quantitative assay of immunoglobulin G. *Immunochemistry*, **1971**, *8*, 871–874.



- 29) Doumas, B. T.; Watson, W. A.; Biggs, H. G. Albumin Standards and Measurement of Serum Albumin with Bromocresol Green. *Clin. Chim. Acta.* **1971**, *31*, 87–96.
- 30) Pinnell, A. E.; Northam, B. E. New Automated Dye-Binding Method for Serum-Albumin Determination with Bromocresol Purple. *Clin. Chem.* **1978**, *24*, 80–86.
- 31) Doumas, B. T.; Peters, T., Jr. Origins of Dye-Binding Methods for Measuring Serum Albumin. *Clin. Chem.* **2009**, *55*, 583–584.
- 32) Shaikh, A.; Seegmiller, J. C.; Borland, T. M.; Burns, B. E.; Ladwig, P. M.; Singh, R. J.; Kumar, R.; Larson, T. S.; Lieske, J. C. Comparison between immunoturbidimetry, size-exclusion chromatography, and LC-MS to quantify urinary albumin. *Clin. Chem.* **2008**, *54*, 1504–1510.
- 33) Ruhn, P. F.; Taylor, J. D.; Hage, D. S. Determination of urinary albumin using high-performance immunoaffinity chromatography and flow injection analysis. *Anal. Chem.* **1994**, *66*, 4265–4271.
- 34) Silver, A.; Dawnay, A.; Landon, J.; Cattell, W. R. Immunoassays for low concentrations of albumin in urine. *Clin. chem.* **1986**, *32*, 1303–1306.
- 35) Kubota, R.; Hamachi, I. Protein Recognition Using Synthetic Small-molecular Binders toward Optical Protein Sensing in vitro and in Live Cells. *Chem. Soc. Rev.* **2015**, *44*, 4454–4471.
- 36) He, X. P.; Zang, Y.; James, T. D.; Li, J.; Chen, G. R. Probing Disease-related Proteins with Fluorogenic Composite Materials. *Chem. Soc. Rev.* **2015**, *44*, 4239–4248.
- 37) Thurley, S.; Roglin, L.; Seitz, O. Hairpin peptide beacon: Dual-labeled PNA-peptide-hybrids for protein detection. *J. Am. Chem. Soc.* **2007**, *129*, 12693–12695.
- 38) Wang, B.; Yu, C. Fluorescence turn-on detection of a protein through the reduced aggregation of a perylene probe. *Angew. Chem., Int. Ed.* **2010**, *49*, 1485–1488.
- 39) Jin, Q.; Feng, L.; Wang, D. D.; Dai, Z. R.; Wang, P.; Zou, L. W.; Liu, Z. H.; Wang, J. Y.; Yu, Y.; Ge, G. B.; Cui, J. N.; Yang, L. A two-photon ratiometric fluorescent probe for imaging carboxylesterase 2 in living cells and tissues. *ACS Appl. Mater. Interfaces* **2015**, *7*, 28474–28481.
- 40) Wu, Y. Y.; Yu, W. T.; Hou, T. C.; Liu, T. K.; Huang, C. L.; Chen, I. C.; Tan, K. T. A selective and sensitive fluorescent albumin probe for the determination of urinary albumin. *Chem. Commun.* **2014**, *50*, 11507–11510.

- 41) Rajasekhar, K.; Achar, C. J.; Govindaraju, T. A red-NIR emissive probe for the selective detection of albumin in urine samples and live cells. *Org. Biomol. Chem.* **2017**, *15*, 1584–1588.
- 42) Reja, S. I.; Khan, I. A.; Bhalla, V.; Kumar, M. A TICT based NIR-fluorescent probe for human serum albumin: a pre-clinical diagnosis in blood serum. *Chem. Commun.* **2016**, *52*, 1182–1185.
- 43) Liu, C.; Yang, W.; Gao, Q.; Du, J.; Luo, H.; Liu, Y.; Yang, C. Differential recognition and quantification of HSA and BSA based on two red-NIR fluorescent probes. *J. Lumin.* **2018**, *197*, 193–199.
- 44) Xu, Y. J.; Su, M. M.; Li, H. L.; Liu, Q. X.; Xu, C.; Yang, Y. S.; Zhu, H. L. A fluorescent sensor for discrimination of HSA from BSA through selectivity evolution. *Anal. Chim. Acta* **2018**, *1043*, 123–131.
- 45) Er, J. C.; Tang, M. K.; Chia, C. G.; Liew, H.; Vendrell, M.; Chang, Y. T. MegaStokes BODIPY-triazoles as environmentally sensitive turn-on fluorescent dyes. *Chem. Sci.* **2013**, *4*, 2168–2176.
- 46) Liu, B.; Bi, X.; McDonald, L.; Pang, Y.; Liu, D.; Pan, C.; Wang, L. Solvatochromic fluorescent probes for recognition of human serum albumin in aqueous solution: insights into structure-property relationship. *Sens. Actuators B: Chem.* **2016**, *236*, 668–674.
- 47) Zhang, P.; Guo, X.; Xiao, Y.; Zhang, Q.; Ding, C. Twisted intramolecular charge transfer (TICT) based fluorescent probe for lighting up serum albumin with high sensitivity in physiological conditions. *Spectrochim. Acta A: Mol. Biomol. Spectrosc.* **2019**, *223*, 117318.
- 48) Shen, P.; Hua, J.; Jin, H.; Du, J.; Liu, C.; Yang, W.; Gao, Q.; Luo, H.; Liu, Y.; Yang, C. Recognition and quantification of HSA: A fluorescence probe across  $\alpha$ -helices of site I and site II. *Sens. Actuators B: Chem.* **2017**, *247*, 587–594.
- 49) Li, J.; Wu, J.; Cui, F.; Zhao, X.; Li, Y.; Lin, Y.; Li, Y.; Hu, J.; Ju, Y. A dual functional fluorescent sensor for human serum albumin and chitosan. *Sens. Actuators B: Chem.* **2017**, *243*, 831–837.
- 50) Li, P.; Wang, Y.; Zhang, S.; Xu, L.; Wang, G.; Cui, J. An ultrasensitive rapid-response fluorescent probe for highly selective detection of HSA. *Tetrahedron Lett.* **2018**, *59*, 1390–1393.

- 51) Luo, Z.; Liu, B.; Zhu, K.; Huang, Y.; Pan, C.; Wang, B.; Wang, L. An environment-sensitive fluorescent probe for quantification of human serum albumin: Design, sensing mechanism, and its application in clinical diagnosis of hypoalbuminemia. *Dyes Pigm.* **2018**, *152*, 60–66.
- 52) Dey, N.; Maji, B.; Bhattacharya, S. Motion Induced Change in Emission as an Effective Strategy for Ratiometric Probing of Human Serum Albumin and Trypsin in Biological Fluids. *Chem. Asian J.* **2018**, *13*, 664–671.
- 53) Yu, Y.; Huang, Y.; Hu, F.; Jin, Y.; Zhang, G.; Zhang, D.; Zhao, R. Self-assembled nanostructures based on activatable red fluorescent dye for site-specific protein probing and conformational transition detection. *Anal. Chem.* **2016**, *88*, 6374–6381.
- 54) Gao, T.; Yang, S.; Cao, X.; Dong, J.; Zhao, N.; Ge, P.; Zeng, W.; Cheng, Z. Smart self-assembled organic nanoprobe for protein-specific detection: design, synthesis, application, and mechanism studies. *Anal. Chem.* **2017**, *89*, 10085–10093.
- 55) Sun, Q.; Wang, W.; Chen, Z.; Yao, Y.; Zhang, W.; Duan, L.; Qian, J. A fluorescence turn-on probe for human (bovine) serum albumin based on the hydrolysis of a dioxaborine group promoted by proteins. *Chem. Commun.* **2017**, *53*, 6432–6435.
- 56) Wang, Z. G.; Yan, X. J.; Liu, H. B.; Zhang, D. L.; Liu, W.; Xie, C. Z.; Li, Q. Z.; Xu, J. Y. A novel hydrazide Schiff base self-assembled nanoprobe for selective detection of human serum albumin and its applications in renal disease surveillance. *J. Mater. Chem. B* **2020**, *8*, 8346–8355.
- 57) Guo, Y.; Chen, Y.; Zhu, X.; Pan, Z.; Zhang, X.; Wang, J.; Fu, N. Self-assembled nanosensor based on squaraine dye for specific recognition and detection of human serum albumin. *Sens. Actuators B: Chem.* **2018**, *255*, 977–985.
- 58) Yan, X. J.; Li, Z.; Liu, H. B.; Wang, Z. G.; Fan, J.; Xie, C. Z.; Li, Q. J.; Xu, J. Y. A chromone hydrazide Schiff base fluorescence probe with high selectivity and sensitivity for the detection and discrimination of human serum albumin (HSA) and bovine serum albumin (BSA). *J. Photochem. Photobiol. A: Chem.* **2022**, *422*, 113576.
- 59) Pei, S.; Li, J.; Zhang, C.; Zhang, G.; Zhou, Y.; Fan, L.; Wang, W.; Shuang, S.; Dong, C. TICT-Based Microenvironment-Sensitive Probe with Turn-on Red Emission for Human Serum Albumin Detection and for Targeting Lipid Droplet Imaging. *ACS Biomater. Sci. Eng.* **2022**, *8*, 253–260.

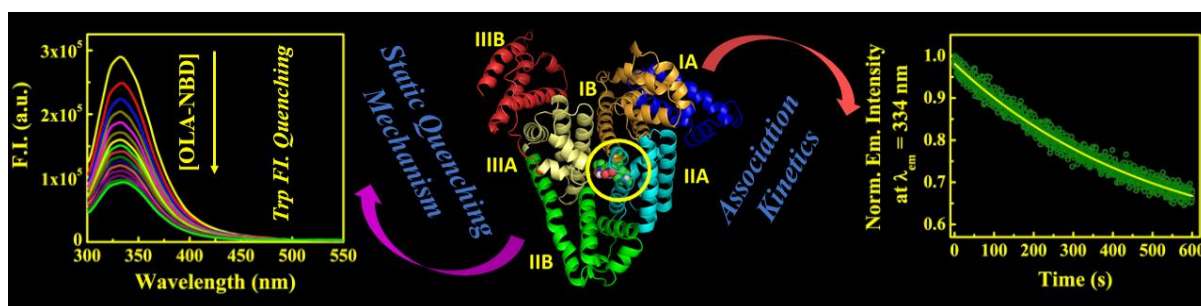
- 60) Zhao, X.; Zheng, W.; Qin, T.; Du, X.; Lei, Y.; Lv, T.; Zhou, M.; Xu, Z.; Wang, L.; Liu, B.; Peng, X. An anti-interference fluorescent probe for point-of-care diagnosis of albuminuria. *Sens. Actuators B: Chem.* **2022**, *351*, 130980.
- 61) Liu, B.; Zeng, C.; Zheng, D.; Zhao, X.; Song, C.; Qin, T.; Xu, Z. A near-infrared dicyanoisophorone-based fluorescent probe for discriminating HSA from BSA. *Spectrochim. Acta A: Mol. Biomol. Spectrosc.* **2022**, *274*, 121081.
- 62) Dey, G.; Gaur, P.; Giri, R.; Ghosh, S. Optical signaling in biofluids: a nondenaturing photostable molecular probe for serum albumins. *Chem. Commun.* **2016**, *52*, 1887–1890.
- 63) Liu, B.; Lv, T.; Zhao, X.; Zhou, M.; Song, C.; Zeng, C.; Qin, T.; Xu, Z. Fluorescence discrimination of HSA from BSA: A close look at the albumin-induced restricted intramolecular rotation of flavonoid probe. *Spectrochim. Acta A: Mol. Biomol. Spectrosc.* **2022**, *264*, 120306.
- 64) Zhang, X.; Chen, Y. Synthesis and fluorescence of dicyanoisophorone derivatives. *Dyes Pigm.* **2013**, *99*, 531–536.
- 65) Zhao, Y.; Wei, K.; Kong, F.; Gao, X.; Xu, K.; Tang, B. Dicyanoisophorone-based near-infrared-emission fluorescent probe for detecting NAD (P) H in living cells and in vivo. *Anal. chem.* **2018**, *91*, 1368–1374.
- 66) Shu, W.; Zang, S.; Wang, C.; Gao, M.; Jing, J.; Zhang, X. An endoplasmic reticulum-targeted ratiometric fluorescent probe for the sensing of hydrogen sulfide in living cells and zebrafish. *Anal. Chem.* **2020**, *92*, 9982–9988.
- 67) Li, H.; Yao, Q.; Sun, W.; Shao, K.; Lu, Y.; Chung, J.; Kim, D.; Fan, J.; Long, S.; Du, J.; Li, Y.; Wang, J.; Yoon, J.; Peng, X. Aminopeptidase N activatable fluorescent probe for tracking metastatic cancer and image-guided surgery via in situ spraying. *J. Am. Chem. Soc.* **2020**, *142*, 6381–6389.
- 68) Wu, Y.; Fu, R.; Mohanty, S.; Nasser, M.; Guo, B.; Ghosh, G. Investigation of integrated effects of hydroxyapatite and VEGF on capillary morphogenesis of endothelial cells. *ACS Appl. Bio Mater.* **2019**, *2*, 2339–2346.
- 69) Liu, T.; Yan, Q. L.; Feng, L.; Ma, X. C.; Tian, X. G.; Yu, Z. L.; Ning, J.; Huo, X. K.; Sun, C. P.; Wang, C.; Cui, J. N. Isolation of  $\gamma$ -glutamyl-transferase rich-bacteria from mouse gut by a near-infrared fluorescent probe with large stokes shift. *Anal. chem.* **2018**, *90*, 9921–9928.

- 70) Larsson, A.; Carlsson, C.; Jonsson, M.; Albinsson, B. Characterization of the Binding of the Fluorescent Dyes YO and YOYO to DNA by Polarized Light Spectroscopy. *J. Am. Chem. Soc.* **1994**, *116*, 8459–8465.
- 71) Sasmal, M.; Bhowmick, R.; Islam, A. S. M.; Bhuiya, S.; Das, S.; Ali, M. Domain-Specific Association of a Phenanthrene–Pyrene-Based Synthetic Fluorescent Probe with Bovine Serum Albumin: Spectroscopic and Molecular Docking Analysis. *ACS Omega* **2018**, *3*, 6293–6304.
- 72) Brouwer, A. M. Standards for photoluminescence quantum yield measurements in solution (IUPAC Technical Report). *Pure Appl. Chem.* **2011**, *83*, 2213–2228.
- 73) Zhu, T.; Du, J.; Cao, W.; Fan, J.; Peng, X. Microenvironment-sensitive fluorescent dyes for recognition of serum albumin in urine and imaging in living cells. *Ind. Eng. Chem. Res.* **2016**, *55*, 527–533.
- 74) Babendure, J. R.; Adams, S. R.; Tsien, R. Y. Aptamers switch on fluorescence of triphenylmethane dyes. *J. Am. Chem. Soc.* **2003**, *125*, 14716–14717.
- 75) Li, Q.; Min, J.; Ahn, Y. H.; Namm, J.; Kim, E. M.; Lui, R.; Kim, H. Y.; Ji, Y.; Wu, H.; Winsniewski, T.; Chang, Y. T. Styryl-Based Compounds as Potential in vivo Imaging Agents for  $\beta$ -Amyloid Plaques. *ChemBioChem* **2007**, *8*, 1679–1687.
- 76) Morris, G. M.; Goodsell, D. S.; Huey, R.; Olson, A. J. Distributed Automated Docking of Flexible Ligands to Proteins: Parallel Applications of AutoDock 2.4. *J. Comput.-Aided Mol. Des.* **1996**, *10*, 293–304.
- 77) Morris, G. M.; Goodsell, D. S.; Halliday, R. S.; Huey, R.; Hart, W. E.; Belew, R. K.; Olson, A. J. Automated Docking Using a Lamarckian Genetic Algorithm and Empirical Binding Free Energy Function. *J. Comput. Chem.* **1998**, *19*, 1639–1662.
- 78) Zhao, R.; Jia, T.; Shi, H.; Huang, C. A versatile probe for serum albumin and its application for monitoring wounds in live zebrafish. *J. Mater. Chem. B.* **2019**, *7*, 2782–2789.
- 79) Sudlow, G.; Birkett, D. J.; Wade, D. N. The Characterization of Two Specific Drug Binding Sites on Human Serum Albumin. *Mol. Pharmacol.* **1975**, *11*, 824–832.
- 80) Sudlow, G.; Birkett, D. J.; Wade, D. N. Further Characterization of Specific Drug Binding Sites on Human Serum Albumin. *Mol. Pharmacol.* **1976**, *12*, 1052–1061.

- 81) Ibrahim, N.; Ibrahim, H.; Kim, S.; Nallet, J. P.; Nepveu, F. Interactions between Antimalarial Indolone-*N*-oxide Derivatives and Human Serum Albumin. *Biomacromolecules* **2010**, *11*, 3341–3351.
- 82) Lakowicz, J. R. Fluorescence Anisotropy. In *Principles of Fluorescence Spectroscopy*, 3rd ed.; Springer: New York, **2006**; pp 353–381.
- 83) Sasmal, M.; Islam, A. S. M.; Bhowmick, R.; Maiti, D.; Dutta, A.; Ali, M. Site-selective interaction of human serum albumin with 4-chloro-7-nitro-1, 2, 3-benzoxadiazole modified olanzapine derivative and effect of  $\beta$ -cyclodextrin on binding: In the light of spectroscopy and molecular docking. *ACS Appl. Bio Mater.* **2019**, *2*, 3551–3561.
- 84) Sedmak, J. J.; Grossberg, S. E. A rapid, sensitive, and versatile assay for protein using Coomassie brilliant blue G250. *Anal. Biochem.* **1977**, *79*, 544–552.
- 85) Kouzuma, T.; Uemastu, Y.; Usami, T.; Imamura, S. Study of glycated amino acid elimination reaction for an improved enzymatic glycated albumin measurement method. *Clin. Chim. Acta* **2004**, *346*, 135–143.

## Chapter 4

Site-Selective Interaction of Human Serum Albumin with 4-Chloro-7-nitro-1,2,3-benzoxadiazole Modified Olanzapine Derivative and Effect of  $\beta$ -Cyclodextrin on Binding: In the Light of Spectroscopy and Molecular Docking





### Abstract:

Here, we present a detailed investigation on the interaction of 4-chloro-7-nitro-1,2,3-benzoxadiazole (NBD) embedded olanzapine derivative (OLA-NBD) with a model transport protein, human serum albumin (HSA). The thermodynamic parameters,  $\Delta H^\circ$ ,  $\Delta S^\circ$ , and  $\Delta G^\circ$ , as evaluated by considering the van't Hoff relationship imply the major contribution of electrostatic/ionic interactions for the HSA–OLA-NBD association. The OLA-NBD induced quenching of HSA emission occurs through static quenching mechanism, indicating a 1:1 association, as portrayed from Benesi–Hildebrand plot, with  $\sim 10^4 \text{ M}^{-1}$  association constant value, and it is in good harmony with the value estimated from anisotropy experiment. The invariance of the time-resolved decay behavior of HSA with added OLA-NBD concentration, along with matching dependency of the binding constant ( $K_b$ ) value on temperature, also supports the occurrence of static quenching. The pronounced blue shift and increased fluorescence enhancement upon interaction with HSA over other biological interferents, makes the OLA-NBD molecule a valuable sensing agent in complex biological environments. The marked increase in fluorescence intensity and average lifetime value of OLA-NBD in the presence of HSA can be attributed to the increased motional constraint imposed by the rigid and nonpolar microenvironment within HSA, which subsequently limits accessible nonradiative decay processes of OLA-NBD. The effect of  $\beta$ -cyclodextrin on HSA–OLA-NBD binding is characterized by a smaller  $K_b$  value revealing that the OLA-NBD molecules are gradually removed from  $\beta$ -CD by HSA to achieve its medicinal outcome of drug delivery. The outcome from circular dichroism (CD) illustrates the variation of HSA secondary structure upon interaction with OLA-NBD. Concurrently, HSA–OLA-NBD association kinetics is also explored by applying the fluorescence technique. The possible interaction zone of OLA-NBD in HSA is investigated from AutoDock-based docking simulation study.

## 4.1 Introduction

Protein molecules are the basic units of all living cells and encompass a number of essential roles in numerous biological functions depending on their wide range structures. Hence, the measurement of binding of small molecules/drugs with a protein is very much crucial. As the structural variation can influence the functional properties of a protein, cautious control over such interactions is very much pertinent.<sup>1</sup> Among the large variety of proteins, serum albumin is a well-known primary constituent of blood plasma. To recognize the pharmacokinetic and pharmacodynamic properties of drug molecules, their binding toward plasma protein is significant, which helps us to understand the drug circulation and to ascertain its free fraction accessible to the target.<sup>2,3</sup>

Human serum albumin (HSA) consists of 585 amino acid residues<sup>4</sup> and is the main globular transport protein of the blood circulatory system, containing ~60% of plasma consistent with 42 mg/mL concentration and contributing ~80% of total colloid osmotic pressure in the body system.<sup>5,6</sup> The secondary structure of free HSA contains about 67%  $\alpha$ -helix with 17 disulphide (S-S) bridges. The tertiary structure has three homologous domains (I, II, and III), each consisting of two subdomains, A and B.<sup>7,8</sup> Trp 214 is the only one tryptophan amino acid residue present in HSA. The ligand binding sites of HSA are mainly located in hydrophobic regions in subdomain IIA at binding site I and subdomain IIIA at binding site II.<sup>9,10</sup> Additionally, crystal structure analysis and drug binding studies proposed that most of the neutral, bulky, and heterocyclic compounds bind at site I by hydrophobic interactions, while most of the aromatic carboxylic acid compounds bind at site II by van der Waals, ionic, and hydrogen-bonding interactions.<sup>7-10</sup> The hydrophobic binding regions play a vital role in drug deposition and efficiency by improving the solubility of various drugs to plasma and tuning their delivery to *in vivo* and *in vitro* cells.<sup>11</sup> Besides this, protein-drug interaction significantly affects the various important properties of drugs like absorption, distribution, metabolism, and excretion properties.<sup>12</sup> HSA is familiar for its high conformational flexibility to an astonishingly wide range of drugs/small molecules.<sup>13-21</sup> Therefore, the study on molecular level binding of drug/small molecules with serum albumins is important and essential for drug development.

Schizophrenia and bipolar disorder treatment are based on the antipsychotics or neuroleptics drugs but they suffer limited usefulness.<sup>22</sup> An atypical antipsychotic drug, olanzapine, is considered to be highly operative for mood stabilizer and schizophrenia treatment, and that

reveals a comprehensive pharmacological profile through a number of receptors.<sup>3,23-25</sup> Here, we have synthesized a 4-chloro-7-nitro-1,2,3-benzoxadiazole (NBD) embedded fluorescent derivative of olanzapine, OLA-NBD, for protein binding studies. We have selected NBD as the fluorophore molecule due to its emission at longer wavelengths and since the small size does not usually influence on the affinity of parent ligand. Also, NBD-containing compounds become highly fluorescent on binding with hydrophobic sites in proteins.<sup>26</sup>

$\beta$ -Cyclodextrin ( $\beta$ -CD) is a cyclic oligomer consisting of seven  $\alpha$ -D-glucopyranose units. A variety of inclusion complexes can be formed by  $\beta$ -CD with a numerous number of inorganic and organic molecules by increasing the stability, bioavailability, and solubility of the guest compounds. It has been also extensively used in organic synthesis, food plant, and pharmacological science.<sup>27</sup> Therefore, it is essential to investigate the effect of  $\beta$ -CD on the HSA–OLA-NBD binding.

The goal of the current work deals with the binding behavior between HSA and OLA-NBD, using various useful spectroscopy techniques. Fluorescence spectroscopy and lifetime studies were executed to explore the quenching mechanism involved in the binding process. Specific binding site was confirmed with the help of site-selective binding and molecular docking experiments. The circular dichroism (CD) spectral investigation was used to analyze the variation of HSA secondary structure upon association with OLA-NBD. Besides this, an attempt was made toward the determination of OLA-NBD–HSA binding kinetics by the fluorescence technique.

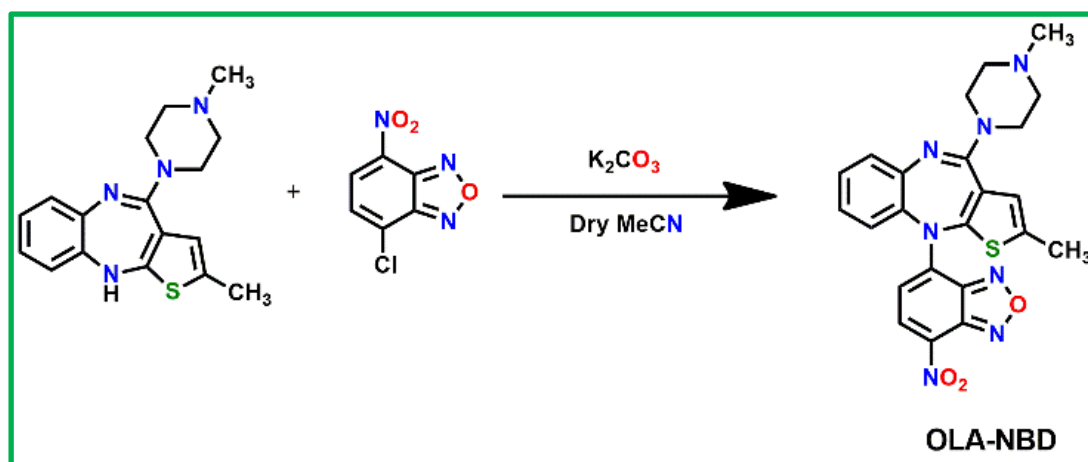
## 4.2 Experimental Section

### 4.2.1 Materials

Olanzapine, 4-chloro-7-nitro-1,2,3-benzoxadiazole (NBD),  $K_2CO_3$ , ibuprofen, warfarin, 8-anilino-1-naphthalene sulfonic acid (ANS), *p*-nitrophenyl acetate (PNPA), and  $\beta$ -cyclodextrin were obtained from Sigma-Aldrich and used as received. All the proteins and enzymes (HSA,  $\beta$ -lactoglobulin, lysozyme, CT-DNA, hemoglobin, cytochrome C, proteinase K, collagen, and trypsin) were also obtained from Sigma Aldrich. Reagent-grade solvents such as methanol, ethanol, dimethylformamide, acetonitrile ( $CH_3CN$ ) etc. (Merck, India) were dried before use according to standard method.

### 4.2.2 Instrumentation

To obtain the Fourier Transform Infrared (FT-IR) spectra in the range 4000-400  $\text{cm}^{-1}$  with a solid KBr disc a Perkin-Elmer RX I FT-IR spectrophotometer was used. An Agilent diode-array UV-Vis Spectrophotometer (Agilent 8453) was used to record the absorption spectra in the range 200-900 nm. The fluorescence spectral measurements were performed on a PTI spectrofluorimeter (Model QM-40) by using a quartz cuvette of 1 cm path length. Both the excitation and emission slit widths were made at 3 nm. A Bruker Avance 600 MHz NMR spectrophotometer was used to record the  $^1\text{H}$ - and  $^{13}\text{C}$ -NMR spectra in dimethyl sulfoxide (DMSO)- $d_6$  by using an internal standard, tetramethyl silane ( $\delta = 0$ ). The ESI-MS $^+$  (m/z) spectra of the probe was recorded on a HRMS spectrophotometer (Waters, Model: QTOF Micro YA263). Fluorescence lifetime studies were carried out by the technique of time correlated single photon counting (TCSPC) measurements with a picosecond diode laser (IBH Nanoled-07) in an IBH fluorocube apparatus. To assemble the fluorescence decay signals a Hamamatsu MCP photomultiplier (R3809) was used and the decays were further scrutinized by the IBH DAS6 software. Circular dichroism (CD) spectral investigations were performed in a PC-driven JASCO J815 (Japan) spectropolarimeter.



Scheme 4.1 Synthesis of OLA-NBD.

### 4.2.3 Synthesis and Characterization of OLA-NBD

OLA-NBD was synthesized by following the literature method<sup>28</sup> in a slightly modified way (Scheme 4.1). Olanzapine (0.312 g, 1 mmol) and  $\text{K}_2\text{CO}_3$  (0.345 g, 2.5 mmol) were mixed in 20 mL of dry  $\text{CH}_3\text{CN}$  solution with constant stirring.

Then NBD-Cl (0.20 g, 1 mmol) in 10 mL of dry CH<sub>3</sub>CN was added dropwise at room temperature, and the reaction mixture was further stirred for 6 h. Then the residue was filtered off by suction and washed several times by CHCl<sub>3</sub>. The combined solution (filtrate and the CHCl<sub>3</sub>) was evaporated in vacuum to get a solid product. The product was then subjected to silica gel column chromatography, and ethyl acetate/methanol (v/v, 8:2) was used as eluent to get a pure deep green solid (yield: 69%). (Scheme 4.1). <sup>1</sup>H NMR (DMSO-*d*<sub>6</sub>): δ in ppm = 8.56 (d, 1H, -ArH), 7.50 (d, 1H, -ArH), 7.37 (t, 1H, -ArH), 7.21 (m, 2H, -ArH), 6.77 (s, 1H, -ArH), 6.61 (d, 1H, -ArH), 3.50 (d, 6H, -CH<sub>2</sub>), 2.48 (s, 3H, -CH<sub>3</sub>), 2.25 (d, 2H, -CH<sub>2</sub>), 2.04 (s, 3H, -CH<sub>3</sub>) (Figure 4.1). <sup>13</sup>C NMR (DMSO-*d*<sub>6</sub>): δ in ppm = 154.35, 144.69, 144.66, 144.29, 143.89, 140.42, 136.13, 129.65, 127.80, 127.03, 127.00, 126.33, 124.38, 122.51, 106.28, 54.47, 45.74, 16.08 (Figure 4.2). ESI-MS<sup>+</sup>: *m/z* = 476.1401 [C<sub>23</sub>H<sub>21</sub>N<sub>7</sub>O<sub>3</sub>S + H<sup>+</sup>] (Figure 4.3). IR Spectrum:  $\tilde{\nu}$  = 1527 cm<sup>-1</sup> (-NO<sub>2</sub>) (Figure 4.4).

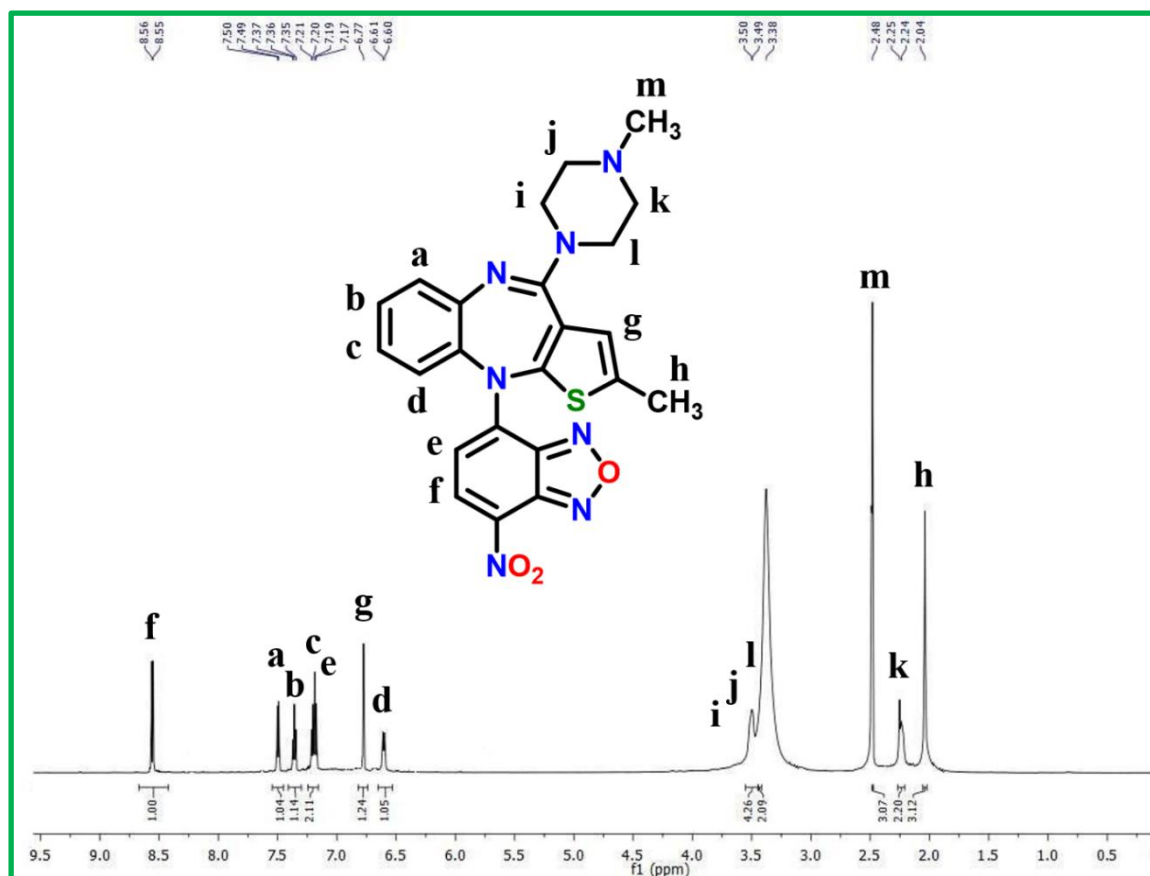


**Figure 4.1** <sup>1</sup>H-NMR spectrum of OLA-NBD in DMSO-*d*<sub>6</sub> in Bruker Avance 600 MHz instrument.

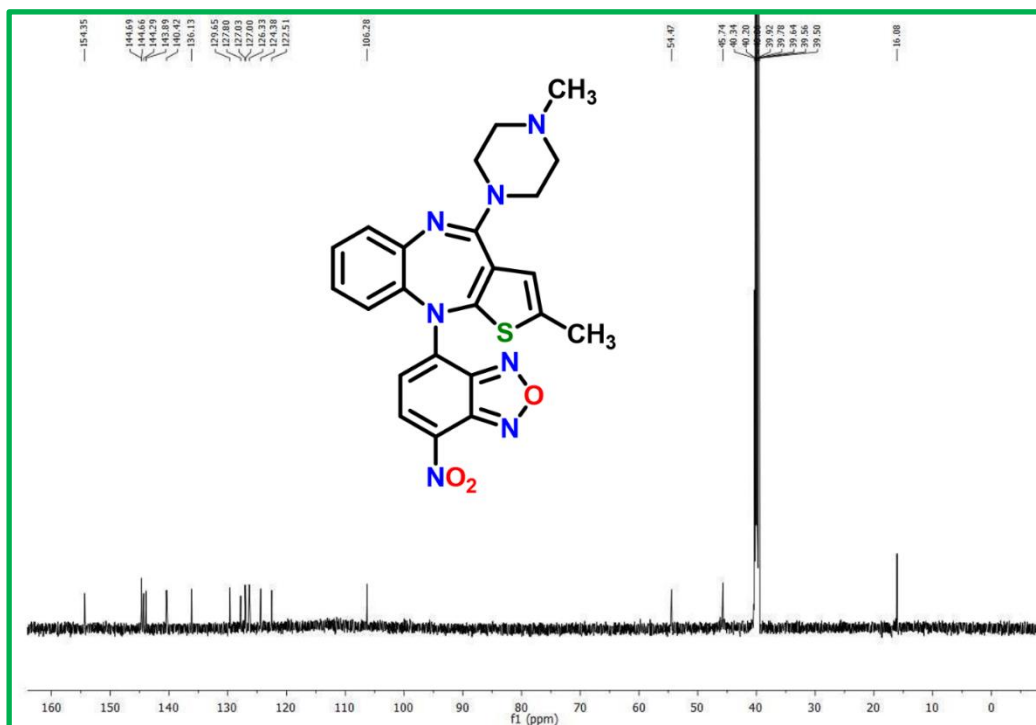


**Figure 4.2**  $^{13}\text{C}$ -NMR spectrum of OLA-NBD in  $\text{DMSO-}d_6$  in Bruker Avance 600 MHz instrument.

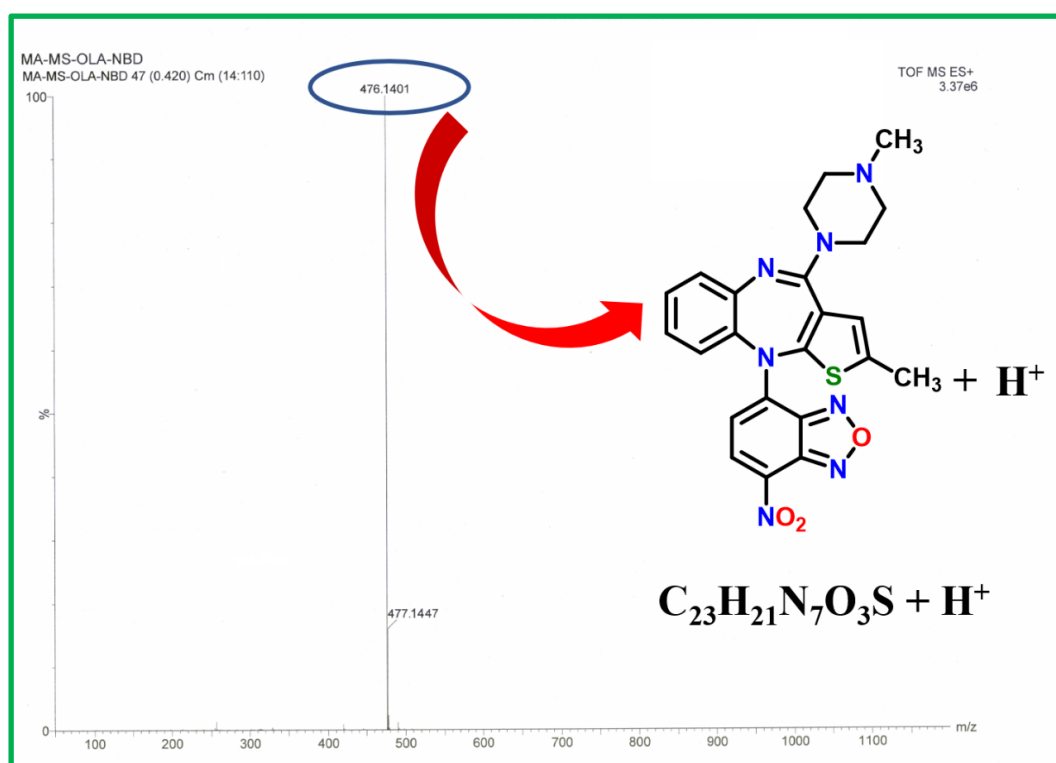


**Figure 4.3** Mass spectrum of OLA-NBD in  $\text{CH}_3\text{CN}$ .

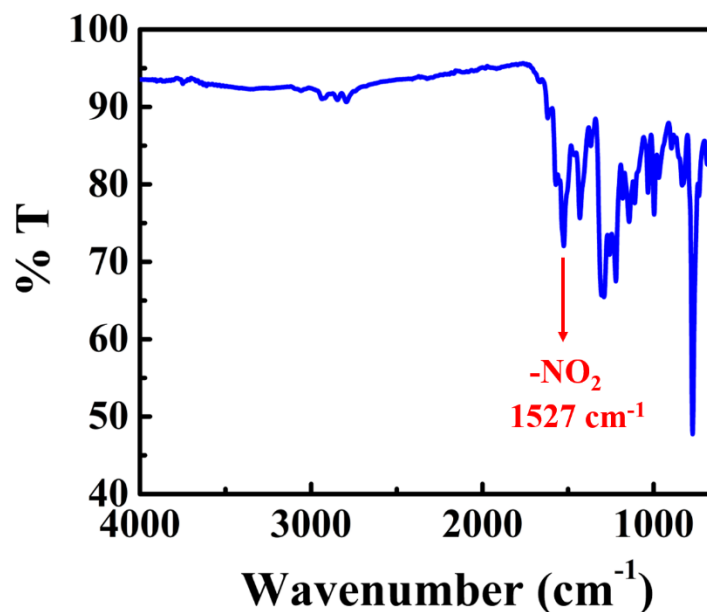


Figure 4.4 IR spectrum of OLA-NBD.

#### 4.2.4 Experimental Solution

A 250 ml 10 mM Tris-HCl buffer solution of pH 7.4 was prepared in deionized Milli pore water and used in all studies. HSA stock solution was prepared in Tris-HCl buffer solution and the exact concentration was evaluated spectrophotometrically by considering the extinction co-efficient value ( $35,000 \text{ M}^{-1} \text{ cm}^{-1}$ ) at 280 nm.<sup>29</sup> Whereas, the 10 ml stock solution of OLA-NBD ( $1.0 \times 10^{-3} \text{ M}$ ) was prepared in  $\text{CH}_3\text{CN}$  due to lack of solubility in water.  $\beta$ -Cyclodextrin stock solution was also prepared in abovesaid buffer solution. The stock solutions of other proteins, enzymes and biomolecules were prepared as required, and the exact concentrations of the protein stock solutions were evaluated spectrophotometrically by considering the absorbance and molar extinction coefficient values at particular wavelengths as relevant. Each solution was mixed thoroughly prior to all the spectral investigations.

#### 4.2.5 UV-Vis and Fluorescence Spectroscopic Studies

All the UV-vis spectra were collected with proper background correction. The absorption titrations were carried out at a fixed concentration of HSA ( $5 \mu\text{M}$ ) and then with the gradual addition of OLA-NBD (0-20  $\mu\text{M}$ ).

For the fluorescence studies, a fixed amount of OLA-NBD ( $5 \mu\text{M}$ ) was titrated with the increasing concentration of HSA (0-48  $\mu\text{M}$ ) upon excitation at 465 nm. Whereas, in another



experiment a fixed amount of HSA (5 μM) was titrated with the increasing concentration of OLA-NBD (0-30 μM) upon excitation at 295 nm. Accompanied by this, the effect of β-Cyclodextrin on the interaction process was also investigated at a constant concentration of HSA (5 μM) and β-Cyclodextrin (1.0 mM) with successive addition of OLA-NBD (0-30 μM). The kinetics of association between OLA-NBD and HSA was monitored at 334 nm on PTI QM-40 spectrofluorimeter. Resonance Rayleigh scattering spectral studies for the HSA–OLA-NBD complex were carried out by synchronous scanning at  $\Delta\lambda = 0$  ( $\lambda_{em} = \lambda_{ex}$ ) in the wavelength range of 200-700 nm. The inner filter effect correction has been made for all the fluorescence spectra presented in the manuscript according to the following equation:<sup>30</sup>

$$I = I_{obs} \times e^{(A_{ex} + A_{em})/2} \quad (1)$$

Where, the corrected and observed emission intensity are denoted by  $I$  and  $I_{obs}$ , respectively.  $A_{ex}$  and  $A_{em}$  designates the absorbance value of the sample at the excitation and emission wavelengths, respectively.

#### 4.2.6 Steady-State Fluorescence Anisotropy

Fluorescence anisotropy ( $r$ ) measurements were carried out by considering the following equation described by Larsson *et al.*<sup>31</sup>

$$r = \frac{I_{VV} - GI_{VH}}{I_{VV} + 2GI_{VH}} \quad (2)$$

Where, the polarizer positions were set at (0°, 0°), (0°, 90°), (90°, 0°), and (90°, 90°) to get  $I_{VV}$ ,  $I_{VH}$ ,  $I_{HV}$ ,  $I_{HH}$  for excitation and emission signals respectively.  $G$  factor is defined as

$$G = \frac{I_{HV}}{I_{HH}} \quad (3)$$

Where,  $I_{HV}$  and  $I_{HH}$  are respectively the vertical and horizontal component of emission polarizer, keeping the excitation polarizer horizontal.  $G$  depends on slit widths and monochromator wavelength. The excitation and emission wavelengths were fixed at 465 and 555 nm respectively.

#### 4.2.7 Esterase-Like Activity Study

The esterase-like activity study was performed to determine the effect of OLA-NBD on the functionality of HSA. Here, the HSA activity is examined by measuring the absorbance value of *p*-nitrophenol ( $\lambda_{abs} = 400$  nm, molar extinction coefficient,  $\epsilon = 17,700 \text{ M}^{-1} \text{ cm}^{-1}$ )<sup>32-34</sup> as

formed by the reaction between the substrate (*p*-nitrophenyl acetate (PNPA)) and the enzyme (HSA). The reaction kinetics was recorded on Agilent 8453 UV-Vis Spectrophotometer. Here, the reaction conditions were maintained as follows: [HSA] = 25  $\mu\text{M}$ , [PNPA] = 50  $\mu\text{M}$ , pH 7.4, temperature = 37  $^{\circ}\text{C}$ . Here, one unit of activity is expressed as to be the quantity of HSA required for releasing 1  $\mu\text{M}$  *p*-nitrophenol per minute at 37  $^{\circ}\text{C}$ .

### 4.2.8 Circular Dichroism (CD) Spectra

All the reported CD spectra were recorded in the wavelength range 195-300 nm under constant purging of nitrogen and a scan speed of 100 nm min<sup>-1</sup>. Here, a fixed concentration of HSA (1.25  $\mu\text{M}$ ) was titrated with the increasing concentration of OLA-NBD from 0  $\mu\text{M}$  to 8  $\mu\text{M}$  in Tris-HCl buffer solution of pH 7.4 at 25  $^{\circ}\text{C}$ . Each CD spectrum was an average of five scans and the baseline correction was performed with Tris-HCl buffer signal.

### 4.2.9 Detection Limit

The detection limit was calculated on the basis of the fluorescence titration with HSA. The fluorescence emission spectrum of OLA-NBD was measured 10 times to calculate the standard deviation of blank measurement. Then, the fluorescence emission at 533 nm was plotted as a function of the concentration of HSA from the corresponding titration experiment to evaluate the slope. The detection limit was then calculated using the following equation:<sup>35</sup>

$$\text{Detection limit} = 3\sigma/k \quad (4)$$

Where “ $\sigma$ ” is the standard deviation of blank measurement, and “ $k$ ” is the slope of the plot of fluorescence emission intensity as a function of [HSA].

### 4.2.10 Fluorescence Lifetime Measurements

The TCSPC measurements were carried out in 10 mM Tris-HCl buffer solution of pH 7.4 for the fluorescence decay of OLA-NBD in the absence and presence of increasing concentration of HSA at 25  $^{\circ}\text{C}$ . Further, the fluorescence decay of HSA was performed in the absence and in the presence of increasing concentration of OLA-NBD to assess its interaction with OLA-NBD. The instrument response function (IRF) was ascertained experimentally by using dilute micellar solution of SDS in water as light signal scatterer. During the TCSPC measurements the photoexcitation was fixed at 450 nm for OLA-NBD, and at 300 nm for HSA. The fluorescence decay data were collected by using eq 5:

$$F(t) = \sum_i \alpha_i \exp\left(-\frac{t}{\tau_i}\right) \quad (5)$$

Where,  $\alpha_i$  represents the  $i$ th pre-exponential factor and  $\tau_i$  denotes the decay time of component  $i$ . The decay time is mentioned to as the lifetime of the excited species. The average lifetimes ( $\langle \tau \rangle$ ) for the fluorescence decay profiles were calculated by using the following equation:<sup>36</sup>

$$\langle \tau \rangle = \frac{\sum_i \alpha_i \tau_i}{\sum_i \alpha_i} \quad (6)$$

#### 4.2.11 Molecular Docking Simulation Study

To recognize the possible binding sites within HSA and the mode of binding of OLA-NBD with HSA, molecular docking study was performed using docking program AutoDock (version 4.2). The X-ray crystal structure of human serum albumin was taken from RCSB Protein Data Bank having PDB ID: 1AO6. To draw the structure of OLA-NBD, Chem3D Ultra 8.0 was used and further modification was carried out by using Gaussian 09W and AutoDock 4.2 programs. Gasteiger charges and polar hydrogen atoms were added to the protein and probe. Grid box with dimensions of  $120 \text{ \AA} \times 120 \text{ \AA} \times 120 \text{ \AA}$  and  $0.403 \text{ \AA}$  grid spacing were specified to enclose the protein using AutoGrid program. The default values shown by the AutoDock program were used for other sets of parameters. The Lamarckian genetic algorithm (LGA) was used to accomplish docking calculations and the grid maps for energy were calculated by AutoGrid.<sup>37-39</sup> The best optimized docked model with lowest binding energy was considered for further study of docking simulations and the output was best viewed by using PyMOL software.

### 4.3 Results and Discussion

#### 4.3.1 Effect of OLA-NBD on the Absorption Spectra of HSA

UV-Vis absorption study is widely recognized in terms of analysis of the structural modifications as well as to understand the complex formation in solution.<sup>40,41</sup> **Figure 4.5A** exhibits the absorption spectra of HSA with the incremental addition of OLA-NBD in aqueous Tris-HCl buffer solution. Absorbance of HSA increases at 280 nm on addition of OLA-NBD, and at the same time, absorbance peak at 465 nm also increases due to OLA-NBD (**Figure 4.5B**). The absorption spectral pattern also changes with added concentration

of OLA-NBD. This finding is well supported toward the complexation between OLA-NBD and HSA.

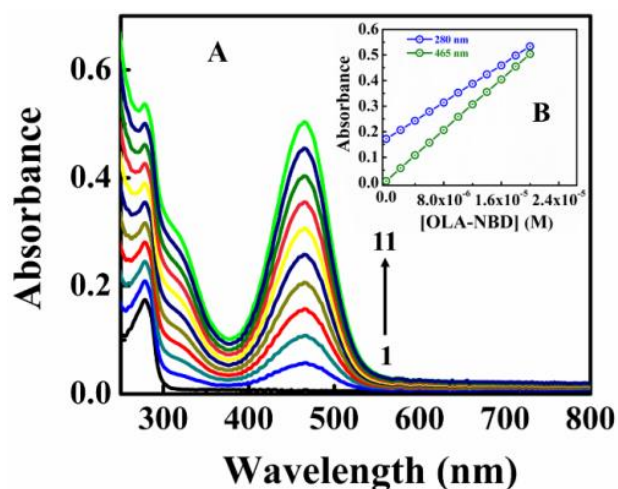


**Figure 4.5** (A) Absorption spectral variations of HSA (5  $\mu\text{M}$ ) with gradual addition of OLA-NBD (0-20  $\mu\text{M}$ ). (B) Inset: plot of absorbance at 280 and 465 nm, respectively, with OLA-NBD concentration.

### 4.3.2 Fluorescence Emission Measurement

Steady-state fluorescence emission measurement is a valuable technique to examine the interactions of drugs/small molecules with proteins. At first, we systematically recorded fluorescence responses of OLA-NBD (5  $\mu\text{M}$ ) in Tris-HCl buffer solution (pH 7.4) by the addition of excess amount (10 equiv.) of different proteins and enzymes, including  $\beta$ -lactoglobulin, lysozyme, CT-DNA, hemoglobin, cytochrome C, proteinase K, collagen, trypsin, and HSA. Here, it was also worth noting that only HSA was capable of enhancing the fluorescence intensity at 533 nm among the different proteins and enzymes tested (**Figure 4.6**). Then, fluorescence titrations were executed to ensure the OLA-NBD–HSA interaction at 5  $\mu\text{M}$  OLA-NBD concentration in aqueous buffer solution with the successive addition of HSA protein. The maximum emission intensity of OLA-NBD is blue-shifted ( $\sim 22$  nm) from 555 to 533 nm in 48  $\mu\text{M}$  HSA solution with simultaneous prominent increase in emission intensity ( $\sim 5$ -fold) upon excitation at 465 nm (**Figure 4.7A**). The modulations of emission intensity and  $\lambda_{\text{em}}^{\text{max}}$  of the OLA-NBD with HSA concentration are more plainly presented in **Figure 4.7B**, which demonstrates an early steep rise of emission intensity up to 20  $\mu\text{M}$  HSA and afterward the achievement of a plateau region likely indicating the saturation of OLA-NBD–HSA interaction.

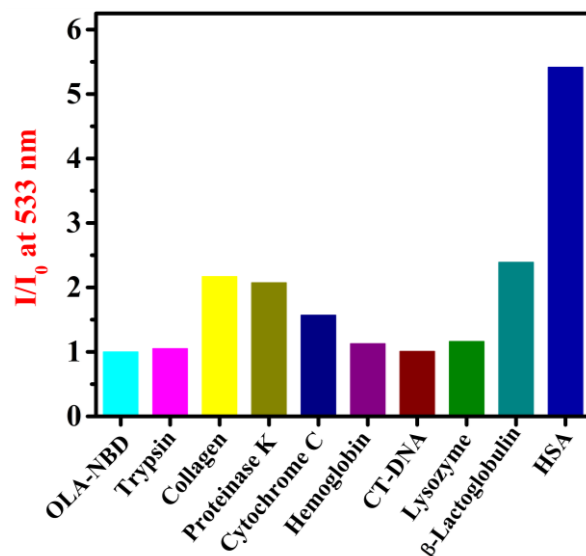


**Figure 4.6** Variations in emission intensity ( $I/I_0$ ) of OLA-NBD (5  $\mu$ M) at 533 nm in Tris-HCl buffer solution (pH 7.4) by the addition of excess amount (10 equiv.) of different proteins and enzymes.  $\lambda_{ex}$  = 465 nm.

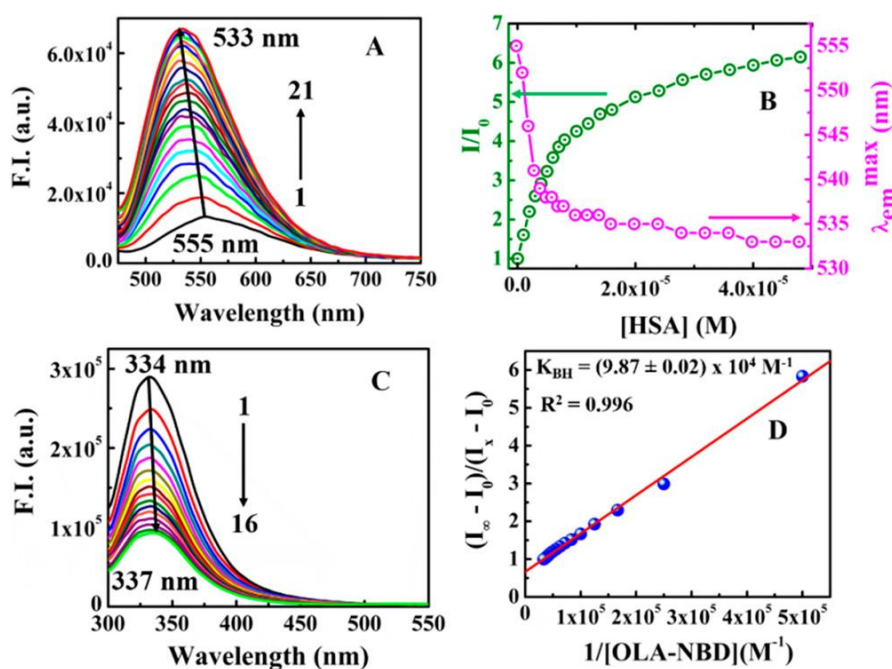


**Figure 4.7** (A) Effect of HSA addition (0-48  $\mu$ M) on the OLA-NBD (5  $\mu$ M) emission spectra. (B) Variation of  $\lambda_{em}^{max}$  and relative intensity of OLA-NBD with HSA. (C) Quenching of HSA (5  $\mu$ M) emission with successive addition of OLA-NBD (0-30  $\mu$ M) at 25  $^{\circ}$ C. (D) Characteristic B-H plot for HSA and OLA-NBD association.  $\lambda_{ex}$  for OLA-NBD and HSA are 465 and 295 nm, respectively.

Such variation of the emission profile in the presence of HSA indicates toward the immense modification of microenvironment surrounding of OLA-NBD within the protein hydrophobic medium compared with the polar aqueous medium. This blue shift in emission band resulting from the reduction in polarity of microenvironment was previously reported.<sup>15,42-45</sup>

Trp, tyrosine (Tyr), and phenylalanine (Phe) are three main amino acid residues responsible for the emission of proteins.<sup>46</sup> Particularly, Trp emission is considered to monitor the structural conformation changes in HSA protein and to elucidate the microenvironment around the HSA bound small molecules.<sup>21</sup> Trp 214 is the only one Trp residue present in subdomain IIA of HSA.<sup>4,46</sup> In aqueous medium, HSA exhibits a emission maximum at 334 nm when it is excited at 295 nm. Excitation was made at 295 nm to reduce the fluorescence contribution from Tyr residue.

To evaluate the binding constant of HSA-OLA-NBD association, a 5  $\mu\text{M}$  concentration of HSA protein was titrated with the incremental addition of OLA-NBD. **Figure 4.7C** displays that upon interaction of OLA-NBD with HSA, the emission intensity is quenched significantly along with a small red shift ( $\sim 3$  nm) of emission maxima from 334 to 337 nm, which indicates that OLA-NBD undergoes strong complexation with HSA and modification of local microenvironment around Trp moiety present in HSA.<sup>47</sup>

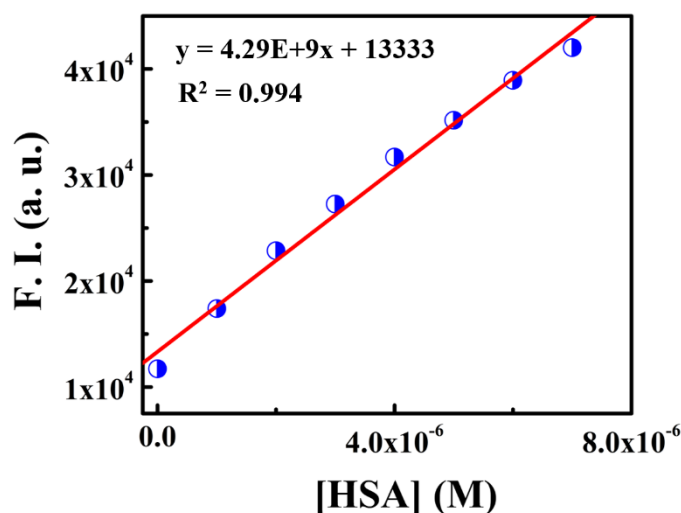
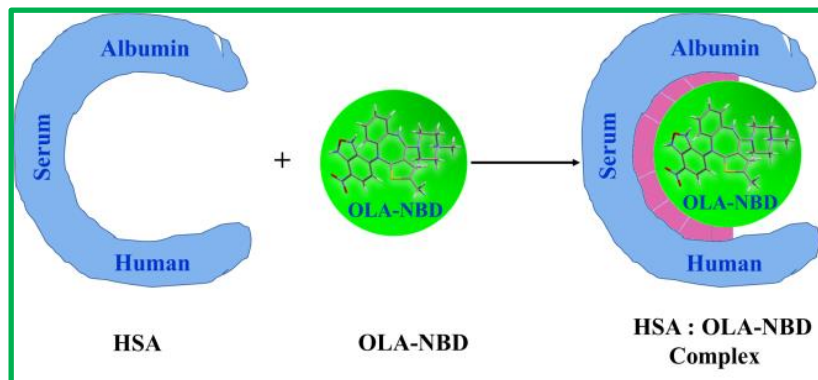


**Figure 4.8** Linear fluorescence response of OLA-NBD (5  $\mu\text{M}$ ) to HSA (0-7  $\mu\text{M}$ ) at 533 nm for LOD determination. The LOD value was estimated from 10 times the standard deviation ( $\sigma$ ) of the fluorescence intensity corresponding to the blank sample (OLA-NBD only). Here,  $\sigma$  value is 85.082. From the graph we get slope =  $4.29 \times 10^9 \text{ M}^{-1}$ .

Moreover, by exploiting the linear dependence of the OLA-NBD emission changes as a function of HSA concentration (Figure 4.8), the limit of detection (LOD) value was estimated to be 59.4 nM.



Scheme 4.2 Complexation of OLA-NBD with HSA in 1:1 Stoichiometry.

### 4.3.3 HSA–OLA-NBD Complexation Equilibrium and Stoichiometric Study

The complexation process of the OLA-NBD with HSA may be portrayed in Scheme 4.2, and the data found from the spectrofluorimetric titration of a constant concentration of HSA with gradual addition of OLA-NBD were examined to evaluate the binding constant by using Benesi-Hildebrand (B-H) equation:<sup>48</sup>

$$\frac{\Delta I_{\max}}{\Delta I} = 1 + \frac{1}{K_{\text{BH}} [\text{OLA-NBD}]} \quad (7)$$

Where  $K_{\text{BH}}$  signifies the association constant. Here,  $\Delta I_{\max} = |I_{\infty} - I_0|$  and  $\Delta I = |I_x - I_0|$ .  $I_0$ ,  $I_x$ , and  $I_{\infty}$  designate the emission intensities of HSA in free state, at an intermediate OLA-NBD concentration and at OLA-NBD concentration when complete saturation occurred, respectively.  $|I_{\infty} - I_0| / |I_x - I_0|$  versus  $1/[\text{OLA-NBD}]$  plot shows a linear variation (Figure 4.7D), which affirms the validity of the eq 7 and supports the 1:1 association between OLA-NBD and HSA. The 1:1 interaction of OLA-NBD with HSA was also confirmed by Job’s plot experiment. In this technique, the fluorescence data were noted by varying the OLA-NBD:HSA molar ratio, while the total molar concentration remained constant.<sup>49</sup> The Job’s plot for OLA-NBD–HSA, that is,  $\Delta I$  at 334 nm versus the mole fraction of OLA-NBD (Figure 4.9) crossed at 0.507, showing that number of OLA-NBD molecules associated with HSA, is close to unity. The calculated value of  $K_{\text{BH}}$  and the related free energy change ( $\Delta G$ ) are tabulated in Table 4.1, inferring strong association of OLA-NBD with HSA.



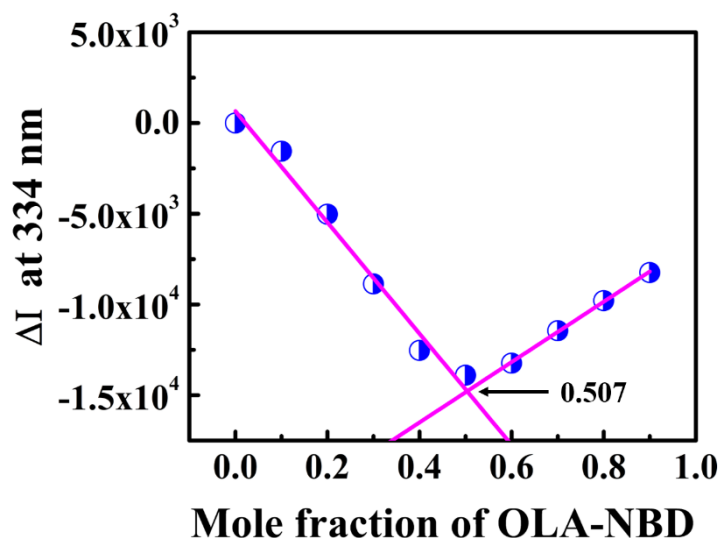


**Figure 4.9** Job's plot for the binding of OLA-NBD to HSA.

**Table 4.1** Binding parameters for association of HSA with OLA-NBD at 25 °C.

method	environment	binding constant ( $10^4 \text{ M}^{-1}$ )	$\Delta G$ (kJ mol <sup>-1</sup> )
Benesi-Hildebrand	HSA-OLA-NBD	(9.87 ± 0.02)	-28.49
fluorescence anisotropy	HSA-OLA-NBD	(10.11 ± 0.23)	-28.55

#### 4.3.4 Intrinsic Fluorescence Quenching of HSA by OLA-NBD

The gradual addition of OLA-NBD (0-30  $\mu\text{M}$ ) into HSA solution (5  $\mu\text{M}$ ) persuades the quenching of HSA fluorescence intensity (Figure 4.7C). This observable fact can be ascribed to the association between OLA-NBD and HSA involving some plausible mechanisms such as ground state complexation, collisional quenching, excited state reactions, molecular rearrangements, energy transfer, etc.<sup>46</sup> The quenching mechanism is usually classified as either static or dynamic. The ground-state association between the fluorophore and the quencher is responsible for former process, whereas collisional encounters between the fluorophore and the quencher at the excited state are responsible for later process.<sup>46,50-52</sup> Static and dynamic quenching processes can be differentiated by their differing temperature dependency and viscosity or by examining the lifetime measurements.<sup>46</sup> Due to the presence

of non-negligible absorbance of OLA-NBD at 295 nm (Figure 4.10) the correction in emission intensity was made to eliminate the inner filter effect by adopting the eq 1.

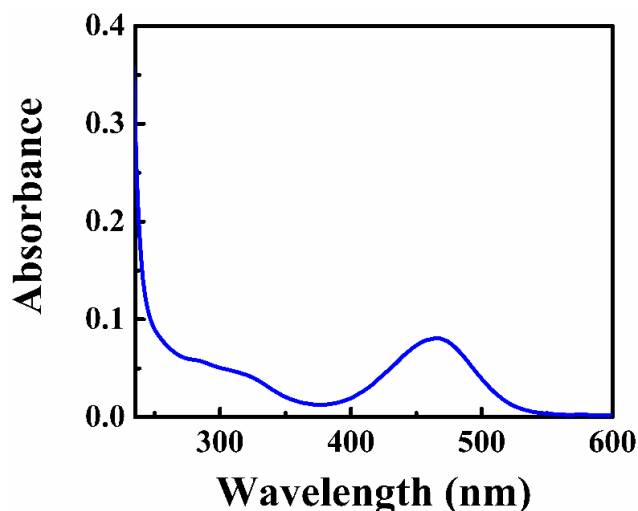


Figure 4.10 Absorption spectra of OLA-NBD (5 μM).

The emission quenching data of HSA–OLA-NBD complexation were examined by the analysis of Stern-Volmer eq 8:<sup>46</sup>

$$\frac{I_0}{I} = 1 + K_{SV}[\text{OLA} - \text{NBD}] = 1 + k_q < \tau_0 > [\text{OLA} - \text{NBD}] \quad (8)$$

Where,  $I_0$  and  $I$  are the HSA emission intensities in the native state and with the increasing concentration of OLA-NBD, respectively.  $K_{SV}$  is the Stern-Volmer constant, and  $k_q$  represents the bimolecular quenching rate constant.  $[\text{OLA-NBD}]$  is the molar concentration of the quencher, and  $< \tau_0 >$  signifies the average lifetime of HSA without OLA-NBD (4.32 ns for HSA). The linear nature of steady-state Stern-Volmer plot, that is,  $I_0/I$  vs.  $[\text{OLA-NBD}]$  (Figure 4.11A) at 298 K indicates that the observed emission quenching of HSA–OLA-NBD conjugate is either due to static or dynamic process. Figure 4.11B displays the trend of linear Stern-Volmer plots at three temperatures, i.e., 283, 293, and 303 K, and associated  $K_{SV}$  and  $k_q$  values are summarized in Table 4.2. The decreasing value of  $K_{SV}$  with the rise in temperature indicates that the quenching process is static rather than dynamic one.<sup>12,20,47</sup> Table 4.2 clearly exhibits that the calculated  $k_q$  values for three temperatures are three orders of magnitude higher than the maximum collisional quenching rate constant value  $2.0 \times 10^{10} \text{ M}^{-1}\text{s}^{-1}$ .<sup>46</sup> This infers the OLA-NBD induced fluorescence quenching of HSA arises through the ground

state complexation between HSA and OLA-NBD or in other words quenching through static process.

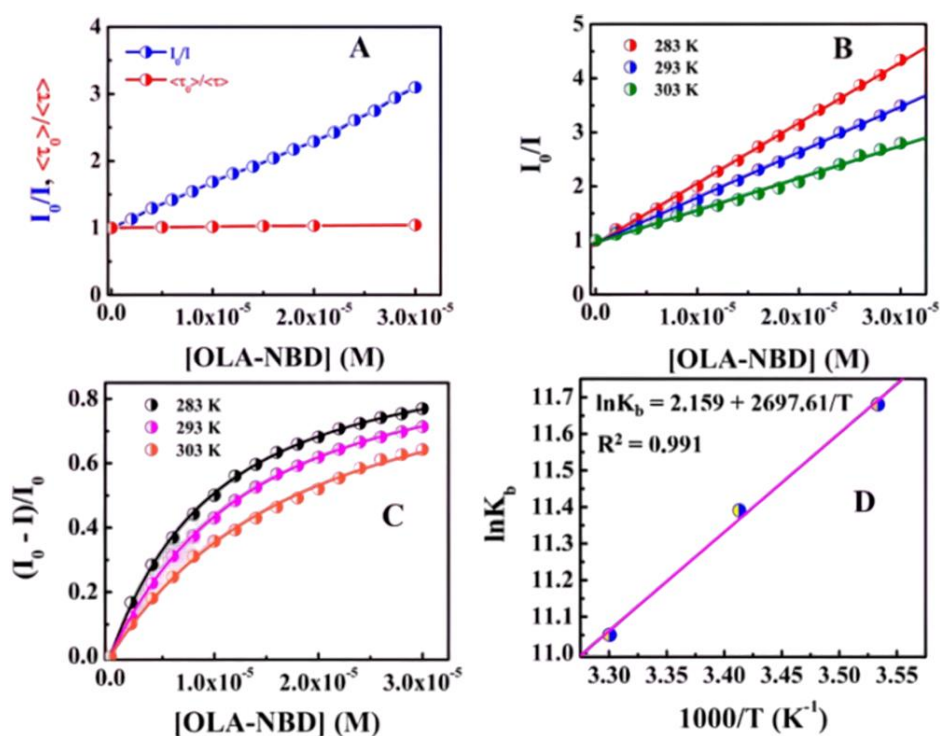


**Figure 4.11** (A) Steady-state ( $I_0/I$ , blue) and time-resolved ( $\langle \tau_0 \rangle / \langle \tau \rangle$ , red) Stern-Volmer plots at 298 K. (B) Characteristic linear Stern-Volmer plots at three different temperatures. (C) Plot of  $(I_0 - I)/I_0$  versus OLA-NBD concentration at different temperatures. (D) Van't Hoff plot for OLA-NBD and HSA association.

**Table 4.2** Stern-Volmer constants ( $K_{SV}$ ), bimolecular quenching rate constants ( $k_q$ ), binding constants ( $K_b$ ), and thermodynamic parameters for the HSA–OLA-NBD association.

$T$ (K)	$K_{SV}$ ( $10^4 M^{-1}$ )	$k_q$ ( $10^{13} M^{-1} s^{-1}$ )	$R^2$	binding constant, $K_b$ ( $10^4 M^{-1}$ )	$\Delta H^0$ (kJ mol $^{-1}$ )	$\Delta S^0$ (J K $^{-1}$ mol $^{-1}$ )	$\Delta G^0$ (kJ mol $^{-1}$ )
283	$11.12 \pm 0.09$	$2.59 \pm 0.09$	0.999	$11.80 \pm 0.13$			-27.50
293	$8.39 \pm 0.06$	$1.94 \pm 0.06$	0.999	$8.92 \pm 0.12$	-22.42	17.95	-27.68
303	$5.96 \pm 0.11$	$1.37 \pm 0.11$	0.994	$6.29 \pm 0.28$			-27.86

### 4.3.5 Determination of HSA-OLA-NBD Binding Constants and Related Thermodynamic Parameters

The binding constant between HSA and OLA-NBD can be evaluated with the help of eqs 9-15, assuming a 1:1 stoichiometric complexation between them.<sup>53</sup> The binding constant ( $K_b$ ) is expressed by eq 10:



$$K_b = \frac{[\text{HSA}:\text{OLA}-\text{NBD}]}{[\text{HSA}]_{\text{free}} [\text{OLA}-\text{NBD}]_{\text{free}}} \quad (10)$$

The free HSA and OLA-NBD concentrations can be defined by

$$[\text{HSA}]_{\text{free}} = [\text{HSA}]_{\text{T}} - [\text{HSA} : \text{OLA} - \text{NBD}] \quad (11)$$

$$[\text{OLA} - \text{NBD}]_{\text{free}} = [\text{OLA} - \text{NBD}]_{\text{T}} - [\text{HSA} : \text{OLA} - \text{NBD}] \quad (12)$$

Where,  $[\text{HSA}]_{\text{T}}$  and  $[\text{OLA} - \text{NBD}]_{\text{T}}$  are the total concentrations of HSA and OLA-NBD, respectively. The concentration of the HSA:OLA-NBD complex is given by

$$[\text{HSA} : \text{OLA} - \text{NBD}] = \frac{1}{2} [([\text{OLA} - \text{NBD}]_{\text{T}} + [\text{HSA}]_{\text{T}} + K_b^{-1}) \pm \sqrt{([\text{OLA} - \text{NBD}]_{\text{T}} + [\text{HSA}]_{\text{T}} + K_b^{-1})^2 - (4[\text{OLA} - \text{NBD}]_{\text{T}}[\text{HSA}]_{\text{T}})}] \quad (13)$$

Eq 14 relates the fluorescence measurements of the above said bimolecular equilibrium:

$$\frac{I_0 - I}{I_0 - I_\infty} = \frac{[\text{HSA}:\text{OLA}-\text{NBD}]}{[\text{HSA}]_{\text{T}}} \quad (14)$$

Here,  $I_0$  and  $I$  denote the fluorescence intensities of HSA in the free state and at different concentration of OLA-NBD, respectively.  $I_\infty$  is the measured fluorescence of HSA at saturation. Replacing eq 13 into eq 14 produces the final equation:

$$\frac{I_0 - I}{I_0 - I_\infty} = \frac{1}{2[\text{HSA}]_{\text{T}}} [([\text{OLA} - \text{NBD}]_{\text{T}} + [\text{HSA}]_{\text{T}} + K_b^{-1}) - \sqrt{([\text{OLA} - \text{NBD}]_{\text{T}} + [\text{HSA}]_{\text{T}} + K_b^{-1})^2 - (4[\text{OLA} - \text{NBD}]_{\text{T}}[\text{HSA}]_{\text{T}})}] \quad (15)$$

Figure 4.11C shows the characteristic  $(I_0 - I)/I_0$  versus  $[\text{OLA}-\text{NBD}]$  plot at three temperatures. The experimental data are best fitted with eq 15, and the binding constant ( $K_b$ )

values for three temperatures thereby obtained are summarized in **Table 4.2**.  $K_b$  value decreases with the rise in temperature and therefore supports the occurrence of static quenching mechanism.<sup>54</sup>

The high value of  $K_b$  indicates a strong association between HSA and OLA-NBD. Hydrogen bonding and hydrophobic, electrostatic, and van der Waal's interactions are the main responsible noncovalent forces for the association of small molecules with proteins.<sup>40,55</sup> To find out the nature of interaction between OLA-NBD and HSA at the ground state in terms of the aforementioned non-covalent forces, the standard enthalpy change ( $\Delta H^0$ ) and standard entropy change ( $\Delta S^0$ ) values can be determined from the van't Hoff relation.<sup>56</sup>

$$\ln K_b = -\frac{\Delta H^0}{RT} + \frac{\Delta S^0}{R} \quad (16)$$

Where,  $R$  denotes the universal gas constant. Then the standard Gibbs free energy ( $\Delta G^0$ ) value is calculated by considering the **eq 17**:

$$\Delta G_{\text{Binding}}^0 = -2.303RT \log K_b = \Delta H^0 - T\Delta S^0 \quad (17)$$

**Figure 4.11D** displays the characteristic  $\ln K_b$  versus  $1/T$  plot, and all the evaluated thermodynamic parameters are presented in **Table 4.2**. In accordance with Ross and Subramanian discussions,<sup>57</sup> the nature of the fundamental forces responsible for an interaction process can be shortly outlined as follows: (i)  $\Delta H^0 > 0$ ,  $\Delta S^0 > 0$  correlate with hydrophobic forces; (ii)  $\Delta H^0 < 0$ ,  $\Delta S^0 < 0$  correlate with van der Waals interaction, hydrogen bond formation; and (iii)  $\Delta H^0 < 0$ ,  $\Delta S^0 > 0$  correlate with electrostatic/ionic interactions. **Table 4.2** indicates that HSA–OLA-NBD binding association is enthalpically and in addition entropically preferred ( $\Delta H^0 < 0$  and  $\Delta S^0 > 0$ ) process. Moreover, the negative value of  $\Delta H^0$  accompanied by a positive value of  $\Delta S^0$  infers the major involvement of electrostatic/ionic interaction for the HSA–OLA-NBD binding process.<sup>40,55</sup> Besides this,  $\Delta G^0 < 0$  also reveals that the binding process is spontaneous.

#### 4.3.6 Steady-State Fluorescence Anisotropy Measurement

Useful information regarding the rigidity of the environment in the instant vicinity of a fluorescent molecular probe can be gathered by steady-state fluorescence anisotropy measurement technique.<sup>47,58</sup> It also delivers the valuable knowledge about the limit to which obstruction of the rotational mobility of the probe can be experienced by a rigid environment

and it is reflected through the variation of anisotropy value. An increment in rigidity of the environment near a fluorescent probe reflects into an augmentation of anisotropy value. **Figure 4.12A** depicts the variation in anisotropy values of OLA-NBD with the increasing HSA concentration in aqueous solution. Initially, a quick increment in the anisotropy ( $r$ ) value was noticed from 0.025 to 0.082 upon addition of 10  $\mu\text{M}$  HSA and then augmented gently to 0.118 until the 45  $\mu\text{M}$  HSA. Evidently, the enhanced anisotropy value directs to the fact that significant motional constraint is imputed on the OLA-NBD by the rigid environment within HSA. The extreme anisotropy ( $r$ ) value, that is, 0.121 was found at 55  $\mu\text{M}$  HSA, and afterward the plateau region was noticed, implying the saturation of interaction between OLA-NBD and HSA. As per the method stated by Ingersoll and Strollo,<sup>59</sup> the apparent binding constant ( $K_b$ ) of OLA-NBD–HSA complexation can be calculated from the **eq 18**:

$$\frac{1}{f_B} = 1 + \frac{1}{K_b[\text{HSA}]} \quad (18)$$

Where,  $f_B$  is the contribution of fractional fluorescence from OLA-NBD bound HSA as expressed by **eq 19**.

$$f_B = \frac{r - r_F}{R(r_B - r) + (r - r_F)} \quad (19)$$

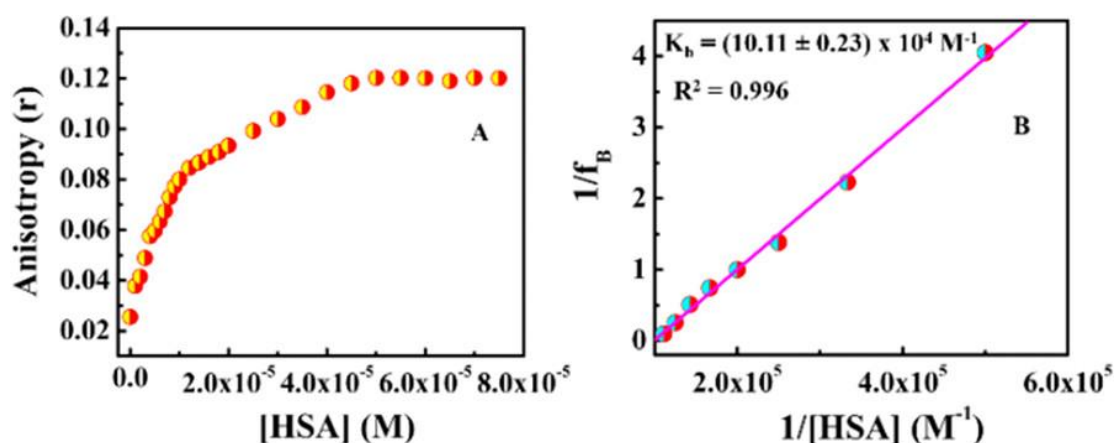


**Figure 4.12** (A) Steady-state anisotropy modulation of OLA-NBD with HSA concentration ( $\lambda_{\text{ex}} = 465 \text{ nm}$ ,  $\lambda_{\text{em}} = 555 \text{ nm}$ ). (B)  $1/f_B$  versus  $1/[\text{HSA}]$  plot for estimating the binding constant of OLA-NBD–HSA complexation by taking the data extracted from anisotropy measurement.

Where,  $r_B$  and  $r_F$  are the bound OLA-NBD–HSA and free OLA-NBD anisotropy values, correspondingly. The correction factor,  $R = I_B/I_F$  is considered here to ensure that OLA-NBD undergoes fluorescence intensity alteration upon binding with HSA. **Figure 4.12B** exhibits the  $1/f_B$  versus  $1/[HSA]$  plot, and the evaluated  $K_b$  value is tabulated in **Table 4.1**. The  $K_b$  value is in excellent agreement with the estimated value from emission titration experiment, and therefore, this measurement method builds up its practical usefulness and utility for the binding constant evaluation.<sup>41,47</sup>

### 4.3.7 Fluorescence Lifetime Measurements

Fluorescence lifetime decay study is a valuable method to analyze the microenvironment nearby the excited probe in the protein medium.<sup>15</sup> The dynamics of OLA-NBD was investigated by the lifetime decay of OLA-NBD in the absence and presence of HSA (**Figure 4.13A**). The decay associated parameters are listed in **Table 4.3**. The free OLA-NBD shows a monoexponential decay in aqueous solution with 0.77 ns lifetime. **Table 4.3** displays that decay pattern of OLA-NBD is altered from monoexponential to biexponential form with two lifetime values in HSA medium and clearly indicates the separation of OLA-NBD into two dissimilar microenvironments on interaction with HSA. The observable increase in average lifetime value ( $\langle \tau \rangle$ ) of OLA-NBD with the increasing amount of HSA (**Table 4.3**) may be due to the increasing motional constraint on OLA-NBD by the rigid and nonpolar environment within HSA and thus provide a decreased nonradiative decay channel.<sup>16</sup>

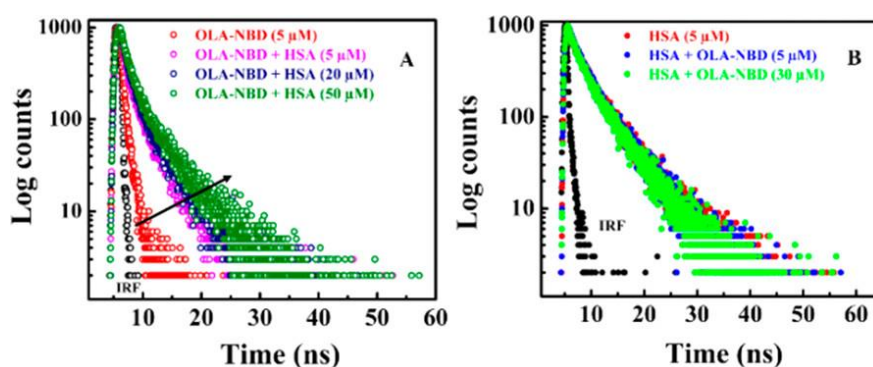


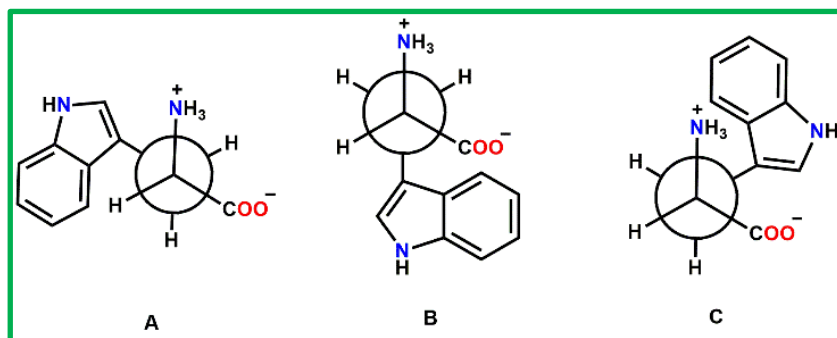
**Figure 4.13** (A) Representative time-resolved fluorescence decay spectra of OLA-NBD (5  $\mu\text{M}$ ) in the absence and with the incremental addition of HSA (0–50  $\mu\text{M}$ ). (B) Fluorescence decay profiles of HSA (5  $\mu\text{M}$ ) in the absence and with the increasing concentration of OLA-NBD (0–30  $\mu\text{M}$ ). IRF represents the instrument response function.



**Table 4.3** Fluorescence lifetime decay parameters of OLA-NBD (5  $\mu\text{M}$ ) with gradual addition of HSA at 25  $^{\circ}\text{C}$ .

system	[HSA] ( $\mu\text{M}$ )	$\tau_1$ (ns)	$\alpha_1$ (%)	$\tau_2$ (ns)	$\alpha_2$ (%)	$\langle\tau\rangle$ (ns)	$\chi^2$
OLA-NBD–HSA	0	0.77	100	–	–	–	1.124
	5	0.71	51.61	3.61	48.39	2.11	1.135
	20	1.00	47.05	4.11	52.95	2.66	1.092
	50	1.20	45.93	4.65	54.07	3.07	1.116

Fluorescence lifetime study of HSA was also done in the absence and in the increasing concentration of OLA-NBD to discriminate the quenching process (static or dynamic). **Figure 4.13B** shows the characteristic decay profiles. The decay associated parameters are presented in **Table 4.4**. The free HSA exhibits a biexponential decay pattern in aqueous solution with  $\langle\tau\rangle$  value of 4.32 ns bearing two lifetime decay constants of 1.68 and 5.41 ns with related amplitude of 29.12% and 70.88%, respectively. This biexponential nature of HSA in the free state has been described prior and ascribed to the presence of one Trp moiety at discrete conformational states.<sup>18</sup> The fluorescence lifetime decay of Trp has been studied by taking a rotamer model stated by Fleming and co-workers.<sup>60</sup> Three probable conformers of Trp are represented as follows:



Here, relatively, the faster component is signified by rotamer C, and conversely, the slower component usually comes out from the speedy interconversion of A and B conformers. However, on nanosecond time scale conversion of comparatively stable C conformer to either B or A form is rather difficult. Additionally, it is believed that on photoexcitation the indole ring undergoes a conformational change from puckered form to planar form, maybe owing to the delocalization of electron density over nitrogen atom with the aromatic moiety.<sup>18</sup>

**Table 4.4** Fluorescence lifetime decay parameters of HSA (5 μM) with gradual addition of OLA-NBD at 25 °C.

system	[OLA-NBD] (μM)	τ <sub>1</sub> (ns)	α <sub>1</sub> (%)	τ <sub>2</sub> (ns)	α <sub>2</sub> (%)	<τ> (ns)	χ <sup>2</sup>
HSA-OLA-NBD	0	1.68	29.12	5.41	70.88	4.32	1.058
	5	1.49	27.83	5.35	72.17	4.27	1.119
	10	1.38	26.46	5.27	73.64	4.24	1.126
	15	1.30	25.17	5.18	74.83	4.20	1.062
	20	1.21	24.05	5.13	75.95	4.18	1.073
	30	1.17	22.86	5.05	77.14	4.16	1.042

Here, we have assigned the average lifetime (< τ >) value rather than more importance on the discrete lifetime decay constant in such biexponential profile. **Table 4.4** displays that < τ > value of HSA marginally decreases from 4.32 ns in aqueous solution to 4.16 ns upon addition of 30 μM OLA-NBD. This minimal reduction of < τ > value in the presence of higher concentration of OLA-NBD is due to the modulation of local microenvironment nearby the Trp moiety upon interaction. A time-resolved Stern-Volmer plot was constructed with the help of < τ > values and by considering the following equation:

$$\frac{\langle \tau_0 \rangle}{\langle \tau \rangle} = 1 + K_{SV}[\text{OLA} - \text{NBD}] \quad (20)$$

Where, < τ<sub>0</sub> > and < τ > are the average lifetime value of HSA in the free state and with the increasing concentration of OLA-NBD, respectively. **Figure 4.11A** depicts the overlap of characteristic steady-state and time-resolved Stern-Volmer plots for the HSA-OLA-NBD interaction, where, time-resolved part is parallel to the x-axis reaffirming the involvement of a static quenching process or in other words ground state complex formation between OLA-NBD and HSA.<sup>61-63</sup>

#### 4.3.8 Hydrophobic Probe ANS Displacement Analysis

ANS displacement experiment was executed to find out the probable binding region of OLA-NBD on HSA. The ANS is a known fluorescent sensitive probe and frequently used to get info about the hydrophobic interaction regions of protein.<sup>49,64-66</sup> Consistent with the protocol, the displacement experiments were carried out with ANS maintaining identical conditions and **Figure 4.14** depicts the plot of change of relative emission (I/I<sub>0</sub>) versus OLA-NBD

concentration. We find that at a 30  $\mu\text{M}$  concentration, OLA-NBD has a better quenching impact on HSA emission than ANS (i.e., OLA-NBD quenched  $\sim 69\%$  and ANS about  $48\%$ ). However, with the addition of OLA-NBD to HSA-ANS associates (1:1 and 1:10), emission intensity was decreased to  $\sim 63\%$  and  $\sim 56\%$ , respectively. This outcome indicates that OLA-NBD moderately competes with ANS for the hydrophobic binding sites of HSA by eliminating the bound ANS molecules.

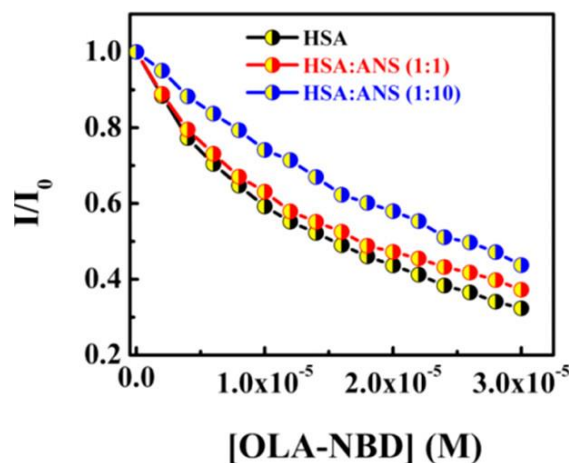


**Figure 4.14** ANS displacement study for the quenching of HSA emission by OLA-NBD at different HSA-ANS ratio (1:0, 1:1 and 1:10).

#### 4.3.9 Site-Specific Binding of OLA-NBD on HSA

The competitive fluorescence binding experiments were implemented to find out the plausible binding site of OLA-NBD on HSA by using two familiar site-specific markers (Warfarin and Ibuprofen). We have done two separate binding experiments to acquire significant information about the OLA-NBD interaction site by analyzing the emission intensity changes of the spectra. Warfarin site-specific marker solely binds at subdomain IIA of site I; in contrast, ibuprofen particularly binds at subdomain IIIA of site II.<sup>9,10,67</sup> In the first set of experiments, OLA-NBD was increasingly added to the HSA-site markers associates (1:1) to monitor the spectral variations (**Figure 4.15A, B**). Upon addition of OLA-NBD into HSA solution, the emission intensity is slightly increased along with a substantial red shift ( $\sim 34$  nm) of  $\lambda_{\text{em}}^{\text{max}}$  from 334 to 368 nm (**Figure 4.15A**). Then successive addition of OLA-NBD into HSA-warfarin associate consequences a regular decrement in emission intensity, implying the effect of OLA-NBD on the Warfarin binding site within HSA. However, in case of Ibuprofen addition, no such significant variation of  $\lambda_{\text{em}}^{\text{max}}$  was detected (**Figure 4.15B**).

The OLA-NBD induces the emission intensity quenching of HSA-Ibuprofen associate almost to the similar range as in the case of free HSA (Figure 4.7C). Hence, the above experimental observations and findings evidently prove that the binding of OLA-NBD to HSA is predominantly located at subdomain IIA of site I.

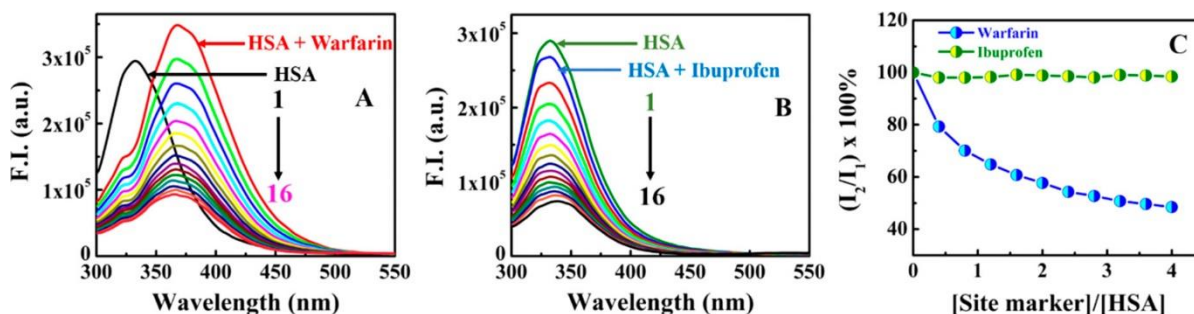


**Figure 4.15** Effect of site markers on the emission of HSA–OLA-NBD. (A) [HSA] = [Warfarin] = 5 μM (B) [HSA] = [Ibuprofen] =5 μM. For both the panel A and B, curve 3-16 represents the addition of OLA-NBD each time 2 μM to a total 28 μM concentration. (C) [HSA] = 5 μM, [OLA-NBD] = 20 μM. Warfarin and ibuprofen site markers are added gradually to a total 20 μM concentration, respectively. λ<sub>ex</sub> of HSA = 295 nm.

In case of second set of experiments, site-specific markers were progressively added to the mixed solution of HSA and OLA-NBD held at a molar ratio of 1:4 to keep the minimum nonspecific binding of the site markers.<sup>17</sup> The emission intensity of the ternary mixture was evaluated from the method stated by Sudlow *et al.*:<sup>10</sup>

$$\frac{I_2}{I_1} \times 100\%$$

Here,  $I_1$  and  $I_2$  denotes the emission intensity of HSA–OLA-NBD in the absence and presence of site-specific markers, respectively. Site markers induced emission spectral variations of HSA–OLA-NBD are depicted in Figure 4.15C, which vividly shows that warfarin contends with OLA-NBD molecules for the binding site I of HSA. Thus, the emission of HSA–OLA-NBD was considerably influenced by warfarin and remained virtually same in the presence of ibuprofen. These results establish that OLA-NBD is likely to bind at site I in subdomain IIA of HSA, inferring the presence of Trp 214 is inside or close to the OLA-NBD binding site, which is in excellent harmony with the results found from the spectrofluorimetric analysis.

#### 4.3.10 Resonance Rayleigh Scattering (RRS) Spectral Investigations

To investigate the interactions of protein molecules with the small molecular probes and to know the molecular recognition, a simple and very sensitive analytical method, RRS is introduced. This technique is very much sensitive to the electrostatic attraction and hydrophobic and hydrogen bonding interactions.<sup>68,69</sup> The resonance Rayleigh scattering spectra of HSA and HSA-OLA-NBD (Figure 4.16) were recorded by synchronous scanning in the wavelength range 200 to 700 nm with  $\Delta\lambda = 0$  nm. In the absence of OLA-NBD, HSA shows a moderate RRS intensity, and then a rapid increment in intensity is noticed with the gradual addition of OLA-NBD, indicating the interaction between OLA-NBD and HSA. This is possibly owing to the greater dimension of HSA-OLA-NBD particles than that of HSA and the ground state complex formation between the two species.

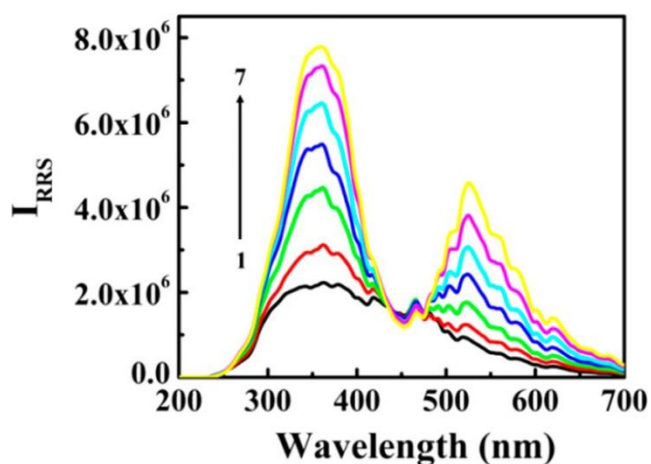


**Figure 4.16** Effect of OLA-NBD concentration (0-35  $\mu\text{M}$ ) on the RRS spectra of HSA-OLA-NBD system.  $[\text{HSA}] = 5 \mu\text{M}$ .

#### 4.3.11 Conformation Investigations: Circular Dichroism Study

The far-UV CD spectra of free HSA in aqueous medium (Figure 4.17) display a characteristic shape with two minima at  $\sim 208$  and  $\sim 222$  nm, vividly indicative of an  $\alpha$ -helix rich secondary structure.<sup>4,7,8,16-18</sup> These two negative bands in the CD profile appears usually due to  $n \rightarrow \pi^*$  charge transfer transition.<sup>70</sup> The CD spectra of HSA experiences a reduction in CD signal with no observable change of the peak wavelengths (Figure 4.17) upon gradual addition of OLA-NBD. This infers OLA-NBD induced alteration of conformation of free HSA concerning the reduction of  $\alpha$ -helicity.

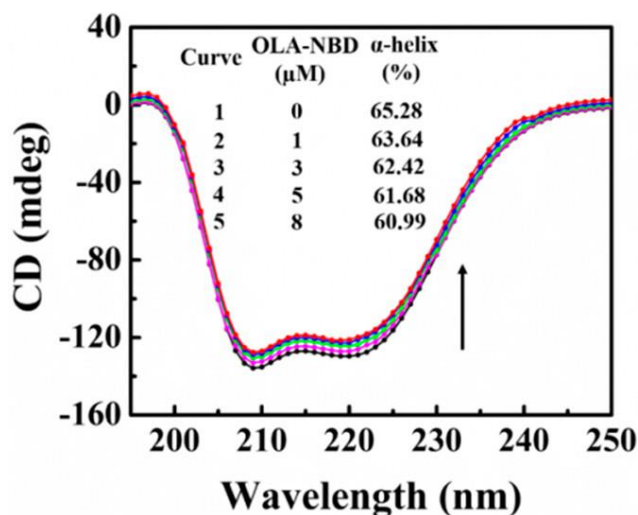


**Figure 4.17** CD spectral profiles of HSA (1.25 μM) with added OLA-NBD at 25 °C. The inset shows the calculated α-helicity (±2%) variation in HSA with the increasing concentration of OLA-NBD.

The percentage α-helicity in HSA is evaluated by adopting the following equation:<sup>16,18</sup>

$$\% \alpha - helix = \frac{-(MRE_{222} - 2340)}{30300} \times 100 \quad (21)$$

Here, mean residue ellipticity (*MRE*) values are assessed from the recorded ellipticity values ( $\theta_{obs}$  in mdeg at 222 nm) using the eq 22:<sup>16,18</sup>

$$MRE (deg.cm^2.dmol^{-1}) = \frac{\theta_{obs}}{C_p n l \times 10} \quad (22)$$

Where, *n* designates the number of amino acid residues (585 for HSA).<sup>4,7,8,16-18</sup>  $C_p$  and *l* are the molar concentration of HSA and the path-length of cell (here 1 cm), respectively. The α-helicity of free HSA is evaluated to be ~65.28 (±2)%, and it is in good agreement with the literature values.<sup>4,7,8,16-18</sup> A reduction in the α-helicity from ~65.28 (±2)% in free HSA to ~60.99 (±2)% with the addition of 8 μM OLA-NBD (inset of **Figure 4.17**) therefore clearly displays OLA-NBD persuaded denaturation of HSA protein.

#### 4.3.12 OLA-NBD Induced Variation of HSA Functionality: Esterase-Like Activity Assay of HSA

Besides the well-known probe binding capacity, a characteristic enzymatic property of HSA can be defined by observing the esterase-like activity assay.<sup>16,18,71,72</sup> The significant effect of

OLA-NBD binding on the conformation of HSA in native state leads us to perform the HSA activity study, as it is important for biological applications. **Figure 4.18A, B** represent the kinetic profiles and relative esterase activity of HSA for releasing of *p*-Nitrophenol on reaction with PNPA in the absence and with the increasing concentration of OLA-NBD. It is observed that the interaction of OLA-NBD with HSA is accompanied by an obvious decrease in the esterase activity of HSA, which is in good agreement with the experimental loss of the free protein structure on binding with OLA-NBD.<sup>16,18</sup>

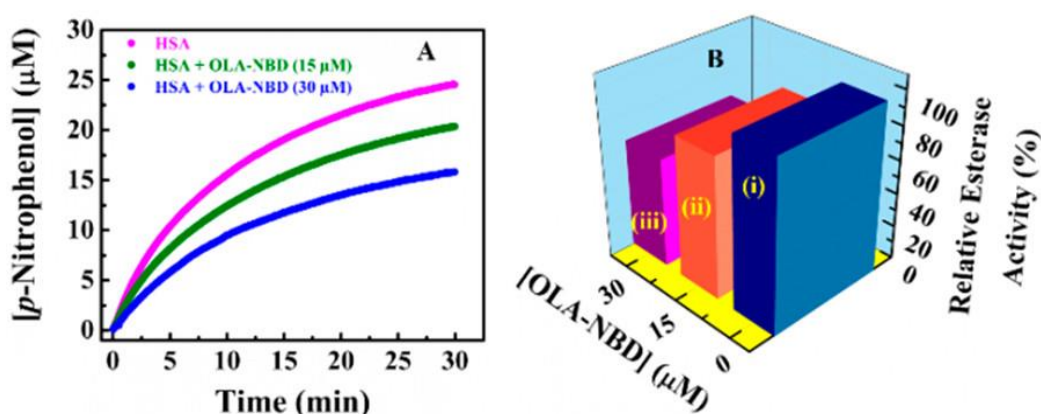


**Figure 4.18** (A) *p*-Nitrophenol (in μM) release kinetic profiles for the reaction between HSA and PNPA in the absence and with the increasing amount of OLA-NBD. (B) OLA-NBD induced variation of relative esterase activity of HSA ([OLA-NBD] = (i) 0, (ii) 15 μM and (iii) 30 μM).  $\lambda_{\text{monitored}} = \lambda_{\text{abs}} = 400 \text{ nm}$ .

#### 4.3.13 Effect of $\beta$ -CD on the Fluorescence Spectra of OLA-NBD

A fluorescence titration was carried out at 5 μM OLA-NBD concentration in aqueous buffer solution with the successive addition of  $\beta$ -CD to find out the binding interaction between OLA-NBD and  $\beta$ -CD. The maximum emission intensity of OLA-NBD is blue shifted (~5 nm) from 555 to 550 nm in 1mM  $\beta$ -CD solution with simultaneous increase of the peak emission intensity when OLA-NBD was excited at 465 nm (**Figure 4.19**). The spectrofluorimetric titration data are further examined to evaluate the binding constant between OLA-NBD and  $\beta$ -CD by using Benesi-Hildebrand equation:

$$\frac{I_{\infty} - I_0}{I_X - I_0} = 1 + \frac{1}{K_{\text{BH}} [\beta\text{-CD}]} \quad (23)$$



Here,  $K_{BH}$  signifies the association constant.  $I_0$ ,  $I_x$ , and  $I_\infty$  designate the emission intensities of OLA-NBD in free state, at an intermediate  $\beta$ -CD concentration, and at  $\beta$ -CD concentration when complete saturation is occurred, respectively.  $|I_\infty - I_0| / |I_x - I_0|$  versus  $1/[\beta\text{-CD}]$  plot shows a linear variation (Figure 4.20) with a binding constant value of  $(1.69 \pm 0.15) \times 10^3 \text{ M}^{-1}$ .

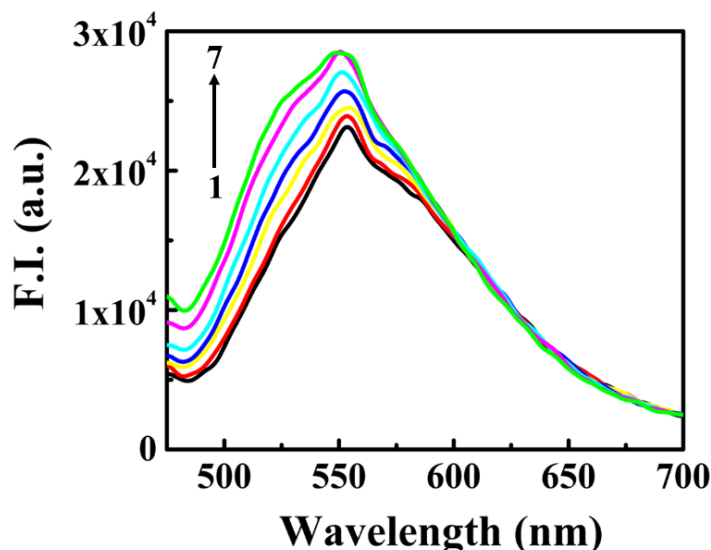


**Figure 4.19** Emission spectra of OLA-NBD in the presence of  $\beta$ -CD in aqueous buffer solution. Spectra 1-7 corresponds to the  $\beta$ -CD concentration 0, 0.1, 0.2, 0.4, 0.6, 0.8 and 1.0 mM respectively.

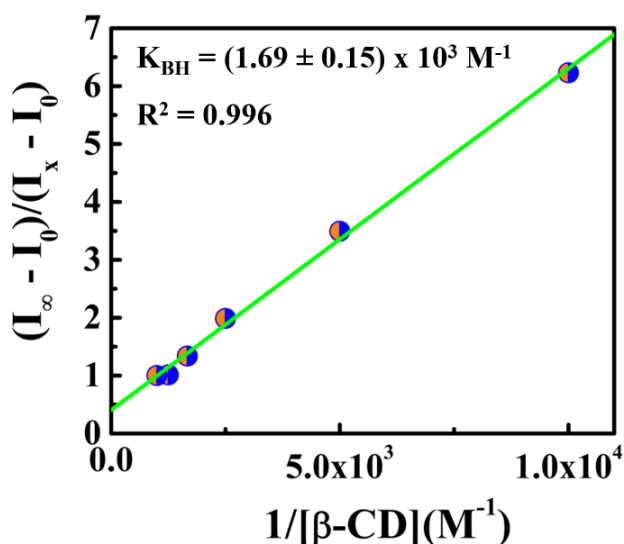


**Figure 4.20** Characteristic Benesi-Hildebrand plot for the complexation of OLA-NBD with  $\beta$ -CD.

#### 4.3.14 Effect of $\beta$ -CD on HSA–OLA-NBD Binding

$\beta$ -Cyclodextrin ( $\beta$ -CD) can form characteristic inclusion complexes with a numerous number of inorganic and organic molecules. It is also extensively used as drug additives to enhance the stability of drug molecules and increase the solubility of water insoluble drug molecules.<sup>27</sup> Here, only the influence of  $\beta$ -CD on HSA–OLA-NBD binding was explored. The OLA-NBD molecule experiences a moderate binding with  $\beta$ -CD (Figures 4.19 and 4.20). This encapsulation method can modify the HSA–OLA-NBD binding association as  $\beta$ -CD behaves like a scabbard that shrouds the OLA-NBD molecule, obstructing it from freely bind with HSA.<sup>73</sup> To recognize the effect of  $\beta$ -CD on HSA–OLA-NBD binding, HSA (5  $\mu$ M) emission was recorded in the presence of 1.0 mM  $\beta$ -CD with the gradual addition of OLA-NBD from 0 to 30  $\mu$ M (Figure 4.21).

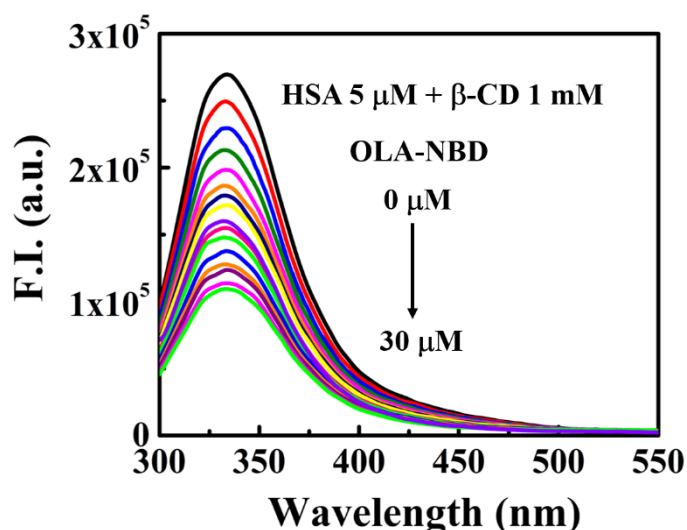


**Figure 4.21** The emission spectra of HSA in the presence of 1.0 mM  $\beta$ -CD with gradual addition of OLA-NBD (0–30  $\mu$ M) at 25  $^{\circ}$ C.

The calculated  $K_{SV}$  and  $K_b$  values from Figures 4.22 and 4.23, respectively, at 25  $^{\circ}$ C in the absence and presence of  $\beta$ -CD are summarized in Table 4.5. The smaller  $K_{SV}$  and  $K_b$  values in the presence of  $\beta$ -CD for the HSA–OLA-NBD binding association indicate that  $\beta$ -CD prevents the direct collision of OLA-NBD molecules with HSA by forming an inclusion complex.<sup>73,74</sup> It also implies that OLA-NBD molecules are progressively unshrouded from  $\beta$ -CD by HSA to accomplish its medicinal outcome upon binding with protein.<sup>69,73-75</sup>

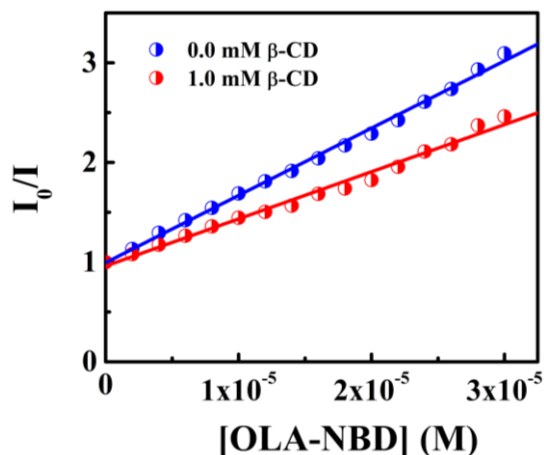


**Figure 4.22** Stern-Volmer plots for the quenching of HSA (5 μM) fluorescence by OLA-NBD (0-30 μM) in the absence and presence of β-CD at 25 °C.

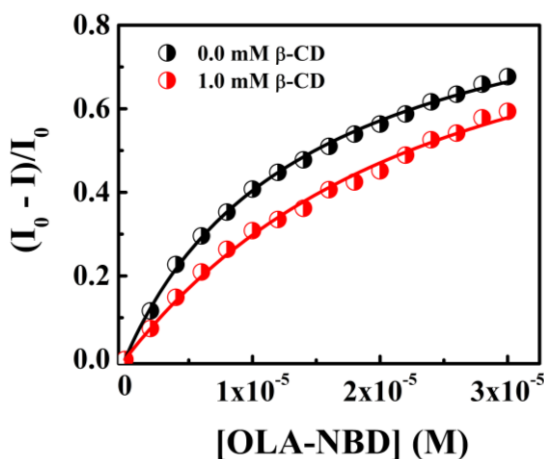


**Figure 4.23** Plot of  $(I_0 - I)/I_0$  vs. OLA-NBD concentration in the absence and presence of β-CD at 25 °C. The solid line displays the best fit.

**Table 4.5** Stern-Volmer constants ( $K_{SV}$ ) and binding constants ( $K_b$ ) for the HSA-OLA-NBD binding association in the absence and presence of β-CD at 25 °C.

[HSA] (μM)	[β-CD] (mM)	$K_{SV}$ ( $10^4 M^{-1}$ )	$R^2$	binding constant, $K_b$ ( $10^4 M^{-1}$ )
5	0.0	$6.74 \pm 0.09$	0.997	$6.38 \pm 0.04$
5	1.0	$4.72 \pm 0.14$	0.995	$5.19 \pm 0.15$

#### 4.3.15 HSA–OLA-NBD Association Kinetics

In the investigation of binding of drug/small molecules with the various proteins, a discussion on the association kinetics is believed to have vital diagnostic implication.<sup>74-78</sup> The association kinetics of the HSA–OLA-NBD composite was investigated under pseudo-first-order conditions by monitoring the emission quenching of HSA at 334 nm upon interaction with OLA-NBD. **Figure 4.24** shows the characteristic emission kinetic trace for the above-mentioned association process at 298 K and it has been fitted by considering a nonlinear regression equation as follows:<sup>79</sup>

$$I(t) = \alpha \exp(-k_a t) + C \quad (24)$$

Where,  $I(t)$  signifies the emission intensity at time  $t$ .  $\alpha$  and  $k_a$  are the amplitude and the apparent association rate constant, respectively corresponding to the exponential factor.  $C$  represents the emission intensity at equilibrium. An apparent rate constant,  $k_a = (1.95 \pm 0.09) \times 10^{-3} \text{ s}^{-1}$  is found for the HSA–OLA-NBD association kinetics at 298 K.

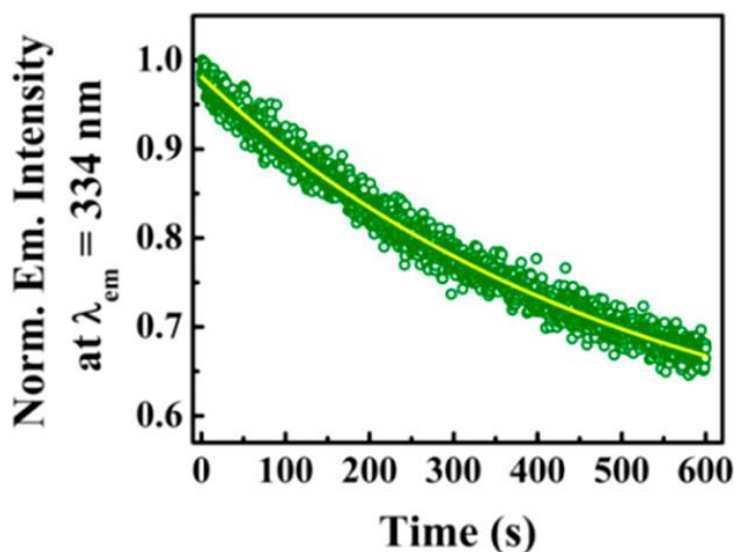


**Figure 4.24** Representative emission kinetic trace for the HSA–OLA-NBD binding association. The kinetic profile defines the time path of HSA emission quenching on interaction with OLA-NBD at 298 K. The raw data are designated by olive-green symbols, and the fitted curve is represented by solid yellow line.  $\lambda_{\text{ex}} = 295 \text{ nm}$ ,  $\lambda_{\text{monitored}} = \lambda_{\text{em}} = 334 \text{ nm}$ ,  $[\text{HSA}] = 1 \text{ }\mu\text{M}$ ,  $[\text{OLA-NBD}] = 20 \text{ }\mu\text{M}$ .

#### 4.3.16 Molecular Docking Results

Herein, we have accomplished the docking study to ascertain the probable OLA-NBD binding site within HSA and the involvement of possible thermodynamic interactions throughout the association process. The minimum binding energy docked conformation was chosen for further investigation.<sup>80,81</sup> The stereo view of molecular docking posture of OLA-NBD with HSA protein is displayed in **Figure 4.25A**, which indicates that the subdomain IIA of site I in HSA is favored for OLA-NBD interaction, and this is well corroborated with the outcome of site-specific marker studies. **Figure 4.25B** exhibits the adjacent amino acid residues (within 4.0 Å) surrounding the OLA-NBD interaction region in subdomain IIA of HSA close to the Trp 214 residue. OLA-NBD molecule is encompassed by several hydrophobic and polar amino acid residues. A variable number of charged and polar residues like Lys 195, Ser 202, Arg 218, Arg 22, and Asp 451 plays a significant role in stabilizing the OLA-NBD–HSA association through electrostatic interactions. Furthermore, Leu 198, Phe 211, Trp 214, Leu 219, and Leu 238 provided a greater stability to the OLA-NBD molecule through hydrophobic interactions. The binding energy for the OLA-NBD–HSA association was found to be  $-5.73 \text{ kcal mol}^{-1}$ . The docking simulation outcome demonstrates that the OLA-NBD molecule binds near to the Trp 214 at site I within HSA, inducing a perturbation of the HSA emission intensity. Hence, molecular docking simulation approach supported the experimental outcomes from a theoretical point of view.

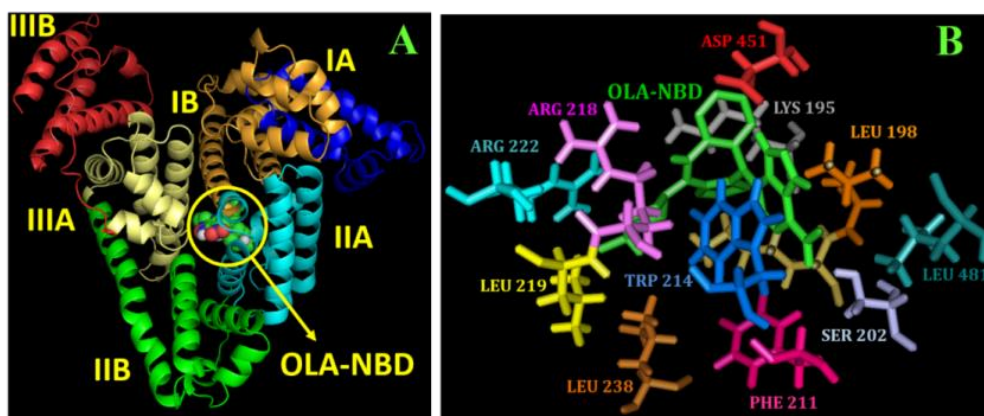


**Figure 4.25** (A) Stereo view of molecular docking posture of OLA-NBD with HSA protein (PDB ID: 1AO6) displayed by yellow circle. (B) Magnified sight of OLA-NBD binding location accompanied by highlighting of the neighboring (within 4.0 Å of the binding site) amino acid residues of HSA.

## 4.4 Conclusions

The present work deals with the various spectroscopic and molecular docking investigation on the interaction of NBD embedded olanzapine derivative (OLA-NBD) with HSA protein. The complexation of OLA-NBD with HSA has been evidently illustrated by UV-Vis spectral change at 280 nm. A gradual enhancement of the emission intensity of OLA-NBD along with the substantial blue shift of  $\lambda_{em}^{max}$  on interaction with HSA is vividly indicates toward the immense modulation of the microenvironment around OLA-NBD within the protein hydrophobic medium compared with the polar aqueous medium. The estimated limit of detection (LOD) value is 59.4 nM. The emission titration of HSA with OLA-NBD resulted an association constant =  $(9.87 \pm 0.02) \times 10^4 \text{ M}^{-1}$ , and it is in excellent harmony with the value estimated from anisotropy experiment. The emission quenching study persuaded by OLA-NBD indicates the presence of static quenching mechanism, which is well corroborated with the results extracted from the time-resolved fluorescence study of HSA with OLA-NBD. Binding constant value decreases with the rise in temperature leading to the decrement in the stability of HSA–OLA-NBD composite, supporting the presence of static quenching mechanism. The negative value of  $\Delta H^0$  accompanied by a positive value of  $\Delta S^0$  infer the major contribution of electrostatic/ionic interaction for the HSA–OLA-NBD binding process. CD outcome illustrates the alteration of the secondary structure of HSA upon interaction with OLA-NBD. The effect of  $\beta$ -Cyclodextrin on HSA–OLA-NBD binding is found to be characterized by a smaller Stern-Volmer quenching and binding constant values, indicating that OLA-NBD molecules are progressively unsheathed from  $\beta$ -CD by HSA to accomplish its medicinal applications. The site-specific binding experiment and molecular docking studies indicate that OLA-NBD binds with HSA in subdomain IIA at the binding site I, that is, close to the Trp 214 amino acid. Hence, the present extrinsic fluorescent molecular probe can be employed as a potential site-specific biomarker for site I binding pocket in the subdomain IIA.

## References

- (1) Peters, T., Jr. *All About Albumins: Biochemistry, Genetics and Medical Applications*; Academic Press: San Diego, CA, 1996; pp 76–132.

- (2) Lázaro, E.; Lowe, P. J.; Briand, X.; Faller, B. New approach to measure protein binding based on a parallel artificial membrane assay and human serum albumin. *J. Med. Chem.* **2008**, *51*, 2009–2017.
- (3) Shahlaei, M.; Rahimi, B.; Ashrafi-Kooshk, M. R.; Sadrjavadi, K.; Khodarahmi, R. Probing of possible olanzapine binding site on human serum albumin: Combination of spectroscopic methods and molecular dynamics simulation. *J. Lumin.* **2015**, *158*, 91–98.
- (4) Carter, D. C.; Ho, J. X. Structure of Serum Albumin. *Adv. Protein Chem.* **1994**, *45*, 153–203.
- (5) Brown, J. R.; Shockley, P. *Lipid-Protein Interactions*; Wiley: New York, 1982; Vol. 1, pp 25–68.
- (6) Ding, F.; Liu, W.; Zhang, L.; Yin, B.; Sun, Y. J. Sulfometuron-methyl binding to human serum albumin: Evidence that sulfometuron-methyl binds at the Sudlow's site I. *Mol. Struct.* **2010**, *968*, 59–66.
- (7) He, X. M.; Carter, D. C. Atomic Structure and Chemistry of Human Serum Albumin. *Nature*, **1992**, *358*, 209–215.
- (8) Peters, T., Jr. Serum Albumin. *Adv. Protein Chem.* **1985**, *37*, 161–245.
- (9) Sudlow, G.; Birkett, D. J.; Wade, D. N. The Characterization of Two Specific Drug Binding Sites on Human Serum Albumin. *Mol. Pharmacol.* **1975**, *11*, 824–832.
- (10) Sudlow, G.; Birkett, D. J.; Wade, D. N. Mol. Further Characterization of Specific Drug Binding Sites on Human Serum Albumin. *Mol. Pharmacol.* **1976**, *12*, 1052–1061.
- (11) Olson, R. E.; Christ, D. D. Chapter 33. Plasma Protein Binding of Drugs. *Annu. Rep. Med. Chem.* **1996**, *31*, 327–336.
- (12) Kandagal, P. B.; Shaikh, S. M. T.; Manjunatha, D. H.; Seetharamappa, J.; Nagaralli, B. S. Spectroscopic studies on the binding of bioactive phenothiazine compounds to human serum albumin. *J. Photochem. Photobiol. A* **2007**, *189*, 121–127.
- (13) Rabbani, G.; Ahn, S. N. Structure, enzymatic activities, glycation and therapeutic potential of human serum albumin: A natural cargo. *Int. J. Biol. Macromol.* **2019**, *123*, 979–990.



- (14) Abou-Zied, O. K.; Al-Shihi, O. I. K. Characterization of Subdomain IIA Binding Site of Human Serum Albumin in its Native, Unfolded, and Refolded States Using Small Molecular Probes. *J. Am. Chem. Soc.* **2008**, *130*, 10793–10801.
- (15) Mallick, A.; Haldar, B.; Chattopadhyay, N. Spectroscopic Investigation on the Interaction of ICT Probe 3-Acetyl-4-oxo-6,7-dihydro-12H Indolo-[2,3-a] Quinolizine with Serum Albumins. *J. Phys. Chem. B* **2005**, *109*, 14683–14690.
- (16) Paul, B. K.; Ghosh, N.; Mukherjee, S. Interplay of Multiple Interaction Forces: Binding of Norfloxacin to Human Serum Albumin. *J. Phys. Chem. B* **2015**, *119*, 13093–13102.
- (17) Ibrahim, N.; Ibrahim, H.; Kim, S.; Nallet, J. P.; Nepveu, F. Interactions between Antimalarial Indolone-*N*-oxide Derivatives and Human Serum Albumin. *Biomacromolecules* **2010**, *11*, 3341–3351.
- (18) Ghosh, N.; Mondal, R.; Mukherjee, S. Hydrophobicity Is the Governing Factor in the Interaction of Human Serum Albumin with Bile Salts. *Langmuir* **2015**, *31*, 1095–1104.
- (19) Ahmad, B.; Parveen, S.; Khan, R. H. Effect of Albumin Conformation on the Binding of Ciprofloxacin to Human Serum Albumin: A Novel Approach Directly Assigning Binding Site. *Biomacromolecules* **2006**, *7*, 1350–1356.
- (20) Sudhamalla, B.; Gokara, M.; Ahalawat, N.; Amooru, D. G.; Subramanyam, R. Molecular Dynamics Simulation and Binding Studies of  $\beta$ -Sitosterol with Human Serum Albumin and Its Biological Relevance. *J. Phys. Chem. B* **2010**, *114*, 9054–9062.
- (21) Sinha, S. S.; Mitra, R. K.; Pal, S. K. Temperature-Dependent Simultaneous Ligand Binding in Human Serum Albumin. *J. Phys. Chem. B* **2008**, *112*, 4884–4891.
- (22) Lieberman, J. A.; Stroup, T. S.; McEvoy, J. P.; Swartz, M. S.; Rosenheck, R. A.; Perkins, D. O.; Keefe, R. S. E.; Davis, S. M.; Davis, C. E.; Lebowitz, B. D.; Severe, J.; Hsiao, J. K. Effectiveness of antipsychotic drugs in patients with chronic schizophrenia. *N. Engl. J. Med.* **2005**, *353*, 1209–1223.
- (23) Albani, J. R. Fluorescence Spectroscopic Study of Interaction between Olanzapine and Bovine Serum Albumin. *Pharm. Anal. Acta* **2015**, *6*, 408.
- (24) Aravagiri, M.; Teper, Y.; Marder, S. R. Pharmacokinetics and tissue distribution of olanzapine in rats. *Biopharm. Drug Dispos.* **1999**, *20*, 369–377.

- (25) Markowitz, J. S.; DeVane, C. L.; Malcolm R. J.; Gefroh, H. A.; Wang, J. S.; Zhu, H. J.; Donovan, J. L. Pharmacokinetics of Olanzapine After Single-Dose Oral Administration of Standard Tablet Versus Normal and Sublingual Administration of an Orally Disintegrating Tablet in Normal Volunteers. *J. Clin. Pharmacol.* **2006**, *46*, 164–171.
- (26) Taliani, S.; Simorini, F.; Sergianni, V.; Motta, C. L.; Settimo, F. D.; Cosimelli, B.; Abignente, E.; Greco, G.; Novellino, E.; Rossi, L.; Gremigni, V.; Spinetti, F.; Chelli, B.; Martini, C. New Fluorescent 2-Phenylindolglyoxylamide Derivatives as Probes Targeting the Peripheral-Type Benzodiazepine Receptor: Design, Synthesis, and Biological Evaluation. *J. Med. Chem.* **2007**, *50*, 404–407.
- (27) Zhang, H.; Huang, X.; Mei, P.; Li, K.; Yan, C. Studies on the Interaction of tricyclazole with  $\beta$ -cyclodextrin and human serum albumin by spectroscopy. *J. Fluoresc.* **2006**, *16*, 287–294.
- (28) Qian, F.; Zhang, C.; Zhang, Y.; He, W.; Gao, X.; Hu, P.; Guo, Z. Visible Light Excitable  $Zn^{2+}$  Fluorescent Sensor Derived from an Intramolecular Charge Transfer Fluorophore and Its in Vitro and in Vivo Application. *J. Am. Chem. Soc.* **2009**, *131*, 1460–1468.
- (29) Moriyama, Y.; Takeda, K. Protective Effects of Small Amounts of Bis(2-ethylhexyl)sulfosuccinate on the Helical Structures of Human and Bovine Serum Albumins in Their Thermal Denaturations. *Langmuir* **2005**, *21*, 5524–5528.
- (30) Ghosh, N.; Mondal, R.; Mukherjee, S. Inverse Temperature Dependence in Static Quenching versus Calorimetric Exploration: Binding Interaction of Chloramphenicol to  $\beta$ -Lactoglobulin. *Langmuir* **2015**, *31*, 8074–8080.
- (31) Larsson, A.; Carlsson, C.; Jonsson, M.; Albinsson, B. Characterization of the Binding of the Fluorescent Dyes YO and YOYO to DNA by Polarized Light Spectroscopy. *J. Am. Chem. Soc.* **1994**, *116*, 8459–8465.
- (32) Ostdal, H.; Andersen, H. Non-Enzymic Protein Induced Hydrolysis of p-Nitrophenyl Acyl Esters in Relation to Lipase/Esterase Assays. *Food Chem.* **1996**, *55*, 55–61.
- (33) Rabbani, G.; Baig, M. H.; Lee, E. J.; Cho, W. K.; Ma, J. Y.; Choi, I. Biophysical Study on the Interaction between Eperisone Hydrochloride and Human Serum Albumin Using Spectroscopic, Calorimetric, and Molecular Docking Analyses. *Mol. Pharmaceutics* **2017**, *14*, 1656–1665.

- (34) Rabbani, G.; Lee, E. J.; Ahmad, K.; Baig, M. H.; Choi, I. Binding of Tolperisone Hydrochloride with Human Serum Albumin: Effects on the Conformation, Thermodynamics, and Activity of HSA. *Mol. Pharmaceutics* **2018**, *15*, 1445–1456.
- (35) Zhu, T.; Du, J.; Cao, W.; Fan, J.; Peng, X. Microenvironment-sensitive fluorescent dyes for recognition of serum albumin in urine and imaging in living cells. *Ind. Eng. Chem. Res.* **2016**, *55*, 527–533.
- (36) Swaminathan, R.; Krishnamoorthy, G.; Periasamy, N. Similarity of fluorescence lifetime distributions for single tryptophan proteins in the random coil state. *Biophys. J.* **1994**, *67*, 2013–2023.
- (37) Morris, G. M.; Goodsell, D. S.; Huey, R.; Olson, A. J. Distributed Automated Docking of Flexible Ligands to Proteins: Parallel Applications of AutoDock 2.4. *J. Comput.-Aided Mol. Des.* **1996**, *10*, 293–304.
- (38) Morris, G. M.; Goodsell, D. S.; Halliday, R. S.; Huey, R.; Hart, W. E.; Belew, R. K.; Olson, A. J. Automated Docking Using a Lamarckian Genetic Algorithm and Empirical Binding Free Energy Function. *J. Comput. Chem.* **1998**, *19*, 1639–1662.
- (39) Ahmad, E.; Rabbani, G.; Zaidi, N.; Singh, S.; Rehan, M.; Khan, M. M.; Rahman, S. H.; Quadri, Z.; Shadab, M.; Ashraf, M. T.; Subbarao, N.; Bhat, R.; Khan, R. H. Stereo-Selectivity of Human Serum Albumin to Enantiomeric and Isoelectronic Pollutants Dissected by Spectroscopy, Calorimetry and Bioinformatics. *PLoS One* **2011**, *6*, e26186.
- (40) Ojha, B.; Das, G. The Interaction of 5-(Alkoxy)naphthalen-1-amine with Bovine Serum Albumin and Its Effect on the Conformation of Protein. *J. Phys. Chem. B* **2010**, *114*, 3979–3986.
- (41) Sasmal, M.; Bhowmick, R.; Islam, A. S. M.; Bhuiya, S.; Das, S.; Ali, M. Domain-Specific Association of a Phenanthrene–Pyrene-Based Synthetic Fluorescent Probe with Bovine Serum Albumin: Spectroscopic and Molecular Docking Analysis. *ACS Omega* **2018**, *3*, 6293–6304.
- (42) Kar, C.; Ojha, B.; Das, G. A Novel Amphiphilic Thiosemicarbazone Derivative for Binding and Selective Sensing of Human Serum Albumin. *Luminescence* **2013**, *28*, 339–344.
- (43) Paul, B. K.; Samanta, A.; Guchhait, N. Exploring Hydrophobic Subdomain IIA of the Protein Bovine Serum Albumin in the Native, Intermediate, Unfolded, and Refolded

- States by a Small Fluorescence Molecular Reporter. *J. Phys. Chem. B* **2010**, *114*, 6183–6196.
- (44) Ganguly, A.; Paul, B. K.; Ghosh, S.; Dalapati, S.; Guchhait, N. Interaction of a Potential Chloride Channel Blocker with a Model Transport Protein: a Spectroscopic and Molecular Docking Investigation. *Phys. Chem. Chem. Phys.* **2014**, *16*, 8465–8475.
- (45) Jana, S.; Ghosh, S.; Dalapati, S.; Guchhait, N. Exploring Structural Change of Protein Bovine Serum Albumin by External Perturbation Using Extrinsic Fluorescence Probe: Spectroscopic Measurement, Molecular Docking and Molecular Dynamics Simulation. *Photochem. Photobiol. Sci.* **2012**, *11*, 323–332.
- (46) Lakowicz, J. R. Quenching of Fluorescence. In *Principles of Fluorescence Spectroscopy*, 3rd ed.; Springer: New York, 2006; pp 278–327.
- (47) Bhuiya, S.; Haque, L.; Das, S. Association of iminium and alkanolamine forms of the benzo[c]phenanthridine alkaloid chelerythrine with human serum albumin: photophysical thermodynamic and theoretical approach. *New J. Chem.* **2018**, *42*, 2180–2196.
- (48) Benesi, M. L.; Hildebrand, J. H. A Spectrophotometric Investigation of the Interaction of Iodine with Aromatic Hydrocarbons. *J. Am. Chem. Soc.* **1949**, *71*, 2703–2707.
- (49) Jash, C.; Payghan, P. V.; Ghoshal, N.; Kumar, G. S. Binding of the Iminium and Alkanolamine Forms of Sanguinarine to Lysozyme: Spectroscopic Analysis, Thermodynamics, and Molecular Modeling Studies. *J. Phys. Chem. B* **2014**, *118*, 13077–13091.
- (50) Afrin, S.; Riyazuddeen; Rabbani, G.; Khan, R. H. Spectroscopic and calorimetric studies of interaction of methimazole with human serum albumin. *J. Lumin.* **2014**, *151*, 219–223.
- (51) Abdullah, S. M. S.; Fatma, S.; Rabbani, G.; Ashraf, J. M. A spectroscopic and molecular docking approach on the binding of tinzaparin sodium with human serum albumin. *J. Mol. Struct.* **2017**, *1127*, 283–288.
- (52) Ishtikhar, M.; Rabbani, G.; Khan, S.; Khan, R. H. Biophysical investigation of thymoquinone binding to ‘N’ and ‘B’ isoforms of human serum albumin: exploring the interaction mechanism and radical scavenging activity. *RSC Adv.* **2015**, *5*, 18218–18232.

- (53) Van de Weert, M.; Stella, L. Fluorescence Quenching and Ligand Binding: A Critical Discussion of a Popular Methodology. *J. Mol. Struct.* **2011**, *998*, 144–150.
- (54) Rabbani, G.; Khan, M. J.; Ahmad, A.; Maskat, M. Y.; Khan, R. H. Effect of copper oxide nanoparticles on the conformation and activity of  $\beta$ -galactosidase. *Colloids Surf., B* **2014**, *123*, 96–105.
- (55) Yin, M. M.; Dong, P.; Chen, W. Q.; Xu, S. P.; Yang, L. Y.; Jiang, F. L.; Liu, Y. Thermodynamics and Mechanisms of the Interactions between Ultrasmall Fluorescent Gold Nanoclusters and Human Serum Albumin,  $\gamma$ -Globulins, and Transferrin: A Spectroscopic Approach. *Langmuir* **2017**, *33*, 5108–5116.
- (56) van Holde, K. E.; Johnson, W. C.; Ho, P. S. Thermodynamics and Biochemistry. In *Principles of Physical Biochemistry, 2nd int. ed.*; Pearson Higher Education: Upper Saddle River, NJ, 2006; pp 72–106.
- (57) Ross, P. D.; Subramanian, S. Thermodynamics of Protein Association Reactions: Forces Contributing to Stability. *Biochemistry* **1981**, *20*, 3096–3102.
- (58) Lakowicz, J. R. Fluorescence Anisotropy. In *Principles of Fluorescence Spectroscopy*, 3rd ed.; Springer: New York, 2006; pp 353–381.
- (59) Ingersoll, C. M.; Strollo, C. M. Steady-State Fluorescence Anisotropy to Investigate Flavonoids Binding to Proteins. *J. Chem. Educ.* **2007**, *84*, 1313–1315.
- (60) Petrich, J. W.; Chang, M. C.; McDonald, D. B.; Fleming, G. R. On the origin of nonexponential fluorescence decay in tryptophan and its derivatives. *J. Am. Chem. Soc.* **1983**, *105*, 3824–3832.
- (61) Ray, D.; Paul, B. K.; Guchhait, N. Differential binding modes of anti-cancer, anti-HIV drugs belonging to isatin family with a model transport protein: a joint refinement from spectroscopic and molecular modeling approaches. *J. Photochem. Photobiol., B* **2013**, *127*, 18-27.
- (62) Chatterjee, S.; Mukherjee, T. K. Spectroscopic Investigation of Interaction between Bovine Serum Albumin and Amine-functionalized Silicon Quantum Dots. *Phys. Chem. Chem. Phys.* **2014**, *16*, 8400–8408.
- (63) Bhuiya, S.; Pradhan, A. B.; Haque, L.; Das, S. Molecular Aspects of the Interaction of Iminium and Alkanolamine Forms of the Anticancer Alkaloid Chelerythrine with Plasma Protein Bovine Serum Albumin. *J. Phys. Chem. B* **2016**, *120*, 5–17.

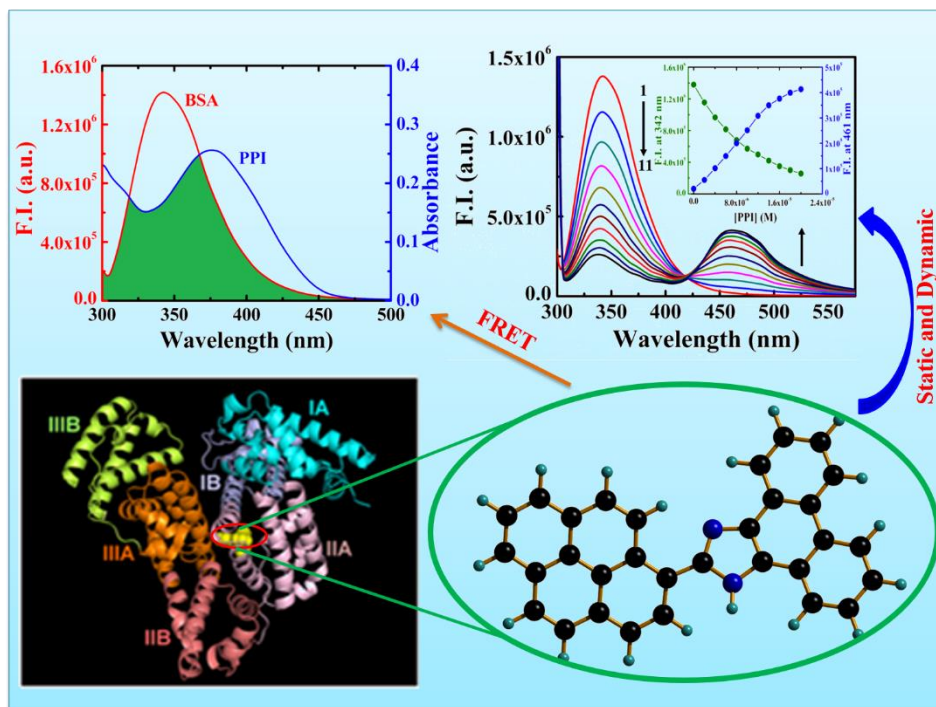
- (64) Rabbani, G.; Ahmad, E.; Khan, M. V.; Ashraf, M. T.; Bhat, R.; Khan, R. H. Impact of structural stability of cold adapted *Candida antarctica* lipase B (CaLB): in relation to pH, chemical and thermal denaturation. *RSC Adv.* **2015**, *5*, 20115–20131.
- (65) Rabbani, G.; Ahmad, E.; Zaidi, N.; Khan, R. H. pH-Dependent Conformational Transitions in Conalbumin (Ovotransferrin), a Metalloproteinase from Hen Egg White. *Cell Biochem. Biophys.* **2011**, *61*, 551–560.
- (66) Rabbani, G.; Ahmad, E.; Zaidi, N.; Fatima, S.; Khan, R. H. pH-Induced Molten Globule State of *Rhizopus niveus* Lipase is More Resistant Against Thermal and Chemical Denaturation Than Its Native State. *Cell Biochem. Biophys.* **2012**, *62*, 487–499.
- (67) Baroni, S.; Mattu, M.; Vannini, A.; Cipollone, R.; Aime, S.; Ascenzi, P.; Fasano, M. Effect of Ibuprofen and Warfarin on the Allosteric Properties of Haem-Human Serum Albumin. A spectroscopic Study. *Eur. J. Biochem.* **2001**, *268*, 6214–6220.
- (68) Madrakian, T.; Bagheri, H.; Afkhami, A.; Soleimani, M. Spectroscopic and molecular docking techniques study of the interaction between oxymetholone and human serum albumin. *J. Lumin.* **2014**, *155*, 218–225.
- (69) Bolattin, M. B.; Nandibewoor, S. T.; Joshi, S. D.; Dixit, S. R.; Chimatadar, S. A. Interaction of Hydralazine with Human Serum Albumin and Effect of  $\beta$ -Cyclodextrin on Binding: Insights from Spectroscopic and Molecular Docking Techniques. *Ind. Eng. Chem. Res.* **2016**, *55*, 5454–5464.
- (70) Yang, P.; Gao, F. *The Principle of Bioinorganic Chemistry*; Science Press: Beijing, 2002; p 349.
- (71) Rabbani, G.; Baig, M. H.; Lee, E. J.; Cho, W. K.; Ma, J. Y.; Choi, I. Biophysical Study on the Interaction between Eperisone Hydrochloride and Human Serum Albumin Using Spectroscopic, Calorimetric, and Molecular Docking Analyses. *Mol. Pharmaceutics* **2017**, *14*, 1656–1665.
- (72) Rabbani, G.; Lee, E. J.; Ahmad, K.; Baig, M. H.; Choi, I. Binding of Tolperisone Hydrochloride with Human Serum Albumin: Effects on the Conformation, Thermodynamics, and Activity of HSA. *Mol. Pharmaceutics* **2018**, *15*, 1445–1456.

- (73) Bogdan, M.; Floare, C. G.; Pirnau, A.; Neamtu, S. Competitive Binding of Tolmetin to  $\beta$ -Cyclodextrin and Human Serum Albumin:  $^1\text{H}$  NMR and Fluorescence Spectroscopy Studies. *J. Solution Chem.* **2017**, *46*, 44–57.
- (74) Bolattin, M. B.; Nandibewoor, S. T.; Joshi, S. D.; Dixit, S. R.; Chimatadar, S. A. Interaction between carisoprodol and bovine serum albumin and effect of  $\beta$ -cyclodextrin on binding: insights from molecular docking and spectroscopic techniques. *RSC Adv.* **2016**, *6*, 63463–63471.
- (75) Zhang, H. X.; Huang, X.; Zhang, M. Thermodynamic studies on the interaction of dioxopromethazine to  $\beta$ -cyclodextrin and bovine serum albumin. *J. Fluoresc.* **2008**, *18*, 753–760.
- (76) Paul, B. K.; Ray, D.; Guchhait, N. Spectral deciphering of the interaction between an intramolecular hydrogen bonded ESIPT drug, 3,5-dichlorosalicylic acid, and a model transport protein. *Phys. Chem. Chem. Phys.* **2012**, *14*, 8892–8902.
- (77) Paul, B. K.; Ghosh, N.; Mukherjee, S. Binding Interaction of a Prospective Chemotherapeutic Antibacterial Drug with  $\beta$ -Lactoglobulin: Results and Challenges. *Langmuir* **2014**, *30*, 5921–5929.
- (78) Banerjee, S.; Chakrabarti, G.; Bhattacharyya, B. Colchicine binding to tubulin monomers: A mechanistic study. *Biochemistry* **1997**, *36*, 5600–5606.
- (79) Canaves, J. M.; Aleu, J.; Lejarreta, M.; Gonzalez-Ros, J. M.; Ferragut, J. A. Effects of pH on the kinetics of the interaction between anthracyclines and lipid bilayers. *Eur. Biophys. J.* **1997**, *26*, 427–431.
- (80) Ahmad, E.; Rabbani, G.; Zaidi, N.; Singh, S.; Rehan, M.; Khan, M. M.; Rahman, S. H.; Quadri, Z.; Shadab, M.; Ashraf, M. T.; Subbarao, N.; Bhat, R.; Khan, R. H. Stereo-Selectivity of Human Serum Albumin to Enantiomeric and Isoelectronic Pollutants Dissected by Spectroscopy, Calorimetry and Bioinformatics. *PLoS One* **2011**, *6*, e26186.
- (81) Varshney, A.; Rehan, M.; Subbarao, N.; Rabbani, G.; Khan, R. H. Elimination of Endogenous Toxin, Creatinine from Blood Plasma Depends on Albumin Conformation: Site Specific Uremic Toxicity & Impaired Drug Binding. *PLoS One* **2011**, *6*, e17230.



## Chapter 5

### Domain-Specific Association of a Phenanthrene-Pyrene-Based Synthetic Fluorescent Probe with Bovine Serum Albumin: Spectroscopic and Molecular Docking Analysis



### Abstract:

In this report, the interaction between a phenanthrene–pyrene-based fluorescent probe (PPI) and bovine serum albumin (BSA), a transport protein, has been explored by steady-state emission spectroscopy, fluorescence anisotropy, far-ultraviolet circular dichroism (CD), time-resolved spectral measurements and molecular docking simulation study. The observed fluorescence intensity enhancement accompanied by a blue-shift of the emission maxima in the presence of BSA can be ascribed to the movement of PPI probe from a more polar aqueous environment to a more hydrophobic protein environment. The binding of the probe causes quenching of BSA fluorescence through both static and dynamic quenching mechanisms, revealing a 1:1 interaction, as delineated from Benesi-Hildebrand plot, with a binding constant of  $\sim 10^5 \text{ M}^{-1}$ , which is in excellent agreement with the binding constant extracted from fluorescence anisotropy measurements. The thermodynamic parameters,  $\Delta H^\circ$ ,  $\Delta S^\circ$ , and  $\Delta G^\circ$  as determined from van't Hoff relationship indicate the predominance of van der Waal's/extensive hydrogen bonding interactions for the binding phenomenon. The molecular docking and site selective binding studies reveal the predominant binding of PPI in subdomain IIA of BSA. From the fluorescence resonance energy transfer study, the average distance between tryptophan 213 of the BSA donor and the PPI acceptor is found to be 3.04 nm. CD study demonstrates the reduction of  $\alpha$ -helical content of BSA protein on binding with PPI, clearly indicating the change of conformation of BSA.

### 5.1 Introduction

The interaction and energetics of protein binding towards small molecules are largely dependent on the microenvironment and molecular architecture arising due to folding/unfolding or even change of the protein structure. The remarkable properties of a small molecule in such a microenvironment bear information related to the binding site, which is essential for drug development and many other investigations.<sup>1-4</sup>

Model globular proteins, such as serum albumins, are important transport proteins and are found plentiful in plasma.<sup>5-8</sup> Bovine serum albumin (BSA), a large globular protein (65000 Da), contains 583 amino acids residues in a single chain.<sup>9</sup> The three domains with different surface charge densities impact BSA adsorption on charged surfaces.<sup>10-11</sup> As for example, the presence of both positively charged residues (lysine and arginine) and negatively charged amino acids (glutamic acid and aspartic acid) on BSA can result in electrostatic interactions with both negatively and positively charged surfaces, respectively.<sup>12,13</sup> Because of the presence of a negatively charged domain, BSA is involved in (a) binding with water, salts, fatty acids, vitamins and hormones and carries them between tissues and cells, (b) removing toxic substances, including pyrogens, from the medium, (c) solubilizing lipids, and is a blocking agent in western blot or enzyme-linked immunosorbent assay applications, and (d) solubilizing other proteins (e.g., labile enzymes). BSA is readily soluble in water and can only be precipitated in the presence of high concentrations of neutral salts such as ammonium sulfate. However, albumin is readily coagulated by heat. So, it is apparent that the BSA can bind a large variety of bioactive molecules by various noncovalent interactions such as hydrophobic, hydrophilic, and ionic interactions. Tryptophan (Trp) 134 and Trp 213 are the two Trp residues present in BSA. It has three domains I, II, and III, each consisting of two subdomains A and B.

The major binding sites of BSA are localized in subdomains, IIA and IIIA, known as site I and site II.<sup>14,15</sup> To infer the protein interaction site with small molecules, site marker fluorescent probes are generally utilized. A great deal of research activities on the structure and function of serum albumins are reported in the literature.<sup>16-27</sup> Nowadays, it is of interest to develop and use special polarity-sensitive fluorescent probes. The main focus of the present work deals with the fluorescence emission and binding aspects of a synthetic fluorophore, a phenanthrene–pyrene based conjugate (PPI) in the hydrophobic milieu of a globular protein, BSA under physiological conditions.

The novelty of the present study stems from the fact that the phenanthrene imidazole molecules<sup>28</sup> act as potential selective biomarkers for inhibition of various enzymatic processes. Here, pyrene moiety has been incorporated with phenanthrene imidazole core as a fluorophore unit to validate the binding proficiency with BSA. The presence of an aryl-heteroatom bond, particularly the C–N bond, is significant for showing different biological activities.<sup>29</sup>

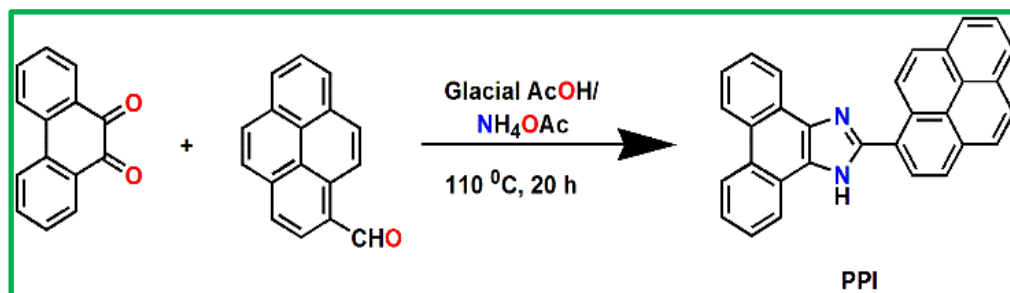
## 5.2 Experimental Section

### 5.2.1 Materials

All the starting materials were of reagent grade. Ibuprofen, warfarin, 8-Anilino-1-naphthalene sulfonic acid (ANS), phenanthrene-9,10-dione and 1-pyrene carboxaldehyde were procured from Sigma-Aldrich and used as received. All the proteins and enzymes (HSA, BSA,  $\beta$ -lactoglobulin, lysozyme, CT-DNA, hemoglobin, cytochrome C, proteinase K, collagen, and trypsin) were also obtained from Sigma Aldrich. Deionized water from Milli-Q source was used throughout the study.

### 5.2.2 Instrumentation

Fourier transform infrared (FTIR) spectra ( $4000\text{--}400\text{ cm}^{-1}$ ) were recorded on a Perkin-Elmer RX I FT-IR spectrophotometer with a solid KBr disc. The UV-vis spectral studies were recorded on an Agilent diode array spectrophotometer (Agilent 8453). Steady-state fluorescence spectra were recorded on a PTI spectrofluorimeter (Model QM-40) by using a fluorescence-free quartz cuvette of 1 cm path length. The excitation and emission slit widths were fixed at 3 nm. A Bruker 300 MHz spectrophotometer was used to run the  $^1\text{H}$ - and  $^{13}\text{C}$ -NMR spectra in dimethyl sulfoxide (DMSO)- $d_6$  with trimethylsilane as an internal standard. The electrospray ionization mass spectra (ESI-MS<sup>+</sup>) (m/z) of the probe was recorded on a HRMS spectrophotometer (QTOF Micro YA263). The time-correlated single photon counting (TCSPC) measurements using a picosecond diode laser (IBH Nanoled-07) in an IBH fluorocube apparatus were used to determine the fluorescence lifetimes. A Hamamatsu MCP photomultiplier (R3809) was used to collect the fluorescence decay data which were further examined by the IBH DAS6 software. CD spectral studies were recorded on a PC-driven JASCO J815 (Japan) spectropolarimeter.



Scheme 5.1 Synthesis of PPI.

### 5.2.3 Synthesis and Characterization of PPI

The probe was synthesized by the previously reported method.<sup>30</sup> with slight modification. A mixture of phenanthrene-9,10-dione (1.04 g, 5 mmol), 1-pyrene carboxaldehyde (1.15 g, 5 mmol) and ammonium acetate (2.89 g, 37.45 mmol) were dissolved in glacial acetic acid (40 mL). Then the resulting solution was refluxed at 110 °C for 20 h in a nitrogen atmosphere, during which time a yellowish green solid was formed. An excess of de-ionized water (30 mL) was added to complete the precipitation. The crude product was collected by filtration, washed with water, and dried by suction (Scheme 5.1). <sup>1</sup>H NMR (DMSO-*d*<sub>6</sub>):  $\delta$  in ppm 10.81 (s, 1H), 9.03 (d, 2H,  $J = 7.8$  Hz), 8.79 (d, 3H,  $J = 6.63$  Hz), 8.70 (d, 1H,  $J = 8.1$  Hz), 8.60 (d, 1H,  $J = 7.92$  Hz), 8.45 (m, 5H), 8.23 (d, 1H,  $J = 7.8$  Hz), 7.87 (t, 4H) (Figure 5.1). <sup>13</sup>C NMR (DMSO-*d*<sub>6</sub>):  $\delta$  in ppm 147.51, 133.49, 131.25, 130.68, 130.06, 129.81, 129.37, 128.98, 128.50, 127.74, 127.58, 127.15, 126.82, 125.24, 124.83, 124.28, 123.79, 123.17, 123.05 (Figure 5.2). ESI-MS<sup>+</sup> (experimental):  $m/z = 419.1546$  [C<sub>31</sub>H<sub>18</sub>N<sub>2</sub> + H<sup>+</sup>], theoretical:  $m/z = 419.1548$  (Figure 5.3). IR Spectrum:  $\tilde{\nu} = 3454$  cm<sup>-1</sup> (-NH), 1646 cm<sup>-1</sup> (-C=N) (Figure 5.4).

### 5.2.4 Experimental Solution

A 10 mM Tris buffer solution (100 mL) of pH 7.4 was prepared in deionized water, which was used in all experiments. A stock solution was prepared by dissolving the required amount of BSA ( $M_{\text{BSA}} = 66400$  g mol<sup>-1</sup>) in pH 7.4 Tris-HCl buffer solution and the exact concentration was determined spectrophotometrically using the molar extinction coefficient 44 000 M<sup>-1</sup> cm<sup>-1</sup> at 280 nm,<sup>31</sup> whereas, the 10 mL stock solution of PPI ( $1.0 \times 10^{-3}$  M) was prepared in dimethyl formamide because of its poor solubility in water. The stock solutions of other proteins, enzymes and biomolecules were prepared as required, and the exact concentrations of the protein stock solutions were evaluated spectrophotometrically by

considering the absorbance and molar extinction coefficient values at particular wavelengths as relevant. Each solution was mixed thoroughly prior to all spectral investigations.

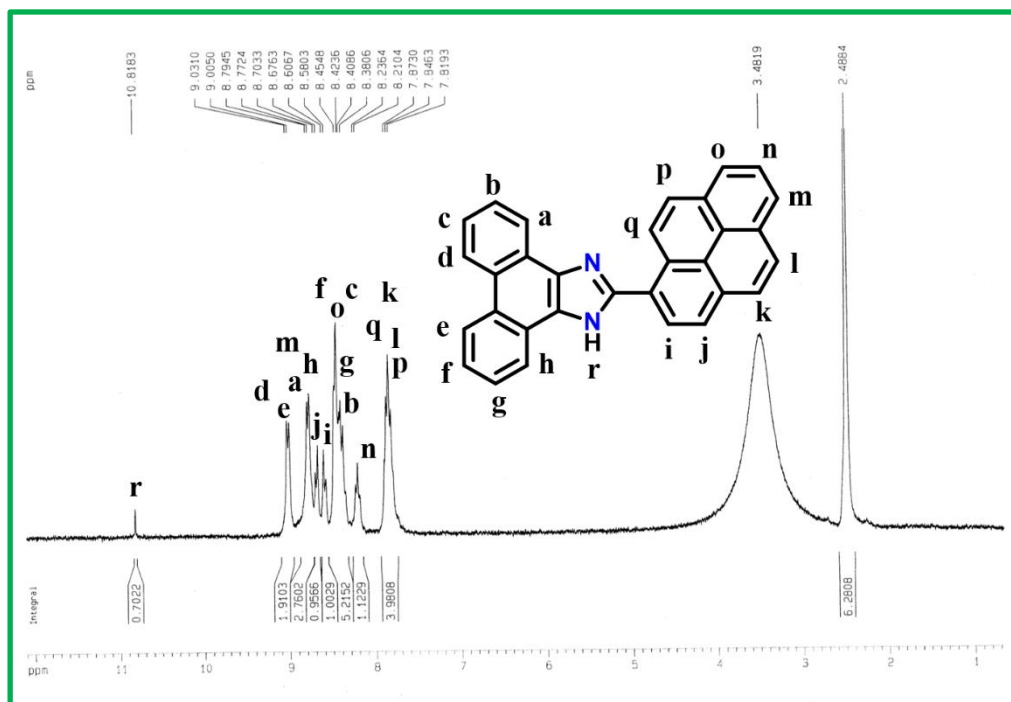


Figure 5.1 <sup>1</sup>H-NMR spectrum of PPI in DMSO-*d*<sub>6</sub> in Bruker 300 MHz instrument.

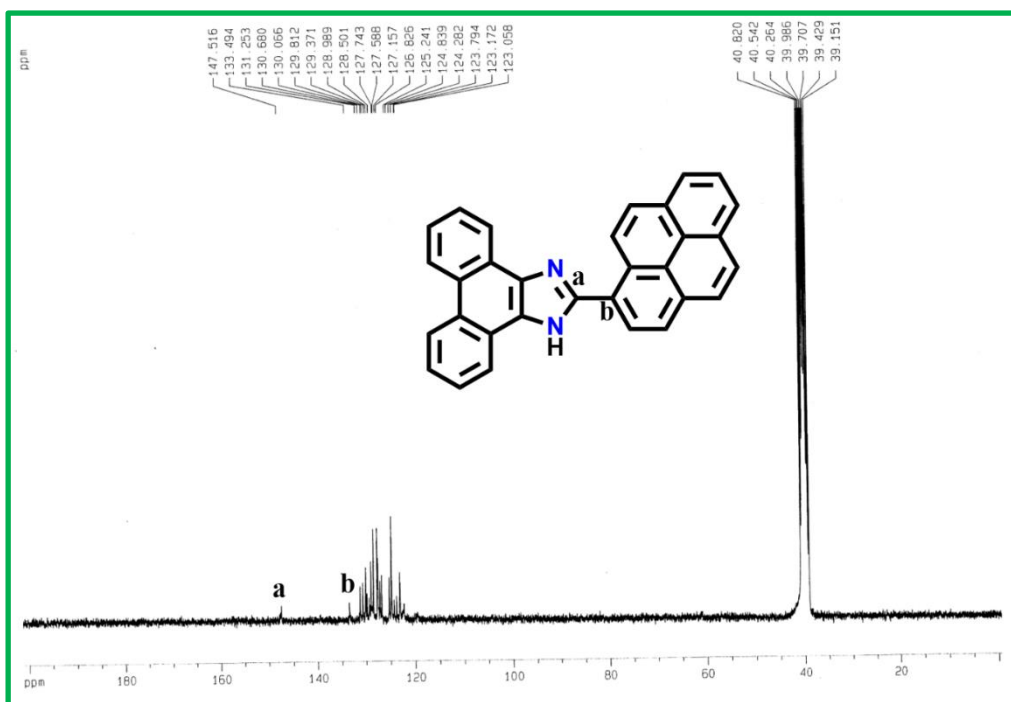


Figure 5.2 <sup>13</sup>C-NMR spectrum of PPI in DMSO-*d*<sub>6</sub> in Bruker 300 MHz instrument.

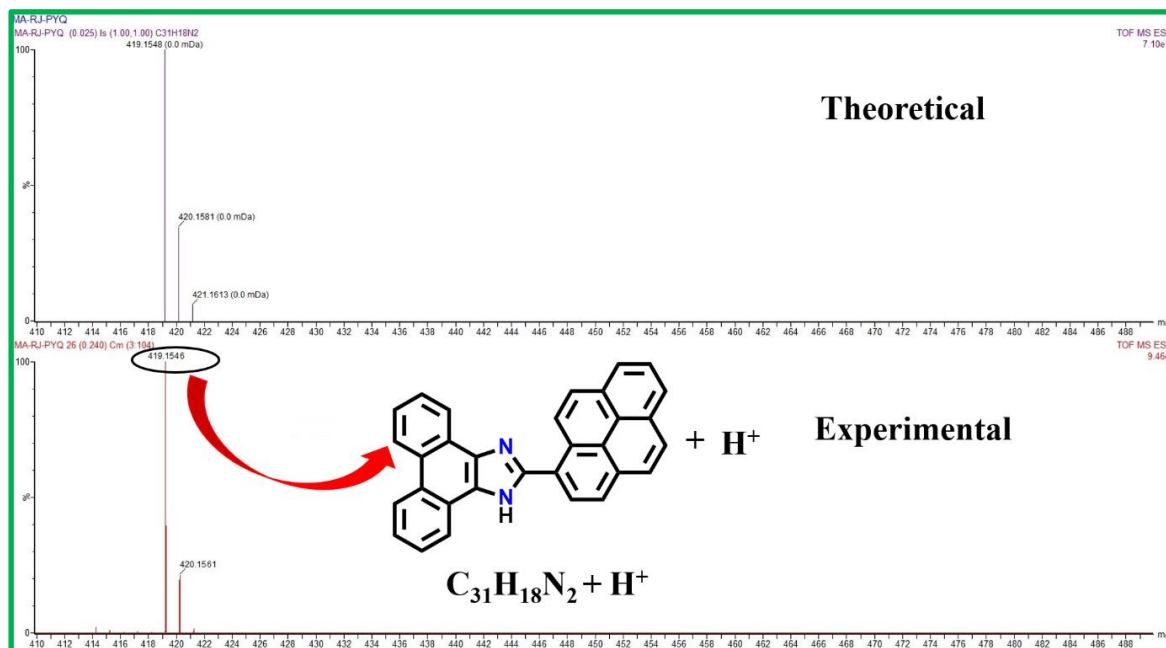


Figure 5.3 Mass spectrum of PPI in CH<sub>3</sub>CN.

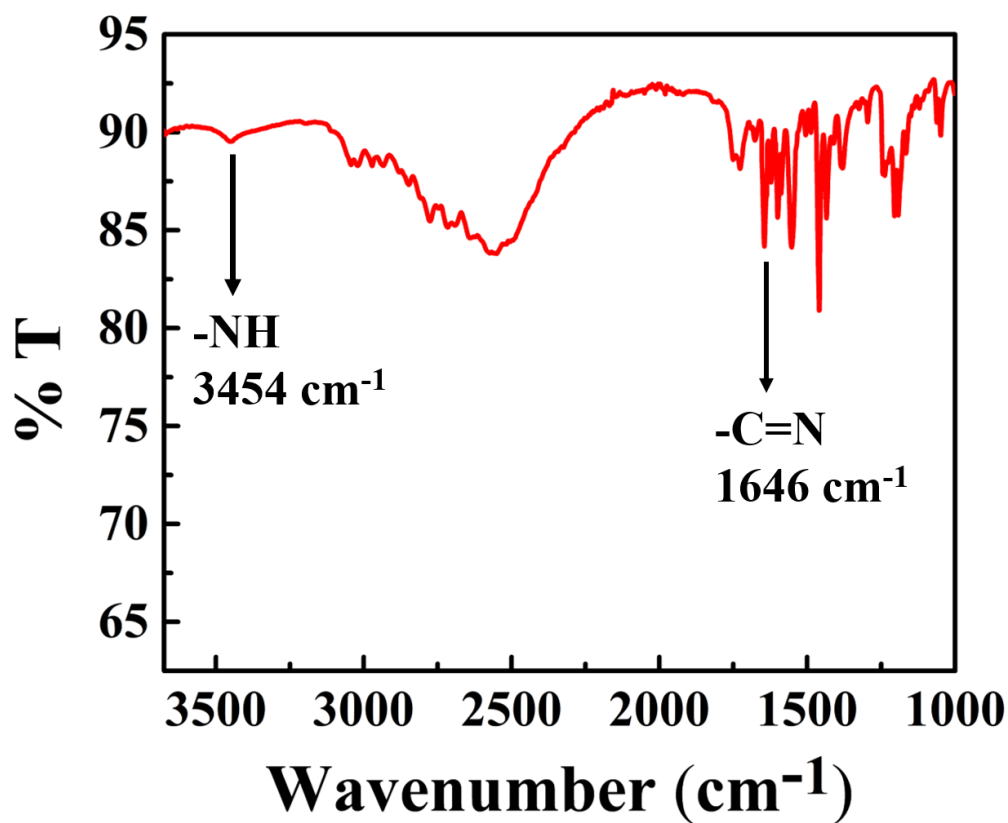


Figure 5.4 IR spectrum of PPI.



### 5.2.5 UV-Vis and Fluorescence Spectroscopic Studies

All the UV-vis spectra were collected with proper background correction. The absorption titrations were performed by keeping BSA concentration fixed at 5  $\mu\text{M}$  with successive increasing the concentration of the PPI solution within the range 0-25  $\mu\text{M}$ .

For the fluorescence studies, a fixed amount of PPI (20  $\mu\text{M}$ ) was titrated with gradual addition of BSA in the range 0-70  $\mu\text{M}$ , upon excitation at 380 nm. Whereas, in another experiment a fixed amount of BSA (10  $\mu\text{M}$ ) was titrated with increasing concentration of PPI within the range 0-20  $\mu\text{M}$  to measure the intrinsic fluorescence of BSA, upon excitation at 295 nm. The titrations were carried out under constant stirring condition.

### 5.2.6 Steady-State Fluorescence Anisotropy

Fluorescence anisotropy ( $r$ ) measurements were carried out by considering the following equation described by Larsson *et al.*<sup>32</sup>

$$r = \frac{I_{VV} - GI_{VH}}{I_{VV} + 2GI_{VH}} \quad (1)$$

Where, the polarizer positions were set at (0°, 0°), (0°, 90°), (90°, 0°), and (90°, 90°) to get  $I_{VV}$ ,  $I_{VH}$ ,  $I_{HV}$ ,  $I_{HH}$  for excitation and emission signals respectively.  $G$  factor is defined as

$$G = \frac{I_{HV}}{I_{HH}} \quad (2)$$

Where,  $I_{HV}$  and  $I_{HH}$  are respectively the vertical and horizontal component of emission polarizer, keeping the excitation polarizer horizontal.  $G$  depends on slit widths and monochromator wavelength. The excitation and emission wavelengths were fixed at 380 and 475 nm respectively.

### 5.2.7 Circular Dichroism (CD) Spectra

All the reported CD spectra were recorded in the wavelength range 195–300 nm under constant purged with nitrogen and a scan speed of 100 nm min<sup>-1</sup>. Here, a fixed concentration of BSA (0.75  $\mu\text{M}$ ) was titrated with the increasing concentration of PPI from 0  $\mu\text{M}$  to 4  $\mu\text{M}$  in Tris-HCl buffer solution of pH 7.4 at 25 °C. Each CD spectrum was an average of five scans and the baseline correction was performed with Tris–HCl buffer signal.

### 5.2.8 Detection Limit

The detection limit was calculated on the basis of the fluorescence titration with BSA. The fluorescence emission spectrum of PPI was measured 10 times to calculate the standard deviation of blank measurement. Then, the fluorescence emission at 457 nm was plotted as a function of the concentration of BSA from the corresponding titration experiment to evaluate the slope. The detection limit was then calculated using the following equation:<sup>33</sup>

$$\text{Detection limit} = 3\sigma/k \quad (3)$$

Where “ $\sigma$ ” is the standard deviation of blank measurement, and “ $k$ ” is the slope of the plot between the fluorescence emission intensity versus [BSA].

### 5.2.9 Fluorescence Lifetime Measurements

The TCSPC measurements were carried out in 10 mM Tris-HCl buffer solution of pH 7.4 for the fluorescence decay of PPI in the absence and in the presence of increasing concentration of BSA at 25 °C. Further, the fluorescence decay of BSA was performed in the absence and in the presence of increasing concentration of PPI to assess the interaction with PPI. The instrument response function (IRF) was ascertained experimentally by using dilute micellar solution of SDS in water as light signal scatterer. During the TCSPC measurements the photoexcitation was fixed at 370 nm for PPI, and at 300 nm for BSA. The fluorescence decay data were collected by using eq 4:

$$F(t) = \sum_i \alpha_i \exp\left(-\frac{t}{\tau_i}\right) \quad (4)$$

Where,  $\alpha_i$  represents the  $i$ th pre-exponential factor and  $\tau_i$  denotes the decay time of component  $i$ . The decay time is mentioned to as the lifetime of the excited species. The average lifetimes ( $\langle \tau \rangle$ ) for the fluorescence decay profiles were calculated by using the following equation:<sup>34</sup>

$$\langle \tau \rangle = \frac{\sum_i \alpha_i \tau_i}{\sum_i \alpha_i} \quad (5)$$

In case of time-resolved anisotropy decay experiment anisotropy decay function  $r(t)$  was formed by using the following equation.<sup>35</sup>

$$r(t) = \frac{I_{\parallel}(t) - GI_{\perp}(t)}{I_{\parallel}(t) + 2GI_{\perp}(t)} \quad (6)$$

Where,  $I_{\parallel}(t)$  and  $I_{\perp}(t)$  represent fluorescence decays gained for parallel and perpendicular emission polarizer, respectively with respect to the vertical excitation polarizer.  $G$  denotes the correction factor for the detector sensitivity of the instrument.

### 5.2.10 Molecular Docking Simulation Study

Molecular docking simulation studies using AutoDock (version 4.2) help to identify the probable binding site and mode of binding of the probe PPI with BSA. The RCSB Protein Data Bank (PDB ID:4JK4) was used as a source of X-ray crystal structure of BSA. The Chem3D Ultra 8.0 was used to draw the probe structure, which was further modified using Gaussian 09W and AutoDock 4.2 programs. Gasteiger partial charges were added to the probe atoms. The non-polar hydrogen atoms were united, and rotatable bonds were defined. Grid maps of  $126 \times 126 \times 126$  Å grid points and 0.403 Å grid spacing were generated using the AutoGrid program. The default values were used for other AutoDock parameters. The Lamarckian genetic algorithm (LGA) was used for docking calculations and the parameters were set to 100 GA runs for each docking simulation upto 250000 energy evaluations. The population size was set to 150 with a crossover rate of 0.8 (LGA). For further analysis of docking simulations, we chose the best optimized docked model with the lowest energy, and this was best viewed in PyMOL software.

## 5.3 Results and Discussion

### 5.3.1 UV-Visible Absorption Study

Absorption spectral study is a useful tool to explore the structural variations and to analyze the complex formation between the protein and probe in solution.<sup>36</sup> UV-vis titrations were carried out at 5 μM BSA concentration, gradually increasing the concentration of PPI (0-25 μM) in aqueous buffer solution. The absorption spectral changes of BSA with a gradual change in the concentration of PPI are shown in **Figure 5.5**. Though PPI has no absorption at 280 nm, gradual addition of PPI results into an increase in absorbance of BSA at 280 nm, with contemporary growing of an absorbance peak at 380 nm due to PPI. The pattern of the absorption spectra at 280 nm also changes with the increase in the concentration of PPI. This observation supports the complexation between PPI and BSA.

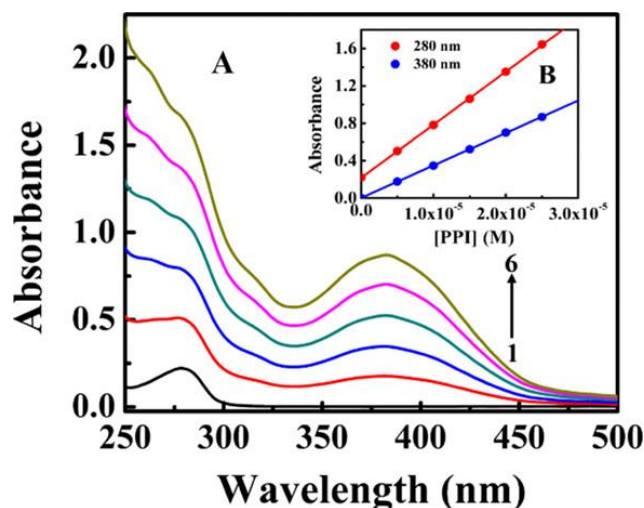


**Figure 5.5** (A) Absorption spectral changes of BSA (5  $\mu\text{M}$ ) with incremental addition of PPI (0-25  $\mu\text{M}$ ) at 25  $^{\circ}\text{C}$ . (B) Inset: absorbance plot at 280 and 380 nm as a function of PPI concentration.

### 5.3.2 Fluorescence Emission Study

Interaction between the protein and probe is well-characterized by the investigation of steady-state fluorescence emission technique. At first, we systematically recorded fluorescence responses of PPI (20  $\mu\text{M}$ ) in Tris-HCl buffer solution (pH 7.4) by the addition of excess amount (10 equiv.) of different proteins and enzymes, including  $\beta$ -lactoglobulin, lysozyme, CT-DNA, hemoglobin, cytochrome C, proteinase K, collagen, trypsin, HSA, and BSA. Here, it was also worth noting that only BSA was capable of enhancing the fluorescence intensity at 457 nm among the different proteins and enzymes tested (**Figure 5.6**). To follow the PPI—BSA interaction, fluorescence titrations were performed at 20  $\mu\text{M}$  PPI concentration in aqueous medium with the incremental addition of BSA. The emission maximum of PPI was shifted from 476 to 457 nm in 70  $\mu\text{M}$  BSA solution with progressive enhancement of the fluorescence intensity (**Figure 5.7A**) when PPI was excited at 380 nm. The fluorescence intensity variations and  $\lambda_{\text{em}}^{\text{max}}$  of PPI as a function of the BSA concentration are more clearly exhibited in **Figure 5.7B**, which represents a steep variation of  $\lambda_{\text{em}}^{\text{max}}$  up to 15  $\mu\text{M}$  BSA followed by attainment of a tableland region, and this fact is a clear indication for an ample modification of the surrounding of PPI within the protein heterogeneous microenvironment. This noticeable blue shift with a concomitant increase in the fluorescence intensity is caused by the alteration in the position of PPI from a more polar aqueous phase to a more hydrophobic protein environment when PPI binds with BSA.

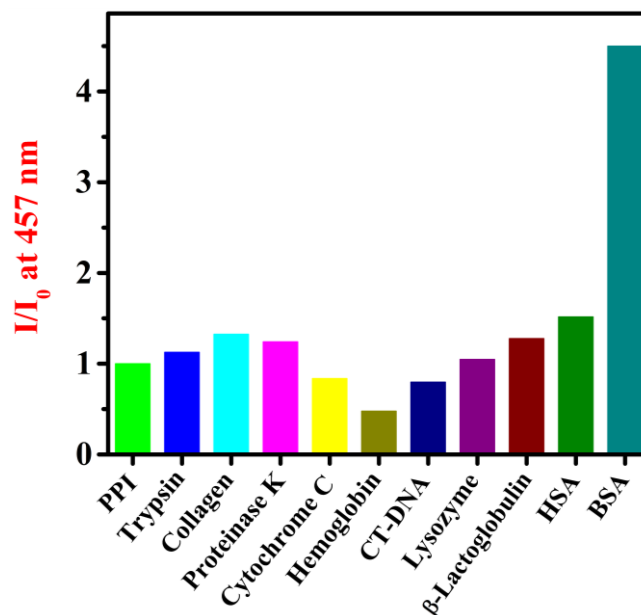


**Figure 5.6** Variations in emission intensity ( $I/I_0$ ) of PPI (20  $\mu\text{M}$ ) at 457 nm in Tris-HCl buffer solution (pH 7.4) by the addition of excess amount (10 equiv.) of different proteins and enzymes.  $\lambda_{\text{ex}} = 380 \text{ nm}$ .

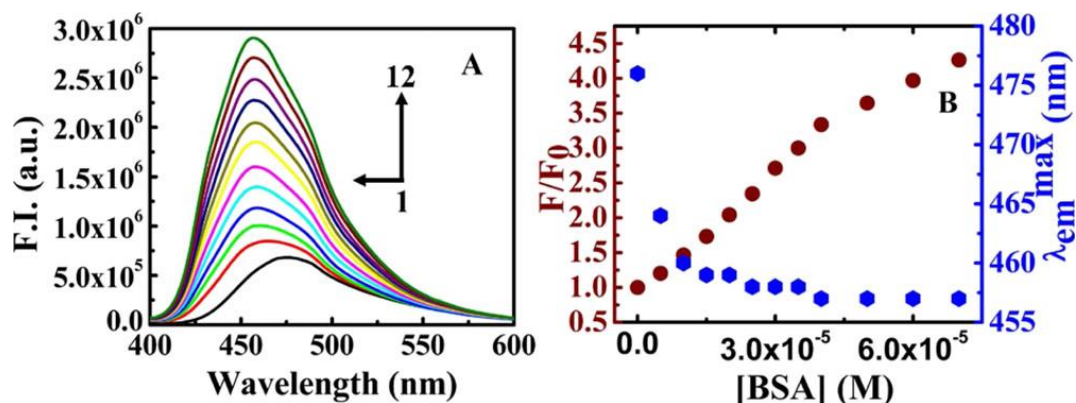


**Figure 5.7** (A) Emission spectra of PPI (20  $\mu\text{M}$ ) with the gradual addition of BSA (0-70  $\mu\text{M}$ ) at 25  $^{\circ}\text{C}$ . (B) Plot of relative variation ( $F/F_0$ ) of the emission intensity and emission maximum ( $\lambda_{\text{em}}^{\text{max}}$ ) of PPI against BSA concentration.

BSA fluorescence comes from the presence of three amino acid residues namely, tyrosine (Tyr), Trp, and Phe. In particular, Trp fluorescence is used to monitor the changes in the structural conformation of the BSA protein and to interpret the local environment of BSA bound PPI.<sup>37-39</sup> There are two Trp moieties in BSA, that is, Trp 134 and Trp 213, which are located in subdomains IB and IIA, respectively. Trp 134 is well-exposed to the hydrophilic region, whereas Trp 213 resides in a hydrophobic cavity of the BSA protein.<sup>40,41</sup>

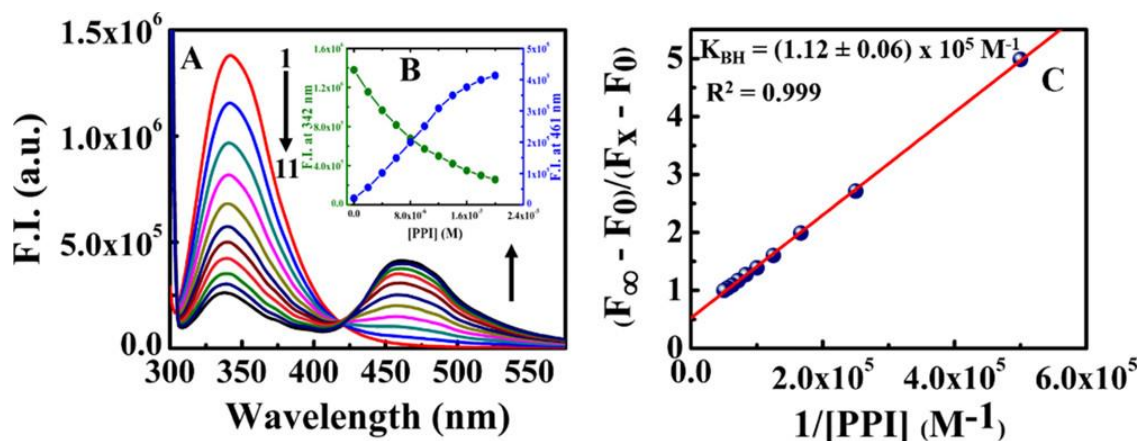


**Figure 5.8** (A) Emission spectra of BSA (10 μM) with the gradual addition of PPI (0-20 μM) at 25 °C. (B) Inset of Figure 5.8A; shows the plot of emission intensity variation at 342 and 461 nm, respectively, as a function of the PPI concentration. (C) Representative Benesi-Hildebrand plot for 1:1 complexation of BSA with PPI.  $\lambda_{\text{ex}}$  for BSA is 295 nm.

BSA shows a strong fluorescence maximum at 342 nm in aqueous buffer solution when the excitation of BSA is made at 295 nm.<sup>42</sup> Excitation at 295 nm was selected to minimize the contribution of the Tyr residue present in BSA. To find out the binding constant for BSA-PPI interaction, in another experiment, the fluorescence titration was performed at 10 μM BSA concentration with the gradual addition of PPI leading to saturation. **Figure 5.8A** shows that the emission intensity of BSA is decreased considerably along with a small blue shift of  $\lambda_{\text{em}}^{\text{max}}$  from 342 to 338 nm with increasing PPI concentration, which in turn implies that PPI binds strongly with BSA and also indicates that the microenvironment around Trp moieties present in BSA is modified on interacting with PPI.<sup>43</sup> There is an important observation that apart from the quenching of emission intensity of BSA at 342 nm, a new emission band is developed at 461 nm. The intensity of this emission band is progressively enhanced with the increasing concentration of PPI. The presence of an isoemissive point at 420 nm is an indication of the equilibrium between the free and bound forms of PPI. Inset of **Figure 5.8A** vividly shows the emission intensity variation at 342 and 461 nm as a function of PPI concentration.

Moreover, by exploiting the linear dependence of the PPI emission changes as a function of BSA concentration (**Figure 5.9**), the limit of detection (LOD) value was estimated to be 6.87 nM.

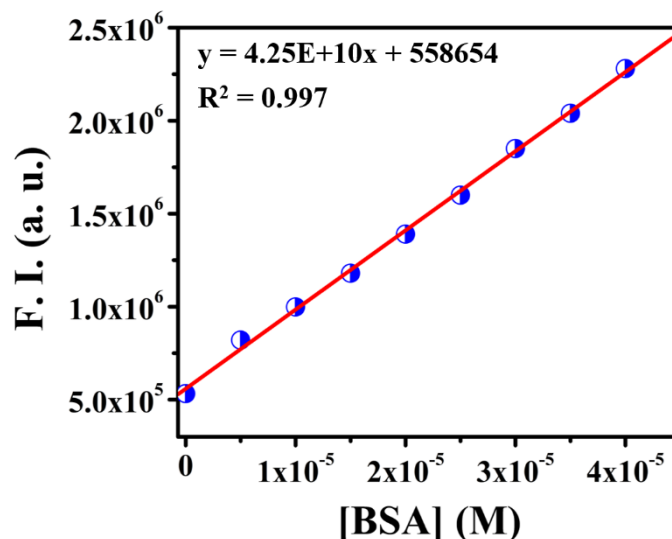


**Figure 5.9** Linear fluorescence response of PPI (20  $\mu\text{M}$ ) to BSA (0-40  $\mu\text{M}$ ) at 457 nm for LOD determination. The LOD value was estimated from 10 times the standard deviation ( $\sigma$ ) of the fluorescence intensity corresponding to the blank sample (PPI only). Here,  $\sigma$  value is 97.589. From the graph we get slope =  $4.25 \times 10^{10} \text{ M}^{-1}$ .

### 5.3.3 Probe-Protein Binding Study

The binding of PPI with BSA can be explained by eqs 7 and 8 considering 1:1 complexation between them.



$$K_{\text{BH}} = \frac{[\text{PPI}:\text{BSA}]}{[\text{PPI}][\text{BSA}]} \quad (8)$$

where  $K_{\text{BH}}$  represents the association constant. The data obtained from the spectrofluorimetric titration of a fixed concentration of BSA with the increasing concentration of PPI are further investigated to find out the binding constant by adopting Benesi-Hildebrand equation.<sup>44</sup>

$$\frac{\Delta F_{\text{max}}}{\Delta F} = 1 + \frac{1}{K_{\text{BH}} [\text{PPI}]} \quad (9)$$

Where,  $\Delta F_{\text{max}} = |F_{\infty} - F_0|$ , and  $\Delta F = |F_x - F_0|$ .  $F_0$ ,  $F_x$ , and  $F_{\infty}$  indicate the emission intensities of BSA in the native state, at an intermediate PPI concentration, and at a PPI concentration when the interaction is saturated, respectively.



$|F_{\infty} - F_0| / |F_x - F_0|$  versus  $1/[PPI]$  plot displays a linear variation (Figure 5.8C), validating the accuracy of eq 9 and supports the 1:1 complexation between PPI and BSA. The 1:1 binding of PPI with BSA was also confirmed by Job's plot analysis using the emission spectral data. In this method, the emission data were recorded by changing the PPI: BSA molar ratio, whereas the total molar concentration of PPI and BSA was constant.<sup>45</sup> The Job's plot for PPI-BSA, that is, the difference in the emission intensity at 342 nm versus the mole fraction of PPI (Figure 5.10) intersected at 0.491, showing the number of PPI molecules binding to BSA to be around unity. The  $K_{BH}$  value, evaluated from the reciprocal of the slope  $1/K_{BH}$  and the corresponding free energy change ( $\Delta G$ ) accompanying the binding process are presented in Table 5.1, implying strong complexation between PPI and BSA.<sup>46</sup>

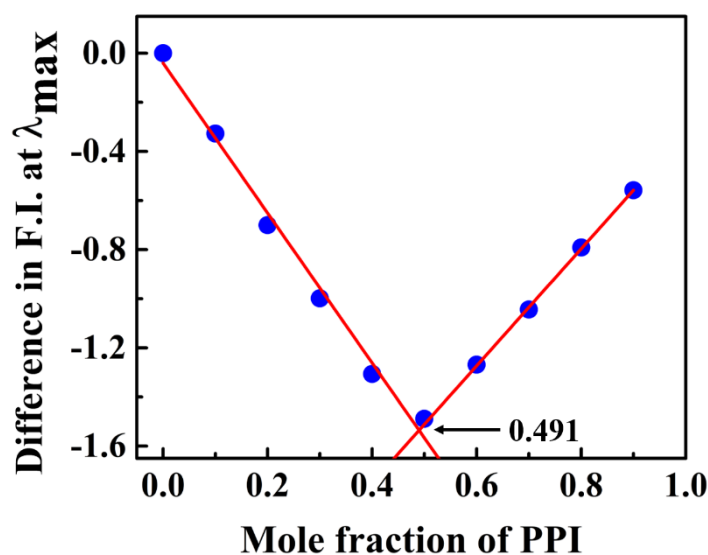


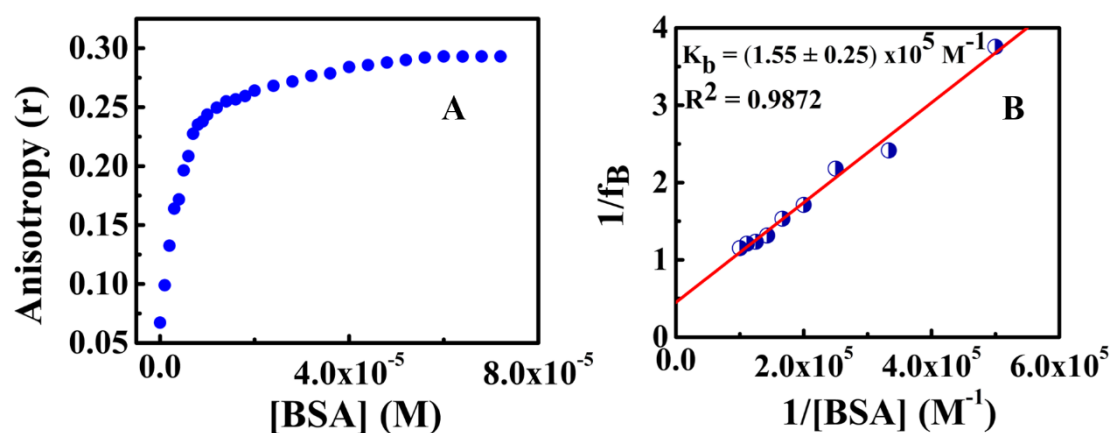
Figure 5.10 Job's plot for the binding of PPI to BSA.

Table 5.1 Binding parameters for the association of PPI with BSA at 25 °C.

method	environment	binding constant ( $10^5 M^{-1}$ )	$\Delta G$ (kJ mol <sup>-1</sup> )
Benesi-Hildebrand	PPI-BSA	(1.12 ± 0.06)	-28.80
fluorescence anisotropy	PPI-BSA	(1.55 ± 0.25)	-29.60

### 5.3.4 Fluorescence Anisotropy Study

To gather information about the rigidity of the surrounding environment of a probe, fluorescence anisotropy measurement is a useful experiment.<sup>47</sup> It also gives information regarding the boundary to which the rigid environment obstructs the rotational mobility of the probe. Enhancement of anisotropy values reflects an increase in the rigidity of the environment around a fluorescent probe. The change in the anisotropy values of PPI with a change in the BSA concentration in aqueous buffer medium is represented in **Figure 5.11A**. Primarily, a rapid enhancement of the anisotropy value from 0.067 to 0.235, till the addition of 8  $\mu\text{M}$  BSA, was observed; then, the increase was gradually to a value of 0.284 till the addition of 40  $\mu\text{M}$  BSA. The increasing value of anisotropy clearly indicates the fact that substantial restriction is imposed on the free motion of PPI molecules with the gradual addition of BSA, and this can be only possible if BSA strongly binds with PPI. The maximum anisotropy value, 0.293, was obtained at 60  $\mu\text{M}$  BSA, and after that, the levelling off of the anisotropy values was observed, which in turn reflects the saturation of association between PPI and BSA.



**Figure 5.11** (A) Anisotropy variation of PPI as a function of the BSA concentration at 25 °C.  $\lambda_{\text{ex}} = 380 \text{ nm}$  and  $\lambda_{\text{em}} = 475 \text{ nm}$  for PPI. (B) Plot of  $1/f_B$  versus  $1/[\text{BSA}]$  for evaluating the binding constant of the PPI-BSA composite from the anisotropy data.

In accordance with Ingersoll and Strollo<sup>48</sup> method, the binding constant of the PPI-BSA composite can be ascertained by adopting the following equation

$$\frac{1}{f_B} = 1 + \frac{1}{K_b[\text{BSA}]} \quad (10)$$

where  $K_b$  denotes the apparent binding constant of the PPI-BSA composite.  $f_B$  corresponds to the fractional fluorescence contribution of PPI bound to BSA, as shown in eq 11.

$$f_B = \frac{r - r_F}{R(r_B - r) + (r - r_F)} \quad (11)$$

where the anisotropy values of bound BSA–PPI and free PPI are denoted by  $r_B$  and  $r_F$ , respectively. The correction factor,  $R$ , that is, the ratio of  $I_B$  and  $I_F$  is taken into consideration to confirm the fact that PPI experiences fluorescence intensity variation on binding with BSA. The double reciprocal plot of  $1/f_B$  versus  $1/[BSA]$  (Figure 5.11B) is a straight line, and from the slope, the calculated value of  $K_b$  is presented in Table 5.1, which is in good accordance with the value obtained from the spectrofluorimetric titration experiment. Thus, this method sets up its practical application and feasibility to find out the binding constant.<sup>43</sup>

### 5.3.5 ANS Displacement Assay

To check the possible binding site of PPI on BSA, the ANS displacement assay was carried out. The fluorescent probe ANS was used to get information about the hydrophobic binding locations of the protein.<sup>45</sup>

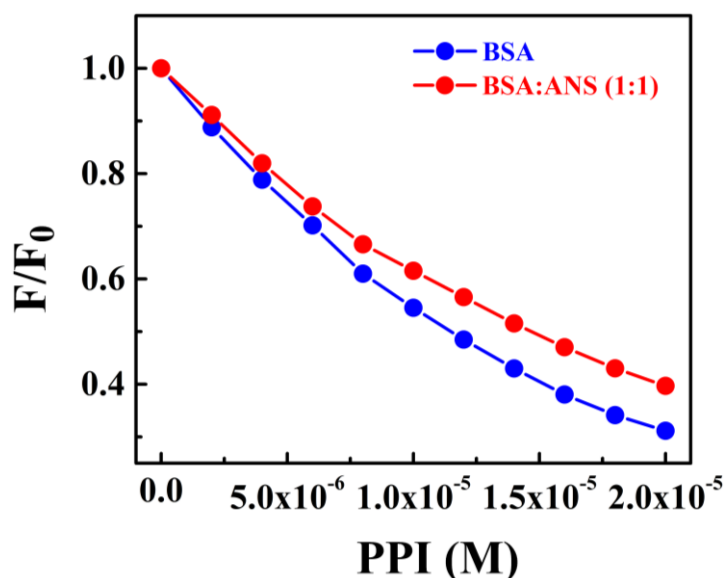
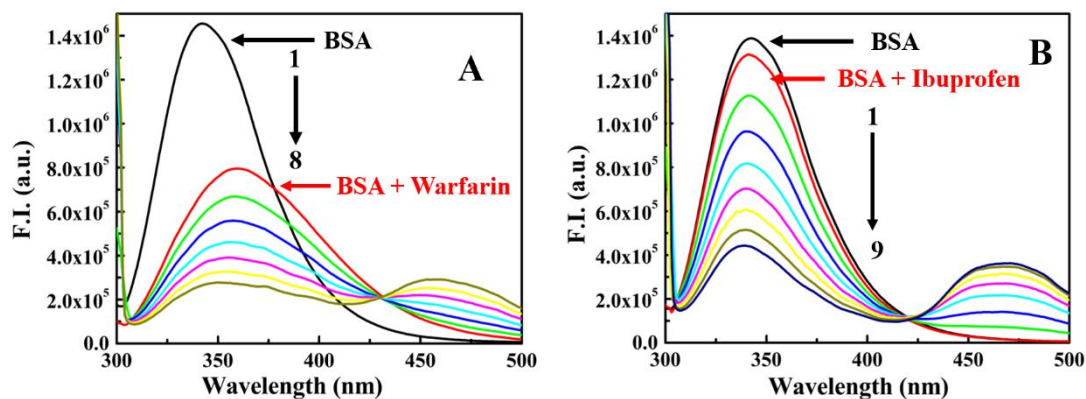


Figure 5.12 ANS displacement study for the quenching of BSA emission by PPI at different BSA-ANS ratio (1:0, 1:1 respectively).

In accordance with the procedure, the displacement studies were accomplished with the introduction of ANS, maintaining similar conditions. **Figure 5.12** represents the plot of  $F/F_0$  versus PPI concentration, which clearly shows that at 20  $\mu\text{M}$  concentration, PPI has a better quenching influence on the emission intensity of BSA than ANS, that is, PPI could quench ~68% and ANS around 51%. The emission intensity of ANS was considerably augmented at 470 nm upon interaction with the hydrophobic regions of BSA, but, when PPI was added to the BSA-ANS composite (1:1), the emission intensity of the composite decreased around 60%. This observation suggested that PPI moderately contend with ANS for the hydrophobic locations of BSA by removing the bound ANS molecules, leading to a decrement in the emission intensity of the BSA-ANS composite.

### 5.3.6 Site-Selective Binding of PPI on BSA

The competitive fluorescence displacement studies were executed to ascertain the BSA binding site in which PPI is located, using two well-known drugs (warfarin and ibuprofen). The range of the binding interaction of the PPI-BSA composite can also be revealed by observing the fluorescence intensity variation of the system.<sup>43</sup> Site marker warfarin exclusively binds at subdomain IIA of site I by hydrophobic interaction, whereas ibuprofen precisely binds at subdomain IIIA of site II through hydrophobic, hydrogen bonding, and electrostatic interactions.<sup>15,43,49,50</sup> Here, PPI was progressively added to the BSA-site marker composites (1:1) in aqueous buffer solution to reveal the spectral change with PPI. **Figure 5.13** represents the spectral changes influenced by the presence of site markers. The introduction of warfarin site marker into the BSA solution significantly quenched the fluorescence intensity associated with a red shift of  $\lambda_{em}$  from 342 to 358 nm (**Figure 5.13A**). Then incremental addition of PPI into the BSA-warfarin composite results in a gradual decrease in the fluorescence intensity, which in turn indicates the PPI influence on the binding of warfarin to BSA. In contrast to warfarin, no meaningful change of BSA fluorescence intensity was observed upon addition of ibuprofen (**Figure 5.13B**). PPI influences the quenching of the fluorescence intensity of BSA-Ibuprofen composite nearly to the same extent as in the absence of Ibuprofen (**Figure 5.8A**). Therefore, the above experimental studies and outcomes clearly establish the fact that the binding of PPI to BSA is principally located at subdomain IIA of site I, which indicates that Trp 213 is inside or in the vicinity of the PPI binding site.



**Figure 5.13** Effect of site markers on the PPI-BSA composite. (A) [BSA] = [Warfarin] = 10  $\mu\text{M}$  with the addition of PPI, each time 2  $\mu\text{M}$ , to a total concentration of 12  $\mu\text{M}$  from curve 3-8 at 25  $^{\circ}\text{C}$ . (B) [BSA] = [Ibuprofen] = 10  $\mu\text{M}$  with the addition of PPI, each time 2  $\mu\text{M}$ , to a total concentration of 14  $\mu\text{M}$  from curve 3-9 at 25  $^{\circ}\text{C}$ .  $\lambda_{\text{ex}}$  of BSA = 295 nm.

### 5.3.7 Study of Fluorescence Quenching Induced by PPI

The incremental addition of PPI into BSA solution induces the quenching of BSA fluorescence (Figure 5.8A). The fluorescence quenching mechanism can be static, owing to the ground-state association between the fluorophore and the quencher, or dynamic, because of collisional encounters between the above said two species at the excited state. These two quenching mechanisms can be discriminated by studying the lifetime measurements or by their varying dependence on temperature and viscosity.<sup>51</sup>

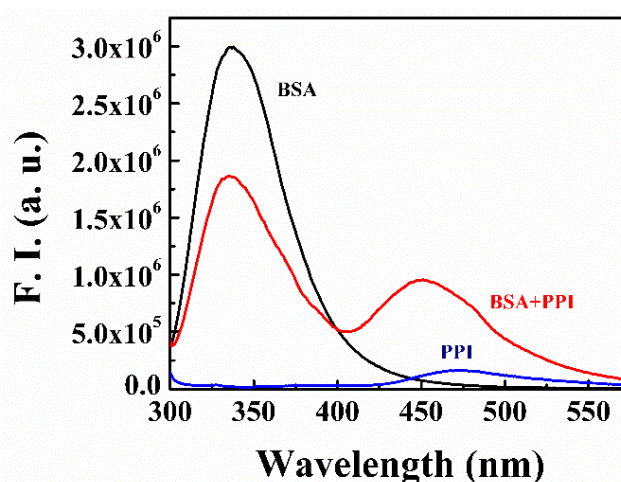


**Figure 5.14** Representative emission profile of BSA(alone), BSA+PPI (1:1) and PPI (alone).  $\lambda_{\text{ex}}$  = 295 nm.

We have performed the emission quenching of Trp present in BSA with the incremental addition of PPI in aqueous buffer solution. Because, PPI has a considerable absorbance at ~280 nm and to avoid the involvement of the inner filter effect to the quenching of BSA fluorescence, the emission intensity was corrected by taking the following relation:<sup>45,52</sup>

$$F = F_{obs} \times e^{(A_{ex} + A_{em})/2} \quad (12)$$

where,  $F$  and  $F_{obs}$  represent the corrected and observed emission intensities, respectively, of the sample under study.  $A_{ex}$  and  $A_{em}$  denotes the absorbance value at the excitation and emission wavelengths, respectively. **Figure 5.14** represents the emission spectrum of PPI at  $\lambda_{ex} = 295$  nm. The probable fluorescence quenching mechanism of BSA-PPI complexation was verified by analyzing the emission data using the well-known Stern-Volmer equation:<sup>51</sup>

$$\frac{F_0}{F} = 1 + K_{SV}[PPI] = 1 + k_q < \tau_0 > [PPI] \quad (13)$$

where,  $F_0$  and  $F$  correspond to the BSA emission intensities in free form and with the successive addition of PPI, respectively.  $K_{SV}$  represents the Stern-Volmer constant, and  $k_q$  is the bimolecular quenching rate constant.  $[PPI]$  and  $< \tau_0 >$  are the molar concentration of the quencher and the average lifetime of a BSA molecule in the absence of PPI, respectively. The involvement of only one type of quenching mechanism, that is, either static or dynamic, is inferred by the linear Stern-Volmer plot.

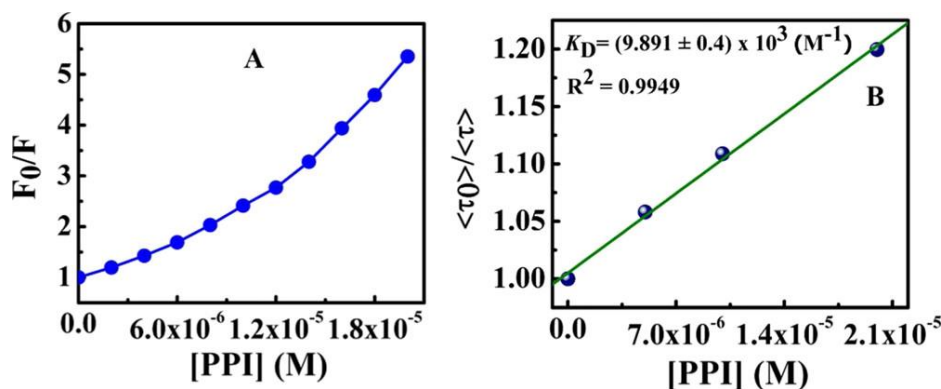


**Figure 5.15** (A) Representative Stern-Volmer plot (from steady-state fluorescence study) for the quenching of BSA (10  $\mu$ M) fluorescence by PPI at 298 K ( $\lambda_{ex} = 295$  nm and  $\lambda_{em} = 342$  nm). (B) Time-resolved Stern-Volmer plot for the quenching of BSA (10  $\mu$ M) fluorescence by PPI at 298 K.

The occurrence of both the above-mentioned quenchings can be inferred, when the plot displays an upward deviation.<sup>38,51,53-55</sup> **Figure 5.15A** displays an upward curvature, signifying the coexistence of static and dynamic quenchings with the same quencher (PPI), and/or the extent of quenching is high at a higher concentration of PPI. Here,  $F_0/F$  is linked with [PPI] by the modified form of Stern-Volmer equation:<sup>51</sup>

$$\frac{F_0}{F} = (1 + K_D[\text{PPI}])(1 + K_S[\text{PPI}]) \quad (14)$$

$$\frac{F_0}{F} = 1 + (K_D + K_S)[\text{PPI}] + K_D K_S [\text{PPI}]^2 \quad (15)$$

where dynamic and static quenching constants are represented by  $K_D$  and  $K_S$ , respectively. The first factor of the right-hand side in **eq 14** represents dynamic quenching, whereas the second factor represents static quenching. The presence of  $[\text{PPI}]^2$  term in **eq 15** accounts for the observation of an upward deviation at high [PPI] when both of the above said quenchings take place for the same fluorophore. The observed dynamic portion can also be ascertained by fluorescence lifetime measurements of BSA against PPI concentration using the following equation:

$$\frac{\langle \tau_0 \rangle}{\langle \tau \rangle} = 1 + K_D[\text{PPI}] = 1 + K_q \langle \tau_0 \rangle [\text{PPI}] \quad (16)$$

where  $\langle \tau_0 \rangle$  and  $\langle \tau \rangle$  correspond to the average lifetime of BSA in native state and with the incremental addition of PPI, respectively. The value of  $K_D = (9.891 \pm 0.4) \times 10^3 \text{ M}^{-1}$  is obtained from the slope of the plot  $\frac{\langle \tau_0 \rangle}{\langle \tau \rangle}$  versus [PPI] (**Figure 5.15B**). The value of  $K_q = K_D / \langle \tau_0 \rangle = (1.64 \pm 0.06) \times 10^{12} \text{ M}^{-1} \text{ s}^{-1}$  is obtained by using the value of  $K_D$  and  $\langle \tau_0 \rangle = 6.01 \text{ ns}$ . The calculated  $K_q$  value is 2 orders of magnitude greater than the maximum diffusion-controlled  $K_q$  value,  $2.0 \times 10^{10} \text{ M}^{-1} \text{ s}^{-1}$ .<sup>51</sup> This implies that the quenching of BSA fluorescence by PPI occurs through Coulombic resonance interaction but not operated by the diffusion process.<sup>38</sup> The fluorescence emission data were further studied by applying the modified Stern-Volmer equation<sup>51,52,56</sup>

$$\frac{F_0}{(F_0 - F)} = \frac{1}{f} + \frac{1}{f \times K_{SV}} \times \frac{1}{[\text{PPI}]} \quad (17)$$



where  $f$  is the maximum accessible fractional initial fluorescence of the protein molecule to the quencher.  $K_{SV}$  and  $f$  values are determined from the intercept and slope of the plot  $F_0/(F_0 - F)$  versus  $1/[PPI]$  (Figure 5.16). The evaluated value of  $K_{SV}$  is  $(5.926 \pm 0.007) \times 10^4 \text{ M}^{-1}$ . The calculated  $f$  value 1.54 indicates that 64.65% of BSA fluorescence is accessible to PPI. The value of  $K_q$  is found to be  $(9.73 \pm 0.01) \times 10^{12} \text{ M}^{-1}\text{s}^{-1}$ , and this high value again establishes the fact that the quenching of BSA is not operated by the diffusion-controlled process.

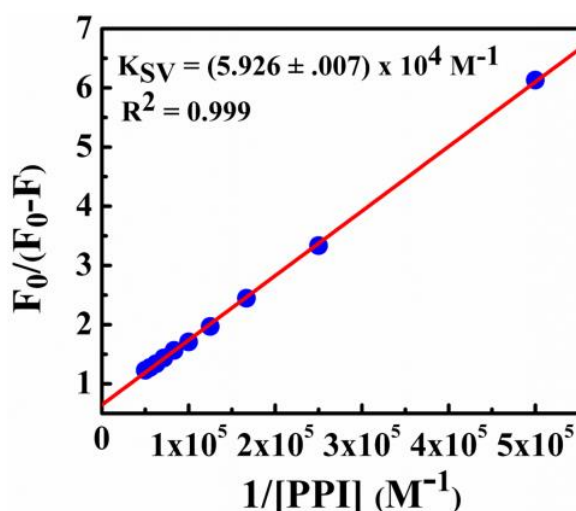


**Figure 5.16** Modified Stern-Volmer plot of PPI induced quenching of BSA (10  $\mu\text{M}$ ) fluorescence at 298 K.

### 5.3.8 Analysis of BSA-PPI Binding Equilibria and Determination of Thermodynamic Parameters

The results obtained from the above dynamic interaction have been utilized to isolate static and dynamic quenching in eq 14. Static quenching is defined by the following equation:



where  $n$  signifies the stoichiometry of the binding process, that is, the number of PPI molecules associated with each BSA molecule. From Figure 5.15A, it is clearly observed that the contribution of dynamic quenching, that is, the upward curvature, becomes considerable only for  $[\text{PPI}] > 8 \mu\text{M}$  (molar ratio  $[\text{PPI}]/[\text{BSA}] > 0.8$ ). So, at a PPI concentration below  $8 \mu\text{M}$ , static quenching can be considered exclusively, as evidenced from a linear dependence of  $F/F_0$  on  $[\text{PPI}]$ .

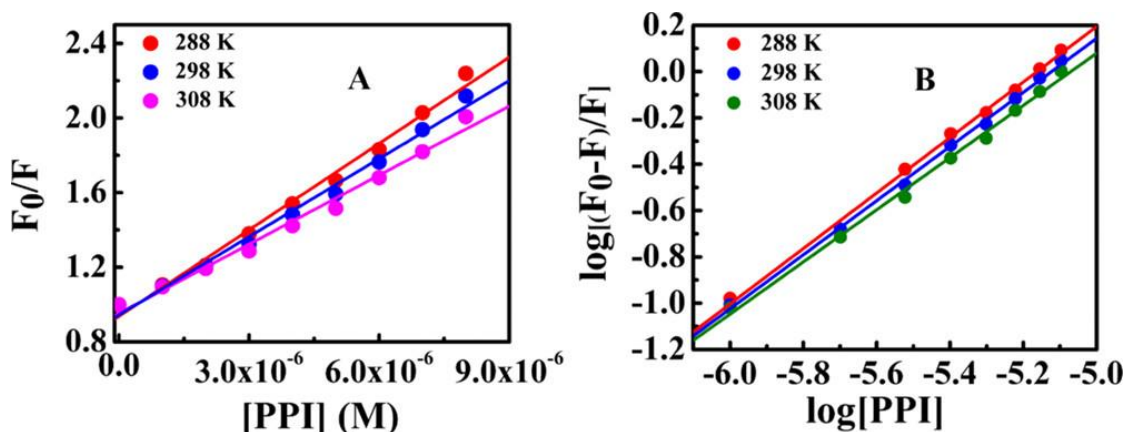


**Figure 5.17** (A) Representative linear Stern-Volmer plots of PPI induced quenching of BSA (10  $\mu\text{M}$ ) fluorescence at low PPI concentrations at different temperatures. (B) Double log plots for the determination of the number of binding sites and the binding constant value of PPI-BSA complexation at different temperatures.

The trend of linear Stern-Volmer quenching plots for  $[\text{PPI}] < 8 \mu\text{M}$  at different temperatures is exhibited in **Figure 5.17A**. By varying the temperature from 288 to 308K, the decreasing tendency of the quenching plot is observed, and the upward deviation becomes insignificant. On the basis of such type of quenching plot and data, the value of the binding constant ( $K_b$ ) and the value of  $n$  (number of binding sites) can be calculated by using **eq 19**:<sup>51,57,58</sup>

$$\log \left[ \frac{(F_0 - F)}{F} \right] = \log K_b + n \log[\text{PPI}] \quad (19)$$

**Table 5.2** Binding constants ( $K_b$ ), number of binding sites ( $n$ ), and thermodynamic parameters for the PPI-BSA system at different temperatures.

Temp. (K)	$K_b$ ( $10^5 \text{ M}^{-1}$ )	$n$	$\Delta H^\circ$ ( $\text{kJ mol}^{-1}$ )	$\Delta S^\circ$ ( $\text{J mol}^{-1}$ )	$\Delta G^\circ$ ( $\text{kJ mol}^{-1}$ )
288	$16.08 \pm 0.08$	$1.19 \pm 0.03$	-41.93	-26.60	-34.27
298	$9.64 \pm 0.11$	$1.16 \pm 0.02$	-41.93	-26.60	-34.01
308	$5.15 \pm 0.16$	$1.12 \pm 0.03$	-41.93	-26.60	-33.74

Figure 5.17B exhibits the representative  $\log[(F_0 - F)/F]$  versus  $\log[\text{PPI}]$  plot at different temperatures, and all numerical parameters thereby obtained are tabulated in Table 5.2, which shows that the  $K_b$  value decreases with increasing temperature. Therefore, it can be expected that static interaction is a temperature-dependent process. The high value of  $K_b$  implies a strong binding affinity of PPI to BSA. Basically, four types of non-covalent forces, namely, van der Waal forces, multiple hydrogen-bonding, hydrophobic, and electrostatic interactions play a vital role in the binding of probes with proteins.<sup>55,59</sup> To ascertain the nature of the ground-state interaction between PPI and BSA in terms of the aforesaid non-covalent forces relevant with the complexation process, related thermodynamic parameters have been estimated by using the following van't Hoff equations<sup>60</sup>

$$\ln K_b = -\frac{\Delta H^\circ}{RT} + \frac{\Delta S^\circ}{R} \quad (20)$$

$$\Delta G^\circ = \Delta H^\circ - T\Delta S^\circ \quad (21)$$

where  $\Delta H^\circ$ ,  $\Delta S^\circ$ , and  $\Delta G^\circ$  are the standard enthalpy, entropy, and free energy changes, respectively for the binding process.  $R$  represents the molar gas constant. The values of  $\Delta H^\circ$  and  $\Delta S^\circ$  are evaluated from the slope and intercept of the  $\ln K_b$  versus  $1/T$  plot (Figure 5.18).  $\Delta G^\circ$  value is then calculated by using eq 21.

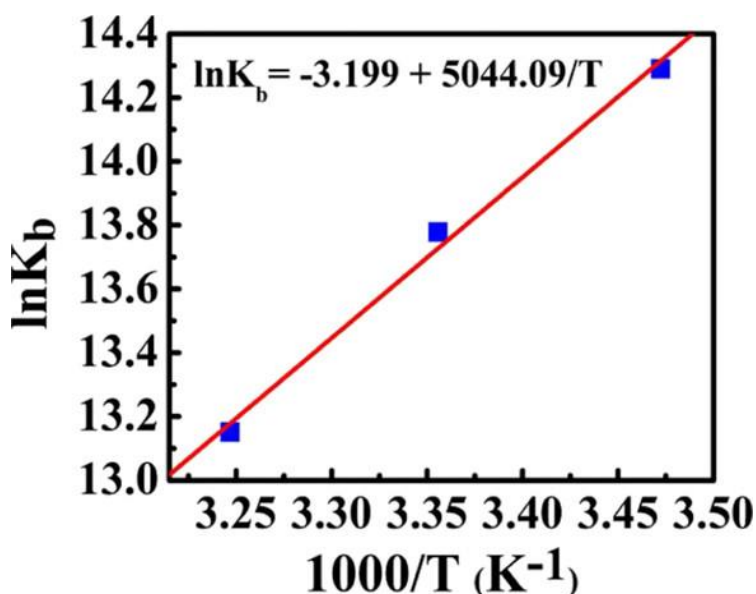
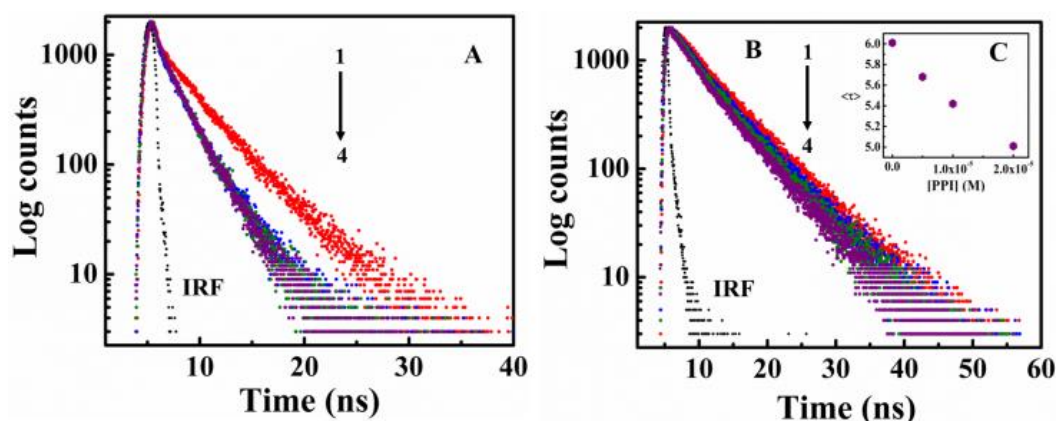


Figure 5.18 van't Hoff plot for the interaction of PPI with BSA at different temperatures.

The values of all related thermodynamic parameters are listed in **Table 5.2**, which show that the value of  $\Delta H^\circ$  is highly negative and  $\Delta S^\circ$  also carries a negative value. This implies that the association of PPI with BSA results from the primary contribution of van der Waals interactions, followed by the involvement of extensive hydrogen bonding interactions between PPI and BSA.<sup>61</sup> Here also, a net negative value of  $\Delta G^\circ$  implies that the interaction between PPI and BSA is spontaneous and thermodynamically favorable.

### 5.3.9 Fluorescence Lifetime Studies

Time-resolved fluorescence decay studies were further accomplished to explore the local microenvironment surrounding the excited probe in the proteinous environment.<sup>17,62</sup> To investigate the dynamics of PPI within the proteinous environment, a nanosecond lifetime decay study of PPI was performed in the absence and with the incremental addition of BSA. Representative decay profiles are shown in **Figure 5.19A**.



**Figure 5.19** (A) Representative time-resolved fluorescence decay spectra of PPI (10 μM) in the absence and presence of increasing concentration of BSA. Spectra 1- 4 corresponds to the BSA concentration 0 μM (red circle), 10 μM (blue circle), 20 μM (olive green circle) and 30 μM (purple circle), respectively at 25 °C. (B) Fluorescence decay spectra of BSA (10 μM) in the absence and presence of increasing concentration of PPI. Spectra 1- 4 corresponds to the PPI concentration 0 μM (red circle), 5 μM (blue circle), 10 μM (olive green circle) and 20 μM (purple circle), respectively at 25 °C. (C) Inset of Figure B; plot shows variation of average lifetime ( $\langle\tau\rangle$ ) of BSA as a function of PPI concentration. IRF represents the instrument response function.

The values of all related parameters are tabulated in **Table 5.3**. The lifetime decay profiles were fitted with a bi-exponential form instead of a mono-exponential form unless the decay curve did not fit well with the mono-exponential form. The best fit for the decay profile was carried out with acceptable values of  $\chi^2$  ( $\chi^2$  within 1.0–1.1). The compound PPI in an aqueous buffer solution is found to display a mono-exponential decay with a lifetime of 4.18 ns. **Table 5.3** reveals that the decay profile is changed from the mono- to bi-exponential form with two lifetime values in the presence of BSA. This is an indication toward separation of PPI into two different environments upon interaction with BSA. Here, we choose to use the average lifetime value in place of more emphasis on the individual fluorescence decay component in such a bi-exponential form. **Table 5.3** shows that the average lifetime ( $\langle\tau\rangle$ ) of PPI gradually decreases with the incremental addition of BSA. The existence of binding interaction is indicated by the meaningful difference in the lifetime values between free PPI and the PPI-BSA composite.

**Table 5.3** Time-resolved fluorescence lifetime decay parameters of PPI (10  $\mu\text{M}$ ) with increasing concentration of BSA at 25  $^\circ\text{C}$ .

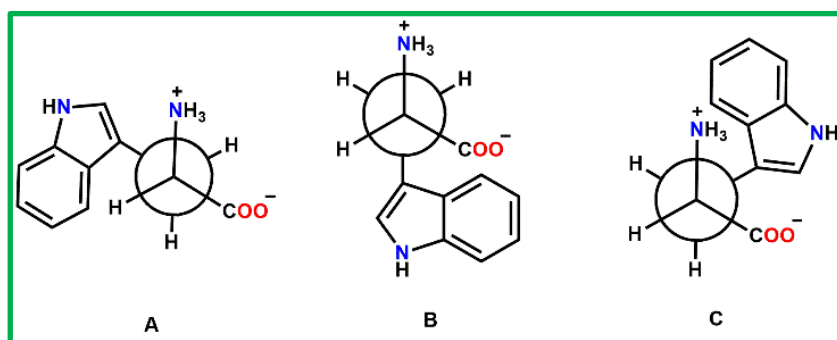
system	[BSA] ( $\mu\text{M}$ )	$\tau_1$ (ns)	$\alpha_1$ (%)	$\tau_2$ (ns)	$\alpha_2$ (%)	$\langle\tau\rangle$ (ns)	$\chi^2$
PPI-BSA	0	4.18	100	-	-	-	1.063
PPI-BSA	10	1.84	67.40	3.58	32.60	2.40	1.029
PPI-BSA	20	1.42	41.23	2.81	58.77	2.23	1.002
PPI-BSA	30	1.34	42.34	2.70	57.66	2.12	1.008

The lifetime decay study was also performed to explore the quenching mechanism (i.e., whether it is static or dynamic or both) of BSA fluorescence by PPI. Here, lifetime decay study of BSA was executed in the absence and with the successive addition of PPI. Representative decay profiles are shown in **Figure 5.19B**. The values of all related parameters are incorporated in **Table 5.4**. The native BSA displays a bi-exponential decay profile in an aqueous medium, with  $\langle\tau\rangle$  value of 6.01 ns having two decay time components of 3.69 and 6.68 ns with the corresponding relative amplitudes of 22.12 and 77.78%, respectively.

**Table 5.4** Time-resolved fluorescence lifetime decay parameters of BSA (10  $\mu$ M) with increasing concentration of PPI at 25  $^{\circ}$ C.

system	[PPI] ( $\mu$ M)	$\tau_1$ (ns)	$\alpha_1$ (%)	$\tau_2$ (ns)	$\alpha_2$ (%)	$\langle\tau\rangle$ (ns)	$\chi^2$
BSA-PPI	0	3.69	22.12	6.68	77.88	6.01	1.021
BSA-PPI	5	3.25	25.13	6.50	74.87	5.68	1.088
BSA-PPI	10	3.11	28.13	6.33	71.87	5.42	1.138
BSA-PPI	20	2.52	31.52	6.07	69.48	5.01	1.081

This bi-exponential decay pattern of the native BSA has been reported earlier and attributed to the existence of two Trp moieties at distinct conformational states in two different local environments.<sup>63,64</sup> Fleming and co-workers<sup>65</sup> have examined the lifetime decays of Trp by considering a model which is based on the conformational rotamers around the  $C^{\alpha} - C^{\beta}$  bond and the comparative charge transfer rate from indole to many electrophiles. The three conformational rotamers of Trp are portrayed below:



Here, the rotamer (C) signifies the faster component and on the contrary, the relatively slower component generally appears from quick interconversion of (A) and (B) rotamers. Nevertheless, the alteration of the relatively stable (C) rotamer to either A or B form is quite impossible on a nanosecond time scale.<sup>66-68</sup> Furthermore, it is supposed that the puckered conformation of the indole ring in the ground state turns into a planar form upon photoexcitation probably due to the delocalization of lone pairs on nitrogen, including the aromatic system.

Generally, the distortion of indole ring planarity is due to the interaction with the quencher, implying the alteration of the microenvironment in the vicinity of Trp, which is the primary cause for a decrease in the lifetime value.<sup>66-68</sup> A quick look at **Table 5.4** reveals that the relative contribution ( $\alpha_2$ ) of the faster decay time component ( $\tau_2$ ) progressively decreases from 77.88 to 69.48%, and at the same time, the relative contribution ( $\alpha_1$ ) of the slower decay time component ( $\tau_1$ ) gradually increases from 22.12 to 31.52%, with the increasing concentration of PPI. **Table 5.4** also shows that the two decay components  $\tau_1$  and  $\tau_2$  are gradually lowered with the increasing concentration of PPI than the respective values for free BSA. The  $\langle\tau\rangle$  value of BSA gradually decreases from 6.01 ns in aqueous buffer solution to 5.01 ns with the gradual addition of PPI (inset of **Figure 5.19B**). The decrease in the  $\langle\tau\rangle$  value is a clear outcome of substantial interactions between BSA and PPI. To investigate the occurrence of dynamic quenching, a time-resolved Stern-Volmer plot was made by using the value of average lifetime, and it can be defined by **eq 16**. **Figure 5.15B** represents the time-resolved Stern-Volmer plot of BSA bound PPI, and it increases linearly with the PPI concentration, which in turn implies the occurrence of dynamic quenching of BSA fluorescence.

### 5.3.10 Time-resolved Anisotropy Decay

The study of lifetime anisotropy decay is useful for garnering knowledge about the rotational motion and relaxation of a fluorescent probe within the proteinous environment.<sup>35</sup> To acquire more information about the neighboring microenvironment of PPI, anisotropy decay study of PPI was performed in aqueous medium in the absence and presence of the BSA protein. The representative anisotropy decay profiles are exhibited in **Figure 5.20**. PPI exhibits a mono-exponential decay profile with a reorientation time of  $\sim 494$  ps, indicating a homogeneous environment around PPI. But interestingly, the anisotropy decay profile of PPI is greatly altered in the presence of BSA leading to a dip-and-rise pattern. This type of pattern signifies the co-occurrence of at least two classes of PPI populations, one with a slower rotational correlation time ( $\tau_{1r}$ ) 6.78 ns having a component ( $\alpha_{1r}$ ) of 88% and another with a faster rotational correlation time ( $\tau_{2r}$ ) 0.79 ns having a component ( $\alpha_{2r}$ ) of 12%. In accordance with the reported literature<sup>69-71</sup> on the explanation of such type of dip-and-rise pattern, the faster motion is ascribed to the existence of solvent-exposed groups or moieties of the probe, whereas, comparatively slower motion corresponds to the bound counterpart.



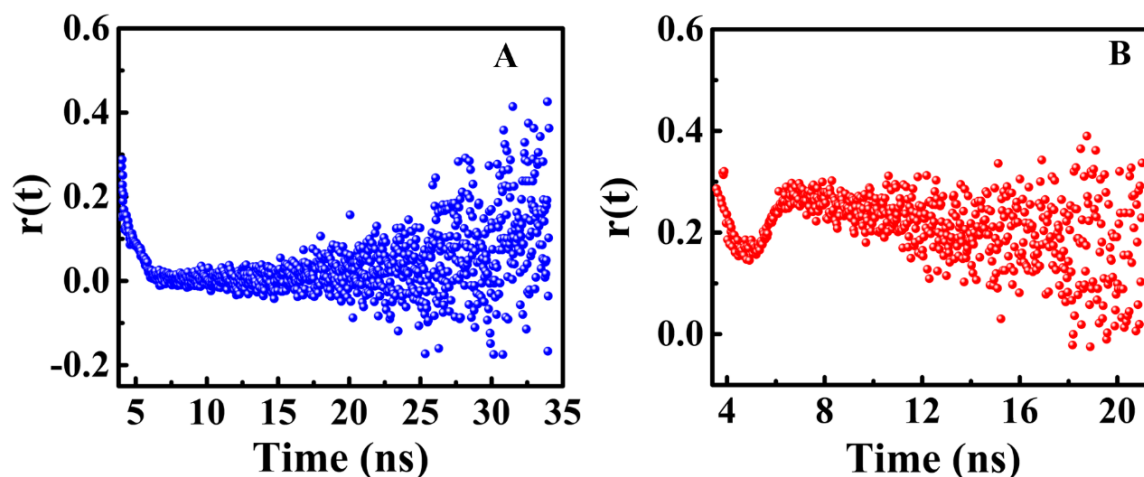


**Figure 5.20** Lifetime anisotropy decay of PPI ( $\lambda_{\text{ex}} = 370$  nm and  $\lambda_{\text{monitored}} = \lambda_{\text{em}}$ ) in the (A) absence of BSA and (B) presence of BSA (20  $\mu\text{M}$ ).

Another probable explanation can be understood in relation with the rotational diffusion of the probe bound to two discrete binding sites (i.e., hydrophilic and hydrophobic zones) in BSA.<sup>72,73</sup> The study of molecular docking (under the Section of Molecular Docking Results) shows in support of plausible location of PPI to be in the hydrophobic binding region (i.e., in subdomain IIA of BSA). Actually, a considerable population in the hydrophilic region (i.e., in subdomain IB of BSA) seems physically not sound for neutral PPI. The above statement is only valid when the components (i.e.,  $\alpha_{1r}$  and  $\alpha_{2r}$ ) reveal the relative PPI population in the two interaction sites. The above-mentioned data obviously shows that the finding probability of PPI in one binding site is appreciably higher than in the other ( $\alpha_{1r} > \alpha_{2r}$ ).<sup>72-76</sup> So, the observed dip-and-rise pattern can therefore be explained by considering the fact that the probe experiences different types of rotational motions in the protein environment.<sup>74-76</sup> Such type of anisotropy decay pattern has been illustrated by the related exponential model, which links the decay parameters with the discrete anisotropy parameters as follows<sup>69-71</sup>

$$r(t) = r(0) \sum_{i=1}^n f_i(t) \exp\left(\frac{-t}{\theta_i}\right) \quad (22)$$

where

$$f_i(t) = \frac{\alpha_i \exp(-t/\tau_i)}{I_T(t)} \quad (23)$$

and

$$I_T(t) = \sum_{i=1}^n \alpha_i \exp(-t/\tau_i) \quad (24)$$

where, the *i*th rotational correlation time is indicated by  $\theta_i$ .  $\alpha_i$  stands for the amplitude of the *i*th lifetime decay component (i.e.,  $\tau_i$ ).  $r(0)$  denotes the limiting anisotropy. Generally, this type of anisotropy decay pattern has been described<sup>69-71</sup> from the outcome of the co-occurrence of two distinctly different lifetime values, which validate the importance of the time-dependent weighing factor  $f_i(t)$ , in narrating such anisotropy profile, as demonstrated in eqs 22 and 23.

### 5.3.11 Binding Distance Measurement Using Fluorescence Resonance Energy Transfer (FRET) between PPI and BSA

FRET is a useful spectroscopic method to delineate the structural conformations of biological and macromolecular systems such as closeness and comparative angular orientation of fluorophores, association of protein-probe composite, and so forth. The binding distance ( $r$ ) between the donor (D) and the acceptor (A) can be evaluated from this useful technique.<sup>77</sup> The efficiency of energy transfer ( $E$ ) between D and A is manifested by the considerable overlap between the emission band of D and the absorption band of A, relative orientation of transition dipoles of D and A, and the distance between D and A, which is generally  $< 8$  nm.<sup>78,79</sup> In our case, Trp residue of the BSA protein acts as the donor unit, PPI acts as the acceptor unit, and the shaded portion represents the spectral overlap region between them (Figure 5.21). In accordance with Förster's theory,  $E$  is defined by the following equation

$$E = 1 - \frac{F}{F_0} = \frac{R_0^6}{R_0^6 + r^6} \quad (25)$$

where  $F_0$  defines the free BSA emission intensity and  $F$  corresponds to the emission intensity of BSA in the presence of PPI. The value of  $R_0$  (i.e., the Förster distance at which the effective transfer of energy is 50%) can be evaluated by using the following relation

$$R_0^6 = (8.79 \times 10^{-25})K^2N^{-4}\varphi J \quad (26)$$

where  $K^2$  indicates the spatial orientation factor of D and A dipole.  $N$  and  $\varphi$  denotes the refractive index of the medium and the quantum yield of D, respectively.

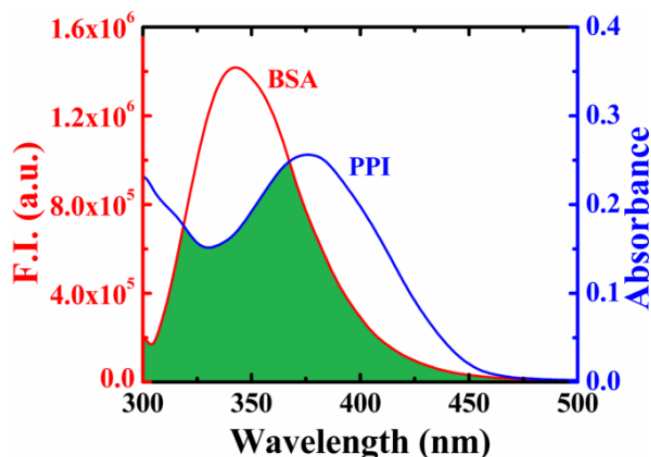


**Figure 5.21** Overlap (shaded region) between the emission spectrum of BSA and the absorption spectrum of PPI at 25 °C. [BSA] = [PPI] = 10 μM at pH 7.4. λ<sub>ex</sub> of BSA = 295 nm.

The overlap integral between the emission spectrum of D and the absorption spectrum of A (**Figure 5.21**) is represented by *J* and its value can be obtained by using the following relation

$$J = \frac{\sum F(\lambda) \varepsilon(\lambda) \lambda^4 \Delta\lambda}{\sum F(\lambda) \Delta\lambda} \quad (27)$$

where *F*(λ) and ε(λ) correspond to the normalized emission intensity of D in the range of λ to (λ + Δλ) and the molar extinction coefficient of A at λ, respectively.<sup>80</sup> In the present case, *K*<sup>2</sup> = 2/3, *N* = 1.336, and φ = 0.15.<sup>56,81</sup> According to the eqs 25–27, parameters evaluated thereby are summarized in **Table 5.5**. The distance *r* between the donor unit BSA and the acceptor unit PPI after the binding interaction was <8 nm and 0.5*R*<sub>0</sub> < *r* < 1.5*R*<sub>0</sub>, infers the occurrence of energy transfer from BSA to PPI with high possibility.<sup>82</sup>

**Table 5.5** FRET parameters for the BSA-PPI composite at 25 °C.

protein	probe	<i>J</i> (cm <sup>3</sup> .L.mol <sup>-1</sup> )	<i>R</i> <sub>0</sub> (nm)	<i>E</i>	<i>r</i> (nm)
BSA	PPI	3.17 × 10 <sup>-14</sup>	3.09	0.54	3.04

### 5.3.12 Conformation Investigations: Circular Dichroism (CD) Study

The variations of the BSA secondary structure with the gradual addition of PPI were carried out by far-UV CD spectral studies in aqueous buffer solution, which show a typical profile (**Figure 5.22**) having two negative bands at ~209 and ~222 nm, clearly indicating the

presence of an  $\alpha$ -helix-rich secondary structure in the BSA protein.<sup>83</sup> These two minima in the CD spectra arises generally because of the  $n \rightarrow \pi^*$  charge transfer transition.<sup>84</sup> **Figure 5.22** shows a decrement in the CD signal with no significant shift of the peak position, implying the PPI-induced conformational change of the native BSA regarding the decrement of the  $\alpha$ -helix content in BSA. The  $\alpha$ -helix percentage in BSA can be determined by considering the following relation<sup>35</sup>

$$\% \alpha - Helix = \frac{-(MRE_{222} - 2340)}{30300} \times 100 \quad (28)$$

where, the observed ellipticity values ( $\theta_{obs}$  in mdeg at 222 nm) are used to evaluate the mean residue ellipticity ( $MRE$ ) value by taking the following relation<sup>35</sup>

$$MRE (deg.cm^2.dmol^{-1}) = \frac{\theta_{obs}}{C_p n l \times 10} \quad (29)$$

where, the molar concentration of BSA is denoted by  $C_p$ .  $n$  indicates the number of amino acid residues (583 for BSA).<sup>5-7,85,86</sup> The cell path length is represented by  $l$  (here 1 cm). The estimated  $\alpha$ -helix content in native BSA is found to be 65.08 ( $\pm 3$ )%, which is in good accordance with the literature value.<sup>5-7,85,86</sup> A decrease in the  $\alpha$ -helix content from  $\sim 65.08$  ( $\pm 3$ )% in the native BSA to  $\sim 59.93$  ( $\pm 3$ )% in the presence of 4  $\mu M$  PPI (inset of **Figure 5.22**) thus obviously shows a PPI-induced perturbation of the secondary structure of BSA.

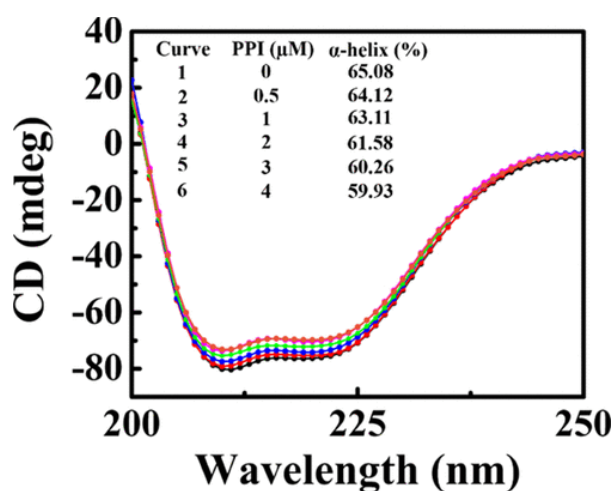


**Figure 5.22** CD spectral profiles of BSA (0.75  $\mu M$ ) with increasing concentrations of PPI at 25  $^{\circ}C$ . The inset exhibits the estimated change in the  $\alpha$ -helix content ( $\pm 3\%$ ) of the BSA with the gradual addition of PPI.

### 5.3.13 Molecular Docking Results

The crystal structure analysis of BSA revealed that it is primarily composed of three homologous domains (I, II, and III), and each domain contains two subdomains (A and B).<sup>87</sup> The major binding sites of BSA for various probes (exogenous and endogenous) are located in subdomains IIA and IIIA, known as Sudlow's sites I and II, respectively.<sup>88</sup> A number of probes or drugs are available, which specifically bind either at site I or site II in BSA.<sup>43,89,90</sup> We have performed molecular docking study to find out whether the probe binds at site I or site II in BSA and the probable interactions involved during the association. Out of 10 different conformers, the lowest binding energy conformer was selected for analysis. The docking results are presented in **Figure 5.23**. Panel **A** in **Figure 5.23** reveals that site I in subdomain IIA of BSA is the preferable binding site for the probe PPI, and this has been supported from site marker experiments. The middle panel shows the magnified view of the microenvironment around the PPI binding site in subdomain IIA of BSA near the Trp 213 residue. The possible hydrogen-bonded interaction between the nitrogen, and nitrogen-bonded hydrogen atoms of PPI with Arg 217 (2.7 Å) and Asp 450 (3.2 Å) plays a crucial role in stabilizing probe-binding (**Figure 5.23C**). In addition, the probe is surrounded by various hydrophobic and polar residues.

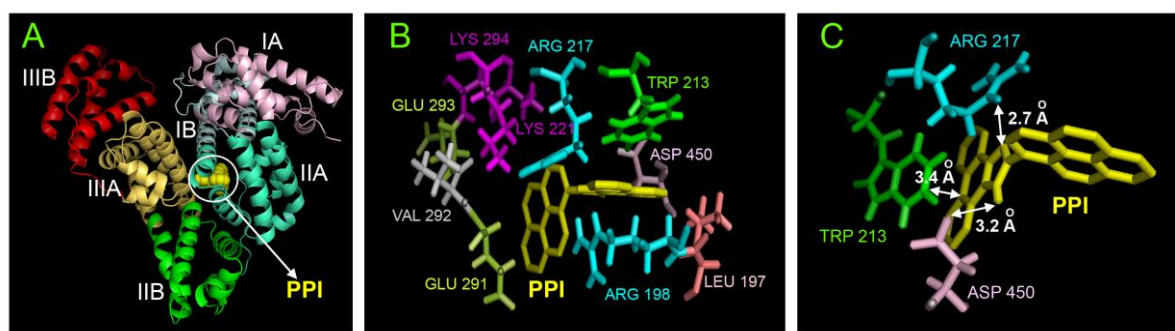


**Figure 5.23** Molecular docking of PPI with the three-dimensional structure of BSA (PDB ID: 4JK4). (A) Docking pose of PPI with BSA shown by the white circle. (B) Magnified view of the binding site of PPI in subdomain IIA. (C) Distance between the neighboring hydrogen-bonded residues and TRP 213 from the probe PPI.

Amino acid residues such as Leu 197, Trp 213, and Val 292 provided an additional stability to the complex through hydrophobic interactions.

Moreover, a number of charged and polar residues such as Arg 198, Arg 217, Lys 221, Lys 294 and so forth play a secondary role in stabilizing the PPI molecule through electrostatic interactions. Thus, docking results suggested that PPI was bound to BSA by three possible interactions, namely hydrophobic, electrostatic, and hydrogen-bonding. According to Zhang *et al.*, increased hydrophobicity is a measure of increased stability.<sup>91</sup> The formation of the hydrogen bond reduces the extent of hydrophilicity and causes a significant increment in the hydrophobicity, which stabilizes the PPI-BSA complex.<sup>92</sup> Distance between the probe and the Trp 213 residue was 3.4 Å (Figure 5.23C), and the free energy (from the docking simulation) for the binding of PPI to subdomain IIA of BSA was found to be -5.01 kcal mol<sup>-1</sup>. It is already known that Trp 134 and Trp 213 residues are responsible for the intrinsic fluorescence of BSA.<sup>37</sup> The docking result illustrates that the probe binds in the near vicinity of Trp 213 in the binding pocket of site I, which in turn causes a perturbation in the fluorescence intensity of BSA, more specifically, quenches the emission of the Trp 213 residue. Thus, molecular docking study supported the experimental findings from the theoretical approach.

## 5.4 Conclusions

Here, we report a phenanthrene-pyrene-based fluorescent probe (PPI) as a molecular reporter to study the micro heterogeneous environment of the BSA protein. The association between BSA and PPI has been clearly demonstrated by the UV-vis spectral change at 280 nm. The observed blue shift of the emission maximum along with an increment of the fluorescence intensity is due to the movement of PPI from a more polar aqueous environment to a more hydrophobic protein environment. The estimated limit of detection (LOD) value is 6.87 nM. The fluorescence titration of BSA with PPI resulted in a binding constant  $(1.12 \pm 0.06) \times 10^5$  M<sup>-1</sup>, which is in excellent agreement with the value obtained from steady-state anisotropy studies. The study on fluorescence quenching induced by PPI reveals the occurrence of both static and dynamic quenching mechanisms. The occurrence of dynamic quenching is indicated by the linear increase in  $\langle\tau_0\rangle/\langle\tau\rangle$  with the increasing concentration of PPI. The ground-state complexation between PPI and BSA is characterized by a large binding constant, which is very sensitive to the temperature because of a negative  $\Delta H^\circ$  value. The complexation process is also associated with a negative  $\Delta S^\circ$ , which implies that the van der Waals interactions and hydrogen-bonding interactions play the most significant roles in stabilizing the BSA-PPI complex. From the FRET study, the average distance between Trp 213 of the

BSA donor and the PPI acceptor is found to be 3.04 nm, and it is close enough for non-radiative energy transfer to occur from BSA to PPI. The CD spectral studies imply the PPI-induced conformational change of the native BSA in terms of decrease of the  $\alpha$ -helix content in BSA. The site-selective binding and molecular docking studies reveal that PPI binds with BSA at site I in subdomain IIA, that is, Trp 213 is near or within the binding site of PPI. The present fluorescent probe having a planar structure could be utilized as a potential site-selective biomarker for site I in subdomain IIA.

### References

- (1) Royer, C. A. Probing Protein Folding and Conformational Transitions with Fluorescence. *Chem. Rev.* **2006**, *106*, 1769–1784.
- (2) Cohen, B. E.; McAnaney, T. B.; Park, E. S.; Jan, Y. N.; Boxer, S. G.; Jan, L. Y. Probing Protein Electrostatics with a Synthetic Fluorescent Amino Acid. *Science* **2002**, *296*, 1700–1703.
- (3) Abou-Zied, O. K.; Al-Shihi, O. I. K. Characterization of Subdomain IIA Binding Site of Human Serum Albumin in its Native, Unfolded, and Refolded States Using Small Molecular Probes. *J. Am. Chem. Soc.* **2008**, *130*, 10793–10801.
- (4) Er, J. C.; Vendrell, M.; Tang, M. K.; Zhai, D.; Chang, Y. T. Fluorescent Dye Cocktail for Multiplex Drug-Site Mapping on Human Serum Albumin. *ACS Comb. Sci.* **2013**, *15*, 452–457.
- (5) Peters, T., Jr. Serum Albumin. *Adv. Protein Chem.* **1985**, *37*, 161–245.
- (6) Brown, J. R. Some aspects of the structure and conformational properties of serum albumin. In *Albumin Structure, Function and Uses*; Foster, J. F., Ed.; Pergamon Press: Oxford, U.K., 1977; pp 53–84.
- (7) He, X. M.; Carter, D. C. Atomic Structure and Chemistry of Human Serum Albumin. *Nature* **1992**, *358*, 209–215.
- (8) Helms, M. K.; Petersen, C. E.; Bhagavan, N. V.; Jameson, D. M. Time-Resolved Fluorescence Studies on Site-Directed Mutants of Human Serum Albumin. *FEBS Lett.* **1997**, *408*, 67–70.
- (9) Peters, T., Jr. *All About Albumins: Biochemistry, Genetics and Medical Applications*; Academic Press: San Diego, CA, 1996; pp 76–132.



- (10) McClellan, S. J.; Franses, E. I. Effect of concentration and denaturation on adsorption and surface tension of bovine serum albumin. *Colloids Surf., B* **2003**, *28*, 63–75.
- (11) Majorek, K. A.; Porebski, P. J.; Dayal, A.; Zimmerman, M. D.; Jablonska, K.; Stewart, A. J.; Chruszcz, M.; Minor, W. Structural and Immunologic Characterization of Bovine, Horse, and Rabbit Serum Albumins. *Mol. Immunol.* **2012**, *52*, 174–182.
- (12) Servagent-Noinville, S.; Revault, M.; Quiquampoix, H.; Baron, M. H. Conformational Changes of Bovine Serum Albumin Induced by Adsorption on Different Clay Surfaces: FTIR Analysis. *J. Colloid Interface Sci.* **2000**, *221*, 273–283.
- (13) Kudelski, A. Influence of electrostatically bound proteins on the structure of linkage monolayers: adsorption of bovine serum albumin on silver and gold substrates coated with monolayers of 2-Mercaptoethanesulphonate. *Vib. Spectrosc.* **2003**, *33*, 197–204.
- (14) Sudlow, G.; Birkett, D. J.; Wade, D. N. The Characterization of Two Specific Drug Binding Sites on Human Serum Albumin. *Mol. Pharmacol.* **1975**, *11*, 824–832.
- (15) Sudlow, G.; Birkett, D. J.; Wade, D. N. Further Characterization of Specific Drug Binding Sites on Human Serum Albumin. *Mol. Pharmacol.* **1976**, *12*, 1052–1061.
- (16) Suzuki, Y.; Yokoyama, K. Design and Synthesis of Intramolecular Charge Transfer–Based Fluorescent Reagents for the Highly–Sensitive Detection of Proteins. *J. Am. Chem. Soc.* **2005**, *127*, 17799–17802.
- (17) Mallick, A.; Halder, B.; Chattopadhyay, N. Spectroscopic Investigation on the Interaction of ICT Probe 3-Acetyl-4-oxo-6,7-dihydro-12H Indolo-[2,3-a] Quinolizine with Serum Albumins. *J. Phys. Chem. B* **2005**, *109*, 14683–14690.
- (18) Das, R.; Guha, D.; Mitra, S.; Kar, S.; Lahiri, S.; Mukherjee, S. Intramolecular Charge Transfer as Probing Reaction: Fluorescence Monitoring of Protein–Surfactant Interaction. *J. Phys. Chem. A* **1997**, *101*, 4042–4047.
- (19) Weber, G. *Light and Life*; McElory, W. D., Glass, B., Eds.; Johns Hopkins: Baltimore, MD, 1961; pp 82-106.
- (20) Barreleiro, P. C. A.; Lindman, B. The Kinetics of DNA–Cationic Vesicle Complex Formation. *J. Phys. Chem. B* **2003**, *107*, 6208–6213.
- (21) Demchenko, A. P. *Topics in Fluorescence Spectroscopy: Biochemical Applications*; Lakowicz, J. R., Ed.; Plenum: New York, 1992; Vol. 3, p 65.

- (22) Cárdenas, M.; Schillén, K.; Pebalk, D.; Nylander, T.; Lindman, B. Interaction between DNA and Charged Colloids Could Be Hydrophobically Driven. *Biomacromolecules* **2005**, *6*, 832–837.
- (23) Haldar, B.; Chakrabarty, A.; Mallick, A.; Mandal, M. C.; Das, P.; Chattopadhyay, N. Fluorometric and Isothermal Titration Calorimetric Studies on Binding Interaction of a Telechelic Polymer with Sodium Alkyl Sulfates of Varying Chain Length. *Langmuir* **2006**, *22*, 3514–3520.
- (24) Chakraborty, A.; Ghosh, S.; Kar, S.; Nath, D. N.; Guchhait, N. Dual emission from (*E*)-3-(4-methylamino-phenyl)-acrylic acid ethyl ester (MAPAEE) and its application as fluorescence probe for studying micellar and protein microenvironment. *J. Mol. Struct.* **2009**, *917*, 148–157.
- (25) Ghosh, S.; Guchhait, N. Chemically Induced Unfolding of Bovine Serum Albumin by Urea and Sodium Dodecyl Sulfate: A Spectral Study with the Polarity-Sensitive Charge-Transfer Fluorescent Probe (*E*)-3-(4-Methyl aminophenyl)acrylic Acid Methyl Ester. *ChemPhysChem* **2009**, *10*, 1664–1671.
- (26) Mahanta, S.; Singh, R. B.; Guchhait, N. Study of Protein–Probe Interaction and Protective Action of Surfactant Sodium Dodecyl Sulphate in Urea-Denatured HSA using Charge Transfer Fluorescence Probe Methyl Ester of *N,N*-Dimethylamino Naphthyl Acrylic Acid. *J. Fluoresc.* **2009**, *19*, 291–303.
- (27) Ghosh, S.; Jana, S.; Nath, D. N.; Guchhait, N. Fluorescent Probing of Protein Bovine Serum Albumin Stability and Denaturation Using Polarity Sensitive Spectral Response of a Charge Transfer Probe. *J. Fluoresc.* **2011**, *21*, 365–374.
- (28) Côté, B.; Boulet, L.; Brideau, C.; Claveau, D.; Ethier, D.; Frenette, R.; Gagnon, M.; Giroux, A.; Guay, J.; Guiral, S.; Mancini, J.; Martins, E.; Massé, F.; Méthot, N.; Riendeau, D.; Rubin, J.; Xu, D.; Yu, H.; Ducharme, Y.; Friesen, R. W. Substituted phenanthrene imidazoles as potent, selective, and orally active mPGES-1 inhibitors. *Bioorg. Med. Chem. Lett.* **2007**, *17*, 6816–6820.
- (29) Guédouar, H.; Aloui, F.; Beltifa, A.; Mansour, H. B.; Hassine, B. B. Synthesis and characterization of phenanthrene derivatives with anticancer property against human colon and epithelial cancer cell lines. *C. R. Chim.* **2017**, *20*, 841-849.

- (30) Subeesh, M. S.; Shanmugasundaram, K.; Sunesh, C. D.; Won, Y. S.; Choe, Y. Utilization of a phenanthroimidazole based fluorophore in light-emitting electrochemical cells. *J. Mater. Chem. C* **2015**, *3*, 4683–4687.
- (31) Anand, U.; Jash, C.; Mukherjee, S. Spectroscopic Probing of the Microenvironment in a Protein-Surfactant Assembly. *J. Phys. Chem. B* **2010**, *114*, 15839–15845.
- (32) Larsson, A.; Carlsson, C.; Jonsson, M.; Albinsson, B. Characterization of the Binding of the Fluorescent Dyes YO and YOYO to DNA by Polarized Light Spectroscopy. *J. Am. Chem. Soc.* **1994**, *116*, 8459–8465.
- (33) Zhu, T.; Du, J.; Cao, W.; Fan, J.; Peng, X. Microenvironment-sensitive fluorescent dyes for recognition of serum albumin in urine and imaging in living cells. *Ind. Eng. Chem. Res.* **2016**, *55*, 527–533.
- (34) Swaminathan, R.; Krishnamoorthy, G.; Periasamy, N. Similarity of fluorescence lifetime distributions for single tryptophan proteins in the random coil state. *Biophys. J.* **1994**, *67*, 2013–2023.
- (35) Paul, B. K.; Ghosh, N.; Mukherjee, S. Interplay of Multiple Interaction Forces: Binding of Norfloxacin to Human Serum Albumin. *J. Phys. Chem. B* **2015**, *119*, 13093–13102.
- (36) Hu, Y. J.; Liu, Y.; Wang, J. B.; Xiao, X. H.; Qu, S. S. Study of the interaction between monoammonium glycyrrhizinate and bovine serum albumin. *J. Pharm. Biomed. Anal.* **2004**, *36*, 915–919.
- (37) Li, D.; Zhu, M.; Xu, C.; Chen, J.; Ji, B. The Effect of Cu<sup>2+</sup> or Fe<sup>3+</sup> on the Noncovalent Binding of Rutin with Bovine Serum Albumin by Spectroscopic Analysis. *Spectrochim. Acta, Part A* **2011**, *78*, 74–79.
- (38) Gentili, P. L.; Ortica, F.; Favaro, G. Static and Dynamic Interaction of a Naturally Occurring Photochromic Molecule with Bovine Serum Albumin Studied by UV–Visible Absorption and Fluorescence Spectroscopy. *J. Phys. Chem. B* **2008**, *112*, 16793–16801.
- (39) Gensch, T.; Hendriks, J.; Hellingwerf, K. Tryptophan fluorescence monitors structural changes accompanying signalling state formation in the photocycle of photoactive yellow protein. *Photochem. Photobiol. Sci.* **2004**, *3*, 531–536.
- (40) Jana, S.; Dalapati, S.; Ghosh, S.; Guchhait, N. Binding interaction between plasma protein bovine serum albumin and flexible charge transfer fluorophore: A spectroscopic

- study in combination with molecular docking and molecular dynamics simulation. *J. Photochem. Photobiol., A* **2012**, *231*, 19–27.
- (41) Sahoo, B. K.; Ghosh, K. S.; Dasgupta, S. Investigating the Binding of Curcumin Derivatives to Bovine Serum Albumin. *Biophys. Chem.* **2008**, *132*, 81–88.
- (42) Burstein, E. A.; Vedenkina, N. S.; Ivkova, M. N. Fluorescence and the Location of Tryptophan residues in Protein Molecules. *Photochem. Photobiol.* **1973**, *18*, 263–279.
- (43) Bhuiya, S.; Pradhan, A. B.; Haque, L.; Das, S. Molecular Aspects of the Interaction of Iminium and Alkanolamine Forms of the Anticancer Alkaloid Chelerythrine with Plasma Protein Bovine Serum Albumin. *J. Phys. Chem. B* **2016**, *120*, 5–17.
- (44) Benesi, H. A.; Hildebrand, J. H. A Spectrophotometric Investigation of the Interaction of Iodine with Aromatic Hydrocarbons. *J. Am. Chem. Soc.* **1949**, *71*, 2703–2707.
- (45) Jash, C.; Payghan, P. V.; Ghoshal, N.; Kumar, G. S. Binding of the Iminium and Alkanolamine Forms of Sanguinarine to Lysozyme: Spectroscopic Analysis, Thermodynamics, and Molecular Modeling Studies. *J. Phys. Chem. B* **2014**, *118*, 13077–13091.
- (46) Ray, D.; Kundu, A.; Pramanik, A.; Guchhait, N. Exploring the Interaction of a Micelle Entrapped Biologically Important Proton Transfer Probe with the Model Transport Protein Bovine Serum Albumin. *J. Phys. Chem. B* **2015**, *119*, 2168–2179.
- (47) Lakowicz, J. R. Fluorescence Anisotropy. In *Principles of Fluorescence Spectroscopy*, 3rd ed.; Springer: New York, USA, 2006; pp 353–381.
- (48) Ingersoll, C. M.; Strollo, C. M. Steady-State Fluorescence Anisotropy to Investigate Flavonoids Binding to Proteins. *J. Chem. Educ.* **2007**, *84*, 1313–1315.
- (49) Baroni, S.; Mattu, M.; Vannini, A.; Cipollone, R.; Aime, S.; Ascenzi, P.; Fasano, M. Effect of Ibuprofen and Warfarin on the Allosteric Properties of Haem-Human Serum Albumin. A spectroscopic Study. *Eur. J. Biochem.* **2001**, *268*, 6214–6220.
- (50) Dufour, C.; Dangles, O. Flavonoid-Serum Albumin Complexation: Determination of Binding Constants and Binding Sites by Fluorescence Spectroscopy. *Biochim. Biophys. Acta, Gen. Subj.* **2005**, *1721*, 164–173.
- (51) Lakowicz, J. R. Quenching of Fluorescence. In *Principles of Fluorescence Spectroscopy*, 3rd ed.; Springer: New York, USA, 2006; pp 278–327.

- (52) Ghosh, N.; Mondal, R.; Mukherjee, S. Inverse Temperature Dependence in Static Quenching versus Calorimetric Exploration: Binding Interaction of Chloramphenicol to  $\beta$ -Lactoglobulin. *Langmuir* **2015**, *31*, 8074–8080.
- (53) Zhang, Y. Z.; Zhou, B.; Liu, Y. X.; Zhou, C. X.; Ding, X. L.; Liu, Y. Fluorescence study on the Interaction of Bovine Serum Albumin with p-Aminoazobenzene. *J. Fluoresc.* **2008**, *18*, 109–118.
- (54) Mandal, P.; Ganguly, T. Fluorescence Spectroscopic Characterization of the Interaction of Human Adult Hemoglobin and Two Isatins, 1-Methylisatin and 1-Phenylisatin: A comparative Study. *J. Phys. Chem. B* **2009**, *113*, 14904–14913.
- (55) Ojha, B.; Das, G. The Interaction of 5-(Alkoxy)naphthalen-1-amine with Bovine Serum Albumin and Its Effect on the Conformation of Protein. *J. Phys. Chem. B* **2010**, *114*, 3979–3986.
- (56) Shaikh, S. M. T.; Seetharamappa, J.; Kandagal, P. B.; Ashoka, S. Binding of the bioactive component isothipendyl hydrochloride with bovine serum albumin. *J. Mol. Struct.* **2006**, *786*, 46–52.
- (57) Bi, S.; Ding, L.; Tian, Y.; Song, D.; Zhou, X.; Liu, X.; Zhang, H. Investigation of the interaction between flavonoids and human serum albumin. *J. Mol. Struct.* **2004**, *703*, 37–45.
- (58) Feng, X. Z.; Lin, Z.; Yang, L. J.; Wang, C.; Bai, C. L. Investigation of the interaction between acridine orange and bovine serum albumin. *Talanta* **1998**, *47*, 1223–1229.
- (59) Patel, R.; Mir, M. U. H.; Maurya, J. K.; Singh, U. K.; Maurya, N.; Parray, M. u. d.; Khan, A. B.; Ali, A. Spectroscopic and molecular modelling analysis of the interaction between ethane-1,2-diyl bis(N,N-dimethyl-N-hexadecyl-ammoniumacetoxo)dichloride and bovine serum albumin. *Luminescence* **2015**, *30*, 1233–1241.
- (60) van Holde, K. E.; Johnson, W. C.; Ho, P. S. Thermodynamics and Biochemistry. In *Principles of Physical Biochemistry*, 2nd ed.; Pearson Higher Education: Upper Saddle River, NJ, USA, 2006; pp 72–106.
- (61) Ross, P. D.; Subramanian, S. Thermodynamics of protein association reactions: forces contributing to stability. *Biochemistry* **1981**, *20*, 3096–3102.

- (62) Das, P.; Mallick, A.; Chakrabarty, A.; Haldar, B.; Chattopadhyay, N. Effect of nanocavity confinement on the rotational relaxation dynamics: 3-acetyl-4-oxo-6,7-dihydro-12H indolo-[2,3-a] quinolizine in micelles. *J. Chem. Phys.* **2006**, *125*, 044516.
- (63) Anand, U.; Jash, C.; Mukherjee, S. Protein unfolding and subsequent refolding: a spectroscopic investigation. *Phys. Chem. Chem. Phys.* **2011**, *13*, 20418–20426.
- (64) Chatterjee, S.; Mukherjee, T. K. Spectroscopic investigation of interaction between bovine serum albumin and amine-functionalized silicon quantum dots. *Phys. Chem. Chem. Phys.* **2014**, *16*, 8400–8408.
- (65) Petrich, J. W.; Chang, M. C.; McDonald, D. B.; Fleming, G. R. On the origin of nonexponential fluorescence decay in tryptophan and its derivatives. *J. Am. Chem. Soc.* **1983**, *105*, 3824–3832.
- (66) Anand, U.; Jash, C.; Boddepalli, R. K.; Shrivastava, A.; Mukherjee, S. Exploring the Mechanism of Fluorescence Quenching in Proteins Induced by Tetracycline. *J. Phys. Chem. B* **2011**, *115*, 6312–6320.
- (67) Anand, U.; Kurup, L.; Mukherjee, S. Deciphering the role of pH in the binding of Ciprofloxacin Hydrochloride to Bovine Serum Albumin. *Phys. Chem. Chem. Phys.* **2012**, *14*, 4250–4258.
- (68) Anand, U.; Mukherjee, S. Reversibility in Protein Folding: Effect of  $\beta$ -Cyclodextrin on Bovine Serum Albumin Unfolded by Sodium Dodecyl Sulphate. *Phys. Chem. Chem. Phys.* **2013**, *15*, 9375–9383.
- (69) Paul, B. K.; Guchhait, N. Modulated Photophysics of an ESIPT Probe 1-Hydroxy-2-naphthaldehyde within Motionally Restricted Environments of Liposome Membranes Having Varying Surface Charges. *J. Phys. Chem. B* **2010**, *114*, 12528–12540.
- (70) Broos, J.; Visser, A. J. W. G.; Engbersen, J. F. J.; Verboom, W.; van Hoek, A.; Reinhoudt, D. N. Flexibility of Enzymes Suspended in Organic Solvents Probed by Time-Resolved Fluorescence Anisotropy. Evidence that Enzyme Activity and Enantioselectivity Are Directly Related to Enzyme Flexibility. *J. Am. Chem. Soc.* **1995**, *117*, 12657–12663.
- (71) Fuentealba, D.; Kato, H.; Nishijima, M.; Fukuhara, G.; Mori, T.; Inoue, Y.; Bohne, C. Explaining the Highly Enantiomeric Photocyclodimerization of 2-Anthracenecarboxylate

- Bound to Human Serum Albumin Using Time-Resolved Anisotropy Studies. *J. Am. Chem. Soc.* **2013**, *135*, 203–209.
- (72) Paul, B. K.; Guchhait, N. Modulation of Prototropic Activity and Rotational Relaxation Dynamics of a Cationic Biological Photosensitizer within the Motionally Constrained Bio-environment of a Protein. *J. Phys. Chem. B* **2011**, *115*, 10322–10334.
- (73) Paul, B. K.; Guchhait, N. Exploring the Strength, Mode, Dynamics, and Kinetics of Binding Interaction of a Cationic Biological Photosensitizer with DNA: Implication on Dissociation of the Drug–DNA Complex via Detergent Sequestration. *J. Phys. Chem. B* **2011**, *115*, 11938–11949.
- (74) Bhattacharya, B.; Nakka, S.; Guruprasad, L.; Samanta, A. Interaction of Bovine Serum Albumin with Dipolar Molecules: Fluorescence and Molecular Docking Studies. *J. Phys. Chem. B* **2009**, *113*, 2143–2150.
- (75) Quitevis, E. L.; Marcus, A. H.; Fayer, M. D. Dynamics of ionic lipophilic probes in micelles: picosecond fluorescence depolarization measurements. *J. Phys. Chem.* **1993**, *97*, 5762–5769.
- (76) Ariola, F. S.; Mudaliar, D. J.; Walvick, R. P.; Heikal, A. A. Dynamics imaging of lipid phases and lipid-marker interactions in model biomembranes. *Phys. Chem. Chem. Phys.* **2006**, *8*, 4517–4529.
- (77) Shahabadi, N.; Maghsudi, M.; Rouhani, S. Study on the Interaction of Food Colourant Quinoline Yellow with Bovine Serum Albumin by Spectroscopic Techniques. *Food Chem.* **2012**, *135*, 1836–1841.
- (78) Valeur, B.; Brochon, J. C. *New Trends in Fluorescence Spectroscopy: Applications to Chemical and Life Science*, 6th ed.; Springer Press: Berlin, 1999; p 25.
- (79) Förster, T. Delocalized excitation and excitation transfer. In *Modern Quantum Chemistry Part III: Action of Light and Organic Crystals*; Sinanoglu, O., Ed.; Academic Press: New York, 1965; pp 93–137.
- (80) Ma, F.; Huang, H. Y.; Zhou, L.; Yang, C.; Zhou, J. H.; Liu, Z. M. Study on the Conformation Changes of Lysozyme Induced by Hypocrellin A: The Mechanism Investigation. *Spectrochim. Acta, Part A* **2012**, *97*, 1159–1165.



- (81) Ding, F.; Huang, J.; Lin, J.; Li, Z.; Liu, F.; Jiang, Z.; Sun, Y. A Study of the Binding of C.I. Mordant Red 3 with Bovine Serum Albumin using Fluorescence Spectroscopy. *Dyes Pigm.* **2009**, *82*, 65–70.
- (82) Kitamura, M.; Murakami, K.; Yamada, K.; Kawai, K.; Kunishima, M. Binding of sulforhodamine B to human serum albumin: a spectroscopic study. *Dyes Pigm.* **2013**, *99*, 588–93.
- (83) Serro, A. P.; Bastos, M.; Pessoa, J. C.; Saramago, B. Bovine Serum Albumin Conformational Changes upon Adsorption on Titania and on Hydroxyapatite and their Relation with Biomineralization. *J. Biomed. Mater. Res., Part A* **2004**, *70*, 420–427.
- (84) Yang, P.; Gao, F. *The Principle of Bioinorganic Chemistry*; Science Press: Beijing, 2002; p 349.
- (85) Berg, J. M.; Tymoczko, J. L.; Stryer, L. Protein Structure and Function. In *Biochemistry*, 5th ed.; W. H. Freeman and Company: New York, 2002; pp 83–136.
- (86) Monti, S.; Manet, I.; Marconi, G. Combination of spectroscopic and computational methods to get an understanding of supramolecular chemistry of drugs: from simple host systems to biomolecules. *Phys. Chem. Chem. Phys.* **2011**, *13*, 20893–20905.
- (87) Carter, D. C.; Ho, J. X. Structure of Serum Albumin. *Adv. Protein Chem.* **1994**, *45*, 153–203.
- (88) Ulrich, K. H. Molecular aspects of ligand binding to serum albumin. *Pharmacol. Rev.* **1981**, *33*, 17–53.
- (89) Chaves, O. A.; da Silva, V. A.; Sant'Anna, C. M. R.; Ferreira, A. B. B.; Ribeiro, T. A. N.; de Carvalho, M. G.; Cesarin-Sobrinho, D.; Netto-Ferreira, J. C. Binding studies of lophirone B with bovine serum albumin (BSA): Combination of spectroscopic and molecular docking techniques. *J. Mol. Struct.* **2017**, *1128*, 606–611.
- (90) Teng, Y.; Zou, L.; Huang, M.; Zong, W. Characterization of the binding of 2-mercaptobenzimidazole to bovine serum albumin. *J. Mol. Recognit.* **2015**, *28*, 232–238.
- (91) Zhang, Y.; Li, Y.; Dong, L.; Li, J.; He, W.; Chen, X.; Hu, Z. Investigation of the interaction between naringin and human serum albumin. *J. Mol. Struct.* **2008**, *875*, 1–8.

- (92) Sahoo, D.; Bhattacharya, P.; Chakravorti, S. Reverse Micelle Induced Flipping of Binding Site and Efficiency of Albumin Protein with an Ionic Styryl Dye. *J. Phys. Chem. B* **2010**, *114*, 10442–10450.

## Chapter 6

---

### Highlights of the Thesis

## Chapter 6: Highlights of the Thesis

---

After the elaborate description, here the overall view of this thesis has been briefly summarized chapterwise. This may be helpful to highlight the aim of our project and may provide an ultimate conclusion how far we have been able to fulfill our dream for the entitled project.

### Chapter 1

This chapter contains a brief description of serum albumins (HSA/BSA) and describes various popular methods for serum albumin detection and estimation, along with a short review of previously reported HSA/BSA detection probes by fluorometric method. Additionally, a very brief overview of the present work is highlighted.

### Chapter 2

In this chapter, we describe the synthesis and characterization of a TICT-based small fluorogenic molecular probe HJRA, which can easily *self-assemble* into nonfluorescent nanoaggregates in aqueous PBS buffer at pH 7.4. The HJRA nanoaggregates can selectively bind with serum albumin proteins (HSA/BSA) in physiological conditions which facilitates the *disassembly* process toward monomer formation. The selective trapping of the HJRA monomer in the subdomain IIA of site I in HSA resulted a rapid turn-on red fluorescent response due to suppression of the TICT action by restricting free intramolecular rotation. HJRA has a detection limit of 1.13 nM (0.0751 mg/L), which is substantially below the normal HSA concentration in healthy urine signifying the high sensitivity of the probe. Analysis of the binding mechanism between HJRA and HSA implies that a combination of various noncovalent bonds including hydrophobic interactions, hydrogen bonds, and  $\pi$ - $\pi$  and cation- $\pi$  interactions are the fundamental forces for encouraging the disassembly process and trapping of the HJRA probe at the site I in HSA. The comparable results and quick response toward the quantification of urinary HSA levels by HJRA method with respect to the Bradford method clearly points toward the superiority of this method compared to the existing ones and may lead to biomedical applications for HSA quantification in urine. Additionally, the probe is also least cytotoxic, cell permeable and suitable for imaging of endogenous and exogenous HSA in living cells.

### Chapter 3

This chapter describes the synthesis and characterization of an ICT-based microenvironment sensitive fluorescent probe DCI-MIN for the detection and quantification of HSA in complicated biological samples with high selectivity and sensitivity. DCI-MIN has excellent photostability and exhibits a clear HSA induced large enhancement in emission intensity (~78-fold) with a significant (~126 nm) Stokes shift. The strong red fluorescence response of DCI-MIN in the presence of HSA can be attributed to the incorporation of DCI-MIN into the site II hydrophobic binding cavity of HSA, that restricts the free rotation of DCI-MIN due to the severe steric hindrance as well as the low polarity of the microenvironment. DCI-MIN displayed high binding affinity to HSA with a  $K_d$  value of  $(0.024 \pm 0.003) \mu\text{M}$ . The probe has a detection limit of 1.01 nM (0.0671 mg/L), which is significantly lower than the normal level of HSA in healthy urine, indicating its high sensitivity and superiority to the earlier reported HSA detection probes. DCI-MIN also shows the ability to perform a variety of useful applications, including the detection and quantification of HSA levels in complex biofluids (human urine and blood samples) as well as the imaging of serum albumin in living cells. As compared to the Bradford assay and the BCG technique, measuring HSA levels in urine and blood samples with DCI-MIN is preferable due to its higher selectivity, faster detection time, and simple operation.

### Chapter 4

This chapter deals with the various spectroscopic and molecular docking investigation on the interaction of NBD embedded olanzapine derivative (OLA-NBD) with HSA protein. A gradual enhancement of the emission intensity of OLA-NBD along with the substantial blue shift of  $\lambda_{em}^{max}$  on interaction with HSA vividly indicates the immense modulation of the microenvironment around OLA-NBD within the protein hydrophobic medium compared with the polar aqueous medium. The estimated limit of detection (LOD) value is 59.4 nM. The fluorescence titration of HSA with OLA-NBD resulted in an association constant of  $(9.87 \pm 0.02) \times 10^4 \text{ M}^{-1}$ . The fluorescence quenching study persuaded by OLA-NBD indicates the presence of a static quenching mechanism, which is well corroborated with the results extracted from the temperature dependent studies and lifetime analysis of HSA with OLA-NBD. The negative value of  $\Delta H^0$  accompanied by a positive value of  $\Delta S^0$  infers the major contribution of electrostatic/ionic interaction for the HSA–OLA-NBD binding process. CD

outcome illustrates the alteration of the secondary structure of HSA upon interaction with OLA-NBD. The effect of  $\beta$ -Cyclodextrin on HSA–OLA-NBD binding is found to be characterized by a smaller Stern-Volmer quenching and binding constant values, indicating that OLA-NBD molecules are progressively unsheathed from  $\beta$ -CD by HSA to accomplish its medicinal applications. The site-specific binding experiment and molecular docking studies indicate that OLA-NBD binds with HSA in subdomain IIA at the binding site I, that is, close to the Trp 214.

### Chapter 5

In this chapter, we represent a phenanthrene-pyrene-based fluorescent probe (PPI) as a molecular reporter to study the micro heterogeneous environment of BSA protein. The observed blue shift of the emission maximum along with an increment of the fluorescence intensity is due to the movement of PPI from a more polar aqueous environment to a more hydrophobic protein environment. The estimated limit of detection (LOD) value is 6.87 nM. The fluorescence titration of BSA with PPI resulted in a binding constant of  $(1.12 \pm 0.06) \times 10^5 \text{ M}^{-1}$ . The study on fluorescence quenching induced by PPI reveals the occurrence of both static and dynamic quenching mechanisms. The occurrence of dynamic quenching is indicated by the linear increase in  $\langle \tau_0 \rangle / \langle \tau \rangle$  with the increasing concentration of PPI. The negative  $\Delta H^\circ$  value accompanied by a negative  $\Delta S^\circ$  value implies the significant contributions of van der Waals interactions and hydrogen-bonding interactions in stabilizing the BSA-PPI complex. From the FRET study, the average distance between Trp 213 of the BSA donor and the PPI acceptor is found to be 3.04 nm, and it is close enough for non-radiative energy transfer to occur from BSA to PPI. The CD spectral studies imply the PPI-induced conformational change of the native BSA in terms of decrease of the  $\alpha$ -helix content in BSA. The site-selective binding and molecular docking studies reveal that PPI binds with BSA at site I in subdomain IIA, that is, Trp 213 is near or within the binding site of PPI.

### List of Publications

1. Domain-Specific Association of a Phenanthrene–Pyrene-Based Synthetic Fluorescent Probe with Bovine Serum Albumin: Spectroscopic and Molecular Docking Analysis. **Sasmal, M.**; Bhowmick, R.; Islam, A. S. M.; Bhuiya, S.; Das, S.; Ali, M. *ACS Omega* **2018**, *3*, 6293–6304.
2. Site-Selective Interaction of Human Serum Albumin with 4-Chloro-7-nitro-1, 2, 3-benzoxadiazole Modified Olanzapine Derivative and Effect of  $\beta$ -Cyclodextrin on Binding: In the light of Spectroscopy and Molecular Docking. **Sasmal, M.**; Islam, A. S. M.; Bhowmick, R.; Maiti, D.; Dutta, A.; Ali, M. *ACS Appl. Bio Mater.* **2019**, *2*, 3551–3561.
3. Serum Albumin Inspired Self-Assembly/Disassembly of a Fluorogenic Nanoprobe for Real-Time Monitoring and Quantification of Urinary Albumin with Live Cell Imaging Application. **Sasmal, M.**; Islam, A. S. M.; Moni, D.; Maiti, D.; Dutta, A.; Ali, M. *ACS Appl. Bio Mater.* **2022**, *5*, 5854–5864.
4. A rhodamine-based turn-on nitric oxide sensor in aqueous medium with endogenous cell imaging: an unusual formation of nitrosohydroxylamine. Alam, R.; Islam, A. S. M.; **Sasmal, M.**; Katarkar, A.; Ali, M. *Org. Biomol. Chem.* **2018**, *16*, 3910–3920.
5. Selective sensing of nitric oxide by a 9, 10-phenanthroquinone–pyridoxal based fluorophore. Maiti, D.; Islam, A. S. M.; **Sasmal, M.**; Prodhan, C.; Ali, M. *Photochem. Photobiol. Sci.* **2018**, *17*, 1213–1221.
6. A rhodamine hydrazide–4-nitroindole-3-carboxaldehyde based turn on  $\text{Hg}^{2+}$  chemosensor: Cytoplasmic live cell imaging, logic gate and memory device applications and computational studies. Bhowmick, R.; Islam, A. S. M.; **Sasmal, M.**; Katarkar, A.; Ali, M. *J. Coord. Chem.* **2018**, *71*, 2065–2081.
7. Design of a Pyrene Scaffold Multifunctional Material: Real-Time Turn-On Chemosensor for Nitric Oxide, AIEE Behavior, and Detection of TNP Explosive. Islam, A. S. M.; **Sasmal, M.**; Maiti, D.; Dutta, A.; Show, B.; Ali, M. *ACS Omega* **2018**, *3*, 10306–10316.



8. Dansyl-appended Cu<sup>II</sup>-complex-based nitroxyl (HNO) sensing with living cell imaging application and DFT studies. Maiti, D.; Islam, A. S. M.; Dutta, A.; **Sasmal, M.**; Prodhan, C.; Ali, M. *Dalton Trans.* **2019**, *48*, 2760–2771.
9. A smart molecular probe for selective recognition of nitric oxide in 100% aqueous solution with cell imaging application and DFT studies. Dutta, A.; Islam, A. S. M.; Maiti, D.; **Sasmal, M.**; Prodhan, C.; Ali, M. *Org. Biomol. Chem.* **2019**, *17*, 2492–2501.
10. Phenazine-Embedded Copper (II) Complex as a Fluorescent Probe for the Detection of NO and HNO with a Bioimaging Application. Islam, A. S. M.; **Sasmal, M.**; Maiti, D.; Dutta, A.; Ganguly, S.; Katarkar, A.; Ali, M. *ACS Appl. Bio Mater.* **2019**, *2*, 1944–1955.
11. A coumarin embedded highly sensitive nitric oxide fluorescent sensor: kinetic assay and bio-imaging Applications. Maiti, D.; Islam, A. S. M.; **Sasmal, M.**; Dutta, A.; Katarkar, A.; Ali, M. *Org. Biomol. Chem.* **2020**, *18*, 8450–8458.
12. Bovine serum albumin interactive one dimensional hexanuclear manganese(iii) complex: synthesis, structure, binding and molecular docking studies. Khatun, R.; Dolai, M.; **Sasmal, M.**; Sepay, M.; Ali, M. *New J. Chem.* **2021**, *45*, 12678–12687.
13. A fluorescein-2-(Pyridin-2-ylmethoxy) benzaldehyde conjugate for fluorogenic turn-ON recognition of Hg<sup>2+</sup> in water and living cells with logic gate and memory device applications. Mohammad, H.; Islam, A. S. M.; **Sasmal, M.**; Prodhan, C.; Ali, M. *Inorganica Chim. Acta* **2022**, *543*, 121165.

# Serum Albumin Inspired Self-Assembly/Disassembly of a Fluorogenic Nanoprobe for Real-Time Monitoring and Quantification of Urinary Albumin with Live Cell Imaging Application

Mihir Sasmal, Abu Saleh Musha Islam, Dolan Moni, Debjani Maiti, Ananya Dutta, and Mahammad Ali\*

Cite This: *ACS Appl. Bio Mater.* 2022, 5, 5854–5864

Read Online

ACCESS |



Metrics &amp; More



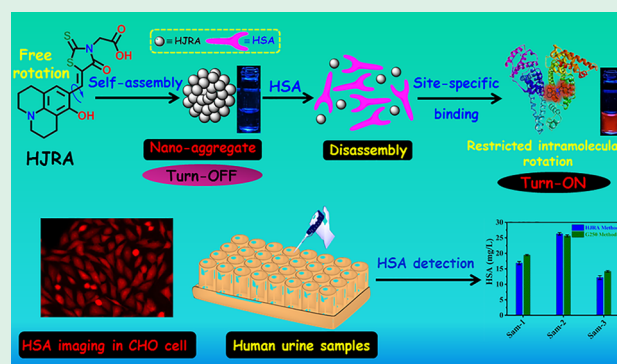
Article Recommendations



Supporting Information

**ABSTRACT:** Abnormal levels (high/low) of urinary human serum albumin (HSA) are associated with a number of diseases and thus act as an essential biomarker for quick therapeutic monitoring and biomedical diagnosis, entailing the urgent development of an effective chemosensor to quantify the albumin levels. Herein, we have rationally designed and developed a small fluorogenic molecular probe, (Z)-2-(5-((8-hydroxy-2,3,6,7-tetrahydro-1H,5H-pyrido[3,2,1-ij]quinolin-9-yl) methylene)-4-oxo-2-thioxothiazolidin-3-yl) acetic acid (HJRA) with a twisted intramolecular charge transfer (TICT) property, which can easily self-assemble into nonfluorescent nanoaggregates in aqueous solution. However, HJRA nanoaggregates can selectively bind with serum albumin proteins (HSA/BSA) in ~100% PBS medium, thereby facilitating the disassembly of nanoaggregates into monomers, exhibiting a clear turn-on red fluorescent response toward HSA and BSA. Analysis of the specific binding mechanism between HJRA and HSA using a site-selective fluorescence displacement assay and molecular docking simulations indicates that a variety of noncovalent interactions are responsible for the disassembly of nanoaggregates with the concomitant trapping of the HJRA monomer at site I in HSA, yielding a substantial red emission caused by the inhibition of intramolecular rotation of HJRA probe inside the hydrophobic cavity of HSA. The limit of detection (LOD) determined by the  $3\sigma/\text{slope}$  method was found to be 1.13 nM, which is substantially below the normal HSA concentration level in healthy urine, signifying the very high sensitivity of the probe toward HSA. The comparable results and quick response toward quantification of HSA in urine by HJRA with respect to the Bradford method clearly point toward the superiority of this method compared to the existing ones and may lead to biomedical applications for HSA quantification in urine. It may also find potential application in live-cell imaging of HSA.

**KEYWORDS:** self-assembly/disassembly, fluorogenic probe, urinary serum albumin, real-time quantification, molecular docking, cell imaging



## INTRODUCTION

Protein detection and quantification are very much crucial in fundamental research, biomedical diagnosis, and therapeutic monitoring.<sup>1,2</sup> Human serum albumin (HSA), a most abundant thiol-containing protein present in very high concentration in blood serum, serves a number of key biological functions including blood osmotic pressure regulation, plasma pH buffering, and fluid transportation in the body and also possesses some antioxidant properties.<sup>3,4</sup> HSA, by virtue of its exceptional ligand-binding ability, functions as a transporter for a wide range of endogenous and exogenous substances, and hence has a significant influence on therapeutic efficacy, cell metabolism, and disease detection.<sup>5–7</sup>

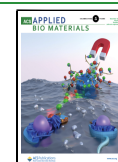
HSA is synthesized exclusively in the liver, primarily in the polysomes of hepatocytes, maintaining a normal level of 35 to 55 g/L in blood plasma in a healthy adult.<sup>8,9</sup> Contrarily,

albumin levels in urine fall below 30 mg/L, probably due to the kidneys preventing essential materials like albumin and other proteins from entering the urine.<sup>10</sup> Nevertheless, an aberrant concentration of albumin in the blood plasma and urine has a direct impact on an individual's health. Hence, albumin levels in body fluids (blood/urine) are commonly employed as health indicators.<sup>9</sup> For example, an HSA deficit in the blood plasma, a case of hypoalbuminemia, may cause chronic hepatitis, kidney disease, liver cirrhosis, and failure.<sup>11</sup>

Received: September 24, 2022

Accepted: November 10, 2022

Published: November 28, 2022



Conversely, excess albumin (30–300 mg/L) in urine can cause microalbuminuria, which has been identified in diabetes mellitus and hypertension, manifesting an early sign of cardiovascular and renal disease.<sup>12–14</sup> Moreover, a patient with a urinary albumin concentration >300 mg/L is diagnosed with macroalbuminuria, indicating a stage where renal damage has progressed to an advanced stage.<sup>15</sup>

Thus, in the last few decades, bioanalytical chemists have paid attention to developing an effective chemosensor for the accurate detection of albumin protein in biological fluids, particularly in urine samples. So far, several analytical approaches like colorimetric (Lowry, Bradford, etc.), radiolabeling, immunoassays, electrophoresis, fluorometry, and LC–MS proteomics-based methods have been established effectively for serum albumin detection in body fluids.<sup>16–19</sup> Traditionally, ELISA technique is used for the measuring of HSA concentration in body fluid like blood, urine, etc.<sup>20</sup> But, its accurate point-of-care testing is limited by the involvement of multistep and time-consuming preparations. However, fluorometry is considered as the most popularly used technique for the accurate quantification of proteins owing to its high selectivity, sensitivity, technical simplicity, rapid responsiveness, and noninvasive benefits along with high-resolution real-time imaging in living cells.<sup>21–25</sup>

In the past few years, fluorophores with typical aggregation-induced emission (AIE) activity have garnered the attention of chemists and biologists to explore the possibility of their biomedical applications.<sup>26–28</sup> As a consequence, a number of AIEgen-based fluorescent molecular probes have been developed for the detection of HSA and BSA.<sup>29–33</sup> Recently, self-assembled molecular probes have been emerging with unique superiority to their individual molecular form as a potent material for protein sensing analysis.<sup>34–36</sup> Molecular self-assembled nanoaggregates with exceptional photostability and biocompatibility offer a wide range of flexibility in chemical design and fine-tuning of optical properties. For instance, a self-assembled probe exhibits no or very little fluorescence due to the aggregation caused quenching (ACQ) effect, but when the probe responds to the target analytes by undergoing disassembly, it will emit strong fluorescence.<sup>37</sup> Besides, there are also few reports where some near-infrared (NIR) dyes bind with HSA to generate HSA–dye nanocomposites for applications in bioimaging, tumor therapeutic diagnosis, and potential drug delivery.<sup>38</sup> However, Thayumanavan and colleagues have successfully employed the *polymer–nanoparticle-disassembly* strategy as a unique technique for the detection of both protein and enzyme.<sup>39–41</sup> On the contrary, only a few examples exist where this disassembly technique was utilized successfully for *small-molecule derived self-assembled nanoaggregated* probes for the HSA and BSA detection.<sup>42–49</sup>

Despite the difficult task in comprehending HSA's complex multidomain structure and remarkable ligand binding ability,<sup>3,50</sup> targetable nanoaggregates with activatable signals based on molecular *self-assembly* may also be useful for exploring noncovalent site-selective interactions. Very recently, a number of fluorescent molecular probes for HSA detection<sup>9,20,51–61</sup> have been published; however, they are incapable of self-assembling into nanoaggregates and have a number of drawbacks, including low sensitivity and selectivity issues, delayed reaction time, poor biocompatibility, etc. Furthermore, several bioprobes have been found to be ineffective and have limited uses in advanced biomedical research because most of them struggle to measure nanomolar

level of HSA present in complex biological fluids owing to their high detection limits, large background signal, and excitation/emission occurring at comparatively shorter wavelengths.

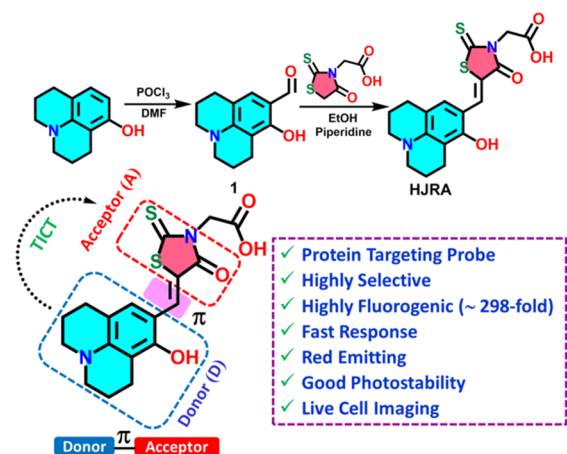
Therefore, in this article, we rationally designed and developed a TICT-based small organic molecular probe HJRA that can easily self-assemble into nonfluorescent nanoaggregates in aqueous solution. However, HJRA nanoaggregates can selectively bind with serum albumins (HSA/BSA), which facilitates the disassembly of nanoaggregates into monomers, exhibiting a noticeable turn-on red fluorescent response toward HSA and BSA in biological environments. Some particular advantages of the probe may include (i) the coupling of disassembly induced emission enhancement with the site-specific recognition mechanism favors the enhancement of the sensitivity and selectivity of the probe; (ii) a very fast (~15 s) fluorescence response time of HJRA toward HSA; (iii) a very low LOD value (1.13 nM), substantially below the normal level of HSA in healthy urine, signifying the high sensitivity of the probe toward HSA; (iv) most strikingly, the outstanding HSA detection capabilities of HJRA in urine, allowing us to develop a rapid and effective way to monitor the health status of people; and (v) finally, the probe may also find potential applications for live-cell imaging of HSA. Here, in addition to the detailed morphological characterization, HSA site marker displacement studies, molecular docking, steady-state fluorescence, and lifetime spectroscopic studies were also conducted to understand the underlying sensing mechanism.

## EXPERIMENTAL SECTION

**Materials.** 8-Hydroxyjulolidine, rhodanine-3-acetic acid, Coomassie Brilliant Blue G-250, ibuprofen, warfarin and glycerol were purchased from Sigma-Aldrich and used as received. All the proteins and enzymes (HSA, BSA,  $\beta$ -lactoglobulin, lysozyme, CT-DNA, hemoglobin, cytochrome C, proteinase K, collagen, pepsin, and trypsin) as well as other biomolecules like glutathione (GSH), creatinine, uric acid, glucose, urea, and all amino acids were also obtained from Sigma-Aldrich. The sodium salts of various anions ( $F^-$ ,  $Cl^-$ ,  $Br^-$ ,  $I^-$ ,  $PO_4^{3-}$ ,  $BrO_3^-$ ,  $ClO_4^-$ ,  $N_3^-$ ,  $NO_2^-$ ,  $NO_3^-$ ,  $SCN^-$ ,  $CH_3COO^-$ ,  $H_2PO_4^-$ ,  $S_2O_3^{2-}$ ,  $SH^-$ ,  $HSO_4^-$ ) and perchlorate salts of different cations ( $Na^+$ ,  $K^+$ ,  $Ca^{2+}$ ,  $Mg^{2+}$ ,  $NH_4^+$ ,  $Mn^{2+}$ ,  $Co^{2+}$ ,  $Ni^{2+}$ ,  $Cu^{2+}$ ,  $Al^{3+}$ ,  $Hg^{2+}$ ,  $Fe^{2+}$ ,  $Zn^{2+}$ ,  $Fe^{3+}$ ) were procured either from Sigma-Aldrich or from other commercial suppliers. Reagent grade (Merck, India) solvents were used for the synthetic purposes and dried prior to use according to the standard procedures. For the spectroscopic studies, deionized water from Milli-Q source and HPLC-grade solvents were used.

**Synthesis of (Z)-2-(5-((8-Hydroxy-2,3,6,7-tetrahydro-1H,5H-pyrido[3,2,1-ij]quinolin-9-yl) methylene)-4-oxo-2-thioxothiazolidin-3-yl) Acetic Acid (HJRA).** In the first step (Scheme 1), compound **1** was synthesized according to the method described in literature,<sup>62</sup> and the detailed synthetic procedure and characterization are given in the Supporting Information. In the next step, for the synthesis of HJRA, compound **1** (0.217 g, 1 mmol) and rhodanine-3-acetic acid (0.191 g, 1 mmol) were dissolved in 10 mL of dry ethanol and a catalytic amount of piperidine was added. Then the reaction mixture was refluxed for 8 h with constant stirring. The residue was then filtered, washed thoroughly with ethanol, and dried in vacuum desiccator overnight to get a solid crude product. The product was then purified by using column chromatography to afford a purple color solid (71% yield) (Scheme 1). <sup>1</sup>H NMR (400 MHz, DMSO-*d*<sub>6</sub>):  $\delta$  in ppm = 13.312 (s, 1H), 9.287 (s, 1H), 8.038 (s, 1H), 6.788 (s, 1H), 4.692 (s, 2H), 3.280–3.224 (m, 4H), 2.652 (t, *J* = 6.1 Hz, 2H), 2.584 (t, *J* = 6.3 Hz, 2H), 1.836 (s, 4H). <sup>13</sup>C NMR (101 MHz, DMSO-*d*<sub>6</sub>):  $\delta$  in ppm = 192.37, 167.73, 166.50, 155.15, 147.74, 131.54, 127.45, 115.32, 109.37, 107.03, 49.65, 48.88, 44.90, 26.92, 21.18, 21.06, 20.28. HRMS (ESI) *m/z*: calcd for [*M* + *H*<sup>+</sup>], 391.0786;

## Scheme 1. Rational Design and Synthesis of HJRA



found, 391.0788. IR Spectrum:  $\nu$  in  $\text{cm}^{-1}$  = 3330, 2823, 1718, 1660, 1170.

**Experimental Solution.** A 500 mL 10 mM phosphate-buffered saline (PBS) solution of pH 7.4 was prepared in deionized water from Milli-Q source and used in all studies. Stock solutions of BSA and HSA (20 mg/mL) were prepared in deionized water. The stock solutions of other proteins, enzymes, and biomolecules were prepared as required, and the exact concentrations of the protein stock solutions were evaluated spectrophotometrically by considering the absorbance and molar extinction coefficient values at particular wavelengths as relevant. Stock solutions of different cations (5 mM for each) and anions (5 mM for each) were prepared by dissolving the required amount of inorganic salts in deionized water. A 10 mL stock solution of HJRA (1 mM) was prepared in spectroscopic grade DMSO and stored in a refrigerator before use.

**Instrumentation and Experimental Methods.** Instrumentation details and the experimental methods adopted for carrying out this work are provided in the Supporting Information.

## RESULTS AND DISCUSSION

**Rational Design and Synthesis of Probe HJRA.** In this article, our main intention was to synthesize a suitably designed novel fluorescent molecular probe that might potentially bind to albumin protein in a site-specific manner. Keeping this in mind, we have developed a TICT mechanism-based molecular probe, HJRA, by incorporating a donor- $\pi$ -acceptor system with julolidine as the electron donor and rhodanine as the electron acceptor moieties (Scheme 1). Here, the selection of modified julolidine fluorophore is based on its outstanding quantum yield<sup>20</sup> and emission wavelength that is nearly as feasible as the Red/NIR region, which in turn is necessary for achieving improved tissue depth penetration and

less autofluorescence. The intention to incorporate hydroxyl group was two fold: (i) to boost the electron-donating ability of the overall moiety as a secondary donor and (ii) to facilitate the formation of stable hydrogen bonds with the amino acid residues of serum albumin protein, which in turn prevents the free molecular rotation of the probe within the protein binding pocket. Moreover, the presence of the hydroxyl group on HJRA may also enhance the aqueous solubility of the probe. A neutral rhodanine moiety was selected for avoiding nonspecific electrostatic interactions and the carboxylic acid functionality makes additional conjugation to a specific protein much easier. Some similar frameworks to the structure of the rhodanine benzylidene conjugates have also been previously reported as protein or RNA aptamer fluorogens, which encourage us to select this probe for our present investigation.<sup>63,64</sup> To achieve our goal, the probe HJRA was synthesized by a simple condensation reaction between compound 1 and rhodanine-3-acetic acid in ethanol (Scheme 1) and well characterized by <sup>1</sup>H NMR (Figure S4), <sup>13</sup>C NMR (Figure S5), HRMS (Figure S6), and IR (Figure S7) spectroscopies.

**Photophysical Properties and Self-Assembly Behavior of HJRA.** Small organic molecules may undergo self-assembly via noncovalent interactions leading to the formation of nanoaggregates, which can greatly alter their optical (absorbance and fluorescence) characteristics.<sup>49</sup> Therefore, to establish the formation of nanoaggregates, we examined the optical properties of HJRA in DMSO/PBS binary mixtures, where a solution of HJRA (2  $\mu\text{M}$ ) in pure DMSO exhibited an intrinsic absorption maximum at 521 nm and a strong emission peak at 585 nm. With the progressive switch of solvent composition from pure DMSO to PBS buffer (pH 7.4), the absorption maximum of HJRA gets shifted from 521 to 539 nm (Figure S8A) and a significant diminishing of emission intensity along with a red shift of emission maxima from 585 to 598 nm (Figure S8B) was observed. All the aforementioned changes in spectral behavior clearly indicate the aggregation of HJRA in aqueous PBS buffer medium, mainly due to the hydrophobic interactions among the HJRA molecules.<sup>48</sup> The nanoaggregate formation was further ascertained by dynamic light scattering (DLS) experiments on a 2  $\mu\text{M}$  HJRA in PBS buffer that displayed the formation of nanoparticles with a 105 nm average diameter (Figure 1A). Moreover, TEM investigation (Figure 1B) vividly established the development of spherical HJRA nanoaggregates with an average diameter of ~97 nm (Figure 1C).

The probe HJRA (2  $\mu\text{M}$ ) displays fluorescent-silent emission band at 598 nm (Figure S9) in ~100% PBS buffer (pH 7.4, containing 0.2% DMSO) upon excitation at 539 nm.

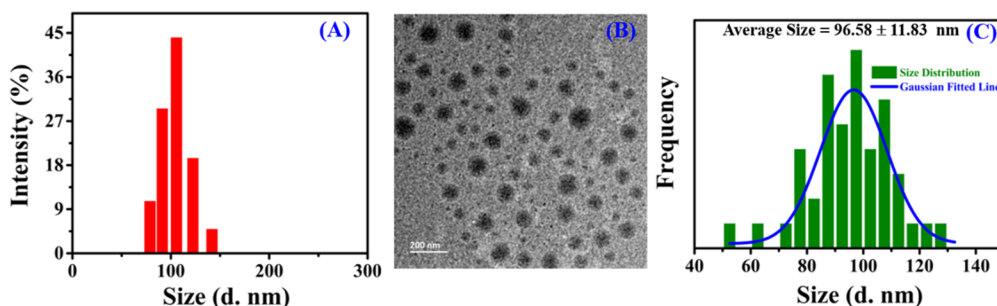


**Figure 1.** (A, B) DLS and TEM images of the nanoaggregates of 2  $\mu\text{M}$  HJRA. (C) Particle size distribution plot of HJRA (2  $\mu\text{M}$ ) nanoaggregates from the TEM image characterization. Scale bar: 200 nm.



The nonemissive status may be due to the formation of loosely packed nanoaggregates resulting aggregation caused quenching (ACQ) effect<sup>46–48</sup> and the presence of twisted intramolecular charge transfer process. Therefore, to establish the involvement of TICT process, change in photophysical (UV–vis absorption and fluorescence) behavior of probe was explored. Thus, HJRA (2  $\mu\text{M}$ ) was added to various organic solvents with different polarity and changes in the absorbance and fluorescence behavior were monitored. As the solvent polarity increases, it was found that the probe showed red shifts of absorption and emission maxima from 495 and 548 nm to 521 and 585 nm in 1,4-dioxane and DMSO, respectively (Figure S10).

Additionally, we have examined the effect of solvent polarity on the fluorescence intensity of HJRA in mixed solvent media of different polarity using PBS/1,4-dioxane and PBS/ethanol in variable compositions. It is expected that the addition of low polarity solvents (1,4-dioxane or ethanol) may disintegrate HJRA nanoaggregates. Indeed, the emission peak of HJRA was blue-shifted with the concomitant enhancement in fluorescence intensity when the volume fraction of 1,4-dioxane and ethanol in the binary combination (PBS/1,4-dioxane and PBS/ethanol) were increased (Figure S11), suggesting the disintegration of HJRA nanoaggregates in low polarity medium.

To further corroborate the occurrence of TICT mechanism, we recorded the fluorescence spectra of HJRA (2  $\mu\text{M}$ ) in mixed solvent media of variable compositions using PBS/glycerol, ethanol/glycerol and ethylene glycol/glycerol having different viscosity. As shown in Figure 2A, the emission

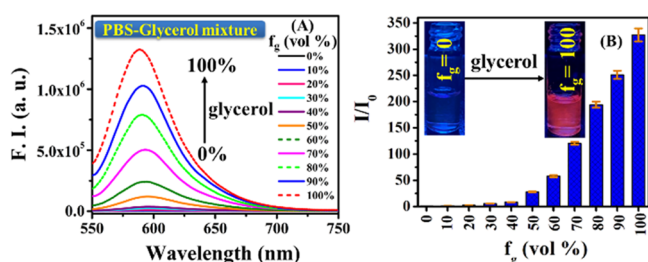
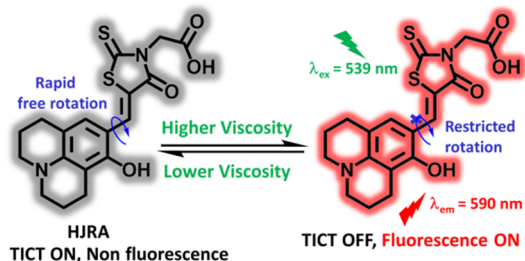


**Figure 2.** (A, B) Fluorescence spectra and corresponding variations in  $I/I_0$  (at 590 nm) of HJRA (2  $\mu\text{M}$ ) in PBS buffer with different fractions of glycerol (v/v, from 0 to 100%). Inset of B, fluorescent photoimages of HJRA with two different  $f_g$  values.  $\lambda_{\text{ex}} = 539$  nm. Error bars: standard deviation ( $n = 3$ ).

intensity of HJRA was increased consistently with the increase in glycerol fraction in PBS/glycerol binary mixture indicating the regular increment in viscosity of the medium. Actually, an  $\sim 314$ -fold increase in emission intensity of HJRA was observed at 590 nm upon increment of the glycerol proportion from 0% to 100% (Figure 2B). Similar changes in fluorescence were also observed upon increasing the glycerol volume fraction in ethanol/glycerol and ethylene glycol/glycerol mixtures (Figure S12). As a consequence, these viscosity-dependent fluorescence modifications evidently demonstrate the restriction imposed on the free intramolecular rotation of HJRA probe by the increase in viscosity, which in turn enhances the fluorescence intensity of HJRA by blocking the nonradiative decay pathways (Scheme 2). Here, it was also worth mentioning that irradiation of the HJRA solution (2  $\mu\text{M}$ ) with a 539 nm light at a power source of 75 W for a period of 30 min did not result in any noticeable changes in the fluorogenic behavior of HJRA (Figure S23). This emphasizes

## Scheme 2. Response Mechanism of HJRA towards Viscosity



the good photostability of HJRA in its operating environment, which is necessary for a biosensor to work effectively.

**Selectivity Study and Optical Response of HJRA toward HSA/BSA.** To explore the selectivity of HJRA, at first, we systematically recorded absorption and fluorescence responses of HJRA (2  $\mu\text{M}$ ) in  $\sim 100\%$  PBS buffer (pH 7.4) by the addition of excess amount (10 equiv.) of different proteins and enzymes, including  $\beta$ -lactoglobulin, lysozyme, CT-DNA, hemoglobin, cytochrome C, proteinase K, collagen, pepsin, trypsin, HSA, and BSA. In PBS buffer medium, HJRA (2  $\mu\text{M}$ ) displays an absorbance maximum at 539 nm (Figure S9). Here, it was found that upon addition of excess HSA/BSA proteins (10 equiv.) to a solution of HJRA, induced certain variations in the absorbance behavior of HJRA. Besides this, no such change in the absorption band of HJRA was noticed in the presence of other proteins, enzymes, and bioanalytes tested (Figure S13A). There is a gradual increase in absorbance at 542 nm was observed upon gradual addition of HSA to a solution of HJRA (Figure S13B). Here, it was also worth noting that only HSA and BSA were capable of providing a substantial turn-on fluorescent response at 582 nm among the different proteins and enzymes tested (Figure 3). As the HJRA

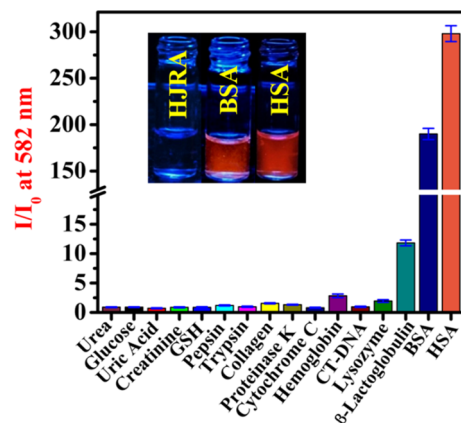


**Figure 3.** Variations in emission intensity ( $I/I_0$  of HJRA (2  $\mu\text{M}$ ) at 582 nm in  $\sim 100\%$  PBS buffer (pH 7.4) by the addition of excess amount (10 equiv.) of different proteins, enzymes and urine interferents. Inset: visual fluorescence changes of HJRA upon addition of HSA and BSA under 356 nm UV light.  $\lambda_{\text{ex}} = 539$  nm. Error bars: standard deviation ( $n = 3$ ).

probe has the potential to be used in urine analysis, we further investigated the impact of other key organic components present in human urine, such as GSH, glucose, urea, uric acid, and creatinine (each at 10 equiv.) on the selective detection of HSA and BSA by HJRA. According to the investigational findings presented in Figure 3, it can be concluded that the

fluorescence emission of HJRA is negligibly changed by these urine interferents under identical experimental environments. Additionally, the selectivity of HJRA ( $2 \mu\text{M}$ ) toward 10 equiv. of different amino acids, 15 equiv. of different cations, and 15 equiv. of various anions was also investigated, resulting in negligible influence on the fluorescence behavior of HJRA at 582 nm (Figure S14–S16, Supporting Information). This suggests that HJRA can serve as a useful analytical method for independently identifying and detecting HSA/BSA.

In this study, the anti-interference capability of HJRA was also investigated by measuring the fluorescence response of HJRA toward HSA in the presence of typical urine interferents as well as other proteins, enzymes, different amino acids, cations and anions. As shown in Figure 4, and Figures S17–

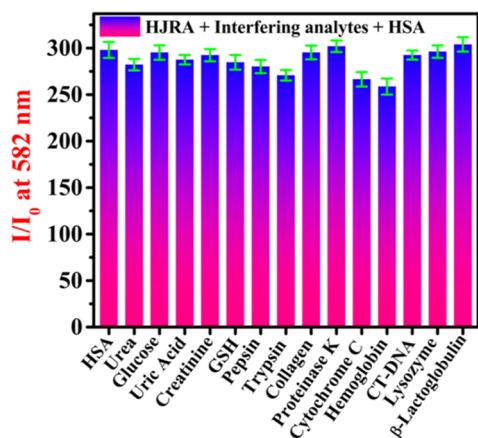


**Figure 4.** Fluorescence responses of HJRA ( $2 \mu\text{M}$ ) toward HSA (10 equiv.) in the presence of excess amount (10 equiv.) of different proteins, enzymes and urine interferents at 582 nm in  $\sim 100\%$  PBS buffer of pH 7.4,  $\lambda_{\text{ex}} = 539 \text{ nm}$ . Error bars: standard deviation ( $n = 3$ ).

S19, when additional interferents were present in the detection system, the fluorescence response of HJRA toward HSA at 582 nm did not alter appreciably in PBS (pH 7.4) buffer medium. Thus, all of them exhibited an interference-free selective fluorescence response of HJRA toward HSA. These findings show that the HJRA probe has exceptional selectivity toward HSA, which can be useful for further cell imaging applications and HSA detection in complicated biological samples.

Interestingly, when the nonemissive HJRA ( $\Phi = 0.0015$ ) interacts with an excess of HSA and BSA in PBS buffer media, it becomes strongly emissive ( $\Phi = 0.4317$  in the presence of HSA) and displays a turn-on red fluorescent response, which in turn allows the scope to identify HSA and BSA with the naked eye under UV light (Figure 3, inset). In fact, it was noticed that the interaction of HJRA ( $2 \mu\text{M}$ ) with HSA and BSA (10 equiv. of each) resulted in  $\sim 298$ -fold and  $\sim 190$ -fold increases in emission intensity at 582 nm, respectively (Figure 3). HSA and BSA have comparable form and functional behaviors, but the difference in microstructure and milieu within their hydrophobic binding zones may affect the extent of interaction of HJRA with proteins and hence the extent of rigidity imposed on the probe. However, in order to comprehend the fluorescent turn-on response of HJRA probe imposed by serum albumin proteins, a quantitative assessment of the interaction between HJRA and HSA is essential. Therefore, a fluorescence titration was carried out keeping  $[\text{HJRA}] = 2 \mu\text{M}$  with the varying HSA concentration between 0 and  $19.6 \mu\text{M}$  in PBS buffer at pH 7.4. It was noticed that the emission intensity

of HJRA was enhanced significantly ( $\sim 298$ -fold) in a  $19.6 \mu\text{M}$  concentration of HSA along with a simultaneous blue shift ( $\sim 16 \text{ nm}$ ) of the emission maxima from 598 to 582 nm upon excitation at 539 nm (Figure 5 and Figure S9). Here, it is

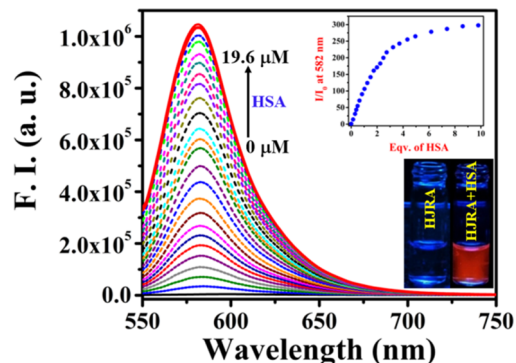


**Figure 5.** Fluorescence spectral changes of HJRA ( $2 \mu\text{M}$ ) in  $\sim 100\%$  PBS buffer (pH 7.4) upon successive addition of HSA. Insets: plot of emission intensity variations ( $I/I_0$  at 582 nm versus equivalent of HSA and visual fluorescence changes of HJRA with the addition of HSA.  $\lambda_{\text{ex}} = 539 \text{ nm}$ .

important to note that as all the emission spectra were collected within 1 min of the bioanalytes being added, the fluorescent response of HJRA to HSA appears to be very quick.

Hence, the time-dependent fluorescence assay of HJRA was conducted in the absence and presence of different HSA concentration to determine the response time. Figure S23 shows that after adding HSA, the emission intensity was increased rapidly and gets saturated within the time of measurement ( $\sim 15 \text{ s}$ ). Therefore, HJRA might be an excellent probe for the real-time measurement of HSA in biological fluids. Here, we also looked at the influence of pH of the medium on HSA sensing by HJRA in the range pH 3 to 10. Without HSA, the emission behavior of the probe ( $2 \mu\text{M}$ ) remained unchanged across the experimental pH range (Figure S22), suggesting that HJRA was relatively stable in various microenvironment. On the other hand, upon addition of 1 equiv of HSA, the emission intensity of HJRA was greatly increased and remained almost constant in the range pH 5 to 7.4, manifesting that the probe is suitable for the detection of HSA in the physiological pH range. The stoichiometry of the reaction between HSA and HJRA was determined by Job's method, which clearly indicates a 1:1 complexation (Figure 6A).

In this study, the fluorescence titration data of HJRA with HSA (*vide supra*) were used to evaluate the dissociation constant ( $K_d$ ) value between the probe and HSA. Following eq S11 when we plot  $(I_0 - I)/(I_0 - I_\infty)$  vs HSA concentration, a nonlinear curve was obtained (Figure S20), which was then solved by using a nonlinear curve fitting approach to give a high binding affinity of HJRA to HSA in terms of the dissociation constant value,  $K_d = (0.64 \pm 0.07) \mu\text{M}$ . Moreover, the emission intensity of HJRA at 582 nm displayed a good linear relationship with the incremental addition of HSA within the concentration range 0– $2.05 \mu\text{M}$  (Figure S21). Based on the  $3\sigma/\text{slope}$  method<sup>58</sup> (see the Supporting Information), the limit of detection (LOD) value was estimated to be  $1.13 \text{ nM}$  ( $0.0751 \text{ mg/L}$ ). A quick inspection of the literature revealed that the present LOD is substantially below the normal HSA concentration in healthy urine, signifying the high sensitivity of

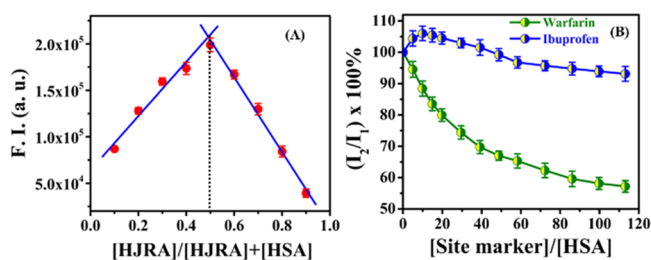


**Figure 6.** (A) Job's plot analysis of HJRA with HSA in different molar ratios keeping the overall concentration at  $2 \mu\text{M}$ . (B) Emission intensity variations of HJRA-HSA composite (HJRA =  $2 \mu\text{M}$ , HSA =  $0.5 \mu\text{M}$ ) in pH 7.4 PBS buffer with the successive addition of warfarin and ibuprofen site markers ( $0$ – $56.6 \mu\text{M}$ ).  $\lambda_{\text{ex}} = 539 \text{ nm}$  and  $\lambda_{\text{em}} = 582 \text{ nm}$ . Error bars: standard deviation ( $n = 3$ ).

the probe and superior to the recently reported other HSA sensing probes.<sup>32,42–44,48,49,51–56,60,61</sup> Besides this, a comparison table has been prepared (Table S2) to list the advantages of this developed method in terms of sensitivity, selectivity, response time, and binding site as compared to the previously reported HSA/BSA detection strategies.

**Site-Specific Binding Study and Probable HSA Sensing Mechanism.** The 1:1 complexation between HJRA and HSA, as delineated by Job's plot, confirms that HJRA binds with HSA protein primarily at one site only. According to the crystal structure study, HSA is a  $\sim 66.5 \text{ kDa}$  complex protein with three distinct domains (domains I, II, and III), each of which contains two subdomains (A and B).<sup>4</sup> The major ligand binding sites of HSA are mostly found in hydrophobic regions of subdomain IIA (binding site I) and subdomain IIIA (binding site II).<sup>65,66</sup> Site I interact with compounds primarily through strong hydrophobic interactions, whereas site II employs a mixture of ionic, van der Waals, and hydrogen bonding interactions.<sup>4,65,66</sup> Therefore, the competitive fluorescence displacement assays were conducted to determine the probable binding location of HJRA on HSA employing two famous site-specific drugs (warfarin for site I and ibuprofen for site II).

Here, in the displacement experiments, the site-specific drugs were incrementally added to a solution of HSA and HJRA in a molar ratio of 1:4 to minimize the nonspecific binding of the site-specific drugs.<sup>67</sup> The change in emission intensity of this ternary mixture were monitored by using the approach stated by Sudlow et al.<sup>66</sup>

$$\frac{I_2}{I_1} 100\%$$

Here,  $I_2$  and  $I_1$  are the emission intensities of the HSA–HJRA mixture in the presence and absence of site-specific drugs, respectively. In the presence of  $56.6 \mu\text{M}$  warfarin, the emission intensity of the HSA–HJRA combination was noticeably reduced by about 43%, implying the displacement of HSA bound HJRA by warfarin (Figure 6B), whereas ibuprofen exhibited no significant change in emission intensity. Hence, these experimental findings clearly indicate that HJRA is most probably housed at subdomain IIA of Site I in HSA.

Then the HSA detection process was explored further to know more about the underlying sensing mechanism. DLS experiment of  $2 \mu\text{M}$  HJRA in  $\sim 100\%$  PBS buffer (pH 7.4) indicated that HJRA can form nanoaggregates with a mean diameter of  $105 \text{ nm}$  (Figure 1A). As the most common cause of AIEgens fluorescence light-up is molecular aggregation, DLS analysis was employed to see if bigger nanoaggregates developed in the presence of HSA protein. Interestingly, after adding of 1 equiv. HSA, the peak at  $105 \text{ nm}$  related to the HJRA nanoaggregates was vanished with the emergence of a new peak at  $9 \text{ nm}$  (Figure 7A) corresponding to the size of the HSA protein in solution (Figure 7c).<sup>38,42</sup> Furthermore, TEM imaging investigations vividly displayed that after the addition of 1 equiv. of HSA, nanoaggregates of HJRA with an average diameter of  $\sim 97 \text{ nm}$  (Figure 1B, C) converted into considerably smaller particles (Figure 7B). These experimental outcomes undoubtedly established the disassembly of the self-assembled nanoaggregates of HJRA upon complexation with HSA. Thus, the fluorescent turn-on response of HJRA to HSA can be attributed to the site-specific binding of HJRA within the hydrophobic cavity of HSA, which in turn suppresses the TICT action by restricting free intramolecular rotation, because of the severe steric hindrance and low-polarity environment inside HSA. Moreover, a steady-state fluorescence anisotropy study was carried out to collect important information about the rigidity of the environment in the immediate proximity of the HJRA probe and it is reflected by the change in anisotropy value.<sup>68,69</sup>

At first, a quick augmentation in the anisotropy value of HJRA ( $2 \mu\text{M}$ ) was noticed from 0.009 to 0.292 upon addition of only  $1.5 \mu\text{M}$  HSA and then the value slowly improved to 0.348 until the addition of  $19.6 \mu\text{M}$  HSA (Figure 8A). Hence, the rising value of anisotropy evidently reveals that considerable motional restriction is imposed on HJRA probes within HSA. Additionally, to determine the source of fluorescence amplification we have also performed the fluorescence lifetime analysis of probe HJRA with the addition of HSA (Figure 8B). Table S1 summarizes the decay related parameters. In  $\sim 100\%$  PBS buffer medium, free HJRA probe

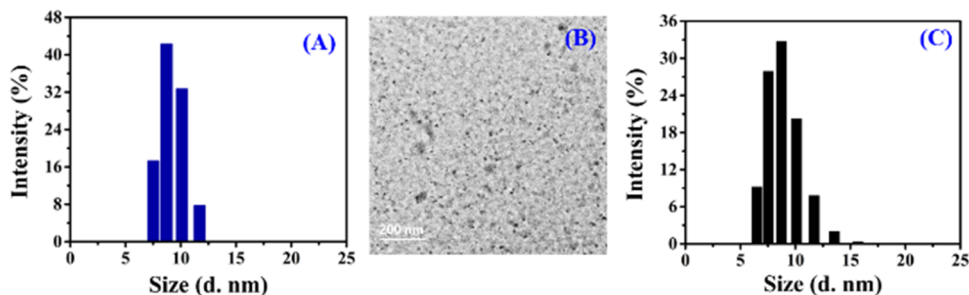


**Figure 7.** (A, B) DLS and TEM images of the HJRA ( $2 \mu\text{M}$ ) after the addition of 1 equiv. of HSA in  $\sim 100\%$  PBS buffer solution (pH 7.4). (C) DLS analysis of only  $2 \mu\text{M}$  HSA. Scale bar:  $200 \text{ nm}$ .



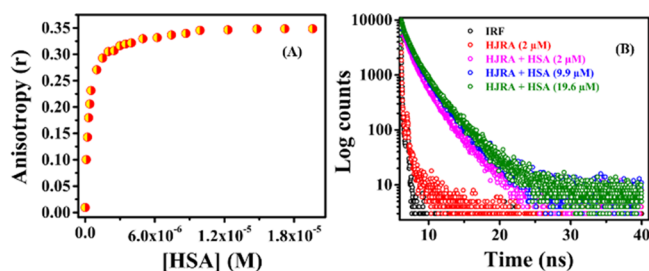


**Figure 8.** (A) Steady-state anisotropy variation of HJRA ( $2 \mu\text{M}$ ) with the increasing concentration of HSA ( $\lambda_{\text{ex}} = 539 \text{ nm}$  and  $\lambda_{\text{em}} = 582 \text{ nm}$ ). (B) Time-resolved fluorescence decay spectra of HJRA ( $2 \mu\text{M}$ ) with the addition of HSA ( $0\text{--}19.6 \mu\text{M}$ ).

displays a triexponential decay with lifetimes of 0.46 ns (34.62%), 0.02 ns (30.96%), and 0.45 ns (34.42%), while after the addition of  $19.6 \mu\text{M}$  of HSA, probe HJRA exhibits a triexponential decay with lifetimes of 1.21 ns (44.17%), 0.29 ns (10.85%), and 2.97 ns (44.98%). The longer lifetime value of HJRA-HSA composite implies that binding of HJRA to HSA decreases the molecular rotational flexibility and blocks the TICT process, thereby lowering the energy loss through nonradiative decay routes.

**Molecular Docking.** Here, we have conducted the molecular docking simulations to determine the probable binding site of HJRA within HSA and the role of relevant interactions during the complexation process.<sup>50,69</sup> From the ten distinct conformers, the docking conformation with lowest binding energy was selected for further investigations. Figure 9A shows the molecular docking pose of HJRA with HSA, indicating that subdomain IIA of site I in HSA is the preferred binding site for the HJRA probe, as evidenced by site-specific drug displacement studies. Several hydrophobic amino acid residues, like Trp 214, Ala 291, Leu 198, Leu 219, and Val 343 provided a better stability to the housed HJRA within HSA through hydrophobic and van der Waals interactions (Figure 9B, D). Some basic and cationic amino acid residues, such as Lys 199, Arg 257, Arg 222, and His 242, are important in forming hydrogen bonds with the oxygen atoms of different

functional groups of HJRA (Figure 9C, D). Furthermore, Lys 195 engages with the aromatic skeleton of HJRA probe through cation– $\pi$  interaction. The indole ring of Trp 214 residue was projected into the binding domain to form a  $\pi$ – $\pi$  bond with HJRA. As shown in Figure 9D, a  $\pi$ -sulfur interaction also occurs between the Tyr 150 residue and the exocyclic sulfur atom of the HJRA probe. Based on the docking experiment, the binding energy for the interaction of HJRA with HSA is  $-6.36 \text{ kcal/mol}$ , suggesting that the interaction process is energetically favorable. The probable HSA sensing mechanism is portrayed in Figure 9E. Primarily, these hydrophobic, electrostatic, and cation– $\pi$  interactions are responsible for the disassembly of the HJRA nanoaggregates which, in turn, facilitated the release and movement of HJRA monomer inside the HSA's hydrophobic cavity. Consequently, various noncovalent bonds that were developed in Site I are responsible for restricting the free rotation of the HJRA probe, making it highly emissive inside the protein domain.

**HSA Quantification in Human Urine Samples.** The quantitative detection of urinary albumin levels has immense clinical importance, although it is often complicated by the presence of other biological interferents and strong auto fluorescence of urine. However, we believe that the probe HJRA may be utilized for selective identification and quantification of the albumin level in urine samples due to its ability of HSA detection over a range of pH 5 to 7.4 (Figure S22) through strong turn-on fluorescence response. Therefore, to establish the practical applicability of the probe HJRA, we collected three urine samples from three healthy male volunteers with no past medical history and diluted ten times by  $\sim 100\%$  PBS buffer (pH 7.4) to assess the endogenous HSA concentration in urine samples using standard addition curve technique. Dilution of urine samples was used to reduce the pH effect and urine background fluorescence.

In our experiment, when HSA ( $0\text{--}20.13 \mu\text{M}$ ) was added to a urine–PBS system containing  $2 \mu\text{M}$  HJRA, the fluorescence intensity increased with the increasing concentration of HSA and reached saturation at  $20.13 \mu\text{M}$  (Figure S25A). Furthermore, in the concentration range of  $0\text{--}2.05 \mu\text{M}$ , the fluorescence intensity increased linearly with HSA (Figure

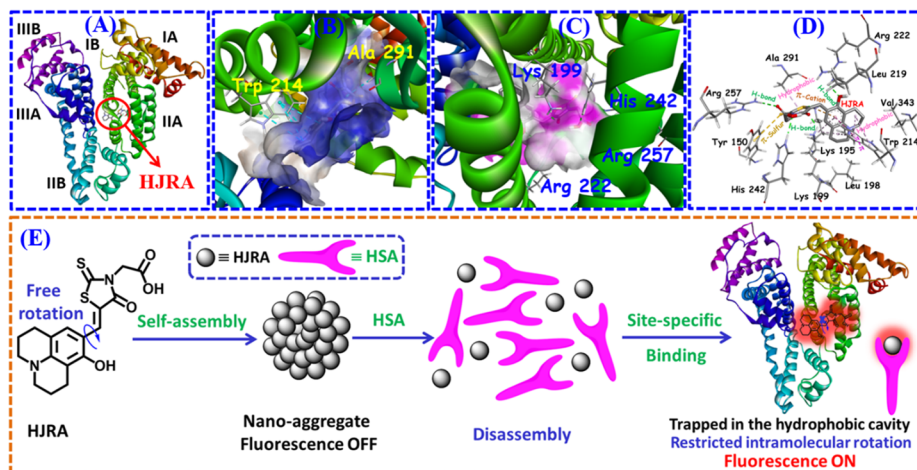


**Figure 9.** (A) Molecular docking posture of HJRA with HSA protein (PDB ID: 1AO6) shown by red circle. (B, C) Magnified view of hydrophobic and hydrogen bonding interactions, respectively, made by HJRA in site I of HSA. (D) Neighboring amino acid residues and responsible forces directly interact for the accommodation of HJRA in site I of HSA. Hydrophobic and  $\pi$ – $\pi$  interactions are displayed as dotted purple lines; H-bonds,  $\pi$ –cation and  $\pi$ –sulfur bonds are indicated as dotted green, orange, and dark orange lines, respectively. (E) Schematic representation of the HSA-mediated disassembly of HJRA nanoaggregates and fluorescence turn-on process.

S25B) and the detection limit was 1.72 nM (0.1143 mg/L) by the  $3\sigma$ /slope method. From the linear relationship of HJRA emission intensity at 582 nm with the increasing HSA concentration, the urinary HSA levels of the three male volunteers were estimated to be 16.84 mg/L, 26.28 mg/L, and 12.76 mg/L, respectively.

For the validation of HSA levels determined by HJRA (fluorescence technique), urine samples were also examined using the Coomassie Brilliant Blue G250 technique,<sup>70</sup> as vividly described in the experimental part of the Supporting Information. Due to the limited sensitivity of Coomassie Brilliant Blue G250 (an albumin binding dye), undiluted urine samples were used in this technique. Based on the standard addition curve of absorbance at 595 nm versus HSA content (mg/L) (Figure 10A), the urinary HSA levels were evaluated

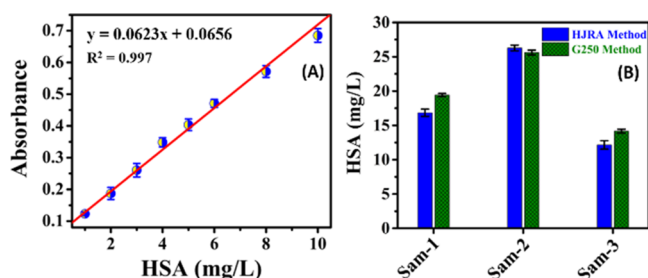


**Figure 10.** (A) Standard addition curve of absorbance versus HSA content (mg/L) by the Coomassie Brilliant Blue G250 method.  $\lambda_{\text{abs}} = 595$  nm. (B) Endogenous HSA quantification in human urine samples by a spectrofluorometric technique using HJRA in comparison with the G250 method. Error bars: standard deviation ( $n = 3$ ).

to be 19.43 mg/L, 25.61 mg/L and 14.05 mg/L, respectively. Remarkably, the urinary HSA levels estimated by the HJRA (Fluorescence) approach were shown to be in good accordance with the G250 method (Figure 10B). Hence, HJRA is an excellent red fluorescent probe for the accurate monitoring and quantifying the endogenous HSA in urine samples.

**Fluorescence Imaging of HSA in Living Cells.** Prior to the intracellular fluorescence imaging studies, a well-known MTT-based assay was performed in the CHO cell line to examine the cytotoxicity of the probe HJRA. As shown in Figure S26, after 24 h of incubation with 10  $\mu\text{M}$  of HJRA, the viability of CHO cells was remained over 82%, suggesting that the probe HJRA has very low cytotoxicity and might be useful in biological applications. Then the cell imaging of endogenous HSA in CHO cells was performed using HJRA. Upon incubation of CHO cells with HJRA (2  $\mu\text{M}$ ) for 30 min a weak red fluorescence was observed (Figure 11B2). Interestingly, the intracellular fluorescence intensity was dramatically reduced in CHO cells when warfarin (30  $\mu\text{M}$ ) was initially incubated for 15 min, followed by incubation with HJRA (2  $\mu\text{M}$ ) for an additional 30 min (Figure 11C2). These findings demonstrated that HJRA has good permeability to the cell membrane, enabling cells to interact with endogenous HSA. However, the fluorescence intensity was significantly enhanced when CHO cells were initially treated with 20  $\mu\text{M}$  HSA for 24 h, followed by further 30 min incubation with 2  $\mu\text{M}$  HJRA (Figure 12A2). In a control study, the intracellular fluorescence intensity was obviously decreased when the CHO cells (incubated with 20  $\mu\text{M}$  HSA for 24 h) were loaded with warfarin (30  $\mu\text{M}$ ) for inhibition (Figure 12B2). In contrast,

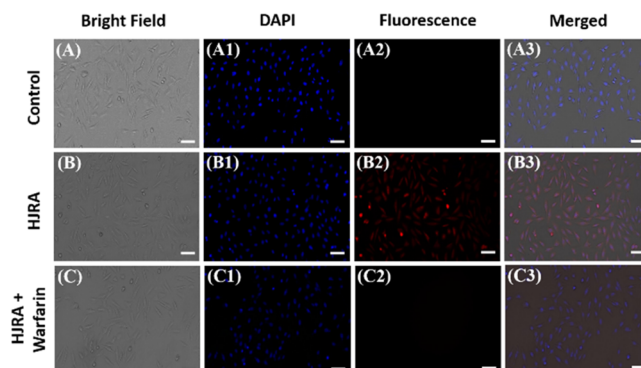


**Figure 11.** Confocal fluorescence imaging of endogenous HSA in living CHO cells. (A–A3) CHO cells as control. (B–B3) CHO cells treated with HJRA (2  $\mu\text{M}$ ) for 30 min and then with DAPI for another 10 min. (C–C3) CHO cells (pretreated with 30  $\mu\text{M}$  warfarin for 15 min) treated with HJRA (2  $\mu\text{M}$ ) for 30 min and then with DAPI for another 10 min.  $\lambda_{\text{ex}}$  for DAPI and HJRA are 352 and 540 nm, respectively. Scale bar = 50  $\mu\text{m}$ .

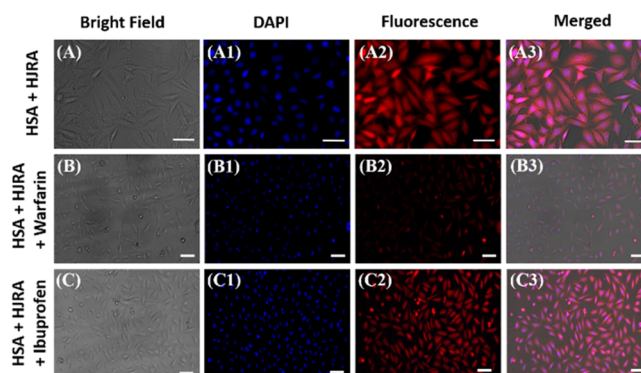


**Figure 12.** Confocal fluorescence imaging of exogenous HSA in living CHO cells. (A–A3) CHO cells (incubated with 20  $\mu\text{M}$  HSA for 24 h) loaded with HJRA (2  $\mu\text{M}$ ) for 30 min and then with DAPI for another 10 min. (B–B3) CHO cells (incubated with 20  $\mu\text{M}$  HSA for 24 h) pretreated with warfarin (30  $\mu\text{M}$ ) for 15 min, then with HJRA (2  $\mu\text{M}$ ) for another 30 min and then further loaded with DAPI for 10 min. (C–C3) CHO cells (incubated with 20  $\mu\text{M}$  HSA for 24 h) pretreated with ibuprofen (30  $\mu\text{M}$ ) for 15 min, then with HJRA (2  $\mu\text{M}$ ) for another 30 min and then further loaded with DAPI for 10 min.  $\lambda_{\text{ex}}$  for DAPI and HJRA are 352 and 540 nm, respectively. Scale bar = 50  $\mu\text{m}$ .

HSA-treated CHO cells loaded with 30  $\mu\text{M}$  ibuprofen followed by incubation with 2  $\mu\text{M}$  HJRA for an additional 30 min showed no change in intracellular fluorescence intensity (Figure 12C2), supporting the spectrum analysis shown in Figure 6B. Costaining with DAPI, a nucleus-targeting dye, followed by microscopic image analysis indicates that HJRA probes are mostly localized in the cytoplasm of CHO cells (Figure S27). These outcomes showed the capability of HJRA to image exogenous HSA in living cells.

## CONCLUSION

In this article, a TICT-based small fluorogenic molecular probe HJRA has been rationally designed and synthesized, which can easily *self-assemble* into nonfluorescent nanoaggregates in aqueous PBS buffer at pH 7.4. The HJRA nanoaggregates can selectively bind with serum albumin proteins (HSA/BSA) in physiological conditions, which facilitates the *disassembly* process toward monomer formation. The selective trapping of



the HJRA monomer in the subdomain IIA of site I in HSA resulted a rapid turn-on red fluorescent response due to suppression of the TICT action by restricting free intramolecular rotation. A similar turn-on response was also noticed in the case of BSA. The limit of detection (LOD) value was estimated to be 1.13 nM (0.0751 mg/L), which is substantially below the normal HSA concentration in healthy urine signifying the high sensitivity of the probe and superior to the recently reported other HSA sensing probes. The underlying HSA sensing mechanism has been well supported by molecular docking, competitive fluorescent displacement assay, and DLS and TEM studies. Analysis of the binding mechanism between HJRA and HSA implies that a combination of various noncovalent bonds including hydrophobic interactions, hydrogen bonds, and  $\pi$ - $\pi$  and cation- $\pi$  interactions are the fundamental forces for encouraging the disassembly process and trapping of the HJRA probe at the site I in HSA. The cell viability experiment reveals the low cytotoxicity of the HJRA probe. The practical applications of the probe were demonstrated by analyzing the healthy urine samples collected from three adults with no previous medical history. The comparable results and quick response toward quantification of HSA in urine by HJRA with respect to the Bradford method clearly points toward the superiority of this method compared to the existing ones and may lead to biomedical applications for HSA quantification in urine. Additionally, the probe may be used to image endogenous and exogenous HSA in living cells. Therefore, one can safely conclude that the HJRA probe can serve as an effective biomarker for the quick biomedical diagnosis of HSA-associated diseases. In conclusion, self-assembly/disassembly strategy opens up a new potential platform for the specific and sensitive detection of various target analytes.

## ■ ASSOCIATED CONTENT

### SI Supporting Information

The Supporting Information is available free of charge at <https://pubs.acs.org/doi/10.1021/acsabm.2c00820>.

Experimental details;  $^1\text{H}$  NMR,  $^{13}\text{C}$  NMR, HRMS, and IR analysis of compound 1 and HJRA; UV-vis and fluorescence spectra of HJRA in different solvents and DMSO/PBS mixtures; fluorescence spectra of HJRA in PBS/1,4-dioxane, PBS/ethanol, ethanol/glycerol and ethylene glycol/glycerol mixtures; absorption responses of HJRA toward different proteins, enzymes, and bioanalytes; fluorescence responses of HJRA toward various amino acids, cations, and anions; interference study; nonlinear plot for the determination of dissociation constant (HJRA-HSA complex); determination of the detection limit; effects of pH on HJRA for the detection of HSA; kinetic study; emission spectra of HJRA with the addition of HSA in urine-PBS system; MTT-based cell viability assay; cell imaging; table for lifetime analysis data; comparison table of the fluorescent probes for the detection of serum albumins (PDF)

## ■ AUTHOR INFORMATION

### Corresponding Author

Mahammad Ali – Department of Chemistry, Jadavpur University, Kolkata 700 032, India; [orcid.org/0000-0003-0756-0468](https://orcid.org/0000-0003-0756-0468); Email: [m\\_ali2062@yahoo.com](mailto:m_ali2062@yahoo.com)

## Authors

Mihir Sasmal – Department of Chemistry, Jadavpur University, Kolkata 700 032, India; [orcid.org/0000-0002-4284-7774](https://orcid.org/0000-0002-4284-7774)

Abu Saleh Musha Islam – School of Chemical Sciences, Indian Association for the Cultivation of Science, Kolkata 700032, India; [orcid.org/0000-0002-2529-8662](https://orcid.org/0000-0002-2529-8662)

Dolan Moni – Department of Chemistry, Jadavpur University, Kolkata 700 032, India

Debjani Maiti – Department of Chemistry, Jadavpur University, Kolkata 700 032, India

Ananya Dutta – Department of Chemistry, Jadavpur University, Kolkata 700 032, India

Complete contact information is available at: <https://pubs.acs.org/doi/10.1021/acsabm.2c00820>

## Notes

The authors declare no competing financial interest.

## ■ ACKNOWLEDGMENTS

Financial supports from CSIR (ref. No. 01(2896)/17/EMR-II), New Delhi and DST (ref. No. 809(Sanc)/ST/P/S&T/4G-9/2104), West Bengal are gratefully acknowledged. M.S. gratefully acknowledges UGC, New Delhi, for the fellowship (UGC-NET, SRF).

## ■ REFERENCES

- (1) Mizukami, S.; Hori, Y.; Kikuchi, K. Small-molecule-based protein-labeling technology in live cell studies: probe-design concepts and applications. *Acc. Chem. Res.* **2014**, *47*, 247–256.
- (2) Kobayashi, H.; Ogawa, M.; Alford, R.; Choyke, P. L.; Urano, Y. New strategies for fluorescent probe design in medical diagnostic imaging. *Chem. Rev.* **2010**, *110*, 2620–2640.
- (3) Fanali, G.; di Masi, A.; Trezza, V.; Marino, M.; Fasano, M.; Ascenzi, P. Human serum albumin: from bench to bedside. *Mol. Aspects Med.* **2012**, *33*, 209–290.
- (4) He, X. M.; Carter, D. C. Atomic structure and chemistry of human serum albumin. *Nature* **1992**, *358*, 209–215.
- (5) Fasano, M.; Curry, S.; Terreno, E.; Galliano, M.; Fanali, G.; Narciso, P.; Notari, S.; Ascenzi, P. The extraordinary ligand binding properties of human serum albumin. *IUBMB Life* **2005**, *57*, 787–769.
- (6) Curry, S.; Mandelkow, H.; Brick, P.; Franks, N. Crystal structure of human serum albumin complexed with fatty acid reveals an asymmetric distribution of binding sites. *Nat. Struct. Biol.* **1998**, *5*, 827–835.
- (7) Ha, C. E.; Bhagavan, N. V. Novel insights into the pleiotropic effects of human serum albumin in health and disease. *Biochim. Biophys. Acta* **2013**, *1830*, 5486–5493.
- (8) Belinskaia, D. A.; Voronina, P. A.; Batalova, A. A.; Goncharov, N. V. Serum Albumin. *Encyclopedia* **2021**, *1*, 65–75.
- (9) Fan, J.; Sun, W.; Wang, Z.; Peng, X.; Li, Y.; Cao, J. A fluorescent probe for site I binding and sensitive discrimination of HSA from BSA. *Chem. Commun.* **2014**, *50*, 9573–9576.
- (10) Alino, V. J.; Yang, K. L. Using liquid crystals as a readout system in urinary albumin assays. *Analyst* **2011**, *136*, 3307–3313.
- (11) Murch, S. H.; Winyard, P. J. D.; Koletzko, S.; Wehner, B.; Cheema, H. A.; Risdon, R. A.; Phillips, A. D.; Meadows, N.; Klein, N. J.; Walker-Smith, J. A. Congenital enterocyte heparan sulphate deficiency with massive albumin loss, secretory diarrhoea, and malnutrition. *Lancet* **1996**, *347*, 1299–1301.
- (12) Peters, T. *All About Albumin: Biochemistry, Genetics and Medical Application*; Academic Press: San Diego, CA, 1996; pp 234–240.
- (13) Hoogenberg, K.; Sluiter, W. J.; Dullaart, R. P. Effect of growth hormone and insulin-like growth factor I on urinary albumin excretion: studies in acromegaly and growth hormone deficiency. *Eur. J. Endocrinol.* **1993**, *129*, 151–157.

- (14) de Zeeuw, D.; Parving, H. H.; Henning, R. Microalbuminuria as an early marker for cardiovascular disease. *J. Am. Soc. Nephrol.* **2006**, *17*, 2100–2105.
- (15) Amin, R.; Widmer, B.; Prevost, A. T.; Schwarze, P.; Cooper, J.; Edge, J.; Marcovecchio, L.; Neil, A.; Dalton, R. N.; Dunger, D. B. Risk of microalbuminuria and progression to macroalbuminuria in a cohort with childhood onset type 1 diabetes: prospective observational study. *BMJ.* **2008**, *336*, 697–701.
- (16) Seegmiller, J. C.; Sviridov, D.; Larson, T. S.; Borland, T. M.; Hortin, G. L.; Lieske, J. C. Comparison of urinary albumin quantification by immunoturbidimetry, competitive immunoassay, and protein-cleavage liquid chromatography-tandem mass spectrometry. *Clin. Chem.* **2009**, *55*, 1991–1994.
- (17) Seegmiller, J. C.; Barnidge, D. R.; Burns, B. E.; Larson, T. S.; Lieske, J. C.; Kumar, R. Quantification of urinary albumin by using protein cleavage and LC-MS/MS. *Clin. Chem.* **2009**, *55*, 1100–1107.
- (18) Lowry, O. H.; Rosebrough, N. J.; Farr, A. L.; Randall, R. J. Protein Measurement with Folin Phenol Reagent. *J. Biol. Chem.* **1951**, *193*, 265–275.
- (19) Bradford, M. M. A rapid and sensitive method for the quantitation of microgram quantities of protein utilizing the principle of protein-dye binding. *Anal. Biochem.* **1976**, *72*, 248–254.
- (20) Wu, Y. Y.; Yu, W. T.; Hou, T. C.; Liu, T. K.; Huang, C. L.; Chen, I. C.; Tan, K. T. A selective and sensitive fluorescent albumin probe for the determination of urinary albumin. *Chem. Commun.* **2014**, *50*, 11507–11510.
- (21) Kubota, R.; Hamachi, I. Protein Recognition Using Synthetic Small-molecular Binders toward Optical Protein Sensing in vitro and in Live Cells. *Chem. Soc. Rev.* **2015**, *44*, 4454–4471.
- (22) He, X. P.; Zang, Y.; James, T. D.; Li, J.; Chen, G. R. Probing Disease-related Proteins with Fluorogenic Composite Materials. *Chem. Soc. Rev.* **2015**, *44*, 4239–4248.
- (23) Thurley, S.; Roglin, L.; Seitz, O. Hairpin peptide beacon: Dual-labeled PNA-peptide-hybrids for protein detection. *J. Am. Chem. Soc.* **2007**, *129*, 12693–12695.
- (24) Wang, B.; Yu, C. Fluorescence turn-on detection of a protein through the reduced aggregation of a perylene probe. *Angew. Chem., Int. Ed.* **2010**, *49*, 1485–1488.
- (25) Jin, Q.; Feng, L.; Wang, D. D.; Dai, Z. R.; Wang, P.; Zou, L. W.; Liu, Z. H.; Wang, J. Y.; Yu, Y.; Ge, G. B.; Cui, J. N.; Yang, L. A two-photon ratiometric fluorescent probe for imaging carboxylesterase 2 in living cells and tissues. *ACS Appl. Mater. Interfaces* **2015**, *7*, 28474–28481.
- (26) Hu, F.; Huang, Y.; Zhang, G.; Zhao, R.; Yang, H.; Zhang, D. Targeted bioimaging and photodynamic therapy of cancer cells with an activatable red fluorescent bioprobe. *Anal. Chem.* **2014**, *86*, 7987–7995.
- (27) Mei, J.; Leung, N. L. C.; Kwok, R. T. K.; Lam, J. W. Y.; Tang, B. Z. Aggregation-induced emission: together we shine, united we soar! *Chem. Rev.* **2015**, *115*, 11718–11940.
- (28) Ding, D.; Li, K.; Liu, B.; Tang, B. Z. Bioprobes Based on AIE Fluorogens. *Acc. Chem. Res.* **2013**, *46*, 2441–2453.
- (29) Yuan, C. X.; Tao, X. T.; Wang, L.; Yang, J. X.; Jiang, M. H. Fluorescent turn-on detection and assay of protein based on lambda (A)-shaped pyridinium salts with aggregation-induced emission characteristics. *J. Phys. Chem. C* **2009**, *113*, 6809–6814.
- (30) Li, W.; Chen, D.; Wang, H.; Luo, S.; Dong, L.; Zhang, Y.; Shi, J.; Tong, B.; Dong, Y. Quantitation of albumin in serum using “turn-on” fluorescent probe with aggregation-enhanced emission characteristics. *ACS Appl. Mater. Interfaces* **2015**, *7*, 26094–26100.
- (31) Hong, Y. N.; Feng, C.; Yu, Y.; Liu, J. Z.; Lam, J. W. Y.; Luo, K. Q.; Tang, B. Z. Quantitation, visualization, and monitoring of conformational transitions of human serum albumin by a tetraphenylethene derivative with aggregation-induced emission characteristics. *Anal. Chem.* **2010**, *82*, 7035–7043.
- (32) Hu, Q.; Yao, B.; Owyong, T. C.; Prashanth, S.; Wang, C.; Zhang, X.; Wong, W. W. H.; Tang, Y.; Hong, Y. Detection of Urinary Albumin Using a “Turn-on” Fluorescent Probe with Aggregation-Induced Emission Characteristics. *Chem. - Asian J.* **2021**, *16*, 1245–1252.
- (33) Yu, Y.; Gong, Q. T.; Lu, W. F.; Liu, Y. H.; Yang, Z. J.; Wang, N.; Yu, X. Q. Aggregation-Induced Emission Probes for Specific Turn-on Quantification of Bovine Serum Albumin. *ACS Appl. Bio Mater.* **2020**, *3*, 5193–5201.
- (34) Molla, M. R.; Prasad, P.; Thayumanavan, S. Protein-induced supramolecular disassembly of amphiphilic polypeptide nanoassemblies. *J. Am. Chem. Soc.* **2015**, *137*, 7286–7289.
- (35) Azagarsamy, M. A.; Yesilyurt, V.; Thayumanavan, S. Disassembly of dendritic micellar containers due to protein binding. *J. Am. Chem. Soc.* **2010**, *132*, 4550–4551.
- (36) Wang, H.; Zhuang, J.; Raghupathi, K. R.; Thayumanavan, S. A supramolecular dissociation strategy for protein sensing. *Chem. Commun.* **2015**, *51*, 17265–17268.
- (37) Ren, C.; Zhang, J.; Chen, M.; Yang, Z. Self-assembling small molecules for the detection of important analytes. *Chem. Soc. Rev.* **2014**, *43*, 7257–7266.
- (38) Chen, Q.; Liu, X.; Zeng, J.; Cheng, Z.; Liu, Z. Albumin-NIR dye self-assembled nanoparticles for photoacoustic pH imaging and pH-responsive photothermal therapy effective for large tumors. *Biomaterials* **2016**, *98*, 23–30.
- (39) Azagarsamy, M. A.; Sokkalingam, P.; Thayumanavan, S. Enzyme-triggered disassembly of dendrimer-based amphiphilic nanocontainers. *J. Am. Chem. Soc.* **2009**, *131*, 14184–14185.
- (40) Guo, J.; Zhuang, J.; Wang, F.; Raghupathi, K. R.; Thayumanavan, S. Protein AND enzyme gated supramolecular disassembly. *J. Am. Chem. Soc.* **2014**, *136*, 2220–2223.
- (41) Amado Torres, D.; Garzoni, M.; Subrahmanyam, A. V.; Pavan, G. M.; Thayumanavan, S. Protein-Triggered Supramolecular Disassembly: Insights Based on Variations in Ligand Location in Amphiphilic Dendrons. *J. Am. Chem. Soc.* **2014**, *136*, 5385–5399.
- (42) Fan, X.; He, Q.; Sun, S.; Li, H.; Pei, Y.; Xu, Y. Nanoparticles Self-assembled from Multiple Interactions: a Novel Near-infrared Fluorescent Sensor for the Detection of Serum Albumin in Human Sera and Turn-on Live-cell Imaging. *Chem. Commun.* **2016**, *52*, 1178–1181.
- (43) Anees, P.; Sreejith, S.; Ajayaghosh, A. Self-assembled near-infrared dye nanoparticles as a selective protein sensor by activation of a dormant fluorophore. *J. Am. Chem. Soc.* **2014**, *136*, 13233–13239.
- (44) Gao, T.; Yang, S.; Cao, X.; Dong, J.; Zhao, N.; Ge, P.; Zeng, W.; Cheng, Z. Smart self-assembled organic nanoprobe for protein-specific detection: design, synthesis, application, and mechanism studies. *Anal. Chem.* **2017**, *89*, 10085–10093.
- (45) Samanta, S.; Halder, S.; Das, G. Twisted-intramolecular-charge-transfer-based turn-on fluorogenic nanoprobe for real-time detection of serum albumin in physiological conditions. *Anal. Chem.* **2018**, *90*, 7561–7568.
- (46) Zheng, Z.; Li, H.; Sun, S.; Xu, Y. Media Dependent Switching of Selectivity and Continuous near Infrared Turn-on Fluorescence Response through Cascade Interactions from Noncovalent to Covalent Binding for Detection of Serum Albumin in Living Cells. *ACS Appl. Mater. Interfaces* **2018**, *10*, 44336–44343.
- (47) Yu, Y.; Huang, Y.; Hu, F.; Jin, Y.; Zhang, G.; Zhang, D.; Zhao, R. Self-assembled nanostructures based on activatable red fluorescent dye for site-specific protein probing and conformational transition detection. *Anal. Chem.* **2016**, *88*, 6374–6381.
- (48) Wang, Z. G.; Yan, X. J.; Liu, H. B.; Zhang, D. L.; Liu, W.; Xie, C. Z.; Li, Q. Z.; Xu, J. Y. A novel hydrazide Schiff base self-assembled nanoprobe for selective detection of human serum albumin and its applications in renal disease surveillance. *J. Mater. Chem. B* **2020**, *8*, 8346–8355.
- (49) Guo, Y.; Chen, Y.; Zhu, X.; Pan, Z.; Zhang, X.; Wang, J.; Fu, N. Self-assembled nanosensor based on squaraine dye for specific recognition and detection of human serum albumin. *Sens. Actuators B: Chem.* **2018**, *255*, 977–985.
- (50) Sasmal, M.; Islam, A. S. M.; Bhowmick, R.; Maiti, D.; Dutta, A.; Ali, M. Site-selective interaction of human serum albumin with 4-chloro-7-nitro-1, 2, 3-benzoxadiazole modified olanzapine derivative

and effect of  $\beta$ -cyclodextrin on binding: In the light of spectroscopy and molecular docking. *ACS Appl. Bio Mater.* **2019**, *2*, 3551–3561.

(51) Wang, Y. R.; Feng, L.; Xu, L.; Li, Y.; Wang, D. D.; Hou, J.; Zhou, K.; Jin, Q.; Ge, G. B.; Cui, J. N.; Yang, L. A rapid-response fluorescent probe for the sensitive and selective detection of human albumin in plasma and cell culture supernatants. *Chem. Commun.* **2016**, *52*, 6064–6067.

(52) Reja, S. I.; Khan, I. A.; Bhalla, V.; Kumar, M. A TICT based NIR-fluorescent probe for human serum albumin: a pre-clinical diagnosis in blood serum. *Chem. Commun.* **2016**, *52*, 1182–1185.

(53) Wang, Y. R.; Feng, L.; Xu, L.; Hou, J.; Jin, Q.; Zhou, N.; Lin, Y.; Cui, J. N.; Ge, G. B. An ultrasensitive and conformation sensitive fluorescent probe for sensing human albumin in complex biological samples. *Sens. Actuators B: Chem.* **2017**, *245*, 923–931.

(54) Rajasekhar, K.; Achar, C. J.; Govindaraju, T. A red-NIR emissive probe for the selective detection of albumin in urine samples and live cells. *Org. Biomol. Chem.* **2017**, *15*, 1584–1588.

(55) Zhu, K.; Lv, T.; Qin, T.; Huang, Y.; Wang, L.; Liu, B. A flavonoid-based fluorescent probe enables the accurate quantification of human serum albumin by minimizing the interference from blood lipids. *Chem. Commun.* **2019**, *55*, 13983–13986.

(56) Dey, G.; Gaur, P.; Giri, R.; Ghosh, S. Optical signaling in biofluids: a non-denaturing photostable molecular probe for serum albumins. *Chem. Commun.* **2016**, *52*, 1887–1890.

(57) Smith, S. E.; Williams, J. M.; Ando, S.; Koide, K. Time-insensitive fluorescent sensor for human serum albumin and its unusual red shift. *Anal. Chem.* **2014**, *86*, 2332–2336.

(58) Zhu, T.; Du, J.; Cao, W.; Fan, J.; Peng, X. Microenvironment-sensitive fluorescent dyes for recognition of serum albumin in urine and imaging in living cells. *Ind. Eng. Chem. Res.* **2016**, *55*, 527–533.

(59) Green, A. M.; Abelt, C. J. Dual-Sensor Fluorescent Probes of Surfactant-Induced Unfolding of Human Serum Albumin. *J. Phys. Chem. B* **2015**, *119*, 3912–3919.

(60) Dey, G.; Singh, V.; Dewangan, J.; Daniel, P. V.; Kamthan, M.; Ghosh, D.; Mondal, P.; Ghosh, S. Renal clearable new NIR probe: precise quantification of albumin in biofluids and fatty liver disease state identification through tissue specific high contrast imaging in vivo. *Anal. Chem.* **2017**, *89*, 10343–10352.

(61) Pei, S.; Li, J.; Zhang, C.; Zhang, G.; Zhou, Y.; Fan, L.; Wang, W.; Shuang, S.; Dong, C. TICT-Based Microenvironment-Sensitive Probe with Turn-on Red Emission for Human Serum Albumin Detection and for Targeting Lipid Droplet Imaging. *ACS Biomater. Sci. Eng.* **2022**, *8*, 253–260.

(62) Van Gompel, J.; Schuster, G. B. Chemiluminescence of organic peroxides: Intramolecular electron-exchange luminescence from a secondary perester. *J. Org. Chem.* **1987**, *52*, 1465–1468.

(63) Pellerano, M.; Naud-Martin, D.; Peyressatre, M.; Prével, C.; Teulade-Fichou, M. P.; Morris, M.; Mahuteau-Betzer, F. TP-2Rho Is a Sensitive Solvatochromic Red-Shifted Probe for Monitoring the Interactions between CDK4 and Cyclin D. *ChemBioChem.* **2016**, *17*, 737–744.

(64) You, M.; Jaffrey, S. R. Structure and mechanism of RNA mimics of green fluorescent protein. *Annu. Rev. Biophys.* **2015**, *44*, 187–206.

(65) Sudlow, G.; Birkett, D. J.; Wade, D. N. The Characterization of Two Specific Drug Binding Sites on Human Serum Albumin. *Mol. Pharmacol.* **1975**, *11*, 824–832.

(66) Sudlow, G.; Birkett, D. J.; Wade, D. N. Further Characterization of Specific Drug Binding Sites on Human Serum Albumin. *Mol. Pharmacol.* **1976**, *12*, 1052–1061.

(67) Ibrahim, N.; Ibrahim, H.; Kim, S.; Nallet, J. P.; Nepveu, F. Interactions between Antimalarial Indolone-*N*-oxide Derivatives and Human Serum Albumin. *Biomacromolecules* **2010**, *11*, 3341–3351.

(68) Lakowicz, J. R. Fluorescence Anisotropy. In *Principles of Fluorescence Spectroscopy*, 3rd ed.; Springer: New York, 2006; pp 353–381.

(69) Sasmal, M.; Bhowmick, R.; Musha Islam, A. S.; Bhuiya, S.; Das, S.; Ali, M. Domain-Specific Association of a Phenanthrene-Pyrene-Based Synthetic Fluorescent Probe with Bovine Serum Albumin:

Spectroscopic and Molecular Docking Analysis. *ACS Omega* **2018**, *3*, 6293–6304.

(70) Sedmak, J. J.; Grossberg, S. E. A rapid, sensitive, and versatile assay for protein using Coomassie brilliant blue G250. *Anal. Biochem.* **1977**, *79*, 544–552.

## Recommended by ACS

### Real-Time Visualization of the Antioxidative Potency of Drugs for the Prevention of Myocardium Ischemia-Reperfusion Injury by a NIR Fluorescent Nanoprobe

Aiping Shi, Juanjuan Peng, *et al.*

NOVEMBER 28, 2022

ACS SENSORS

READ 

### Rapid Point-of-Care Quantification of Human Serum Albumin in Urine Based on Ratiometric Fluorescence Signaling Driven by Intramolecular H-Bonding

Sourav Sarkar, Kyo Han Ahn, *et al.*

NOVEMBER 22, 2022

ACS SENSORS

READ 

### Erythrocyte Membrane-Camouflaged Aggregation-Induced Emission Nanoparticles for Fetal Intestinal Maturation Assessment

Jun Dai, Shixuan Wang, *et al.*

DECEMBER 06, 2022

ANALYTICAL CHEMISTRY

READ 

### Aggregation and Binding-Directed FRET Modulation of Conjugated Polymer Materials for Selective and Point-of-Care Monitoring of Serum Albumins

Sameer Hussain, Ruixia Gao, *et al.*

JULY 18, 2022

ANALYTICAL CHEMISTRY

READ 

Get More Suggestions >



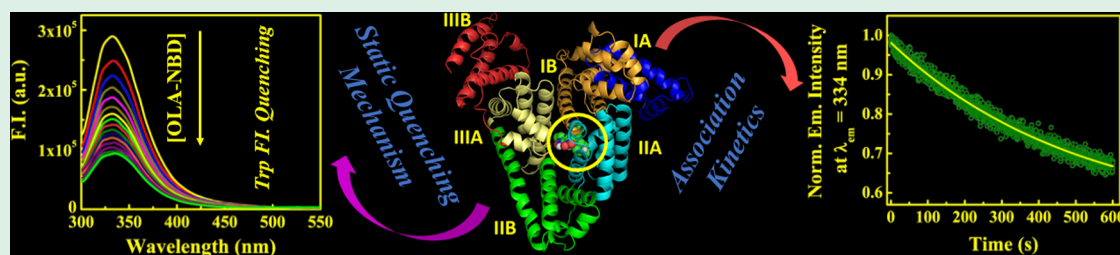
# Site-Selective Interaction of Human Serum Albumin with 4-Chloro-7-nitro-1,2,3-benzoxadiazole Modified Olanzapine Derivative and Effect of $\beta$ -Cyclodextrin on Binding: In the Light of Spectroscopy and Molecular Docking

Mihir Sasmal,<sup>†</sup> Abu Saleh Musha Islam,<sup>†</sup> Rahul Bhowmick,<sup>†</sup> Debjani Maiti,<sup>†</sup> Ananya Dutta,<sup>†</sup> and Mahammad Ali<sup>\*,†,‡</sup>

<sup>†</sup>Department of Chemistry, Jadavpur University, 188, Raja S. C. Mullick Road, Kolkata 700 032, India

<sup>‡</sup>Vice-Chancellor, Aliah University, II-A/27, Action Area II, Newtown, Kolkata, West Bengal 700160, India

## Supporting Information



**ABSTRACT:** Here, we present a detailed investigation on the interaction of 4-chloro-7-nitro-1,2,3-benzoxadiazole (NBD) embedded olanzapine derivative (OLA-NBD) with a model transport protein, human serum albumin (HSA). The thermodynamic parameters,  $\Delta H^\circ$ ,  $\Delta S^\circ$ , and  $\Delta G^\circ$ , as evaluated by considering the van't Hoff relationship imply the major contribution of electrostatic/ionic interactions for the HSA–OLA-NBD association. The OLA-NBD induced quenching of HSA emission occurs through static quenching mechanism, indicating a 1:1 association, as portrayed from Benesi–Hildebrand plot, with  $\sim 10^4 \text{ M}^{-1}$  association constant value, and it is in good harmony with the value estimated from anisotropy experiment. The invariance of the time-resolved decay behavior of HSA with added OLA-NBD concentration, along with matching dependency of the binding constant ( $K_b$ ) value on temperature, also supports the occurrence of static quenching. The effect of  $\beta$ -cyclodextrin on HSA–OLA-NBD binding is characterized by a smaller  $K_b$  value revealing that the OLA-NBD molecules are gradually removed from  $\beta$ -CD by HSA to achieve its medicinal outcome of drug delivery. The outcome from circular dichroism (CD) illustrates the variation of HSA secondary structure upon interaction with OLA-NBD. Concurrently, HSA–OLA-NBD association kinetics is also explored by applying the fluorescence technique. The possible interaction zone of OLA-NBD in HSA is investigated from AutoDock-based docking simulation study.

**KEYWORDS:** olanzapine-NBD derivative, human serum albumin,  $\beta$ -cyclodextrin, static quenching, circular dichroism, association kinetics, molecular docking

## INTRODUCTION

Protein molecules are the basic units of all living cells and encompass a number of essential roles in numerous biological functions depending on their wide range structures. Hence, the measurement of binding of small molecules/drugs with a protein is very much crucial. As the structural variation can influence the functional properties of a protein, cautious control over such interactions is very much pertinent.<sup>1</sup> Among the large variety of proteins, serum albumin is a well-known primary constituent of blood plasma. To recognize the pharmacokinetic and pharmacodynamic properties of drug molecules, their binding toward plasma protein is significant, which helps us to understand the drug circulation and to ascertain its free fraction accessible to the target.<sup>2,3</sup>

Human serum albumin (HSA) consists of 585 amino acid residues<sup>4</sup> and is the main globular transport protein of the blood circulatory system, containing  $\sim 60\%$  of plasma consistent with 42 mg/mL concentration and contributing  $\sim 80\%$  of total colloid osmotic pressure in the body system.<sup>5,6</sup> The secondary structure of free HSA contains about 67%  $\alpha$ -helix with 17 disulfide (S–S) bridges. The tertiary structure has three homologous domains (I, II, and III), each consisting of two subdomains, A and B.<sup>7,8</sup> Trp 214 is the only one tryptophan amino acid residue present in HSA. The ligand binding sites of HSA are mainly located in hydrophobic regions in subdomain IIA at binding site I and

Received: May 21, 2019

Accepted: July 16, 2019

Published: July 16, 2019

subdomain IIIA at binding site II.<sup>9,10</sup> Additionally, crystal structure analysis and drug binding studies proposed that most of the neutral, bulky, and heterocyclic compounds bind at site I by hydrophobic interactions, while most of the aromatic carboxylic acid compounds bind at site II by van der Waals, ionic, and hydrogen-bonding interactions.<sup>7–10</sup> The hydrophobic binding regions play a vital role in drug deposition and efficiency by improving the solubility of various drugs to plasma and tuning their delivery to *in vivo* and *in vitro* cells.<sup>11</sup> Besides this, protein–drug interaction significantly affects the various important properties of drugs like absorption, distribution, metabolism, and excretion properties.<sup>12</sup> HSA is familiar for its high conformational flexibility to an astonishingly wide range of drugs/small molecules.<sup>13–21</sup> Therefore, the study on molecular level binding of drug/small molecules with serum albumins is important and essential for drug development.

Schizophrenia and bipolar disorder treatment are based on the antipsychotics or neuroleptics drugs but they suffer limited usefulness.<sup>22</sup> An atypical antipsychotic drug, olanzapine, is considered to be highly operative for mood stabilizer and schizophrenia treatment, and that reveals a comprehensive pharmacological profile through a number of receptors.<sup>3,23–25</sup> Here, we have synthesized a 4-chloro-7-nitro-1,2,3-benzoxadiazole (NBD) embedded fluorescent derivative of olanzapine, OLA-NBD, for protein binding studies. We have selected NBD as the fluorophore molecule due to its emission at longer wavelengths and since the small size does not usually influence on the affinity of parent ligand. Also, NBD-containing compounds become highly fluorescent on binding with hydrophobic sites in proteins.<sup>26</sup>

$\beta$ -Cyclodextrin ( $\beta$ -CD) is a cyclic oligomer consisting of seven  $\alpha$ -D-glucopyranose units. A variety of inclusion complexes can be formed by  $\beta$ -CD with a numerous number of inorganic and organic molecules by increasing the stability, bioavailability, and solubility of the guest compounds. It has been also extensively used in organic synthesis, food plant, and pharmacological science.<sup>27</sup> Therefore, it is essential to investigate the effect of  $\beta$ -CD on the HSA–OLA-NBD binding.

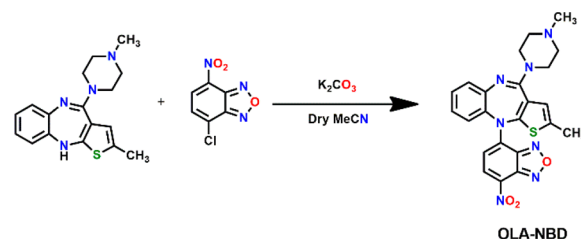
The goal of the current work deals with the binding behavior between HSA and OLA-NBD, using various useful spectroscopy techniques. Fluorescence spectroscopy and lifetime studies were executed to explore the quenching mechanism involved in the binding process. Specific binding site was confirmed with the help of site-selective binding and molecular docking experiments. The circular dichroism (CD) spectral investigation was used to analyze the variation of HSA secondary structure upon association with OLA-NBD. Besides this, an attempt was made toward the determination of OLA-NBD–HSA binding kinetics by the fluorescence technique.

## EXPERIMENTAL SECTION

**Materials.** Olanzapine, 4-chloro-7-nitro-1,2,3-benzoxadiazole (NBD),  $K_2CO_3$ , ibuprofen, warfarin, HSA, 8-anilino-1-naphthalene sulfonic acid (ANS), *p*-nitrophenyl acetate (PNPA), and  $\beta$ -cyclodextrin were obtained from Sigma-Aldrich and used as received. Reagent-grade solvents such as methanol, ethanol, dimethylformamide, acetonitrile ( $CH_3CN$ ), etc. (Merck, India) were dried before use according to standard method.

**Synthesis of 4-(2-Methyl-4-(4-methylpiperazin-1-yl)-10H-benzo[b]thieno[2,3-e][1,4]diazepin-10-yl)-7-nitrobenzo[c][1,2,5]oxadiazole (OLA-NBD).** OLA-NBD was synthesized by following the literature method<sup>28</sup> in a slightly modified way (Scheme 1). Olanzapine (0.312 g, 1 mmol) and  $K_2CO_3$  (0.345 g, 2.5 mmol) were mixed in 20 mL of dry  $CH_3CN$  solution with constant stirring. Then

## Scheme 1. Synthesis of OLA-NBD



NBD-Cl (0.20 g, 1 mmol) in 10 mL of dry  $CH_3CN$  was added dropwise at room temperature, and the reaction mixture was further stirred for 6 h. Then the residue was filtered off by suction and washed several times by  $CHCl_3$ . The combined solution (filtrate and the  $CHCl_3$ ) was evaporated in vacuum to get a solid product. The product was then subjected to silica gel column chromatography, and ethyl acetate/methanol (v/v, 8:2) was used as eluent to get a pure deep green solid (yield: 69%) (Scheme 1).  $^1H$  NMR ( $DMSO-d_6$ ):  $\delta$  in ppm = 8.56 (d, 1H, –ArH), 7.50 (d, 1H, –ArH), 7.37 (t, 1H, –ArH), 7.21 (m, 2H, –ArH), 6.77 (s, 1H, –ArH), 6.61 (d, 1H, –ArH), 3.50 (d, 6H, – $CH_2$ ), 2.48 (s, 3H, – $CH_3$ ), 2.25 (d, 2H, – $CH_2$ ), 2.04 (s, 3H, – $CH_3$ ) (Figure S1).  $^{13}C$  NMR ( $DMSO-d_6$ ):  $\delta$  in ppm = 154.35, 144.69, 144.66, 144.29, 143.89, 140.42, 136.13, 129.65, 127.80, 127.03, 127.00, 126.33, 124.38, 122.51, 106.28, 54.47, 45.74, 16.08 (Figure S2). ESI-MS<sup>+</sup>:  $m/z$  = 476.1401 [ $C_{23}H_{21}N_7O_3S + H^+$ ] (Figure S3). IR Spectrum:  $\tilde{\nu}$  = 1527  $cm^{-1}$  (– $NO_2$ ) (Figure S4).

**Physical Instrumentations and Experimental Methods.** All details of instrumental specifications, preparation of experimental solution, and procedures adopted for carrying out the whole work are provided in the Supporting Information.

## RESULTS AND DISCUSSION

### Effect of OLA-NBD on Absorption Spectra of HSA.

UV–vis absorption study is widely recognized in terms of analysis of the structural modifications as well as to understand the complex formation in solution.<sup>29,30</sup> Figure 1A exhibits the

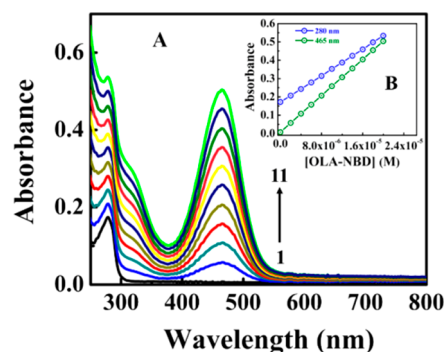


**Figure 1.** (A) Absorption spectral variations of HSA (5  $\mu M$ ) with gradual addition of OLA-NBD (0–20  $\mu M$ ). (B) Inset: plot of absorbance at 280 and 465 nm, respectively, with OLA-NBD concentration.

absorption spectra of HSA with the incremental addition of OLA-NBD in aqueous Tris-HCl buffer solution. Absorbance of HSA increases at 280 nm on addition of OLA-NBD, and at the same time, absorbance peak at 465 nm also increases due to OLA-NBD (Figure 1B). The absorption spectral pattern also changes with added concentration of OLA-NBD. This finding is well supported toward the complexation between OLA-NBD and HSA.

**Fluorescence Emission Measurement.** Steady-state fluorescence emission measurement is a valuable technique to



examine the interactions of drugs/small molecules with proteins. Fluorescence titrations were executed to ensure the OLA-NBD–HSA interaction at 5  $\mu\text{M}$  OLA-NBD concentration in aqueous buffer solution with the successive addition of HSA protein. The maximum emission intensity of OLA-NBD is blue-shifted ( $\sim 22$  nm) from 555 to 533 nm in 48  $\mu\text{M}$  HSA solution with simultaneous prominent increase in emission intensity ( $\sim 5$ -fold) upon excitation at 465 nm (Figure 2A). The

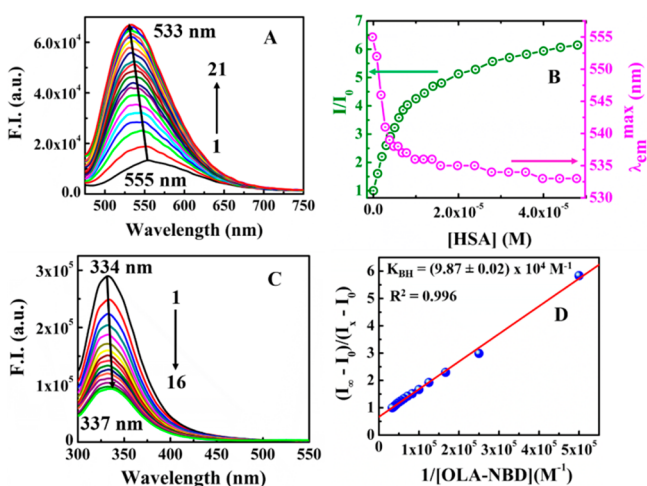


**Figure 2.** (A) Effect of HSA addition (0–48  $\mu\text{M}$ ) on the OLA-NBD (5  $\mu\text{M}$ ) emission spectra. (B) Variation of  $\lambda_{\text{em}}^{\text{max}}$  and relative intensity of OLA-NBD with HSA. (C) Quenching of HSA (5  $\mu\text{M}$ ) emission with successive addition of OLA-NBD (0–30  $\mu\text{M}$ ) at 25  $^{\circ}\text{C}$ . (D) Characteristic B–H plot for HSA and OLA-NBD association.  $\lambda_{\text{ex}}$  for OLA-NBD and HSA are 465 and 295 nm, respectively.

modulations of emission intensity and  $\lambda_{\text{em}}^{\text{max}}$  of the OLA-NBD with HSA concentration are more plainly presented in Figure 2B, which demonstrates an early steep rise of emission intensity up to 20  $\mu\text{M}$  HSA and afterward the achievement of a plateau region likely indicating the saturation of OLA-NBD–HSA interaction. Such variation of the emission profile in the presence of HSA indicates toward the immense modification of microenvironment surrounding of OLA-NBD within the protein hydrophobic medium compared with the polar aqueous medium. This blue shift in emission band resulting from the reduction in polarity of microenvironment was previously reported.<sup>15,31–34</sup>

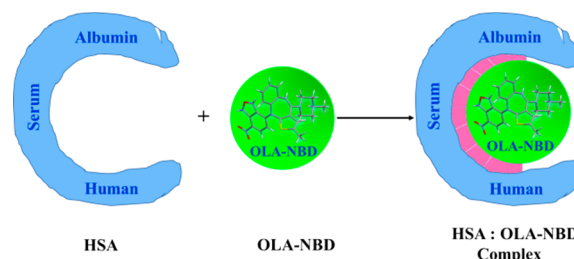
Trp, tyrosine (Tyr), and phenylalanine (Phe) are three main amino acid residues responsible for the emission of proteins.<sup>35</sup> Particularly, Trp emission is considered to monitor the structural conformation changes in HSA protein and to elucidate the microenvironment around the HSA bound small molecules.<sup>21</sup> Trp 214 is the only one Trp residue present in subdomain IIA of HSA.<sup>4,35</sup> In aqueous medium, HSA exhibits a emission maximum at 334 nm when it is excited at 295 nm. Excitation was made at 295 nm to reduce the fluorescence contribution from Tyr residue.

To evaluate the binding constant of HSA-OLA-NBD association, a 5  $\mu\text{M}$  concentration of HSA protein was titrated with the incremental addition of OLA-NBD. Figure 2C displays that upon interaction of OLA-NBD with HSA, the emission intensity is quenched significantly along with a small red shift ( $\sim 3$  nm) of emission maxima from 334 to 337 nm, which indicates that OLA-NBD undergoes strong complexation with

HSA and modification of local microenvironment around Trp moiety present in HSA.<sup>36</sup>

**HSA–OLA-NBD Complexation Equilibrium and Stoichiometric Study.** The complexation process of the OLA-NBD with HSA may be portrayed in Scheme 2, and the data

### Scheme 2. Complexation of OLA-NBD with HSA in 1:1 Stoichiometry



found from the spectrofluorimetric titration of a constant concentration of HSA with gradual addition of OLA-NBD were examined to evaluate the binding constant by using Benesi–Hildebrand (B–H) equation:<sup>37</sup>

$$\frac{\Delta I_{\text{max}}}{\Delta I} = 1 + \frac{1}{K_{\text{BH}}[\text{OLA-NBD}]} \quad (1)$$

where  $K_{\text{BH}}$  signifies the association constant. Here,  $\Delta I_{\text{max}} = |I_{\infty} - I_0|$  and  $\Delta I = |I_x - I_0|$ .  $I_0$ ,  $I_x$ , and  $I_{\infty}$  designate the emission intensities of HSA in free state, at an intermediate OLA-NBD concentration, and at OLA-NBD concentration when complete saturation occurred, respectively.  $|I_{\infty} - I_0|/|I_x - I_0|$  versus  $1/[\text{OLA-NBD}]$  plot shows a linear variation (Figure 2D), which affirms the validity of eq 1 and supports the 1:1 association between OLA-NBD and HSA. The 1:1 interaction of OLA-NBD with HSA was also confirmed by Job's plot experiment.

In this technique, the fluorescence data were noted by varying the OLA-NBD:HSA molar ratio, while the total molar concentration remained constant.<sup>38</sup> The Job's plot for OLA-NBD–HSA, that is,  $\Delta I$  at 334 nm versus the mole fraction of OLA-NBD (Figure S5) crossed at 0.507, showing that number of OLA-NBD molecules associated with HSA, is close to unity. The calculated value of  $K_{\text{BH}}$  and the related free energy change ( $\Delta G$ ) are tabulated in Table 1, inferring strong association of OLA-NBD with HSA.

**Table 1.** Binding Parameters for Association of HSA with OLA-NBD at 25  $^{\circ}\text{C}$

method	environment	binding constant ( $10^4 \text{ M}^{-1}$ )	$\Delta G$ ( $\text{kJ mol}^{-1}$ )
Benesi–Hildebrand	HSA–OLA-NBD	(9.87 $\pm$ 0.02)	–28.49
fluorescence anisotropy	HSA–OLA-NBD	(10.11 $\pm$ 0.23)	–28.55

**Intrinsic Fluorescence Quenching of HSA by OLA-NBD.** The gradual addition of OLA-NBD (0–30  $\mu\text{M}$ ) into HSA solution (5  $\mu\text{M}$ ) persuades the quenching of HSA fluorescence intensity (Figure 2C). This observable fact can be ascribed to the association between OLA-NBD and HSA involving some plausible mechanisms such as ground state complexation, collisional quenching, excited state reactions, molecular rearrangements, energy transfer, etc.<sup>35</sup> The quenching mechanism is usually classified as either static or dynamic. The ground-state association between the fluorophore and the quencher is

responsible for former process, whereas collisional encounters between the fluorophore and the quencher at the excited state are responsible for later process.<sup>35,39–41</sup> Static and dynamic quenching processes can be differentiated by their differing temperature dependency and viscosity or by examining the lifetime measurements.<sup>35</sup> Because of the presence of non-negligible absorbance of OLA-NBD at 295 nm (Figure S6), the correction in emission intensity was made to eliminate the inner filter effect by adopting the eq S1, narrated in the Supporting Information.

The emission quenching data of HSA–OLA-NBD complexation were examined by the analysis of Stern–Volmer equation, eq 2:<sup>35</sup>

$$\frac{I_0}{I} = 1 + K_{SV}[\text{OLA-NBD}] = 1 + k_q \langle \tau_0 \rangle [\text{OLA-NBD}] \quad (2)$$

where  $I_0$  and  $I$  are the HSA emission intensities in the native state and with the increasing concentration of OLA-NBD, respectively.  $K_{SV}$  is the Stern–Volmer constant, and  $k_q$  represents the bimolecular quenching rate constant.  $[\text{OLA-NBD}]$  is the molar concentration of the quencher, and  $\langle \tau_0 \rangle$  signifies the average lifetime of HSA without OLA-NBD (4.32 ns for HSA). The linear nature of steady-state Stern–Volmer plot, that is,  $I_0/I$  versus  $[\text{OLA-NBD}]$  (Figure 3A) at 298 K indicates that the

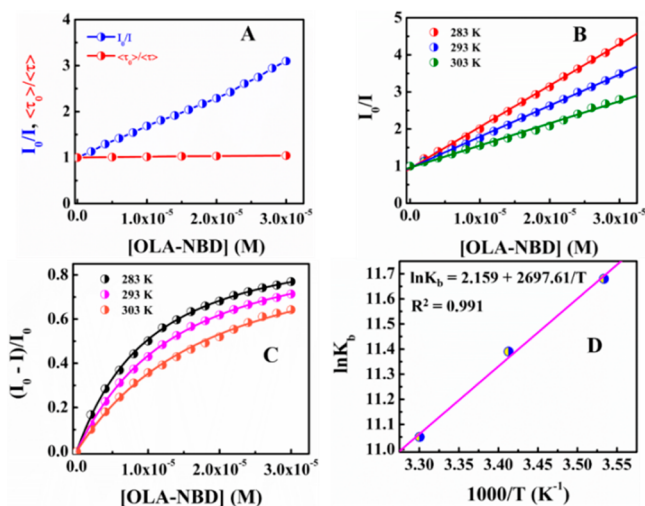


**Figure 3.** (A) Steady-state ( $I_0/I$ , blue) and time-resolved ( $\langle \tau_0 \rangle / \langle \tau \rangle$ , red) Stern–Volmer plots at 298 K. (B) Characteristic linear Stern–Volmer plots at three different temperatures. (C) Plot of  $(I_0 - I)/I_0$  versus OLA-NBD concentration at different temperatures. (D) Van't Hoff plot for OLA-NBD and HSA association.

observed emission quenching of HSA–OLA-NBD conjugate is either due to static or dynamic process. Figure 3B displays the trend of linear Stern–Volmer plots at three temperatures, that is, 283, 293, and 303 K, and associated  $K_{SV}$  and  $k_q$  values are summarized in Table 2. The decreasing value of  $K_{SV}$  with the rise

in temperature indicates that the quenching process is static rather than dynamic one.<sup>12,20,36</sup> Table 2 clearly exhibits that the calculated  $k_q$  values for three temperatures are three orders of magnitude higher than the maximum collisional quenching rate constant value  $2.0 \times 10^{10} \text{ M}^{-1} \text{ s}^{-1}$ .<sup>35</sup>

This infers the OLA-NBD induced fluorescence quenching of HSA arises through the ground state complexation between HSA and OLA-NBD or in other words quenching through static process.

**Determination of HSA–OLA-NBD Binding Constants and Related Thermodynamic Parameters.** The binding constant between HSA and OLA-NBD can be evaluated with the help of eqs 3–9, assuming a 1:1 stoichiometric complexation between them.<sup>42</sup> The binding constant ( $K_b$ ) is expressed by eq 4:



$$K_b = \frac{[\text{HSA:OLA-NBD}]}{[\text{HSA}]_{\text{free}}[\text{OLA-NBD}]_{\text{free}}} \quad (4)$$

The free HSA and OLA-NBD concentrations can be defined by

$$[\text{HSA}]_{\text{free}} = [\text{HSA}]_T - [\text{HSA:OLA-NBD}] \quad (5)$$

$$[\text{OLA-NBD}]_{\text{free}} = [\text{OLA-NBD}]_T - [\text{HSA:OLA-NBD}] \quad (6)$$

where  $[\text{HSA}]_T$  and  $[\text{OLA-NBD}]_T$  are the total concentrations of HSA and OLA-NBD, respectively. The concentration of the HSA:OLA-NBD complex is given by

$$[\text{HSA:OLA-NBD}] = \frac{1}{2} \left[ ([\text{OLA-NBD}]_T + [\text{HSA}]_T + K_b^{-1}) \pm \sqrt{([\text{OLA-NBD}]_T + [\text{HSA}]_T + K_b^{-1})^2 - 4[\text{OLA-NBD}]_T[\text{HSA}]_T} \right] \quad (7)$$

Equation 8 relates the fluorescence measurements of the above said bimolecular equilibrium:

$$\frac{I_0 - I}{I_0 - I_\infty} = \frac{[\text{HSA:OLA-NBD}]}{[\text{HSA}]_T} \quad (8)$$

Here,  $I_0$  and  $I$  denote the fluorescence intensities of HSA in the free state and at different concentration of OLA-NBD, respectively.  $I_\infty$  is the measured fluorescence of HSA at saturation. Replacing eq 7 into eq 8 produces the final equation:

$$\frac{I_0 - I}{I_0 - I_\infty} = \frac{1}{2[\text{HSA}]_T} \left[ ([\text{OLA-NBD}]_T + [\text{HSA}]_T + K_b^{-1}) - \sqrt{([\text{OLA-NBD}]_T + [\text{HSA}]_T + K_b^{-1})^2 - 4[\text{OLA-NBD}]_T[\text{HSA}]_T} \right] \quad (9)$$

Figure 3C shows the characteristic  $(I_0 - I)/I_0$  versus  $[\text{OLA-NBD}]$  plot at three temperatures. The experimental data are best fitted with eq 9, and the binding constant ( $K_b$ ) values for three temperatures thereby obtained are summarized in Table 2.  $K_b$  value decreases with the rise in temperature and therefore supports the occurrence of static quenching mechanism.<sup>43</sup>

**Table 2.** Stern–Volmer Constants ( $K_{SV}$ ), Bimolecular Quenching Rate Constants ( $k_q$ ), Binding Constants ( $K_b$ ), and Thermodynamic Parameters for HSA–OLA-NBD Association

T (K)	$K_{SV}$ ( $10^4 \text{ M}^{-1}$ )	$k_q$ ( $10^{13} \text{ M}^{-1} \text{ s}^{-1}$ )	$R^2$	binding constant, $K_b$ ( $10^4 \text{ M}^{-1}$ )	$\Delta H^0$ (kJ mol <sup>-1</sup> )	$\Delta S^0$ (J K <sup>-1</sup> mol <sup>-1</sup> )	$\Delta G^0$ (kJ mol <sup>-1</sup> )
283	$11.12 \pm 0.09$	$2.59 \pm 0.09$	0.999	$11.80 \pm 0.13$			-27.50
293	$8.39 \pm 0.06$	$1.94 \pm 0.06$	0.999	$8.92 \pm 0.12$	-22.42	17.95	-27.68
303	$5.96 \pm 0.11$	$1.37 \pm 0.11$	0.994	$6.29 \pm 0.28$			-27.86

The high value of  $K_b$  indicates a strong association between HSA and OLA-NBD. Hydrogen bonding and hydrophobic, electrostatic, and van der Waal's interactions are the main responsible noncovalent forces for the association of small molecules with proteins.<sup>29,44</sup> To find out the nature of interaction between OLA-NBD and HSA at the ground state in terms of the aforementioned noncovalent forces, the standard enthalpy change ( $\Delta H^0$ ) and standard entropy change ( $\Delta S^0$ ) values can be determined from the van't Hoff relation:<sup>45</sup>

$$\ln K_b = -\frac{\Delta H^0}{RT} + \frac{\Delta S^0}{R} \quad (10)$$

where  $R$  denotes the universal gas constant. Then the standard Gibbs free energy ( $\Delta G^0$ ) value is calculated by considering the eq 11:

$$\Delta G_{\text{Binding}}^0 = -2.303RT \log K_b = \Delta H^0 - T\Delta S^0 \quad (11)$$

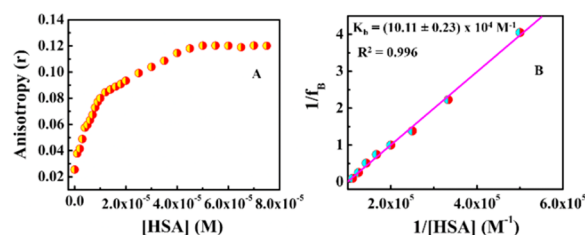
Figure 3D displays the characteristic  $\ln K_b$  versus  $1/T$  plot, and all the evaluated thermodynamic parameters are presented in Table 2. In accordance with Ross and Subramanian discussions,<sup>46</sup> the nature of the fundamental forces responsible for an interaction process can be shortly outlined as follows: (i)  $\Delta H^0 > 0$ ,  $\Delta S^0 > 0$  correlate with hydrophobic forces; (ii)  $\Delta H^0 < 0$ ,  $\Delta S^0 < 0$  correlate with van der Waals interaction, hydrogen bond formation; and (iii)  $\Delta H^0 < 0$ ,  $\Delta S^0 > 0$  correlate with electrostatic/ionic interactions.

Table 2 indicates that HSA–OLA-NBD binding association is enthalpically and in addition entropically preferred ( $\Delta H^0 < 0$  and  $\Delta S^0 > 0$ ) process.

Moreover, the negative value of  $\Delta H^0$  accompanied by a positive value of  $\Delta S^0$  infers the major involvement of electrostatic/ionic interaction for the HSA–OLA-NBD binding process.<sup>29,44</sup> Besides this,  $\Delta G^0 < 0$  also reveals that the binding process is spontaneous.

#### Steady-State Fluorescence Anisotropy Measurement.

Useful information regarding the rigidity of the environment in the instant vicinity of a fluorescent molecular probe can be gathered by steady-state fluorescence anisotropy measurement technique.<sup>47</sup> It also delivers the valuable knowledge about the limit to which obstruction of the rotational mobility of the probe can be experienced by a rigid environment, and it is reflected through the variation of anisotropy value. An increment in rigidity of the environment near a fluorescent probe reflects into an augmentation of anisotropy value. Figure 4A depicts the variation in anisotropy values of OLA-NBD with the increasing HSA concentration in aqueous solution. Initially, a quick increment in the anisotropy ( $r$ ) value was noticed from 0.025 to



**Figure 4.** (A) Steady-state anisotropy modulation of OLA-NBD with HSA concentration ( $\lambda_{\text{ex}} = 465$  nm,  $\lambda_{\text{em}} = 555$  nm). (B)  $1/f_B$  versus  $1/[HSA]$  plot for estimating the binding constant of OLA-NBD–HSA complexation by taking the data extracted from anisotropy measurement.

0.082 upon addition of 10  $\mu\text{M}$  HSA and then augmented gently to 0.118 until the 45  $\mu\text{M}$  HSA. Evidently, the enhanced anisotropy value directs to the fact that significant motional constraint is imputed on the OLA-NBD by the rigid environment within HSA. The extreme anisotropy ( $r$ ) value, that is, 0.121 was found at 55  $\mu\text{M}$  HSA, and afterward the plateau region was noticed, implying the saturation of interaction between OLA-NBD and HSA. As per the method stated by Ingersoll and Strollo,<sup>48</sup> the apparent binding constant ( $K_b$ ) of OLA-NBD–HSA complexation can be calculated from eq 12:

$$\frac{1}{f_B} = 1 + \frac{1}{K_b[HSA]} \quad (12)$$

where  $f_B$  is the contribution of fractional fluorescence from OLA-NBD bound HSA as expressed by eq 13:

$$f_B = \frac{r - r_F}{R(r_B - r) + (r - r_F)} \quad (13)$$

where  $r_B$  and  $r_F$  are the bound OLA-NBD–HSA and free OLA-NBD anisotropy values, correspondingly. The correction factor,  $R = I_B/I_F$  is considered here to ensure that OLA-NBD undergoes fluorescence intensity alteration upon binding with HSA. Figure 4B exhibits the  $1/f_B$  versus  $1/[HSA]$  plot, and the evaluated  $K_b$  value is tabulated in Table 1. The  $K_b$  value is in excellent agreement with the estimated value from emission titration experiment, and therefore, this measurement method builds up its practical usefulness and utility for the binding constant evaluation.<sup>30,36</sup>

**Fluorescence Lifetime Measurements.** Fluorescence lifetime decay study is a valuable method to analyze the microenvironment nearby the excited probe in the protein medium.<sup>15</sup> The dynamics of OLA-NBD was investigated by the lifetime decay of OLA-NBD in the absence and presence of HSA (Figure 5A). The decay associated parameters are listed in Table

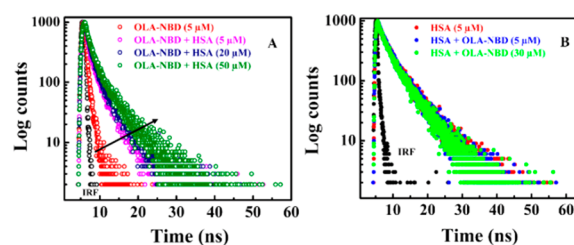


**Figure 5.** (A) Representative time-resolved fluorescence decay spectra of OLA-NBD (5  $\mu\text{M}$ ) in the absence and with the incremental addition of HSA (0–50  $\mu\text{M}$ ). (B) Fluorescence decay profiles of HSA (5  $\mu\text{M}$ ) in the absence and with the increasing concentration of OLA-NBD (0–30  $\mu\text{M}$ ). IRF represents the instrument response function.

3. The free OLA-NBD shows a monoexponential decay in aqueous solution with 0.77 ns lifetime. Table 3 displays that decay pattern of OLA-NBD is altered from monoexponential to biexponential form with two lifetime values in HSA medium and clearly indicates the separation of OLA-NBD into two dissimilar microenvironments on interaction with HSA. The observable increase in average lifetime value ( $\langle\tau\rangle$ ) of OLA-NBD with the increasing amount of HSA (Table 3) may be due to the increasing motional constraint on OLA-NBD by the rigid and nonpolar environment within HSA and thus provide a decreased nonradiative decay channel.<sup>16</sup>

Fluorescence lifetime study of HSA was also done in the absence and in the increasing concentration of OLA-NBD to



**Table 3. Fluorescence Lifetime Decay Parameters of OLA-NBD (5  $\mu\text{M}$ ) with Gradual Addition of HSA at 25  $^{\circ}\text{C}$** 

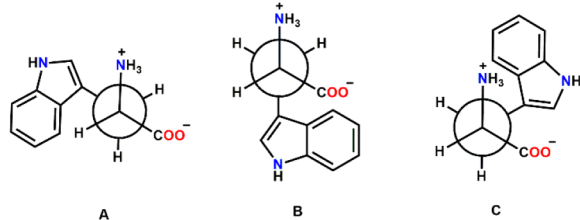
system	[HSA] ( $\mu\text{M}$ )	$\tau_1$ (ns)	$\alpha_1$ (%)	$\tau_2$ (ns)	$\alpha_2$ (%)	$\langle\tau\rangle$ (ns)	$\chi^2$
OLA-NBD–HSA	0	0.77	100				1.124
	5	0.71	51.61	3.61	48.39	2.11	1.135
	20	1.00	47.05	4.11	52.95	2.66	1.092
	50	1.20	45.93	4.65	54.07	3.07	1.116

**Table 4. Fluorescence Lifetime Decay Parameters of HSA (5  $\mu\text{M}$ ) with Gradual Addition of OLA-NBD at 25  $^{\circ}\text{C}$** 

system	[OLA-NBD] ( $\mu\text{M}$ )	$\tau_1$ (ns)	$\alpha_1$ (%)	$\tau_2$ (ns)	$\alpha_2$ (%)	$\langle\tau\rangle$ (ns)	$\chi^2$
HSA–OLA-NBD	0	1.68	29.12	5.41	70.88	4.32	1.058
	5	1.49	27.83	5.35	72.17	4.27	1.119
	10	1.38	26.46	5.27	73.64	4.24	1.126
	15	1.30	25.17	5.18	74.83	4.20	1.062
	20	1.21	24.05	5.13	75.95	4.18	1.073
	30	1.17	22.86	5.05	77.14	4.16	1.042

discriminate the quenching process (static or dynamic). Figure 5B shows the characteristic decay profiles. The decay associated parameters are presented in Table 4. The free HSA exhibits a biexponential decay pattern in aqueous solution with  $\langle\tau\rangle$  value of 4.32 ns bearing two lifetime decay constants of 1.68 and 5.41 ns with related amplitude of 29.12% and 70.88%, respectively.

This biexponential nature of HSA in the free state has been described prior and ascribed to the presence of one Trp moiety at discrete conformational states.<sup>18</sup> The fluorescence lifetime decay of Trp has been studied by taking a rotamer model stated by Fleming and co-workers.<sup>49</sup> Three probable conformers of Trp are represented as follows:



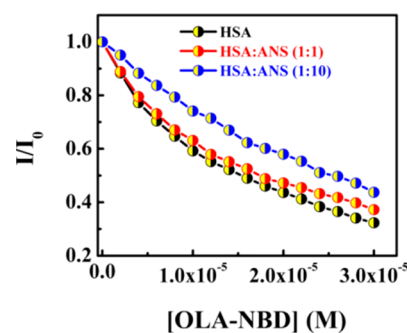
Here, relatively, the faster component is signified by rotamer C, and conversely, the slower component usually comes out from the speedy interconversion of A and B conformers. However, on nanosecond time scale conversion of comparatively stable C conformer to either B or A form is rather difficult. Additionally, it is believed that on photoexcitation the indole ring undergoes a conformational change from puckered form to planar form, maybe owing to the delocalization of electron density over nitrogen atom with the aromatic moiety.<sup>18</sup> Here, we have assigned the average lifetime ( $\langle\tau\rangle$ ) value rather than more importance on the discrete lifetime decay constant in such biexponential profile. Table 4 displays that  $\langle\tau\rangle$  value of HSA marginally decreases from 4.32 ns in aqueous solution to 4.16 ns upon addition of 30  $\mu\text{M}$  OLA-NBD. This minimal reduction of  $\langle\tau\rangle$  value in the presence of higher concentration of OLA-NBD is due to the modulation of local microenvironment nearby the Trp moiety upon interaction. A time-resolved Stern–Volmer plot was constructed with the help of  $\langle\tau\rangle$  values and by considering the following equation:

$$\frac{\langle\tau_0\rangle}{\langle\tau\rangle} = 1 + K_{\text{SV}}[\text{OLA-NBD}] \quad (14)$$

where  $\langle\tau_0\rangle$  and  $\langle\tau\rangle$  are the average lifetime value of HSA in the free state and with the increasing concentration of OLA-NBD, respectively. Figure 3A depicts the overlap of characteristic

steady-state and time-resolved Stern–Volmer plots for the HSA–OLA-NBD interaction, where, time-resolved part is parallel to the  $x$ -axis reaffirming the involvement of a static quenching process or in other words ground state complex formation between OLA-NBD and HSA.<sup>50–52</sup>

**Hydrophobic Probe ANS Displacement Analysis.** ANS displacement experiment was executed to find out the probable binding region of OLA-NBD on HSA. The ANS is a known fluorescent sensitive probe and frequently used to get info about the hydrophobic interaction regions of protein.<sup>38,53–55</sup> Consistent with the protocol, the displacement experiments were carried out with ANS maintaining identical conditions, and Figure 6 depicts the plot of change of relative emission ( $I/I_0$ )

**Figure 6.** ANS displacement study for the quenching of HSA emission by OLA-NBD at different HSA-ANS ratio (1:0, 1:1, and 1:10).

versus OLA-NBD concentration. We find that at a 30  $\mu\text{M}$  concentration, OLA-NBD has a better quenching impact on HSA emission than ANS (i.e., OLA-NBD quenched  $\sim 69\%$  and ANS about 48%). However, with the addition of OLA-NBD to HSA-ANS associates (1:1 and 1:10), emission intensity was decreased to  $\sim 63\%$  and  $\sim 56\%$ , respectively. This outcome indicates that OLA-NBD moderately competes with ANS for the hydrophobic binding sites of HSA by eliminating the bound ANS molecules.

**Site-Specific Binding of OLA-NBD on HSA.** The competitive fluorescence binding experiments were implemented to find out the plausible binding site of OLA-NBD on HSA by using two familiar site-specific markers (Warfarin and Ibuprofen). We have done two separate binding experiments to acquire significant information about the OLA-NBD interaction site by analyzing the emission intensity changes of the spectra. Warfarin site-specific marker solely binds at subdomain IIA of

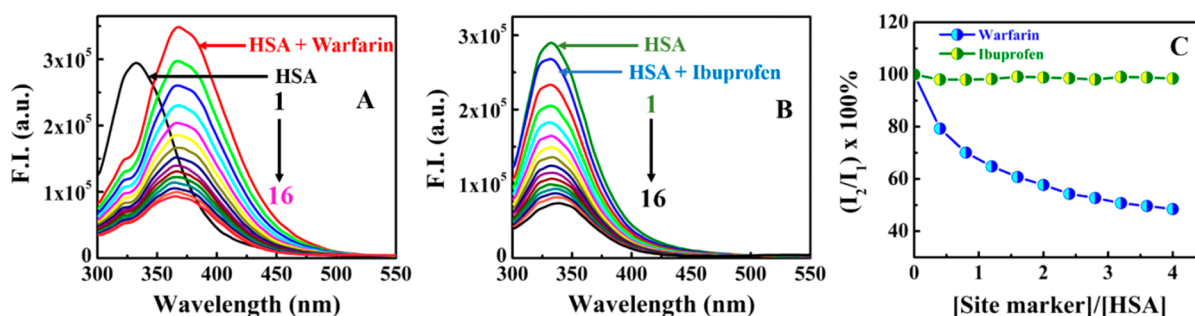


**Figure 7.** Effect of site markers on the emission of HSA–OLA-NBD. (A)  $[HSA] = [Warfarin] = 5 \mu M$  (B)  $[HSA] = [Ibuprofen] = 5 \mu M$ . For both the panel A and B, curve 3–16 represents the addition of OLA-NBD each time  $2 \mu M$  to a total  $28 \mu M$  concentration. (C)  $[HSA] = 5 \mu M$ ,  $[OLA-NBD] = 20 \mu M$ . Warfarin and ibuprofen site markers are added gradually to a total  $20 \mu M$  concentration, respectively.  $\lambda_{ex}$  of HSA =  $295 \text{ nm}$ .

site I; in contrast, ibuprofen particularly binds at subdomain IIIA of site II.<sup>9,10,56</sup> In the first set of experiments, OLA-NBD was increasingly added to the HSA-site markers associates (1:1) to monitor the spectral variations (Figure 7A,B). Upon addition of OLA-NBD into HSA solution, the emission intensity is slightly increased along with a substantial red shift ( $\sim 34 \text{ nm}$ ) of  $\lambda_{em}^{max}$  from  $334$  to  $368 \text{ nm}$  (Figure 7A). Then successive addition of OLA-NBD into HSA-warfarin associate consequences a regular decrement in emission intensity, implying the effect of OLA-NBD on the Warfarin binding site within HSA. However, in case of Ibuprofen addition, no such significant variation of  $\lambda_{em}^{max}$  was detected (Figure 7B). The OLA-NBD induces the emission intensity quenching of HSA-Ibuprofen associate almost to the similar range as in the case of free HSA (Figure 7C). Hence, the above experimental observations and findings evidently prove that the binding of OLA-NBD to HSA is predominantly located at subdomain IIA of site I.

In case of second set of experiments, site-specific markers were progressively added to the mixed solution of HSA and OLA-NBD held at a molar ratio of 1:4 to keep the minimum nonspecific binding of the site markers.<sup>17</sup> The emission intensity of the ternary mixture was evaluated from the method stated by Sudlow et al.<sup>10</sup>

$$\frac{I_2}{I_1} \times 100\%$$

Here,  $I_1$  and  $I_2$  denotes the emission intensity of HSA–OLA-NBD in the absence and presence of site-specific markers, respectively. Site markers induced emission spectral variations of HSA–OLA-NBD are depicted in Figure 7C, which vividly shows that warfarin contends with OLA-NBD molecules for the binding site I of HSA. Thus, the emission of HSA–OLA-NBD was considerably influenced by warfarin and remained virtually same in the presence of ibuprofen.

These results establish that OLA-NBD is likely to bind at site I in subdomain IIA of HSA, inferring the presence of Trp 214 is inside or close to the OLA-NBD binding site, which is in excellent harmony with the results found from the spectrofluorimetric analysis.

**Resonance Rayleigh Scattering (RRS) Spectral Investigations.** To investigate the interactions of protein molecules with the small molecular probes and to know the molecular recognition, a simple and very sensitive analytical method, RRS, is introduced. This technique is very much sensitive to the electrostatic attraction and hydrophobic and hydrogen bonding interactions.<sup>57,58</sup> The resonance Rayleigh scattering spectra of HSA and HSA–OLA-NBD (Figure 8) were recorded by

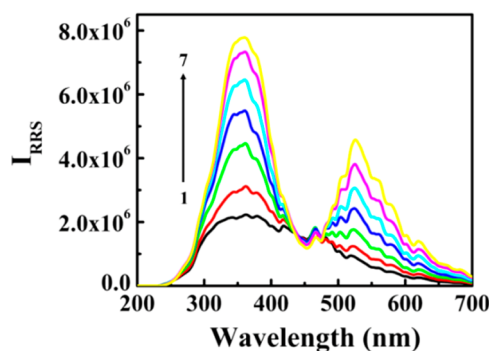


**Figure 8.** Effect of OLA-NBD concentration ( $0$ – $35 \mu M$ ) on the RRS spectra of HSA–OLA-NBD system.  $[HSA] = 5 \mu M$ .

synchronous scanning in the wavelength range  $200$  to  $700 \text{ nm}$  with  $\Delta\lambda = 0 \text{ nm}$ . In the absence of OLA-NBD, HSA shows a moderate RRS intensity, and then a rapid increment in intensity is noticed with the gradual addition of OLA-NBD, indicating the interaction between OLA-NBD and HSA. This is possibly owing to the greater dimension of HSA–OLA-NBD particles than that of HSA and the ground state complex formation between the two species.

**Conformation Investigations: Circular Dichroism Study.** The far-UV CD spectra of free HSA in aqueous medium (Figure 9) display a characteristic shape with two minima at  $\sim 208$  and  $\sim 222 \text{ nm}$ , vividly indicative of an  $\alpha$ -helix rich secondary structure.<sup>4,7,8,16–18</sup> These two negative bands in the CD profile appears usually due to  $n \rightarrow \pi^*$  charge transfer transition.<sup>59</sup> The CD spectra of HSA experiences a reduction in

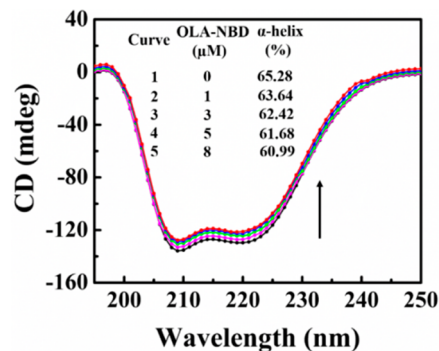


**Figure 9.** CD spectral profiles of HSA ( $1.25 \mu M$ ) with added OLA-NBD at  $25 \text{ }^\circ\text{C}$ . The inset shows the calculated  $\alpha$ -helicity ( $\pm 2\%$ ) variation in HSA with the increasing concentration of OLA-NBD.

CD signal with no observable change of the peak wavelengths (Figure 9) upon gradual addition of OLA-NBD. This infers OLA-NBD induced alteration of conformation of free HSA concerning the reduction of  $\alpha$ -helicity.

The percentage  $\alpha$ -helicity in HSA is evaluated by adopting the following equation:<sup>16,18</sup>

$$\% \alpha\text{-helix} = \frac{-(MRE_{222} - 2340)}{30300} \times 100 \quad (15)$$

Here, mean residue ellipticity ( $MRE$ ) values are assessed from the recorded ellipticity values ( $\theta_{obs}$  in mdeg at 222 nm) using eq 16:<sup>16,18</sup>

$$MRE(\text{deg}\cdot\text{cm}^2\cdot\text{dmol}^{-1}) = \frac{\theta_{obs}}{C_p n l \times 10} \quad (16)$$

where  $n$  designates the number of amino acid residues (585 for HSA).<sup>4,7,8,16–18</sup>  $C_p$  and  $l$  are the molar concentration of HSA and the path-length of cell (here 1 cm), respectively. The  $\alpha$ -helicity of free HSA is evaluated to be  $\sim 65.28 (\pm 2)\%$ , and it is in good agreement with the literature values.<sup>4,7,8,16–18</sup> A reduction in the  $\alpha$ -helicity from  $\sim 65.28 (\pm 2)\%$  in free HSA to  $\sim 60.99 (\pm 2)\%$  with the addition of  $8 \mu\text{M}$  OLA-NBD (inset of Figure 9) therefore clearly displays OLA-NBD persuaded denaturation of HSA protein.

**OLA-NBD Induced Variation of HSA Functionality: Esterase-like Activity Assay of HSA.** Besides the well-known probe binding capacity, a characteristic enzymatic property of HSA can be defined by observing the esterase-like activity assay.<sup>16,18,60,61</sup> The significant effect of OLA-NBD binding on the conformation of HSA in native state leads us to perform the HSA activity study, as it is important for biological applications. Figure 10A and B represent the kinetic profiles and relative

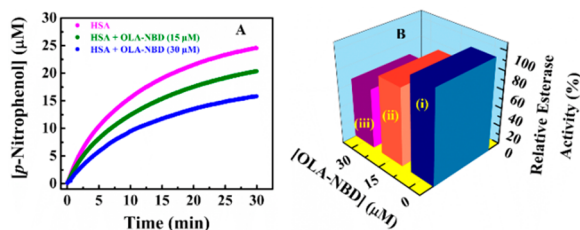


**Figure 10.** (A)  $p$ -Nitrophenol (in  $\mu\text{M}$ ) release kinetic profiles for the reaction between HSA and PNPA in the absence and with the increasing amount of OLA-NBD. (B) OLA-NBD induced variation of relative esterase activity of HSA ( $[\text{OLA-NBD}] =$  (i) 0, (ii)  $15 \mu\text{M}$ , and (iii)  $30 \mu\text{M}$ ).  $\lambda_{\text{monitored}} = \lambda_{\text{abs}} = 400 \text{ nm}$ .

esterase activity of HSA for releasing of  $p$ -Nitrophenol on reaction with PNPA in the absence and with the increasing concentration of OLA-NBD. It is observed that the interaction of OLA-NBD with HSA is accompanied by an obvious decrease in the esterase activity of HSA, which is in good agreement with the experimental loss of the free protein structure on binding with OLA-NBD.<sup>16,18</sup>

**Effect of  $\beta$ -CD on HSA–OLA-NBD Binding.**  $\beta$ -Cyclodextrin ( $\beta$ -CD) can form characteristic inclusion complexes with a numerous number of inorganic and organic molecules. It is also extensively used as drug additives to enhance the stability of drug molecules and increase the solubility of water insoluble drug molecules.<sup>27</sup> Here, only the influence of  $\beta$ -CD on HSA–OLA-NBD binding was explored. The OLA-NBD molecule experiences a moderate binding with  $\beta$ -CD (Figures S7 and S8),

as discussed in the Supporting Information. This encapsulation method can modify the HSA–OLA-NBD binding association as  $\beta$ -CD behaves like a scabbard that shrouds the OLA-NBD molecule, obstructing it from freely bind with HSA.<sup>62</sup> To recognize the effect of  $\beta$ -CD on HSA–OLA-NBD binding, HSA ( $5 \mu\text{M}$ ) emission was recorded in the presence of  $1.0 \text{ mM}$   $\beta$ -CD with the gradual addition of OLA-NBD from 0 to  $30 \mu\text{M}$  (Figure S9). The calculated  $K_{SV}$  and  $K_b$  values from Figures S10 and S11, respectively, at  $25 \text{ }^\circ\text{C}$  in the absence and presence of  $\beta$ -CD are summarized in Table 5. The smaller  $K_{SV}$  and  $K_b$  values in the

**Table 5.** Stern–Volmer Constants ( $K_{SV}$ ) and Binding Constants ( $K_b$ ) for HSA–OLA-NBD Binding Association in the Absence and Presence of  $\beta$ -CD at  $25 \text{ }^\circ\text{C}$

[HSA] ( $\mu\text{M}$ )	$[\beta\text{-CD}]$ (mM)	$K_{SV}$ ( $10^4 \text{ M}^{-1}$ )	$R^2$	binding constant, $K_b$ ( $10^4 \text{ M}^{-1}$ )
5	0.0	$6.74 \pm 0.09$	0.997	$6.38 \pm 0.04$
5	1.0	$4.72 \pm 0.14$	0.995	$5.19 \pm 0.15$

presence of  $\beta$ -CD for the HSA–OLA-NBD binding association indicate that  $\beta$ -CD prevents the direct collision of OLA-NBD molecules with HSA by forming an inclusion complex.<sup>62,63</sup> It also implies that OLA-NBD molecules are progressively unsheathed from  $\beta$ -CD by HSA to accomplish its medicinal outcome upon binding with protein.<sup>58,62–64</sup>

**HSA–OLA-NBD Association Kinetics.** In the investigation of binding of drug/small molecules with the various proteins, a discussion on the association kinetics is believed to have vital diagnostic implication.<sup>63–67</sup> The association kinetics of the HSA–OLA-NBD composite was investigated under pseudo-first-order conditions by monitoring the emission quenching of HSA at  $334 \text{ nm}$  upon interaction with OLA-NBD. Figure 11

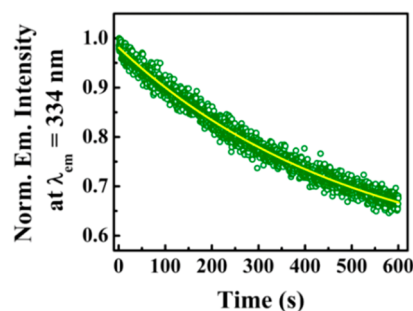


**Figure 11.** Representative emission kinetic trace for the HSA–OLA-NBD binding association. The kinetic profile defines the time path of HSA emission quenching on interaction with OLA-NBD at  $298 \text{ K}$ . The raw data are designated by olive-green symbols, and the fitted curve is represented by solid yellow line.  $\lambda_{\text{ex}} = 295 \text{ nm}$ ,  $\lambda_{\text{monitored}} = \lambda_{\text{em}} = 334 \text{ nm}$ ,  $[\text{HSA}] = 1 \mu\text{M}$ ,  $[\text{OLA-NBD}] = 20 \mu\text{M}$ .

shows the characteristic emission kinetic trace for the above-mentioned association process at  $298 \text{ K}$ , and it has been fitted by considering a nonlinear regression equation as follows:<sup>68</sup>

$$I(t) = \alpha \exp(-k_a t) + C \quad (17)$$

where  $I(t)$  signifies the emission intensity at time  $t$ .  $\alpha$  and  $k_a$  are the amplitude and the apparent association rate constant, respectively, corresponding to the exponential factor.  $C$  represents the emission intensity at equilibrium. An apparent rate constant,  $k_a = (1.95 \pm 0.09) \times 10^{-3} \text{ s}^{-1}$  is found for the HSA–OLA-NBD association kinetics at  $298 \text{ K}$ .



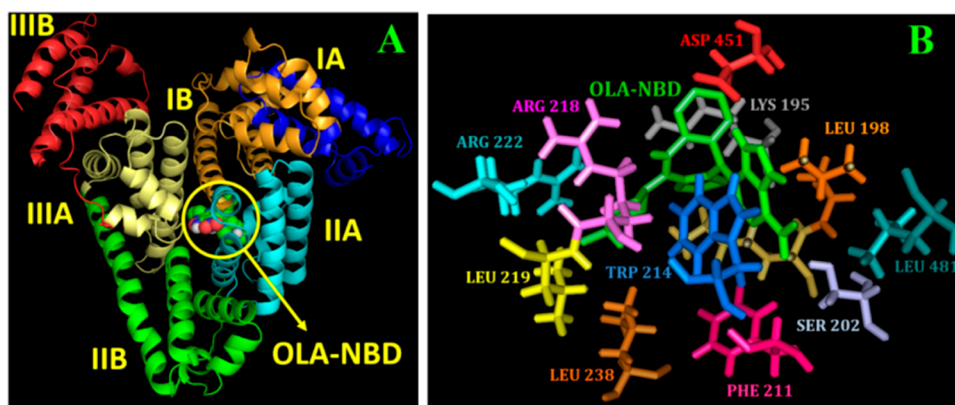


**Figure 12.** (A) Stereo view of molecular docking posture of OLA-NBD with HSA protein (PDB ID: 1A06) displayed by yellow circle. (B) Magnified sight of OLA-NBD binding location accompanied by highlighting of the neighboring (within 4.0 Å of the binding site) amino acid residues of HSA.

**Molecular Docking Results.** Herein, we have accomplished the docking study to ascertain the probable OLA-NBD binding site within HSA and the involvement of possible thermodynamic interactions throughout the association process. The minimum binding energy docked conformation was chosen for further investigation.<sup>69,70</sup> The stereo view of molecular docking posture of OLA-NBD with HSA protein is displayed in Figure 12A, which indicates that the subdomain IIA of site I in HSA is favored for OLA-NBD interaction, and this is well corroborated with the outcome of site-specific marker studies. Figure 12B exhibits the adjacent amino acid residues (within 4.0 Å) surrounding the OLA-NBD interaction region in subdomain IIA of HSA close to the Trp 214 residue. OLA-NBD molecule is encompassed by several hydrophobic and polar amino acid residues. A variable number of charged and polar residues like Lys 195, Ser 202, Arg 218, Arg 222, and Asp 451 plays a significant role in stabilizing the OLA-NBD–HSA association through electrostatic interactions. Furthermore, Leu 198, Phe 211, Trp 214, Leu 219, and Leu 238 provided greater stability to the OLA-NBD molecule through hydrophobic interactions. The binding energy for the OLA-NBD–HSA association was found to be  $-5.73 \text{ kcal mol}^{-1}$ . The docking simulation outcome demonstrates that the OLA-NBD molecule binds near to the Trp 214 at site I within HSA, inducing a perturbation of the HSA emission intensity. Hence, molecular docking simulation approach supported the experimental outcomes from a theoretical point of view.

## CONCLUSION

The present work deals with the various spectroscopic and molecular docking investigation on the interaction of NBD embedded olanzapine derivative (OLA-NBD) with HSA protein. The complexation of OLA-NBD with HSA has been evidently illustrated by UV–vis spectral change at 280 nm. A gradual enhancement of the emission intensity of OLA-NBD along with the substantial blue shift of  $\lambda_{em}^{max}$  on interaction with HSA is vividly indicates toward the immense modulation of the microenvironment around OLA-NBD within the protein hydrophobic medium compared with the polar aqueous medium. The emission titration of HSA with OLA-NBD resulted an association constant =  $(9.87 \pm 0.02) \times 10^4 \text{ M}^{-1}$ , and it is in excellent harmony with the value estimated from anisotropy experiment. The emission quenching study persuaded by OLA-NBD indicates the presence of static quenching mechanism, which is well corroborated with the results extracted

from the time-resolved fluorescence study of HSA with OLA-NBD. Binding constant value decreases with the rise in temperature leading to the decrement in the stability of HSA–OLA-NBD composite, supporting the presence of static quenching mechanism. The negative value of  $\Delta H^0$  accompanied by a positive value of  $\Delta S^0$  infer the major contribution of electrostatic/ionic interaction for the HSA–OLA-NBD binding process. CD outcome illustrates the alteration of the secondary structure of HSA upon interaction with OLA-NBD. The effect of  $\beta$ -cyclodextrin on HSA–OLA-NBD binding is found to be characterized by smaller Stern–Volmer quenching and binding constant values, indicating that OLA-NBD molecules are progressively unsheathed from  $\beta$ -CD by HSA to accomplish its medicinal applications. The site-specific binding experiment and molecular docking studies indicate that OLA-NBD binds with HSA in subdomain IIA at the binding site I, that is, close to the Trp 214 amino acid. Hence, the present extrinsic fluorescent molecular probe can be employed as a potential site-specific biomarker for site I binding pocket in the subdomain IIA.

## ASSOCIATED CONTENT

### Supporting Information

The Supporting Information is available free of charge on the ACS Publications website at DOI: 10.1021/acsabm.9b00429.

Characterization data for OLA-NBD; Job's plot; experimental methods and instrumental specifications; effect of  $\beta$ -cyclodextrin on fluorescence spectra of OLA-NBD (PDF)

## AUTHOR INFORMATION

### Corresponding Author

\*E-mail: m\_ali2062@yahoo.com.

### ORCID

Mihir Sasmal: 0000-0002-4284-7774

Abu Saleh Musha Islam: 0000-0002-2529-8662

Mahammad Ali: 0000-0003-0756-0468

### Notes

The authors declare no competing financial interest.

## ACKNOWLEDGMENTS

Financial support from DST (Ref. No. 809(Sanc)/ST/P/S&T/4G-9/2104), West Bengal and CSIR (Ref. No. 01(2896)/17/EMR-II), New Delhi, India are gratefully acknowledged. M.S. is



grateful for the UGC-NET Fellowship (SRF) UGC, New Delhi, India.

## REFERENCES

- (1) Peters, T., Jr. *All About Albumins: Biochemistry, Genetics and Medical Applications*; Academic Press: San Diego, CA, 1996; pp 76–132.
- (2) Lázaro, E.; Lowe, P. J.; Briand, X.; Faller, B. New approach to measure protein binding based on a parallel artificial membrane assay and human serum albumin. *J. Med. Chem.* **2008**, *51*, 2009–2017.
- (3) Shahlaei, M.; Rahimi, B.; Ashrafi-Kooshk, M. R.; Sadrajavadi, K.; Khodarahmi, R. Probing of possible olanzapine binding site on human serum albumin: Combination of spectroscopic methods and molecular dynamics simulation. *J. Lumin.* **2015**, *158*, 91–98.
- (4) Carter, D. C.; Ho, J. X. Structure of Serum Albumin. *Adv. Protein Chem.* **1994**, *45*, 153–203.
- (5) Brown, J. R.; Shockley, P. *Lipid-Protein Interactions*; Wiley: New York, 1982; Vol. 1, pp 25–68.
- (6) Ding, F.; Liu, W.; Zhang, L.; Yin, B.; Sun, Y. J. Sulfometuron-methyl binding to human serum albumin: Evidence that sulfometuron-methyl binds at the Sudlow's site I. *J. Mol. Struct.* **2010**, *968*, 59–66.
- (7) He, X. M.; Carter, D. C. Atomic Structure and Chemistry of Human Serum Albumin. *Nature* **1992**, *358*, 209–215.
- (8) Peters, T., Jr. Serum Albumin. *Adv. Protein Chem.* **1985**, *37*, 161–245.
- (9) Sudlow, G.; Birkett, D. J.; Wade, D. N. The Characterization of Two Specific Drug Binding Sites on Human Serum Albumin. *Mol. Pharmacol.* **1975**, *11*, 824–832.
- (10) Sudlow, G.; Birkett, D. J.; Wade, D.; Mol, N. Further Characterization of Specific Drug Binding Sites on Human Serum Albumin. *Mol. Pharmacol.* **1976**, *12*, 1052–1061.
- (11) Olson, R. E.; Christ, D. D. Chapter 33. Plasma Protein Binding of Drugs. *Annu. Rep. Med. Chem.* **1996**, *31*, 327–336.
- (12) Kandagal, P. B.; Shaikh, S. M. T.; Manjunatha, D. H.; Seetharamappa, J.; Nagaralli, B. S. Spectroscopic studies on the binding of bioactive phenothiazine compounds to human serum albumin. *J. Photochem. Photobiol., A* **2007**, *189*, 121–127.
- (13) Rabbani, G.; Ahn, S. N. Structure, enzymatic activities, glycation and therapeutic potential of human serum albumin: A natural cargo. *Int. J. Biol. Macromol.* **2019**, *123*, 979–990.
- (14) Abou-Zied, O. K.; Al-Shihi, O. I. K. Characterization of Subdomain IIA Binding Site of Human Serum Albumin in its Native, Unfolded, and Refolded States Using Small Molecular Probes. *J. Am. Chem. Soc.* **2008**, *130*, 10793–10801.
- (15) Mallick, A.; Haldar, B.; Chattopadhyay, N. Spectroscopic Investigation on the Interaction of ICT Probe 3-Acetyl-4-oxo-6,7-dihydro-12H Indolo-[2,3-a] Quinolizine with Serum Albumins. *J. Phys. Chem. B* **2005**, *109*, 14683–14690.
- (16) Paul, B. K.; Ghosh, N.; Mukherjee, S. Interplay of Multiple Interaction Forces: Binding of Norfloxacin to Human Serum Albumin. *J. Phys. Chem. B* **2015**, *119*, 13093–13102.
- (17) Ibrahim, N.; Ibrahim, H.; Kim, S.; Nallet, J. P.; Nepveu, F. Interactions between Antimalarial Indolone-N-oxide Derivatives and Human Serum Albumin. *Biomacromolecules* **2010**, *11*, 3341–3351.
- (18) Ghosh, N.; Mondal, R.; Mukherjee, S. Hydrophobicity Is the Governing Factor in the Interaction of Human Serum Albumin with Bile Salts. *Langmuir* **2015**, *31*, 1095–1104.
- (19) Ahmad, B.; Parveen, S.; Khan, R. H. Effect of Albumin Conformation on the Binding of Ciprofloxacin to Human Serum Albumin: A Novel Approach Directly Assigning Binding Site. *Biomacromolecules* **2006**, *7*, 1350–1356.
- (20) Sudhamalla, B.; Gokara, M.; Ahalawat, N.; Amooru, D. G.; Subramanyam, R. Molecular Dynamics Simulation and Binding Studies of  $\beta$ -Sitosterol with Human Serum Albumin and Its Biological Relevance. *J. Phys. Chem. B* **2010**, *114*, 9054–9062.
- (21) Sinha, S. S.; Mitra, R. K.; Pal, S. K. Temperature-Dependent Simultaneous Ligand Binding in Human Serum Albumin. *J. Phys. Chem. B* **2008**, *112*, 4884–4891.
- (22) Lieberman, J. A.; Stroup, T. S.; McEvoy, J. P.; Swartz, M. S.; Rosenheck, R. A.; Perkins, D. O.; Keefe, R. S. E.; Davis, S. M.; Davis, C. E.; Lebowitz, B. D.; Severe, J.; Hsiao, J. K. Effectiveness of antipsychotic drugs in patients with chronic schizophrenia. *N. Engl. J. Med.* **2005**, *353*, 1209–1223.
- (23) Albani, J. R. Fluorescence Spectroscopic Study of Interaction between Olanzapine and Bovine Serum Albumin. *Pharm. Anal. Acta* **2015**, *6*, 408.
- (24) Aravagiri, M.; Teper, Y.; Marder, S. R. Pharmacokinetics and tissue distribution of olanzapine in rats. *Biopharm. Drug Dispos.* **1999**, *20*, 369–377.
- (25) Markowitz, J. S.; DeVane, C. L.; Malcolm, R. J.; Gefroh, H. A.; Wang, J. S.; Zhu, H. J.; Donovan, J. L. Pharmacokinetics of Olanzapine After Single-Dose Oral Administration of Standard Tablet Versus Normal and Sublingual Administration of an Orally Disintegrating Tablet in Normal Volunteers. *J. Clin. Pharmacol.* **2006**, *46*, 164–171.
- (26) Taliani, S.; Simorini, F.; Sergianni, V.; Motta, C. L.; Settimo, F. D.; Cosimelli, B.; Abignente, E.; Greco, G.; Novellino, E.; Rossi, L.; Gremigni, V.; Spinetti, F.; Chelli, B.; Martini, C. New Fluorescent 2-Phenylindolglyoxylamide Derivatives as Probes Targeting the Peripheral-Type Benzodiazepine Receptor: Design, Synthesis, and Biological Evaluation. *J. Med. Chem.* **2007**, *50*, 404–407.
- (27) Zhang, H.; Huang, X.; Mei, P.; Li, K.; Yan, C. Studies on the Interaction of tricyclazole with  $\beta$ -cyclodextrin and human serum albumin by spectroscopy. *J. Fluoresc.* **2006**, *16*, 287–294.
- (28) Qian, F.; Zhang, C.; Zhang, Y.; He, W.; Gao, X.; Hu, P.; Guo, Z. Visible Light Excitable  $Zn^{2+}$  Fluorescent Sensor Derived from an Intramolecular Charge Transfer Fluorophore and Its in Vitro and in Vivo Application. *J. Am. Chem. Soc.* **2009**, *131*, 1460–1468.
- (29) Ojha, B.; Das, G. The Interaction of 5-(Alkoxy)naphthalen-1-amine with Bovine Serum Albumin and Its Effect on the Conformation of Protein. *J. Phys. Chem. B* **2010**, *114*, 3979–3986.
- (30) Sasmal, M.; Bhowmick, R.; Islam, A. S. M.; Bhuiya, S.; Das, S.; Ali, M. Domain-Specific Association of a Phenanthrene–Pyrene-Based Synthetic Fluorescent Probe with Bovine Serum Albumin: Spectroscopic and Molecular Docking Analysis. *ACS Omega* **2018**, *3*, 6293–6304.
- (31) Kar, C.; Ojha, B.; Das, G. A Novel Amphiphilic Thiosemicarbazone Derivative for Binding and Selective Sensing of Human Serum Albumin. *Luminescence* **2013**, *28*, 339–344.
- (32) Paul, B. K.; Samanta, A.; Guchhait, N. Exploring Hydrophobic Subdomain IIA of the Protein Bovine Serum Albumin in the Native, Intermediate, Unfolded, and Refolded States by a Small Fluorescence Molecular Reporter. *J. Phys. Chem. B* **2010**, *114*, 6183–6196.
- (33) Ganguly, A.; Paul, B. K.; Ghosh, S.; Dalapati, S.; Guchhait, N. Interaction of a Potential Chloride Channel Blocker with a Model Transport Protein: a Spectroscopic and Molecular Docking Investigation. *Phys. Chem. Chem. Phys.* **2014**, *16*, 8465–8475.
- (34) Jana, S.; Ghosh, S.; Dalapati, S.; Guchhait, N. Exploring Structural Change of Protein Bovine Serum Albumin by External Perturbation Using Extrinsic Fluorescence Probe: Spectroscopic Measurement, Molecular Docking and Molecular Dynamics Simulation. *Photochem. Photobiol. Sci.* **2012**, *11*, 323–332.
- (35) Lakowicz, J. R. Fluorescence Anisotropy. In *Principles of Fluorescence Spectroscopy*, 3rd ed.; Springer: New York, 2006; pp 353–381.
- (36) Bhuiya, S.; Haque, L.; Das, S. Association of iminium and alkanolamine forms of the benzo[c]phenanthridine alkaloid chelerythrine with human serum albumin: photophysical thermodynamic and theoretical approach. *New J. Chem.* **2018**, *42*, 2180–2196.
- (37) Benesi, M. L.; Hildebrand, J. H. A Spectrophotometric Investigation of the Interaction of Iodine with Aromatic Hydrocarbons. *J. Am. Chem. Soc.* **1949**, *71*, 2703–2707.
- (38) Jash, C.; Payghan, P. V.; Ghoshal, N.; Kumar, G. S. Binding of the Iminium and Alkanolamine Forms of Sanguinarine to Lysozyme: Spectroscopic Analysis, Thermodynamics, and Molecular Modeling Studies. *J. Phys. Chem. B* **2014**, *118*, 13077–13091.

- (39) Afrin, S.; Riyazuddeen; Rabbani, G.; Khan, R. H. Spectroscopic and calorimetric studies of interaction of methimazole with human serum albumin. *J. Lumin.* **2014**, *151*, 219–223.
- (40) Abdullah, S. M. S.; Fatma, S.; Rabbani, G.; Ashraf, J. M. A spectroscopic and molecular docking approach on the binding of tinzaparin sodium with human serum albumin. *J. Mol. Struct.* **2017**, *1127*, 283–288.
- (41) Ishtikhar, M.; Rabbani, G.; Khan, S.; Khan, R. H. Biophysical investigation of thymoquinone binding to 'N' and 'B' isoforms of human serum albumin: exploring the interaction mechanism and radical scavenging activity. *RSC Adv.* **2015**, *5*, 18218–18232.
- (42) Van de Weert, M.; Stella, L. Fluorescence Quenching and Ligand Binding: A Critical Discussion of a Popular Methodology. *J. Mol. Struct.* **2011**, *998*, 144–150.
- (43) Rabbani, G.; Khan, M. J.; Ahmad, A.; Maskat, M. Y.; Khan, R. H. Effect of copper oxide nanoparticles on the conformation and activity of  $\beta$ -galactosidase. *Colloids Surf., B* **2014**, *123*, 96–105.
- (44) Yin, M. M.; Dong, P.; Chen, W. Q.; Xu, S. P.; Yang, L. Y.; Jiang, F. L.; Liu, Y. Thermodynamics and Mechanisms of the Interactions between Ultrasmall Fluorescent Gold Nanoclusters and Human Serum Albumin,  $\gamma$ -Globulins, and Transferrin: A Spectroscopic Approach. *Langmuir* **2017**, *33*, 5108–5116.
- (45) van Holde, K. E.; Johnson, W. C.; Ho, P. S. Thermodynamics and Biochemistry. In *Principles of Physical Biochemistry*, 2nd int. ed.; Pearson Higher Education: Upper Saddle River, NJ, 2006; pp 72–106.
- (46) Ross, P. D.; Subramanian, S. Thermodynamics of Protein Association Reactions: Forces Contributing to Stability. *Biochemistry* **1981**, *20*, 3096–3102.
- (47) Lakowicz, J. R. Fluorescence Anisotropy. In *Principles of Fluorescence Spectroscopy*, 3rd ed.; Springer: New York, 2006; pp 353–381.
- (48) Ingersoll, C. M.; Strollo, C. M. Steady-State Fluorescence Anisotropy to Investigate Flavonoids Binding to Proteins. *J. Chem. Educ.* **2007**, *84*, 1313–1315.
- (49) Petrich, J. W.; Chang, M. C.; McDonald, D. B.; Fleming, G. R. On the origin of nonexponential fluorescence decay in tryptophan and its derivatives. *J. Am. Chem. Soc.* **1983**, *105*, 3824–3832.
- (50) Ray, D.; Paul, B. K.; Guchhait, N. Differential binding modes of anti-cancer, anti-HIV drugs belonging to isatin family with a model transport protein: a joint refinement from spectroscopic and molecular modeling approaches. *J. Photochem. Photobiol., B* **2013**, *127*, 18–27.
- (51) Chatterjee, S.; Mukherjee, T. K. Spectroscopic Investigation of Interaction between Bovine Serum Albumin and Amine-functionalized Silicon Quantum Dots. *Phys. Chem. Chem. Phys.* **2014**, *16*, 8400–8408.
- (52) Bhuiya, S.; Pradhan, A. B.; Haque, L.; Das, S. Molecular Aspects of the Interaction of Iminium and Alkanolamine Forms of the Anticancer Alkaloid Chelerythrine with Plasma Protein Bovine Serum Albumin. *J. Phys. Chem. B* **2016**, *120*, 5–17.
- (53) Rabbani, G.; Ahmad, E.; Khan, M. V.; Ashraf, M. T.; Bhat, R.; Khan, R. H. Impact of structural stability of cold adapted *Candida antarctica* lipase B (CaLB): in relation to pH, chemical and thermal denaturation. *RSC Adv.* **2015**, *5*, 20115–20131.
- (54) Rabbani, G.; Ahmad, E.; Zaidi, N.; Khan, R. H. pH-Dependent Conformational Transitions in Conalbumin (Ovotransferrin), a Metalloproteinase from Hen Egg White. *Cell Biochem. Biophys.* **2011**, *61*, 551–560.
- (55) Rabbani, G.; Ahmad, E.; Zaidi, N.; Fatima, S.; Khan, R. H. pH-Induced Molten Globule State of *Rhizopus niveus* Lipase is More Resistant Against Thermal and Chemical Denaturation Than Its Native State. *Cell Biochem. Biophys.* **2012**, *62*, 487–499.
- (56) Baroni, S.; Mattu, M.; Vannini, A.; Cipollone, R.; Aime, S.; Ascenzi, P.; Fasano, M. Effect of Ibuprofen and Warfarin on the Allosteric Properties of Haem-Human Serum Albumin. A spectroscopic Study. *Eur. J. Biochem.* **2001**, *268*, 6214–6220.
- (57) Madrakian, T.; Bagheri, H.; Afkhami, A.; Soleimani, M. Spectroscopic and molecular docking techniques study of the interaction between oxymetholone and human serum albumin. *J. Lumin.* **2014**, *155*, 218–225.
- (58) Bolattin, M. B.; Nandibewoor, S. T.; Joshi, S. D.; Dixit, S. R.; Chimatadar, S. A. Interaction of Hydralazine with Human Serum Albumin and Effect of  $\beta$ -Cyclodextrin on Binding: Insights from Spectroscopic and Molecular Docking Techniques. *Ind. Eng. Chem. Res.* **2016**, *55*, 5454–5464.
- (59) Yang, P.; Gao, F. *The Principle of Bioinorganic Chemistry*; Science Press: Beijing, 2002; p 349.
- (60) Rabbani, G.; Baig, M. H.; Lee, E. J.; Cho, W. K.; Ma, J. Y.; Choi, I. Biophysical Study on the Interaction between Eperisone Hydrochloride and Human Serum Albumin Using Spectroscopic, Calorimetric, and Molecular Docking Analyses. *Mol. Pharmaceutics* **2017**, *14*, 1656–1665.
- (61) Rabbani, G.; Lee, E. J.; Ahmad, K.; Baig, M. H.; Choi, I. Binding of Tolperisone Hydrochloride with Human Serum Albumin: Effects on the Conformation, Thermodynamics, and Activity of HSA. *Mol. Pharmaceutics* **2018**, *15*, 1445–1456.
- (62) Bogdan, M.; Floare, C. G.; Pirnau, A.; Neamtu, S. Competitive Binding of Tolmetin to  $\beta$ -Cyclodextrin and Human Serum Albumin:  $^1\text{H}$  NMR and Fluorescence Spectroscopy Studies. *J. Solution Chem.* **2017**, *46*, 44–57.
- (63) Bolattin, M. B.; Nandibewoor, S. T.; Joshi, S. D.; Dixit, S. R.; Chimatadar, S. A. Interaction between carisoprodol and bovine serum albumin and effect of  $\beta$ -cyclodextrin on binding: insights from molecular docking and spectroscopic techniques. *RSC Adv.* **2016**, *6*, 63463–63471.
- (64) Zhang, H. X.; Huang, X.; Zhang, M. Thermodynamic studies on the interaction of dioxopromethazine to  $\beta$ -cyclodextrin and bovine serum albumin. *J. Fluoresc.* **2008**, *18*, 753–760.
- (65) Paul, B. K.; Ray, D.; Guchhait, N. Spectral deciphering of the interaction between an intramolecular hydrogen bonded ES IPT drug, 3,5-dichlorosalicylic acid, and a model transport protein. *Phys. Chem. Chem. Phys.* **2012**, *14*, 8892–8902.
- (66) Paul, B. K.; Ghosh, N.; Mukherjee, S. Binding Interaction of a Prospective Chemotherapeutic Antibacterial Drug with  $\beta$ -Lactoglobulin: Results and Challenges. *Langmuir* **2014**, *30*, 5921–5929.
- (67) Banerjee, S.; Chakrabarti, G.; Bhattacharyya, B. Colchicine binding to tubulin monomers: A mechanistic study. *Biochemistry* **1997**, *36*, 5600–5606.
- (68) Canaves, J. M.; Aleu, J.; Lejarreta, M.; Gonzalez-Ros, J. M.; Ferragut, J. A. Effects of pH on the kinetics of the interaction between anthracyclines and lipid bilayers. *Eur. Biophys. J.* **1997**, *26*, 427–431.
- (69) Ahmad, E.; Rabbani, G.; Zaidi, N.; Singh, S.; Rehan, M.; Khan, M. M.; Rahman, S. H.; Quadri, Z.; Shadab, M.; Ashraf, M. T.; Subbarao, N.; Bhat, R.; Khan, R. H. Stereo-Selectivity of Human Serum Albumin to Enantiomeric and Isoelectronic Pollutants Dissected by Spectroscopy, Calorimetry and Bioinformatics. *PLoS One* **2011**, *6*, No. e26186.
- (70) Varshney, A.; Rehan, M.; Subbarao, N.; Rabbani, G.; Khan, R. H. Elimination of Endogenous Toxin, Creatinine from Blood Plasma Depends on Albumin Conformation: Site Specific Uremic Toxicity & Impaired Drug Binding. *PLoS One* **2011**, *6*, No. e17230.

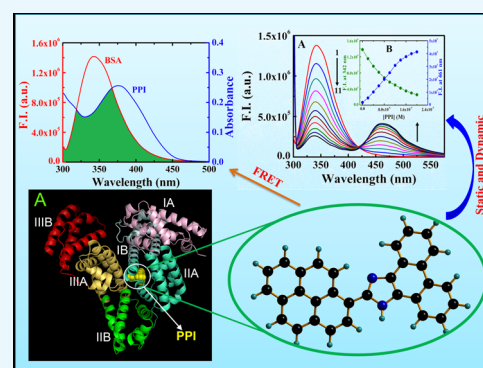
# Domain-Specific Association of a Phenanthrene–Pyrene-Based Synthetic Fluorescent Probe with Bovine Serum Albumin: Spectroscopic and Molecular Docking Analysis

Mihir Sasmal, Rahul Bhowmick, Abu Saleh Musha Islam, Sutanwi Bhuiya, Suman Das,<sup>1</sup> and Mahammad Ali<sup>2\*</sup>

Department of Chemistry, Jadavpur University, 188, Raja S. C. Mullick Road, Kolkata 700 032, India

## Supporting Information

**ABSTRACT:** In this report, the interaction between a phenanthrene–pyrene-based fluorescent probe (PPI) and bovine serum albumin (BSA), a transport protein, has been explored by steady-state emission spectroscopy, fluorescence anisotropy, far-ultraviolet circular dichroism (CD), time-resolved spectral measurements, and molecular docking simulation study. The blue shift along with emission enhancement indicates the interaction between PPI and BSA. The binding of the probe causes quenching of BSA fluorescence through both static and dynamic quenching mechanisms, revealing a 1:1 interaction, as delineated from Benesi–Hildebrand plot, with a binding constant of  $\sim 10^5$  M<sup>-1</sup>, which is in excellent agreement with the binding constant extracted from fluorescence anisotropy measurements. The thermodynamic parameters,  $\Delta H^\circ$ ,  $\Delta S^\circ$ , and  $\Delta G^\circ$ , as determined from van't Hoff relationship indicate the predominance of van der Waals/extensive hydrogen-bonding interactions for the binding phenomenon. The molecular docking and site-selective binding studies reveal the predominant binding of PPI in subdomain IIA of BSA. From the fluorescence resonance energy transfer study, the average distance between tryptophan 213 of the BSA donor and the PPI acceptor is found to be 3.04 nm. CD study demonstrates the reduction of  $\alpha$ -helical content of BSA protein on binding with PPI, clearly indicating the change of conformation of BSA.



## INTRODUCTION

The interaction and energetics of protein binding toward small molecules are largely dependent on the microenvironment and molecular architecture arising due to folding/unfolding or even change of the protein structure. The remarkable properties of a small molecule in such a microenvironment bear information related to the binding site, which is essential for drug development and many other investigations.<sup>1–4</sup>

Model globular proteins, such as serum albumins, are important transport proteins and are found plentiful in plasma.<sup>5–8</sup> Bovine serum albumin (BSA), a large globular protein (65 000 Da), contains 583 amino acid residues in a single chain.<sup>9</sup> The three domains with different surface charge densities impact BSA adsorption on charged surfaces.<sup>10,11</sup> As for example, the presence of both positively charged residues (lysine and arginine) and negatively charged amino acids (glutamic acid and aspartic acid) on BSA can result in electrostatic interactions with both negatively and positively charged surfaces, respectively.<sup>12,13</sup> Because of the presence of a negatively charged domain, BSA is involved in (a) binding with water, salts, fatty acids, vitamins, and hormones and carries them between tissues and cells, (b) removing toxic substances, including pyrogens, from the medium, (c) solubilizing lipids and is a blocking agent in western blot or enzyme-linked

immunosorbent assay applications, and (d) solubilizing other proteins (e.g., labile enzymes). BSA is readily soluble in water and can only be precipitated in the presence of high concentrations of neutral salts such as ammonium sulfate. However, albumin is readily coagulated by heat. So, it is apparent that the BSA can bind a large variety of bioactive molecules by various noncovalent interactions such as hydrophobic, hydrophilic, and ionic interactions. Tryptophan (Trp) 134 and Trp 213 are the two Trp residues present in BSA. It has three domains I, II, and III, each consisting of two subdomains A and B.

The major binding sites of BSA are localized in subdomains, IIA and IIIA, known as site I.<sup>14,15</sup> To infer the protein interaction site with small molecules, site marker fluorescent probes are generally utilized. A great deal of research activities on the structure and function of serum albumins are reported in the literature.<sup>16–27</sup> Nowadays, it is of interest to develop and use special polarity-sensitive fluorescent probes. The main focus of the present work deals with the fluorescence emission and binding aspects of a synthetic

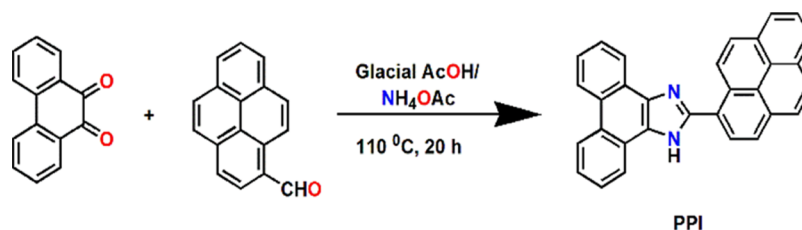
Received: January 30, 2018

Accepted: June 1, 2018

Published: June 12, 2018



Scheme 1. Synthesis of PPI



fluorescent probe, a phenanthrene–pyrene based conjugate (PPI), in the hydrophobic milieu of a globular protein, BSA, under physiological conditions.

The novelty of the present study stems from the fact that the phenanthrene imidazole molecules<sup>28</sup> act as potential selective biomarkers for inhibition of various enzymatic processes. Here, pyrene moiety has been incorporated with phenanthrene imidazole core as a fluorophore unit to validate the binding proficiency with BSA. The presence of an aryl-heteroatom bond, particularly the C–N bond, is significant for showing different biological activities.<sup>29</sup>

## RESULTS AND DISCUSSION

PPI was synthesized from phenanthrene-9,10-dione, 1-pyrene carboxaldehyde, and ammonium acetate in glacial acetic acid, as shown in Scheme 1, and characterized by proton nuclear magnetic resonance (<sup>1</sup>H NMR) (Figure S1), <sup>13</sup>C NMR (Figure S2), high-resolution mass spectrometry (HRMS) (Figure S3), and infrared (Figure S4) spectroscopy.

**Ultraviolet–Visible (UV–vis) Absorption Study.** Absorption spectral study is a useful tool to explore the structural variations and to analyze the complex formation between the protein and probe in solution.<sup>30</sup> UV–vis titrations were carried out at 5 μM BSA concentration, gradually increasing the concentration of PPI (0–25 μM) in aqueous buffer solution. The absorption spectral changes of BSA with a gradual change in the concentration of PPI are shown in Figure 1. Though PPI

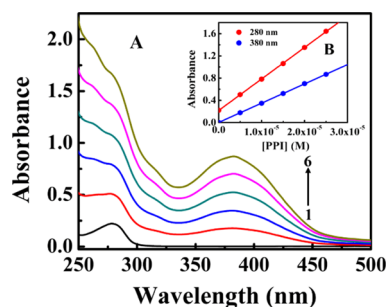


**Figure 1.** (A) Absorption spectral changes of BSA (5 μM) with incremental addition of PPI (0–25 μM) at 25 °C. (B) Inset: absorbance plot at 280 and 380 nm as a function of PPI concentration.

has no absorption at 280 nm, gradual addition of PPI results in an increase in absorbance of BSA at 280 nm, with contemporary growing of an absorbance peak at 380 nm due to PPI. The pattern of the absorption spectra at 280 nm also changes with the increase in the concentration of PPI. This observation supports the complexation between PPI and BSA.

**Fluorescence Emission Study.** Interaction between the protein and probe is well-characterized by the investigation of steady-state fluorescence emission technique. To follow the PPI–BSA interaction, fluorescence titrations were performed

at 20 μM PPI concentration in aqueous medium with the incremental addition of BSA. The emission maximum of PPI was shifted from 476 to 457 nm in 70 μM BSA solution with progressive enhancement of the fluorescence intensity (Figure 2A) when PPI was excited at 380 nm. The fluorescence

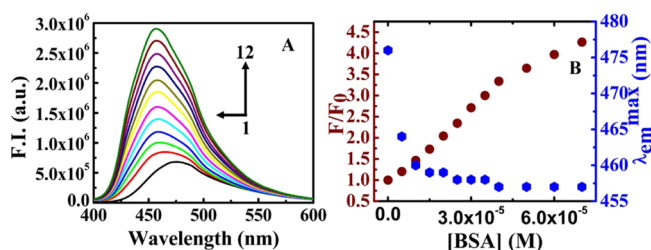


**Figure 2.** (A) Emission spectra of PPI (20 μM) with the gradual addition of BSA (0–70 μM) at 25 °C. (B) Plot of relative variation ( $F/F_0$ ) of the emission intensity and emission maximum ( $\lambda_{em}^{max}$ ) of PPI against BSA concentration.

intensity variations and  $\lambda_{em}^{max}$  of PPI as a function of the BSA concentration are more clearly exhibited in Figure 2B, which represents a steep variation of  $\lambda_{em}^{max}$  up to 15 μM BSA, followed by attainment of a tableland region, and this fact is a clear indication for an ample modification of the surrounding of PPI within the protein heterogeneous microenvironment.

This noticeable blue shift with a concomitant increase in the fluorescence intensity is caused by the alteration in the position of PPI from a more polar aqueous phase to a more hydrophobic protein environment when PPI binds with BSA. BSA fluorescence comes from the presence of three amino acid residues namely, tyrosine (Tyr), Trp, and phenylalanine. In particular, Trp fluorescence is used to monitor the changes in the structural conformation of the BSA protein and to interpret the local environment of BSA-bound PPI.<sup>31–33</sup> There are two Trp moieties in BSA, that is, Trp 134 and Trp 213, which are located in subdomains IB and IIA, respectively. Trp 134 is well-exposed to the hydrophilic region, whereas Trp 213 resides in a hydrophobic cavity of the BSA protein.<sup>34,35</sup>

BSA shows a strong fluorescence maximum at 342 nm in aqueous buffer solution when the excitation of BSA is made at 295 nm.<sup>36</sup> Excitation at 295 nm was selected to minimize the contribution of the Tyr residue present in BSA. To find out the binding constant for BSA–PPI interaction, in another experiment, the fluorescence titration was performed at 10 μM BSA concentration with the gradual addition of PPI leading to saturation. Figure 3A shows that the emission intensity of BSA is decreased considerably along with a small blue shift of  $\lambda_{em}^{max}$  from 342 to 338 nm with increasing PPI concentration, which in turn implies that PPI binds strongly with BSA and also indicates that the microenvironment around Trp moieties present in BSA is modified on interacting with PPI.<sup>37</sup> There is an important observation that apart from the quenching of

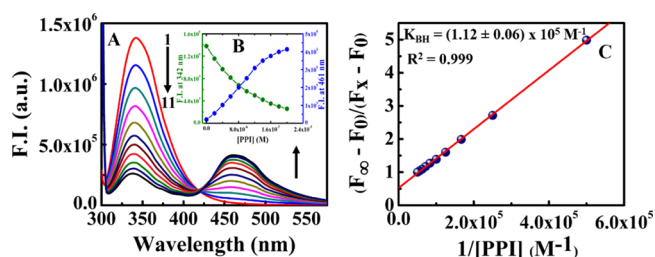


**Figure 3.** (A) Emission spectra of BSA (10  $\mu\text{M}$ ) with the gradual addition of PPI (0–20  $\mu\text{M}$ ) at 25  $^{\circ}\text{C}$ . (B) Inset of Figure 3A; shows the plot of emission intensity variation at 342 and 461 nm, respectively, as a function of the PPI concentration. (C) Representative Benesi–Hildebrand plot for 1:1 complexation of BSA with PPI.  $\lambda_{\text{ex}}$  for BSA is 295 nm.

emission intensity of BSA at 342 nm, a new emission band is developed at 461 nm. The intensity of this emission band is progressively enhanced with the increasing concentration of PPI. The presence of an isoemissive point at 420 nm is an indication of the equilibrium between the free and bound forms of PPI. Inset of Figure 3A vividly shows the emission intensity variation at 342 and 461 nm as a function of PPI concentration.

**Probe-Protein Binding Study.** The binding of PPI with BSA can be explained by eqs 1 and 2, considering 1:1 complexation between them.



$$K_{\text{BH}} = \frac{[\text{PPI:BSA}]}{[\text{PPI}][\text{BSA}]} \quad (2)$$

where  $K_{\text{BH}}$  represents the association constant. The data obtained from the spectrofluorimetric titration of a fixed concentration of BSA with the increasing concentration of PPI are further investigated to find out the binding constant by adopting Benesi–Hildebrand equation.<sup>38</sup>

$$\frac{\Delta F_{\text{max}}}{\Delta F} = 1 + \frac{1}{K_{\text{BH}}[\text{PPI}]} \quad (3)$$

where  $\Delta F_{\text{max}} = |F_{\infty} - F_0|$  and  $\Delta F = |F_x - F_0|$ .  $F_0$ ,  $F_x$ , and  $F_{\infty}$  indicate the emission intensities of BSA in the native state, at an intermediate PPI concentration, and at a PPI concentration when the interaction is saturated, respectively.  $|F_{\infty} - F_0|/|F_x - F_0|$  versus  $1/[\text{PPI}]$  plot displays a linear variation (Figure 3C), validating the accuracy of eq 3, and supports the 1:1 complexation between PPI and BSA. The 1:1 binding of PPI with BSA was also confirmed by Job's plot analysis using the emission spectral data. In this method, the emission data were recorded by changing the PPI:BSA molar ratio, whereas the total molar concentration of PPI and BSA was constant.<sup>39</sup> The Job's plot for PPI–BSA, that is, the difference in the emission intensity at 342 nm versus the mole fraction of PPI (Figure S5), intersected at 0.491, showing the number of PPI molecules binding to BSA to be around unity. The  $K_{\text{BH}}$  value, evaluated from the reciprocal of the slope  $1/K_{\text{BH}}$ , and the corresponding free energy change ( $\Delta G$ ) accompanying the binding process are presented in Table 1, implying strong complexation between PPI and BSA.<sup>40</sup>

**Fluorescence Anisotropy Study.** To gather information about the rigidity of the surrounding environment of a probe, fluorescence anisotropy measurement is a useful experiment.<sup>41</sup> It also gives information regarding the boundary to which the rigid environment obstructs the rotational mobility of the

**Table 1. Binding Parameters for the Association of PPI with BSA at 25  $^{\circ}\text{C}$**

method	environment	binding constant ( $10^5 \text{ M}^{-1}$ )	$\Delta G$ ( $\text{KJ mol}^{-1}$ )
Benesi–Hildebrand	PPI–BSA	(1.12 $\pm$ 0.06)	–28.80
fluorescence anisotropy	PPI–BSA	(1.55 $\pm$ 0.25)	–29.60

probe. Enhancement of anisotropy values reflects an increase in the rigidity of the environment around a fluorescent probe. The change in the anisotropy values of PPI with a change in the BSA concentration in aqueous buffer medium is represented in Figure 4A. Primarily, a rapid enhancement of the anisotropy

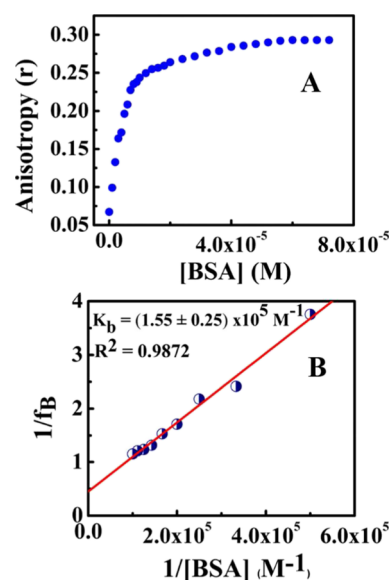


**Figure 4.** (A) Anisotropy variation of PPI as a function of the BSA concentration at 25  $^{\circ}\text{C}$ .  $\lambda_{\text{ex}} = 380 \text{ nm}$  and  $\lambda_{\text{em}} = 475 \text{ nm}$  for PPI. (B) Plot of  $1/f_{\text{B}}$  vs  $1/[\text{BSA}]$  for evaluating the binding constant of the PPI–BSA composite from the anisotropy data.

value from 0.067 to 0.235, till the addition of 8  $\mu\text{M}$  BSA, was observed; then, the increase was gradual to a value of 0.284 till the addition of 40  $\mu\text{M}$  BSA. The increasing value of anisotropy clearly indicates the fact that substantial restriction is imposed on the free motion of PPI molecules with the gradual addition of BSA, and this can be only possible if BSA strongly binds with PPI. The maximum anisotropy value, 0.293, was obtained at 60  $\mu\text{M}$  BSA, and after that, the levelling off of the anisotropy values was observed, which in turn reflects the saturation of association between PPI and BSA.

In accordance with Ingersoll and Strollo<sup>42</sup> method, the binding constant of the PPI–BSA composite can be ascertained by adopting the following equation

$$\frac{1}{f_{\text{B}}} = 1 + \frac{1}{K_{\text{b}}[\text{BSA}]} \quad (4)$$

where  $K_{\text{b}}$  denotes the apparent binding constant of the PPI–BSA composite.  $f_{\text{B}}$  corresponds to the fractional fluorescence contribution of PPI bound to BSA, as shown in eq 5.

$$f_{\text{B}} = \frac{r - r_{\text{F}}}{R(r_{\text{B}} - r) + (r - r_{\text{F}})} \quad (5)$$

where the anisotropy values of bound BSA–PPI and free PPI are denoted by  $r_B$  and  $r_F$ , respectively. The correction factor,  $R$ , that is, the ratio of  $I_B$  and  $I_F$ , is taken into consideration to confirm the fact that PPI experiences fluorescence intensity variation on binding with BSA. The double reciprocal plot of  $1/f_B$  versus  $1/[BSA]$  (Figure 4B) is a straight line, and from the slope, the calculated value of  $K_b$  is presented in Table 1, which is in good accordance with the value obtained from the spectrofluorimetric titration experiment. Thus, this method sets up its practical application and feasibility to find out the binding constant.<sup>37</sup>

**8-Anilino-1-naphthalene Sulfonic Acid (ANS) Displacement Assay.** To check the possible binding site of PPI on BSA, the ANS displacement assay was carried out. The fluorescent probe ANS was used to get information about the hydrophobic binding locations of the protein.<sup>39</sup> In accordance with the procedure, the displacement studies were accomplished with the introduction of ANS, maintaining similar conditions. Figure S6 represents the plot of  $F/F_0$  versus PPI concentration, which clearly shows that at 20  $\mu\text{M}$  concentration, PPI has a better quenching influence on the emission intensity of BSA than ANS, that is, PPI could quench  $\sim 68\%$  and ANS around 51%. The emission intensity of ANS was considerably augmented at 470 nm upon interaction with the hydrophobic regions of BSA, but when PPI was added to the BSA–ANS composite (1:1), the emission intensity of the composite decreased around 60%. This observation suggested that PPI moderately contends with ANS for the hydrophobic locations of BSA by removing the bound ANS molecules, leading to a decrement in the emission intensity of the BSA–ANS composite.

**Site-Selective Binding of PPI on BSA.** The competitive fluorescence displacement studies were executed to ascertain the BSA binding site in which PPI is located, using two well-known drugs (warfarin and ibuprofen). The range of the binding interaction of the PPI–BSA composite can also be revealed by observing the fluorescence intensity variation of the system.<sup>37</sup> Site marker warfarin exclusively binds at subdomain IIA of site I by hydrophobic interaction, whereas ibuprofen precisely binds at subdomain IIIA of site II through hydrophobic, hydrogen-bonding, and electrostatic interactions.<sup>15,37,43,44</sup> Here, PPI was progressively added to the BSA–site marker composites (1:1) in aqueous buffer solution to reveal the spectral change with PPI. Figure 5 represents the spectral changes influenced by the presence of site markers.

The introduction of warfarin site marker into the BSA solution significantly quenched the fluorescence intensity associated with a red shift of  $\lambda_{em}$  from 342 to 358 nm (Figure 5A). Then, incremental addition of PPI into the BSA–warfarin composite results in a gradual decrease in the fluorescence intensity, which in turn indicates the PPI influence on the binding of warfarin to BSA. In contrast to warfarin, no meaningful change of BSA fluorescence intensity was observed upon addition of ibuprofen (Figure 5B). PPI influences the quenching of fluorescence intensity of the BSA–ibuprofen composite nearly to the same extent as in the absence of ibuprofen (Figure 3A). Therefore, the above experimental studies and outcomes clearly establish the fact that the binding of PPI to BSA is principally located at subdomain IIA of site I, which indicates that Trp 213 is inside or in the vicinity of the PPI binding site.

**Study of Fluorescence Quenching Induced by PPI.** The incremental addition of PPI into BSA solution induces the

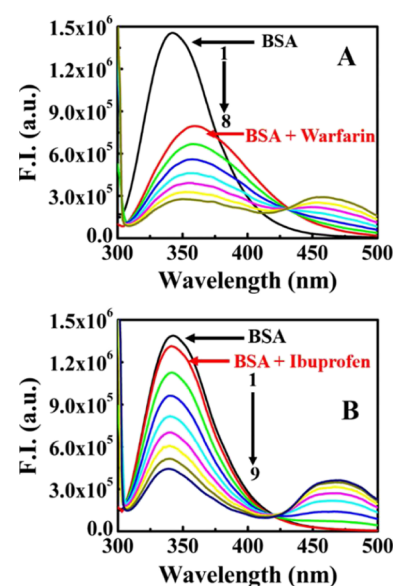


**Figure 5.** Effect of site markers on the PPI–BSA composite. (A)  $[BSA] = [Warfarin] = 10 \mu\text{M}$  with the addition of PPI, each time 2  $\mu\text{M}$ , to a total concentration of 12  $\mu\text{M}$  from curves 3–8 at 25  $^\circ\text{C}$ . (B)  $[BSA] = [Ibuprofen] = 10 \mu\text{M}$  with the addition of PPI, each time 2  $\mu\text{M}$ , to a total concentration of 14  $\mu\text{M}$  from curves 3–9 at 25  $^\circ\text{C}$ .  $\lambda_{ex}$  of BSA = 295 nm.

quenching of BSA fluorescence (Figure 3A). The fluorescence quenching mechanism can be static, owing to the ground-state association between the fluorophore and the quencher, or dynamic because of collisional encounters between the above said two species at the excited state. These two quenching mechanisms can be discriminated by studying the lifetime measurements or by their varying dependence on temperature and viscosity.<sup>45</sup> We have performed the emission quenching of Trp present in BSA with the incremental addition of PPI in aqueous buffer solution. Because PPI has a considerable absorbance at  $\sim 280$  nm and to avoid the involvement of the inner filter effect to the quenching of BSA fluorescence, the emission intensity was corrected by taking the following relation<sup>39,46</sup>

$$F = F_{obs} \times e^{(A_{ex} + A_{em})/2} \quad (6)$$

where,  $F$  and  $F_{obs}$  represent the corrected and observed emission intensities, respectively, of the sample under study.  $A_{ex}$  and  $A_{em}$  denote the absorbance value at the excitation and emission wavelengths, respectively. Figure S7 represents the emission spectrum of PPI at  $\lambda_{ex} = 295$  nm. The probable fluorescence quenching mechanism of BSA–PPI complexation was verified by analyzing the emission data using the well-known Stern–Volmer equation<sup>45</sup>

$$\frac{F_0}{F} = 1 + K_{SV}[PPI] = 1 + k_q \langle \tau_0 \rangle [PPI] \quad (7)$$

where,  $F_0$  and  $F$  correspond to the BSA emission intensities in free form and with the successive addition of PPI, respectively.  $K_{SV}$  represents the Stern–Volmer constant, and  $k_q$  is the bimolecular quenching rate constant.  $[PPI]$  and  $\langle \tau_0 \rangle$  are the molar concentration of the quencher and the average lifetime of a BSA molecule in the absence of PPI, respectively. The involvement of only one type of quenching mechanism, that is, either static or dynamic, is inferred by the linear Stern–Volmer plot. The occurrence of both the abovementioned quenchings



can be inferred, when the plot displays an upward deviation.<sup>32,45,47–49</sup> Figure 6A displays an upward curvature,

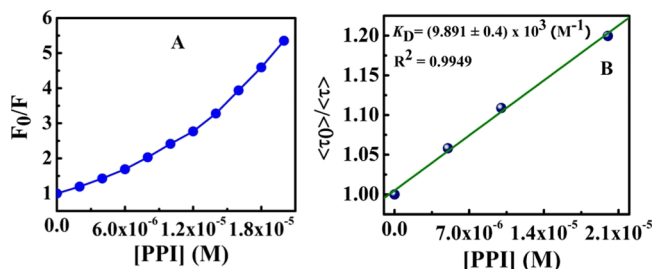


**Figure 6.** (A) Representative Stern–Volmer plot (from steady-state fluorescence study) for the quenching of BSA (10  $\mu\text{M}$ ) fluorescence by PPI at 298 K ( $\lambda_{\text{ex}} = 295$  nm and  $\lambda_{\text{em}} = 342$  nm). (B) Time-resolved Stern–Volmer plot for the quenching of BSA (10  $\mu\text{M}$ ) fluorescence by PPI at 298 K.

signifying the coexistence of static and dynamic quenchings with the same quencher (PPI), and/or the extent of quenching is high at a higher concentration of PPI. Here,  $F_0/F$  is linked with [PPI] by the modified form of Stern–Volmer equation<sup>45</sup>

$$\frac{F_0}{F} = (1 + K_D[\text{PPI}])(1 + K_S[\text{PPI}]) \quad (8)$$

$$\frac{F_0}{F} = 1 + (K_D + K_S)[\text{PPI}] + K_D K_S [\text{PPI}]^2 \quad (9)$$

where dynamic and static quenching constants are represented by  $K_D$  and  $K_S$ , respectively. The first factor of the right-hand side in eq 8 represents dynamic quenching, whereas the second factor represents static quenching. The presence of  $[\text{PPI}]^2$  term in eq 9 accounts for the observation of an upward deviation at high [PPI] when both of the above said quenchings take place for the same quencher. The observed dynamic portion can also be ascertained by fluorescence lifetime measurements of BSA against PPI concentration using the following equation

$$\frac{\langle\tau_0\rangle}{\langle\tau\rangle} = 1 + K_D[\text{PPI}] = 1 + K_q\langle\tau_0\rangle[\text{PPI}] \quad (10)$$

where  $\langle\tau_0\rangle$  and  $\langle\tau\rangle$  correspond to the average lifetime of BSA in native state and with the incremental addition of PPI, respectively. The value of  $K_D = (9.891 \pm 0.4) \times 10^3 \text{ M}^{-1}$  is obtained from the slope of the plot  $\langle\tau_0\rangle/\langle\tau\rangle$  versus [PPI] (Figure 6B). The value of  $K_q = K_D/\langle\tau_0\rangle = (1.64 \pm 0.06) \times 10^{12} \text{ M}^{-1} \text{ s}^{-1}$  is obtained by using the value of  $K_D$  and  $\langle\tau_0\rangle = 6.01$  ns. The calculated  $K_q$  value is 2 orders of magnitude greater than the maximum diffusion-controlled  $K_q$  value,  $2.0 \times 10^{10} \text{ M}^{-1} \text{ s}^{-1}$ .<sup>45</sup> This implies that the quenching of BSA fluorescence by PPI occurs through Coulombic resonance interaction but not operated by the diffusion process.<sup>32</sup> The fluorescence emission data were further studied by applying the modified Stern–Volmer equation<sup>45,46,50</sup>

$$\frac{F_0}{(F_0 - F)} = \frac{1}{f} + \frac{1}{f \times K_{\text{SV}}} \times \frac{1}{[\text{PPI}]} \quad (11)$$

where  $f$  is the maximum accessible fractional initial fluorescence of the protein molecule to the quencher.  $K_{\text{SV}}$  and  $f$  values are determined from the intercept and slope of the plot  $F_0/(F_0 - F)$  versus  $1/[\text{PPI}]$  (Figure S8). The evaluated value of  $K_{\text{SV}}$  is  $(5.926 \pm 0.007) \times 10^4 \text{ M}^{-1}$ . The calculated  $f$  value 1.54 indicates that 64.65% of BSA fluorescence is accessible to PPI.

The value of  $K_q$  is found to be  $(9.73 \pm 0.01) \times 10^{12} \text{ M}^{-1} \text{ s}^{-1}$ , and this high value again establishes the fact that the quenching of BSA is not operated by the diffusion-controlled process.

**Analysis of BSA–PPI Binding Equilibria and Determination of Thermodynamic Parameters.** The results obtained from the above dynamic interaction have been utilized to isolate static and dynamic quenchings in eq 8. Static quenching is defined by the following equation



where  $n$  signifies the stoichiometry of the binding process, that is, the number of PPI molecules associated with each BSA molecule. From Figure 6A, it is clearly observed that the contribution of dynamic quenching, that is, the upward curvature, becomes considerable only for  $[\text{PPI}] > 8 \mu\text{M}$  (molar ratio  $[\text{PPI}]/[\text{BSA}] > 0.8$ ). So, at a PPI concentration below  $8 \mu\text{M}$ , static quenching can be considered exclusively, as evidenced from a linear dependence of  $F/F_0$  on [PPI]. The trend of linear Stern–Volmer quenching plots for  $[\text{PPI}] < 8 \mu\text{M}$  at different temperatures is exhibited in Figure 7A. By

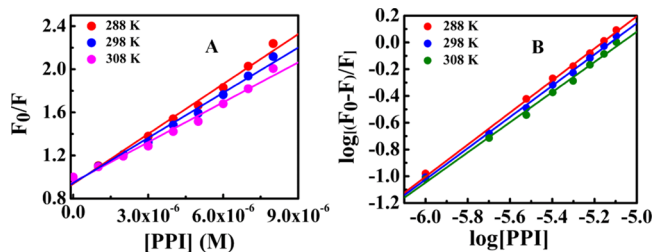


**Figure 7.** (A) Representative linear Stern–Volmer plots of PPI-induced quenching of BSA (10  $\mu\text{M}$ ) fluorescence at low PPI concentrations at different temperatures. (B) Double log plots for the determination of the number of binding sites and the binding constant value of PPI–BSA complexation at different temperatures.

varying the temperature from 288 to 308 K, the decreasing tendency of the quenching plot is observed, and the upward deviation becomes insignificant. On the basis of such type of quenching plot and data, the value of the binding constant ( $K_b$ ) and the value of  $n$  (number of binding sites) can be calculated by using eq 13<sup>45,51,52</sup>

$$\log\left[\frac{(F_0 - F)}{F}\right] = \log K_b + n \log[\text{PPI}] \quad (13)$$

Figure 7B exhibits the representative  $\log[(F_0 - F)/F]$  versus  $\log[\text{PPI}]$  plot at different temperatures, and all numerical parameters thereby obtained are tabulated in Table S1, which shows that the  $K_b$  value decreases with increasing temperature. Therefore, it can be expected that static interaction is a temperature-dependent process. The high value of  $K_b$  implies a strong binding affinity of PPI to BSA. Basically, four types of noncovalent forces, namely, van der Waal forces, multiple hydrogen-bonding, hydrophobic, and electrostatic interactions play a vital role in the binding of probes with proteins.<sup>49,53</sup> To ascertain the nature of the ground-state interaction between PPI and BSA in terms of the aforesaid noncovalent forces relevant with the complexation process, related thermodynamic parameters have been estimated by using the following van't Hoff equations<sup>54</sup>

$$\ln K_b = -\frac{\Delta H^\circ}{RT} + \frac{\Delta S^\circ}{R} \quad (14)$$



$$\Delta G^\circ = \Delta H^\circ - T\Delta S^\circ \quad (15)$$

where  $\Delta H^\circ$ ,  $\Delta S^\circ$ , and  $\Delta G^\circ$  are the standard enthalpy, entropy, and free energy changes, respectively, for the binding process.  $R$  represents the molar gas constant. The values of  $\Delta H^\circ$  and  $\Delta S^\circ$  are evaluated from the slope and intercept of the  $\ln K_b$  versus  $1/T$  plot (Figure 8).  $\Delta G^\circ$  value is then calculated by using eq

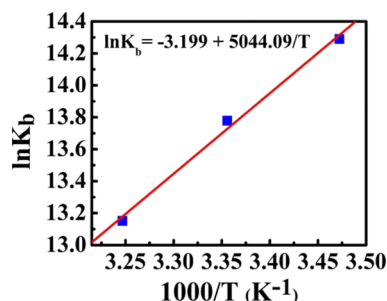


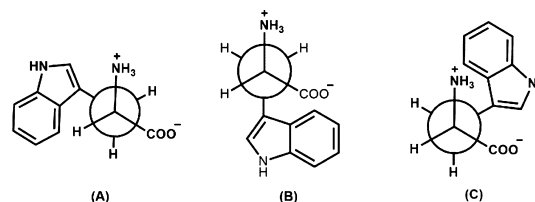
**Figure 8.** van't Hoff plot for the interaction of PPI with BSA at different temperatures.

15. The values of all related thermodynamic parameters are listed in Table S1, which show that the value of  $\Delta H^\circ$  is highly negative and  $\Delta S^\circ$  also carries a negative value. This implies that the association of PPI with BSA results from the primary contribution of van der Waals interactions, followed by the involvement of extensive hydrogen bonding interactions between PPI and BSA.<sup>55</sup> Here also, a net negative value of  $\Delta G^\circ$  implies that the interaction between PPI and BSA is spontaneous and thermodynamically favorable.

**Fluorescence Lifetime Studies.** Time-resolved fluorescence decay studies were further accomplished to explore the local microenvironment surrounding the excited probe in the proteinous environment.<sup>17,56</sup> To investigate the dynamics of PPI within the proteinous environment, a nanosecond lifetime decay study of PPI was performed in the absence and with the incremental addition of BSA. Representative decay profiles are shown in Figure S9A. The values of all related parameters are tabulated in Table S2. The lifetime decay profiles were fitted with a biexponential form instead of a monoexponential form, unless the decay curve did not fit well with the monoexponential form. The best fit for the decay profiles was carried out with acceptable values of  $\chi^2$  ( $\chi^2$  within 1.0–1.1). The probe PPI in an aqueous buffer solution is found to display a monoexponential decay with a lifetime of 4.18 ns. Table S2 reveals that the decay profile is changed from the mono- to biexponential form with two lifetime values in the presence of BSA. This is an indication toward separation of PPI into two different environments upon interaction with BSA. Here, we choose to use the average lifetime value in place of more emphasis on the individual fluorescence decay component in such a biexponential form. Table S2 shows that the average lifetime ( $\langle\tau\rangle$ ) of PPI gradually decreases with the incremental addition of BSA. The existence of binding interaction is indicated by the meaningful difference in the lifetime values between free PPI and the PPI–BSA composite.

The lifetime decay study was also performed to explore the quenching mechanism (i.e., whether it is static or dynamic or both) of BSA fluorescence by PPI. Here, lifetime decay study of BSA was executed in the absence and with the successive addition of PPI. Representative decay profiles are shown in Figure S9B. The values of all related parameters are incorporated in Table S3. The native BSA displays a

biexponential decay profile in an aqueous medium, with  $\langle\tau\rangle$  value of 6.01 ns having two decay time components of 3.69 and 6.68 ns with the corresponding relative amplitudes of 22.12 and 77.78%, respectively. This biexponential decay pattern of the native BSA has been reported earlier and attributed to the existence of two Trp moieties at distinct conformational states in two different local environments.<sup>57,58</sup> Fleming and co-workers<sup>59</sup> have examined the lifetime decays of Trp by considering a model, which is based on the conformational rotamers around the  $C^\alpha$ – $C^\beta$  bond and the comparative charge transfer rate from indole to many electrophiles. The three conformational rotamers of Trp are portrayed below:



Here, the rotamer (C) signifies the faster component, and on the contrary, the relatively slower component generally appears from quick interconversion of (A) and (B) rotamers. Nevertheless, the alteration of the relatively stable (C) rotamer to either A or B form is quite impossible on a nanosecond time scale.<sup>60–62</sup> Furthermore, it is supposed that the puckered conformation of the indole ring in the ground state turns into a planar form upon photoexcitation probably due to the delocalization of lone pairs on nitrogen, including the aromatic system. Generally, the distortion of indole ring planarity is due to the interaction with the quencher, implying the alteration of the microenvironment in the vicinity of Trp, which is the primary cause for a decrease in the lifetime value.<sup>60–62</sup> A quick look at Table S3 reveals that the relative contribution ( $\alpha_2$ ) of the faster decay time component ( $\tau_2$ ) progressively decreases from 77.88 to 69.48%, and at the same time, the relative contribution ( $\alpha_1$ ) of the slower decay time component ( $\tau_1$ ) gradually increases from 22.12 to 31.52%, with the increasing concentration of PPI. Table S3 also shows that the two decay components  $\tau_1$  and  $\tau_2$  are gradually lowered with the increasing concentration of PPI than the respective values for free BSA. The  $\langle\tau\rangle$  value of BSA gradually decreases from 6.01 ns in aqueous buffer solution to 5.01 ns with the gradual addition of PPI (inset of Figure S9B). The decrease in the  $\langle\tau\rangle$  value is a clear outcome of substantial interactions between BSA and PPI. To investigate the occurrence of dynamic quenching, a time-resolved Stern–Volmer plot was made by using the value of average lifetime, and it can be defined by eq 10. Figure 6B represents the time-resolved Stern–Volmer plot of BSA bound PPI, and it increases linearly with the PPI concentration, which in turn implies the occurrence of dynamic quenching of BSA fluorescence.

**Time-Resolved Anisotropy Decay.** The study of lifetime anisotropy decay is useful for garnering knowledge about the rotational motion and relaxation of a fluorescent probe within the proteinous environment.<sup>63</sup> To acquire more information about the neighboring microenvironment of PPI, anisotropy decay study of PPI was performed in aqueous medium in the absence and presence of the BSA protein. The representative anisotropy decay profiles are exhibited in Figure 9. PPI exhibits a monoexponential decay profile with a reorientation time of  $\sim 494$  ps, indicating a homogeneous environment around PPI. But interestingly, the anisotropy decay profile of PPI is greatly

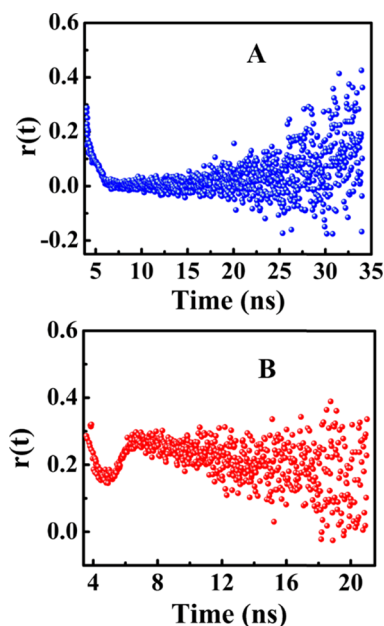


**Figure 9.** Lifetime anisotropy decay of PPI ( $\lambda_{\text{ex}} = 370$  nm and  $\lambda_{\text{monitored}} = \lambda_{\text{em}}$ ) in the (A) absence of BSA and (B) presence of BSA ( $20 \mu\text{M}$ ).

altered in the presence of BSA leading to a dip-and-rise pattern. This type of pattern signifies the co-occurrence of at least two classes of PPI populations, one with a slower rotational correlation time ( $\tau_{1r}$ ) 6.78 ns having a component ( $\alpha_{1r}$ ) of 88% and another with a faster rotational correlation time ( $\tau_{2r}$ ) 0.79 ns having a component ( $\alpha_{2r}$ ) of 12%. In accordance with the reported literature<sup>64–66</sup> on the explanation of such type of dip-and-rise pattern, the faster motion is ascribed to the existence of solvent-exposed groups or moieties of the probe, whereas, comparatively slower motion corresponds to the bound counterpart. Another probable explanation can be understood in relation with the rotational diffusion of the probe bound to two discrete binding sites (i.e., hydrophilic and hydrophobic zones) in BSA.<sup>67,68</sup> The study of molecular docking (under the Section of [Molecular Docking Results](#)) shows in support of plausible location of PPI to be in the hydrophobic binding region (i.e., in subdomain IIA of BSA). Actually, a considerable population in the hydrophilic region (i.e., in subdomain IB of BSA) seems physically not sound for neutral PPI. The above statement is only valid when the components (i.e.,  $\alpha_{1r}$  and  $\alpha_{2r}$ ) reveal the relative PPI population in the two interaction sites. The abovementioned data obviously show that the finding probability of PPI in one binding site is appreciably higher than in the other ( $\alpha_{1r} > \alpha_{2r}$ ).<sup>67–71</sup> So, the observed dip-and-rise pattern can therefore be explained by considering the fact that the probe experiences different types of rotational motions in the protein environment.<sup>69–71</sup> Such type of anisotropy decay pattern has been illustrated by the related exponential model, which links the decay parameters with the discrete anisotropy parameters as follows<sup>64–66</sup>

$$r(t) = r(0) \sum_{i=1}^n f_i(t) \exp\left(\frac{-t}{\theta_i}\right) \quad (16)$$

where

$$f_i(t) = \frac{\alpha_i \exp(-t/\tau_i)}{I_T(t)} \quad (17)$$

and

$$I_T(t) = \sum_{i=1}^n \alpha_i \exp(-t/\tau_i) \quad (18)$$

where, the  $i$ th rotational correlation time is indicated by  $\theta_i$ .  $\alpha_i$  stands for the amplitude of the  $i$ th lifetime decay component (i.e.,  $\tau_i$ ).  $r(0)$  denotes the limiting anisotropy. Generally, this type of anisotropy decay pattern has been described<sup>64–66</sup> from the outcome of the co-occurrence of two distinctly different lifetime values, which validate the importance of the time-dependent weighing factor  $f_i(t)$  in narrating such anisotropy profile, as demonstrated in eqs 16 and 17.

**Binding-Distance Measurement Using Fluorescence Resonance Energy Transfer (FRET) between PPI and BSA.** FRET is a useful spectroscopic method to delineate the structural conformations of biological and macromolecular systems such as closeness and comparative angular orientation of fluorophores, association of protein–probe composite, and so forth. The binding distance ( $r$ ) between the donor (D) and the acceptor (A) can be evaluated from this useful technique.<sup>72</sup> The efficiency of energy transfer ( $E$ ) between D and A is manifested by the considerable overlap between the emission band of D and the absorption band of A, relative orientation of transition dipoles of D and A, and the distance between D and A, which is generally  $< 8$  nm.<sup>73,74</sup> In our case, Trp residue of the BSA protein acts as the donor unit, PPI acts as the acceptor unit, and the shaded portion represents the spectral overlap

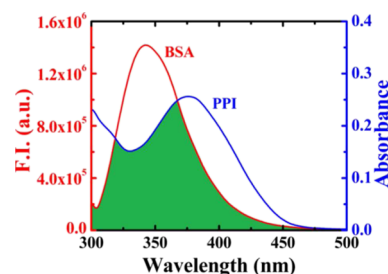


**Figure 10.** Overlap (shaded region) between the emission spectrum of BSA and the absorption spectrum of PPI at 25 °C.  $[\text{BSA}] = [\text{PPI}] = 10 \mu\text{M}$  at pH 7.4.  $\lambda_{\text{ex}}$  of BSA = 295 nm.

region between them (Figure 10). In accordance with Förster's theory,  $E$  is defined by the following equation

$$E = 1 - \frac{F}{F_0} = \frac{R_0^6}{R_0^6 + r^6} \quad (19)$$

where  $F_0$  defines the free BSA emission intensity and  $F$  corresponds to the emission intensity of BSA in the presence of PPI. The value of  $R_0$  (i.e., the Förster distance at which the effective transfer of energy is 50%) can be evaluated by using the following relation

$$R_0^6 = (8.79 \times 10^{-25}) K^2 N^{-4} \phi J \quad (20)$$

where  $K^2$  indicates the spatial orientation factor of D and A dipole.  $N$  and  $\phi$  denote the refractive index of the medium and the quantum yield of D, respectively. The overlap integral between the emission spectrum of D and the absorption spectrum of A (Figure 10) is represented by  $J$ , and its value can be obtained by using the following relation

$$J = \frac{\sum F(\lambda)\epsilon(\lambda)\lambda^4\Delta\lambda}{\sum F(\lambda)\Delta\lambda} \quad (21)$$

where,  $F(\lambda)$  and  $\epsilon(\lambda)$  correspond to the normalized emission intensity of D in the range of  $\lambda$  to  $(\lambda + \Delta\lambda)$  and the molar extinction coefficient of A at  $\lambda$ , respectively.<sup>75</sup> In the present case,  $K^2 = 2/3$ ,  $N = 1.336$ , and  $\varphi = 0.15$ .<sup>50,76</sup> According to eqs 19–21, parameters evaluated thereby are summarized in Table 2. The distance  $r$  between the donor unit BSA and the acceptor

**Table 2.** FRET Parameters for the BSA–PPI Composite at 25 °C

protein	probe	$J$ ( $\text{cm}^3\cdot\text{L}\cdot\text{mol}^{-1}$ )	$R_0$ (nm)	$E$	$r$ (nm)
BSA	PPI	$3.17 \times 10^{-14}$	3.09	0.54	3.04

unit PPI after the binding interaction was  $<8$  nm, and  $0.5R_0 < r < 1.5R_0$  infers the occurrence of energy transfer from BSA to PPI with high possibility.<sup>77</sup>

**Conformation Investigations: Circular Dichroism (CD) Study.** The variations of the BSA secondary structure with the gradual addition of PPI were carried out by far-UV circular dichroism (CD) spectral studies in aqueous buffer solution, which show a typical profile (Figure 11) having two negative

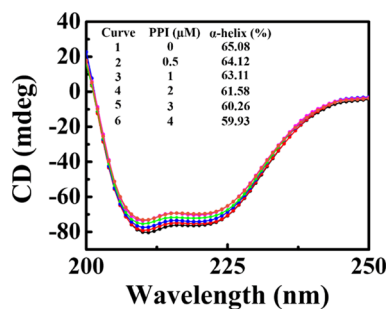


**Figure 11.** CD spectral profiles of BSA (0.75  $\mu\text{M}$ ) with increasing concentrations of PPI at 25 °C. The inset exhibits the estimated change in the  $\alpha$ -helix content ( $\pm 3\%$ ) of BSA with the gradual addition of PPI.

bands at  $\sim 209$  and  $\sim 222$  nm, clearly indicating the presence of an  $\alpha$ -helix-rich secondary structure in the BSA protein.<sup>78</sup> These two minima in the CD spectra arise generally because of the  $n \rightarrow \pi^*$  charge transfer transition.<sup>79</sup> Figure 11 shows a decrement in the CD signal with no significant shift of the peak position, implying the PPI-induced conformational change of the native BSA regarding the decrement of the  $\alpha$ -helix content in BSA. The  $\alpha$ -helix percentage in BSA can be determined by considering the following relation<sup>63</sup>

$$\% \alpha\text{-helix} = \frac{-(\text{MRE}_{222} - 2340)}{30\,300} \times 100 \quad (22)$$

where, the observed ellipticity values ( $\theta_{\text{obs}}$  in mdeg at 222 nm) are used to evaluate the mean residue ellipticity (MRE) value by taking the following relation<sup>63</sup>

$$\text{MRE} (\text{deg}\cdot\text{cm}^2\cdot\text{dmo}^{-1}) = \frac{\theta_{\text{obs}}}{C_p n l \times 10} \quad (23)$$

where, the molar concentration of BSA is denoted by  $C_p$ .  $n$  indicates the number of amino acid residues (583 for BSA).<sup>5–7,80,81</sup> The cell path length is represented by  $l$  (here 1 cm). The estimated  $\alpha$ -helix content in native BSA is found to be 65.08 ( $\pm 3$ )%, which is in good accordance with the literature value.<sup>5–7,80,81</sup> A decrease in the  $\alpha$ -helix content from  $\sim 65.08$  ( $\pm 3$ )% in the native BSA to  $\sim 59.93$  ( $\pm 3$ )% in the presence of 4  $\mu\text{M}$  PPI (inset of Figure 11) thus obviously shows a PPI-induced perturbation of the secondary structure of BSA.

**Molecular Docking Results.** The crystal structure analysis of BSA revealed that it is primarily composed of three homologous domains (I, II, and III), and each domain contains two subdomains (A and B).<sup>82</sup> The major binding sites of BSA for various probes (exogenous and endogenous) are located in subdomains IIA and IIIA, known as Sudlow's sites I and II, respectively.<sup>83</sup> A number of probes or drugs are available, which specifically bind either at site I or site II in BSA.<sup>37,84,85</sup> We have performed molecular docking study to find out whether the probe binds at site I or site II in BSA and the probable interactions involved during the association. Out of 10 different conformers, the lowest binding energy conformer was selected for analysis. The docking results are presented in Figure 12. Panel A in Figure 12 reveals that site I in subdomain IIA of BSA is the preferable binding site for the probe PPI, and this has been supported from site marker experiments. The middle panel shows the magnified view of the microenvironment around the PPI binding site in subdomain IIA of BSA near the Trp 213 residue. The possible hydrogen-bonded interaction between the nitrogen and nitrogen-bonded hydrogen atoms of PPI with Arg 217 (2.7 Å) and Asp 450 (3.2 Å) plays a crucial role in stabilizing probe-binding (Figure 12C). In addition, the probe is surrounded by various hydrophobic and polar residues. Amino acid residues such as Leu 197, Trp 213, and Val 292 provided an additional stability to the complex through hydrophobic interactions. Moreover, a number of charged and polar residues such as Arg 198, Arg 217, Lys 221, Lys 294, and so forth play a secondary role in stabilizing the PPI molecule through electrostatic interactions. Thus, docking results suggested that PPI was bound to BSA by three possible interactions, namely hydrophobic, electrostatic, and hydrogen-

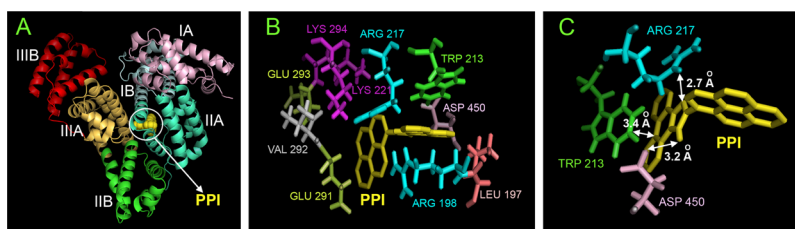


**Figure 12.** Molecular docking of PPI with the three-dimensional structure of BSA (PDB ID: 4JK4). (A) Docking pose of PPI with BSA shown by the white circle. (B) Magnified view of the binding site of PPI in subdomain IIA. (C) Distance between the neighboring hydrogen-bonded residues and TRP 213 from the probe (PPI) molecule.



bonding. According to Zhang et al., increased hydrophobicity is a measure of increased stability.<sup>86</sup> The formation of the hydrogen bond reduces the extent of hydrophilicity and causes a significant increment in the hydrophobicity, which stabilizes the PPI–BSA complex.<sup>87</sup> Distance between the probe and the Trp 213 residue was 3.4 Å (Figure 12C), and the free energy (from the docking simulation) for the binding of PPI to subdomain IIA of BSA was found to be  $-5.01 \text{ kcal mol}^{-1}$ . It is already known that Trp 134 and Trp 213 residues are responsible for the intrinsic fluorescence of BSA.<sup>31</sup> The docking result illustrates that the probe binds in the near vicinity of Trp 213 in the binding pocket of site I, which in turn causes a perturbation in the fluorescence intensity of BSA, more specifically, quenches the emission of the Trp 213 residue. Thus, molecular docking study supported the experimental findings from the theoretical approach.

## CONCLUSIONS

Here, we report a phenanthrene–pyrene-based fluorescent probe (PPI) as a molecular reporter to study the microheterogeneous environment of the BSA protein. The association between BSA and PPI has been clearly demonstrated by the UV–vis spectral change at 280 nm. The observed blue shift of the emission maximum along with an increment of the fluorescence intensity is due to the movement of PPI from a more polar aqueous environment to a more hydrophobic protein environment. The fluorescence titration of BSA with PPI resulted in a binding constant of  $(1.12 \pm 0.06) \times 10^5 \text{ M}^{-1}$ , which is in excellent agreement with the value obtained from steady-state anisotropy studies. The study on fluorescence quenching induced by PPI reveals the occurrence of both static and dynamic quenching mechanisms. The occurrence of dynamic quenching is indicated by the linear increase in  $\langle\tau_0\rangle/\langle\tau\rangle$  with the increasing concentration of PPI. The ground-state complexation between PPI and BSA is characterized by a large binding constant, which is very sensitive to the temperature because of a negative  $\Delta H^\circ$  value. The complexation process is also associated with a negative  $\Delta S^\circ$ , which implies that the van der Waals interactions and hydrogen-bonding interactions play the most significant roles in stabilizing the BSA–PPI complex. From the FRET study, the average distance between Trp 213 of the BSA donor and the PPI acceptor is found to be 3.04 nm, and it is close enough for nonradiative energy transfer to occur from BSA to PPI. The CD spectral studies imply PPI-induced conformational change of the native BSA in terms of decrease of the  $\alpha$ -helix content in BSA. The site-selective binding and molecular docking studies reveal that PPI binds with BSA at site I in subdomain IIA, that is, Trp 213 is near or within the binding site of PPI. The present fluorescent probe having a planar structure could be utilized as a potential site-selective biomarker for site I in subdomain IIA.

## EXPERIMENTAL SECTION

**Materials.** All starting materials were of reagent grade. BSA, ibuprofen, warfarin, ANS, phenanthrene-9,10-dione, and 1-pyrene carboxaldehyde were procured from Sigma-Aldrich and used as received. Deionized water from Milli-Q source was used throughout the study.

**Physical Measurements.** Fourier transform infrared (FTIR) spectra ( $4000\text{--}400 \text{ cm}^{-1}$ ) were recorded on a PerkinElmer RX I FTIR spectrophotometer with a solid KBr

disc. The UV–vis spectral studies were recorded on an Agilent diode array spectrophotometer (Agilent 8453). Steady-state fluorescence spectra were recorded on a PTI spectrofluorimeter (Model QM-40) by using a fluorescence-free quartz cuvette of 1 cm path length. The excitation and emission slit widths were fixed at 3 nm. A Bruker 300 MHz spectrophotometer was used to run the  $^1\text{H}$  and  $^{13}\text{C}$  NMR spectra in dimethyl sulfoxide ( $\text{DMSO-}d_6$ ) with trimethylsilane as an internal standard. The electrospray ionization mass spectra (ESI-MS<sup>+</sup>) ( $m/z$ ) of the probe was recorded on a HRMS spectrophotometer (QTOF Micro YA263). The time-correlated single-photon counting measurements using a picosecond diode laser (IBH Nanoled-07) in an IBH fluorocube apparatus were used to determine the fluorescence lifetimes. A Hamamatsu MCP photomultiplier (R3809) was used to collect the fluorescence decay data, which were further examined by the IBH DAS6 software. CD spectral studies were recorded on a PC-driven JASCO J815 (Japan) spectropolarimeter.

**Synthesis of 2-(Pyren-1-yl)-1H-phenanthro[9,10-d]-imidazole (PPI).** The probe was synthesized by the previously reported method<sup>88</sup> with slight modification. A mixture of phenanthrene-9,10-dione (1.04 g, 5 mmol), 1-pyrene carboxaldehyde (1.15 g, 5 mmol), and ammonium acetate (2.89 g, 37.45 mmol) were dissolved in glacial acetic acid (40 mL). Then, the resulting solution was refluxed at  $110^\circ\text{C}$  for 20 h in a nitrogen atmosphere, during which time a yellowish green solid was formed. An excess of deionized water (30 mL) was added to complete the precipitation. The crude product was collected by filtration, washed with water, and dried by suction (Scheme 1).  $^1\text{H}$  NMR ( $\text{DMSO-}d_6$ ):  $\delta$  in ppm 10.81 (s, 1H), 9.03 (d, 2H,  $J = 7.8 \text{ Hz}$ ), 8.79 (d, 3H,  $J = 6.63 \text{ Hz}$ ), 8.70 (d, 1H,  $J = 8.1 \text{ Hz}$ ), 8.60 (d, 1H,  $J = 7.92 \text{ Hz}$ ), 8.45 (m, 5H), 8.23 (d, 1H,  $J = 7.8 \text{ Hz}$ ), 7.87 (t, 4H) (Figure S1).  $^{13}\text{C}$  NMR ( $\text{DMSO-}d_6$ ):  $\delta$  in ppm 147.51, 133.49, 131.25, 130.68, 130.06, 129.81, 129.37, 128.98, 128.50, 127.74, 127.58, 127.15, 126.82, 125.24, 124.83, 124.28, 123.79, 123.17, 123.05 (Figure S2). ESI-MS<sup>+</sup> (experimental):  $m/z$ : 419.1546 [ $\text{C}_{31}\text{H}_{18}\text{N}_2 + \text{H}^+$ ], theoretical:  $m/z$ : 419.1548 (Figure S3). IR spectrum:  $\tilde{\nu}$ :  $3454 \text{ cm}^{-1}$  (–NH),  $1646 \text{ cm}^{-1}$  (–C=N) (Figure S4).

**Experimental Solution.** A 10 mM Tris buffer solution (100 mL) of pH 7.4 was prepared in deionized water, which was used in all experiments. A stock solution was prepared by dissolving the required amount of BSA ( $M_{\text{BSA}} = 66\,400 \text{ g mol}^{-1}$ ) in pH 7.4 Tris-HCl buffer solution, and the exact concentration was determined spectrophotometrically using the molar extinction coefficient  $44\,000 \text{ M}^{-1} \text{ cm}^{-1}$  at 280 nm,<sup>89</sup> whereas the 10 mL stock solution of PPI ( $1.0 \times 10^{-3} \text{ M}$ ) was prepared in dimethyl formamide because of its poor solubility in water. Each solution was mixed properly before all spectral experiments at  $25^\circ\text{C}$ .

**Methods.** All details of experimental methods are provided in the Supporting Information.

**Molecular Docking Simulation Study.** Molecular docking simulation studies using AutoDock (version 4.2) help to identify the probable binding site and mode of binding of the probe PPI with BSA. The RCSB Protein Data Bank (PDB ID: 4JK4) was used as a source of X-ray crystal structure of BSA. The Chem3D Ultra 8.0 was used to draw the probe structure, which was further modified using Gaussian 09W and AutoDock 4.2 programs. Gasteiger partial charges were added to the probe atoms. The nonpolar hydrogen atoms were united, and rotatable bonds were defined. Grid maps of  $126 \times 126 \times 126 \text{ \AA}$  grid points and  $0.403 \text{ \AA}$  grid spacing were generated

using the AutoGrid program. The default values were used for other AutoDock parameters. The Lamarckian genetic algorithm (LGA) was used for docking calculations and the parameters were set to 100 GA runs for each docking simulation upto 250 000 energy evaluations. The population size was set to 150 with a crossover rate of 0.8 (LGA). For further analysis of docking simulations, we chose the best optimized docked model with the lowest energy, and this was best viewed in PyMOL software.

## ■ ASSOCIATED CONTENT

### ■ Supporting Information

The Supporting Information is available free of charge on the ACS Publications website at DOI: [10.1021/acsomega.8b00186](https://doi.org/10.1021/acsomega.8b00186).

Characterization data of compound PPI:  $^1\text{H}$  NMR,  $^{13}\text{C}$  NMR, HRMS, and IR; Job's plot for the binding of PPI to BSA; plot for ANS displacement study; modified Stern–Volmer plot of PPI-induced quenching of BSA; lifetime spectra of PPI in the absence and presence of BSA; lifetime spectra of BSA in the absence and presence of PPI; table for experimentally calculated quenching data and lifetime data; and experimental methods (PDF)

## ■ AUTHOR INFORMATION

### Corresponding Author

\*E-mail: [m\\_ali2062@yahoo.com](mailto:m_ali2062@yahoo.com). Fax: 91-33-2414-6223 (M.A.).

### ORCID

Suman Das: 0000-0002-4148-1002

Mahammad Ali: 0000-0003-0756-0468

### Notes

The authors declare no competing financial interest.

## ■ ACKNOWLEDGMENTS

Financial supports from the CSIR (ref. 01(2896)/17/EMR-II), New Delhi and the DST (ref. no. 809(Sanc)/ST/P/S&T/4G-9/2104), West Bengal are gratefully acknowledged. M.S. gratefully acknowledges the UGC, New Delhi for the fellowship (UGC-NET, JRF). R.B. thanks the CSIR, New Delhi for the fellowship (SRF).

## ■ REFERENCES

- (1) Royer, C. A. Probing Protein Folding and Conformational Transitions with Fluorescence. *Chem. Rev.* **2006**, *106*, 1769–1784.
- (2) Cohen, B. E.; McAnaney, T. B.; Park, E. S.; Jan, Y. N.; Boxer, S. G.; Jan, L. Y. Probing Protein Electrostatics with a Synthetic Fluorescent Amino Acid. *Science* **2002**, *296*, 1700–1703.
- (3) Abou-Zied, O. K.; Al-Shihi, O. I. K. Characterization of Subdomain IIA Binding Site of Human Serum Albumin in its Native, Unfolded, and Refolded States Using Small Molecular Probes. *J. Am. Chem. Soc.* **2008**, *130*, 10793–10801.
- (4) Er, J. C.; Vendrell, M.; Tang, M. K.; Zhai, D.; Chang, Y.-T. Fluorescent Dye Cocktail for Multiplex Drug-Site Mapping on Human Serum Albumin. *ACS Comb. Sci.* **2013**, *15*, 452–457.
- (5) Peters, T., Jr. Serum Albumin. *Adv. Protein Chem.* **1985**, *37*, 161–245.
- (6) Brown, J. R. Some aspects of the structure and conformational properties of serum albumin. In *Albumin Structure, Function and Uses*; Foster, J. F., Ed.; Pergamon Press: Oxford, U.K., 1977; pp 53–84.
- (7) He, X. M.; Carter, D. C. Atomic Structure and Chemistry of Human Serum Albumin. *Nature* **1992**, *358*, 209–215.

(8) Helms, M. K.; Petersen, C. E.; Bhagavan, N. V.; Jameson, D. M. Time-Resolved Fluorescence Studies on Site-Directed Mutants of Human Serum Albumin. *FEBS Lett.* **1997**, *408*, 67–70.

(9) Peters, T., Jr. *All About Albumins: Biochemistry, Genetics and Medical Applications*; Academic Press: San Diego, CA, 1996; pp 76–132.

(10) McClellan, S. J.; Franses, E. I. Effect of concentration and denaturation on adsorption and surface tension of bovine serum albumin. *Colloids Surf., B* **2003**, *28*, 63–75.

(11) Majorek, K. A.; Porebski, P. J.; Dayal, A.; Zimmerman, M. D.; Jablonska, K.; Stewart, A. J.; Chruszcz, M.; Minor, W. Structural and Immunologic Characterization of Bovine, Horse, and Rabbit Serum Albumins. *Mol. Immunol.* **2012**, *52*, 174–182.

(12) Servagent-Noinville, S.; Revault, M.; Quiquampoix, H.; Baron, M.-H. Conformational Changes of Bovine Serum Albumin Induced by Adsorption on Different Clay Surfaces: FTIR Analysis. *J. Colloid Interface Sci.* **2000**, *221*, 273–283.

(13) Kudelski, A. Influence of electrostatically bound proteins on the structure of linkage monolayers: adsorption of bovine serum albumin on silver and gold substrates coated with monolayers of 2-Mercaptoethanesulphonate. *Vib. Spectrosc.* **2003**, *33*, 197–204.

(14) Sudlow, G.; Birkett, D. J.; Wade, D. N. The Characterization of Two Specific Drug Binding Sites on Human Serum Albumin. *Mol. Pharmacol.* **1975**, *11*, 824–832.

(15) Sudlow, G.; Birkett, D. J.; Wade, D. N. Further Characterization of Specific Drug Binding Sites on Human Serum Albumin. *Mol. Pharmacol.* **1976**, *12*, 1052–1061.

(16) Suzuki, Y.; Yokoyama, K. Design and Synthesis of Intramolecular Charge Transfer-Based Fluorescent Reagents for the Highly-Sensitive Detection of Proteins. *J. Am. Chem. Soc.* **2005**, *127*, 17799–17802.

(17) Mallick, A.; Haldar, B.; Chattopadhyay, N. Spectroscopic Investigation on the Interaction of ICT Probe 3-Acetyl-4-oxo-6,7-dihydro-12H Indolo-[2,3-a] Quinolizine with Serum Albumins. *J. Phys. Chem. B* **2005**, *109*, 14683–14690.

(18) Das, R.; Guha, D.; Mitra, S.; Kar, S.; Lahiri, S.; Mukherjee, S. Intramolecular Charge Transfer as Probing Reaction: Fluorescence Monitoring of Protein–Surfactant Interaction. *J. Phys. Chem. A* **1997**, *101*, 4042–4047.

(19) Weber, G. *Light and Life*; McElory, W. D., Glass, B., Eds.; Johns Hopkins: Baltimore, MD, 1961; pp 82–106.

(20) Barreleiro, P. C. A.; Lindman, B. The Kinetics of DNA–Cationic Vesicle Complex Formation. *J. Phys. Chem. B* **2003**, *107*, 6208–6213.

(21) Demchenko, A. P. *Topics in Fluorescence Spectroscopy: Biochemical Applications*; Lakowicz, J. R., Ed.; Plenum: New York, 1992; Vol. 3, p 65.

(22) Cárdenas, M.; Schillén, K.; Pebalk, D.; Nylander, T.; Lindman, B. Interaction between DNA and Charged Colloids Could Be Hydrophobically Driven. *Biomacromolecules* **2005**, *6*, 832–837.

(23) Haldar, B.; Chakrabarty, A.; Mallick, A.; Mandal, M. C.; Das, P.; Chattopadhyay, N. Fluorometric and Isothermal Titration Calorimetric Studies on Binding Interaction of a Telechelic Polymer with Sodium Alkyl Sulfates of Varying Chain Length. *Langmuir* **2006**, *22*, 3514–3520.

(24) Chakrabarty, A.; Ghosh, S.; Kar, S.; Nath, D. N.; Guchhait, N. Dual emission from (*E*)-3-(4-methylamino-phenyl)-acrylic acid ethyl ester (MAPAEE) and its application as fluorescence probe for studying micellar and protein microenvironment. *J. Mol. Struct.* **2009**, *917*, 148–157.

(25) Ghosh, S.; Guchhait, N. Chemically Induced Unfolding of Bovine Serum Albumin by Urea and Sodium Dodecyl Sulfate: A Spectral Study with the Polarity-Sensitive Charge-Transfer Fluorescent Probe (*E*)-3-(4-Methyl aminophenyl)acrylic Acid Methyl Ester. *ChemPhysChem* **2009**, *10*, 1664–1671.

(26) Mahanta, S.; Singh, R. B.; Guchhait, N. Study of Protein–Probe Interaction and Protective Action of Surfactant Sodium Dodecyl Sulphate in Urea-Denatured HSA using Charge Transfer Fluorescence

Probe Methyl Ester of *N,N*-Dimethylamino Naphthyl Acrylic Acid. *J. Fluoresc.* **2009**, *19*, 291–302.

(27) Ghosh, S.; Jana, S.; Nath, D.; Guchhait, N. Fluorescent Probing of Protein Bovine Serum Albumin Stability and Denaturation Using Polarity Sensitive Spectral Response of a Charge Transfer Probe. *J. Fluoresc.* **2011**, *21*, 365–374.

(28) Côté, B.; Boulet, L.; Brideau, C.; Claveau, D.; Ethier, D.; Frenette, R.; Gagnon, M.; Giroux, A.; Guay, J.; Guiral, S.; Mancini, J.; Martins, E.; Massé, F.; Méthot, N.; Riendeau, D.; Rubin, J.; Xu, D.; Yu, H.; Ducharme, Y.; Friesen, R. W. Substituted phenanthrene imidazoles as potent, selective, and orally active mPGES-1 inhibitors. *Bioorg. Med. Chem. Lett.* **2007**, *17*, 6816–6820.

(29) Guédouar, H.; Aloui, F.; Beltifa, A.; Mansour, H. B.; Hassine, B. B. Synthesis and characterization of phenanthrene derivatives with anticancer property against human colon and epithelial cancer cell lines. *C. R. Chim.* **2017**, *20*, 841–849.

(30) Hu, Y.-J.; Liu, Y.; Wang, J.-B.; Xiao, X.-H.; Qu, S.-S. Study of the interaction between monoammonium glycyrrhizinate and bovine serum albumin. *J. Pharm. Biomed. Anal.* **2004**, *36*, 915–919.

(31) Li, D.; Zhu, M.; Xu, C.; Chen, J.; Ji, B. The Effect of  $\text{Cu}^{2+}$  or  $\text{Fe}^{3+}$  on the Noncovalent Binding of Rutin with Bovine Serum Albumin by Spectroscopic Analysis. *Spectrochim. Acta, Part A* **2011**, *78*, 74–79.

(32) Gentili, P. L.; Ortica, F.; Favaro, G. Static and Dynamic Interaction of a Naturally Occurring Photochromic Molecule with Bovine Serum Albumin Studied by UV–Visible Absorption and Fluorescence Spectroscopy. *J. Phys. Chem. B* **2008**, *112*, 16793–16801.

(33) Gensch, T.; Hendriks, J.; Hellingwerf, K. J. Tryptophan fluorescence monitors structural changes accompanying signalling state formation in the photocycle of photoactive yellow protein. *Photochem. Photobiol. Sci.* **2004**, *3*, 531–536.

(34) Jana, S.; Dalapati, S.; Ghosh, S.; Guchhait, N. Binding interaction between plasma protein bovine serum albumin and flexible charge transfer fluorophore: A spectroscopic study in combination with molecular docking and molecular dynamics simulation. *J. Photochem. Photobiol., A* **2012**, *231*, 19–27.

(35) Sahoo, B. K.; Ghosh, K. S.; Dasgupta, S. Investigating the Binding of Curcumin Derivatives to Bovine Serum Albumin. *Biophys. Chem.* **2008**, *132*, 81–88.

(36) Burstein, E. A.; Vedenkina, N. S.; Ivkova, M. N. Fluorescence and the Location of Tryptophan residues in Protein Molecules. *Photochem. Photobiol.* **1973**, *18*, 263–279.

(37) Bhuiya, S.; Pradhan, A. B.; Haque, L.; Das, S. Molecular Aspects of the Interaction of Iminium and Alkanolamine Forms of the Anticancer Alkaloid Chelerythrine with Plasma Protein Bovine Serum Albumin. *J. Phys. Chem. B* **2016**, *120*, 5–17.

(38) Benesi, H. A.; Hildebrand, J. H. A Spectrophotometric Investigation of the Interaction of Iodine with Aromatic Hydrocarbons. *J. Am. Chem. Soc.* **1949**, *71*, 2703–2707.

(39) Jash, C.; Payghan, P. V.; Ghoshal, N.; Kumar, G. S. Binding of the Iminium and Alkanolamine Forms of Sanguinarine to Lysozyme: Spectroscopic Analysis, Thermodynamics, and Molecular Modeling Studies. *J. Phys. Chem. B* **2014**, *118*, 13077–13091.

(40) Ray, D.; Kundu, A.; Pramanik, A.; Guchhait, N. Exploring the Interaction of a Micelle Entrapped Biologically Important Proton Transfer Probe with the Model Transport Protein Bovine Serum Albumin. *J. Phys. Chem. B* **2015**, *119*, 2168–2179.

(41) Lakowicz, J. R. Fluorescence Anisotropy. *Principles of Fluorescence Spectroscopy*, 3rd ed.; Springer: New York, USA, 2006; pp 353–381.

(42) Ingersoll, C. M.; Strollo, C. M. Steady-State Fluorescence Anisotropy to Investigate Flavonoids Binding to Proteins. *J. Chem. Educ.* **2007**, *84*, 1313–1315.

(43) Baroni, S.; Mattu, M.; Vannini, A.; Cipollone, R.; Aime, S.; Ascenzi, P.; Fasano, M. Effect of Ibuprofen and Warfarin on the Allosteric Properties of Haem-Human Serum Albumin. A spectroscopic Study. *Eur. J. Biochem.* **2001**, *268*, 6214–6220.

(44) Dufour, C.; Dangles, O. Flavonoid-Serum Albumin Complexation: Determination of Binding Constants and Binding Sites by

Fluorescence Spectroscopy. *Biochim. Biophys. Acta, Gen. Subj.* **2005**, *1721*, 164–173.

(45) Lakowicz, J. R. Quenching of Fluorescence. *Principles of Fluorescence Spectroscopy*, 3rd ed.; Springer: New York, USA, 2006; pp 278–327.

(46) Ghosh, N.; Mondal, R.; Mukherjee, S. Inverse Temperature Dependence in Static Quenching versus Calorimetric Exploration: Binding Interaction of Chloramphenicol to  $\beta$ -Lactoglobulin. *Langmuir* **2015**, *31*, 8074–8080.

(47) Zhang, Y.-Z.; Zhou, B.; Liu, Y.-X.; Zhou, C.-X.; Ding, X.-L.; Liu, Y. Fluorescence study on the Interaction of Bovine Serum Albumin with *p*-Aminoazobenzene. *J. Fluoresc.* **2008**, *18*, 109–118.

(48) Mandal, P.; Ganguly, T. Fluorescence Spectroscopic Characterization of the Interaction of Human Adult Hemoglobin and Two Isatins, 1-Methylisatin and 1-Phenylisatin: A comparative Study. *J. Phys. Chem. B* **2009**, *113*, 14904–14913.

(49) Ojha, B.; Das, G. The Interaction of 5-(Alkoxy)naphthalen-1-amine with Bovine Serum Albumin and Its Effect on the Conformation of Protein. *J. Phys. Chem. B* **2010**, *114*, 3979–3986.

(50) Shaikh, S. M. T.; Seetharamappa, J.; Kandagal, P. B.; Ashoka, S. Binding of the bioactive component isothipendyl hydrochloride with bovine serum albumin. *J. Mol. Struct.* **2006**, *786*, 46–52.

(51) Bi, S.; Ding, L.; Tian, Y.; Song, D.; Zhou, X.; Liu, X.; Zhang, H. Investigation of the interaction between flavonoids and human serum albumin. *J. Mol. Struct.* **2004**, *703*, 37–45.

(52) Feng, X.-Z.; Lin, Z.; Yang, L.-J.; Wang, C.; Bai, C.-L. Investigation of the interaction between acridine orange and bovine serum albumin. *Talanta* **1998**, *47*, 1223–1229.

(53) Patel, R.; Mir, M. U. H.; Maurya, J. K.; Singh, U. K.; Maurya, N.; Parray, M. u. d.; Khan, A. B.; Ali, A. Spectroscopic and molecular modelling analysis of the interaction between ethane-1,2-diyl bis(*N,N*-dimethyl-*N*-hexadecyl-ammoniumacetoxo)dichloride and bovine serum albumin. *Luminescence* **2015**, *30*, 1233–1241.

(54) van Holde, K. E.; Johnson, W. C.; Ho, P. S. Thermodynamics and Biochemistry. *Principles of Physical Biochemistry*, 2nd ed.; Pearson Higher Education: Upper Saddle River, NJ, USA, 2006; pp 72–106.

(55) Ross, P. D.; Subramanian, S. Thermodynamics of protein association reactions: forces contributing to stability. *Biochemistry* **1981**, *20*, 3096–3102.

(56) Das, P.; Mallick, A.; Chakrabarty, A.; Haldar, B.; Chattopadhyay, N. Effect of nanocavity confinement on the rotational relaxation dynamics: 3-acetyl-4-oxo-6,7-dihydro-12H indolo-[2,3-*a*] quinolizine in micelles. *J. Chem. Phys.* **2006**, *125*, 044516.

(57) Anand, U.; Jash, C.; Mukherjee, S. Protein unfolding and subsequent refolding: a spectroscopic investigation. *Phys. Chem. Chem. Phys.* **2011**, *13*, 20418–20426.

(58) Chatterjee, S.; Mukherjee, T. K. Spectroscopic investigation of interaction between bovine serum albumin and amine-functionalized silicon quantum dots. *Phys. Chem. Chem. Phys.* **2014**, *16*, 8400–8408.

(59) Petrich, J. W.; Chang, M. C.; McDonald, D. B.; Fleming, G. R. On the origin of nonexponential fluorescence decay in tryptophan and its derivatives. *J. Am. Chem. Soc.* **1983**, *105*, 3824–3832.

(60) Anand, U.; Jash, C.; Boddepalli, R. K.; Shrivastava, A.; Mukherjee, S. Exploring the Mechanism of Fluorescence Quenching in Proteins Induced by Tetracycline. *J. Phys. Chem. B* **2011**, *115*, 6312–6320.

(61) Anand, U.; Kurup, L.; Mukherjee, S. Deciphering the role of pH in the binding of Ciprofloxacin Hydrochloride to Bovine Serum Albumin. *Phys. Chem. Chem. Phys.* **2012**, *14*, 4250–4258.

(62) Anand, U.; Mukherjee, S. Reversibility in Protein Folding: Effect of  $\beta$ -Cyclodextrin on Bovine Serum Albumin Unfolded by Sodium Dodecyl Sulphate. *Phys. Chem. Chem. Phys.* **2013**, *15*, 9375–9383.

(63) Paul, B. K.; Ghosh, N.; Mukherjee, S. Interplay of Multiple Interaction Forces: Binding of Norfloxacin to Human Serum Albumin. *J. Phys. Chem. B* **2015**, *119*, 13093–13102.

(64) Paul, B. K.; Guchhait, N. Modulated Photophysics of an ESIPT Probe 1-Hydroxy-2-naphthaldehyde within Motionally Restricted Environments of Liposome Membranes Having Varying Surface Charges. *J. Phys. Chem. B* **2010**, *114*, 12528–12540.



- (65) Broos, J.; Visser, A. J. W. G.; Engbersen, J. F. J.; Verboom, W.; van Hoek, A.; Reinhoudt, D. N. Flexibility of Enzymes Suspended in Organic Solvents Probed by Time-Resolved Fluorescence Anisotropy. Evidence that Enzyme Activity and Enantioselectivity Are Directly Related to Enzyme Flexibility. *J. Am. Chem. Soc.* **1995**, *117*, 12657–12663.
- (66) Fuentealba, D.; Kato, H.; Nishijima, M.; Fukuhara, G.; Mori, T.; Inoue, Y.; Bohne, C. Explaining the Highly Enantiomeric Photocyclodimerization of 2-Anthracenecarboxylate Bound to Human Serum Albumin Using Time-Resolved Anisotropy Studies. *J. Am. Chem. Soc.* **2013**, *135*, 203–209.
- (67) Paul, B. K.; Guchhait, N. Modulation of Prototropic Activity and Rotational Relaxation Dynamics of a Cationic Biological Photosensitizer within the Motionally Constrained Bio-environment of a Protein. *J. Phys. Chem. B* **2011**, *115*, 10322–10334.
- (68) Paul, B. K.; Guchhait, N. Exploring the Strength, Mode, Dynamics, and Kinetics of Binding Interaction of a Cationic Biological Photosensitizer with DNA: Implication on Dissociation of the Drug–DNA Complex via Detergent Sequestration. *J. Phys. Chem. B* **2011**, *115*, 11938–11949.
- (69) Bhattacharya, B.; Nakka, S.; Guruprasad, L.; Samanta, A. Interaction of Bovine Serum Albumin with Dipolar Molecules: Fluorescence and Molecular Docking Studies. *J. Phys. Chem. B* **2009**, *113*, 2143–2150.
- (70) Quitevis, E. L.; Marcus, A. H.; Fayer, M. D. Dynamics of ionic lipophilic probes in micelles: picosecond fluorescence depolarization measurements. *J. Phys. Chem.* **1993**, *97*, 5762–5769.
- (71) Ariola, F. S.; Mudaliar, D. J.; Walvick, R. P.; Heikal, A. A. Dynamics imaging of lipid phases and lipid-marker interactions in model biomembranes. *Phys. Chem. Chem. Phys.* **2006**, *8*, 4517–4529.
- (72) Shahabadi, N.; Maghsudi, M.; Rouhani, S. Study on the Interaction of Food Colourant Quinoline Yellow with Bovine Serum Albumin by Spectroscopic Techniques. *Food Chem.* **2012**, *135*, 1836–1841.
- (73) Valeur, B.; Brochon, J. C. *New Trends in Fluorescence Spectroscopy: Applications to Chemical and Life Science*, 6th ed.; Springer Press: Berlin, 1999; p 25.
- (74) Förster, T. Delocalized excitation and excitation transfer. In *Modern Quantum Chemistry Part III: Action of Light and Organic Crystals*; Sinanoglu, O., Ed.; Academic Press: New York, 1965; pp 93–137.
- (75) Ma, F.; Huang, H.-Y.; Zhou, L.; Yang, C.; Zhou, J.-H.; Liu, Z.-M. Study on the Conformation Changes of Lysozyme Induced by Hypocrellin A: The Mechanism Investigation. *Spectrochim. Acta, Part A* **2012**, *97*, 1159–1165.
- (76) Ding, F.; Huang, J.; Lin, J.; Li, Z.; Liu, F.; Jiang, Z.; Sun, Y. A Study of the Binding of C.I. Mordant Red 3 with Bovine Serum Albumin using Fluorescence Spectroscopy. *Dyes Pigm.* **2009**, *82*, 65–70.
- (77) Kitamura, M.; Murakami, K.; Yamada, K.; Kawai, K.; Kunishima, M. Binding of sulforhodamine B to human serum albumin: a spectroscopic study. *Dyes Pigm.* **2013**, *99*, 588–593.
- (78) Serro, A. P.; Bastos, M.; Pessoa, J. C.; Saramago, B. Bovine Serum Albumin Conformational Changes upon Adsorption on Titania and on Hydroxyapatite and their Relation with Biomineralization. *J. Biomed. Mater. Res., Part A* **2004**, *70*, 420–427.
- (79) Yang, P.; Gao, F. *The Principle of Bioinorganic Chemistry*; Science Press: Beijing, 2002; p 349.
- (80) Berg, J. M.; Tymoczko, J. L.; Stryer, L. Protein Structure and Function. *Biochemistry*, 5th ed.; W. H. Freeman and Company: New York, 2002; pp 83–136.
- (81) Monti, S.; Manet, I.; Marconi, G. Combination of spectroscopic and computational methods to get an understanding of supramolecular chemistry of drugs: from simple host systems to biomolecules. *Phys. Chem. Chem. Phys.* **2011**, *13*, 20893–20905.
- (82) Carter, D. C.; Ho, J. X. Structure of Serum Albumin. *Adv. Protein Chem.* **1994**, *45*, 153–203.
- (83) Ulrich, K. H. Molecular aspects of ligand binding to serum albumin. *Pharmacol. Rev.* **1981**, *33*, 17–53.
- (84) Chaves, O. A.; da Silva, V. A.; Sant’Anna, C. M. R.; Ferreira, A. B. B.; Ribeiro, T. A. N.; de Carvalho, M. G.; Cesarin-Sobrinho, D.; Netto-Ferreira, J. C. Binding studies of lophirone B with bovine serum albumin (BSA): Combination of spectroscopic and molecular docking techniques. *J. Mol. Struct.* **2017**, *1128*, 606–611.
- (85) Teng, Y.; Zou, L.; Huang, M.; Zong, W. Characterization of the binding of 2-mercaptobenzimidazole to bovine serum albumin. *J. Mol. Recognit.* **2015**, *28*, 232–238.
- (86) Zhang, Y.; Li, Y.; Dong, L.; Li, J.; He, W.; Chen, X.; Hu, Z. Investigation of the interaction between naringin and human serum albumin. *J. Mol. Struct.* **2008**, *875*, 1–8.
- (87) Sahoo, D.; Bhattacharya, P.; Chakravorti, S. Reverse Micelle Induced Flipping of Binding Site and Efficiency of Albumin Protein with an Ionic Styryl Dye. *J. Phys. Chem. B* **2010**, *114*, 10442–10450.
- (88) Subeesh, M. S.; Shanmugasundaram, K.; Sunesh, C. D.; Won, Y. S.; Choe, Y. Utilization of a phenanthroimidazole based fluorophore in light-emitting electrochemical cells. *J. Mater. Chem. C* **2015**, *3*, 4683–4687.
- (89) Anand, U.; Jash, C.; Mukherjee, S. Spectroscopic Probing of the Microenvironment in a Protein-Surfactant Assembly. *J. Phys. Chem. B* **2010**, *114*, 15839–15845.